Calc–silicate xenolith – magma interactions in the Rustenburg Layered Suite, Bushveld Complex

Bavisha Koovarjee

UNIVERSITY OF THE
WITWATERSRAND,
JOHANNESBURG

A thesis submitted to the Faculty of Science, University of the Witwatersrand, Johannesburg, in fulfilment of the requirements for the degree of Doctor of Philosophy

Johannesburg, 2022

DECLARATION

I declare that this thesis is my own, unaided work. It is being submitted for the Degree of Doctor of Philosophy at the University of the Witwatersrand, Johannesburg. It has not been submitted for any degree or examination at any other University.

(Signature of candidate)

03rd day of February 2022 at Rondebosch, Cape Town

ABSTRACT

The mafic-ultramafic Rustenburg Layered Suite (RLS) of the 2.05 Ga Bushveld Complex hosts xenoliths ranging in size from a few centimetres to tens of kilometres and comprising a variety of rock types derived principally from the chemical and clastic sedimentary rocks of the Transvaal Supergroup. This study investigates a rare case of a calc-silicate xenolith from an underground exposure at Rowland Shaft, Lonmin Platinum, near Marikana in the Western Limb, and drillcores through xenoliths in the Platreef in the Northern Limb on Zwartfontein Farm with the specific aim of investigating interactions between the xenoliths and RLS magma. In the Marikana xenolith, Perple_X modelling of the peak assemblage of monticellite + forsterite + spinel indicates T_{max} conditions between 975 and 1125 °C at P between 0.6–1.6 kbar and X_{CO_2} ~1. Centimetre-thick forsterite- and spinel-rich layers on the western edge of the xenolith are interpreted primarily as relict sedimentary layering; however, a vesuvianite-rich rim is interpreted as the product of hydrous retrograde fluid infiltration ($X_{CO_2} < 0.1$) at T ~400–700 °C. The xenolith is hosted in mottled anorthosite of the Upper Critical Zone but is flanked by an ~25 cm wide contact zone that contains several small (<10 cm) calc-silicate fragments displaying the same peak assemblage as the main xenolith. These fragments are also surrounded by vesuvianite and/or vesuvianite + grossular symplectites. The matrix of the contact zone comprises almost pure anorthite plagioclase (An_{99}) and Ca-Tschermak clinopyroxene with wollastonite exsolution lamellae. The plagioclase and pyroxene display a pseudo-ophitic texture, which is partially replaced by thin grossular coronas. Also present in the matrix are discrete grains of poikilitic uvarovitic garnet cored by chromite grains. In addition to the calc-silicate fragments, the contact zone contains several irregular-elongate garnet masses and a clast comprising 3 disrupted cm-scale chromitite stringers. EPM and LA-ICP-MS analysis of the "chromite" grains shows zoning from Cr-rich cores to rims characterised by Al and Fe^{3+} that resemble the spinels within the calc-silicate xenolith, suggesting increased hybridisation of the magmatic system during their growth. Cr-rich garnet similarly shows core to rim zonation from uvarovitic and grossularitic compositions. When combined with the unusually calcic plagioclase and the Ca-Al-Fe^{3+} clinopyroxene, these features are consistent with crystallisation of a hybrid magma that became increasingly contaminated by a xenolith component, with concomitant

increase in oxygen fugacity. Bulk-rock XRF, micro-XRF and stable isotope data confirm that length-scales of chemical interaction ranged from cm to dm scale and may have varied, depending on specific elements. Overall, however, decarbonation of the xenolith resulted in a Mg-silicate-rich restite and produced the unusual calcic mineral compositions in the contact zone. The $\delta^{18}O$ values of 7.62‰–12.67‰ and 8.63‰–9.8‰ for the plagioclase and pyroxene, respectively, in the contact zone contrast with those in the mottled anorthosite (6.42–6.62‰ and 5.81‰). The unusual location of the 7 cm thick chromitite stringer in the contact zone is interpreted as disruption and entrainment of a portion of the UG1 chromitite layer, which lies 20 m stratigraphically above the xenolith, as the xenolith sank through the partially crystalline magma as a result of decarbonation-driven density increase. Migration/displacement of the xenolith is supported by the steep dip and near-orthogonal strike of bedding in the xenolith relative to the RLS layering.

Although peak monticellite + forsterite + diopside + spinel assemblages are preserved locally, calc-silicate xenoliths in the Platreef in the Northern Limb of the Bushveld Complex show strong retrograde re-equilibration, dominated by serpentine. While the intercalated Platreef is characterised by abundant parapyroxenite, which is interpreted as the product of crystallisation/metasomatism of hybrid magma and metasediment, the extreme calcic plagioclase and clinopyroxene compositions seen at Marikana are absent. However, stable isotopes show elevated $\delta^{18}O$ values that agree with previous studies from the Northern Limb. Unlike at Marikana, the close proximity of the footwall sediments of the Transvaal Supergroup to the xenoliths suggests that discrete xenolith-magma interactions were overwhelmed by carbonates that have been completely digested by magma and voluminous fluids derived from prograde metamorphism of the Transvaal Supergroup footwall in the vicinity of the Zwartfontein cores.

ACKNOWLEDGEMENTS

First and most importantly, I would like to express my sincerest gratitude to Prof. Roger Gibson. Your continued guidance and support were invaluable. Thank you for your patience and all conversations we had over the years. You were my true inspiration in completing this project. My appreciation goes out to Prof. Paul Nex for his constant assistance, advice and for sparking my interest in this topic since I was an undergraduate. Thank you both for taking me on as a Ph.D. candidate and supervising this project. It was a privilege and honour to gain insight from your exceptional scientific knowledge throughout my studies.

This project would not be possible without the financial support I received from the Department of Science and Innovation-National Research Foundation (DSI-NRF), the Centre of Excellence for Integrated Mineral and Energy Resource Analysis (DSI-NRF CIMERA), and the Postgraduate Merit Awards (PGMA) from the University of the Witwatersrand.

I would like to thank Lonmin Platinum and Dennis Hoffman for providing access to samples. Managing geologist at Rowland Shaft in Marikana, Pieter van Zyl, is thanked for accommodating an underground mine visit and senior geologist, Godfrey Ndou, is thanked for providing access to the Akanani core yard in Mokopane and for his assistance with sampling.

A special appreciation goes to Prof. Chris Harris and friend Sherissa Roopnarain at the University of Cape Town for giving me the enriching opportunity to learn about oxygen isotopes and so much more over such a short period of time. Thanks to Dr. Peter Horvath for his advice and assistance with Electron Microprobe analysis and X-ray element mapping. Dr. Deon van Niekerk and Rhodes University are thanked for access to the Electron Microprobe. The microprobe was partially funded by NRF National Equipment Program grant (UID 74464). Thank you to Deshentree Chetty at Mintek for conducting micro-XRF analysis.

I would like to acknowledge and extend my gratitude to the numerous staff members at the School of Geosciences, University of the Witwatersrand for their assistance with sample

preparation, analysis, advice and encouragement. Special thanks go to: Mr. Caiphas Majola and Mr. Sam Tshabalala for preparing polished thin-sections, Mr. Marumo Ntsoane for his help with crushing and milling, Mr. Thomas Stapley, Dr. Sarah Gylnn and Dr. Grant Bybee for their advice on mineral separation, Dr. Alan Wilson and Mr. Marlin Patchappa for XRF analysis, Prof. Glen Nwaila, Dr. Peter Horvath and Ms. Nonkuselo Madlakana for advice on using Perple_X thermodynamic calculation software, and Prof. Robert Bolhar for assistance with LA-ICP-MS. Dr. Asinine Tshibubudze, Prof. Tamiru Abiye and Prof. Rais Latypov are thanked for their support and encouragement. I would like to extend a special thanks to Prof. Gill Drennan for her support and encouragement.

So many people have played an important role in helping me achieve this goal. Specifically, I would like to thank my parents and extended family for their constant love and unrelenting support. Thank you to my close friends for your motivation and always keeping up with me. To my dear friends in the Earth Lab thank you for the interesting conversations, 'office rules', coffee breaks and late nights. Most importantly thank you for going on this journey with me.

CONTENTS

LIST OF FIGURES

LIST OF TABLES

CHAPTER 1: INTRODUCTION

1.1 Introduction

The Bushveld Complex (BC) in South Africa is home to world's largest layered mafic intrusion, the Rustenburg Layered Suite (RLS) which is one of largest resources of platinum group elements (PGE), Cr and V. For this reason, the BC together with the RLS has been subject to intense research over the past three decades. Despite the vast body of research there is no concensus on the effects that crustal contamination may have had on the RLS magma and localised ore mineralisation, if any (Cawthorn and Walraven, 1998; Cawthorn, 1999; Zeh *et al*., 2015). Calc-silicate xenoliths in the RLS are relatively rare, but their presence provides the opportunity to investigate the effects that calcareous rock may have on the igneous rock assemblage of the RLS during its emplacement. The vast majority of calc-silicate xenoliths in the RLS are found in Northern Limb where a portion of the footwall to the RLS is dolomite; relatively fewer occurences are recorded in the Eastern Limb, with only one being recorded in the Western Limb. The newly-discovered calc-silicate xenolith located in the Western Limb that is the primary focus of this study is compared with xenoliths in the Northern Limb. Prior studies conducted on xenoliths located in the Eastern Limb have focussed primarily on the metamorphic mineral assemblages and their usefulness in determining pressure and temperature conditions (REFS). With the exception of Willemse and Bensch (1964), no work has been done on (1) the physical and chemical interaction between the xenoliths and the RLS magma, during which potential exists for the decarbonating calc-silicate xenolith to contaminate the enclosing magma and (2) the implications that xenolith-magma interactions have for chromite-spinel chemistry. Koovarjee (2015) studied the first recorded calc-silicate xenolith in the Western Limb and demonstrated that some chemical interaction between the the xenolith and magma occurred. Sharman-Harris *et al*. (2005) studied the interaction between the Platreef and its calc-silicate footwall in the Northern Limb, and the possible influence on PGE-mineralisation.

In order to the distinguish the different types of interactions of magmas which readily interact with their surroundings, which can be solid wall-rocks or other magmas, Heinonen *et al*. (2021)

attempted to more rigorously define the terms used to describe the different types of interactions. This was done because some previous definitions are unclear and create confusion; for example, Heinonen *et al*. (2021) highlighted that Gary *et al*. (1972; p. 42) described *assimilation* as: 'The process of incorporating solid or fluid foreign material, that is, wall-rock, into magma. Such a magma, or the rock it produces may be called a *hybrid* or *anomalous*', but that Neuendorf *et al*. (2005; p. 40) stated that assimilation is: 'The incorporation and digestion of xenoliths and their chemical constituents into a body of magma. Such a magma, or the rock it produces, may be called *hybrid* or *contaminated*.' Thus, Heinonen *et al*. (2020) proposed clarification on the terms used to describe magma interaction with its surroundings as follows: (1) *hybridisation* is the complete chemical mixing of two melts; (2) *mingling* indicates physical mixing of melts that remain chemically separated; (3) *assimilation* is the complete mixing of a melt and an initially solid wall-rock, and (4) *stoping* occurs when the melt and wall-rock block remain chemically separated. All of the above terms are considered mixtures, where hybridisation and assimilation result in homogeneous products, and mingling and stoping result in heterogeneous products (Heinonen *et al*., 2021).

In order to investigate xenolith-magma interactions in the RLS, this project combines petrography, electron-microprobe analysis, stable isotope analysis and laser ablation inductively coupled plasma mass spectrometry (LA-ICP-MS). Spatially controlled sampling was done to fully analyse and interpret the implications of the interaction/contamination between the xenoliths and magma. Petrography and electron-microprobe analysis was used to (1) identify prograde and retrograde mineral assemblages and constrain pressure and temperature (*P-T*) conditions; (2) determine mineral chemistry; (3) establish the paragenetic sequence, and (4) identify any evidence of chemical interaction/contamination between the xenolith and RLS magma. Stable isotope studies were used to track the extent of contamination of the RLS magma by the xenolithic material. LA-ICP-MS was used to analyse trace elements in spinel grains in order to determine their origin in different parts of the xenolith-magma system.

1.2 Regional geology

1.2.1 The Transvaal Supergroup

The Transvaal Supergroup is a late Archean to Paleoproterozoic (2.67-2.07 Ga) package of sedimentary rocks and minor volcanics distributed over a large portion of the northern and western parts of the Kaapvaal Craton (Eriksson *et al*., 2001) (Figure 1.1). It consists of the protobasinal Wolkberg, Chuniespoort and Pretoria Groups (Eriksson and Reczko, 1995; Eriksson *et al*., 2001) (Figure 1.2). The sequence of rocks was deposited in the Transvaal and Griqualand basins, which are separated by the Vryburg Rise. It reaches a maximum thickness of 12 km in the Transvaal Basin (Eriksson *et al*., 2001). The sediments were deposited on the Kaapvaal craton after the deposition and lithification of the 3.0–2.7 Ga Witwatersrand and Ventersdorp Supergroups, although the lowermost portion of the Transvaal Supergroup may have been deposited concurrently with the 2.7 Ga Ventersdorp Supergroup (Catuneanu and Eriksson, 1999; Alexandre *et al*., 2006).

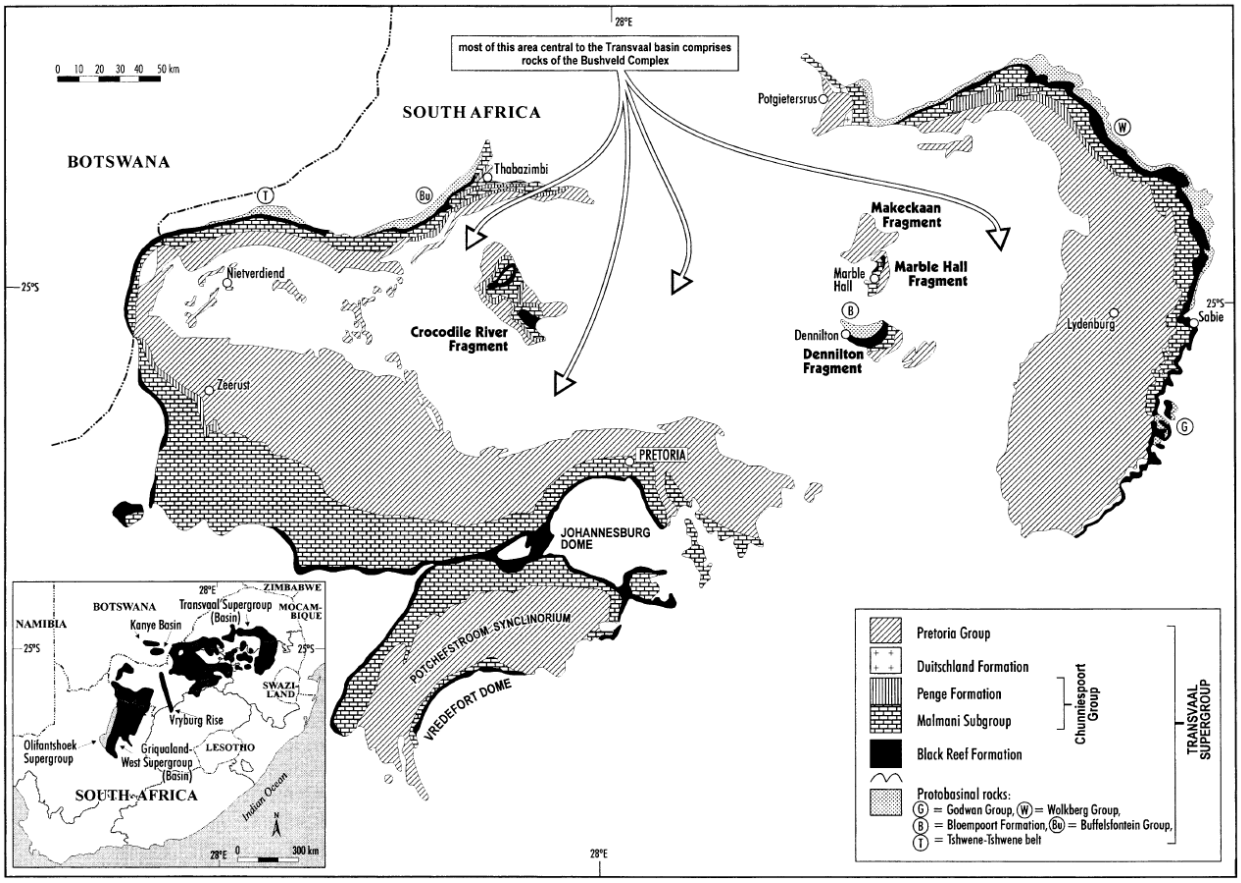

Figure 1.1: Geological map of the Transvaal Supergroup highlighting the Transvaal Basin rocks, including the Protobasinal rocks, the Black Reef Formation, Chuniespoort and Pretoria Groups (Eriksson *et al*., 2001).

The Wolkberg Group conglomerates and sandstones, as well as volcanic rocks of basaltic, andesitic and acidic compositions, form the base of the Transvaal Supergroup (Catuneanu and Eriksson, 1999; Eriksson *et al*., 2001). Unconformably overlying the Wolkberg Group is the Black Reef Formation, composed of quartzite and conglomerate, succeeded by the Chuniespoort Group, composed mainly of dolomite, chert, limestone, carbonaceous shale and quartzite of the Malmani Subgroup (Catuneanu and Eriksson, 1999; Eriksson *et al*., 2001). The Chuniespoort Group is conformably overlain by banded ironstones of the Penge Formation, followed by the Duitschland Formation, composed mainly of dolomitic shale, dolomite and quartzite (Catuneanu and Eriksson, 1999). The succeeding Pretoria Group comprises 14 formations and is composed of shales, quartz arenites, subordinate carbonates, and volcanic rocks (Catuneanu

and Eriksson, 1999; Kinnaird, 2005). The lower nine formations are preserved throughout the basin. The upper five formations have been affected by post-sedimentation erosion and have been truncated by the Bushveld Complex intrusion (Catuneanu and Eriksson, 1999; Eriksson *et al*., 2001). The Transvaal Supergroup contains several potential sources of calc-silicate rock, including the Malmani Subgroup, the Duitschland Formation and discrete units in the predominantly siliciclastic Pretoria Group (Catuneanu and Eriksson, 1999; Eriksson *et al*., 2001). It is generally asumed that calc-silicate xenoliths within the Bushveld Complex originate from the Transvaal Supergroup (Willemse and Bench, 1964; Wallmach *et al*., 1989; Kinnaird *et al*., 2002; Harris and Chaumba, 2001) as fragments of the original sediment were dislodged and emplaced within the intruding magma (Daly, 1928; Hartzer 1995). Magma of the Bushveld Complex intruded into ~11 km of the Transvaal Supergroup stratigraphy (Eriksson *et a*l., 1995) and is predominantly located within the Transvaal Supergroup, with the Pretoria Group generally forming the floor rocks, except in the Northern Limb (Eriksson and Reczko, 1995; Eriksson *et al*., 1995).

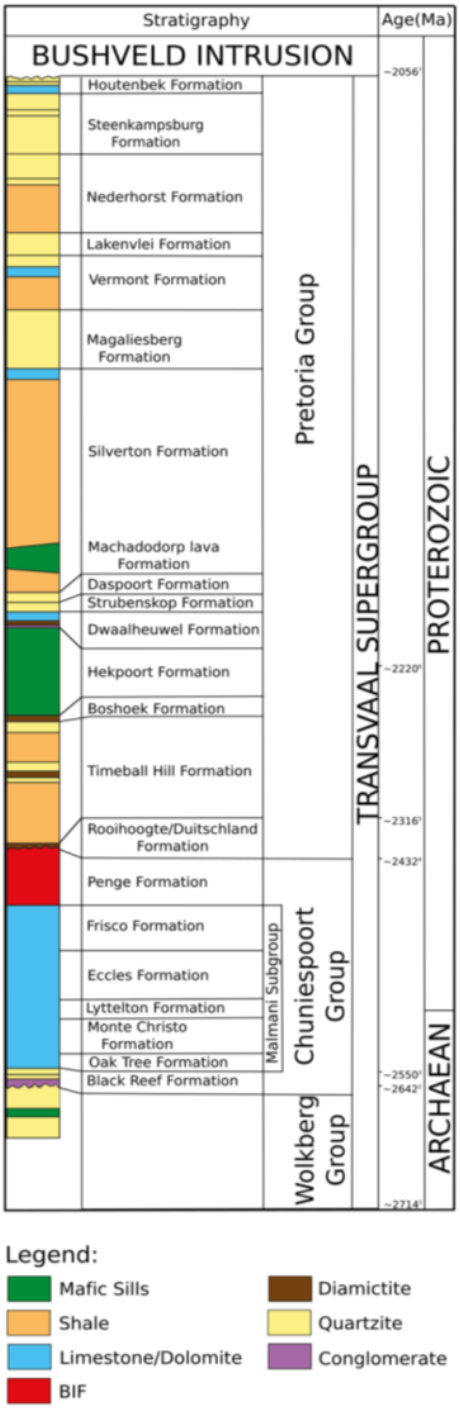

Figure 1.2: Stratigraphic column through the Transvaal Supergroup showing regions from which calc-silicate xenoliths may have originated (blue) (adapted from Catuneanu and Eriksson, 1999; Sharman-Harris *et al.*, 2005).

1.2.2 The Bushveld Complex

The 2055.91 ± 0.26 Ma (Zeh *et al*., 2015) Bushveld Complex was emplaced into the Kaapvaal craton and is located in the north-east of South Africa (Cawthorn and Walraven, 1998; Cawthorn, 1999; Zeh *et al*., 2015). The Complex encompasses a sequence of four compositionally variable ultramafic to felsic lithological units that include the intrusive ultramafic to mafic Rustenburg Layered Suite (RLS) and Rashoop Granophyre Suite, and the felsic extrusive Rooiberg Group and Lebowa Granite Suite (Walraven *et al*., 1990; Schweizter *et al*., 1997). The Bushveld Complex crops out as four lobes or limbs (Northern, Eastern, Far Western and Western), with a further limb (South-eastern or Bethal Limb) unexposed (Figure 1.3). All the limbs dip inwards towards the centre of the Complex, giving it an elongate-basin shape (Eales and Cawthorn, 1996; Kinnaird *et al*., 2002). The RLS intrudes the Chuniespoort and Pretoria Groups of the Transvaal Supergroup (Cawthorn *et al*., 2002; Kinnaird *et al*., 2002) and therefore, the footwall lithologies of the Bushveld Complex include various sedimentary rock-types, with the exception of a section in the Northern Limb that has a footwall of granitic gneiss (Eales and Cawthorn, 1996).

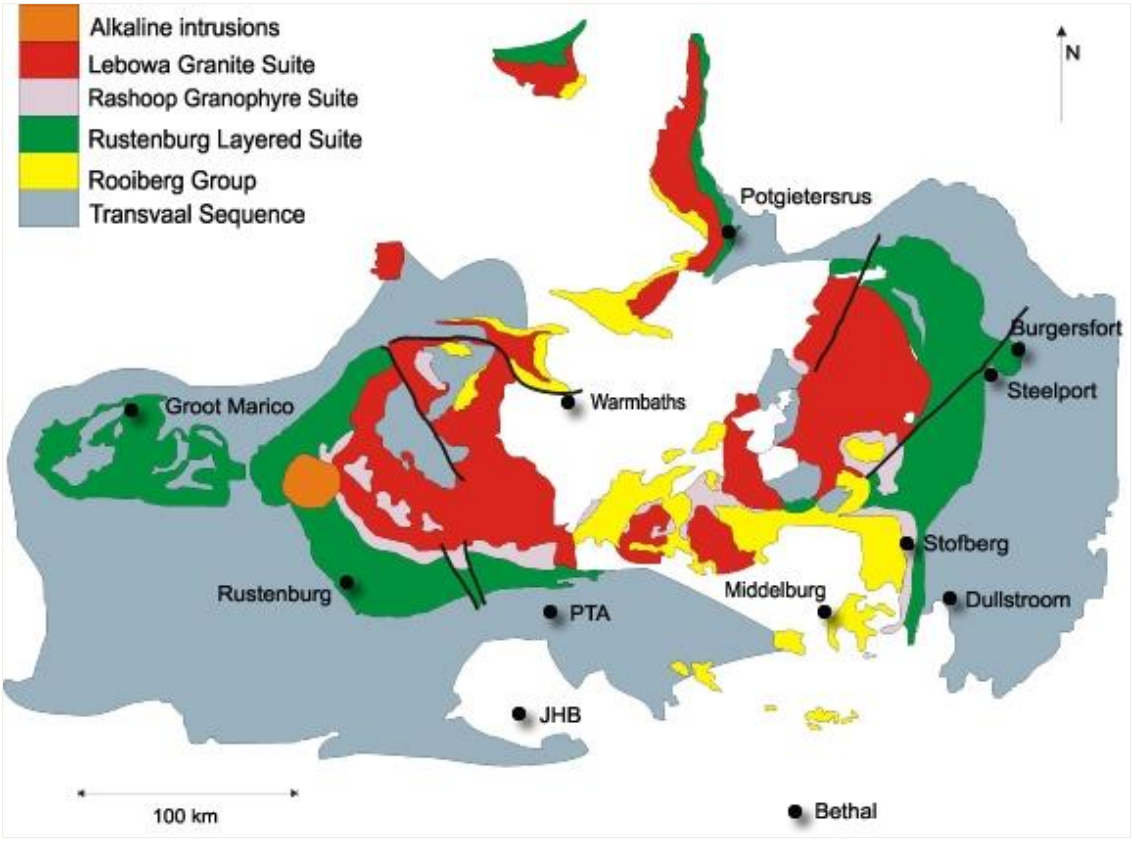

Figure 1.3: Geological map showing the simplified geological components of the Bushveld Igneous Complex (Kinnaird, 2005).

1.2.3 The Rustenburg Layered Suite (RLS)

The RLS is the world's largest layered ultramafic to mafic intrusion, with a maximum thickness of 7–9 km, covering an area >90 000 km^2 (Finn *et al*., 2015) and an estimated volume of 370 000 – 700 000 km^3 (Cawthorn and Walraven 1998; Zeh *et al*., 2015). It is thought to have formed by numerous injections of magma into a single chamber, which resulted in comprehensive layering of the rocks (Eales and Cawthorn, 1996; Kinnaird *et al*., 2005). The RLS is largely divided into five zones, namely, the Marginal (MaZ), Lower (LZ), Critical (CZ), Main (MZ) and Upper (UZ) zones (Figure 1.4), underlain by the Basal Ultramafic Sequence (BUS) however, not all zones are found in all limbs (Eales and Cawthorn, 1996; Kinnaird *et al*., 2002; Wilson, 2015).

1.2.3.1 The Western and Eastern Limbs of the RLS

The ≥ 750 m thick BUS identified at the base of the RLS in the Eastern Limb comprises numerous layers of Mg-rich pyroxenites, harzburgites and dunites (Wilson, 2015; Wilson et al., 2017). The unlayered, heterogeneous noritic MaZ (≤ 800 m thick) is composed of multi-intrusive generations of noritic rock (Eales and Cawthorn, 1996; Cawthorn and Walraven 1998). The overlying LZ is composed of pyroxenite and harzburgite, attaining a maximum thickness of ~1584 m in the Olifants River trough in the Eastern Limb. The CZ (1300–1800 m thick) contains the world's largest platinum group elements (PGEs) and chromite deposits. PGEs are hosted by the Merensky Reef and the Upper Group 2 (UG2) chromitite. Large reserves of chromite occur in the chromitite layers of the Lower (LG), Middle (MG) and Upper (UG) Groups (Eales and Cawthorn, 1996).

The Critical Zone is subdivided into upper and lower zones: the lower Critical Zone (LCZ) is composed of orthopyroxenite cumulates. The upper Critical Zone (UCZ) comprises chromitite, harzburgite and pyroxenite at the base, through norite to anorthosite (Kinnaird *et al*., 2002). The transition between the two sub-zones is characterised by two chromitite layers at the base of the lowermost layer of anorthosite (Eales and Cawthorn, 1996; Kinnaird *et al*., 2002). The Merensky Reef forms at the base of the MZ (3000–3400 m), which comprises mainly norite and gabbronorite and lacks olivine, chromite-spinel, fine-scale layering and lithological variation that are seen in the underlying zones. Mottled anorthosite occurs within two narrow intervals, and pyroxenites are rare (Eales and Cawthorn, 1996; Barnes and Maier, 2002). The first occurrence of magnetite marks the boundary between the MZ and the UZ. The UZ (~2000 m thick) is composed of anorthosite, troctolite, ferrogabbro and diorite, with multiple magnetitite layers (Eales and Cawthorn, 1996; Kinnaird *et al*., 2002; Campbell, 2011).

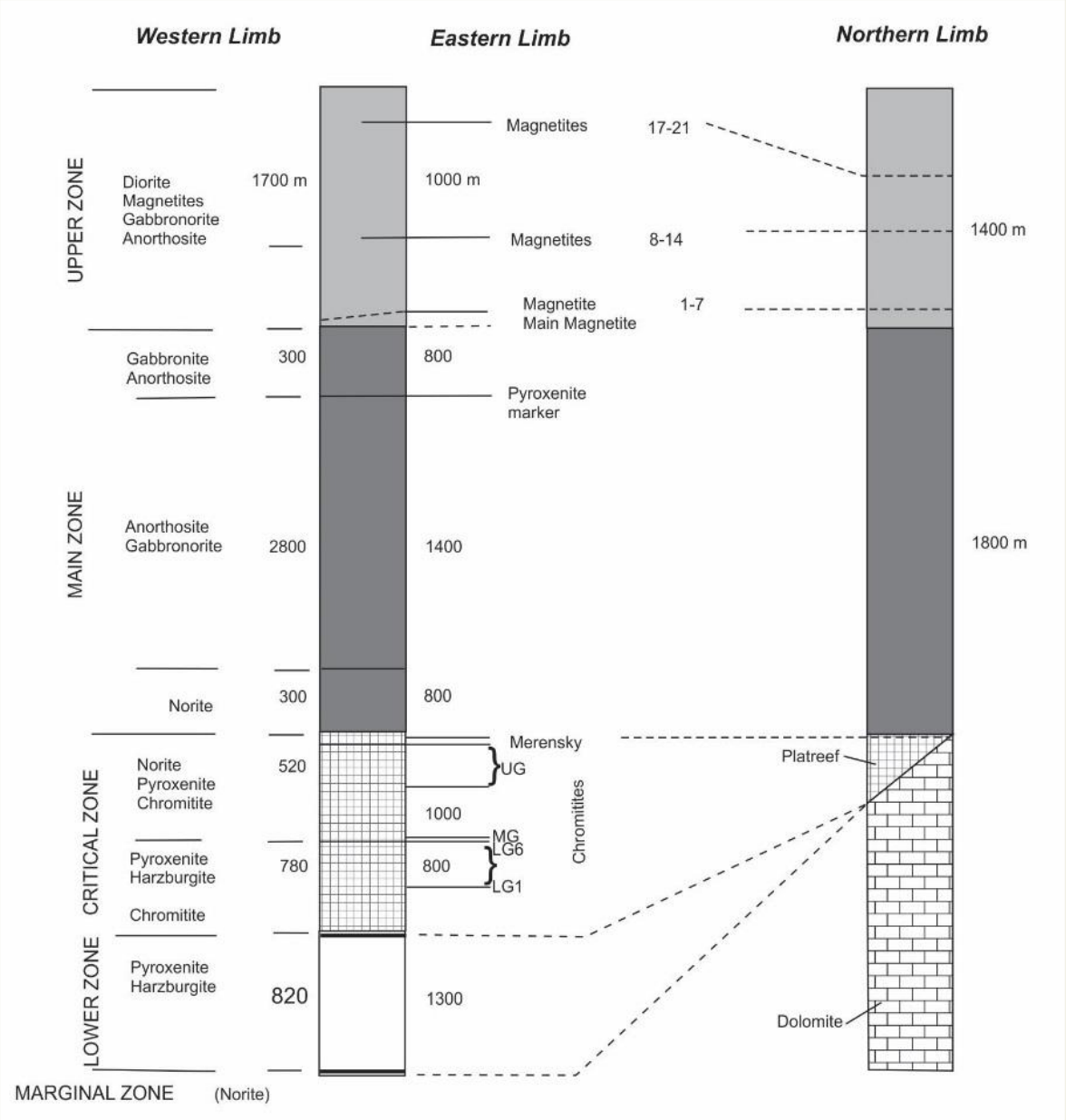

Figure 1.4: Simplified stratigraphy of the Rustenburg Layered Suite showing the main geological zones and significant layers, together with the thicknesses of each zone for the Eastern, Western and Northern limbs. The Western and Eastern limbs have an approximate thickness of 7200 m and 8100 m, respectively (reproduced from Cawthorn and Lee, 1998).

1.2.3.2 The Northern Limb of the RLS

The Northern Limb (Figure 1.5) extends northwards from immediately south of Mokopane (formerly Potgietersrus) for 110 km (Figure 1.3) (Van der Merwe, 1976; Armitage, 2002; Sharman-Harris *et al*., 2005). The Northern Limb is divided from the bulk of the RLS (Western and Eastern limbs) by the Zebedielia Fault of the Thabazimbi-Murchison Lineament (Good and de Wit, 1997), and shows numerous significant differences from the other limbs.

The MaZ is composed of norite, but is very poorly developed (Sharman-Harris *et al.*, 2005; Kinnaird *et al*., 2005). According to Van der Merwe (1978) the thickness of norite and dolerite is variable (ranging from a few centimetres to tens of metres). Xenoliths of variable compositions, including carbonate rocks, are found in the MaZ (Van der Merwe, 1978). South of Mokopane the LZ is best developed, with a maximum thickness of ~1600 m (Hulbert and von Gruenewaldt, 1985). Further north in the Southern and Central domains, the LZ occurs as satellite bodies. It is composed of harzburgites, orthopyroxenite cumulates, olivine-orthopyroxenite and a few chromitite layers (Van der Merwe, 1976; Sharman-Harris *et al.*, 2005). The CZ is not as well developed in the Northern Limb compared to the rest of the RLS (Gain and Mostert, 1982; Harris and Chaumba, 2001). Numerous authors (Wagner, 1929; White, 1994; Hulbert, 1983) consider the UG2 chromitite and the Merensky Reef, occurring in the Western and Eastern limbs, equivalent to the Grasvalley norite-pyroxenite-anorthosite (GNPA) chromitite layer and Platreef, respectively. According to MacDonald *et al.* (2005), the GNPA and Platreef may have formed from a separate magma and not from the same magma that produced the CZ in the Western and Eastern limbs. Studies by Yudovskaya and Kinnaird (2010) suggest that the Northern Limb formed independently (of the rest of the RLS) and was fed from a separate sub-chamber during emplacement of the CZ.

The Platreef forms the base of the CZ and is composed of medium-to coarse-grained pyroxenite and minor amounts of norite, which host xenoliths of variable composition (Lee, 1996; Harris and Chaumba, 2001). It has a maximum thickness of ~400 m in the south; in the north, it ranges from a few metres to 30 m (Armitage *et al*., 2002; Kinnaird *et al*., 2005). The Platreef is

sporadically mineralised with PGEs, Ni and Cu, which occur between the footwall and MZ. Variation in lithological composition is due to magmatic interaction with the footwall, and variation in thickness can be attributed to the structure of the footwall (Buchanan *et al*., 1982; Nex, 2005).

Overlying the Platreef is the MZ (~2200 m) which is composed of gabbro, anorthosite, pyroxenite and troctolite (van der Merwe, 1987). The MZ in the Northern, Western and Eastern limbs is similar. The ~1100 m thick UZ is composed of magnetitite, gabbro and anorthosite. The UZ in the Northern Limb is similar to the UZ in the Western and Eastern limbs (Van der Merwe, 1987; Ashwal *et al*., 2005).

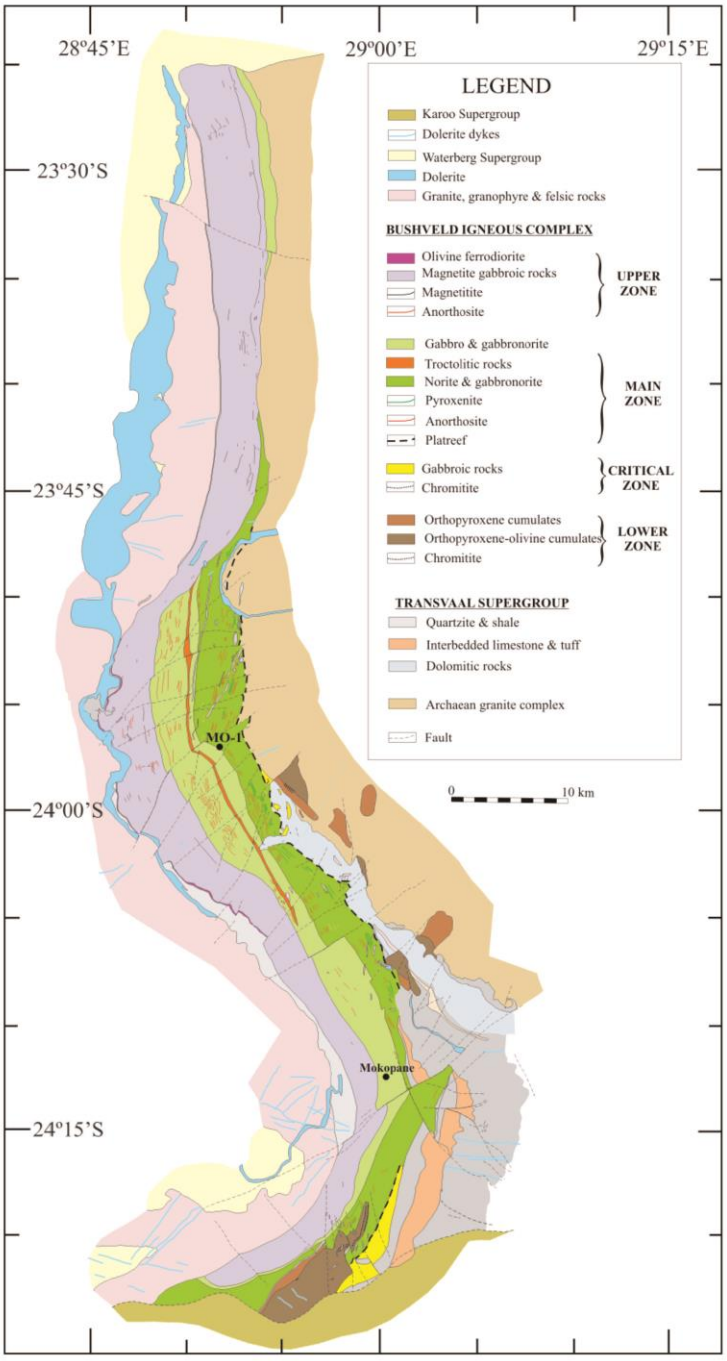

Figure 1.5: Geological map of the exposed Northern Limb of the Bushveld Complex and its footwall comprising the Transvaal Supergroup sedimentary rocks and Archean Basement Complex granitoids (Van der Merwe, 1978; Ashwal *et al*., 2005).

1.3 Previous work

1.3.1 Carbonates in the Transvaal Supergroup

The oldest and most extensive sequence of dolomites and subordinate limestones in the Transvaal Supergroup is found in the Malmani Subgroup of the Chuniespoort Group. Exposures of these lithologies surround the Bushveld Complex (Figure 1.1). The Chuniespoort Group has a maximum thickness of 1200 m and is subdivided into five formations; the basal Oaktree, Monte Cristo, Lyttelton, Eccles and uppermost Frisco Formations (Button, 1973; Eriksson and Altermann, 2008; Catuneanu and Eriksson, 1999) (Figure 1.2). Each formation is characterised by the variability of its chert content, type of stromatolites, as well as the accompanying interbedded lithologies, including carbonaceous mudstone, shales, and quartzites.

The Duitschland Formation, which outcrops in the Mokopane area, has a maximum thickness of 1100 m and is composed of dolomitic mudstones interbedded with dolomite and/or quartzite and chert breccias (Eriksson and Reczko, 1995; Catuneanu and Eriksson, 1999). The top of the formation is characterised by dolomite containing bornite and chalcopyrite (Sharman-Harris, 2006). It is suggested that fine, muddy and calcareous material was eroded from the Malmani dolomites and deposited into a continental basin to form the Duitschland Formation (Eriksson and Reczko, 1995; Catuneanu and Eriksson, 1999).

The deposition of the Duitschland Formation was followed by an ~80 million-year gap in sedimentation (Eriksson and Reczko, 1995). The succeeding Pretoria Group contains several dolomitic horizons; however, none are as extensively developed as the Malmani dolomites. In the Rooihoogte, Magaliesberg and upper five formations of the Pretoria Group, lenses of stromatolitic dolomite/carbonate occur. The Silverton Formation hosts a $\leq$ 100 m thick layer of marble within the uppermost shale, and dolomitic lenses are found in carbonaceous mudstones (Button, 1973; Eriksson and Clendenin, 1990; Eriksson *et al*., 1995).

1.3.2 Calc-silicate xenoliths in the RLS

Calc-silicate xenoliths are relatively rare in the RLS, having been reported in the Eastern Limb (Upper, Critical and Marginal Zones) and Northern Limb (Marginal and Lower Zones and the Platreef) (Willemse and Bensch, 1964; Gain and Mostert, 1982) more commonly than the Western Limb. They almost certainly originate from carbonates in the Transvaal Supergroup (Wallmach *et al*., 1989; Wallmach *et al*., 1995). According to Wallmach *et al.* (1989), the xenoliths are generally elliptical or wedge-shaped and are typically small, usually less than several hundred m^3. The xenoliths show mineralogical evidence of prograde dehydration and decarbonation, and partial retrograde hydration (Wallmach *et al*., 1989; Wallmach *et al*., 1995; Buick *et al*., 2000). They host several uncommon minerals, such as kalsilite ($KAlSiO_4$), owing to the extreme temperatures achieved (Willemse and Bensch, 1964), and cuspidine ($Ca_4Si_2O_7(OH,F)_2$), foshagite ($Ca_4Si_3O_9(OH)_2$) and hillebrandite ($Ca_2SiO_3(OH)_2$), which formed during retrograde metamorphism (Buick *et al.*, 2000).

1.3.2.1 Eastern Limb

Willemse and Bensch (1964) undertook one of the first and most extensive studies on calc-silicate xenoliths in the Bushveld Complex, and it is the only previous study that considers xenolith-magma interactions. Prior research had consisted simply of reference to metamorphic, carbonate-rich, inclusions. Willemse and Bensch (1964) focused on ten localities where the calc-silicate xenoliths occur in the Marginal and Upper Zones and identified metamorphic minerals that included akermanite, monticellite, olivine, wollastonite, calcite, spinel, garnet, vesuvianite and clinopyroxene. However, they concluded that four dominant mineral constituents exist in the xenolith cores, namely, 1) monticellite-akermanite, 2) clinopyroxene, 3) olivine, and 4) vesuvianite, and noted that different localities are dominated by (but not limited to) one of the four constituents.

According to Willemse and Bensch (1964) the monticellite-akermanite dominant xenoliths (found at Localities C, E, F, G, I and J of their study) comprise alternating bands of the aforementioned minerals interlayered with clinopyroxene. The clinopyroxene is Al- and Ca-rich

and has a high Fe^{3+}/Fe^{2+} ratio, and was named 'fassaite' by Willemse and Bensch (1964). (It should be noted that 'fassaite' is considered obsolete by Morimoto *et al*. (1988)). The xenolith contact with igneous rock is characterised by dark green monomineralic clinopyroxene (diopsidic in composition) and in some cases garnet is present for ≤ 5 cm from the contact of the igneous rock. Plagioclase is most commonly observed near the xenolith-igneous rock contact and has a composition of An_{75}. In some places (e.g., their Locality F), Willemse and Bensch (1964) noted that fragments of xenoliths were peeled off at the xenolith-magma contact, subsequently incorporated into the magma and even completely digested by the magma. Wollastonite appears to be the product of smaller xenolithic fragments being completely digested by the surrounding magma in some localities. This mineral is almost never present in the main xenolithic body and is most commonly observed in contact zones. In other cases (Localities E and G) cm-scale *lit-par-lit* injection of norite occurs into fragments of peeled-off calc-silicate rock. At Localities C and E, the igneous rock up to 3 mm from the contact with the xenolith comprises plagioclase (An_{80}) and interstitial diopside (this rock is considered gabbroic in composition). Beyond the aforementioned 3 mm thick band the igneous assemblage comprises clinopyroxene, orthopyroxene and plagioclase ($An_{50–55}$). According to Willemse and Bensch (1964), the igneous rock on the contact with the xenolith is commonly richer in Ca and Mg compared to igneous rock further away. The authors also noted that there is no definite evidence to indicate what happened to unsaturated minerals such as monticellite, akermanite, olivine or spinel on the xenolith-magma contact. However, they suggested that these minerals were replaced by orthopyroxene, clinopyroxene or wollastonite, depending on the Ca-content of the precursor minerals. In summary, the composition of the igneous rock on the contact with the xenoliths is affected by the xenolith; in several cases the immediate adjoining rock is gabbroic in composition for a few millimetres whereas the igneous rock further away is the more typical norite (Willemse and Bensch, 1964).

In one case (Locality A of Willemse and Bensch, (1964)), where a xenolith predominantly comprises olivine (high Mg content indicates olivine is forsterite-rich), a clear zonal distribution of mineral assemblages is observed relative to the contact with the gabbroic RLS magmatic

rock, as follows: (1) xenolith core (forsterite); (2) spinel zone; (3) spinel-clinopyroxene zone; (4); vesuvianite zone; (5) garnet-clinopyroxene zone, and (6) clinopyroxene-garnet zone (Willemse and Bensch, 1964). The spinel occurs as idioblastic grains and hosts magnetite lamellae. The clinopyroxenes are Al- and Ca-rich, have a high Fe^{3+}/Fe^{2+} ratio, and occur as massive, granular and fibrous grains. Vesuvianite occurs in two varieties, namely, massive pinkish-red and fibrous greenish-yellow, and the garnet is predominantly grossular–andradite-rich. Minor serpentine is found in the forsterite and spinel cracks in the xenolith core. Immediately adjacent to the clinopyroxene-garnet zone a 1.5 mm thick gabbro chill zone is observed. Plagioclase composition in the chill zone is $An_{75–80}$, whereas further away from the contact the plagioclase composition is $An_{52–60}$. Willemse and Bensch (1964) studied the chemical variation of major elements between the xenolith core and surrounding gabbro using Barth Standard Cells. The results showed that there is no major variation in Si between the zones. The vesuvianite and garnet-rich zones contain the highest concentration of Al. The maximum Fe concentration is observed in the outermost garnet-rich zone. The Ca concentration increases away from the xenolith core and Mg increases towards the xenolith core. According to Willemse and Bensch (1964), the forsterite-rich core and the associated zonation is a metamorphic artefact. The prograde heating of an impure dolomitic limestone results in dedolomitisation, which produced the forsterite-rich, spinel-bearing marble. The aforementioned authors noted that the presence of a gabbro chill zone indicates that the system is essentially a closed one that allows for only minor escape of fluid, thus creating a pressure gradient in an outward direction from the xenolith. Therefore, all fluids migrated away from the xenolith together with Ca (in the form of $CaCO_3$). Given that calcium carbonate is more soluble than magnesium silicate, a forsterite-rich, spinel-bearing core is left behind. Towards the margin of the xenolith Ca-, Mg- and Al-rich pyroxene formed to produce pyroxene-rich zones. Slightly away from the margin, minerals rich in Ca and poor in Mg form, while Al and Fe may have been introduced from a magmatic source and this is where the vesuvianite and garnet-rich zones were later produced. Based on the observations above Willemse and Bensch (1964) concluded that the zoned nature of the mineral assemblages surrounding the forsterite-rich xenolith core is produced as a result of outward migration of CO_2 and $CaCO_3$ during prograde metamorphism.

Two varieties of pyroxene-rich xenoliths were observed by Willemse and Bensch (1964). The first type (Locality D) comprises predominantly clinopyroxene (Al-, Fe^{3+}- and Ca-rich) at the core that it is surrounded by a vesuvianite zone followed by a garnet zone, which occurs adjacent to gabbronorite. The outermost (garnet) zone hosts plagioclase and clinopyroxene inclusions which may originate from the surrounding gabbronorite (and were subsequently encroached by garnet). Willemse and Bensch (1964) suggested that the zoned nature of this pyroxene-rich xenolith, together with the significant amounts of garnet and vesuvianite, indicate that the protolith was a carbonate rock. The second type of pyroxene-rich xenolith (Locality H) comprises diopside associated with vesuvianite, grossular-rich garnet and Ca-rich plagioclase ($An_{90–95}$). This xenolith is unique because it hosts chromite and uvarovitic garnet. The chromite occurs as individual grains in uvarovite, diopside and plagioclase, and as veinlets in diopside. Uvarovitic garnet occurs in zones with chromite that have undergone metamorphic or metasomatic processes and require the addition of CaO (Frankel, 1959). Willemse and Bensch (1964) noted uvarovitic garnet in the Marginal Zone, where it is intimately associated with chromite and preferentially concentrated at the contact between chromite and pyroxene. They also noted the presence of feldspar where uvarovitic garnet is less massive, and that the garnet commonly surrounds the chromite grains (Willemse and Bensch, 1964).

The vesuvianite-rich xenoliths (Locality B) generally display a zonal distribution of mineral assemblages relative to the contact with the magmatic rock (gabbro), as follows: (1) greenish-yellow vesuvianite zone; (2) milky-white spotted zone comprising turbid vesuvianite, fibrous clinopyroxene and garnet; (3) garnet zone; (4) vesuvianite-garnet zone, and (5) pyroxene diorite comprising clinopyroxene and plagioclase. The xenolith-igneous rock contact is marked by an increase in grain-size of the pyroxene diorite. Minerals in the vesuvianite-garnet zone are never in direct contact with the pyroxene diorite – fine-grained albite separates the two zones. Willemse and Bensch (1964) stated that zoning on the pyroxene diorite and xenolith contact and the distribution of the pyroxene diorite indicate that the rock is born out of the surrounding igneous rock, namely, gabbro and is not sedimentary in origin.

Willemse and Bensch (1964) identified two types of xenoliths. One indicates clear evidence of being sedimentary in origin (Localities B, C, D, E, F, G, I and J), while the others, rich in olivine (Locality A) and pyroxene (H), may have uncertain provenance. The xenoliths rich in olivine and pyroxene may represent highly altered carbonate rocks where migration of certain components took place. It is generally accepted that the xenoliths originate from the Transvaal Supergroup (Willemse and Bensch, 1964). Given that the composition of the xenoliths matches those of limestone from the aureole of the Bushveld Complex and the mineral association between garnet and vesuvianite, and the presence of Al-, Fe^{3+}- and Ca-rich clinopyroxene is characteristic of contact metamorphic environments of limestone according to Willemse and Bensch (1964).

According to Willemse and Bensch (1964), the xenoliths also show different degrees of alteration during prograde metamorphism, owing to their differences in size: smaller xenoliths probably underwent more complete alteration than larger xenoliths owing to their smaller volume. The pyroxene and olivine-rich xenoliths are comparatively smaller than the monticellite-akermanite xenoliths and the zonal distribution of minerals and/or mineral assemblages on the margins are typically observed in the smaller xenoliths. Smaller xenoliths may have broken off larger ones, in which case both xenoliths comprise the same carbonate rock type. However, the smaller xenolith would have been subjected to more intense metamorphic conditions, subsequently producing the zonation described above. Movement through the magma potentially destroyed the above described zonation in some cases. It is possible that xenoliths in the upper and lower parts of the RLS show mineralogical differences because the amount of volatiles in the magma differed. The researchers suggested that the lower parts of the RLS were volatile-deficient and could be considered as ‘dry’ (Willemse and Bensch, 1964), whereas the xenoliths in the upper parts of the RLS were in a ‘wetter’ magma (Willemse and Bensch, 1964; Wallmach *et al*., 1995).

Wallmach *et al.* (1989) suggested differences in mineral assemblages between calc-silicate xenoliths in the Marginal and Lower Critical Zones owing to the different peak pressure

conditions (Figure 1.6). The important mineral assemblages described in the Marginal Zone xenoliths are:

1) calcite – akermanite – monticellite
2) calcite – forsterite – monticellite
3) akermanite – diopside – monticellite
4) diopside – forsterite – monticellite,

while those in the lower Critical Zone xenoliths are:

5) calcite – periclase – monticellite
6) merwinite – akermanite – monticellite
7) forsterite – periclase – monticellite (Wallmach *et al*., 1989).

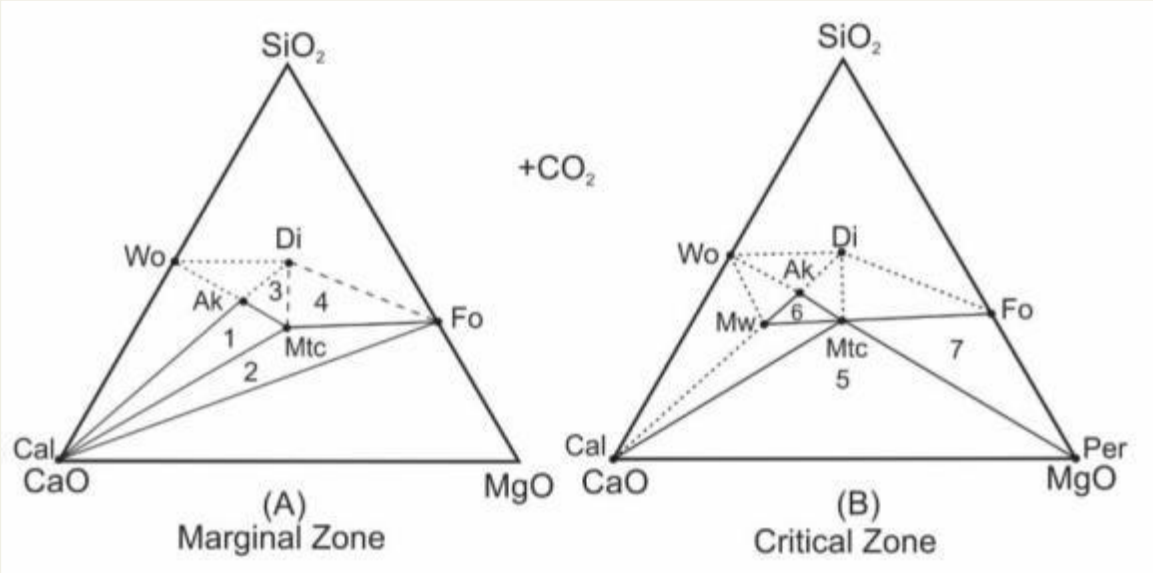

Figure 1.6: CaO – MgO – SiO_2 ternary plots illustrating mineral phases and assemblages in xenoliths located in the Marginal (a) and lower Critical (b) Zones from Wallmach *et al*. (1989). The solid and dashed lines connect minerals which coexist during prograde and retrograde metamorphism, respectively; minerals that do not coexist are connected by dotted lines. The numbers (1–7) refer to mineral assemblages listed above. Abbreviations: Cal = calcite, Wo = wollastonite, Di = diopside, Ak = akermanite, Mtc = monticellite, Mw = merwinite, Per = periclase and Fo = forsterite (Whitney and Evans, 2010).

Wallmach *et al.* (1995) found that monticellite and wollastonite in a xenolith from the Upper Zone were formed from akermanite under retrograde metamorphic temperatures of ~700 °C, and that vesuvianite formed from melilite, wollastonite, monticellite, and/or diopside between 400 and 600 °C. In the Critical and Marginal Zones, vesuvianite is rare, and melilite, monticellite and periclase are present. Wallmach *et al.* (1989; 1995) concluded that the Upper Zone magma was more volatile rich, which could be attributed to the variation in pervasive hydrous fluids that were present in the magma (Wallmach *et al*., 1995)

Estimated peak metamorphic constraints for the xenoliths range from 1100–1200 °C, <1.5 kbar in the Upper Zone (Wallmach *et al.,* 1995) to <1390 °C, <2.3 kbar in the Critical Zone, and <1390 °C, <3.1 kbar in the Marginal Zone (Wallmach *et al.,* 1989).

According to Buick *et al*. (2000) retrogression of xenoliths in the Marginal and Upper Zones produced cuspidine ($Ca_4Si_2O_7(OH,F)_2$), foshagite ($Ca_4Si_3O_9(OH)_2$) and hillebrandite ($Ca_2SiO_3(OH)_2$), that are generally found in veins. However, little is known about the pressure and temperature conditions of their formation. It is also difficult to determine the composition of the fluids that led to their growth (Buick *et al.*, 2000). Cuspidine formed either before retrograde metamorphism, early in the cooling history by fluorine-bearing fluid infiltration, or by the reaction of fluorine-rich minerals that may have been present during the peak metamorphism. Foshagite formed at ~400 °C during low-temperature retrograde reactions and replaced vesuvianite (Henry, 1999). Hillebrandite is intergrown with foshagite and, thus, likely formed at ~400 °C (Buick *et al.*, 2000). Buick *et al*. (2000) concluded that the three minerals are likely to have formed as a result of late infiltration of fluids between temperatures of 600–700 °C (cuspidine) and 250–400 °C (foshagite and hillebrandite).

1.3.2.2 Western Limb

Kinnaird *et al.* (2002) noted the occurrence of a calc-silicate xenolith underground at Rowland Shaft, Marikana, Lonmin Operations, upper Critical Zone in the Western Bushveld Complex. This is the first recorded occurrence of a calc-silicate xenolith in the Western Limb. A preliminary

study was conducted by Koovarjee (2015) on a limited number of samples; a more detailed investigation is presented here with a larger sample suite.

1.3.2.3 Northern Limb

Gain and Mostert (1982) studied calc-silicate xenoliths in the Northern Platreef (Figure 1.5). The authors focused on the role these xenoliths played in PGE and sulphide mineralisation and put less emphasis on metamorphic mineral assemblages and *P-T* conditions. According to Gain and Mostert (1982), larger xenoliths preserve high-temperature metamorphic mineral assemblages. High-temperature minerals include forsterite, monticellite, diopside, and less common vesuvianite and hercynite. The study listed prograde and retrograde assemblages, which included serpentine, hydrogrossular and talc after forsterite and monticellite, tremolite after diopside and hercynite after magnetite. Retrograde minerals were found at the margins of large xenoliths and in small xenoliths. Gain and Mostert (1982) describe the contacts between the xenoliths and surrounding magmatic rock as gradational and associated with the development of pegmatoidal material. The researchers identified alteration zones (up to 20 m in width) in the immediate surrounding magmatic rock, which they speculated could have been produced by dehydration and decarbonation of the xenolith. The authors noted the absorption of CO_2 instead of H_2O by the magma was more likely at the time of prograde metamorphism, and proposed that H_2O remained within the confines of the xenolith and later resulted in retrograde metamorphism and serpentinisation. Figure 1.7 depicts three possible examples of how a xenolith and its surrounding alteration zone may appear based on examples from the Platreef (Gain and Mostert, 1982). Example 1 shows a uniformly shaped xenolith surrounded by a uniform alteration zone. In example 2 an irregularly shaped xenolith is surrounded by an alteration zone that may be wider in areas where protrusions occur in the original shape of the xenolith. Example 3 depicts an originally large xenolith that has undergone physical breakup through fracturing and fragmentation into smaller pieces, subsequently exposing smaller portions to magma interactions and producing a relatively larger alteration zone. Gain and Mostert (1982) suggested that CO_2, H_2O and S released from the breakup of calc-silicate xenoliths within the magmatic rock led to oversaturation and acted as an external source of

sulphur. This, in turn, resulted in the precipitation of immiscible sulphides and thus, mineralisation of PGEs, Ni and Cu took place. Pronost *et al.* (2008) also recognised this process as a potential mechanism aiding mineralisation.

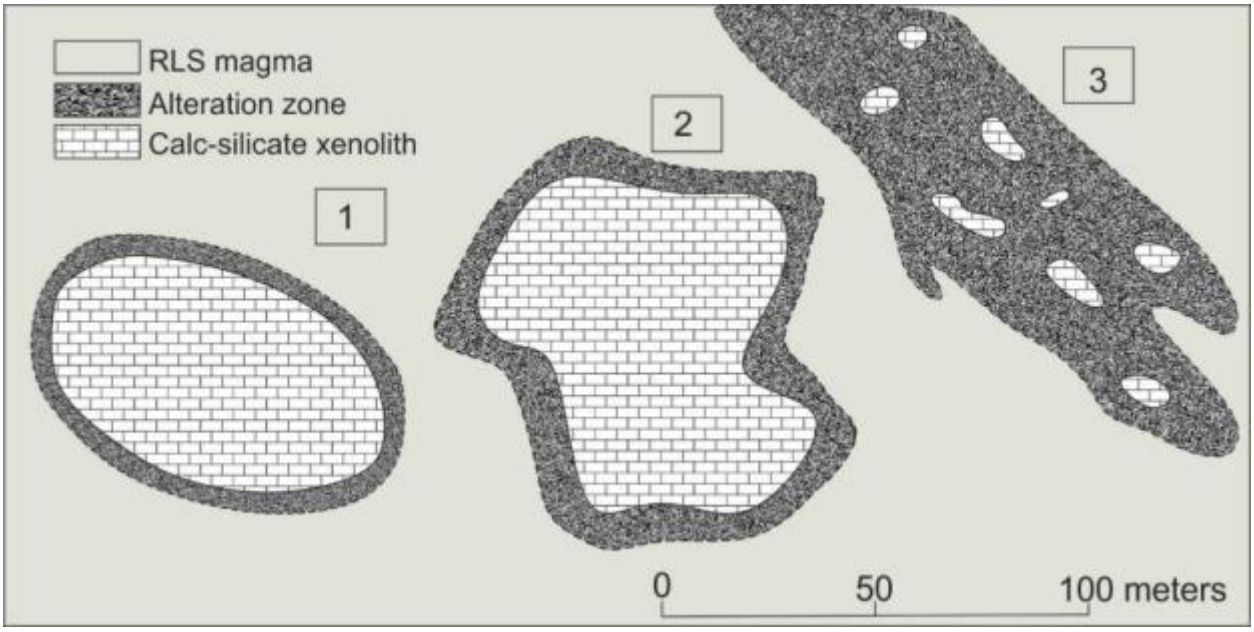

Figure 1.7: Simplified cross-section showing the different occurrences of calc-silicate xenoliths and surrounding alteration zones in the RLS magma reproduced from on Gain and Mostert (1982).

Lee (1996) noted that the zones immediately surrounding calc-silicate xenoliths were enriched by sulphides that hosted PGEs, Cu and Ni. Kinnaird *et al.* (2005) and Sharman-Harris *et al.* (2005) made the same observation for calc-silicate xenoliths in the Main Zone and suggested that these xenoliths played an important role in triggering localised mineralisation. Mitchell and Scoon (2012) also recognised that calc-silicate xenoliths may be associated with localised regions of high-grade PGEs, but they concluded that this mechanism for mineralisation in the Northern Limb may not be applicable on a regional scale.

Although Johnson *et al*. (2010; 2011) placed less emphasis on determining *P-T* conditions using the mineral assemblages in calc-silicate xenoliths in the Northern Limb, they studied quartz-absent Fe and Al-rich metapelite xenoliths located in the Platreef. Metapelite xenoliths, which

most likely originate from the Timeball Formation of the Transvaal Supergroup, are common in the Platreef and vary in size from a few centimetres to several metres across (Johnson *et al*., 2011). Peak metamorphic constraints derived from these xenoliths are ~2.5 kbar and ≥ 900 °C. The xenoliths display textural (with coarser grains at the margins) and mineralogical zonation, and always show sharp contacts with the magma. Micro-diatextite is observed in small xenoliths and at the margins of larger xenoliths. It should be noted that larger individual xenoliths may have been disaggregated during the emplacement of the magma. The presence of micro-diatextite indicates rapid melting took place owing to the high temperature attained by the xenolith as it was incorporated in the Platreef magma. Prograde dehydration of the xenoliths assisted melting as H_2O migrated to the xenoliths' margins. Sheets and veins of granite are observed above larger xenoliths and are considered to be the melt that partially crystallised within conduits through which melt escaped from the xenoliths (Johnson *et al*., 2010).

1.3.3 Carbonate–magma interactions in layered intrusions

Carbonate—magma interactions are not particularly rare and occurrences have been investigated in several volcanic and plutonic environments (e.g., Wenzel *et al*., 2002; Barnes *et al*., 2005; Freda *et al*., 2008). Various studies that document carbonate—magma interactions consider the localised effects that carbonate assimilation has on the immediate surrounding igneous assemblage or the evolution of the magma (Tilley and Harwood, 1931; Joesten, 1977; Owens, 2000; Wenzel *et al*., 2002; Barnes *et al*., 2005; Freda *et al*., 2008; Gaeta *et al*., 2009; Mollo *et al*., 2010). These studies note that skarn rocks develop at the carbonate—magma interface and that contamination of the magma is commonly marked by the crystallisation of Ca-rich minerals, particularly clinopyroxene, and by higher $\delta^{18}O$ values relative to the magmatic component (Barbieri *et al*., 1975; Gaeta *et al*., 2009). In some cases, skarn rock can act as a barrier between the carbonate rocks and magma, preventing extensive assimilation and further exchange of components (Owens, 2000; Gaeta *et al*., 2009; Mollo *et al*., 2010).

Tilley and Harwood (1931) investigated olivine-dolerite intrusions adjacent to carbonate-rich country-rock at Scawt Hill, Ireland, and found that localised assimilation of $CaCO_3$ by the doleritic magma produced augite instead of hypersthene and converted olivine to orthopyroxenes. According to them, this left a residual liquid that was rich in plagioclase, Fe and Na. They inferred that increasing amounts of $CaCO_3$ assimilation led to the development of augite-plagioclase-nepheline-rich rocks. Joesten (1977) studied reactions between alkali gabbro magma and limestone in the Christmas Mountains, Texas, and noted that a ≤3 m thick contact zone, within which nepheline pyroxenite is the main constituent, lies adjacent to a ≤1 m thick calc-silicate skarn at the xenolith contact. According to Joesten (1977), the sinuous nature of the pyroxenite-skarn contact and the presence of small rounded (as opposed to angular) calc-silicate xenoliths in the pyroxenite suggest that the magma-carbonate interaction involved local solution of the country rock. This is supported by their observation of skarn away from the main limestone xenolith. In both the above cases clinopyroxene in the contact zones adjacent to the xenoliths is enriched in Ca, Al, Fe^{3+} and Ti (Tilley and Harwood, 1931; Joesten, 1977).

More recent studies have noted that the crystallisation of Ca-rich minerals (most commonly diopside) affects the stability of liquidus phases in the magma and that the magma becomes increasingly depleted in Si as Ca-rich minerals form (Barnes *et al*., 2005; Freda *et al*., 2008). This desilication reaction:

$$CaCO_3^{solid} + SiO_2^{melt} + MgO^{melt} \rightarrow diopside^{solid} + CO_2$$ (Marziano *et al*. 2008)

is typical for contaminated basaltic/gabbroic magmas. This indicates that the dissolution of $CaCO_3$ in silicate melts will produce silica-undersaturated melts as SiO_2 is consumed to produce diopside and, by this notion, it is implied that the extent of carbonate assimilation is controlled by MgO content of the magma (Mollo *et al*., 2010). According to Gaeta *et al*. (2009) and references therein, magma emplaced in a carbonate-rich rock is associated with skarns and cumulates abundant in Ca-Tschermak-rich clinopyroxene. Skarns that contain glass and that grade into a cumulate reaction zone indicate high-temperature formation and are considered

magmatic, rather than metasomatic, skarns (Fulignati *et al*., 2004; Gaeta *et al*., 2009; Mollo *et al*., 2010). Gaeta *et al*. (2009) suggested that rocks composed of Ca-Tschermak-rich clinopyroxene should be considered as the product of a CaO-rich silicate melt and, thus, that the resultant assimilation of this melt is more appropriately considered to be magma contamination than the ingestion of carbonate wall rock only. Thus, assimilation reactions must also consider magmatic components such as MgO and Al_2O_3 (Gaeta *et al*., 2009; Mollo *et al*., 2010).

In the Colli Albani Volcanic District (CAVD) in Italy the subvolcanic magmatic system was emplaced in carbonate-rich (limestone) country-rock (Chiarabba *et al*., 1997). Gaeta *et al*. (2009) demonstrated that, through assimilation-fractional-crystallisation processes, magmas in the CAVD are contaminated by Ca-rich melts. The volcanic districts of Italy generally comprise Fo-olivine and Cr-spinel-bearing basanitic, trachybasaltic and tephritic volcanics (Perini *et al*., 2004). However, these compositions are not observed in the CAVD plumbing system and Gaeta *et al*. (2009) showed that carbonate assimilation produced cumulates involving magnesian olivine (Fo_{90}) and Ca-Tschermak-rich clinopyroxene, and contain Al-rich spinel instead. Gaeta *et al*. (2009) noted that calc-silicate xenoliths cannot be solely responsible for the magma contamination and differentiation seen at CAVD and considered that larger-scale magma-carbonate interactions must exist, that is, in order to account for the contamination effects, extensive wall-rock assimilation must have occurred beyond what is suggested by the proportion of surviving xenolithic material.

Whitley *et al*. (2020) studied magmatic and metasomatic effects of carbonate-magma interactions that are recorded in calc-silicate xenoliths in the Merapi volcanic region, Indonesia. The Merapi plumbing system intrudes ≤11 km of limestones and marls, and metamorphosed xenoliths are commonly observed within the eruptive deposits (Chadwick *et al*., 2007). Whitley *et al*. (2020) suggested that ≥30% crustal carbonate assimilation took place during the genesis of magma and that this contributes to large volumes of CO_2 liberation during syn-magmatic

activity. This is associated with intensifying explosivity at Merapi (Borisova *et a*l., 2013; Carr *et al*., 2018).

Whitley *et al*. (2020) identified two types of xenoliths at Merapi: (1) magmatic skarn xenoliths, which are formed within the magma, and (2) metasomatic exoskarn xenoliths, which originate from the contact aureole. Magmatic skarn xenoliths are zoned, with the edges characterised by Ca-rich glass, plagioclase (An_{37-100}) and magnetite, surrounding cores composed of wollastonite, Ca-Tschermak-rich clinopyroxene, plagioclase (An_{47-100}), garnet (grossular-andradite) and quartz. Exoskarn xenoliths are unzoned, contain no glass and comprise garnet (grossular-andradite), wollastonite, Ca-Tschermak-rich clinopyroxene, plagioclase (An_{100}), quartz and calcite granoblasts, indicating sub-solidus formation (Whitley *et al*., 2020). According to them, magmatic skarn xenoliths are syn-magmatic and form as a result of 'dissolution' of limestone that produces a Ca-rich magmatic melt from which Ca-rich/skarn minerals can precipitate. This is supported by the presence of Ca-rich glass and Ca-rich melt inclusions. Whitley *et al*. (2020) suggested that the magmatic skarn xenoliths provide new insights into how the cumulate-forming processes at the Merapi–wall-rock occur: carbonate assimilation influences the mineralogy of cumulates as shown by Wenzel *et al*. (2002) and Gaeta *et al*. (2009). Assimilation and resultant Ca enrichment of the magmatic melt increases the stability of clinopyroxene and, in more evolved melts, plagioclase as well (Mollo *et al*., 2010). This results in a wall-rock that grades from a cumulate-rich zone adjacent to the magma body, and can be considered as the endoskarn, to exoskarn assemblages at the limestone contact (Whitley *et al*., 2020).

Calc-silicate xenoliths have been identified in the Lower Zone of the Kiglapait Intrusion, Labrador (Owens, 2000). These xenoliths commonly show mineral assemblages of diopside + forsterite + monticellite + spinel ± akermanite at the core and are surrounded by a 'reaction' zone comprising clinopyroxene + spinel + magnetite. It should be noted that clinopyroxene is not a recognised cumulus phase at this stratigraphic level in the intrusion (Morse, 1981) and, hence, its presence here is interpreted as evidence of carbonate-magma interaction (Owens, 2000). Clinopyroxene compositions are Ca-, Al-, and Fe^{3+}-rich (Ca-Tschermak-rich). The

presence of Fe^{3+} indicates that contamination by the xenolith caused an increase in fO_2, resulting in oxidising conditions (Owens, 2000; Wenzel *et al*., 2002). The troctolite host rock immediately adjacent to the reaction zone displays fine pyroxene blebs in Ca-rich plagioclase (An_{100}). The An content of plagioclase decreases to An_{60} ~2 cm away from the reaction zone. Morse (1981) suggested that the reaction zone may have acted as a barrier to further diffusion of components outwards from the xenolith and, therefore, that any contamination of the magma must have occurred before the development of the reaction zone (Owens, 2000; Gaeta *et al*., 2009; Mollo *et al*., 2010). Owens (2000) concluded that the xenoliths lost Ca, and possibly Mg, while gaining Si, Al and Fe from the surrounding magma, and that the low amounts of pyroxene in some samples may indicate less diffusion of Si in those examples versus other, more pyroxene-rich, samples.

Silica-poor dolomitic xenoliths located in the Ioko-Dovyren Intrusion in the North Baikal Region of Russia form Mg-skarns that may have undergone partial melting during incorporation in a mafic magma of dunite composition (Wenzel *et al*., 2002). Two dominant mineral assemblages have been identified: (1) periclase (now brucite pseudomorphs) + forsterite + spinel, which occurs in the xenolith cores, and (2) olivine + spinel ± monticellite occurring at the margins. Wenzel *et al*. (2002) suggested that rapid heating and decomposition of the dolomitic xenolith produced calcite + periclase + CO_2. Peak metamorphism took place at ~1200 °C and ~1 kbar and, as the magma continued to heat the xenolith, $CaCO_3$ migrated away from the xenolith, leaving behind a Ca-free brucite/periclase + forsterite + spinel skarn. This $CaCO_3$ subsequently mixed with the surrounding magma. Evidence of calcite mixing with the magma may be indicated by crystallisation in the dunites of Ca-rich forsterite and Ca-Tschermak-rich clinopyroxene. Wenzel *et al*. (2002) concluded that the changes in composition of the dunites surrounding the xenoliths were caused by contamination of the magma by CaO and that the source of CaO could have been calcite melt. However, no evidence of calcite melt has been observed. Contamination from the decarbonating xenolith added CO_2 into the magma, resulting in an increase in fO_2 (Wenzel *et al*., 2002).

Carbonate-magma interactions have also been studied in the Platreef in the Northern Limb of the RLS, where RLS magma interacted with the dolomitic Transvaal Supergroup footwall (Gain and Mostert, 1982; Klemd *et al*., 2020). The effects of carbonate assimilation on the magma have been documented using $\delta^{18}O$ compositions (section 6.3 and references therein). The most obvious physical manifestations of this interaction are: (1) the presence of calc-silicate xenoliths in the Platreef and Main Zone, and (2) the development of parapyroxenite (Gain and Mostert, 1982; Kinnaird *et al*., 2005), namely, diopside-rich metasomatic or metamorphic rocks and hybrid rocks that contain significant amounts of clinopyroxene of both metamorphic and magmatic origin that formed as a result of carbonate-magma interactions (Wagner, 1929; Kinnaird *et al*., 2005). Parapyroxenites in the Platreef are predominantly found where the footwall is dolomite (Kinnaird *et al*., 2005; Klemd *et al*., 2020). Clinopyroxene in the Platreef is predominantly diopsidic in composition, with higher Ca and lower Si, Fe and Na compared to pyroxene in magmatic pyroxenite (Pronost *et al*., 2008; Klemd *et al*., 2020). In norites and pyroxenites, orthopyroxene is the only cumulus phase, and Harris and Chaumba (2001) showed that the assimilation of carbonates in the Platreef does not favour the crystallisation of clinopyroxene or forsterite over orthopyroxene. Therefore, norites and pyroxenites show typical igneous mineralogy, but nonetheless show a shift in $\delta^{18}O$ measurements.

1.4 Aims and objectives

While previous studies in the RLS have demonstrated similar peak metamorphic conditions being achieved in the different zones of the Eastern Limb of the RLS, mineralogical variations in calc-silicate xenoliths have been attributed to the nature of the protolith and inherited sedimentary layering (e.g., Willemse and Bensch, 1964). The effects of metamorphism and metasomatism and the different degrees of retrogression (Willemse and Bensch, 1964; Buick et al., 2000) have also played a role in the mineralogical variation of xenoliths. This raises the question of length scales of chemical equilibration and whether solid-state or fluid-assisted diffusion of elements took place at different times in the evolution of the xenolith-magma system, as well as the origin of fluids operating in the aforementioned system, that is, an

internal source from the xenolith and/or magma, or an external source from post-crystallization fluid influx. This project aims to investigate interactions and the effects, if any, these calc-silicate xenoliths may have on the magma and any localised mineralisation in the RLS. Borehole core samples collected from the Platreef of the Northern Limb (Zwartfontein farm) were examined together with samples collected from a xenolith located underground at Rowland Shaft, Marikana (Western Limb).

Transmitted and reflected light petrography, backscattered scanning electron microscopy (BSEM), X-ray Fluorescence (XRF) and micro-XRF, electron-microprobe analysis (EMPA), X-ray element mapping, stable isotope analysis, and laser ablation inductively coupled plasma mass spectrometry (LA-ICP-MS) were used to:

- Spatially constrain the variation in the mineral assemblages and mineral compositions across the contact zone between the RLS magmatic rocks and the calc-silicate xenoliths, with the aim of understanding the degree of the chemical interaction between the magma and the xenolith (using petrographic methods, BSEM, EMPA, X-ray element mapping).

- Model the prograde heating and retrograde cooling history of the xenolith to constrain the relative timing of crystallisation and reactions in the xenolith (using Perple_X thermodynamic modelling software).

- Determine the sequence of the mineral growth in the xenolith and the contact zone with regard to crystallisation and cooling of the RLS magma from microtextural analysis.

- Examine the physical and chemical interaction between the xenolith and RLS magma, and to determine the extent of contamination/interaction (cm- to m-scale) using stable isotope signatures of the mineral separates.

- Analyse the chemical interaction between the xenoliths and the RLS magma to determine the possible origin of spinels (magmatic or metamorphic) and the role the interaction between the xenolith and magma played in the local ore mineralisation. LA-ICP-MS was employed to analyse trace elements because the variations in trace element concentration is much larger than major elements, and trace elements are sensitive to processes that major elements may not be sensitive to.

CHAPTER 2: PETROLOGY AND MAJOR ELEMENT GEOCHEMISTRY

2.1 Introduction

This study involved spatially controlled sampling for each xenolith of interest in order to investigate the variation in mineral assemblages across the contact zones between xenoliths and RLS igneous rock. In each case, samples were collected from the xenolith interior and close to the likely edge of the xenolith as well as from its immediate surroundings, based on visible mineralogical and textural differences; however, as discussed in the ensuing chapters, the xenolith-magma interface is somewhat complex as a result of metasomatic and low-T hydration effects. Reference RLS igneous rock samples away from each xenolith were also obtained. Boreholes that intersect calc-silicate xenoliths in the Platreef on Zwartfontein farm in the Northern Limb were considered because borehole core provided the opportunity for spatially well-constrained sampling to be employed. However, zonation of minerals and textures similar to the Marikana occurrence between xenolith and igneous rocks is not as easily distinguishable in the Zwartfontein xenoliths. The Marikana example provides an appreciation of the complex spatial relationships between various parts of the system which cannot be seen at Zwartfontein owing to the one-dimensional nature of the cores.

2.2 Marikana

Samples were collected underground from Rowland Shaft, Marikana, Lonmin Operations, ~27 km east of Rustenburg (Figure 2.1) from a single xenolith situated ~20 m below the UG 1 chromitite layer (upper Critical Zone). Specifically, the xenolith is located on the 26 Level Tram Cross-cut North. It is partially exposed in the sidewall of the cross-cut (Figure 2.2A). The true dimensions of the xenolith could not be determined because at the time of sampling the xenolith and most of its surrounding were covered in shotcrete. However, the xenolith was exposed over a height of 5 m and length of 7 m. The condition of the outcrop was poor and highly friable. Samples were collected from parts of the xenolith that appear unaltered as well as parts that show mineralogical or textural variation. The eastern edge of the xenolith was not identified as it was obscured by shotcrete. The western edge is partially exposed, and sampling

was done at all accessible areas where change in mineralogy or texture was evident. The xenolith and its surroundings will be described below.

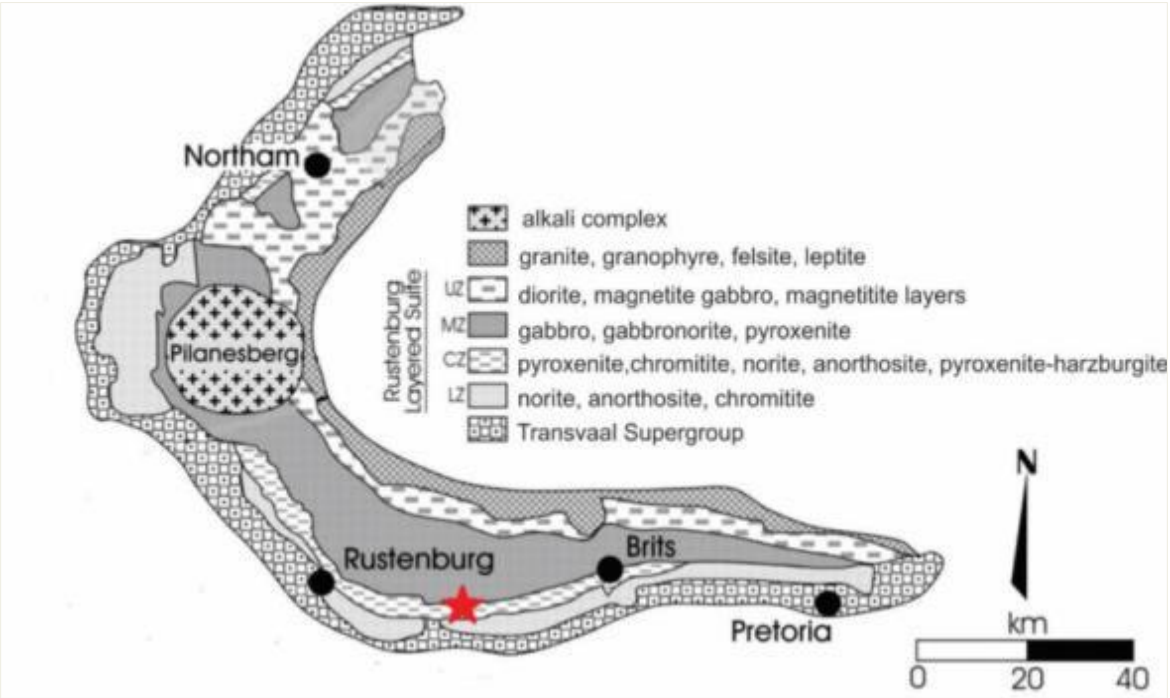

Figure 2.1: Geological map of the Western Limb of the Bushveld Complex showing the location of Rowland Shaft (red star). UZ = Upper Zone, MZ = Main Zone, CZ = Critical Zone and LZ = Lower Zone (reproduced from Smith *et al*., 2003).

2.2.1 Xenolith and the contact zone

The exposed xenolith is predominantly massive and composed of grey to cream/yellow monticellite, medium grey forsterite and black spinel. However, internal compositional, textural and structural variabilities are observed and will be described from east to west of the outcrop with the aid of the schematic diagram shown in Figure 2.2B. Overall layering within the xenolith appears to strike 171° and dip 65° W, which is approximately orthogonal to the E-W-striking, gently N-dipping, magmatic layering. The eastern layer of the exposed xenolith is ~4 m to 4.5 m thick; comprises medium to coarse-grained monticellite, forsterite (~5 mm to 15 mm) and fine-grained spinel (> 1 mm to 3 mm) (Figure 2.3A). This layer contains an irregular, 7 cm long

spinel-rich patch (Figure 2.3B). The edges of the spinel patch contain interstitial monticellite, whereas the centre is dominantly spinel. It is characterised by sub-vertical, broadly E-W-striking fractures that show a dm spacing and moderately-steeply W-plunging oblique-slip to subhorizontal slickenlines in clay-rich fault gouge. The intermediate layer is 1.5 m wide and comprises fine to medium-grained monticellite and forsterite (1 mm to 3 mm), and has a sugary textural appearance. The layer is characterised by ~8 cm to 10 cm thick pegmatoidal bands composed predominantly of monticellite up to ~20 mm, spinel grains ~10 mm in size, and lacks forsterite (Figure 2.3C). The westernmost layer (1.5 m to 2 m thick); comprises medium to coarse-grained monticellite and forsterite (4 mm to 15 mm) and shows a poikilitic texture, with dark spinel (< 1 mm to 3 mm) inclusions. For the purpose of this study the term *main xenolithic body* will refer to xenoliths that are at least 1 m thick, show a predominantly medium to coarse-grained texture, and are relatively massive, but may be structurally and texturally heterogeneous as described in the above case.

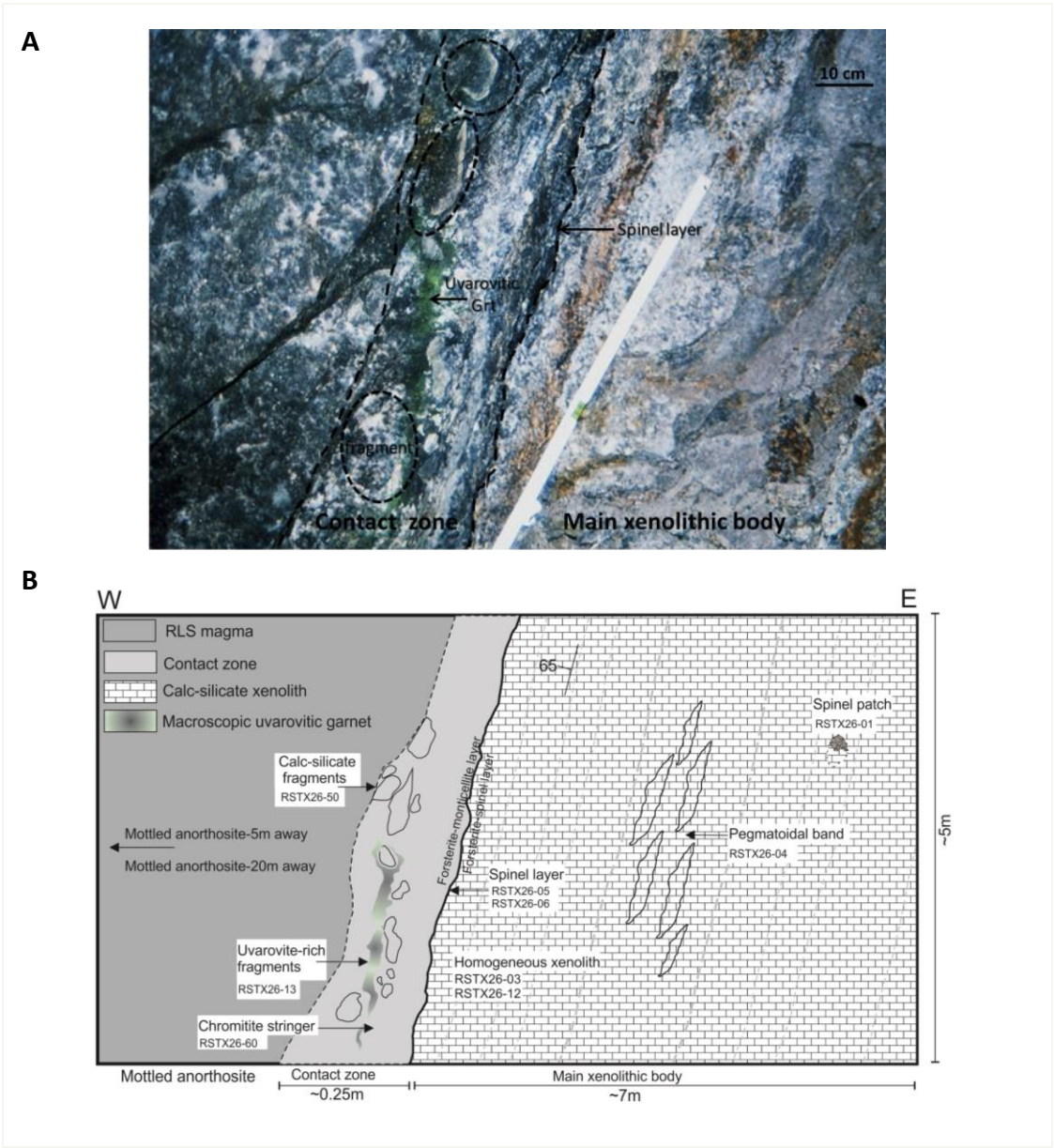

Figure 2.2: Marikana xenolith exposed in the sidewall underground, 26 Level, Tram Cross-cut North, Rowland Shaft. (A) Photograph of the sample site showing the western portion of the xenolith (right), contact zone and surrounding igneous rock (left). Fragments of calc-silicate rock in the contact zone are circled and apple-green uvarovitic garnet is labelled. The dark grey spikes and patches in the xenolith are shadow effects on joints, not mineral variation. (B) Schematic diagram of the xenolith and surrounding contact zone showing the approximate locations of the samples and the corresponding sample identification numbers.

Figure 2.3: Hand samples of the Marikana xenolith showing differences in mineral texture and proportions. (A) Largely homogeneous xenolith; grey forsterite, cream/yellowish monticellite and black spinel (RSTX26-12). (B) Spinel-rich patch surrounded by monticellite (RSTX26-01). (C) Pegmatoidal band with large black spinel grains predominantly included in cream/yellowish monticellite and surrounded predominantly by fine-grained grey forsterite (RSTX26-04).

The western flank of the main xenolithic body is defined by a series of distinct cm-scale layers (Figure 2.4) as follows: (1) forsterite-spinel layer; (2) spinel layer; (3) a forsterite-monticellite layer, which is texturally different from the xenolith core; (4) a highly altered vesuvianite layer containing a thin, but distinct, serpentine band; (5) a clinopyroxene layer, and (6) a highly heterogeneous zone within which a chromitite stringer is found and fragments of calc-silicate minerals, uvarovitic garnet, Cr-spinel, pyroxene and plagioclase occur; this is considered the contact zone (Figures 2.2).

The western end of the main xenolithic body is characterised by a ≥ 3 cm-thick layer which is deficient in monticellite and consists of medium grey forsterite (0.5 cm to 2 cm) and black spinel (0.5 mm to 3 mm), hereinafter referred to as the forsterite-spinel layer. The spinel layer is in sharp contact with the forsterite-spinel layer (Figure 2.4) and consists of fine-grained (<0.5 mm to 1 mm) spinel. The maximum thickness of the spinel layer is ~1.5 cm and it appears to be disrupted by the calc-silicate minerals of the forsterite-spinel layer. The medium grey forsterite-monticellite layer is found next; it is fine-grained and ≥ 1 cm thick and also displays a sharp contact with the spinel layer. The forsterite-monticellite layer shows compositional similarity with the xenolith itself, consisting of monticellite, forsterite (>1 mm to 5 mm in size) and disseminated spinel (< 0.5 mm to 1 mm). It appears disrupted by the vesuvianite layer. The ~3 cm-thick, highly altered vesuvianite layer follows and displays a gradational contact with the forsterite-monticellite layer. This zone is fine to medium-grained, displays grey to yellow colours and predominantly consists of vesuvianite, spinel and minor monticellite. It is characterised by a ~2 mm-thick band of green-black serpentine that separates two mineralogically different bands: (1) vesuvianite (alteration hinders grain-size determination), spinel (< 1 mm) and monticellite (< 1 mm) which grades in colour from medium grey to cream/yellowish grey, and (2) greyish white vesuvianite (1 mm to 2 mm) and spinel (< 1 mm). There is a gradational contact between the highly altered vesuvianite layer and the clinopyroxene layer. The latter is ≥ 5 cm thick, medium-grained (1 mm to 3 mm) and monomineralic. It is progressively lighter towards the xenolith, ranging in colour from dark to medium green, and consisting almost exclusively of clinopyroxene.

Figure 2.4: Hand sample (RSTX26-05) showing the zonation of minerals immediately adjacent to the xenolith. (1) The forsterite-spinel layer adjacent to the spinel layer (2). This is followed by forsterite-monticellite layer (3), followed by the vesuvianite layer (4), within which a serpentine band occurs, and the clinopyroxene layer (5).

The contact zone displays a variety of colours ranging from dark to apple green to cream/white-grey. It has an observed thickness of ~25 cm, and the grain size varies from fine to coarse (Figure 2.2A). The matrix of the contact zone is grey to white, comprising plagioclase (< 1 mm to 2 mm) and clinopyroxene (< 1 mm to 4 mm) with variable amounts of apple green garnet (1 mm to 2 mm). In the matrix, calc-silicate rock fragments are visible and are rounded to sub-rounded to irregular (Figures 2.2 and 2.5). The long axes of the fragments varies from ~2 cm to 10 cm. The fragments generally display zonation of their own on a smaller scale, consisting of a grey core of monticellite, surrounded by cream to yellow vesuvianite, followed by apple-green garnet (1 mm to 2 mm) which commonly hosts spinel (< 1mm) and clinopyroxene (<2 mm to 6 mm). Garnet occurs in friable, discontinuous aggregates that are distributed irregularly within the contact zone. Both the calc-silicate fragments and garnet aggregates are enclosed by the plagioclase-clinopyroxene matrix (Figure 2.5). The occurrence of the fragments in this zone provides visual evidence that there has been an outward movement of the calc-silicate minerals from the main xenolithic body. Within this zone is a chromitite stringer (Figure 2.6), the total thickness of which is ~7 cm, but which splits into 3 thinner layers that are intercalated with mottled anorthosite. For the purpose of this study, the three layers of interest are labelled according to their proximity to the xenolith (Figure 2.6).

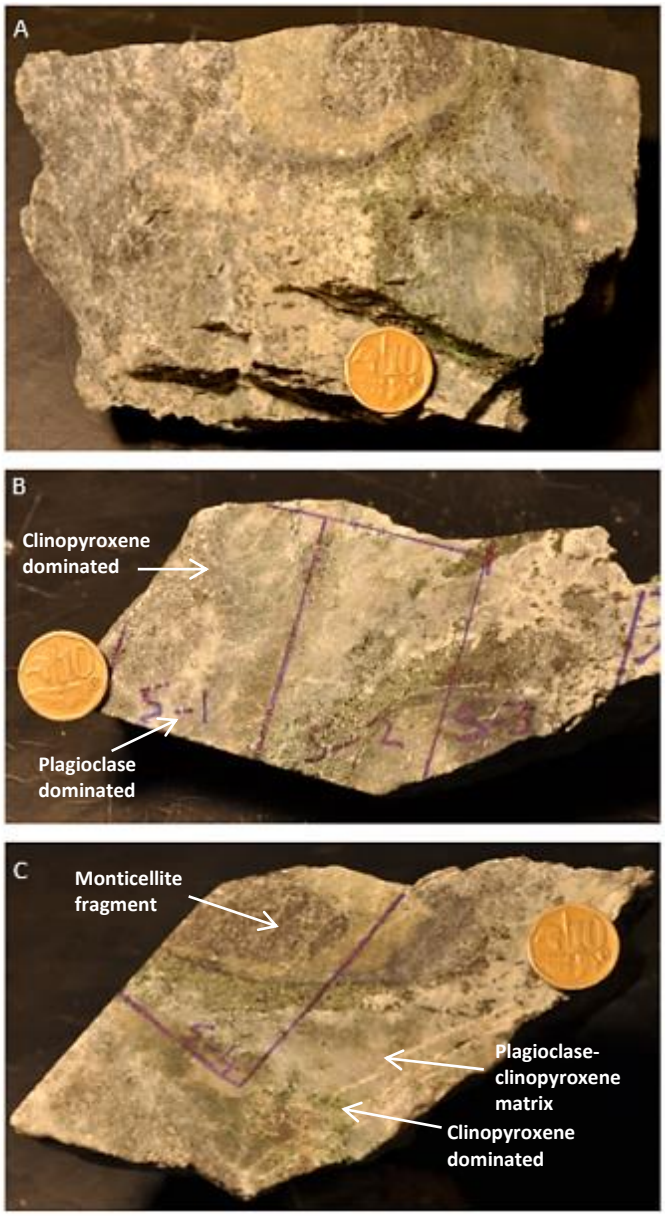

Figure 2.5: Hand samples of the calc-silicate fragments found in the contact zone. The cores of these fragments are commonly grey, and are surrounded by vesuvianite adjacent to a variety of other minerals, but most commonly, include uvarovite garnet and clinopyroxene. Greyish-white plagioclase and grey-green pyroxene comprise the matrix (A). Thin sections were cut for samples RSTX26-51, RSTX26-52 and RSTX26-53 (B) and RSTX26-54 (C).

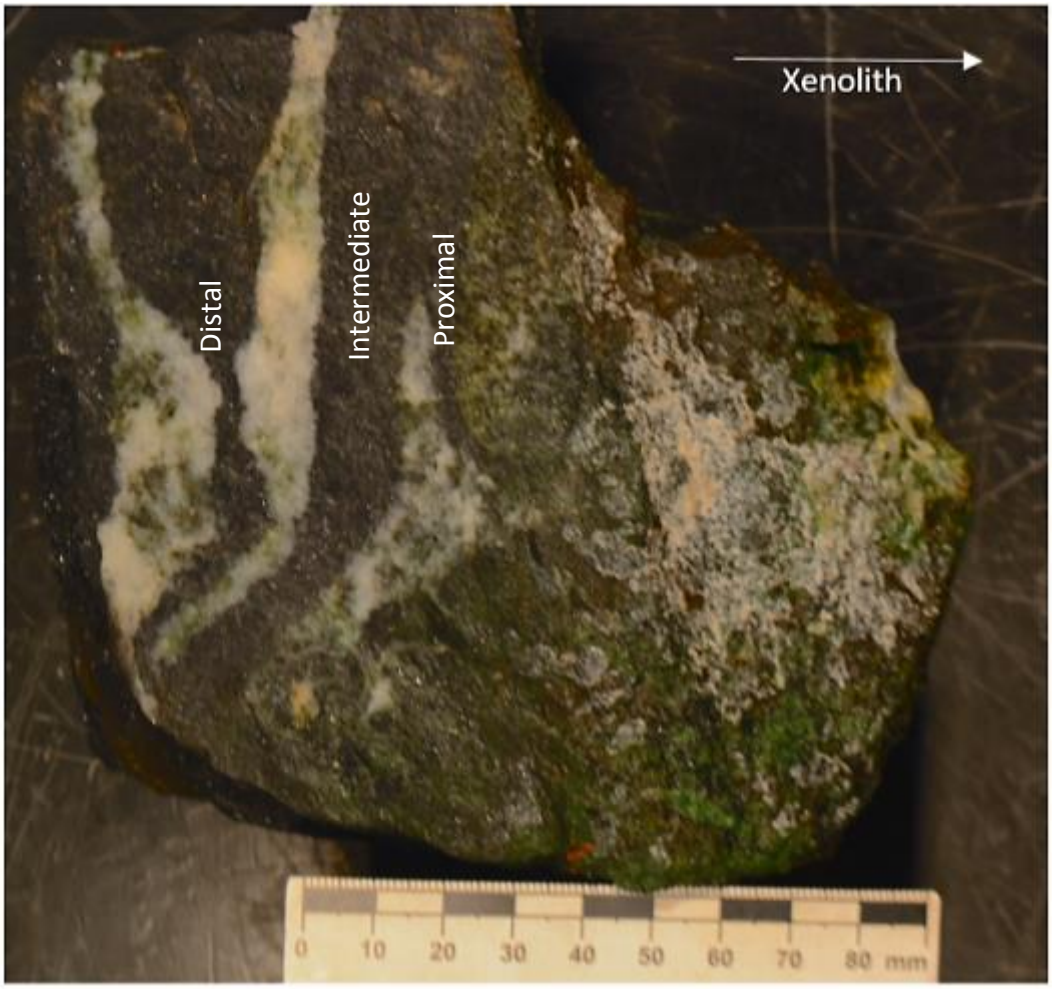

Figure 2.6: Hand sample of the chromitite stringer found in the contact zone. The stringer (left) is distal to the xenolith, while macroscopic apple-green uvarovite and diopside (right) is proximal to the xenolith. The stringer is split into three thinner bands of variable thickness, between which anorthosite occurs (white plagioclase and green pyroxene). Thin sections cut from this sample include RSTX2-61 (stringer proximal to the xenolith), RSTX26-62 (intermediate/stringer found between the other two) and RSTX26-63 (stringer distal to the xenolith).

2.2.2 Igneous rock: mottled anorthosite

The contact between the *contact zone* and the enclosing igneous rock was not observed because, at the time of main sample collection, the xenolith and most of its surroundings were covered by shotcrete. The mottled anorthosite (Figure 2.7A) was sampled 5 m and 20 m from the western edge of the xenolith. It consists predominantly of white to cream plagioclase with

patches (mottles) of greyish green pyroxene. The mottles range in size from 1 cm to 8 cm and comprise 15% to 20% of the samples. The UG 1 chromitite layer was also sampled 20 m away from the xenolith (Figure 2.7B). The layer comprises euhedral chromite grains that range in size from < 1 mm to 2 mm and interstitial plagioclase.

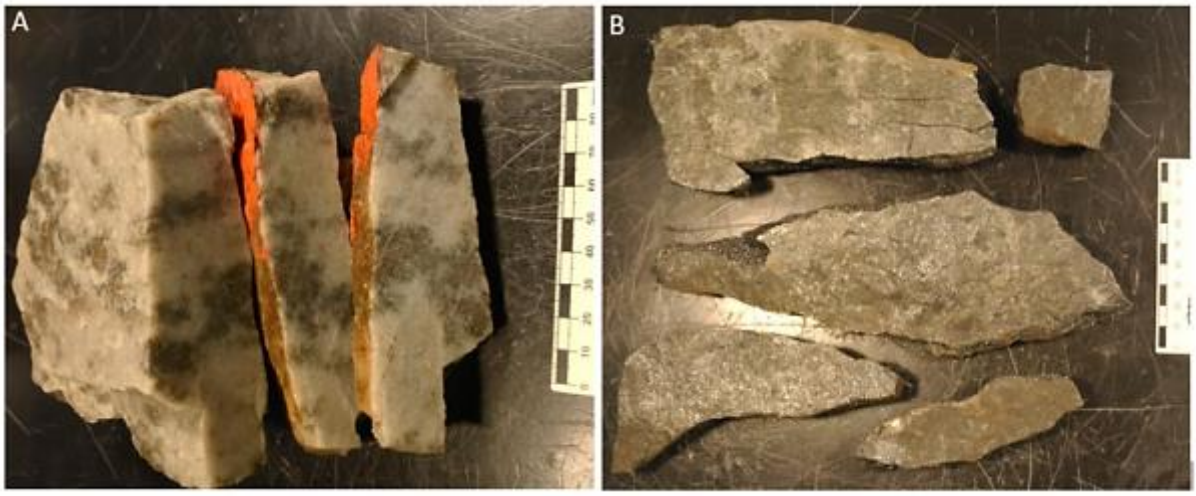

Figure 2.7: (A) Mottled anorthosite collected 5 m (RSTX26-A5) and 20 m (RSTX26-A20) away from the xenolith, and (B) UG 1 chromitite collected 20 m away from the xenolith.

2.2.3 Whole-rock geochemistry and micro-XRF

Whole-rock major and trace elements were analysed from six zones (Table 2.1) from the Marikana sample suite. Detailed sample preparation, methodology, and full XRF major and trace element data are presented in Appendix 1A–B. The methodology employed for micro-XRF is outlined in Appendix C.

Samples analysed for whole-rock geochemistry were selected from locations representing (1) the main xenolithic body (from the western layer (Figure 2.3) where rocks are layered, but homogenous in composition); (2) the forsterite-spinel layer; (3) the forsterite-monticellite layer, both of which are adjacent to the spinel layer (Figure 2.4); (4) the contact zone (from the plagioclase-clinopyroxene matrix which includes clusters of uvarovitic garnet); (5) 5 m away from the main xenolithic body and (6) 20 m away from the main xenolithic body. These were

further compared with the average norite compositions in UG1 Footwall, recorded by Eales *et al*. (1990) (Appendix 1) in order to evaluate if the matrix found in the contact zone shows a greater compositional similarity with anorthosite or norite. The norite compositions were considered because the surrounding igneous rock in Figure 2.2A appears to be richer in clinopyroxene than typical mottled anorthosite sampled herein. The norite compositions (Eales *et al*., 1990) include:

(1) Average of six norites near the top of the unit, and

(2) Average of four norites near the base of noritic suite (Eales *et al*., 1990).

No XRF analysis was done for the spinel layer, chromitite stringer and samples containing calc-silicate fragments in the contact zone because of their significant heterogeneity, as described above.

Table 2. 1: Whole-rock compositions of samples from the Marikana xenolith, mottled anorthosite, and norite (Eales *et al*., 1990)

Sample ID	RSTX26-12	RSTX26-06A	RSTX26-06C	RSTX26-50	RSTX26-A5	RSTX26-A20		
Sample description	Main xenolith	Forsterite-spinel layer	Forsterite-monticellite layer	Contact zone	Mottled anorthosite 5 m away	Mottled anorthosite 20 m away	Average of 6 norites near top UG1 unit (Eales *et al*., 1990)	Average of 4 norites at the base of noritic suite (Eales *et al*., 1990)
(wt%)								
SiO_2	36.13	34.23	33.92	40.96	48.93	49.1	52.68	52.05
Al_2O_3	3.98	2.65	6.78	15.88	30.87	29.60	11.75	14.81
Fe_2O_3	0.62	1.02	0.65	0.71	0.09	0.17	0.78	0.72
FeO	5.01	8.23	5.26	5.72	0.73	1.35	7.77	7.21
Fetot	5.63	9.25	5.91	6.43	0.82	1.52	8.55	7.93
MnO	0.53	0.57	0.56	0.14	0.01	0.02	0.17	0.16
MgO	36.77	52.73	25.63	8.62	0.46	1.26	19.14	15.27
CaO	16.93	1.02	27.11	26.34	15.20	14.60	6.31	8.17
Na_2O	0.03	0.06	bdl	0.04	2.43	2.40	1.14	1.46
K_2O	0.03	0.03	0.03	0.03	0.18	0.18	0.13	0.05
TiO_2	0.20	0.28	0.19	0.53	0.05	0.07	0.11	0.08
P_2O_5	0.01	0.01	0.01	0.01	0.01	0.01	0.02	0.01
Cr_2O_3	<0.01	0.04	0.27	1.23	0.01	0.01	0.29	0.24
NiO	0.01	0.01	0.01	0.02	bdl	bdl	0.05	0.04
TOTAL	**100.25**	**100.88**	**100.42**	**100.23**	**98.97**	**98.77**	**100.34**	**100.28**

Binary variation plots were selected to determine whether or not correlations exist between the major elements (Figure 2.8). Based on Figure 2.8A, layers with higher MgO concentration contain lower Al_2O_3 concentration. The same applies for MgO vs CaO (Figure 2.8B); layers with high CaO concentration contain lower MgO concentration, with the exception of mottled anorthosite and norite, however, there is no consistent trend from xenolith to igneous rock. SiO_2 vs MgO, FeO (total) or CaO, and CaO vs Al_2O_3 (Figure 2.8E to D) show no obvious trends. There is no correlation between CaO and Al_2O_3 or FeO (total). In general Figure 2.8 does not define any strong correlations between the major oxides. However, it highlights two outliers, namely: (1) the forsterite-spinel layer, because its composition is dominated by MgO and FeO; and (2) the contact zone matrix sample, which is composed of a relatively higher amount of all major oxides when compared to the xenolith samples (which is predominantly composed of CaO, MgO and FeO) and mottled anorthosite, which contains greater amounts of Al_2O_3 and SiO_2. Outliers are present in the sample suite because the variation in mineralogy and composition from xenolith compared to the contact zone and igneous rock does not display gradual or steady change over a large area, instead variations occur quite dramatically within a small area. These dramatic changes in composition prevent the development of obvious trends.

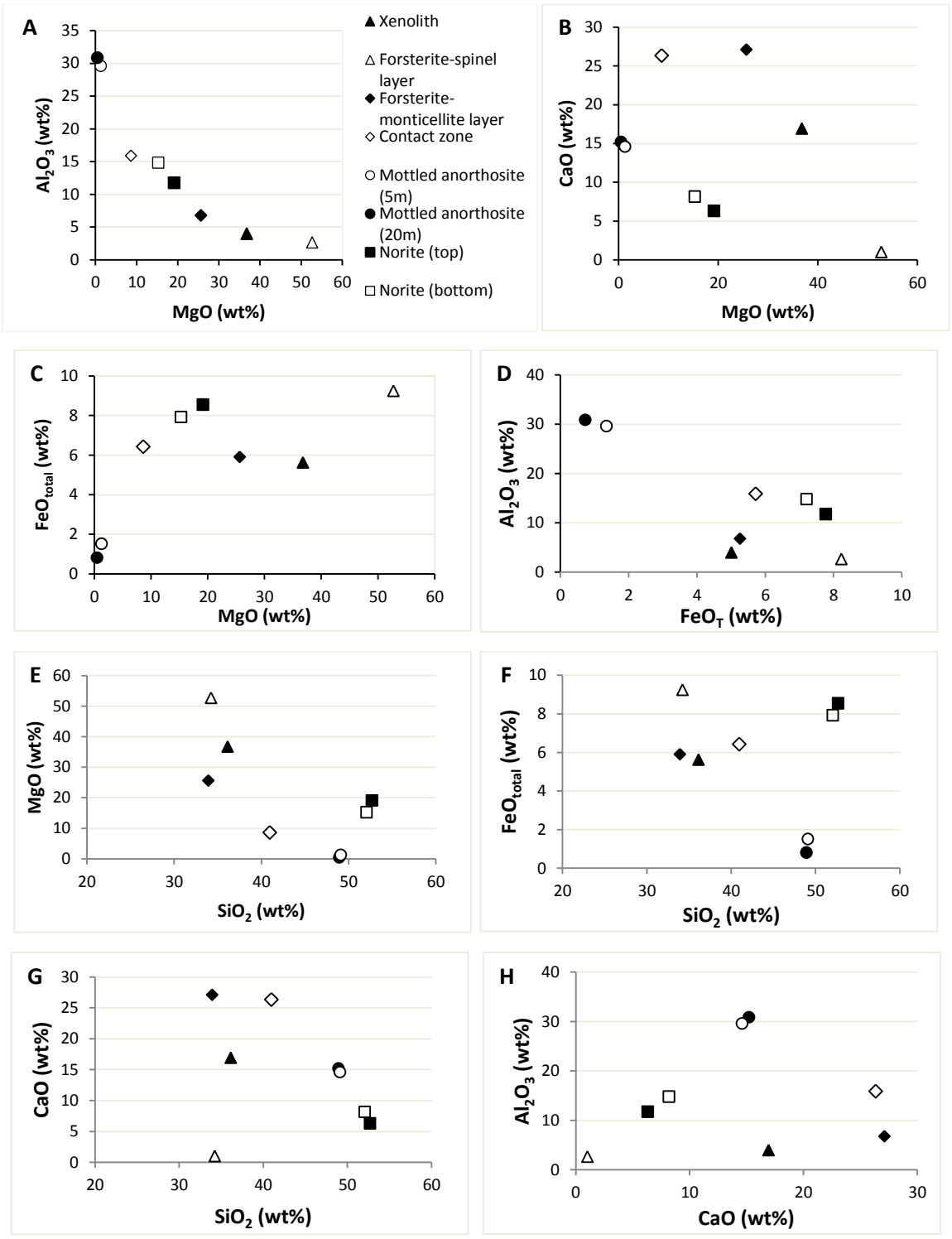

Figure 2.8: Binary variation plots representing the correlations between major elements Al_2O_3, MgO, SiO_2, CaO and FeO from Marikana xenolith and its surrounding lithologies.

Given that binary variation diagrams (Figure 2.8) do not define obvious correlations between major elements, the variation in major element concentration over a spatial range was examined. Therefore, the main xenolithic body and the mottled anorthosite and/or norite are considered as endmembers (Figure 2.9). It should be noted that the variation in major elements between endmembers was also described in a previous study by Willemse and Bensch (1964) detailed in section 1.3.2.1 for xenoliths in the Eastern Limb.

The CaO concentration ranges from 1.02 wt% to 27.11 wt% (Figure 2.9). It decreases significantly from the main xenolithic body towards the forsterite-spinel layer and increases by ~26 wt% less than 2 cm away in the forsterite-monticellite layer (Figures 2.4 and 2.10). In the contact zone the CaO concentration is 26.34 wt%. This contrasts with mottled anorthosite, which displays concentrations of 15.20 wt% and 14.60 wt% in samples 5 m and 20 m away, respectively (Figure 2.9A). CaO concentration in norite units ranges from 6.31 wt% near the top of the UG 1 chromitite to 8.17 wt% at the base of the noritic suite (Eales *et al*., 1990) (Figure 2.9B). Micro-XRF element maps indicate that Ca increases from the calc-silicate fragments into the contact zone matrix (Figure 2.11). The MgO concentration displays a large range from 8.62 wt% to 52.73 wt% between the xenolith and contact zone. MgO is in greatest concentration in the forsterite-spinel layer, given that only forsterite and spinel are present, while the main xenolith displays 36.77 wt% MgO. From the forsterite-spinel layer to the contact zone, MgO shows a decrease from 25.63 wt% to 8.62 wt%. Micro-XRF element maps confirm that Mg decreases from the forsterite-spinel layer towards the forsterite-monticellite layer (Figure 2.10). The lowest concentrations are recorded as 0.46 wt% and 1.26 wt% in mottled anorthosite 5 m and 20 m away, respectively (Figure 2.9A). The norites from Eales *et al*. (1990) show higher MgO concentrations compared to mottled anorthosite: 19.14 wt% in norite units near the top of the UG 1 chromitite and 15.27 wt% at the base of the noritic suite (Figure 2.9B).

The Al_2O_3 content ranges from 2.65 wt% (forsterite-spinel layer) to 15.88 wt% (contact zone). There is a slight drop in Al_2O_3 content from the main xenolith (3.98 wt%) to the forsterite-spinel layer (2.65 wt%), and an increase between the forsterite-monticellite layer (6.78 wt%) and the

contact zone (15.88 wt%). Mottled anorthosite displays a high concentration of Al_2O_3 with 30.87 wt% and 29.60 wt% recorded 5 m and 20 m away from the main xenolithic body, respectively (Figure 2.9A). The norites show lower Al_2O_3 concentrations compared to mottled anorthosite: 11.75 wt% in norite units near the top of the UG 1 chromitite and 14.81 wt% at the base of the noritic suite (Eales *et al*., 1990) (Figure 2.9B). The SiO_2 concentration ranges from 33.92 wt% to 40.96 wt% between the main xenolithic body and the contact zone. In the mottled anorthosites 5 m and 20 m away from the main xenolithic body, SiO_2 contents of 48.93 wt% and 49.10 wt% are recorded, respectively (Figure 2.9A). The highest concentrations are observed in the norites: 52.68 wt% in units near the top of the UG 1 chromitite and 52.05 wt% at the base of the noritic suite (Eales *et al*., 1990) (Figure 2.9B). Overall, SiO_2 increases towards the magmatic rock.

Total FeO concentration in the main xenolithic body is 5.63 wt%. The highest concentration occurs in the forsterite-spinel layer (9.25 wt%), there is a decrease towards the forsterite-monticellite layer (5.91 wt%) and a slight increase in the contact zone (6.43 wt%). The lowest concentrations are recorded in mottled anorthosite as 0.90 wt% (5 m away) and 1.67 wt% (20 m away). The norites show higher $FeO_{(total)}$ concentrations compared to mottled anorthosite: 8.55 wt% in norite units near the top of the UG 1 chromitite and 7.93 wt% at the base of the noritic suite (Eales *et al*., 1990) (Figure 2.9B). The Cr_2O_3 concentrations are multiplied by a factor of 20 to fit the scale of the plot in Figure 2.9. Negligible amounts of Cr_2O_3 are evident in samples between the main xenolithic body and the forsterite-spinel layer. In the forsterite-spinel layer Cr_2O_3 concentration is 0.26 wt%. The contact zone records the highest Cr_2O_3 concentration as 1.23 wt%. Figure 2.11 indicates that the Cr is mostly concentrated in spinel bands surrounding the calc-silicate fragments. Negligible Cr_2O_3 concentrations are recorded in mottled anorthosites (Figure 2.9A), and minor amounts in the norites (Eales *et al*., 1990) (Figure 2.9B). Micro-XRF element maps for the chromitite stringer (Figure 2.12) indicate that Cr and Fe concentrations are highest in the distal stringer and lowest in the proximal chromitite stringer. In the mottled anorthosite intercalations between the chromitite stringers,

Ca decreases from the distal stringer towards the proximal layer, while Al appears to be relatively constant (Figure 2.12).

Minor amounts of TiO_2, MnO and Na_2O occur in the samples (Table 2.1) and show no significant variation from xenolith to igneous rocks. Negligible amounts of TiO_2 are observed in the mottled anorthosites and norites. The highest TiO_2 concentration is recorded in the contact zone (0.53 wt%), and it ranges from 0.20 wt% to 0.28 wt% in the main xenolithic body and forsterite-spinel layer. The greatest concentration of MnO is in the forsterite-spinel layer (0.57 wt%), and negligible amounts occur in the igneous rocks. Mottled anorthosite contains the highest Na_2O content (2.40 wt%–2.43 wt%), whereas norites contain minor amounts (1.14 wt%–1.46 wt%) (Eales *et al*., 1990), and negligible concentrations occur in all other samples.

The variation in major elements between the main xenolithic body, across the various layers (forsterite-spinel, spinel and forsterite-monticellite layers) and the contact zone can be attributed to the layered nature of the xenolith. For example the CaO and MgO content may reflect the variable monticellite and forsterite proportions in the xenolith compared to the forsterite-spinel and forsterite-monticellite layers. Alternatively, an example from Willemse and Bensch (1964) can be considered to explain the major element variation. The aforementioned authors noted that the xenolith at location A of their study exhibited a defined zonation of mineral assemblages across the xenolith-igneous rock contact (described in section 1.3.2.1). Willemse and Bensch (1964) suggested that the defined zonation of mineral assemblages may be attributed to the outward migration of CaO (in the form of $CaCO_3$) from the xenolith core to the margins of the xenolith which is adjacent to the igneous rock contact. The outward migration of CaO resulted in the MgO-rich xenolith core (which is predominantly composed of forsterite and is spinel-bearing) and the zones closer to the igneous rock become subsequently richer in CaO (Willemse and Bensch 1964). A similar phenomenon is observed herein where CaO content is significantly lower in the forsterite-spinel layer, whereas a higher CaO content is observed in the forsterite-monticellite layer and contact zone. The MgO content shows the

opposite trend. A summary of the samples and corresponding whole-rock data is shown in Figure 2.13.

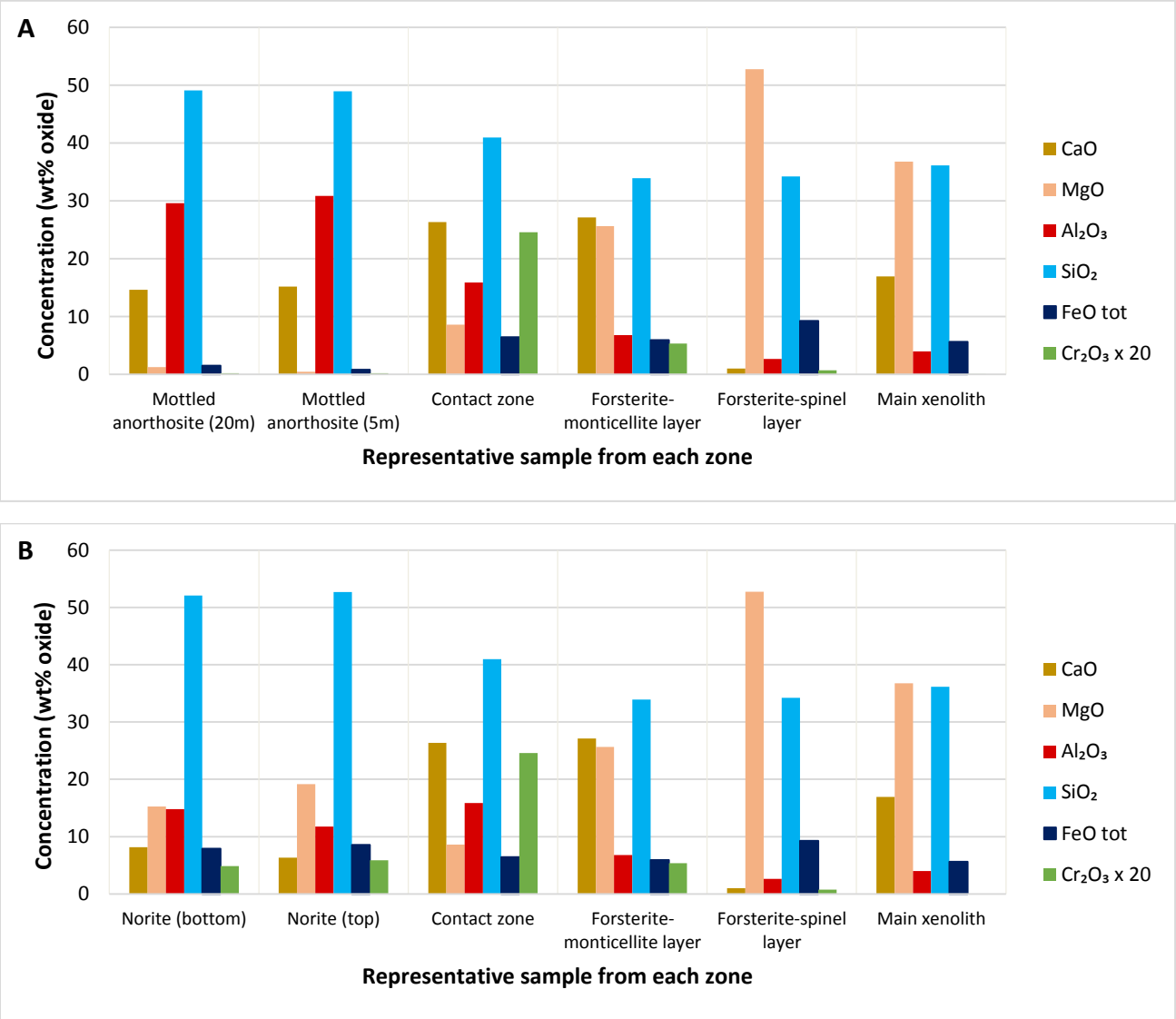

Figure 2.9: Histogram depicting the oxide (wt%) concentration in samples from the Marikana xenolith and its surroundings. A illustrates the variation between the main xenolithic body, contact zone and mottled anorthosites. B illustrates the variation between the main xenolithic body, contact zone and norites studied by Eales *et al*. (1990).

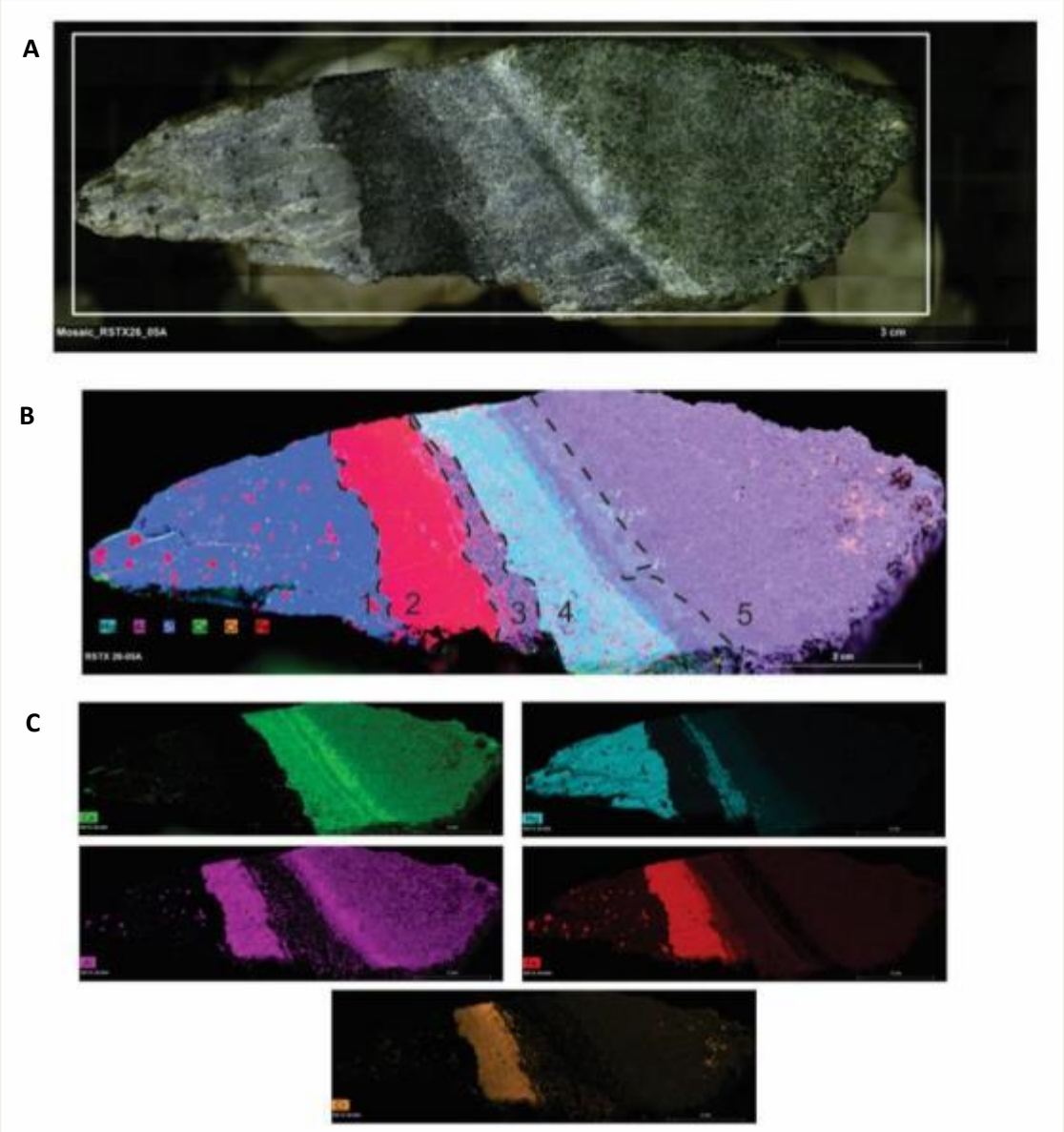

Figure 2.10: Micro-XRF element map for sample RSTX26-05A showing the zonation of minerals immediately adjacent to the xenolith. (A) Mosaic showing mapped area in white rectangle. (B) A composite of selected major elements and (C) individual element maps showing Ca, Mg, Al, Fe and Cr. (1) The forsterite-spinel layer adjacent to the spinel layer (2). This is followed by forsterite-monticellite layer (3), followed by the vesuvianite layer (4), within which a serpentine band occurs, and the clinopyroxene layer (5).

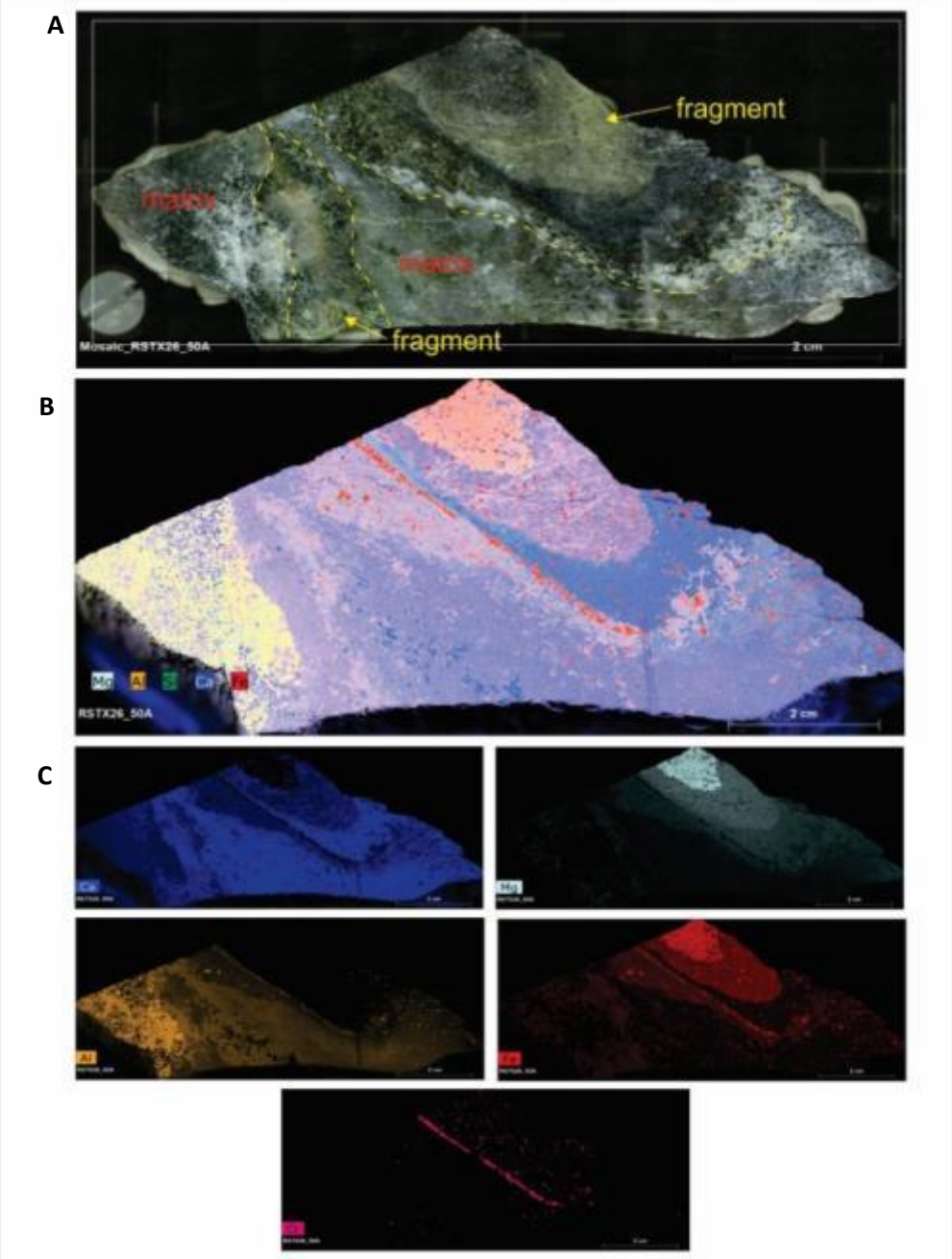

Figure 2.11: Micro-XRF element map for sample RSTX26-50A containing fragments of calc-silicate minerals in the contact zone. (A) Mosaic showing mapped area in white rectangle and indicating fragment and matrix zones. (B) A composite of selected major elements and (C) individual element maps showing Ca, Mg, Al, Fe and Cr.

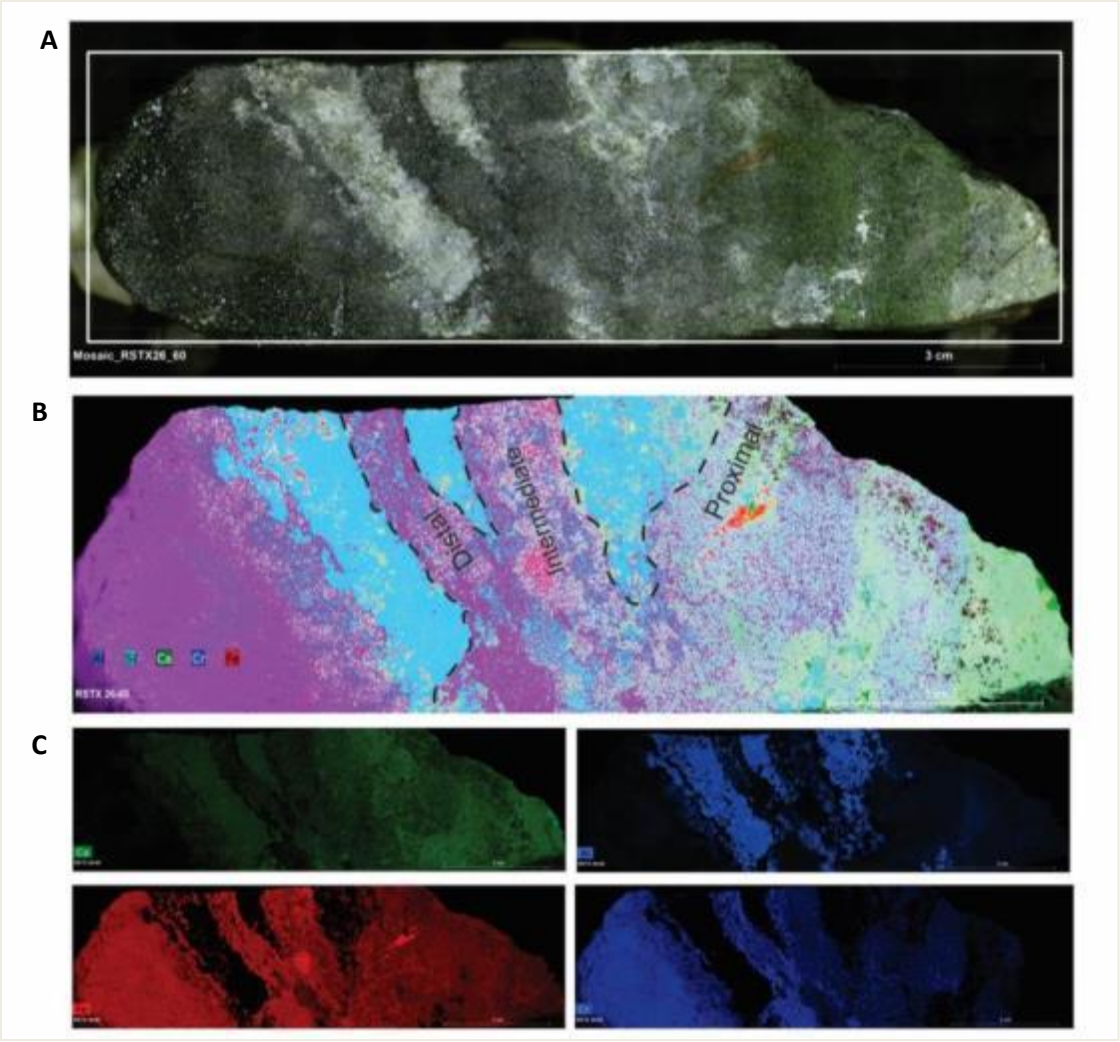

Figure 2.12 Micro-XRF element maps for sample RSTX26-60 containing the chromitite stringer in the contact zone. (A) Mosaic showing mapped area in white rectangle. (B) A composite of selected major elements indicating the proximal, intermediate and distal stringers and (C) individual element maps showing Ca, Al, Fe and Cr.

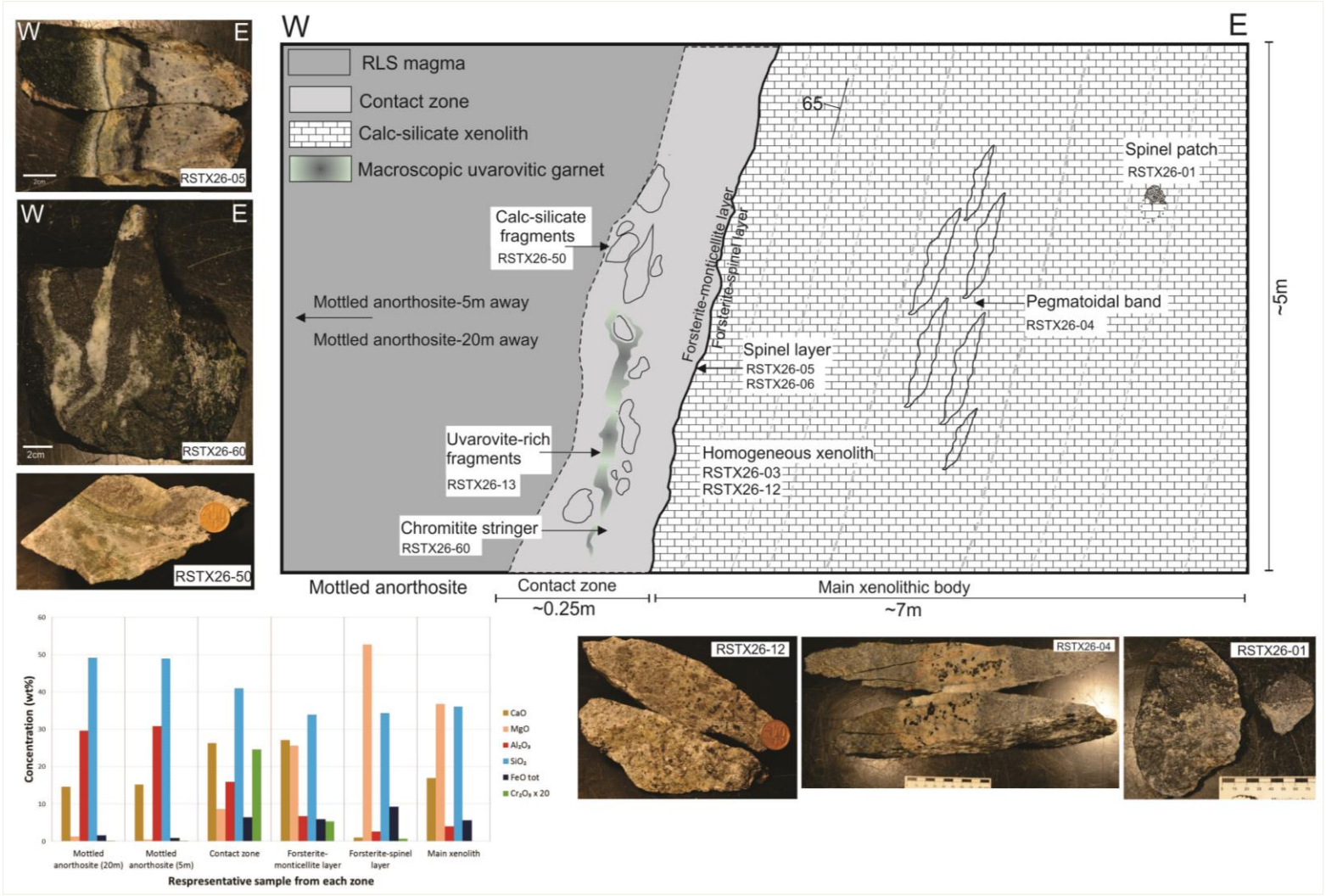

Figure 2.13: Schematic diagram of the Marikana xenolith, Western Limb and surrounding contact zone in the sidewall of Tram Cross-cut 26 underground at Rowland Shaft showing the approximate locations of samples, the corresponding sample identification and whole-rock geochemical data.

2.3 Zwartfontein

Three boreholes that intersect calc-silicate xenoliths in the northern domain of the Northern Limb on Zwartfontein farm, where the footwall is Malmani dolomite and granite (Figure 2.14), were examined and sampled. Cores ZF 116, ZF 116ED1 and ZF 109ED1, ZF 24D1 were selected chiefly because they host large calc-silicate xenoliths that occur over a large range of depth. Unaltered xenoliths were sampled from each core together with the probable edges of xenoliths. The continuity that cores provide allows for scrutiny of the contact relationships. However, determining the edge of the xenoliths (contacts between xenoliths and igneous rock) in the Platreef proved to be difficult because of the presence of parapyroxenite and the high degree of alteration. Parapyroxenite and igneous lithologies surrounding the probable edges of the xenolith were sampled adjacent to the xenoliths up to several metres away from the xenoliths. See Appendix 2 for detailed borehole descriptions.

All sampled rocks were described and classified in accordance with the Platreef Rock Type Manual (Nex *et al*., 2006) which was produced to assist in the classification of Platreef lithologies, given that these rocks have interacted with the footwall and are extremely diverse compared to rocks in the rest of the RLS. The Manual describes and classifies rocks based on internationally recognised terminology. However, it also includes informal terminology in order to account for the uniqueness of the Platreef lithologies (Nex *et al*., 2006). These informal terminologies will be described below where necessary and relevant to rocks from this sample suite. Lithologies encountered in the borehole cores are predominantly pyroxenite, calc-silicate xenoliths, hybrid rocks and parapyroxenites.

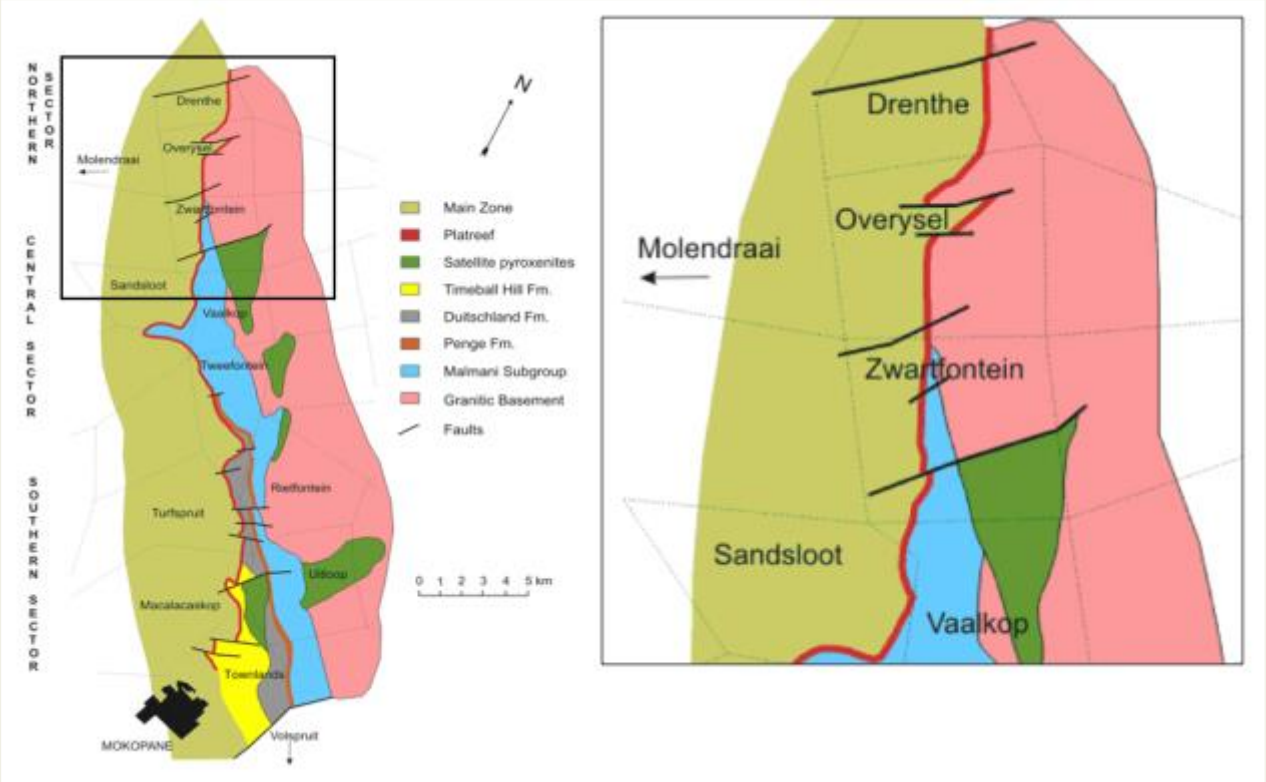

Figure 2.14: Simplified geological map of the Northern Limb with an enlargement of the northern domain, indicating the location of Zwartfontein farm (reproduced from Nex and Kinnaird, (2004) after Van der Merwe, (1978)).

2.3.1 Xenoliths, hybrid rocks and parapyroxenites

According to Bates and Jackson (1987) a calc-silicate forms during metamorphism of limestone or dolomite and contains Ca-bearing silicates like diopside and wollastonite. In the Platreef, according to Nex *et al*. (2006), minerals such as tremolite, forsterite, diopside, periclase, wollastonite, grossular, monticellite, akermanite, spurrite, merwinite and larnite may be found. However, some of these minerals are extremely difficult to identify using hand samples only (Nex *et al*., 2006). Numerous calc-silicate xenoliths are intersected within individual boreholes and, in some cases, they show a great deal of variability in size and mineralogy. They are evident as interlayers within the Platreef package and display a variety of colours including white, cream, grey, and pale to dark green. Most commonly, the xenoliths are coarse-grained and comprise forsterite, monticellite and clinopyroxene, and they are commonly highly

serpentinised (dark-green to black). In one case, a monomineralic clinopyroxene xenolith occurs in sharp contact with pyroxenite (Figure 2.15A). The vertical widths of these calc-silicate xenoliths vary from tens of cm to 3–4 m. Multiple xenoliths in close proximity to one another, interlayered with heterogeneous igneous rock or parapyroxenite, may be distinct xenoliths, or a once-larger xenolith that was fragmented during the emplacement of the magma. In borehole ZF116 a texturally and mineralogically distinct medium-grained xenolith exhibits cream and grey-black layering and patches comprising clinopyroxene and calcite that grades into more regular, mm-scale, grey to yellow fine-grained layers (Figure 2.15B) that comprise serpentine, calcite and other very fine Ca-bearing silicates, but lack forsterite, monticellite and clinopyroxene. In some cases, these layers appear to be continuous and undisturbed, while others exhibit deformation in the form of disharmonic micro-folding (Figure 2.15B).

Figure 2.15: Borehole core (A) ZF 109 ED 1 that intersects coarse-grained monticellite, forsterite and clinopyroxene xenolith (top) displaying green, grey and cream to white colours (~1155 m) and medium-grained, green monomineralic (clinopyroxene) xenolith in borehole (~1162 m). (B) Borehole ZF116 showing medium-grained xenolith (top) that comprises clinopyroxene and calcite (~1453 m) and grades into fine-grained layers (bottom) of serpentine, calcite and other Ca-bearing silicates (~1454 m).

Hybrid rocks are common in the cores. According to the Platreef Rock Type Manual (Nex *et al*., 2006) a hybrid rock is composed of magmatic and metamorphic/metasedimentary components. The hybrid rocks found in borehole ZF 116 ED1 (Figure 2.16) exhibit textural and compositional heterogeneity throughout the core; grain size varies from fine to coarse-grained (Figure 2.16A). These commonly comprise medium-grained feldspathic pyroxenite (igneous) surrounded by medium to dark green clinopyroxene (medium to coarse-grained) and greyish white to cream forsterite (medium-grained) of metamorphic origin (Figure 2.16B).

Serpentinisation is widespread in the hybrid rocks. Fragments of what appear to have been calc-silicate material, now completely serpentinised, occur as well (Figure 2.16C).

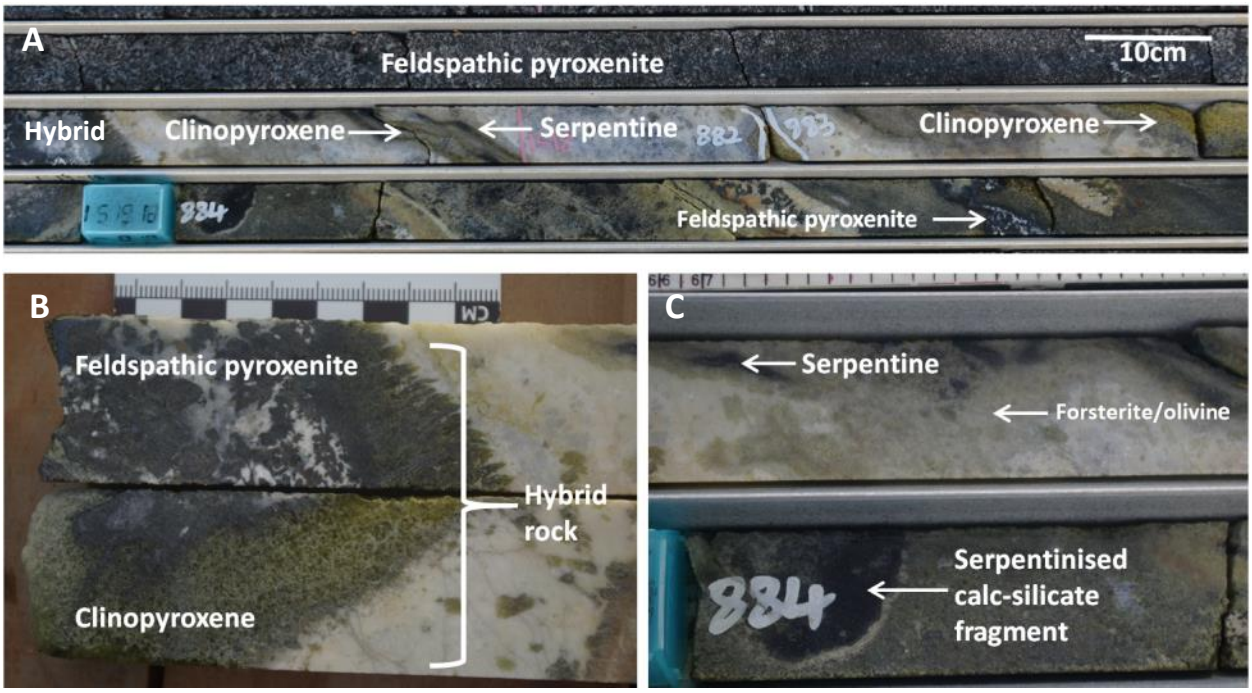

Figure 2.16: Hybrid rock intersections in borehole ZF 116ED1. (A) Feldspathic pyroxenite adjacent to hybrid rock. The unit is texturally and mineralogically heterogeneous between ~1517 and 1519 m depth. (B) Layer of feldspathic pyroxene (left) surrounded by medium to coarse-grained clinopyroxene (medium to dark green) (~1517 m). (C) Completely serpentinised fragment of calc-silicate rock surrounded by highly altered cream mineral and green diopside (~1518 m).

According to Wagner (1929), parapyroxenite is regarded as a metamorphic rock containing metamorphic clinopyroxene. Parapyroxenite is not an internationally recognised term and, according to Bates and Jackson (1987), it should be classified as a calc-silicate. However, in the Platreef, parapyroxenites and calc-silicate *xenoliths*, in particular, can be distinguished from each other (Nex *et al.,* 2006). The term parapyroxenite is used if: (1) the rock displays a metamorphic texture instead of an igneous texture, (2) the rock appears to be a mix of pyroxenite and calc-silicate, or (3) the rock does not fit into any other classification (Nex *et al.,* 2006).

Parapyroxenite occurs throughout the boreholes, indicating that it is a common lithology in the Platreef. The parapyroxenites observed in this sample suite (Figure 2.17) are predominantly medium to coarse-grained, pale green to dark grey and comprise clinopyroxene and serpentine with forsterite and minor calcite and plagioclase. Other units host disseminated sulphides, predominantly pyrrhotite and chalcopyrite. Some units (which surround a calc-silicate xenolith) are characterised by miarolitic cavities that contain calcite and biotite. In this sample suite, several features that distinguish parapyroxenite (Figure 2.17) from the calc-silicate xenoliths are evident: parapyroxenites are always darker (dark green to black) and do not exhibit white/cream colours like calc-silicate xenoliths; parapyroxenite mineralogy includes plagioclase, orthopyroxene and clinopyroxene, minor biotite and sulphides, whereas the calc-silicate xenoliths do not contain the abovementioned minerals (with the exception of clinopyroxene); the texture of the calc-silicate xenoliths makes them variable from the parapyroxenite: calc-silicate xenoliths display recrystallization of coarse interlocking grains and are locally layered, while parapyroxenites in this sample suite are highly altered, making individual grains difficult to identify in most cases, and are never layered.

Figure 2.17: Parapyroxenite associated with serpentine in borehole ZF 116 (~1445 m depth). In some cases (bottom) plagioclase is observed with completely serpentinised grains (black).

2.3.2 Platreef igneous/magmatic lithologies

The xenoliths are most commonly hosted by parapyroxenite, but the main igneous lithologies that surround the parapyroxenite and, in fewer cases, the calc-silicate xenolith directly, include pyroxenite and feldspathic pyroxenite (Figure 2.18A). Pyroxenite contains > 90% cumulus orthopyroxene and clinopyroxene, with minor (≤ 10%) intercumulus plagioclase. It is dark grey-green, typically medium to coarse-grained, with minor biotite and disseminated sulphides (pyrrhotite and chalcopyrite). In some cases it is cross-cut by serpentine veins. Where plagioclase composes > 10% of the rock it is called a feldspathic pyroxenite in the Platreef. Using the International Union of Geological Sciences (IUGS) scheme, a rock containing 85–90% orthopyroxene/clinopyroxene and 10–15% plagioclase would be classified as a norite; however, in the Platreef, the same rock is termed a feldspathic pyroxenite, which implies that it may have economic value and host high PGE grades (Nex *et al*., 2006). Feldspathic pyroxenites vary in grain size from medium to coarse. Pegmatoidal zones of feldspathic pyroxenite (Figure 2.15B) ≤ 20 cm wide are observed and the amount of interstitial plagioclase shows variation. Minor disseminated sulphides (pyrrhotite and chalcopyrite) and biotite are identified in the pegmatoidal zones. In some cases pegmatoidal zones are cross-cut by serpentine veins.

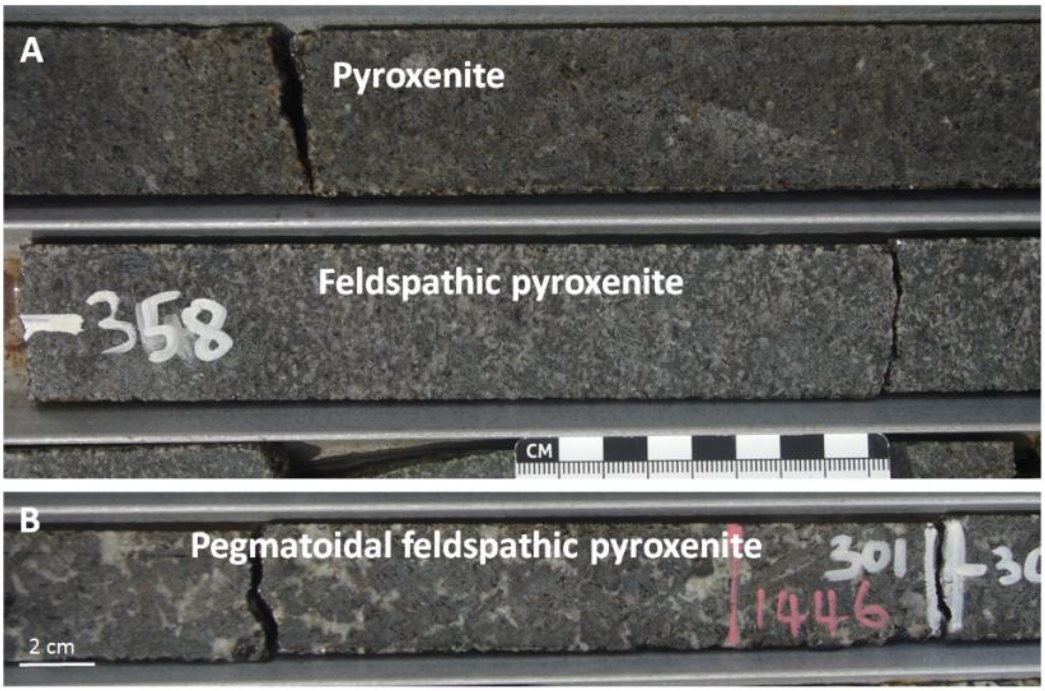

Figure 2.18: (A) Pyroxenite and feldspathic pyroxenite in borehole ZF 116 (~1487 m to 1489 m). Pyroxenite is dark grey/green, while feldspathic pyroxenite contains cumulus plagioclase. (B) Pegmatoidal feldspathic pyroxenite found in borehole ZF 116 (~1446 m).

2.3.3 Whole-rock geochemistry

Whole-rock data for the Platreef package were acquired from previously studied samples constituting the Platreef Rock Type Manual (Nex *et al*., 2006) and shown in Appendix 1D. Samples analysed for the Platreef Manual (Nex *et al*., 2006) relevant to this study include calc-silicates, parapyroxenite, feldspathic pyroxenite and pyroxenite. The calc-silicate xenoliths show considerable variation between samples (Figure 2.19). Major oxides Al_2O_3, Fe_2O_3, CaO and MgO show large ranges of 1.95 wt%–13.49 wt%, 1.22 wt%–17.89 wt%, 10.83 wt%–31.88 wt%, and 1.90 wt%–23.96 wt%, respectively. One xenolith (N31) shows a significant concentration of MnO (12.28 wt%). These compositional differences can be attributed to numerous factors, which include the composition of the source rock and degree of sub-solidus fluid-rock alteration. Parapyroxenites also show large ranges; the greatest range is between Fe_2O_3 (5.16 wt%–17.46 wt%) and MgO (8.24 wt%–13.12 wt%). Smaller ranges exist between Al_2O_3 (from

3.27 wt% to 5.21 wt%) and CaO (from 21.16 wt% to 23.98 wt%). For the igneous samples; the Al_2O_3 content ranges from 6.30 wt% to 13.88 wt%, and CaO from 5.14 wt% to 8.45 wt%. The MgO shows a large range (12.30 wt%–21.11 wt%) and Fe_2O_3 ranges from 9.47 wt% to 13.26 wt%.

Binary variation plots (Figure 2.20) were selected to determine whether or not correlations between major elements exist between the Platreef samples. Overall the data show a scattered trend and no correlation between major oxides is defined.

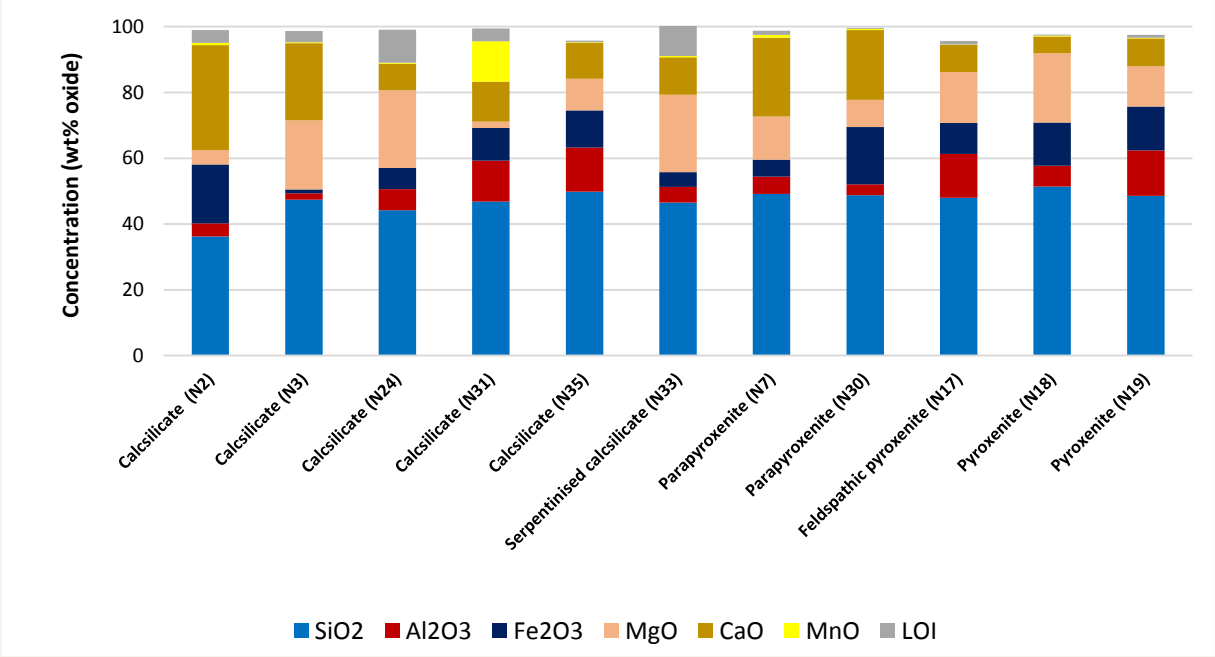

Figure 2.19: Graphical representation of major oxide concentrations of calc-silicates, parapyroxenites and igneous rocks found in the Platreef (data from Nex *et al*., 2006).

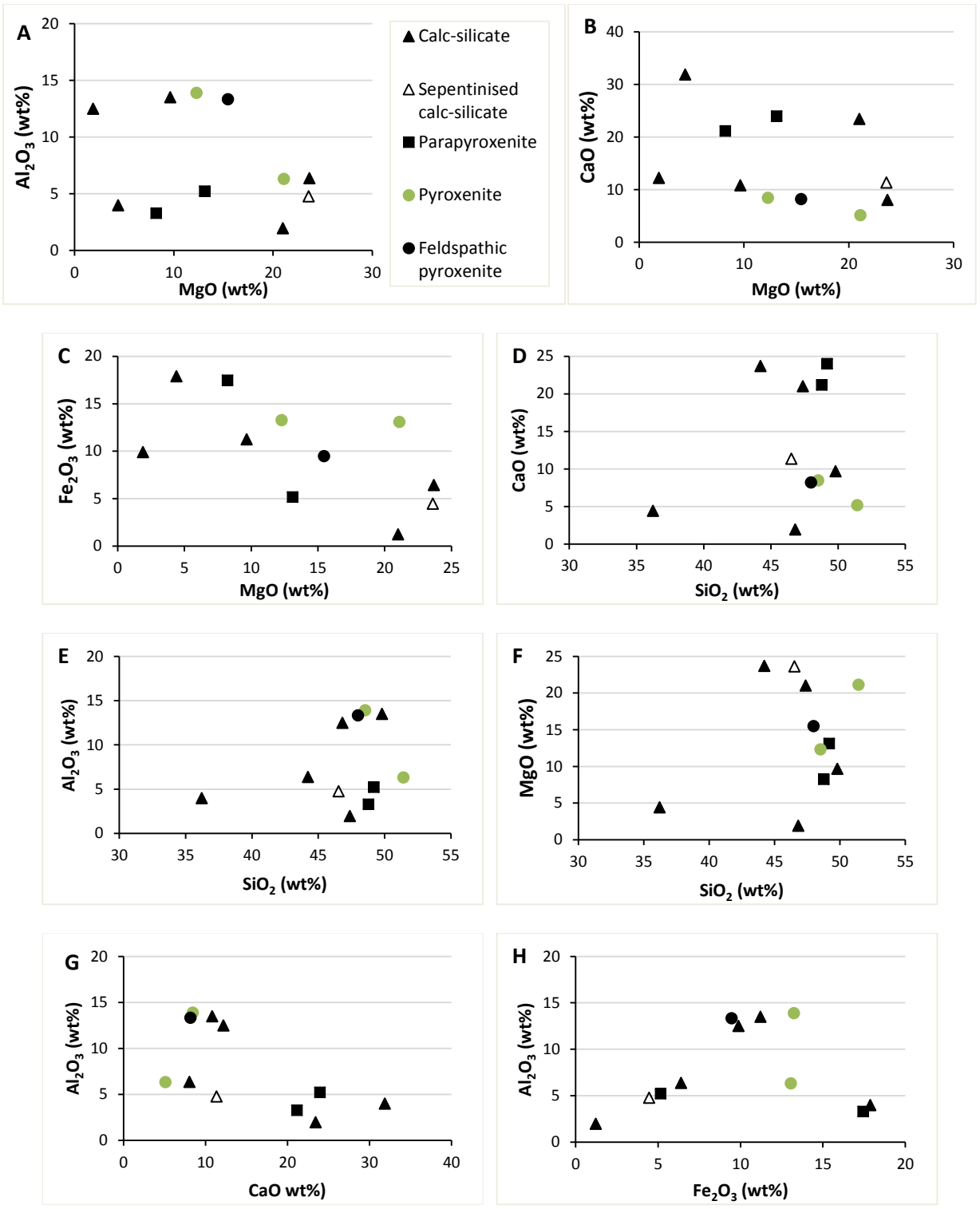

Figure 2.20: Binary variation plots representing the correlations between major elements Al_2O_3, MgO, SiO_2, CaO and Fe_2O_3 for Platreef lithologies (data from Nex *et al*., 2006).

2.4 Discussion and summary

This study involves the investigation of one calc-silicate xenolith in the upper Critical Zone in the Western Limb of the RLS and it is compared with numerous calc-silicate xenoliths located in three boreholes that intersect the Platreef, Northern Limb on Zwartfontein farm. The main xenolithic bodies in both the Marikana and Zwartfontein occurrences, where less altered, are predominantly composed of monticellite, forsterite and spinel. However, the Zwartfontein xenoliths show a greater variability in mineralogy and, additionally, host clinopyroxene. In one case an entire xenolith comprises monomineralic clinopyroxene, whereas in Marikana a layer of monomineralic clinopyroxene is observed only at the western edge of the xenolith (Figure 2.4). In the case of the Marikana xenolith the aforementioned layer appears to be similar to the monomineralic clinopyroxene zone described by Willemse and Bensch (1964) which occurs along the xenolith-igneous rock contact in an occurrence in the Eastern Limb.

Given that only borehole core is available for study in Zwartfontein, it has proved difficult to identify xenolith edges and similar zonation of mineral assemblages and/or minerals like those described by Willemse and Bensch (1964) in section 1.3.2.1. The difficulty in identifying xenolith edges can be attributed to the inability to distinguish whether or not xenoliths of variable thicknesses, interlayered with heterogeneous igneous rock or parapyroxenite in close proximity with each other, are individual xenoliths, that is, single and independent fragments of dolomitic rock that became isolated from the dolomitic footwall, metamorphosed and relocated within the Platreef package; or whether they represent a single large xenolith that was fragmented into smaller pieces during the emplacement of Platreef magma.

The contact between the main xenolithic body and either the *contact zone* and/or the igneous rock is not easily identified. In the Western Limb occurrence, the reason is because, at the time of sampling, the sidewall was covered with shotcrete. However, sufficient evidence (see Chapters 3 and 4) indicates that the contacts are gradational rather than sharp. The spinel layer, although mineralogically different from the xenolith, does not mark the edge of the xenolith because calc-silicate rock layers occur adjacent to the spinel layer towards the contact

zone (Figure 2.4). Visual evidence shows fragments of calc-silicate rock present in the contact zone. This could have occurred as (1) fragments were isolated from the main xenolithic body and moved outwards towards the magma during interaction with the magma, or (2) it represents a zone within which calc-silicate rock and magma mingling occurred in which case the calc-silicate rock was not completely digested by the magma, leaving behind fragments. In both cases, interaction between the calc-silicate rock and the magma has taken place and developed a zone where both metamorphic and igneous minerals and textures are evident.

CHAPTER 3: THIN-SECTION MICROSCOPY

3.1 Introduction

This chapter provides a summary of the observations made from a total of 73 polished thin-sections, 20 from the Western Limb and 48 from the Platreef (see Appendix 3 for description of all polished thin-sections). All samples were examined in transmitted and reflected light; the latter was particularly used to identify oxides and sulphides in the Western Limb and Platreef rocks, respectively. Backscattered electron (BSE) images were also used where necessary.

Multiple thin-sections were selected from the different zones, that is, xenolith, contact, and igneous rock because each zone showed a great deal of macroscopic variability. Variations within individual zones were also sampled where there was a change in (1) texture, as observed in the main xenolithic body at Marikana, and (2) mineralogy, as observed in the contact zone. The modal abundance of minerals present was estimated visually, and documented together with texture and alteration. These observations were used to determine the variation in mineralogy between and within zones, establish the paragenetic sequence, and identify any mineral and textural signs of interaction between the xenolith and RLS magma. This petrographic study begins with descriptions of the main xenolithic body, followed by the contact zone, and lastly, the surrounding igneous rocks in order to establish the spatial variation in mineralogy. All mineral abbreviations are after Whitney and Evans (2010).

3.2 Marikana

3.2.1 Main xenolithic body

Samples from the main xenolithic body are coarse-grained and are composed of three main phases: monticellite (70%), forsterite (20%) and spinel (10%) (Figure 3.1). Monticellite grains are idioblastic to hypidioblastic and vary in size from 0.2 cm to 1.5 cm. The grains display undulose extinction and irregular boundaries against the other minerals. Monticellite commonly exhibits sub-parallel fractures, and in some cases, the fractures are filled with a micro-crystalline rust-coloured mineral. In a few cases, monticellite interpenetrates forsterite. Forsterite exists as

idioblastic to hypidioblastic grains and varies in size from 0.5 cm to 1.5 cm. It shows strong, pale green to pink pleochroism. Backscattered electron (BSE) imagery confirmed the presence of thin monticellite exsolution lamellae in forsterite (Figure 3.2). Spinel occurs as idioblastic to hypidioblastic grains enclosed in both forsterite and monticellite and, less commonly, interstitially along the boundaries of forsterite and monticellite. The crystal sizes vary from 0.1 mm to 3 mm. No compositional variation is apparent in transmitted light and all spinel grains are dark brown. However, BSE images (Figure 3.2) confirmed complex compositional variation of individual spinel grains. The spinel exhibits exsolution textures involving Fe-Ti spinel (magnetite) lamellae and host Mg-Al spinel (spinel, *sensu stricto*) that was confirmed by EMPA (section 4.3.5). The magnetite exsolution lamellae range in size from < 50 µm to 500 µm and comprise ~25% to ~30% of the spinel grains. The lamellae appear to be crystallographically aligned in some cases; in other cases magnetite occurs as irregular patches; it also occurs as discontinuous rims along some grains; and appears as very fine dust (Figure 3.2).

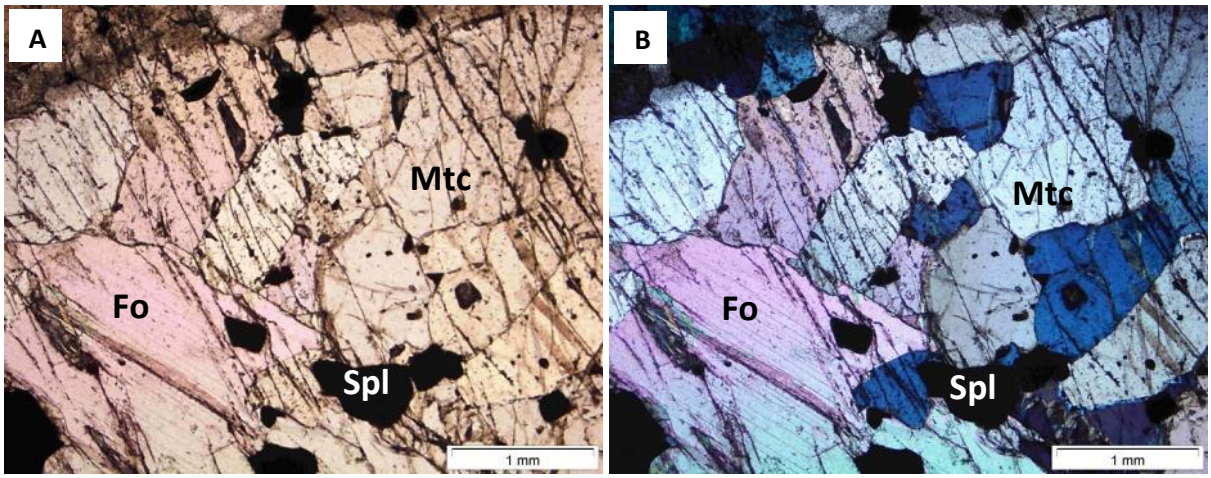

Figure 3.1: Photomicrograph of the Western Limb calc-silicate xenolith (from the main xenolithic body, RSTX26-12) (A) PPL, (B) XPL. Monticellite can be distinguished by planar to irregular fractures, whereas forsterite has fewer fractures and very fine exsolution lamellae. Alteration occurs along the fractures. Abbreviations: Mtc = monticellite, Fo = forsterite, Spl = spinel.

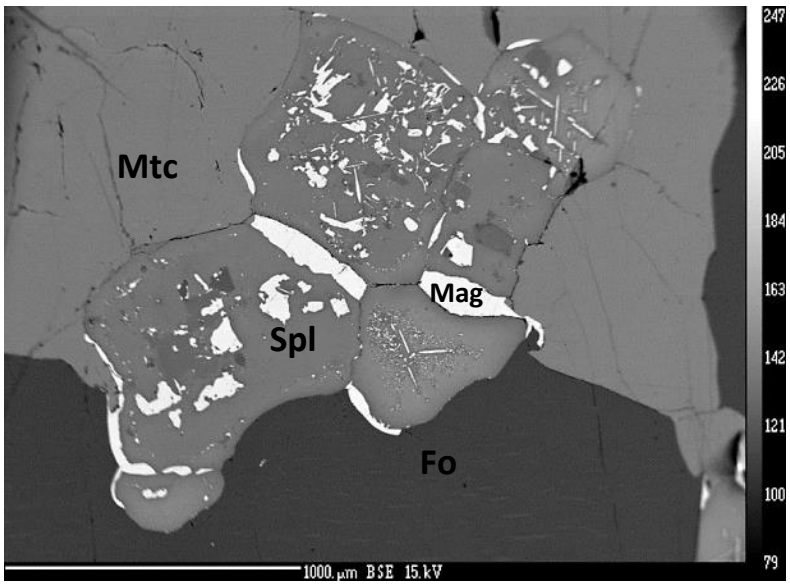

Figure 3.2: BSE image depicting spinel exsolution textures (main xenolithic body, RSTX26-12), where white lamellae are Fe-Ti spinel (magnetite). Dark grey areas surrounding the white lamellae are zones of Fe depletion; medium grey areas are Mg-Al spinel. The exsolution lamellae mineral (magnetite) occurs as discontinuous rims along the grain boundaries of the Mg-Al spinel. Some of the lamellae patterns in the spinel appear to be crystallographically aligned, while others occur as irregular patches to fine dust. The monticellite exsolution lamellae in forsterite are visible at the bottom of the image. Abbreviations: Mtc = monticellite, Fo = forsterite, Spl = spinel, Mag = magnetite.

Variations in mineral modal abundance are observed in the form of the spinel patch and pegmatoidal band (located in the main xenolithic body, Figure 2.2). Both contain minor amounts of calcite but no forsterite. The sample from the spinel patch is composed of idioblastic spinel (90%) and hypidioblastic monticellite (10%), which is interstitial (Figure 3.3A). Spinel varies in size from 0.1 mm to 2 mm, is brown and displays zonation, where the cores are a darker brown than the rims. Data from EMPA (section 4.3.5) indicate that these spinel grains are Al-Mg-Fe-bearing, and that Mg decreases and Fe increases slightly towards the rim. Immediately surrounding the spinel patch is an area dominated by monticellite (90%) and spinel (10%), with minor calcite (Figure 3.3B). Monticellite grains are idioblastic to hypidioblastic and vary in size from 0.1 cm to 1 cm. Minor calcite was identified in one case and it occurs interstitially to the monticellite, as depicted in Figure 3.3B, and does not occur anywhere else in

this sample. Spinel occurs as black idioblastic to hypidioblastic grains and varies in size from 0.1 to 2 mm. It is commonly enclosed by monticellite or lies at the edges of monticellite grains.

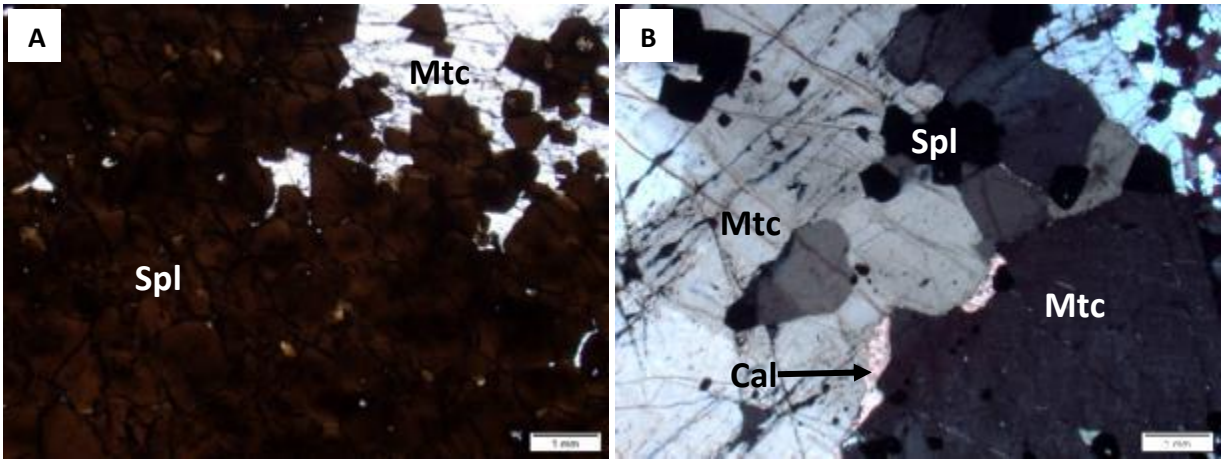

Figure 3.3: Photomicrographs of the spinel patch and surrounding monticellite (RSTX26-01). (A) The spinel patch is predominantly composed of zoned spinel with minor monticellite (PPL). (B) Coarse monticellite with interstitial calcite and idioblastic spinel. The arrow points to interstitial calcite (XPL). Abbreviations: Mtc = monticellite, Cal = calcite, Spl = spinel.

Pegmatoidal bands show features similar to the area immediately surrounding the spinel patch. They are composed of monticellite (95%) and spinel (5%). Monticellite grains are idioblastic to hypidioblastic and vary in size from 0.1 cm to 2 cm, but most grains are coarser than monticellite elsewhere in the xenolithic body. The spinel grains are very variable and range from idioblastic to hypidioblastic polygonal, and from 0.2 mm to 7 mm (Figure 3.4A). Zonation is observed in the larger polygonal to idioblastic spinel grains, where the cores are richer in Al (light brown) and the rims are richer in Fe (dark brown) (see section 4.3.5). The cores of these spinel grains may contain a minor amount of calcite (Figure 3.4B). Finer spinel grains, as well as the rims of the larger polygonal grains are characterised by magnetite exsolution lamellae (Figure 3.5). The lamellae range in size from < 10 µm to 150 µm and occur as globular to irregular patches.

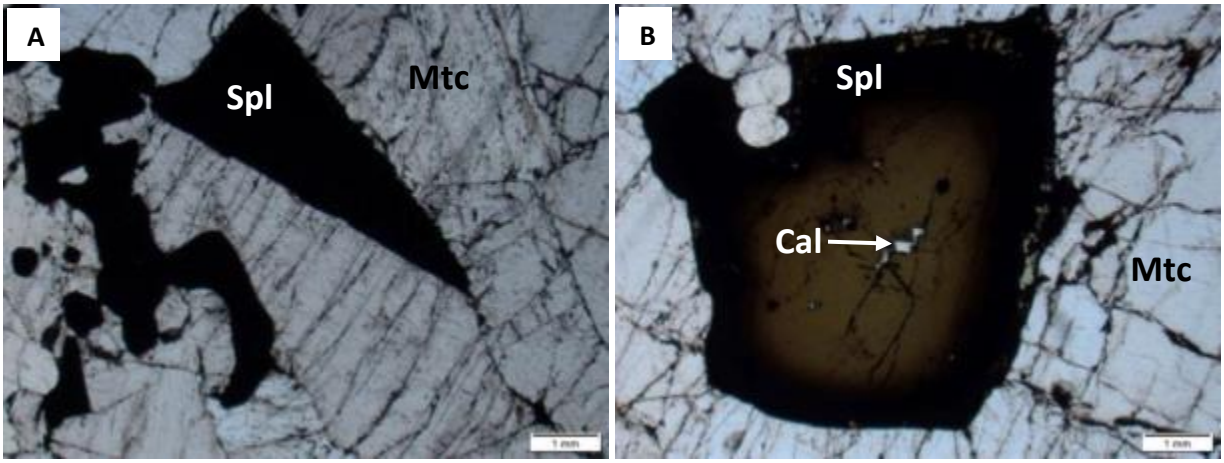

Figure 3.4: Photomicrographs of spinel found in the pegmatoidal bands (RSTX26-04), both in PPL. (A) Idioblastic to hypidioblastic polygonal spinel showing zonation and exsolution textures observed in BSE images. (B) Large spinel crystal showing zonation, with calcite in the centre (depicted by the arrow). Abbreviations: Mtc = monticellite, Cal = calcite, Spl = spinel.

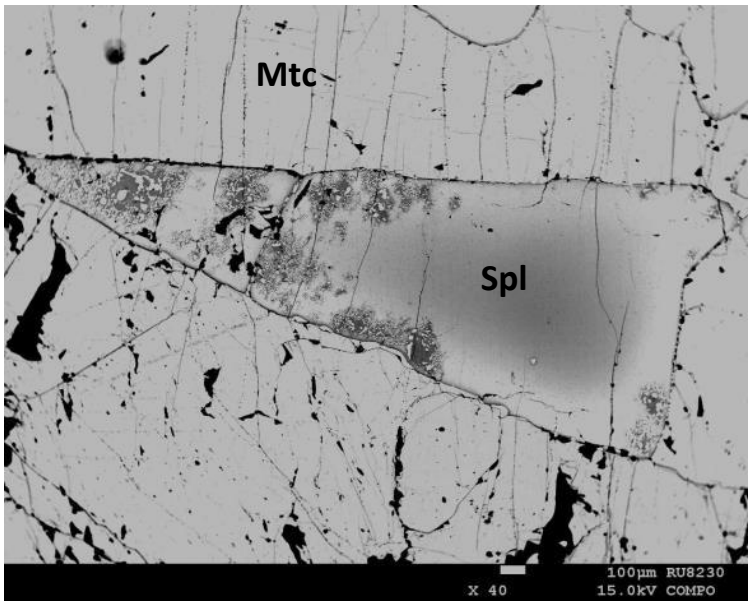

Figure 3.5: BSE image of spinel found in the pegmatoidal bands (RSTX26-04). The individual grains (triangular in this image) exhibit zoning, where the darker core is slightly richer in Al and the rim is richer in Fe. Mg remains relatively constant throughout the crystal. The rims are characterised by exsolution; white lamellae are magnetite (Fe-Ti spinel); dark grey mineral surrounding the white lamellae are zones of Fe depletion, and medium grey mineral is Mg-Al spinel. Abbreviations: Mtc = monticellite, Spl = spinel.

The forsterite-spinel layer, which is adjacent to the spinel layer (Figure 3.6), is composed of two phases: forsterite and spinel. BSE imaging (Figure 3.7) depicts textural and chemical variation of this spinel.

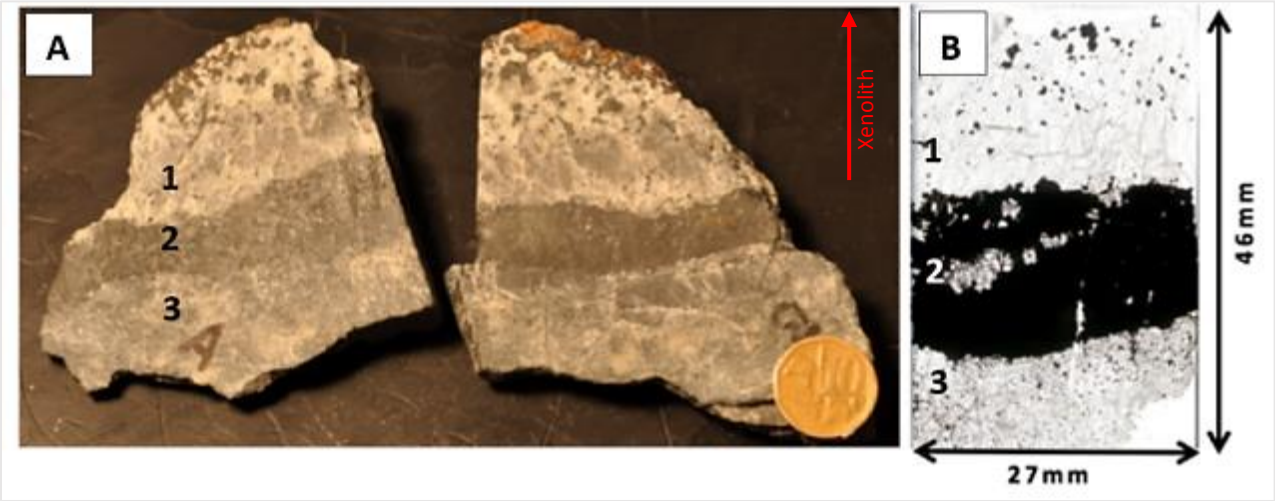

Figure 3.6: Sample from the western end of the main xenolithic body showing (1) the forsterite-spinel layer, (2) the spinel layer and (3) the forsterite-monticellite layer (RSTX26-06). (A) Photograph showing banding of the rock and (B) the corresponding thin-section scan of the sample.

The forsterite-spinel layer (1) comprises idioblastic to hypidioblastic forsterite (90%) grains varying in size from 0.5 cm to 2 cm. Dark to light brown (in transmitted light) spinel grains (10%) are idioblastic to hypidioblastic and vary in size from 0.5 mm to 3 mm. Spinel exhibits exsolution textures in transmitted light, but it is more clearly observed in BSE images (Figure 3.7A) where white is magnetite (Fe-Ti spinel), dark grey mineral is least-enriched in Fe, and medium grey mineral is Mg-Al spinel. Spinel in the forsterite-spinel layer is dominated by magnetite lamellae (70%) which display a patchy appearance; and the margins are Fe-poor (Figure 3.7A). The magnetite lamellae located in the margin of the spinel layer (adjacent to the forsterite-spinel layer) comprises 40% of the spinel host; ranges in size from < 10 µm to 250 µm; and occurs as globular shaped and crystallographically aligned laths (Figure 3.7B).

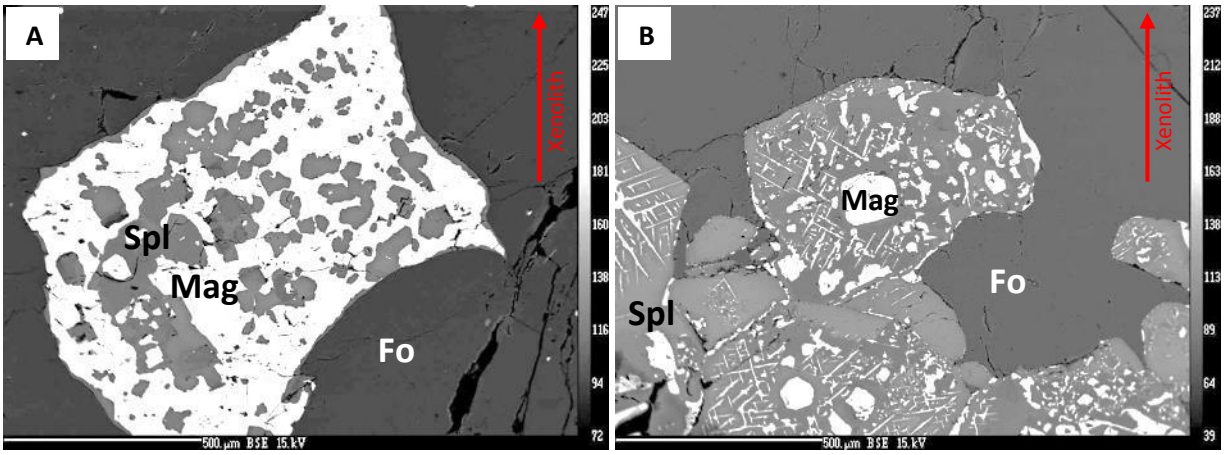

Figure 3.7: BSE images of (A) spinel in the forsterite-spinel layer (RSTX26-06, see Figure 3.6, label 1). (B) Spinel located in the margin of the spinel layer (adjacent to the forsterite-spinel layer) (Figure 3.6 top of label 2). Spinel exhibits exsolution textures where white is magnetite (Fe-Ti spinel), dark grey where Fe is least enriched; medium grey mineral is Mg-Al spinel. The red arrow indicates the direction of the main xenolithic body. Abbreviations: Fo = forsterite, Spl = spinel, Mag = magnetite.

The spinel layer (2) is ~0.5 to 1.5 cm thick (Figure 3.6) and is composed of 90% spinel and 10% forsterite. The spinel grains are idioblastic and range in size from 0.25 mm to 1 mm; in transmitted light, the spinel exhibits various shades of brown and black (Figure 3.8A). The black areas are magnetite (Fe-Ti-rich) lamellae, commonly irregularly surrounded by light brown spinel, which is the least enriched in Fe; the medium brown areas are Mg-Al spinel (section 4.3.5). The spinel layer is granoblastic with well-developed triple-junctions identified in BSE images. Magnetite lamellae range in size from < 10 µm to 250 µm and comprise 10% to 15% of the host spinel (Figure 3.8B).

Immediately adjacent to the spinel layer, the forsterite-monticellite layer (3) is composed of 60% idioblastic forsterite grains that vary in size from 0.5 mm to 0.5 cm with the exception of a single, large (~2 cm) crystal immediately adjacent to the spinel layer and 15% hypidioblastic monticellite. The idioblastic spinel grains (25%), which are finer than those in the forsterite-spinel layer of the xenolith and spinel layer, vary in size from 0.1 mm to 1 mm (Figure 3.8C). Spinel is more uniformly distributed in this layer and exhibits green to brown shades (Figure

3.8C). Backscattered electron images depict exsolution textures (Figure 3.8 B and D): light grey/white lamellae are magnetite (Fe-Ti spinel), dark grey regions surrounding the light grey/white lamellae are zones of Fe depletion, and medium grey represents Mg-Al spinel. The magnetite lamellae in layer 3 vary in size from < 10 μm to 100 μm and comprise ~15% of the host spinel. The exsolution lamellae in layers 2 and 3 appear to be crystallographically controlled, but magnetite also occurs as discontinuous rims along some grain boundaries and as globular to irregular patches. There is a decrease in the proportion of magnetite in the host spinel outward from the forsterite-spinel layer; spinel in the forsterite-spinel layer (layer 1 in Figure 3.6) is the most magnetite-rich and spinel in the forsterite-monticellite layer (layer 3 in Figure 3.6) is the least magnetite-rich.

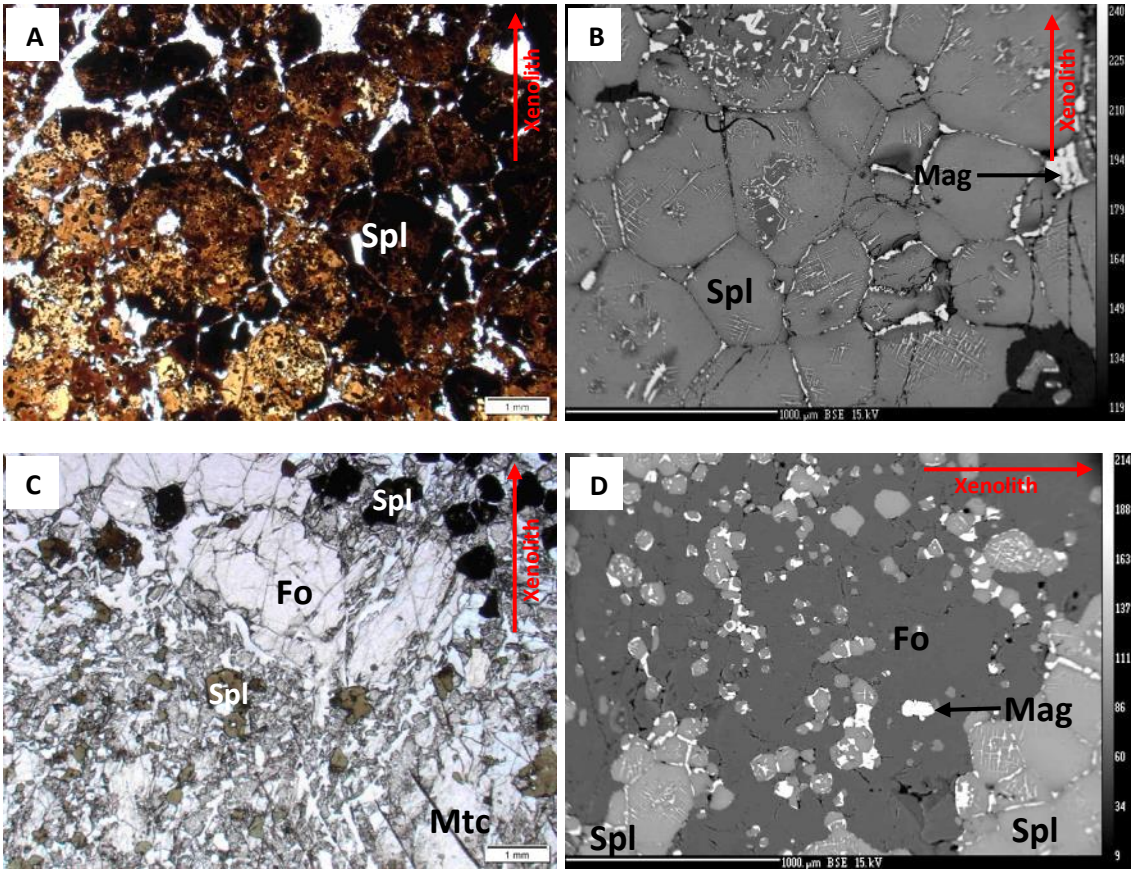

Figure 3.8: Spinel layer (RSTX26-06) exhibiting multiple shades of brown and representing compositional variation in the photomicrograph (A) and BSE image (B) showing grains in the spinel layer that exhibit a granoblastic texture with well-developed triple-junctions. (C) Spinel found in the forsterite-monticellite layer are green in colour and compostionally different; Mg-Al spinel are composed of less Fe. (D) BSE image of forsterite and spinel found in the forsterite-monticellite layer. Light grey/white lamellae are Fe-Ti spinel, dark grey mineral surrounding the light grey/white lamellae are zones of Fe depletion and medium grey mineral is Mg-Al spinel (B and D). The red arrow indicates the direction of the main xenolithic body. Abbreviations: Spl = spinel, Mag = magnetite, Fo = forsterite, Mtc = monticellite.

The 3 cm-thick, highly altered vesuvianite layer adjacent to the forsterite-monticellite layer (Figure 2.4) is divided into 2 sublayers by an ~2 mm wide serpentine band. The layer proximal to the xenolith is composed of vesuvianite (45%), spinel (20%), monticellite (15%) and forsterite (20%). Xenoblastic vesuvianite has been altered and displays light to turbid brown shades. It encloses idioblastic to hypidioblastic brown to green spinel, which varies in size from 0.1 mm to 0.8 mm. Monticellite is hypidioblastic to xenoblastic and varies in size from < 0.1 mm to 1 mm.

The forsterite content (hypidioblastic to xenoblastic grains varying in size from 0.4 mm to 2.5 mm) increases towards the serpentine band (Figure 3.9), whereas monticellite decreases. The layer distal to the xenolith is composed of vesuvianite (90%) and spinel (10%). The vesuvianite is xenoblastic and displays a variety of shades of brown. The degree of alteration is much higher in this zone, making it difficult to identify any other features. Green spinel is idioblastic to hypidioblastic and finer, at ~0.2 mm (Figure 3.9A).

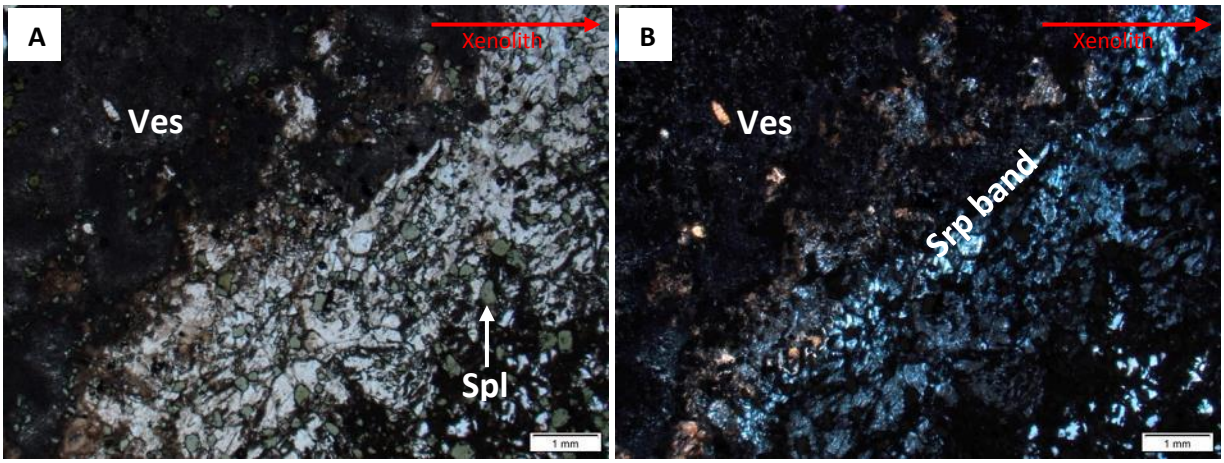

Figure 3.9: Photomicrograph depicting the highly altered vesuvianite zone (RSTX-26-05). (A) In PPL green spinel can be seen throughout the thin-section. (B) In XPL an ~2 mm serpentine band ("Srp band" in image) is evident separating the vesuvianite, monticellite and spinel area from the vesuvianite and spinel area, which shows greater alteration. The red arrow indicates the direction of the main xenolithic body. Abbreviations: Ves = vesuvianite, Spl = spinel, Srp = serpentine.

3.2.2 Contact zone

In this zone, rocks appear to be a mixture of two components, that is, zoned calc-silicate rock fragments and garnet masses (metasedimentary) surrounded by a plagioclase-diopside-dominated matrix, with minor spinel and garnet, in which the two principal components vary significantly in relative proportions, and a chromitite stringer (igneous); thus, this zone hosts the most variable mineral assemblages and complex textures. Important features will be described which include: the calc-silicate rock fragments and the chromitite stringer, together with the minerals associated with them.

Calc-silicate rock fragments are composed of calc-silicate minerals, particularly monticellite. The cores of these fragments are generally dark grey (Figure 2.5). The sample chosen for petrographic study (Figure 3.10) measures 1.8 cm along the long axis and contains a core of monticellite that shows increasing turbidity towards the margin. The minerals surrounding the fragment are fractured, with the degree of fracturing decreasing away from the monticellite core. Well-defined zonation of minerals is evident in this sample: the edge of the monticellite core is characterised by a band (< 0.1 mm to 0.5 mm thick) of zoned spinel grains with dark brown cores and light brown rims. EMPA (section 4.3.5) indicates the cores are Cr-rich and rims are Mg-Al-rich. This is followed by a highly fractured ~2 mm-thick band of diopside (confirmed by EMPA in section 4.3.3). Adjacent to this band (left of thin-section) is a layer that comprises idioblastic to hypidioblastic monticellite (30%, varying in size from 0.5 mm to 1 m); idioblastic to hypidioblastic vesuvianite (25%, varying in size from 0.5 mm to 1.5 mm); idioblastic to hypidioblastic diopside (25%, varying from 0.1 mm to 6 mm); garnet (10%, varying in size from 0.2 mm to 1 mm); and idioblastic spinel (10%). In this layer vesuvianite displays a high degree of alteration and varies from light to dark turbid brown; it appears to replace pre-existing minerals such as monticellite. Diopside occurs in close association with monticellite, vesuvianite and garnet. The garnet grains range from apple-green to pale green (uvarovite) and colourless (grossular) (section 4.3.6.1); and commonly occur as irregularly shaped clusters surrounded by diopside. Spinel occurs in different associations: enclosed in garnet; without garnet, but in association with diopside; with vesuvianite, and also as a rim around the monticellite fragment (Figure 3.10). The spinel composition varies, as indicated by the different shades of brown, as well as by the occurrence of green spinel, which may be confused with uvarovitic garnet. Individual spinel grains, as well as those that rim the monticellite fragments, are zoned.

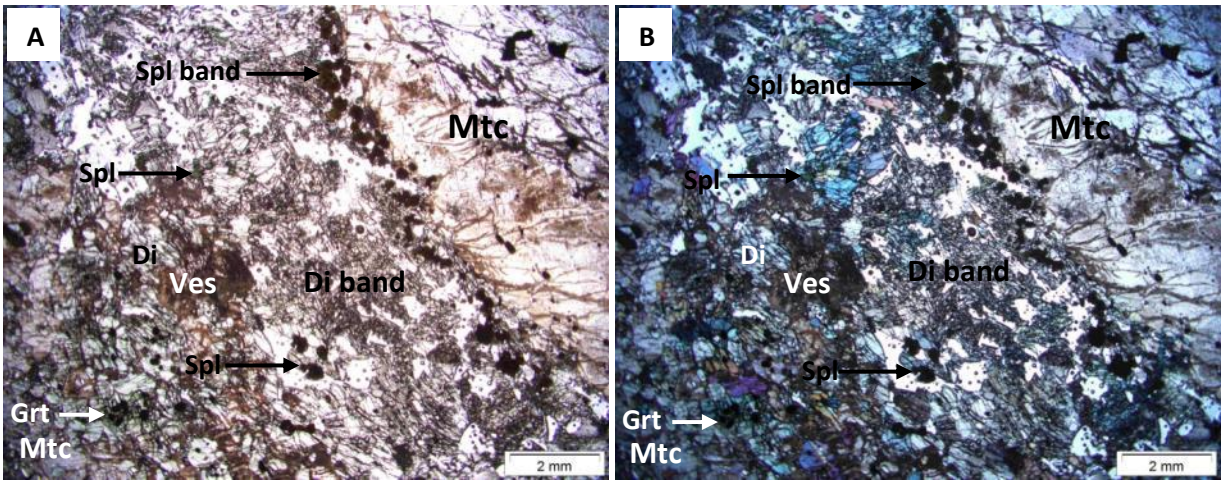

Figure 3.10: Photomicrograph showing calc-silicate fragment RSTX26-52 from the contact zone. Unaltered monticellite occurs in the core of the fragment (right), while altered monticellite occurs closer to the margin. The fragment core is rimmed by zoned spinel, with Cr-rich cores and Mg-Al-rich rims (see section 4.3.5). Diopside closest to the fragment shows the highest degree of fracturing. Green spinel occurs with the diopside. Beyond this region the degree of fracturing decreases and monticellite, diopside and garnet, together with altered vesuvianite, occur. (A) in PPL, (B) in XPL. Abbreviations: Mtc = monticellite, Di = diopside, Spl = spinel, Ves = vesuvianite, Grt = garnet.

Calc-silicate fragments are surrounded by a greyish-white matrix (Figure 2.5), which is dominated by plagioclase (50%). The samples chosen for petrographic study can be divided into plagioclase (Figure 3.11 A and B) and clinopyroxene domains (Figure 3.11 C and D). Plagioclase (0.5 mm to 2 mm in size) occurs in different associations: zones that comprise mostly euhedral to subhedral plagioclase, and zones where diopside is interstitial to subhedral plagioclase. In the latter, diopside (30%) grains are anhedral, varying in size from 0.5 mm to 4 mm. In some cases, diopside inclusions are present in the plagioclase, but more commonly diopside acts as the interstitial phase (Figure 3.11 A and B). In the clinopyroxene-bearing domain wollastonite exsolution lamellae occur in the diopside grains. The garnet is pale green (Cr-bearing/uvarovitic) (5%) to colourless (grossular) (15%). The pale green garnet occurs as circular clusters/aggregates in which the core exhibits the darkest shade of green (Cr-rich) and the rim is colourless (Al-rich) (Figure 3.12 C and D). Grossular also occurs as reaction rims between plagioclase and diopside. Many features are better observed in BSE images and include

grossular reaction rims between plagioclase and diopside; circular clusters/aggregates of Cr-bearing (uvarovitic) garnet which exhibit sieve-like textures; diopside inclusions in plagioclase as small as 10 μm; and wollastonite exsolution hosted by diopside (Figure 3.12A). Grossular reaction rims give the plagioclase an irregular shape. However, the lath shape consistent with a cumulus igneous texture is still visible (Figure 3.11 C and D). In some cases, uvarovitic garnet aggregates are characterised by Cr-spinel at the core (Figure 3.12B). Cr-spinel constitutes < 1% and is always enclosed by uvarovitic garnet.

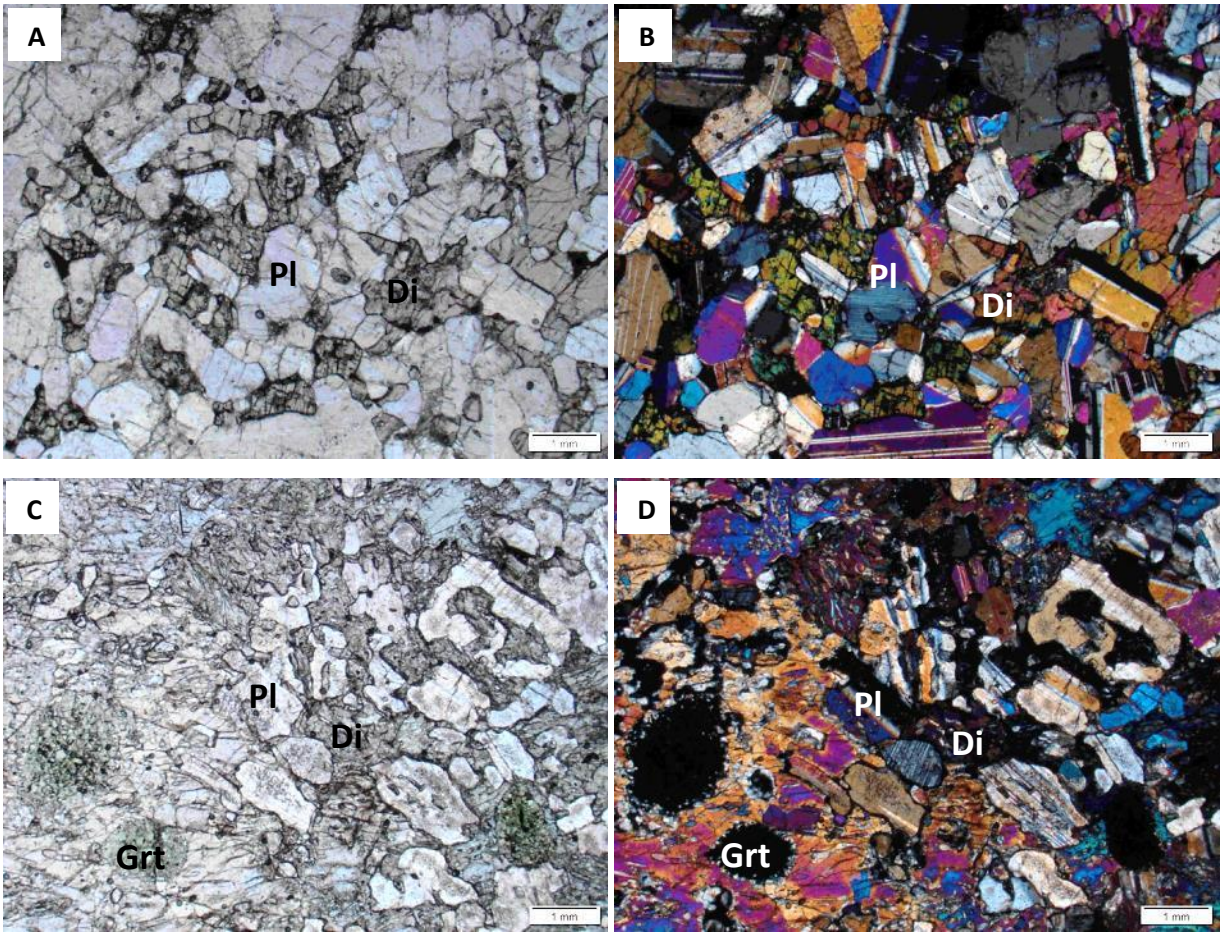

Figure 3.11: Photomicrograph showing a plagioclase dominated sample from the contact zone matrix (RSTX26-51) in PPL (left) and XPL (right). (A and B) Subhedral plagioclase with interstitial diopside gives this part of the sample a cumulus igneous texture. (C and D) In some cases, plagioclase cores appear to be darker in PPL due to the presence of numerous small (< 10 µm) diopside inclusions. Aggregates of zoned garnet with Cr-rich cores and grossular rims occur in the same sample, and are visible at the bottom of the photomicrograph. Garnet is pale green in PPL and isotropic in XPL. Abbreviations: Pl = plagioclase, Di = diopside, Grt = garnet.

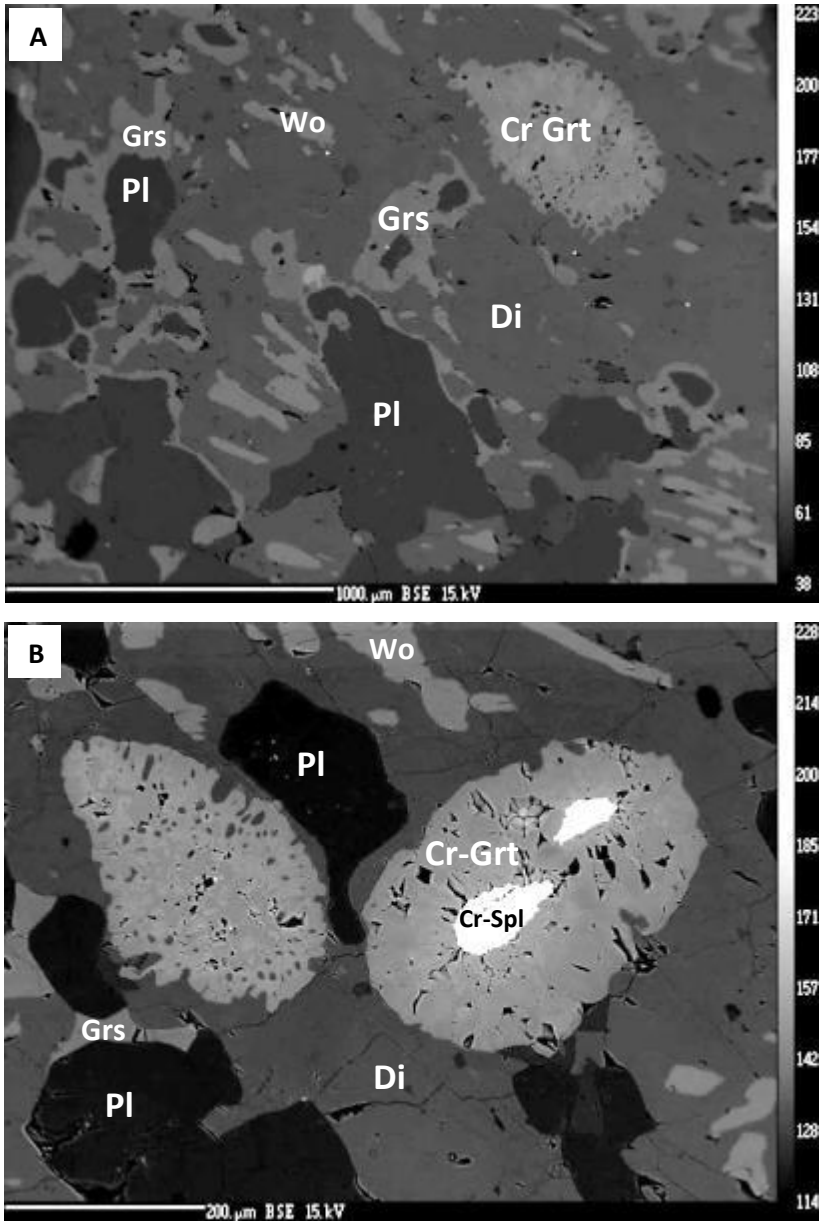

Figure 3.12: BSE images depicting complex features in the contact zone sample RSTX26-51 that cannot be identified in thin-section analysis. (A) Grossular occurs as reaction rims between plagioclase and clinopyroxene. Cr-rich garnet forms clusters/aggregates, and sub-grains are zoned with Cr-rich cores and Al-rich rims. Diopside hosts wollastonite inclusions, which show a preferred (NW-SE orientation on the image) crystallographic alignment (consistent with exsolution). Diopside inclusions are visible in plagioclase. (B) Cr-rich garnet clusters with Cr-spinel at the core. Abbreviations: Cr Grt = chrome-bearing garnet, Di = diopside, Grs = grossular, Pl = plagioclase and Wo = wollastonite.

Symplectites are also found in the contact zone. Symplectites are intimate intergrowths of two or more minerals that grow simultaneously (Winter, 2010). Those found in association with the calc-silicate fragments host individual vesuvianite vermicules that vary in length from 1 mm to 3 mm. It appears that a grossular-vesuvianite symplectite formed between plagioclase and Al-rich clinopyroxene (Figure 3.13). The overall composition of the garnet (grossular) remains relatively constant throughout the symplectite, with slight variation in the Al content of the grossular, as indicated by EMPA (section 4.3.6.1)

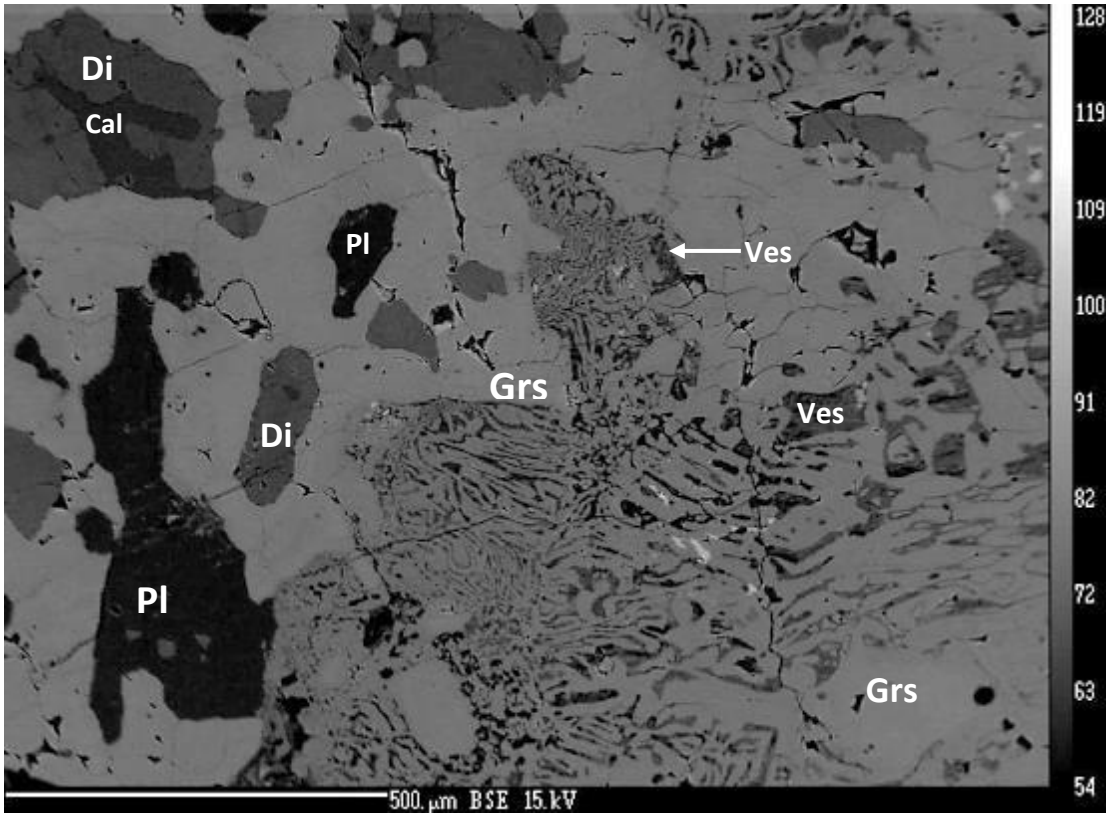

Figure 3.13: BSE image of grossular-vesuvianite symplectites between a calc-silicate fragment and surrounding matrix (left) in sample RSTX26-54 from the contact zone. Vesuvianite forms the dark 1 mm to 3 mm long vermicules in light grey grossular.

Sample RSTX26-61 collected from the Cr-stringer (Figure 2.6) proximal to the xenolith (Figure 3.14) is composed of diopside (40%), garnet (35%) and Cr-spinel (25%). Diopside grains are idioblastic to hypidioblastic and range in size from 0.2 mm to 2.5 mm. Pale to apple green Cr-bearing garnet occurs as circular idioblastic clusters/aggregates (from 0.2 mm to 0.5 mm in size) and Cr-spinel is commonly found in the centres of the garnet clusters/aggregates. The garnet-Cr-spinel relationship is similar to those observed in calc-silicate fragment samples (Figures 3.11 and 3.13). Cr-spinel is euhedral and varies is size from 0.1 mm to 0.5 mm in size. EMPA (section 4.3.5) confirms that the spinel grains are zoned; the cores are Cr-rich and the rims are Al-rich.

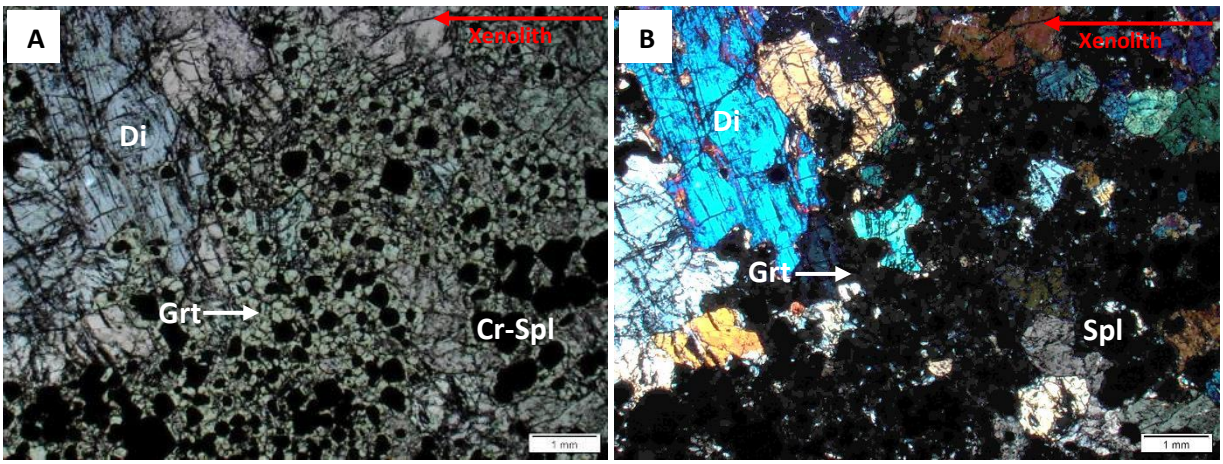

Figure 3.14: Photomicrograph of sample RSTX26-61 collected from the ~7 cm-thick Cr-stringer that splits into three thinner ones. The Cr-stringer proximal to the xenolith, on the right of the image, is Cr-spinel surrounded by clusters/aggregates of Cr-bearing garnet and diopside (top left). The red arrow indicates the direction of the main xenolithic body. (A) in PPL, (B) in XPL. Abbreviations: Di = diopside, Grt = garnet, Spl = spinel.

The intermediate chromitite stringer (Figure 3.15 A and B) comprises plagioclase (40%), diopside (25%), Cr-spinel (35%) and garnet (< 1%). Cumulus plagioclase is euhedral to subhedral, varies in size from 0.4 mm to 1.5 mm, and displays alteration which gives the grains a dusty to turbid appearance in some cases. The degree of alteration decreases to the right of the sample (Figure 3.15 A and B) which is adjacent to the distal chromitite stringer. Diopside is interstitial to plagioclase, subhedral to anhedral and ranges in size from 0.1 mm to 2.3 mm.

Euhedral Cr-spinel grains range in size from 0.1 mm to 0.3 mm and exhibit a similar zonation as in the proximal sample. Garnet occurs in minor amounts where it rims a few Cr-spinel grains.

The chromitite stringer distal from the xenolith (Figure 3.15 C and D) comprises plagioclase (55%), diopside (5%), garnet (5%) and spinel (35%). Plagioclase occurs as euhedral to subhedral grains (from 0.5 mm to 2 mm in size) with minor interstitial diopside, reminiscent of mottled anorthosite in the RLS (Section 3.3.3). The Cr-spinel is euhedral and varies in size from 0.1 to 0.5 mm. Cr-spinel grains in the intermediate and distal samples are enclosed in both plagioclase and diopside and, more rarely, are interstitial. This implies that Cr-spinel was the first mineral to crystallise, followed by plagioclase and diopside. Cr-spinel is not uniformly distributed throughout the samples, but instead occurs as bands/stringers (Figures 3.14 and 3.15). According to EMPA (section 4.3.5), the cores of the Cr-spinel are compositionally similar to that of the UG 1 chromite. However, Cr-spinel grains that form the stringers show slight zonation, with Cr-rich cores and Al-rich rims. The intermediate and distal samples display an overall igneous texture. However, some features indicate that this rock is a hybrid, particularly the occurrence of uvarovitic garnet that appears to surround Cr-spinel in some cases; and the presence of plagioclase-diopside symplectites. These symplectites are found in close association with the Cr-stringer. Individual diopside vermicules vary in length from < 10 to 120 µm (Figure 3.16). The symplectite encloses only a few spinel grains and is texturally zoned with relatively fewer diopside vermicules at its margins. Host (plagioclase) and vermicule (diopside) compositions are confirmed by EMPA (sections 4.3.5 and 4.3.6, respectively).

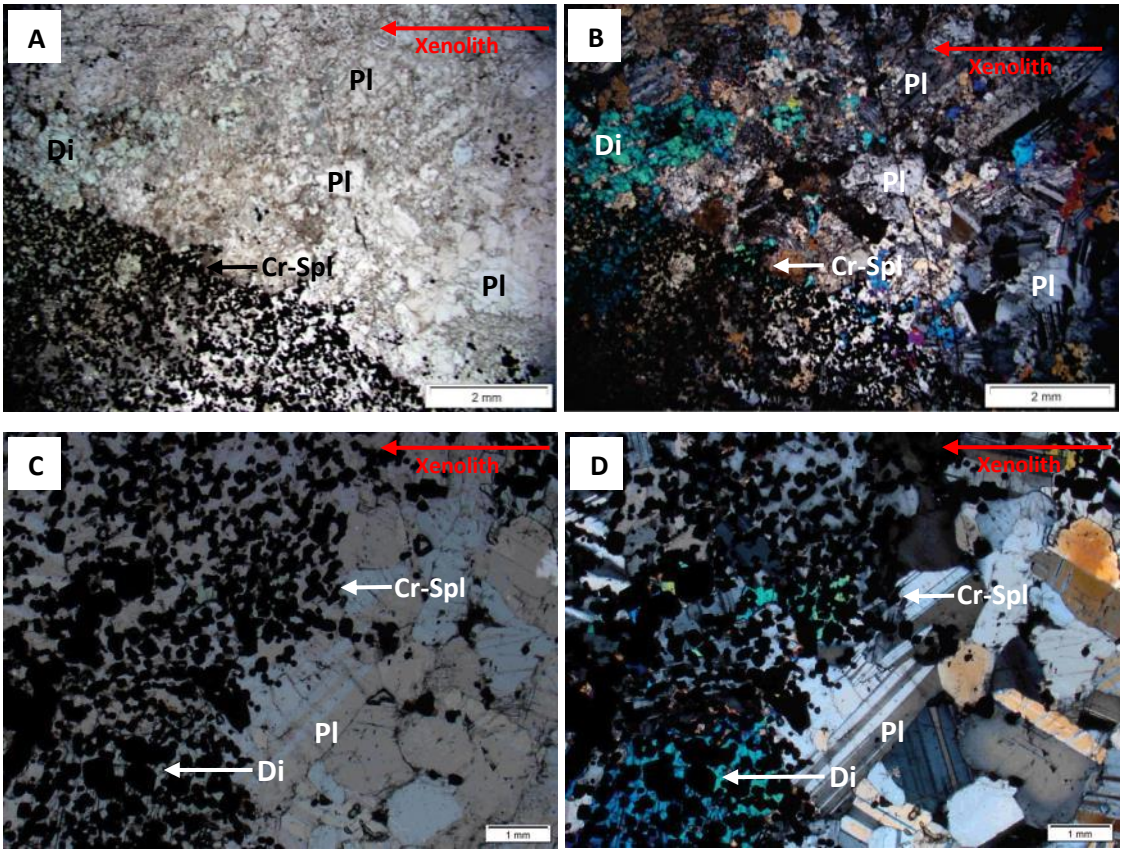

Figure 3.15: Photomicrographs of sample RSTX26-62 collected from the intermediate Cr-stringer (A and B) and RSTX26-63, distal Cr-stringer (C and D). On the left, euhedral Cr-spinel grains occur forming the stringers. On the right, interlocking euhedral to subhedral laths of plagioclase enclose minor amounts of spinel. Interstitial diopside displays second-order birefringence colours. (A and C) in PPL, (B and D) in XPL. The red arrow indicates the direction of the main xenolithic body. Abbreviations: Pl = plagioclase, Di = diopside, Spl = spinel.

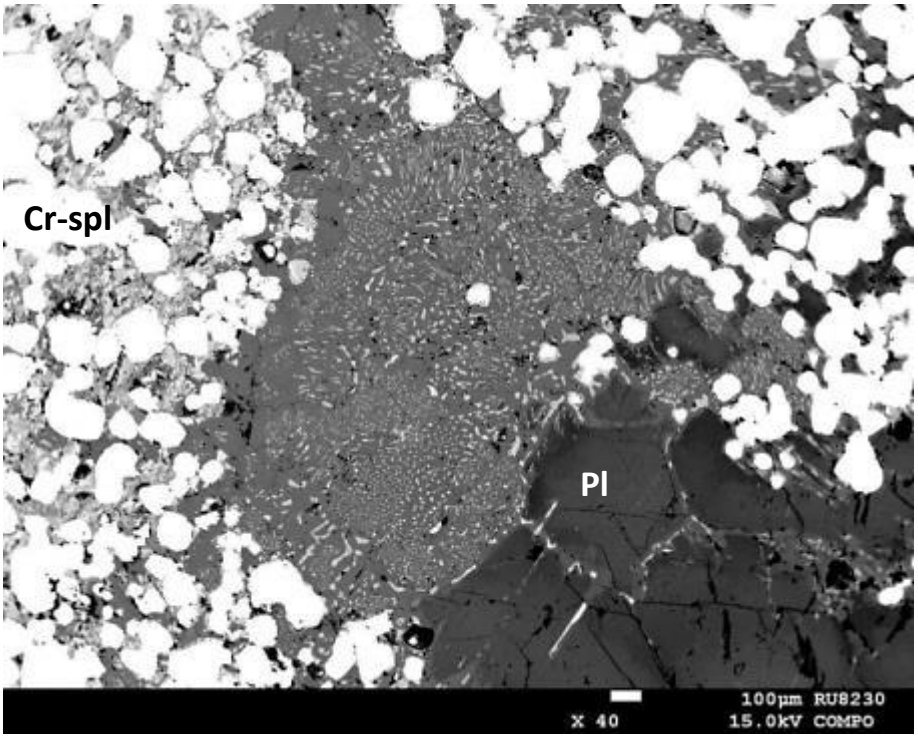

Figure 3.16: BSE image of plagioclase-diopside symplectites found in chromitite stringer distal to the xenolith (RSTX26-63) from the hybridised zone. Diopside forms the whitish to light grey < 10 to 120 µm long vermicules in darker grey plagioclase. Abbreviations: Pl = plagioclase, Spl = spinel.

3.2.3 Igneous rock

The host rock enclosing the Marikana xenolith and its contact zone is mottled anorthosite (Figure 3.17), which was sampled 5 m and 20 m away from the main xenolithic body as no closer samples could be obtained. Petrographically, the two samples show little difference. The assemblage is composed of three phases: plagioclase (90%), clinopyroxene (7%) and orthopyroxene (3%). Euhedral to subhedral plagioclase grains vary in size from 0.2 to 3 mm (Figure 3.18). Interstitial orthopyroxene and clinopyroxene forms the mottles that vary in size from 0.1 to 0.5 mm. Neither of the samples show any textural signs of alteration.

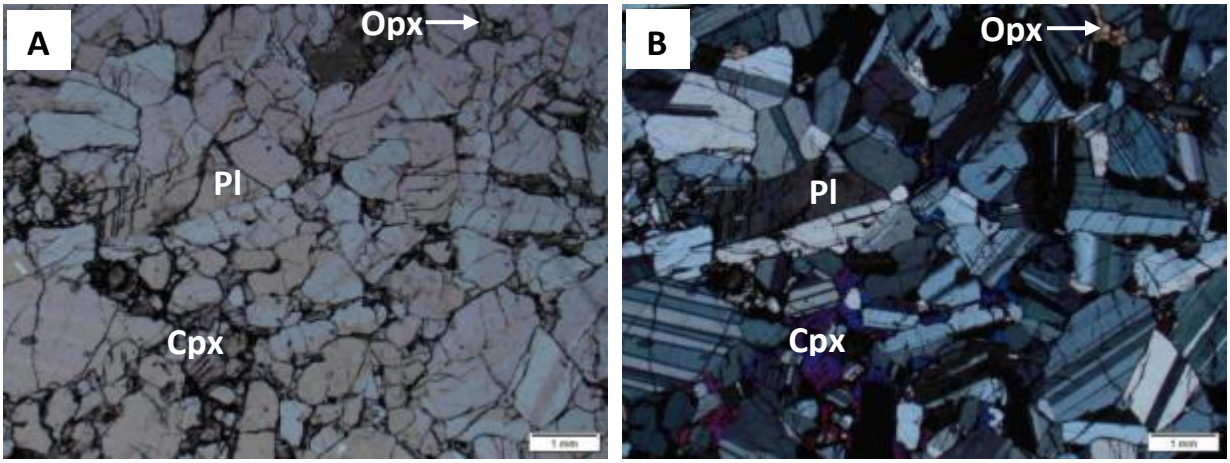

Figure 3.17: Photomicrograph of typical mottled anorthosite found 5 m from the main xenolithic body (RSTX26-A5), (A) in PPL and (B) in XPL. Cumulus plagioclase occurs with interstitial orthopyroxene and clinopyroxene (displaying second-order interference colours). Abbreviations: Pl = plagioclase, Opx = orthopyroxene, Cpx = clinopyroxene.

3.3 Zwartfontein

3.3.1 Main xenolithic bodies

On Zwartfontein farm three boreholes, ZF 116, ZF 116ED1 and ZF 109ED1, that intersect calc-silicate xenoliths were sampled. Each xenolith shows variable mineral compositions and textures and will be described under the same heading.

The xenolith in borehole ZF 116 is medium-grained and is composed of four petrographically identifiable phases: forsterite (30%), monticellite (25%), diopside (15%), and spinel (15%) (Figure 3.18). In addition to these four phases, an extremely fine-crystalline mineral (15%) is evident; however, its composition could not be determined using either petrographic methods or EMPA. The mineral may have been formed after alteration of a high-grade Ca-rich mineral as it pseudomorphs coarse grains similar in size to the other peak assemblage minerals. Forsterite grains are idioblastic to hypidioblastic and vary in size from 1 mm to 5 mm. BSE images and EMPA confirm that forsterite contains exsolution lamellae of monticellite (Figure 3.19). Monticellite is hypidioblastic and varies from 0.5 mm to 1 cm. The mineral displays undulose extinction. Clinopyroxene (confirmed as zoned diopside by EMPA in section 4.3.6) occurs as hypidioblastic to xenoblastic grains varying in size from 0.2 mm to 4 mm, and displays more planar to irregular fractures than the other minerals (Figure 3.19). Idioblastic to hypidioblastic spinel varies in size from 0.2 to 4 mm; it is commonly enclosed by monticellite and diopside, but also occurs as euhedral grains along crystal boundaries. Grains are dark to medium green and a few of them display zonation textures, with the cores slightly richer in Fe and Ti compared to the rims (section 4.4.7). The fine-crystalline Ca-rich aggregate (as indicated by EMPA) is evident as dark brown to black zones in transmitted light, and appears to be an alteration product of a pre-existing mineral as, in some cases, the grain boundary can still be identified. The individual grains are smaller in size than the EMPA beam and a stoichiometric analysis was not obtained (section 4.4.1).

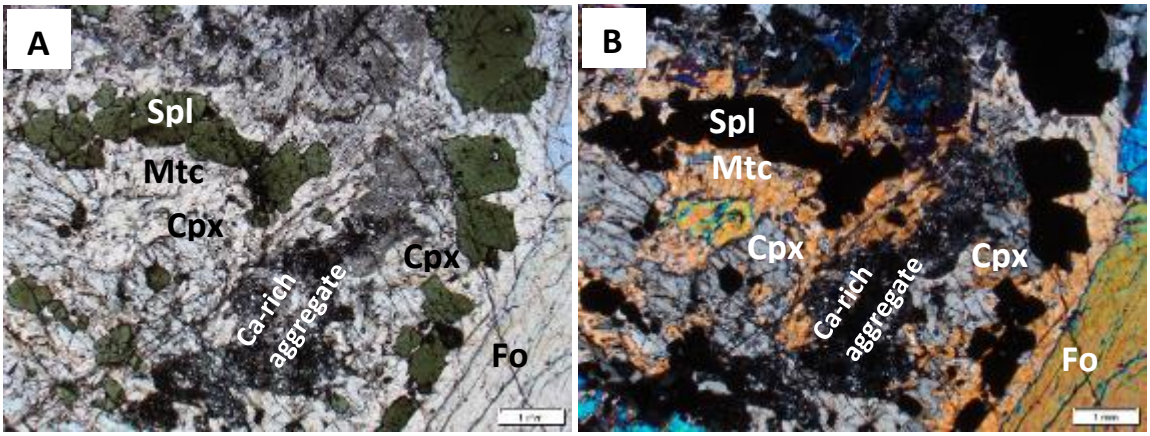

Figure 3.18: Photomicrograph of the calc-silicate xenolith (A156-7) found in borehole ZF 116 (A) in PPL and (B) in XPL. Forsterite occurs in the bottom right and contains monticellite exsolution lamellae (see Figure 3.18). Monticellite is in close association with grey diopside. Brown-black fine-crystalline (Ca-rich aggregate) alteration occurs in the centre and gives this area a turbid appearance. Abbreviations: Mtc = monticellite, Fo = forsterite, Cpx = clinopyroxene, Spl = spinel.

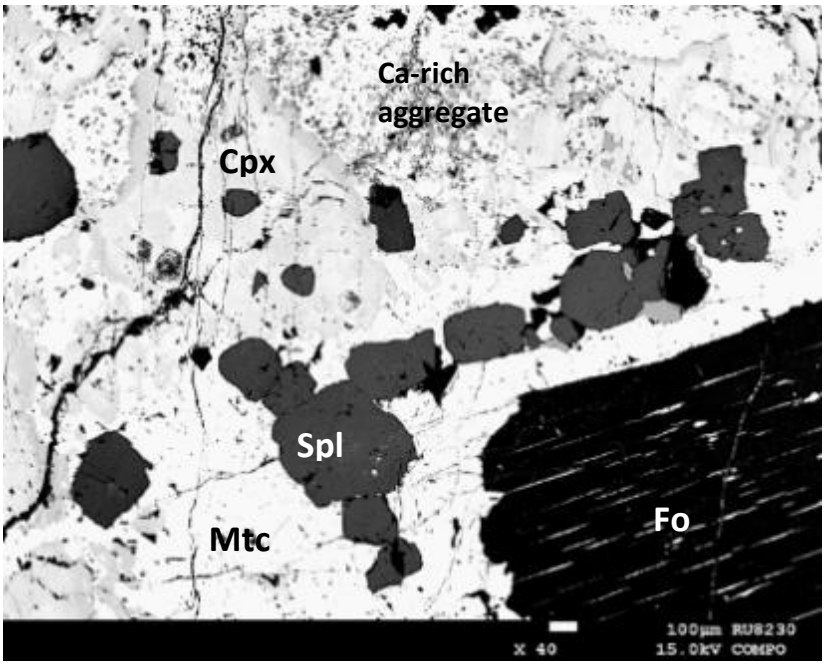

Figure 3.19: BSE image of the xenolith (A156-7) depicting monticellite exsolution lamellae in forsterite (bottom right). Unidentifiable Ca-rich, fine-crystalline alteration occurs at the top of the image. Mg, Al, Fe spinel occur with monticellite and zoned diopside. Abbreviations: Mtc = monticellite, Fo = forsterite, Cpx = clinopyroxene, Spl = spinel.

The calc-silicate xenolith in borehole ZF 109ED1 is composed of six phases: clinopyroxene (45%), calcite (10%), anhydrite (5%), serpentine (25%) (after forsterite), magnetite (5%) and an extremely fine-crystalline, Ca-rich aggregate (10%) (Figure 3.20). Clinopyroxene (confirmed as diopside by EMPA in section 4.3.3) occurs as idioblastic to hypidioblastic grains that vary in size from 1 mm to 1 cm, and displays planar to irregular fracturing. In some cases, it hosts calcite inclusions. Locally, it displays interpenetrated boundaries with anhydrite. Calcite is hypidioblastic to xenoblastic and varies in size from 0.8 mm to 1.5 mm. In some cases, it is interstitial to grains that have been completely serpentinised. Anhydrite exhibits simple twinning and is commonly found with calcite; it is idioblastic to hypidioblastic and varies in size from 2 mm to 5 mm. This sample shows extensive serpentinisation. In some cases, individual idioblastic to hypidioblastic grains with well-defined grain boundaries have been completely serpentinised (Figure 3.20). In other cases, the degree of alteration is too high to identify grain-size or grain-shape. However, these serpentine zones are associated with an extremely fine-crystalline Ca-rich aggregate which occurs along crystal boundaries and within cross-cutting veins. Minor amounts of magnetite occur in association with serpentine (Figure 3.21).

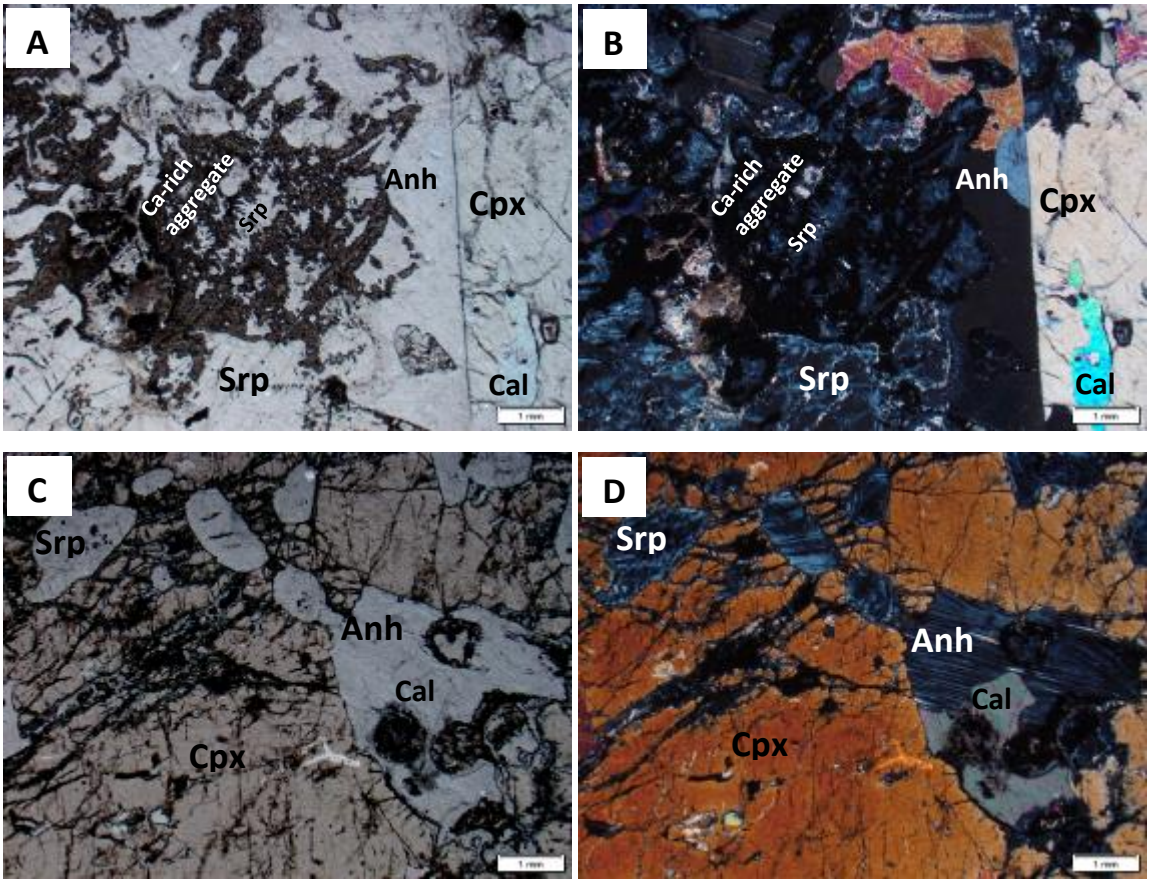

Figure 3.20: Photomicrographs of the xenolith in borehole ZF 109 ED 1, sample C435-2. A and C in PPL and B and D in XPL. Coarse-grained diopside exhibits irregular fracturing and is in close association with calcite, which occurs as inclusions. Brown-black, fine-crystalline Ca-rich aggregate occurs along boundaries and within veins, and gives this area a turbid appearance ("Fine gr" in image) (A and B). Anhydrite exhibits simple twinning. Idioblastic-hypidioblastic grains that have been completely serpentinised occur in C and D. Abbreviations: Cpx = clinopyroxene, Cal = calcite, Anh = Anhydrite, Srp = serpentine.

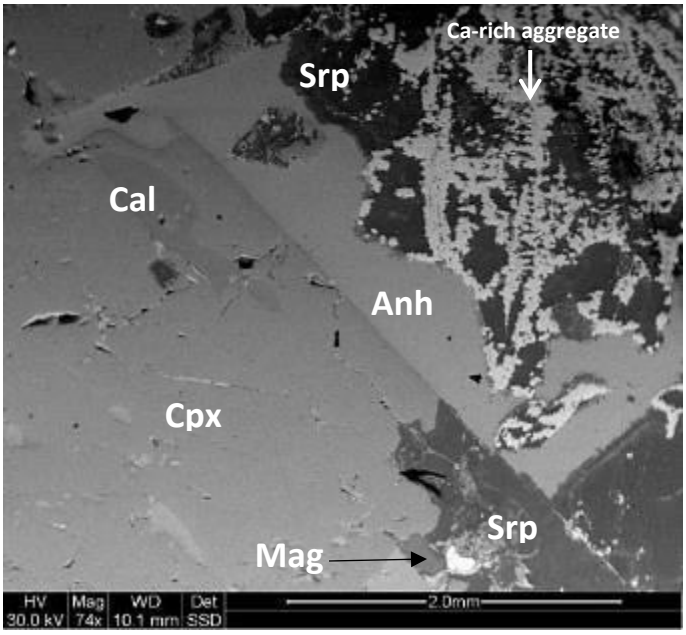

Figure 3.21: BSE image of the xenolith in borehole ZF 109 ED 1, sample C435-2, depicting the fine-crystalline mineral that occurs in close association with serpentine along grain boundaries and within veins ("Fine gr" in image). Magnetite is identified by EMPA at the bottom on the image, indicated by the arrow. Abbreviations: Cpx = clinopyroxene, Cal = calcite, Anh = Anhydrite, Srp = serpentine, Mag = magnetite.

The xenolith in borehole ZF 116ED1 is fine-grained and composed of two major phases: calcite (35%) and serpentine (40%) (Figure 3.22). In addition to these minerals, an extremely fine-crystalline aggregate (25%) is evident; like the other xenoliths, this aggregate has not been stoichiometrically resolved owing to its micro-crystalline size. However, EMPA indicated that it is Ca-rich, which could indicate that it is an alteration product of a mineral such as monticellite. Calcite is idioblastic to hypidioblastic and varies in size from 0.1 mm to 0.5 mm. Serpentine (after forsterite) is idioblastic to hypidioblastic; the boundaries of the pre-existing mineral are visible, and vary in size from 0.5 mm to 1 mm. In Chapter 2 the borehole samples were described as layered; however, in thin-section these layers are not easily distinguished. In some cases, there are zones richer in serpentine, but well-defined layers are not evident.

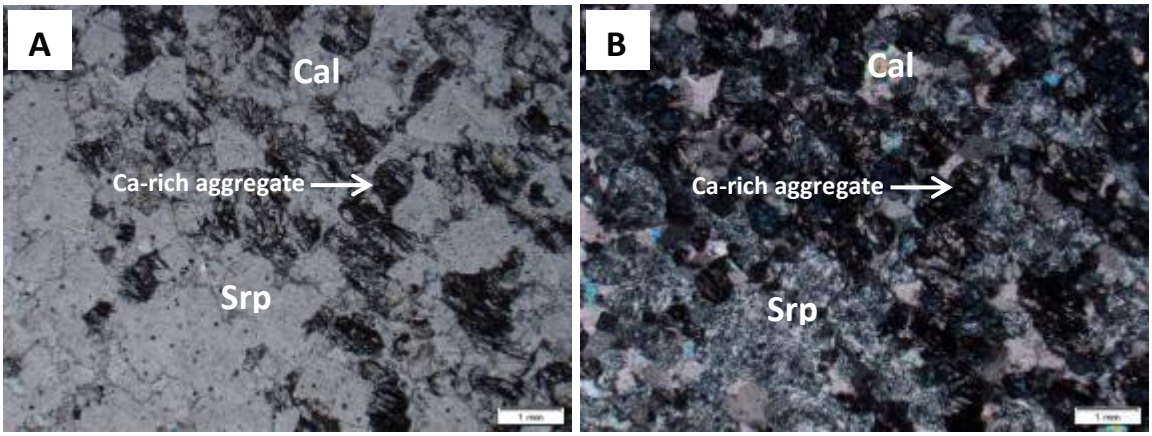

Figure 3.22: Photomicrograph of the fine-crystalline xenolith located in ZF 116 ED1, sample A312-3, (A) in PPL and (B) in XPL. Idioblastic to hypidioblastic calcite, and a phase now completely replaced by serpentine is depicted in association with a brown to black, extremely fine-grained, Ca-rich aggregate (possibly after monticellite). Abbreviations: Cal = calcite, Srp = serpentine.

3.3.2 Hybrid rock and parapyroxenites

Samples analysed from the contact zone include those rock types which appear to be hybrid rock according to Nex *et al*. (2006). In the sample suite hybrid rocks comprise of metamorphic minerals similar to the xenoliths; however, the modal abundances of these minerals vary significantly throughout the zone and appear to be a mix of igneous and metamorphic minerals. Analysis was hampered by high levels of serpentinisation (See Appendix 3).

The best example of hybrid rock was taken from borehole ZF 116 ED1 (Figure 3.23) where an igneous rock, exhibiting igneous mineral textures, is adjacent to a metamorphic rock. The igneous rock (top of Figure 3.23A and B) is composed of 60% cumulus pyroxene and 40% interstitial plagioclase, and can be considered as feldspathic pyroxenite. Pyroxene and plagioclase crystal size varies from 1 mm to 3 mm. Orthopyroxene exhibits planar to irregular fracturing and clinopyroxene displays intricate exsolution patterns. Both minerals are crosscut by veins that are filled with a micro-crystalline, rust-coloured mineral. The metamorphic rock immediately at the contact with feldspathic pyroxenite exhibits fine-crystalline clinopyroxene that is possibly an alteration product of a pre-existing mineral (i.e., the aggregates are

pseudomorphs after larger grains) and can be identified at the bottom of Figure 3.23A and B. In some cases, medium to coarse relict grain boundaries are observed that host fine-crystalline clinopyroxene. The grain size increases from fine to coarse further away from the feldspathic pyroxenite (Figure 3.23C and D). The coarsest clinopyroxene grains vary in size from 1 mm to 6 mm, are elongate, and idioblastic to hypidioblastic. A highly altered mineral occurs interstitially to the large clinopyroxene.

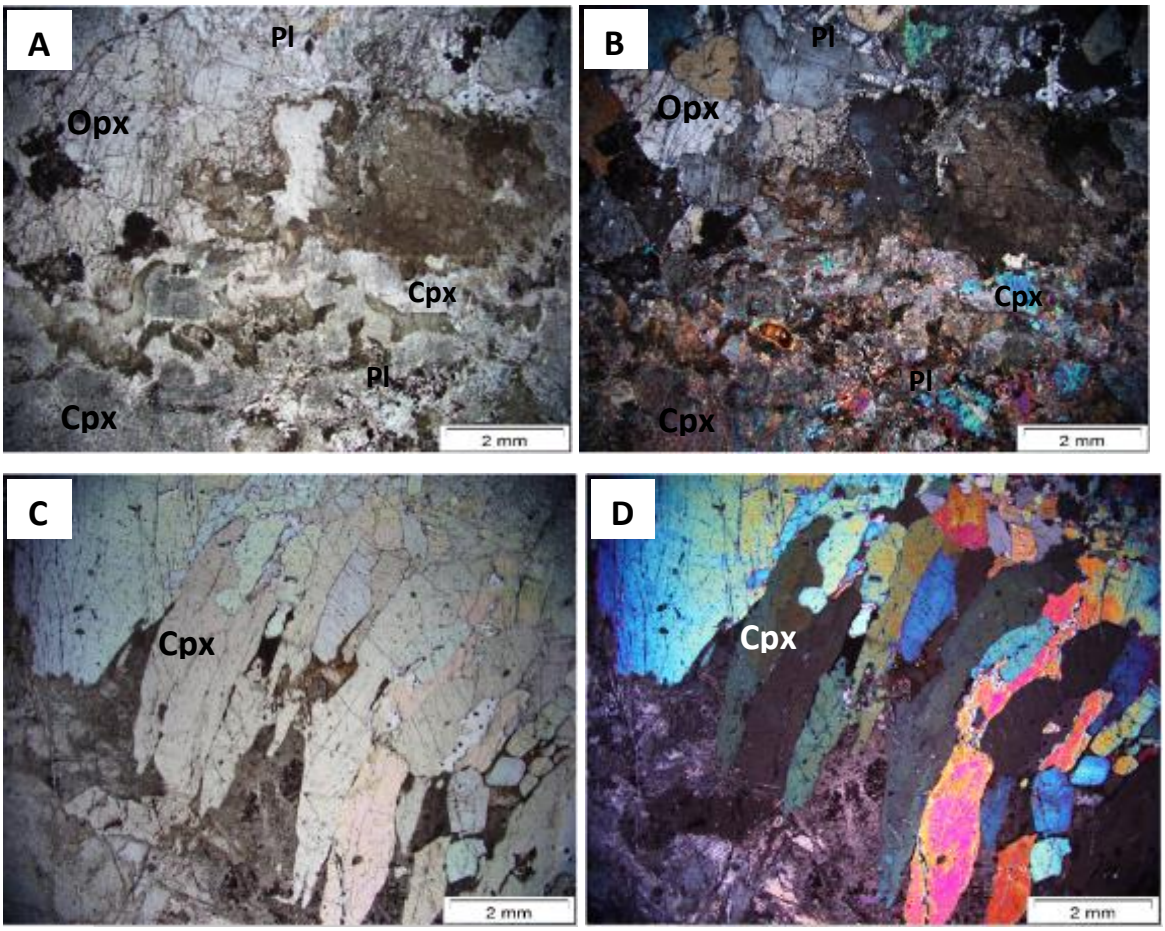

Figure 3.23: Photomicrographs of a sample collected from the contact zone located in ZF 116 ED1, sample B882-4. A and C in PPL and B and D in XPL. The igneous component comprises plagioclase and pyroxene (A and B) which lie adjacent to the metamorphic component. This component is composed predominantly of diopside (C and D), with the exception of the altered mineral found at the bottom of images C and D that appears to be highly altered plagioclase. Abbreviations: Pl = plagioclase, Opx = orthopyroxene, Cpx = clinopyroxene.

Parapyroxenites (Figure 3.24) are commonly associated with the calc-silicate xenoliths. They are composed of ~70–75% idioblastic to hypidioblastic clinopyroxene (ranging in size from 0.5 mm to 4 mm) with minor interstitial plagioclase (≤ 20%), ranging in size from 0.5 mm to 2 mm. In some cases, biotite (< 5%, < 0.5 mm in size) and disseminated sulphides (pyrrhotite, pyrite, chalcopyrite and pentlandite; < 2%, ranging in size from < 0.5 mm to 3 mm) occur. Serpentinisation is common and constitutes up to 10% of the sample; magnetite occur with the serpentine. Sericite, and alteration of minerals such as plagioclase to dark brown clays, is evident and the minerals commonly display a high degree of fracturing.

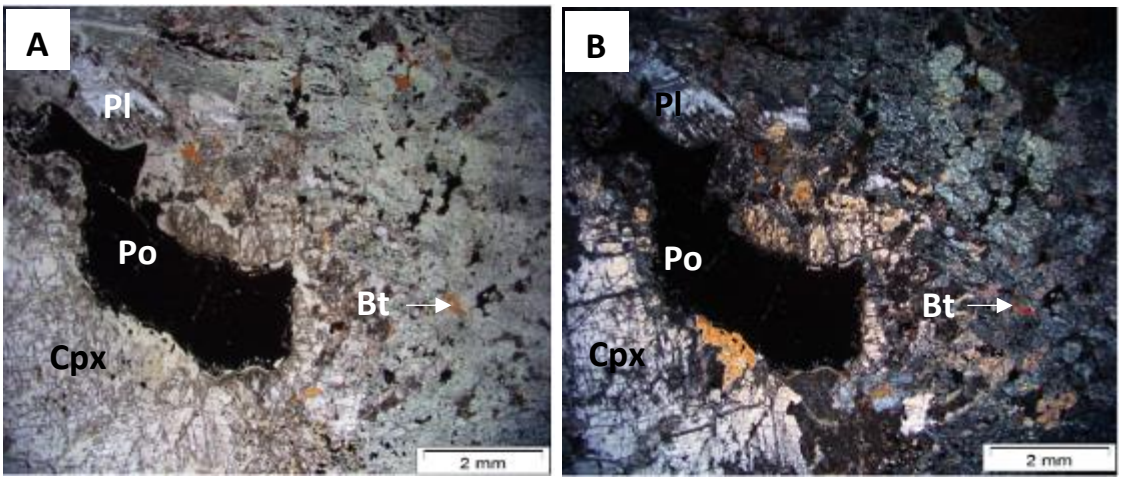

Figure 3.24: Photomicrograph of parapyroxenite found in association with the xenoliths in ZF116, sample A291-1. (A) in PPL and (B) in XPL. The sample is composed predominantly of clinopyroxene, which displays a high degree of fracturing, with minor interstitial plagioclase and biotite. In this sample, coarse pyrrhotite is evident. Abbreviations: Pl = plagioclase, Po = pyrrhotite, Bt = biotite, Di = diopside.

3.3.3 Igneous rock

Pyroxenite is composed of cumulus pyroxene (90–95%) and interstitial plagioclase (5–10%) (Figure 3.25). Commonly medium to coarse-grained, pyroxene varies in size from 0.5 mm to 5 mm and displays fracturing. Accessory minerals are sulphides (commonly disseminated pyrrhotite, pyrite, chalcopyrite and pentlandite), and biotite. Microcrystalline alteration is predominantly evident in the form of serpentine, which occurs as pseudomorphous aggregates

and veins. Magnetite is evident in association with serpentine. Sericite is evident in association with plagioclase. Sericitisation and alteration of minerals to dark brown clays also occurs. The dark brown clay minerals are found within the pyroxene and plagioclase in some cases.

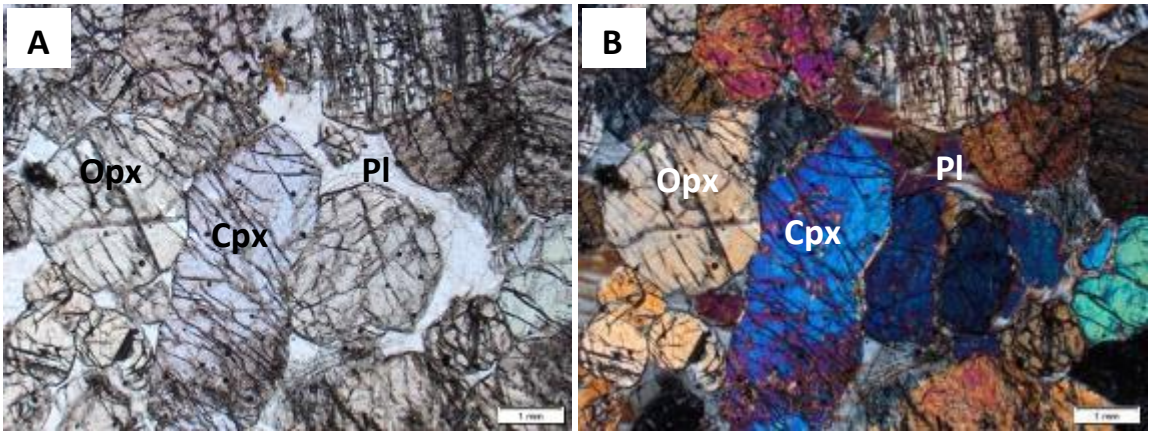

Figure 3.25: Photomicrograph of typical pyroxenite associated with xenoliths found in borehole ZF 116 sample A24. (A) in PPL and (B) in XPL. Cumulus pyroxene occurs with minor interstitial plagioclase. Abbreviations: Pl = plagioclase, Opx = orthopyroxene, Cpx = clinopyroxene.

3.4 Discussion and summary

The petrographic study summarises the mineralogical and textural variation in the main xenolithic bodies, contact zones and adjacent host igneous rock, as well the similarities and differences between xenoliths and the surrounding zones located in the Marikana and Zwartfontein cases. This summary is outlined in Table 3.1.

Table 3. 1: Summary of minerals and characteristic features in Marikana and Zwartfontein sample suites

Mineral/characteristics	Marikana			Zwartfontein		
	Main xenolith	Contact zone	Igneous rock	Main xenoliths	Hybrid rock or parapyroxenites	Igneous rock
Monticellite	X*	X		X ZF116		
Forsterite	X			X ZF116 ZF 116ED1 ZF 109ED1	X ZF 116ED1	
Spinel	X	X		X ZF116		
Calcite	0*			X ZF116 ZF 116ED1 ZF 109ED1		
Chromite/Cr-spinel		X	X			
Clinopyroxene		X	X	X ZF116 ZF 116ED1 ZF 109ED1	X ZF116 ZF 116ED1 ZF 109ED1	X ZF116 ZF 116ED1 ZF 109ED1
Orthopyroxene			0		X ZF 116ED1	X ZF116 ZF 116ED1 ZF 109ED1
Plagioclase		X	X		X ZF 116ED1	X ZF116 ZF 116ED1 ZF 109ED1
Garnet		X				
Vesuvianite		X				
Wollastonite		X				
Serpentine		0		X ZF 116ED1 ZF 109ED1	X ZF116 ZF 116ED1 ZF 109ED1	X ZF116 ZF 116ED1 ZF 109ED1
Magnetite	X			0 ZF 109ED1		
Sulphides					0 ZF116 ZF 116ED1 ZF 109ED1	0 ZF116 ZF 116ED1 ZF 109ED1
Anhydrite				X ZF 109ED1		
Fine-crystalline Ca-rich aggregate				X ZF116 ZF 116ED1 ZF 109ED1		
Pegmatoids	Monticellite-spinel dominant bands					Feldspathic pyroxenite and pyroxenite
Fragments		Monticellite			Serpentinised	
Prograde assemblages	Mtc+Fo+Spl			Mtc+Fo+Di+Spl Di+Cal+Anh		
Retrograde assemblages/minerals		Grt+Ves+Wo		Srp+Mag	Srp+Mag	
Zonation of minerals/mineral assemblages	Western contact	Monticellite fragments				
Evidence of xenolith-magma interactions		Monticellite fragments Pseudo-ophitic igneous texture Cr-spinel			Serpentine fragments Rock comprised igneous and metamorphic	

*X = major mineral constituting >5% of sample, *0 = minor mineral constituting <5% of sample.

The main xenolithic body at Marikana comprises coarse-grained monticellite, forsterite and spinel. In the Zwartfontein case a similar assemblage is observed in one xenolith (borehole ZF 116), with the addition of clinopyroxene. At Zwartfontein, mineral assemblages show variation between xenoliths and when compared to the Marikana xenolith; (1) xenoliths commonly contain clinopyroxene; (2) forsterite is inferred to have originally been present from the pseudomorphous serpentine in some samples and; (3) all xenoliths contain extremely fine-crystalline pseudomorphous Ca-rich aggregates that could not be identified by petrographic and EMP methods, which we speculate could be a product of alteration after monticellite. The xenolith ZF 116 lacks calcite and serpentine, xenolith ZF 109ED1 hosts anhydrite and xenolith ZF 116ED1 lacks clinopyroxene, monticellite and forsterite, and predominantly contains calcite, serpentine and fine-crystalline Ca-rich aggregates. Variations in the mineral assemblages in Zwartfontein may be due to a number of factors; (1) even though all xenoliths are composed of calc-silicate minerals there may be differences in the inherent nature of the protolith; (2) the degree of metamorphism endured by each xenolith and; (3) the degree to which fluids may have interacted with each xenolith (Gain and Mostert, 1982).

At Marikana, calcite occurs in only trace amounts (< 1%) in the main xenolithic body where textural and mineralogical variation is observed, that is, in the spinel patch and pegmatoidal band, which are mineralogically different to the main xenolithic body. The spinel patch and pegmatoidal band lack forsterite and host texturally variable spinel; zoned spinel is found only in these samples. (Despite the difference, these samples are still considered part of the main xenolithic body.) At Zwartfontein, calcite is present in xenoliths ZF 116ED1 (35%) and ZF 109ED1 (10%). At Marikana, although some grains of spinel found in the main xenolithic body display zonation textures (light brown to dark brown), most of the spinel exhibits exsolution textures. Both zoned spinel and spinel exhibiting exsolution textures occur in the main xenolithic body. The Marikana contact zone hosts Cr-spinel. Zonation textures are evident in the contact zone rather than exsolution. At Zwartfontein, spinel is only found in xenolith ZF 116, and exhibits brown to green zonation. No exsolution textures are observed. Sulphides, including pyrrhotite, pyrite, chalcopyrite and pentlandite are evident in Zwartfontein parapyroxenite and pyroxenite

but are absent in the xenoliths at both sites. No garnet is evident in Zwartfontein, whereas in the Marikana case, garnet is abundant in the contact zone where it is found in close association with Cr-spinel, occurring as reaction coronas between plagioclase and clinopyroxene and involved in symplectites with vesuvianite. Serpentine in the Marikana xenolith occurs as a single 2 mm-wide band, whereas in Zwartfontein it is ubiquitous. Serpentinisation in the Zwartfontein samples may indicate low-grade retrograde effects (Pronost *et al*., 2008) that did not take place in the Marikana case, possibly owing to the closer proximity of the former setting with the RLS footwall in the Northern limb. All samples, including the igneous package of rocks, exhibit some degree of serpentinisation, suggesting that high degrees of serpentinisation are linked to fluids from the footwall (Holwell and McDonald, 2006).

Fragments of calc-silicate rock found at Zwartfontein are completely serpentinised. At Marikana, monticellite fragments are found in the contact zone adjacent to the main xenolith. These fragments of calc-silicate rock originate from the xenolith, and possibly disaggregated during interaction with the magma. They appear to depict, on a smaller scale, a similar phenomenon that occurs between the main xenolithic body and the surrounding contact zone, that is, monticellite and spinel occur at the centre/core of the fragments; however, the forsterite seen in the main xenolithic body is absent. A layer of spinel surrounds the monticellite fragment, followed by a layer of clinopyroxene, beyond which vesuvianite, clinopyroxene and uvarovitic garnet occur. This zonation of minerals is similar to that which occurs on a larger scale between the xenolith and contact zone shown in Figure 2.4.

CHAPTER 4: MINERAL CHEMISTRY

4.1 Introduction

Mineral chemistry data for monticellite, forsterite, spinel, garnet, pyroxene, chromite, vesuvianite, plagioclase, calcite, anhydrite and serpentine from 22 polished thin-sections were collected using electron microprobe analysis (EMPA) at Rhodes University and the University of the Witwatersrand. EMPA was used to obtain mineral chemical data and any evidence of zonation of grains, as well as to investigate the chemical variation in mineral phases between the xenolith, contact zones, and surrounding igneous rock. The analyses are summarised in Table 4.1, and mineral chemical data are included in Appendix 4. The chemical data and X-ray element mapping indicate compositional heterogeneity on a variety of scales, between zones (Figure 2.2, Chapter 2), within individual zones between samples, and within individual samples.

4.2 Methods

Eight samples were analysed quantitatively using a CAMECA SXFiveFE EMPA equipped with five wavelength dispersive spectrometers at the Microscopy and Microanalysis Unit of the University of the Witwatersrand. A total of 302 analyses were done. Owing to prolonged downtime of the CAMECA instrument, quantitative mineral chemical analyses for 14 samples were additionally obtained by using four wavelength dispersive spectrometers on a JEOL JXA-8230 electron probe micro-analyser at Rhodes University, Grahamstown. A total of 459 points were analysed. Detailed methodology is noted in Appendix 4A. On average, five grains per mineral per thin-section were analysed. Individual grains that appeared inhomogeneous or zoned were analysed from core to rim with up to 5 points, depending on the grain size. In total, 761 points were analysed.

Table 4. 1: Summary of the minerals analysed using the electron microprobe (and number of analyses per mineral per zone)

Sample description	Marikana						Zwartfontein		Total
	Xenolith	Contact zone			Igneous rock		Xenolith	Contact zone	
		Forsterite-spinel layer, spinel layer and forsterite-monticellite layer	Calc-silicate rock fragment and surrounding matrix	Chromitite stringer	Mottled Anorthosite	UG1			
Monticellite	dominant (36)	intermediate (8)					intermediate (15)		59
Forsterite	intermediate (18)	dominant (20)					intermediate (7)		45
Spinel	intermediate (67)	intermediate (57)	intermediate (24)				intermediate (18)		166
Garnet			intermediate (70)	dominant (27)					97
Pyroxene			dominant (65)	intermediate (42)	accessory (23)		intermediate (17)	intermediate (38)	185
Chromite/ chrome spinel				intermediate (25)		dominant (7)			32
Vesuvianite			intermediate (16)					intermediate (18)	34
Plagioclase			intermediate (37)	intermediate (31)	dominant (42)	intermediate (5)			115
Calcite	accessory (5)						accessory (8)		13
Anhydrite							accessory (4)		4
Serpentine							intermediate (11)		11
Total	126	85	212	125	65	12	80	56	761

4.3 Marikana

A total of 18 thin-sections were analysed, eight using the CAMECA and ten using the JEOL instruments. Thin-sections analysed at Rhodes University have the name “JEOL” affixed to the end of the sample numbers/names in all legends, while thin-sections analysed at the University of the Witwatersrand have no name/reference to an electron microprobe instrument affixed to the sample numbers. Table 4.2 provides a summary and brief description of all thin-sections analysed.

Table 4. 2: Summary and brief description of all thin-sections analysed

	Sample name	Sample description	Mineral assemblage	Microprobe
Xenolith	RSTX26-12	Main xenolith body	Fo + Mtc +Spl	CAMECA
	RSTX26-03	Main xenolith body	Fo + Mtc +Spl	JEOL
	RSTX26-01	Spinel patch	Mtc + Spl+ Cal	
	RSTX26-04	Pegmatoidal patch	Mtc +Spl + Cal	
Western contact of xenolith	RSTX26-05 (A,B,C)	Spinel layer and immediate surroundings		JEOL
	RSTX26-05 A	Forsterite-spinel layer	Fo + Spl	
	RSTX26-05 B	Spinel layer	Spl	
	RSTX26-05 C	Forsterite-monticellite layer	Fo + Mtc + Spl	
	RSTX26-06 (A, B, C)	Spinel layer and immediate surroundings		CAMECA
	RSTX26-06 A	Forsterite-spinel layer	Fo + Spl	
	RSTX26-06 B	Spinel layer	Spl	
	RSTX26-06 C	Forsterite-monticellite layer	Fo + Mtc + Spl	
Contact zone	RSTX26-13	Fragment	Di + Grt + Spl + Wo	CAMECA
	RSTX26-51	Matrix	Pl + Di + Grt + Wo	
	RSTX26-52	Fragment	Di + Grt + Spl + Ves + Mtc	
	RSTX26-53 A	Matrix	Pl + Di + Grt + Ves	
	RSTX26-53 B	Fragment	Di + Grt + Spl	
	RSTX26-54	Matrix	Pl + Di + Grt + Ves	
	RSTX26-61	Chromitite stringer proximal to xenolith	Di + Grt + Spl	JEOL
	RSTX26-62	Chromitite stringer intermediate	Pl + Di + Grt + Spl	
	RSTX26-63	Chromitite stringer distal to xenolith	Pl + Di + Grt + Spl	
Host rock	RSTX26-A5	Mottled anorthosite 5 m away from the main xenolith body	Pl + Di	JEOL
	RSTX26-A20	Mottled anorthosite 20 m away from the main xenolith body	Pl + Di	
	RSTX26-UG1	UG 1 Chromitite 20 m away from the main xenolithic body	Pl + Spl	

4.3.1 Monticellite and forsterite

Monticellite ($CaMgSiO_4$) and/or forsterite (Mg_2SiO_4) dominate in the main bulk of the xenolith, and occur in the forsterite-spinel layer and the forsterite-monticellite layer at the edge of the xenolith and calc-silicate fragments in the contact zone. Minor monticellite is found in the contact zone. Representative analyses of monticellite and forsterite are shown in Tables 4.3 and 4.4, respectively, and monticellite and forsterite compositions are shown on the Ca-Mg-Fe ternary diagram in Figure 4.1. Mg in monticellite ranges from 0.89 apfu to 0.97 apfu (based on four oxygens per formula unit), and Fe ranges from 0.05 apfu to 0.12 apfu. The X_{Mg} [where X_{Mg} = $Mg/(Mg + Fe_T)$] ranges from 0.88 to 0.95 (Figure 4.2A), where X_{Mg} is slightly lower (0.88 to 0.93) in the forsterite-monticellite layer compared to the main xenolithic body (between 0.94 – 0.95), with a slight decrease in the samples containing pegmatoidal monticellite grains (X_{Mg} = 0.93).

In samples adjacent to the spinel layer (forsterite-monticellite layer) only minor amounts of monticellite are evident, and X_{Mg} ranges from 0.88 to 0.93. The Fe content increases from the main xenolithic body to the forsterite-monticellite layer from 0.04 apfu to 0.12 apfu. Ca remains constant throughout the sample suite, between 0.96 – 0.97 apfu.

Forsterite compositions show little to no variation, with values of Fo_{97-98} (Figure 4.2B) in samples found in the main xenolithic body, as well as in the forsterite-spinel layer, the spinel layer and the forsterite-monticellite layer. However, the forsterite-monticellite layer shows lower Mg values, between Fo_{94-96} (1.94 apfu – 1.96 apfu). Fe increases from the xenolith (0.04 apfu – 0.06 apfu) to the forsterite-spinel layer, where it is at its highest concentration in the forsterite-monticellite layer (0.07 apfu – 0.11 apfu). Most grains contain an average of 0.015 apfu Ca. No forsterite was identified in the contact zone. Overall, trends indicate that Mg in both monticellite and forsterite decreases from the main xenolithic body to the western edge of the xenolith, while Fe^{2+} appears to behave inversely.

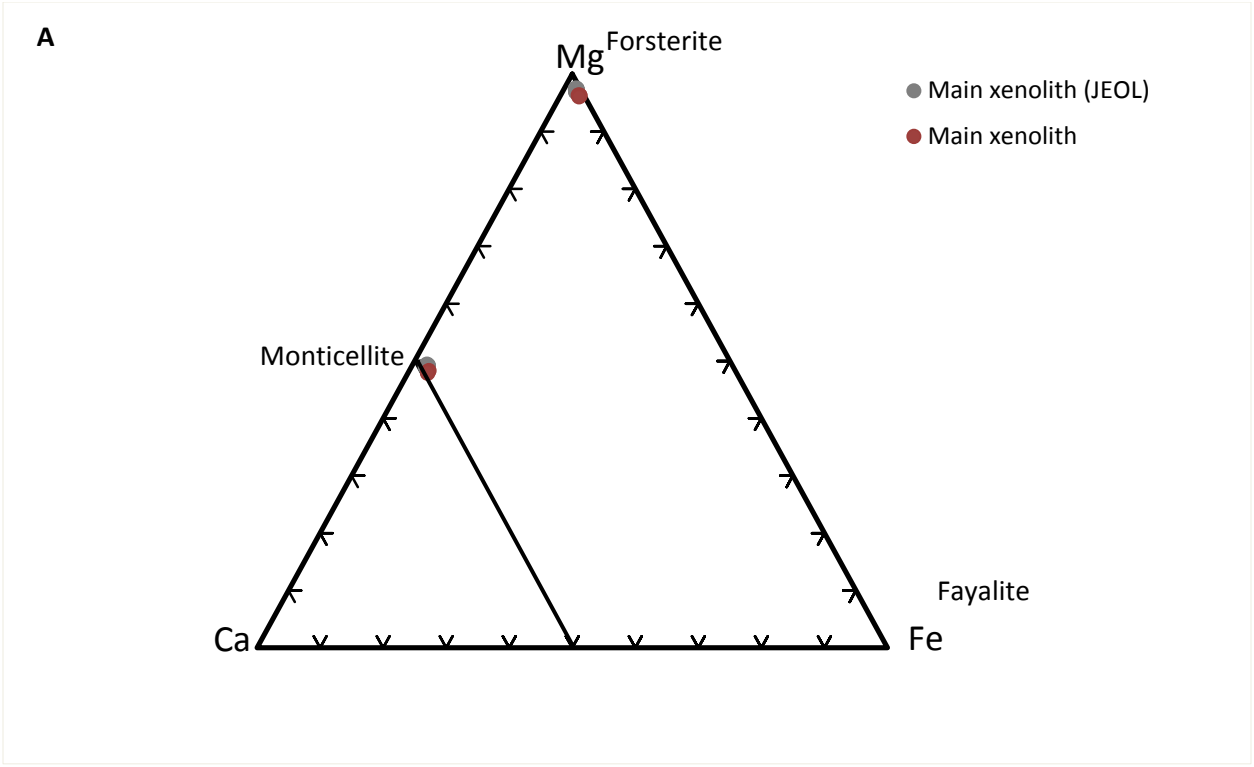
A
Mg
Forsterite
Main xenolith (JEOL)
Main xenolith
Monticellite
Fayalite
Ca
Fe

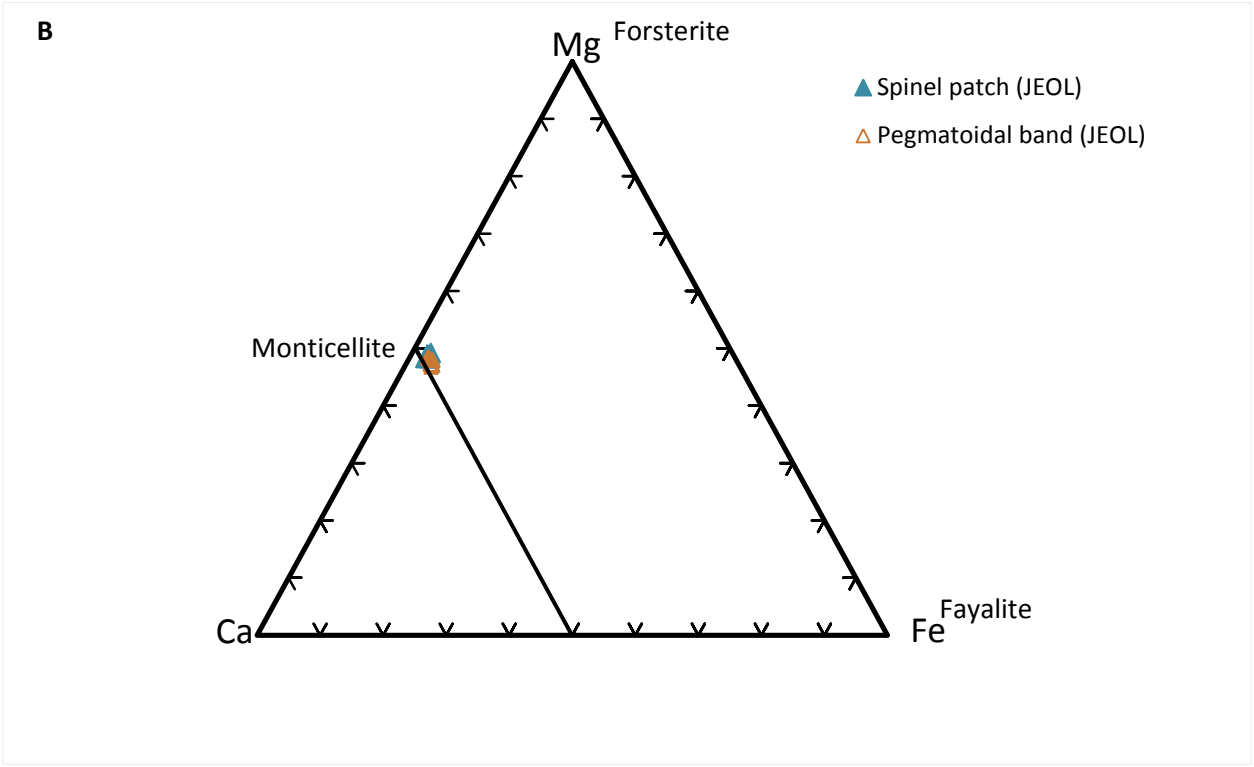
B
Mg
Forsterite
Spinel patch (JEOL)
Pegmatoidal band (JEOL)
Monticellite
Ca
Fe
Fayalite

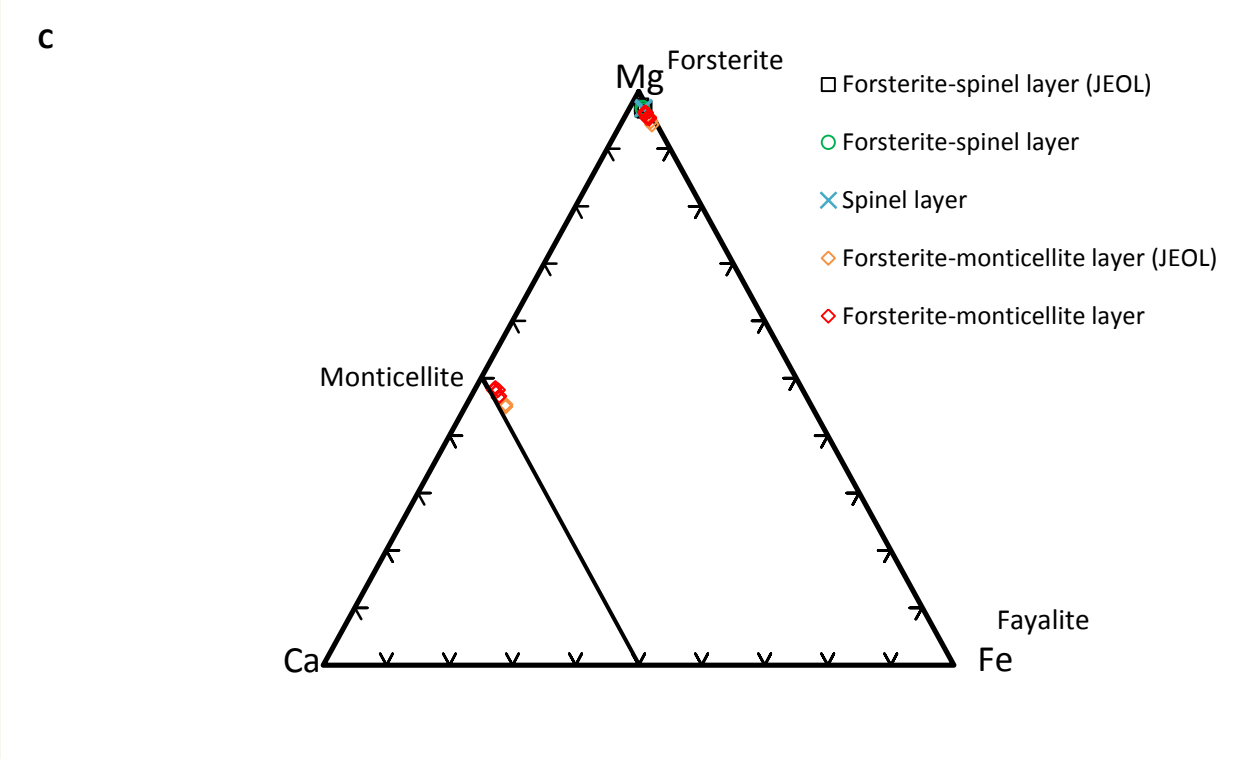

Figure 4.1: Monticellite and forsterite compositions for the Marikana xenolith illustrated based on the proportions of Ca-Mg-Fe. (A) Monticellite and forsterite show little variation in the main xenolithic body. (B) No forsterite is evident in samples containing patches of spinel and pegmatoidal grains. (C) The forsterite-spinel, spinel and forsterite-monticellite layers are slightly more Fe rich and less Mg rich than the xenolith compositions.

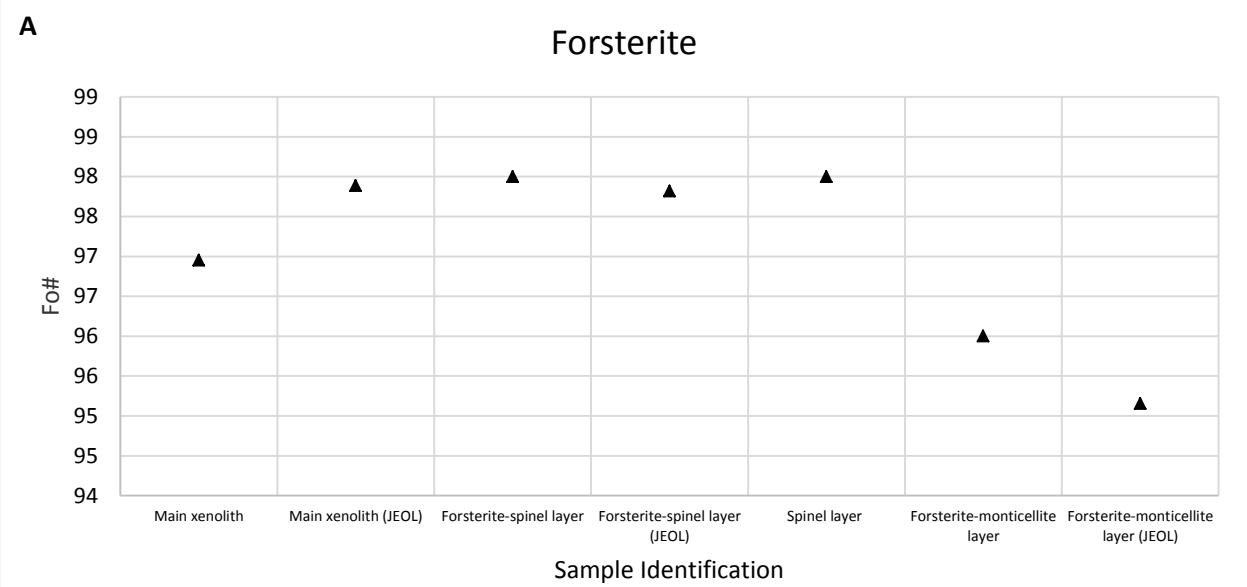

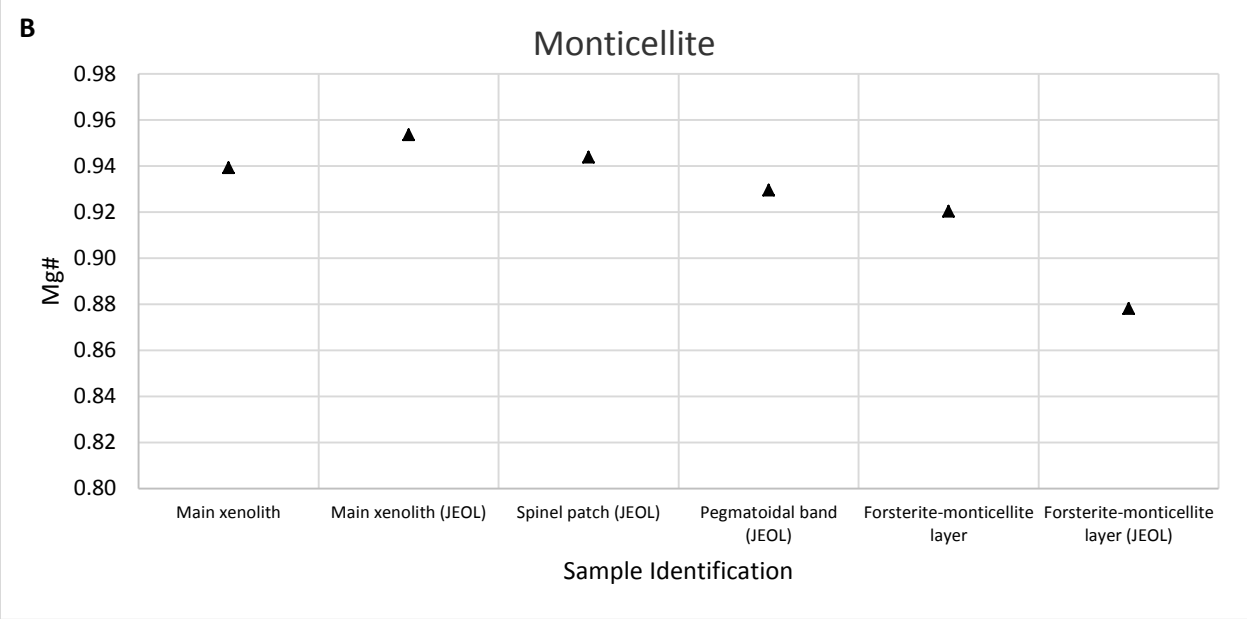

Figure 4.2: Plots of Fo# (A) and X_{Mg} (B) averages per sample in different locations from the Marikana xenoliths. Samples from the main xenolithic body are plotted on the left; samples found in the westernmost sector of the xenolith are plotted on the right in order to depict the compositional variation in a spatial context. Trends show that X_{Mg} and Fo# decrease from the main xenolithic body to forsterite-monticellite layer.

X_{Mg} decreases in both monticellite and forsterite towards the forsterite-monticellite layer, while Fe increases towards the forsterite-monticellite layer. Although the Ca content in monticellite

(from the main xenolithic body to forsterite-monticellite layer) remains consistent, at 0.96 apfu–0.97 apfu, it should be noted that there is no monticellite evident in the forsterite-spinel layer. This indicates that there is a decrease in Ca towards the forsterite-spinel layer as the Ca-rich phase (monticellite) becomes less prevalent.

Table 4. 3: Representative chemical compositions of monticellite from the Marikana xenolith

Sample	Main xenolith (CAMECA)	Forsterite-monticellite layer (CAMECA)	Main xenolith (JEOL)	Spinel patch (JEOL)	Pegmatoidal band (JEOL)	Forsterite-monticellite layer JEOL
Mineral	**Mtc**	**Mtc**	**Mtc**	**Mtc**	**Mtc**	**Mtc**
SiO_2	37.65	37.37	37.98	37.86	37.70	37.08
Al_2O_3	bdl	0.01	0.01	bdl	bdl	bdl
TiO_2	0.03	0.02	0.03	0.03	0.03	0.04
Cr_2O_3	0.02	0.02	0.01	0.02	0.03	0.02
FeO	2.78	3.62	2.14	2.58	3.22	5.45
MnO	0.57	0.57	0.56	0.52	0.57	0.64
MgO	24.08	23.49	24.67	24.28	23.78	22.03
CaO	34.03	33.62	33.88	33.81	33.66	32.83
Na_2O	0.01	0.01	0.01	bdl	0.01	0.01
K_2O	bdl	bdl	0.02	0.02	0.02	0.02
Total	99.15	98.73	99.30	99.08	99.02	98.13
			Number of ions based on 4 Oxygens			
Si	1.00	1.00	1.00	1.00	1.00	1.01
Al	bdl	bdl	bdl	bdl	bdl	bdl
Ti	bdl	bdl	bdl	bdl	bdl	bdl
Cr	bdl	bdl	bdl	bdl	bdl	bdl
Fe^{2+}	0.06	0.08	0.05	0.06	0.07	0.12
Mn	0.01	0.01	0.01	0.01	0.01	0.01
Mg	0.95	0.94	0.97	0.96	0.94	0.89
Ca	0.97	0.96	0.96	0.96	0.96	0.95
Na	bdl	bdl	bdl	bdl	bdl	bdl
K	bdl	bdl	bdl	bdl	bdl	bdl
Total	3.00	3.00	3.00	3.00	3.00	2.99
Mg#	0.94	0.92	0.95	0.94	0.93	0.88

Table 4. 4: Representative chemical compositions of forsterite from the Marikana xenolith

Sample	Main xenolith CAMECA	Forsterite-spinel layer (CAMECA)	Spinel layer (CAMECA)	Forsterite-monticellite layer (CAMECA)	Main xenolith (JEOL)	Forsterite-spinel layer (CAMECA)	Forsterite-monticellite layer (CAMECA)
Mineral	**Fo**	**Fo**	**Fo**	**Fo**	**Fo**	**Fo**	**Fo**
SiO_2	42.16	41.89	42.10	41.89	42.05	41.52	41.86
Al_2O_3	0.02	0.02	bdl	0.02	0.06	0.01	0.01
TiO_2	0.02	0.01	0.02	0.01	0.03	0.01	0.02
Cr_2O_3	0.01	0.01	0.01	0.02	0.02	0.01	0.02
FeO	3.07	3.91	2.31	2.18	2.13	4.81	2.17
MnO	0.55	0.54	0.47	0.50	0.52	0.50	0.50
MgO	54.72	53.96	55.21	55.45	55.34	52.96	54.64
CaO	0.60	0.62	0.54	0.67	0.56	0.56	0.60
Na_2O	bdl	bdl	bdl	bdl	bdl	0.01	bdl
K_2O	bdl	bdl	bdl	bdl	0.02	0.02	0.02
Total	101.14	100.96	100.65	100.75	100.74	100.41	99.84
			Number of ions based on 4 Oxygens				
Si	0.99	0.99	0.99	0.99	0.99	0.99	1.00
Al	bdl	bdl	bdl	bdl	bdl	bdl	bdl
Ti	bdl	bdl	bdl	bdl	bdl	bdl	bdl
Cr	bdl	bdl	bdl	bdl	bdl	bdl	bdl
Fe^{2+}	0.06	0.08	0.05	0.04	0.04	0.10	0.04
Mn	0.01	0.01	0.01	0.01	0.01	0.01	0.01
Mg	1.92	1.91	1.94	1.95	1.95	1.89	1.94
Ca	0.02	0.02	0.01	0.02	0.01	0.01	0.02
Na	bdl	bdl	bdl	bdl	bdl	bdl	bdl
K	bdl	bdl	bdl	bdl	bdl	bdl	bdl
Total	3.01	3.01	3.01	3.01	3.01	3.01	3.00
Mg#	0.97	0.96	0.98	0.98	0.98	0.95	0.98

4.3.2 Calcite

EMPA confirmed the occurrence of calcite ($CaCO_3$) in the main xenolithic samples containing patches of spinel (RSTS26-01) and pegmatoidal grains of monticellite (RSTX26-04). A representative chemical composition is shown in Appendix 4B. Calcite is composed of 1.99 apfu Ca, minor amounts of Sr and Mg, and negligible amounts of Ba.

4.3.3 Pyroxene

Pyroxenes are found in the contact zone matrix and surrounding calc-silicate fragments, the chromitite stringer, and mottled anorthosite (Table 4.5). They occur in numerous mineral assemblages and display several textural features that are illustrated in Chapter 3. Pyroxene compositions have been classified according to Morimoto *et al*. (1988), as approved by the International Mineralogical Association; a general pyroxene classification diagram is provided in Figure 4.3. Clinopyroxenes, including diopside ($CaMgSi_2O_6$) and hedenbergite ($CaFeSi_2O_6$), are present and more abundant than orthopyroxenes, such as enstatite ($Mg_2Si_2O_6$). The pyroxenoid wollastonite ($Ca_2Si_2O_6$) is also present in the sample suite. A variety of ionic substitutions is evident in the clinopyroxene and cannot be accounted for in the general classification diagram of Morimoto *et al*. (1988). Therefore, adjectival modifiers for mineral names are used to indicate unusual, but significant, amounts of chemical constituents, such Al, Fe^{3+} or Cr. Representative analyses of pyroxene in the sample suite are shown in Table 4.6, with the number of ions based on six oxygens. The Fe^{2+}/Fe^{3+} estimations were calculated based the method described by Droop (1987).

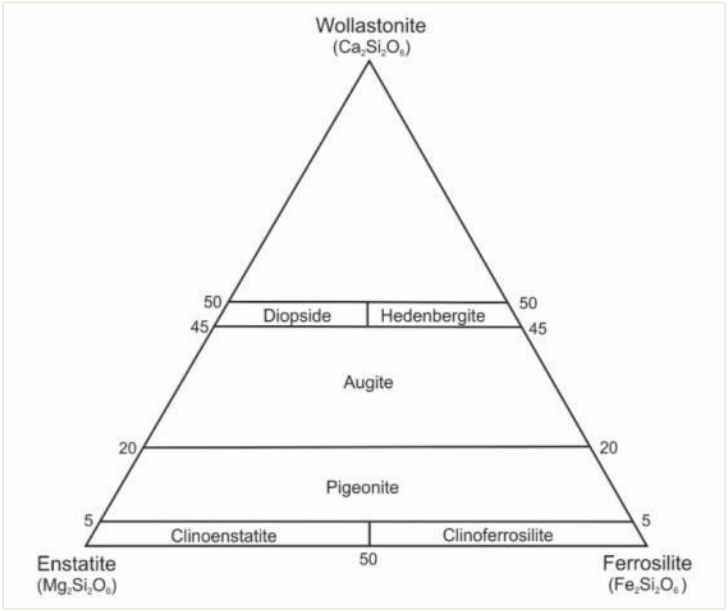

Figure 4.3: General pyroxene classification diagram according to Morimoto *et al*. (1988).

Table 4. 5: Summary of samples containing pyroxene and the associated mineral assemblages from the Marikana sample suite

Sample name	Sample description	Mineral assemblage
RSTX26-13	Fragment - surrounding calc-silicate minerals	Di + Grt + Spl + Wo
RSTX26-51	Matrix - involved in coronas	Pl + Di + Grt + Wo
RSTX26-52	Fragment - surrounding calc-silicate minerals	Di + Grt + Spl + Ves + Mtc
RSTX26-53 A	Matrix - involved in coronas	Pl + Di + Grt + Ves
RSTX26-53 B	Fragment - surrounding calc-silicate minerals	Di + Grt + Spl
RSTX26-54	Matrix - involved in coronas	Pl + Di + Grt + Ves
RSTX26-61	Chromitite stringer proximal to xenolith	Di + Grt + Spl
RSTX26-62	Chromitite stringer intermediate	Pl + Di + Grt + Spl
RSTX26-63	Chromitite stringer distal to xenolith	Pl + Di + Grt + Spl
RSTX26-A5	Mottled anorthosite 5 m away from the main xenolith body	Pl + Di
RSTX26-A20	Mottled anorthosite 20 m away from the main xenolith body	Pl + Di

Clinopyroxene found in the matrix of the contact zone occurs in conjunction with plagioclase and is evident in three samples (RSTX26-51, RSTX26-53A and RSTX26-54). The clinopyroxene in the matrix shows broadly similar compositions, but with some variation. Pyroxenes are characterised by high amounts of Al (up to 0.77 apfu) (Figure 4.5) and can therefore be termed Al-diopside (Morimoto *et al*., 1988). According to Figure 4.4, pyroxene from sample RSTX26-53 is diopsidic, and ranges from Wo_{57}-En_{33}-Fs_{10} to Wo_{59}-En_{33}-Fs_{8}. Clinopyroxene in sample RSTX26-51 shows a range from Wo_{52}-En_{42}-Fs_{6} to Wo_{61}-En_{30}-Fs_{9}, with an Al content of 0.50 apfu – 0.67 apfu. Sample RSTX26-54 shows a range from Wo_{55}-En_{36}-Fs_{9} to Wo_{62}-En_{30}-Fs_{8} and Al shows a significant variation from 0.51 apfu to 0.77 apfu. Element mapping shows that Al-diopside immediately adjacent to plagioclase or garnet reaction coronas between the pyroxene and plagioclase has a higher Al content than cores of the pyroxene grains (Figure 4.6).

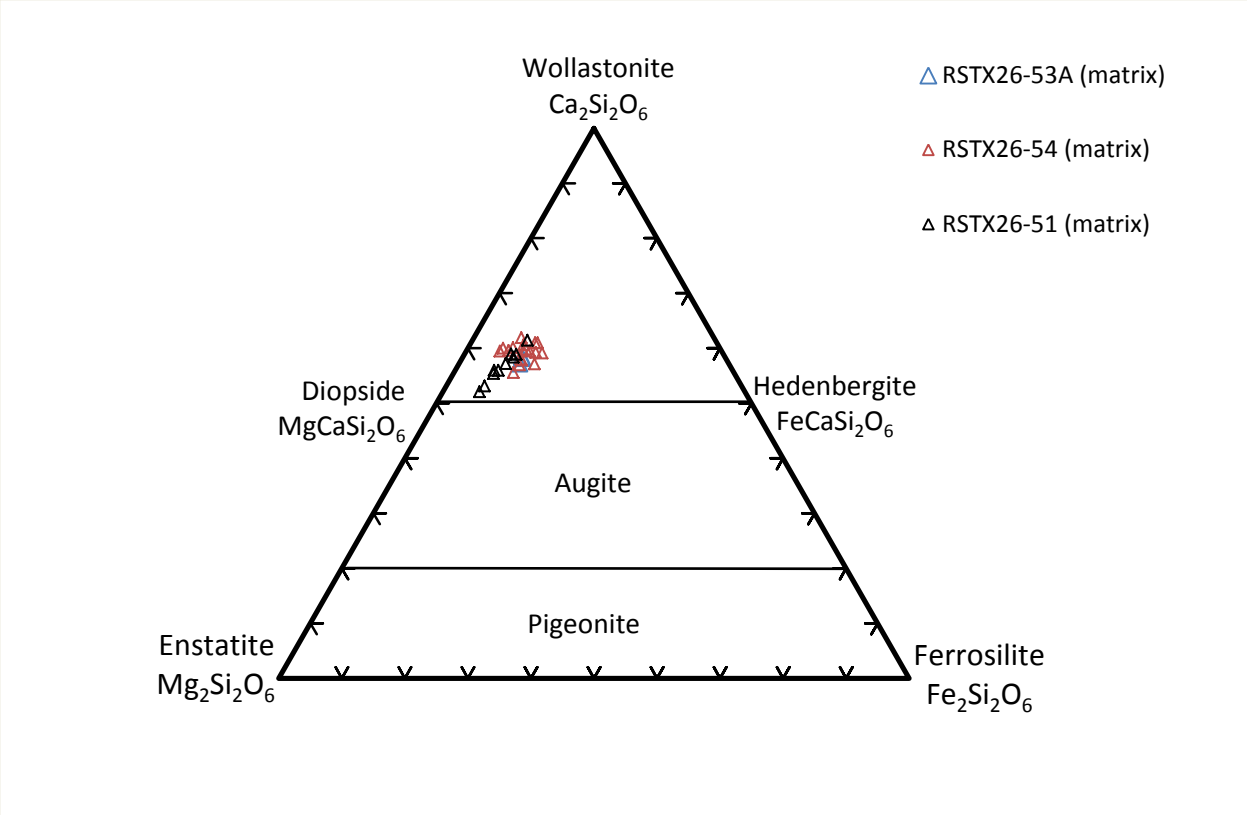

Figure 4.4: Ternary plot for pyroxene endmembers wollastonite, enstatite and ferrosilite, representing clinopyroxene compositions from the matrix in the contact zone for the Marikana sample suite.

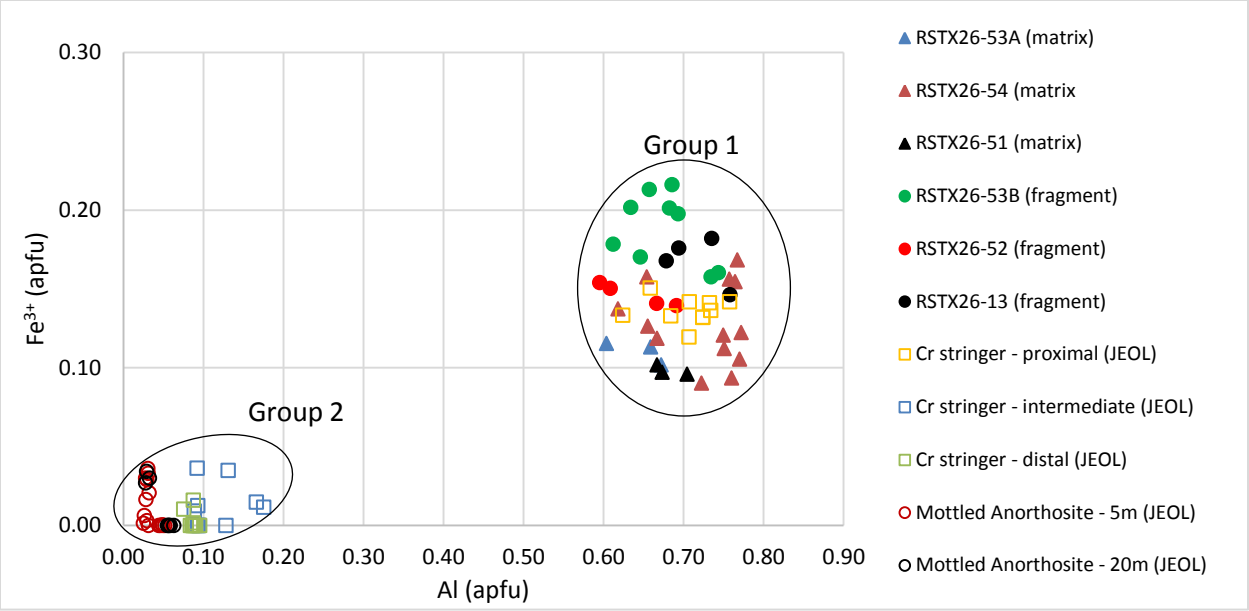

Figure 4.5: Cation-cation plot of Al and Fe^{3+} representing all clinopyroxenes in the Marikana sample suite showing two distinct groups. Group 1 comprises samples found in the contact zone; Group 2 comprises mottled anorthosite samples, as well as samples from the chromitite stringer distal to the xenolith.

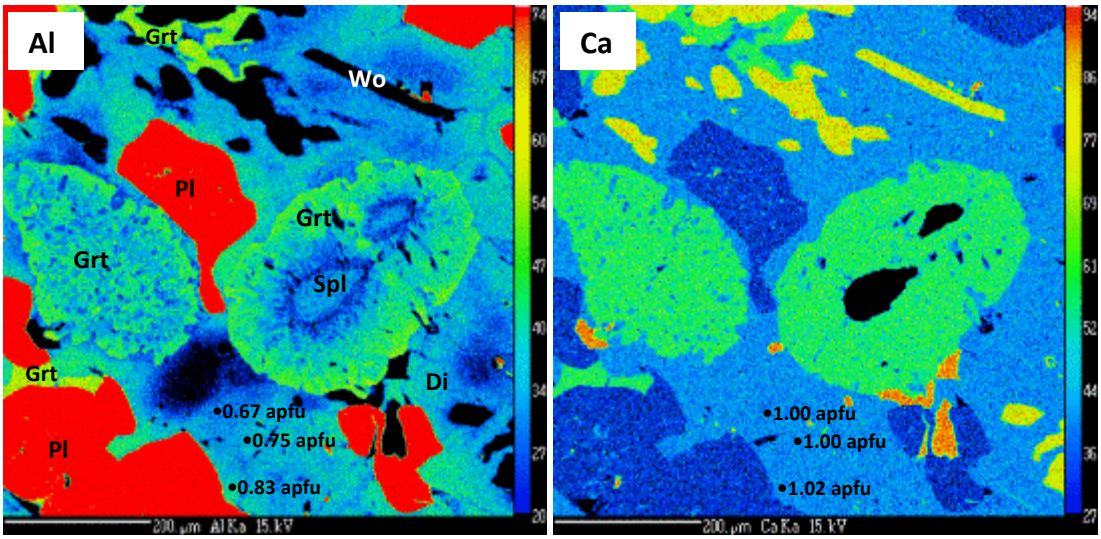

Figure 4.6: Element map with superimposed cation data showing clinopyroxene-plagioclase coronas that produce garnet in sample RSTX26-51 (Marikana contact zone). Al is at highest concentration adjacent to plagioclase and decreases further away from plagioclase grain boundaries. Ca remains constant throughout the grains. Coronas are also observed in BSE image in Figure 3.13.

Clinopyroxene is also found in samples RSTX26-53, RSTX26-52 and RSTX26-13 that contain calc-silicate fragments, together with Cr-spinel and garnet. Clinopyroxene in RSTX26-53 ranges from Wo_{56}-En_{32}-Fs_{12} to Wo_{59}-En_{30}-Fs_{11} (Figure 4.7). Clinopyroxene chemical composition indicates that it is Al-diopside as well and the Al content shows a variation from 0.63 to 0.71 apfu (Figure 4.5). Sample RSTX26-52 shows a range from Wo_{54}-En_{38}-Fs_{8} to Wo_{59}-En_{29}-Fs_{12}, while Al ranges from 0.43 apfu to 0.69 apfu. Al-diopside analysed in sample RSTX26-13 varies from Wo_{58}-En_{30}-Fe_{12} to Wo_{60}-En_{28}-Fe_{12} and Al shows a range from 0.68 apfu to 0.76 apfu. According to the EMPA results for these samples it appears that the Al content is lower in Al-diopside immediately adjacent to garnet, and increases further away from garnet (Figure 4.8). Wollastonite is found in the contact zone and most commonly occurs as elongate inclusions in Al-diopside in the matrix surrounding calc-silicate fragments. The average composition of wollastonite is Wo_{99}-$Di_{0.3}$-$Hd_{0.7}$ (Figure 4.7).

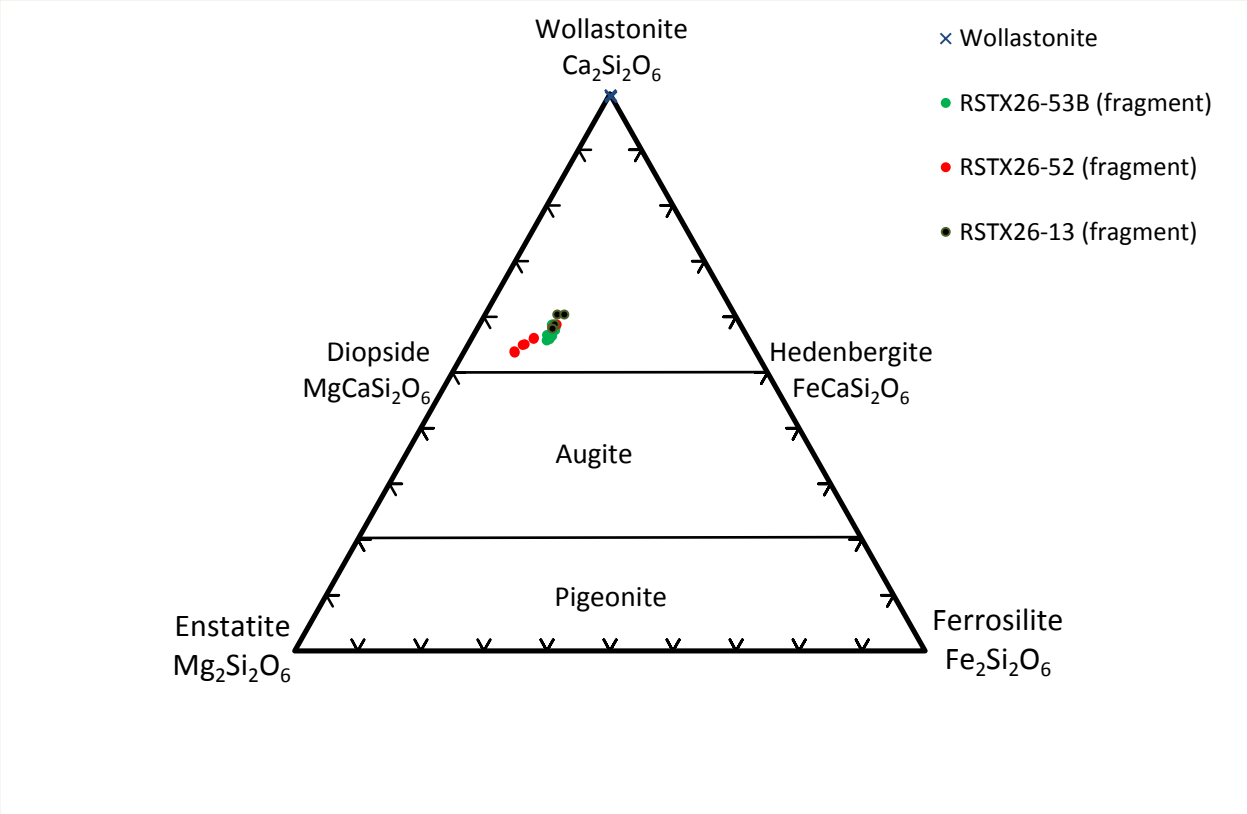

Figure 4.7: Ternary plot for pyroxene endmembers wollastonite, enstatite and ferrosilite representing compositions of clinopyroxene found in fragments for the Marikana sample suite.

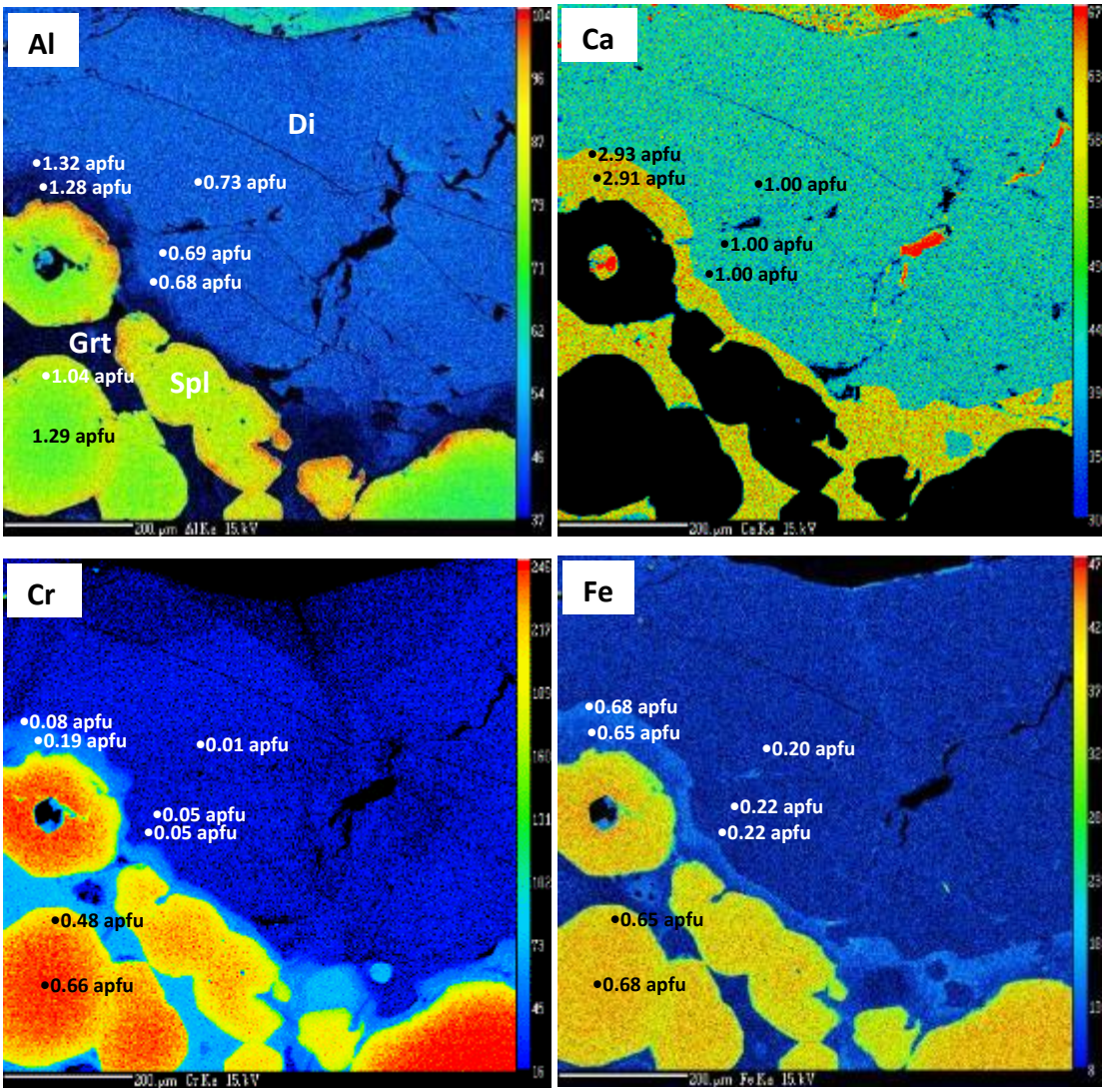

Figure 4.8: Element map showing Al-diopside, garnet and spinel in fragment RSTX26-53B from the Marikana contact zone. No zonation is detected in diopside. Zonation is not well developed for Cr and Al in garnet; however, the EMPA data show that there is a decrease in Cr and an increase in Al from core to rim. Ca remains constant and Fe_T increases slightly at the rims of garnet. Spinel grains display clear Cr zonation from core to rim.

The chromitite stringer sample shows variation in clinopyroxene composition based on whether the pyroxene is proximal, intermediate or distal from the xenolith (Figure 4.9). Even though the distance between the most proximal and distal samples to the xenolith is ≤ 5 cm there is a significant compositional variation. The sample proximal to the xenolith (labelled *Cr-stringer proximal* in figures) shows compositions similar to samples from the contact zone matrix and

surrounding the calc-silicate fragments, and can be termed Al-diopside. Compositions range from Wo_{56}-En_{34}-Fs_{10} to Wo_{59}-En_{29}-Fs_{12}, while Al content varies from 0.68 apfu to 0.76 apfu (Figure 4.5). Clinopyroxene in the intermediate sample contains significantly less Ca and more Mg than the proximal sample, ranging from Wo_{49}-En_{44}-Fs_{7} to Wo_{51}-En_{37}-Fs_{12}, while the Al content is significantly less, between 0.10 apfu and 0.17 apfu. This is still considered Al-diopside according to Morimoto *et al*. (1988) because the sample contains ≥ 0.1 Al apfu. Clinopyroxene in the distal sample contains even less Ca and more Mg and shows a variation from Wo_{45}-En_{47}-Fs_{8} to Wo_{49}-En_{44}-Fs_{7}, with Al having an average of 0.09 apfu; therefore it is classified as diopside.

The mottled anorthosite located 5 m away from the main xenolithic body contains both clinopyroxene and orthopyroxene. The clinopyroxene composition varies from Wo_{45}-En_{43}-Fs_{12} to Wo_{46}-En_{44}-Fs_{10} (Figure 4.9), while the Al content varies from 0.03 apfu to 0.05 apfu (Figure 4.5). Clinopyroxene in mottled anorthosite located 20 m away from the xenolith exhibits a compositional range from Wo_{42}-En_{41}-Fs_{17} to Wo_{44}-En_{40}-Fs_{16}, with an Al content of 0.06 apfu. All clinopyroxene in these rocks is augite. Orthopyroxene in the mottled anorthosite located 5 m from the xenolith shows a slight compositional range from Wo_{1}-En_{70}-Fs_{29} to Wo_{2}-En_{69}-Fs_{29}. In the sample 20 m away from the xenolith the orthopyroxene has a compositional range from Wo_{2}-En_{69}-Fs_{29} to Wo_{5}-En_{59}-Fs_{36}. The Al content remains constant at 0.03 apfu.

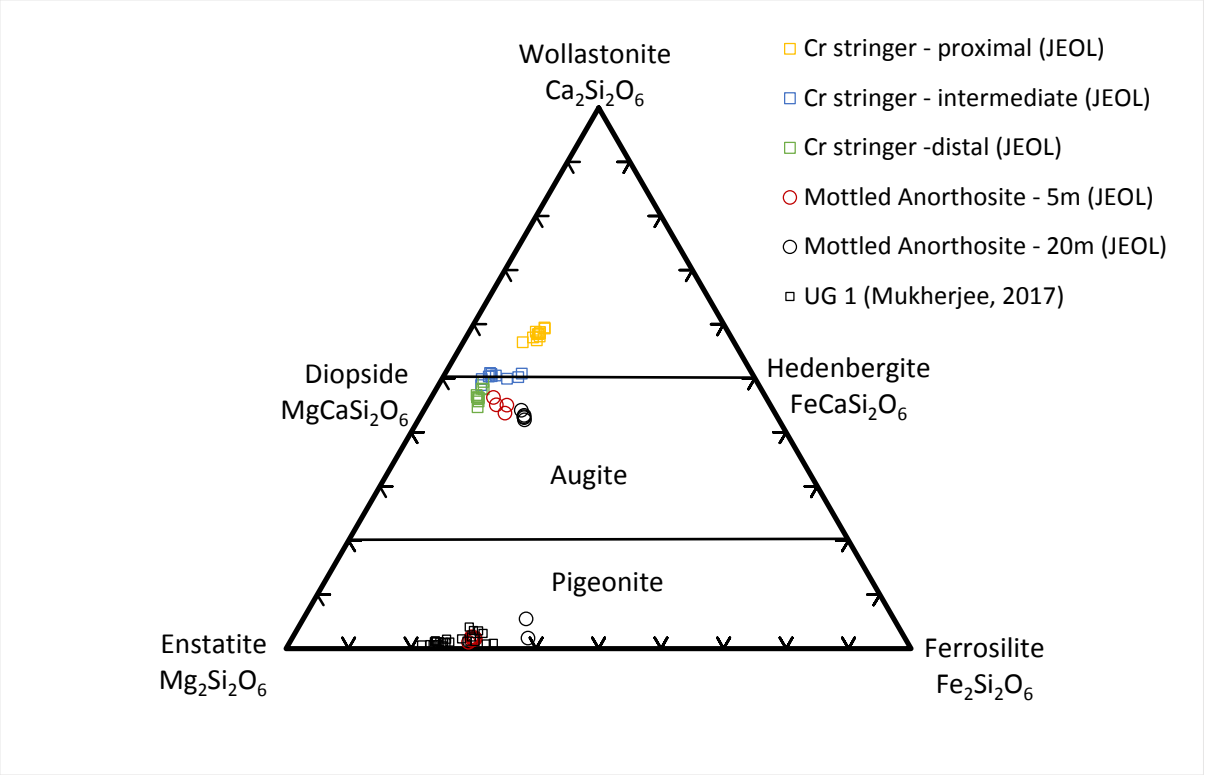

Figure 4.9: Ternary plot for pyroxene endmembers wollastonite, enstatite and ferrosilite representing compositions from the chromitite stringer, mottled anorthosite, and UG 1 from the Marikana sample suite.

Table 4. 6: Representative chemical compositions of pyroxene from the Marikana sample suite

Sample	RSTX26-53A (CAMECA)	RSTX26-53A (CAMECA)	RSTX26-53B (CAMECA)	RSTX26-51 (CAMECA)	RSTX26-52 (CAMECA)	RSTX26-54 (CAMECA)	RSTX26-54 (CAMECA)	RSTX26-13 (CAMECA)	RSTX26-13 (CAMECA)
mineral	Cpx	Wo	Cpx	Cpx	Cpx	Cpx	Wo	Cpx	Wo
SiO_2	42.88	51.03	37.84	45.03	43.61	41.98	50.86	40.47	51.58
TiO_2	0.31	0.03	1.25	0.32	0.39	0.35	0.01	0.45	0.01
Al_2O_3	15.62	0.06	15.03	12.37	12.52	16.82	0.07	16.14	0.10
Cr_2O_3	0.14	bdl	0.48	0.44	0.66	0.25	0.02	1.50	0.02
FeO	5.18	0.28	4.30	4.02	5.48	4.96	0.12	6.48	0.23
MnO	0.08	0.11	0.05	0.06	0.05	0.06	0.07	0.08	0.14
MgO	9.96	bdl	8.74	11.63	11.03	9.71	bdl	8.69	0.02
CaO	25.17	47.28	31.43	25.19	24.69	25.21	47.79	24.97	47.27
Na_2O	0.01	0.01	0.17	0.01	bdl	0.01	bdl	0.02	0.01
Total	99.33	98.79	99.12	99.06	98.42	99.34	98.92	98.77	99.36
Number of ions based on 6 Oxygens									
Si	1.59	2.00	1.41	1.67	1.63	1.56	1.99	1.52	2.01
Ti	0.01	bdl	0.04	0.01	0.01	0.01	bdl	0.01	bdl
Al	0.68	bdl	0.66	0.54	0.55	0.73	bdl	0.72	bdl
Fe^{3+}	0.12	bdl	0.12	0.09	0.14	0.13	bdl	0.17	bdl
Cr^{3+}	bdl	bdl	0.01	0.01	0.02	0.01	bdl	0.04	bdl
Fe^{2+}	0.05	0.01	0.01	0.03	0.04	0.03	bdl	0.04	0.01
Mn	bdl	bdl	bdl	bdl	bdl	bdl	bdl	bdl	bdl
Mg	0.55	bdl	0.49	0.64	0.62	0.54	bdl	0.49	bdl
Ca	1.00	1.98	1.25	1.00	0.99	1.00	2.00	1.01	1.97
Na	bdl	bdl	0.01	bdl	bdl	bdl	bdl	bdl	bdl
Total	4.00	4.00	4.00	4.00	4.00	4.00	4.00	4.00	4.00
Wo	62.72	99.54	70.58	59.94	60.41	64.06	100.00	65.82	99.58
En	34.47	0.00	28.58	38.16	37.38	34.25	0.00	31.83	0.04
Fs	2.80	0.46	0.85	1.90	2.21	1.70	0.00	2.35	0.38
Total	100.00	100.00	100.00	100.00	100.00	100.00	100.00	100.00	100.00

Table 4.6 *(continued)*

Sample	RSTX26-61(JEOL)	RSTX26-62 (JEOL)	RSTX26-63(JEOL)	RSTX26-A5 (JEOL)	RSTX26-A5 (JEOL)	RSTX26-A20 (JEOL)	RSTX26-A20 (JEOL)
mineral	Cpx	Cpx	Cpx	Opx	Cpx	Opx	Cpx
SiO_2	**41.32**	51.83	52.10	53.55	53.79	52.12	52.20
TiO_2	0.54	0.27	0.25	0.24	0.33	0.29	0.53
Al_2O_3	15.92	2.64	4.66	0.67	1.03	0.68	1.30
Cr_2O_3	0.74	0.73	0.63	0.22	0.37	0.09	0.32
FeO	6.10	5.35	4.42	18.71	6.89	22.60	10.21
MnO	0.10	0.15	0.12	0.33	0.14	0.40	0.23
MgO	9.32	14.24	14.38	25.06	16.96	20.82	13.88
CaO	24.49	24.15	22.46	0.88	18.56	2.62	20.34
Na_2O	0.01	0.14	0.33	0.01	0.14	0.01	0.21
Total	98.52	99.36	99.03	99.65	98.07	99.61	99.01
			Number of ions based on 6 Oxygens				
Si	1.55	1.92	1.93	1.97	2.01	1.96	1.97
Ti	0.02	0.01	0.01	0.01	0.01	0.01	0.01
Al	0.71	0.12	0.20	0.03	0.05	0.03	0.06
Fe3+	0.14	0.01	0.01	0.02	bdl	0.03	bdl
Cr3+	0.02	0.02	0.02	0.01	0.01	bdl	0.01
Fe2+	0.06	0.15	0.13	0.56	0.22	0.68	0.32
Mn	bdl	bdl	bdl	0.01	bdl	0.01	0.01
Mg	0.52	0.79	0.79	1.37	0.95	1.17	0.78
Ca	0.99	0.96	0.89	0.03	0.74	0.11	0.82
Na	bdl	0.01	0.02	bdl	0.01	bdl	0.02
Total	4.00	4.00	4.00	4.00	4.00	4.00	4.00
Wo	63.08	50.49	51.35	1.76	38.84	5.40	42.71
En	33.36	41.39	41.71	69.94	49.87	59.76	40.55
Fs	3.56	8.12	6.94	28.30	11.29	34.83	16.74
Total	100.00	100.00	100.00	100.00	100.00	100.00	100.00

Variations in cation proportions with X_{Mg} [X_{Mg} = Mg / (Mg + Fe_T)] in all the analysed clinopyroxenes are illustrated in Figures 4.10 – 4.12. In samples containing garnet coronas, values of X_{Mg} range from 0.70 to 0.87; higher values in Al-diopside appear adjacent to plagioclase and garnet and lower values are found away from these boundaries. Al-diopside associated with the calc-silicate fragments shows a range of X_{Mg} values from 0.70 to 0.83, but shows no apparent trend. Al-diopside found in the proximal sample associated with the chromitite stringer shows an average X_{Mg} of 0.73. The intermediate sample shows an average value of 0.83 and the distal sample 0.86. Clinopyroxene in mottled anorthosite 5 m away from the main xenolithic body has an average of 0.78; 20 m away the average X_{Mg} is 0.71. Although there is no real correlation between the two components, clustering of samples into two groups is evident (Figure 4.10). Group 1 contains samples that are found in the contact zone and sample from the chromitite stringer proximal to the xenolith. Group 2 contains mottled anorthosite, as well as samples from the chromitite stringer intermediate and distal to the xenolith.

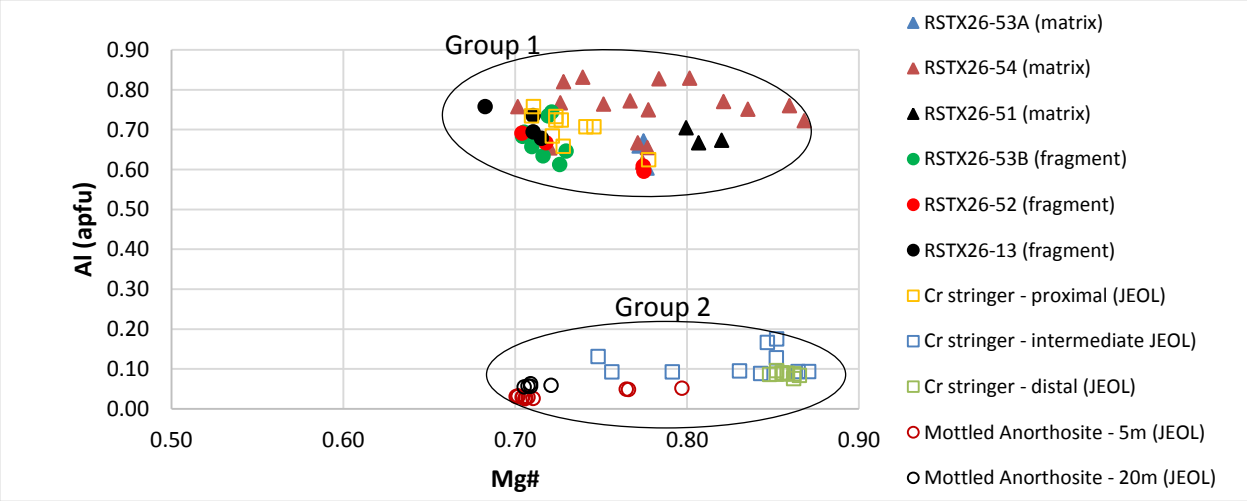

Figure 4.10: Plot depicting the correlation between Mg# and Al representing all clinopyroxene from the Marikana sample suite.

Fe_T in clinopyroxene (Figure 4.11) varies from 0.09 apfu to 0.21 apfu in samples from the contact zone matrix, with lower values appearing adjacent to plagioclase and garnet. Higher

values are observed in Al-diopside further away from these minerals. In samples containing fragments of calc-silicate rock (with spinel and garnet) the Fe_T shows variability between samples. Samples RSTX26-53 and RSTX26-13 show similar values, with an average of ~0.20 apfu – 0.21 apfu, but sample RSTX26-52 shows Fe_T ranging from 0.15 apfu to 0.21 apfu, with higher values evident in Al-diopside adjacent to garnet. Clinopyroxene in proximal, intermediate and distal samples associated with the chromitite stringer shows little Fe_T variation, with average values of 0.19 apfu, 0.14 apfu and 0.14 apfu, respectively. Clinopyroxene Fe_T values in mottled anorthosite 5 m away from the xenolith are ~0.24 apfu, and ~0.32 apfu in the sample 20 m away. Two trends are evident in Figure 4.11 and therefore samples can be divided into two groups. Group 1 hosts samples that are located in the contact zone where X_{Mg} increases from 0.68 to 0.88 as Fe_T decreases from 0.21 apfu to 0.11 apfu. The magmatic trend observed in Group 2 includes samples from the chromitite stringer intermediate and distal from the xenolith. Clinopyroxene X_{Mg} decreases from the chromitite stringer to the mottled anorthosite (from 0.87 to 0.71) and Fe_T increases from 0.12 apfu to 0.32 apfu.

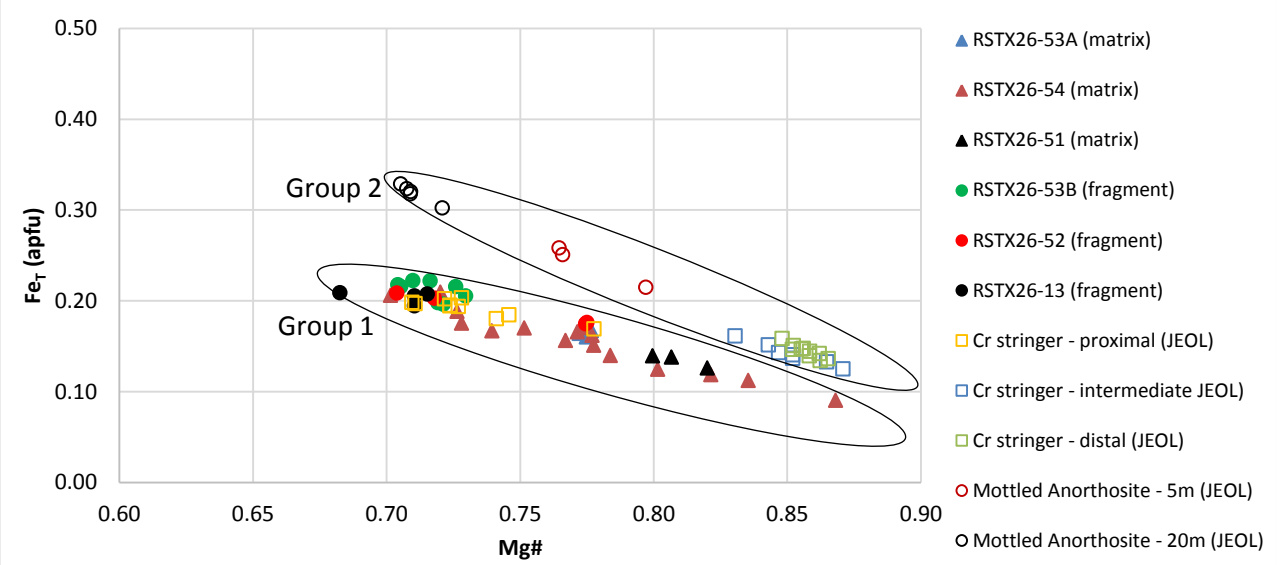

Figure 4.11: Plot depicting the correlation between Fe_T and Mg# representing all clinopyroxene from the Marikana sample suite.

Mottled anorthosite 5 m and 20 m away from the main xenolithic body contains clinopyroxene with an average Cr content of 0.01 apfu (Figure 4.12). UG 1 enstatite analysed by Mukherjee (2017) contains 0.01 Cr apfu (unpublished data). Cr values in clinopyroxene show little variability in samples from the contact zone matrix (bdl – 0.01 apfu). In samples that do not contain Cr-spinel or Cr-bearing garnet (uvarovite), little to no Cr is detected in clinopyroxene. However, in clinopyroxene that is adjacent to the Cr-bearing minerals, ≤0.03 apfu Cr is detected. In samples containing calc-silicate fragments (with a mineral assemblage of Cr-spinel + garnet (uvarovite) + Al-diopside) a slight zonation in Cr is observed in clinopyroxene, with Al-diopside immediately adjacent to garnet containing higher amounts of Cr (≤ 0.06 apfu in one sample) and Al-diopside away from garnet showing a lower Cr content (0.01 – 0.02 apfu). The same zonation is observed for the chromitite stringer proximal to the xenolith (ranging from 0.01 to 0.05 apfu). The intermediate and distal chromitite stringers show no zonation of Cr content in diopside, with an average 0.02 apfu.

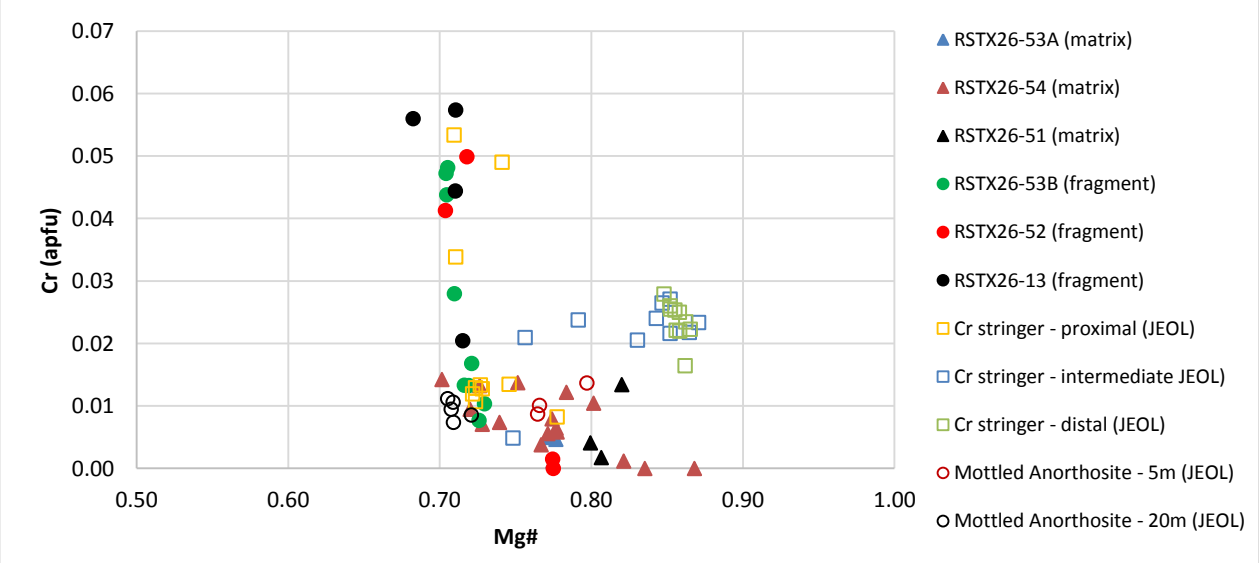

Figure 4.12: Plot depicting the correlation between Mg# and Cr representing all clinopyroxene from the Marikana sample suite.

Five metres away from the xenolith, the Ca content in clinopyroxene in mottled anorthosite ranges between 0.84 apfu and 0.87 apfu (Figure 4.13). Twenty metres away from the xenolith,

in mottled anorthosite, Ca decreases further and exhibits a range between 0.82 apfu – 0.85 apfu. The aforementioned samples lie in Group 2. The Ca content of Al-diopside remains constant (~1.00 apfu) in all samples from the contact zone matrix, calc-silicate fragments and the proximal chromitite stringer. These samples lie in Group 1. There is a slight decrease in the Ca content observed in the intermediate chromitite stringer, showing a range from 0.93 to 0.97 Ca pfu. A further decrease in Ca content is shown in the distal sample associated with the chromitite stringer (0.84 apfu to 0.95 apfu).

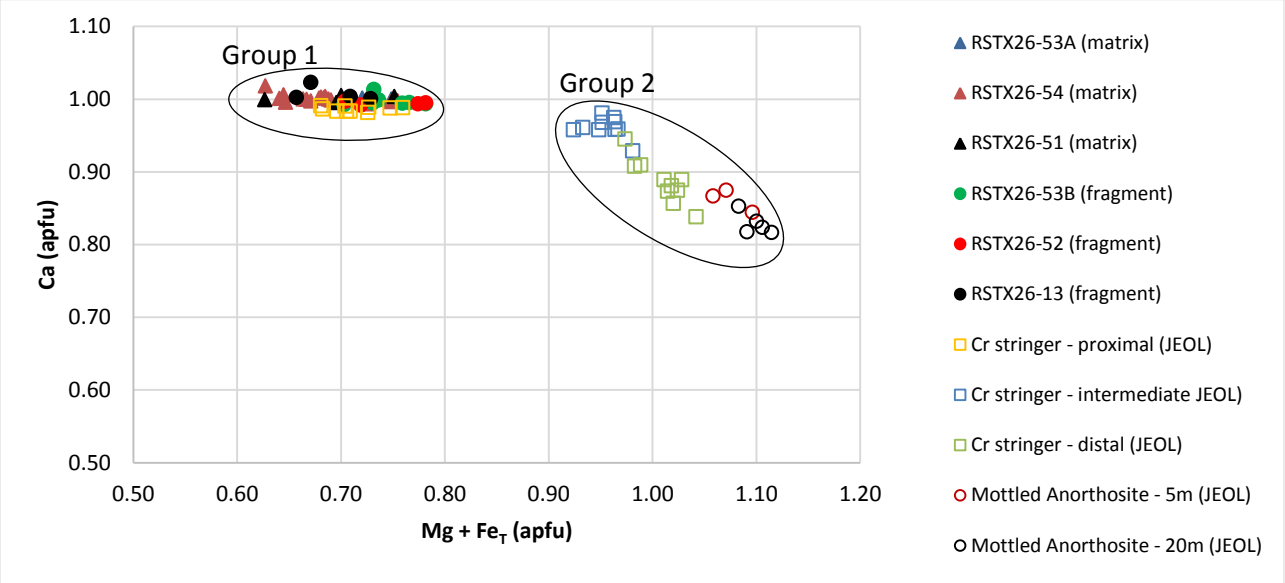

Figure 4.13: Plot depicting the correlation between Mg + Fe_T and Ca representing all clinopyroxene from the Marikana sample suite.

Mg + Fe_T plotted against Al (Figure 4.14) shows some correlation in samples found in the contact zone, Group 1. There appears to be a decrease in Mg + Fe_T (from 0.78 apfu to 0.63 apfu) as Al increases from 0.60 apfu to 0.86 apfu. Samples in Group 2 include the chromitite stringer samples intermediate and distal to the xenolith, as well as the mottled anorthosite. Only the chromitite stringer sample intermediate to the xenolith shows a slight trend: as Al decreases from 0.18 apfu to 0.09 apfu, Mg + Fe_T increases from 0.93 apfu to 0.99 apfu.

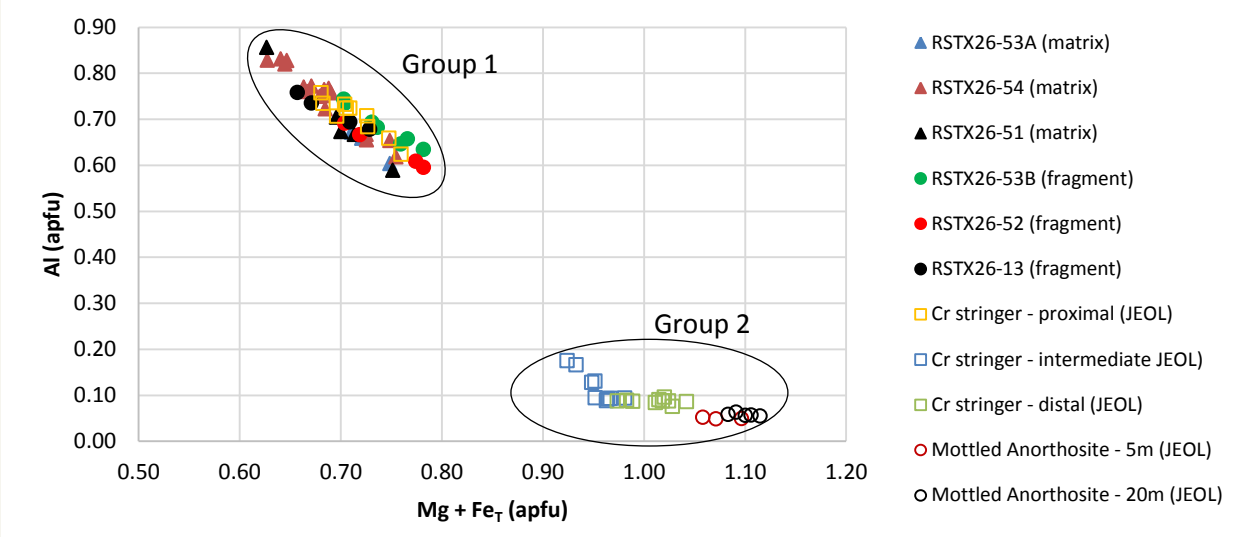

Figure 4.14: Plot depicting the correlation between Mg + Fe_T and Ca representing all clinopyroxene from the Marikana sample suite.

All major constituents found in clinopyroxene are summarised in Figure 4.15. Ca is in greatest concentration in the contact zone, particularly in the matrix surrounding calc-silicate rock fragments and in the matrix, and the proximal chromitite stringer. A decrease in Ca is observed in the intermediate and distal chromitite stringer, and the mottled anorthosite. Lower Mg concentrations are observed in samples containing calc-silicate rock fragments, the matrix (of the contact zone) and proximal chromitite stringer. Mg increases in the intermediate and distal chromitite stringer and there is a slight decrease in mottled anorthosite relative to the aforementioned samples. Al and Fe^{3+} behave inversely to Mg; with a larger decrease in Al content and relatively small but notable Fe^{3+} content between the proximal chromitite stringer and intermediate chromitite stringer. The Fe^{2+} content shows the most gradual variability, with an increase from the contact zone towards mottled anorthosite.

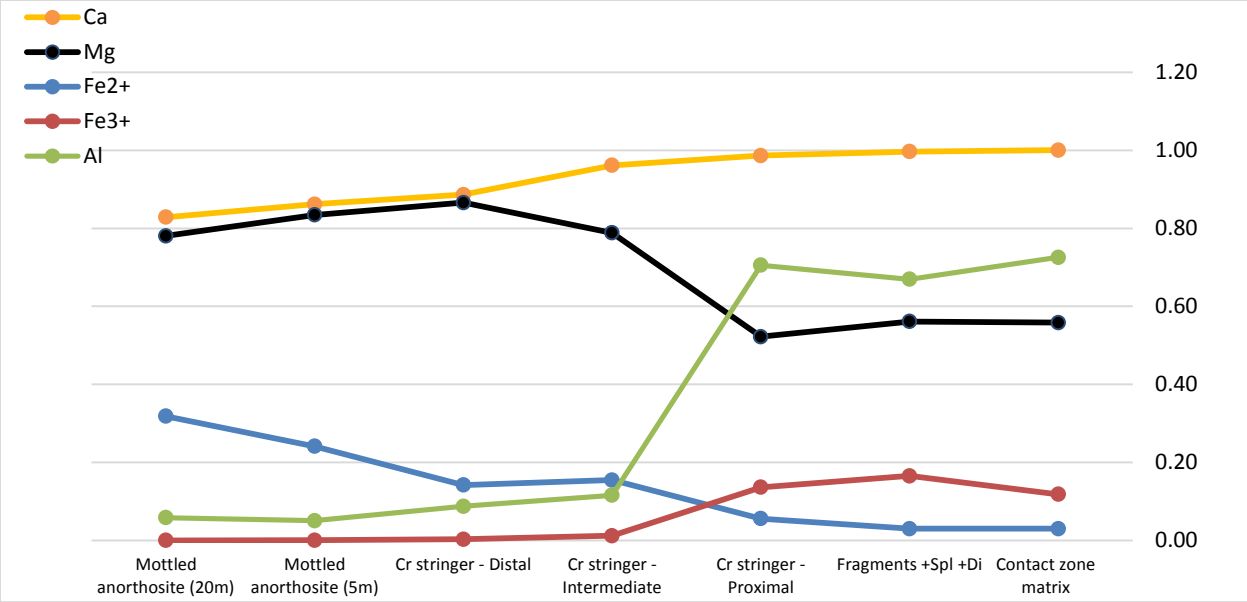

Figure 4.15: Plots showing pyroxene compositional variation (cations per formula unit) averaged for each sample from the Marikana contact zone through to the mottled anorthosite. The purpose of this figure is to illustrate the overall compositional variation spatially, from the contact zone to the igneous rock.

4.3.4 Feldspar

All feldspars analysed are Ca-rich, therefore only plagioclase feldspars [$Na(AlSi_3O_8)$ – $Ca(Al_2Si_2O_8)$] are of interest. The number of ions is based on eight oxygens. Plagioclase is found in the matrix of the contact zone, the chromitite stringer, mottled anorthosite and the UG 1 chromitite layer. Plagioclase exhibits various textural features and occurs in several mineral assemblages that are summarised in Table 4.7.

Table 4. 7: Summary of samples containing plagioclase and the associated mineral assemblages from the Marikana sample suite

Sample Name	Sample description	Mineral assemblage
RSTX26-51	Matrix - involved in coronas	Di + Grt + Pl
RSTX26-53 A	Matrix - involved in coronas	Pl + Di + Grt
RSTX26-54	Matrix - involved in coronas	Di + Grt + Pl
RSTX26-62	Cr-stringer intermediate	Di + Pl + Grt + Spl
RSTX26-63	Cr-stringer distal from xenolith	Di + Pl + Grt + Spl
RSTX26-A5	Mottled anorthosite 5 m away from the main xenolith body	Di + Pl
RSTX26-A20	Mottled anorthosite 20 m away from the main xenolith body	Di + Pl
RSTX26-UG1	UG 1 chromitite 20 m away from the main xenolithic body	Pl + Cr-Spl

In the contact zone, plagioclase commonly appears euhedral to subhedral with interstitial Al-diopside in thin-section (Figure 3.11); however, BSE images indicate that plagioclase is flanked by garnet coronas that occur adjacent to Al-diopside, signifying a metamorphic overprint (Figure 3.12A). A general variation in cation proportions across the sample suite is shown in Figure 4.16. Plagioclase in the contact zone is extremely calcic compared with grains found in mottled anorthosite and the UG 1 chromitite layer (Figure 4.17). Al and Ca remain constant at 1.99 apfu–2.00 apfu and 0.99 apfu–1.00 apfu, respectively. Representative analyses of plagioclase are shown in Table 4.8. Si shows an inverse relationship with Al, consistent with charge balance requirements.

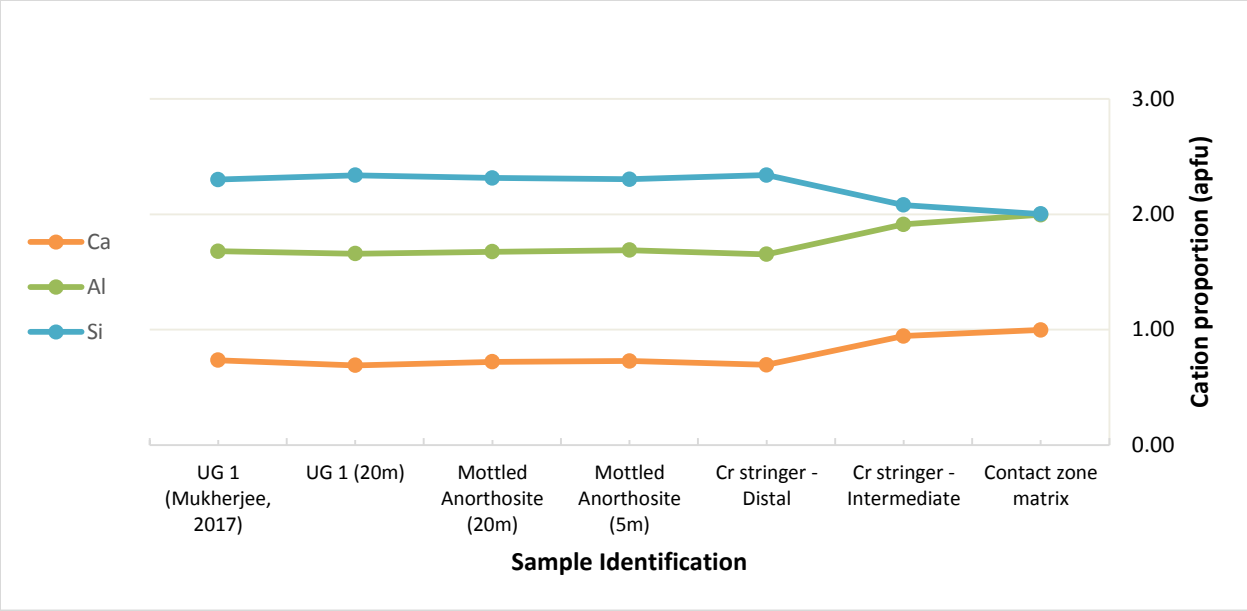

Figure 4.16: Plot showing variation in plagioclase composition (cations per formula unit) averaged for each sample from the Marikana contact zone through to the UG 1 chromitite layer and compared with unpublished data collected by Mukherjee (2017) from the UG1 chromitite layer. The purpose of this figure is to illustrate the overall compositional variation spatially, from contact zone to the igneous rock.

Table 4. 8: Representative chemical compositions of plagioclase from the Marikana sample suite

Sample	RSTX26-53A (CAMECA)	RSTX26-51 (CAMECA)	RSTX26-54 (CAMECA)	RSTX26-62 (JEOL)	RSTX26-63 (JEOL)	RSTX26-63 (JEOL)	RSTX26-63 (JEOL)	RSTX26-A5 (JEOL)	RSTX26-A20 (JEOL)	RSTX26-UG1 (JEOL)
comment					rim	core	symplectite			
SiO_2	43.01	42.83	42.92	45.34	52.99	50.43	44.61	50.72	51.27	51.57
Al_2O_3	36.31	36.23	36.35	35.37	30.20	31.82	35.87	31.56	31.42	31.04
FeO	0.14	0.13	0.06	0.18	0.16	0.16	0.06	0.23	0.33	0.15
CaO	19.93	19.85	20.07	19.21	13.30	15.36	19.81	14.95	14.82	14.20
Na_2O	0.03	0.03	0.02	0.41	3.57	2.54	0.15	2.65	2.72	3.09
K_2O	0.01	0.03	bdl	0.03	0.30	0.19	0.03	0.18	0.20	0.16
BaO	0.03	0.03	0.03							
Total	99.45	99.12	99.44	100.54	100.52	100.50	100.52	100.29	100.75	100.20
					Number of ions based on 8 Oxygens					
Si	2.00	2.00	2.00	2.08	2.39	2.29	2.05	2.30	2.32	2.34
Al	1.99	2.00	2.00	1.91	1.60	1.70	1.94	1.69	1.67	1.66
Fe	0.01	0.01	bdl	0.01	0.01	0.01	bdl	0.01	0.01	0.01
Ca	0.99	0.99	1.00	0.92	0.73	0.68	0.98	0.73	0.72	0.69
Na	bdl	bdl	bdl	0.06	0.24	0.28	0.01	0.23	0.24	0.27
K	bdl	bdl	bdl	bdl	0.01	0.01	bdl	0.01	0.01	0.01
Ba	bdl	bdl	bdl							
Total	5.00	5.00	5.00	4.98	4.98	4.97	4.99	4.97	4.97	4.97
Ab	0.28	0.31	0.15	3.68	32.11	22.77	1.32	24.03	24.63	22.35
An	99.66	99.54	99.83	96.14	66.11	76.10	98.52	74.90	74.18	76.12
Or	0.06	0.16	0.02	0.19	1.79	1.13	0.16	1.07	1.20	1.53
Total	100.00	100.00	100.00	100.00	100.00	100.00	100.00	100.00	100.00	100.00

Plagioclase found in the host rock (mottled anorthosite) 5 m away from the main xenolithic body shows no zonation and appears to be similar to typical plagioclase in mottled anorthosite found in the RLS (Cawthorn and Ashwal, 2009). The average composition is An_{75}-Ab_{24}-Or_1 (Figure 4.17A) and can be considered as bytownite (Al comprises ~1.69 apfu, Ca ~0.73, and Na 0.23 apfu). Plagioclase that occurs in mottled anorthosite 20 m away from the main xenolithic body exhibits the same textural features and has essentially the same composition of An_{74}-Ab_{25}-Or_1 (Al comprises ~1.68 apfu, Ca ~0.72 and Na 0.23 apfu). UG 1 chromitite plagioclase displays a similar composition to the mottled anorthosite, An_{71}-Ab_{28}-Or_1, although it contains slightly less Ca (Al comprises ~1.66 apfu, Ca ~0.68 and Na 0.28 apfu).

A wide range of plagioclase compositions occurs in the chromitite stringer (Figure 4.17B). Anorthite ($An_{>96}$; Al remains constant at 1.94 apfu, Ca varies between 0.97–0.98 apfu and Na between 0.01 apfu and 0.02 apfu) occurs in a symplectitic intergrowth with diopside in the distal chromitite stringer (RSTX26-63) (Figure 4.18). Inclusions found in diopside are also pure anorthite ($An_{>96}$; Al constitutes 1.94 apfu, Ca ~0.95 apfu and Na 0.03 apfu). The plagioclase in the distal chromitite stringer consists of euhedral to subhedral cumulate grains with well-defined grain boundaries (Figure 3.15 C and D), confirmed in BSE images (Figure 4.18). The EMPA results indicate that plagioclase grains in the distal chromitite stringer are compositionally zoned, with Ca decreasing from the cores (An_{81-74}; bytownite) to rims (An_{73-61}; labradorite). Less than two centimetres away, in sample RSTX26-62 (chromitite stringer intermediate to the xenolith), the cumulus plagioclase approaches pure anorthite ($An_{>94}$; Al constitutes ~1.91 apfu, Ca ~0.94 apfu and Na 0.04 apfu). There is no plagioclase recorded in the proximal chromitite stringer. Even more highly calcic plagioclase, almost pure anorthite (An_{99}) (Figure 4.17C), occurs in reaction coronas with garnet found in the matrix of the contact zone samples RSTX26-53A, RSTX26-51, and RSTX26-54.

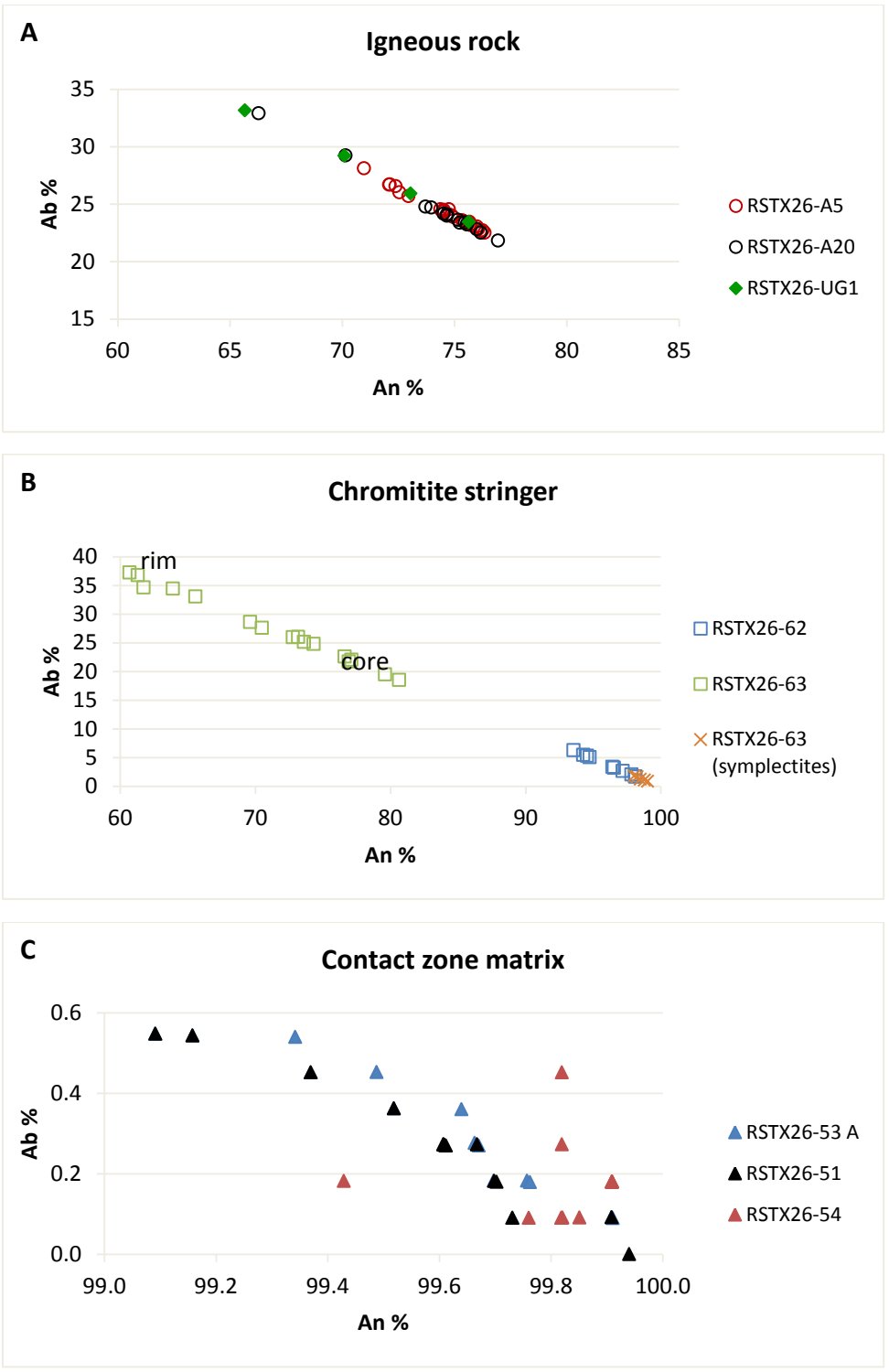

Figure 4.17: Plots depicting anorthite and albite proportions for plagioclase in igneous rock (A), the chromitite stringers (B) and the matrix in the contact zone (C) from the Marikana sample suite.

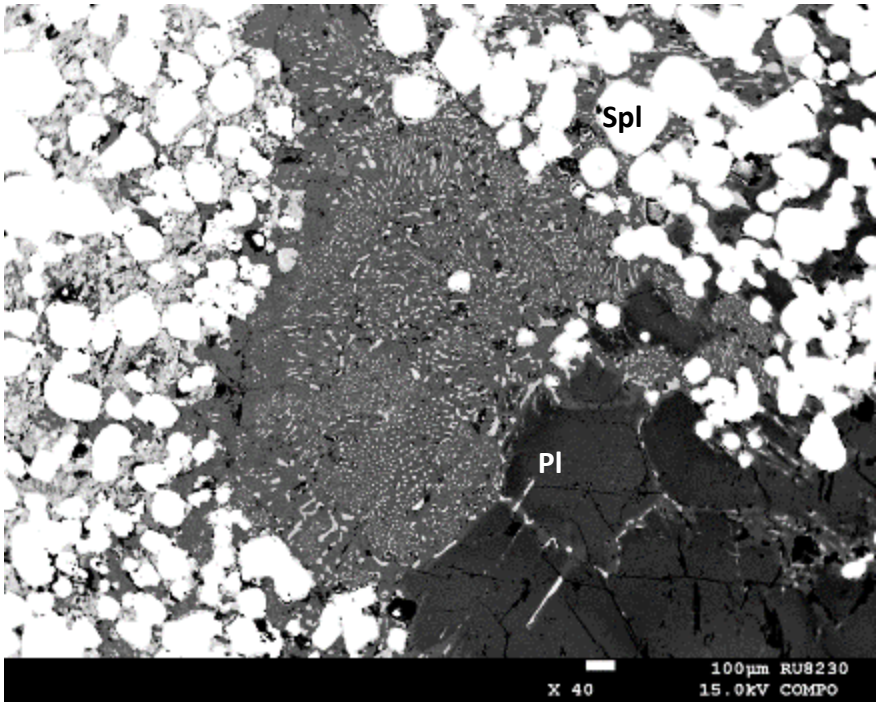

Figure 4.18: BSE image of diopside vermicules in symplectitic intergrowths with plagioclase ($An_{>96}$), surrounded by a Cr-spinel – matrix containing even finer diopside – plagioclase symplectites (RSTX26-63 – Cr-stringer distal). Plagioclase with well-defined grain boundaries is observed in the bottom right. No accurate chemical data could be recorded for the diopside vermicules owing to their small size compared to the beam diameter.

The chemical data indicate a similar clustering of plagioclase into two distinct groups (Figure 4.19) as for the clinopyroxenes. Group 1 hosts samples found in the contact zone and contains more Ca and Al than Group 2, with the exception of sample RSTX26-63 (chromitite stringer distal from the xenolith) which lies in Group 2. Plagioclase in the chromitite stringer (intermediate to the xenolith) contains compositions that approach pure anorthite (An_{94}), while 2 cm away, the chromitite stringer distal to the xenolith plagioclase shows a significant drop in An content: these grains are zoned; the cores are richer in Ca (An_{70-80}) relative to the rims (An_{60-70}). The rims contain An contents similar to plagioclase found in the RLS (Cawthorn and Ashwal, 2009). Mottled anorthosite and UG 1 plagioclase compositions correspond to Group 2. Mottled

anorthosite samples 5 m and 20 m away from the main xenolithic body show similar compositional trends as UG 1 plagioclase.

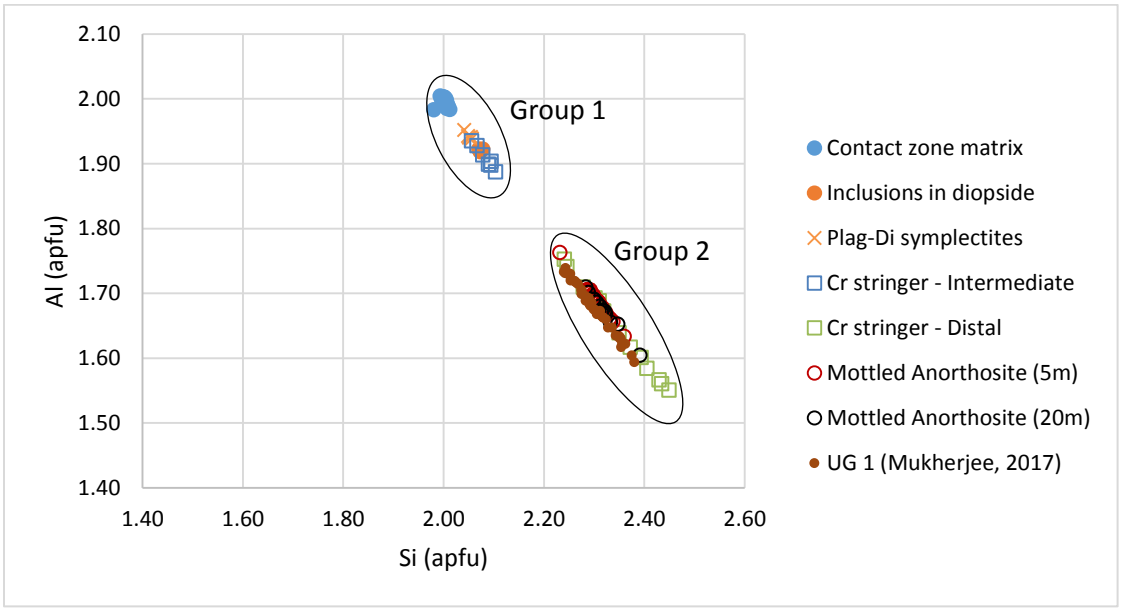

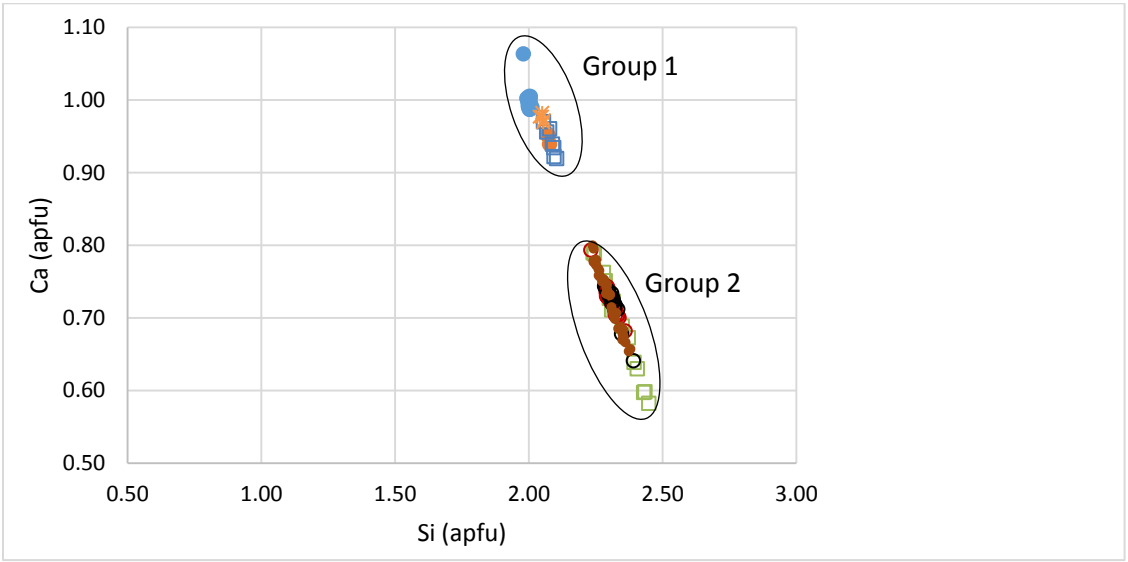

Figure 4.19: Cation-cation correlation diagrams between (A) Si vs Al and (B) Si vs Ca for plagioclase found throughout the Marikana sample suite. All samples were analysed using JEOL instrument, except samples labelled *coronas*.

4.3.5 Spinel

The general formula for spinel is $A^{2+}B^{3+}{}_2O^{2-}{}_4$ and allows a subdivision into three subgroups based on the trivalent ion (Burdett, 1982). These subgroups are spinel (Al), magnetite (Fe^{3+}) and chromite (Cr). Divalent ions include Mg, Fe^{2+}, Mn, Zn and Ni. Spinels are named based on the dominant divalent and trivalent cations, and classified according to Figure 4.20 (Deer *et al*., 1989). The number of cations is based on four oxygens. The Fe^{2+}/Fe^{3+} estimations were calculated based the method described by Droop (1987).

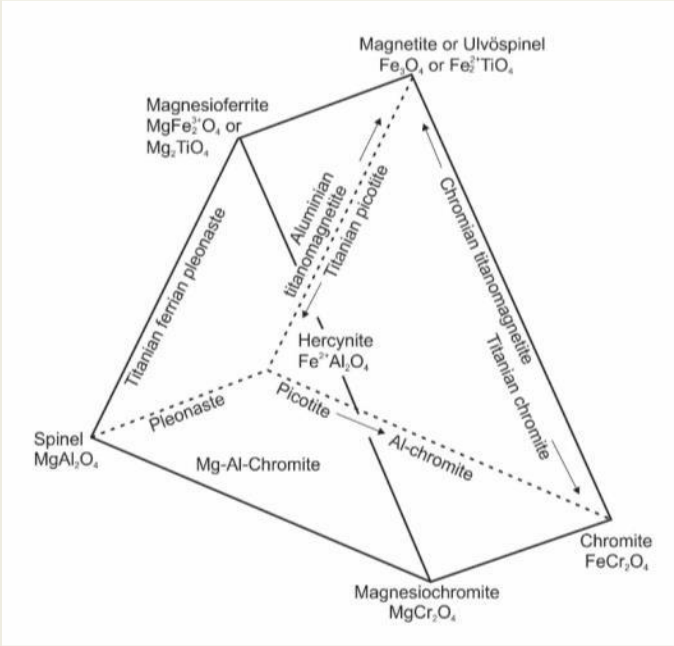

Figure 4.20: General classification diagram and nomenclature for multicomponent spinel (after Deer *et al.,* 1989).

Spinel is the only mineral that is found throughout the Marikana sample suite, but its composition varies across (Figure 4.21) and within different zones (xenolith and contact zones). The compositional variation in spinels is mainly due to variable Al, Mg, Fe, Cr and minor amounts of Ti in some samples across the sample suite from xenolith to the host anorthosite. Broad patterns can be discerned, such as the increased occurrence in Cr and Fe^{2+} within the contact zone (and a decrease in Mg and Fe^{3+}). However, the occurrence of spinel is even more

complex than depicted in Figure 4.21 owing to its presence in numerous mineral associations and textural features; for instance, exsolution is prevalent in spinel in the xenolithic body, and zonation is common in the contact zone. Table 4.9 summarises the occurrence of spinel throughout the sample suite. Representative analyses of spinel are shown in Table 4.10.

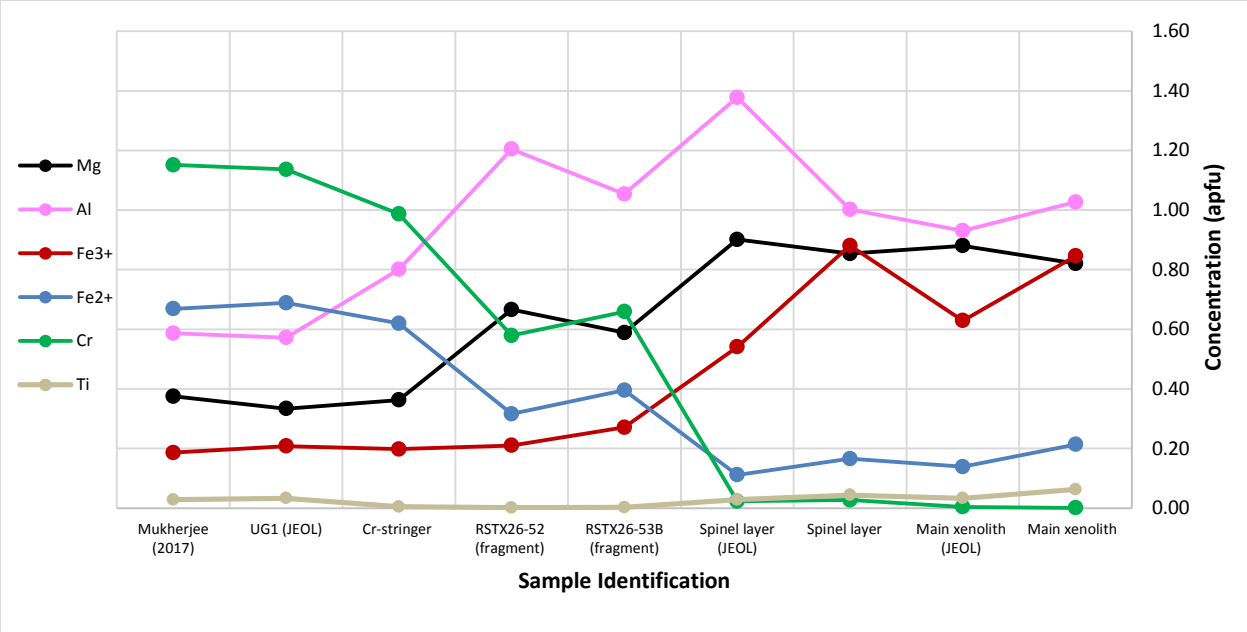

Figure 4.21: Plots showing spinel composition (cations per formula unit) averaged for each sample from the xenolith and contact zones through to the UG 1 chromitite layer and compared with unpublished data collected by Mukherjee (2017) from the UG1 chromitite layer. The purpose of this figure is to illustrate the overall compositional variation spatially, from xenolith to the mottled anorthosite in the Marikana sample suite.

Table 4. 9: Summary of the occurrence of spinel throughout the Marikana sample suite

Sample name		Sample description	Mineral assemblage	Microprobe
Xenolith	RSTX26-12	Main xenolith body	Fo + Mtc +Spl	CAMECA
	RSTX26-03	Main xenolith body	Fo + Mtc +Spl	JEOL
	RSTX26-01	Spinel patch	Mtc +Spl + Cal	JEOL
	RSTX26-04	Pegmatoidal patch	Mtc + Spl+ Cal	JEOL
Western contact of xenolith	RSTX26-05 (A, B, C)	Spinel layer and immediate surroundings		JEOL
	RSTX26-05 A	Forsterite-spinel layer	Fo + Spl	
	RSTX26-05 B	Spinel layer	Spl	
	RSTX26-05 C	Forsterite-monticellite layer	Fo + Mtc + Spl	
	RSTX26-06 (A, B, C)	Spinel layer and immediate surroundings		CAMECA
	RSTX26-06 A	Proximal to xenolith	Fo + Spl	
	RSTX26-06 B	Spinel layer	Spl	
	RSTX26-06 C	Distal from xenolith	Fo + Mtc + Spl	
Contact zone	RSTX26-53B	Fragment	Di + Grt + Spl	CAMECA
	RSTX26-52	Fragment	Di + Grt + Ves +Mtc + Spl	CAMECA
	RSTX26-61	Chromitite stringer proximal to xenolith	Di + Grt + Spl	JEOL
	RSTX26-62	Chromitite stringer intermediate	Di + Grt + Pl + Spl	
	RSTX26-63	Chromitite stringer distal from xenolith	Di + Grt + Pl + Spl	
Igneous Rock	RSTX26-UG1	UG 1 chromitite 20 m away from the main xenolithic body	Pl + Spl	JEOL

Figure 4.22 illustrates the spinel compositional variation throughout the Marikana sample suite. Spinel that is found in the xenolith and western contact of the xenolith exhibits similar compositions. These spinels show exsolution textures and are Mg-Al-rich spinel (spinel, *sensu stricto*), with Fe-rich (magnetite) exsolution lamellae. In the contact zone, the spinel exhibits different compositional trends, with the major difference being the presence of Cr. Zonation is evident, with Cr decreasing and Al increasing from core to rim.

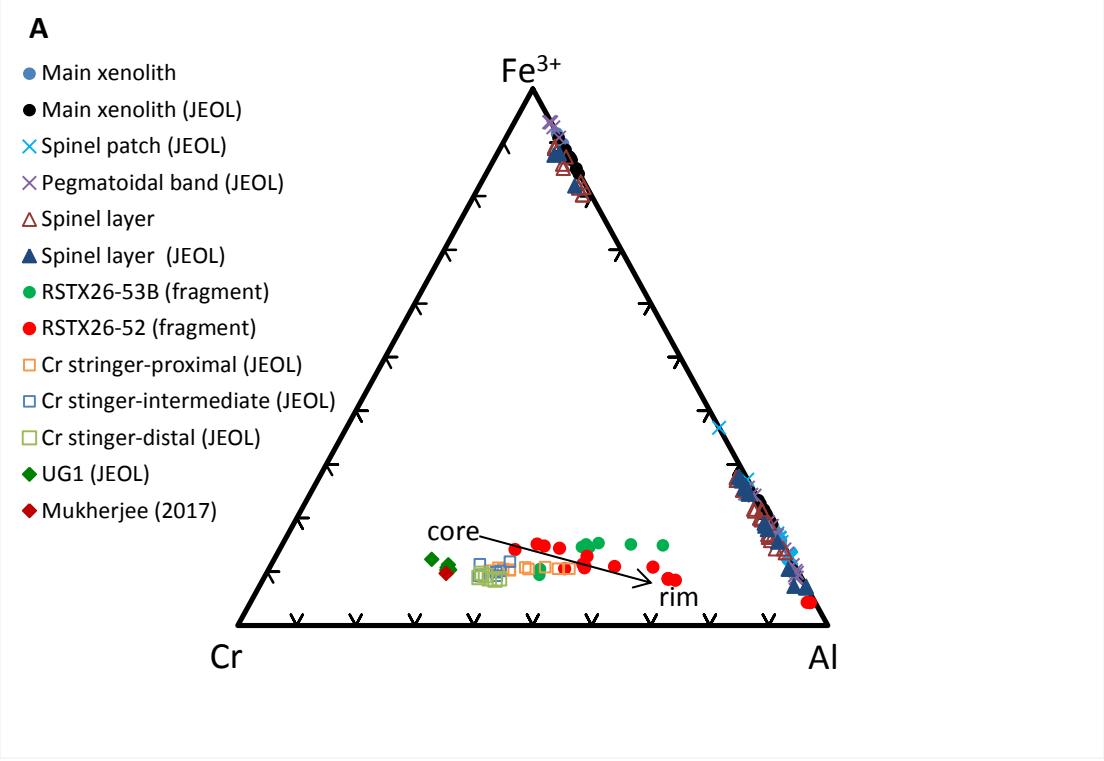

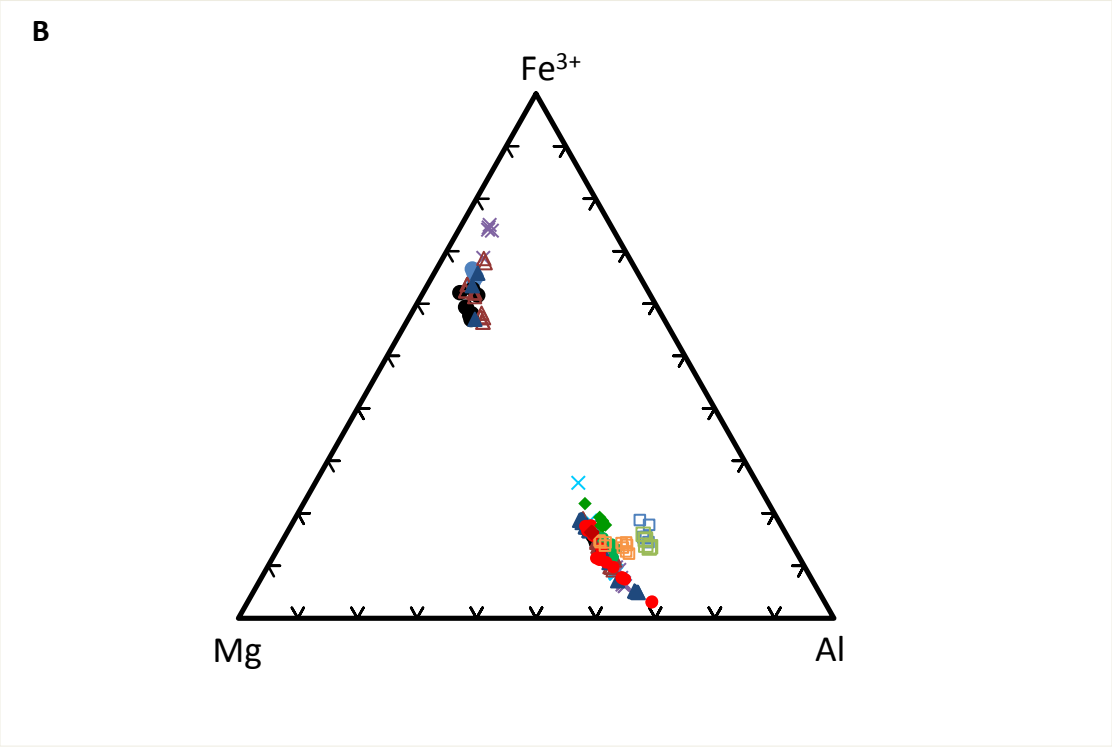

Figure 4.22: Ternary plots of spinel compositions throughout the Marikana sample suite. (A) trivalent ion plot ($Fe^{3+,}$ Cr, Al and (B)) plot for Fe^{3+}, Mg, Al (all calculated in atoms per formula unit).

Cation-cation proportions for all samples are depicted in Figure 4.23, which shows that three compositionally variable spinel groups are evident in the sample suite. Group 1 consists of the Fe-rich exsolution lamellae in spinel from xenolithic samples (main xenolith, pegmatoidal patch and spinel layer); all analyses can be termed magnetite. Group 2 covers the host spinel in the main xenolith, pegmatoidal patch and spinel layer samples. This spinel is Al-rich and can be termed spinel, *sensu stricto.* The spinel grains from the spinel patch samples are evident in Group 2 only, as they are homogeneous and no exsolution is evident. Group 3 includes Cr-rich spinel from samples that are found in the contact zone, which exhibit core-to-rim zonation, and are Cr-spinel/chromite.

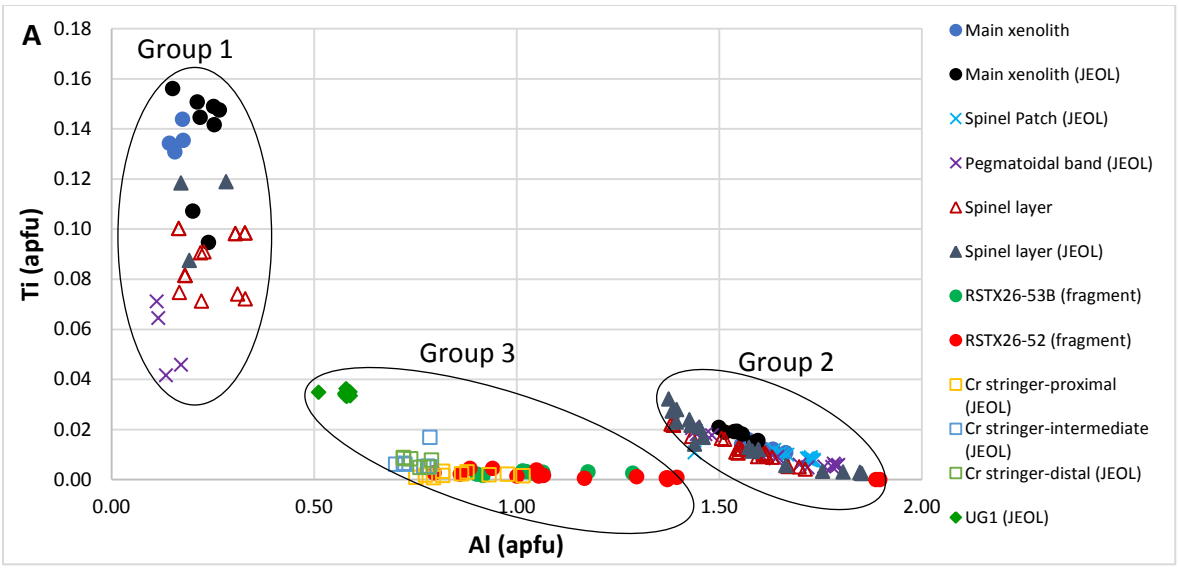
A
Group 1
Group 3
Group 2
Ti (apfu)
Al (apfu)
0.00
0.02
0.04
0.06
0.08
0.10
0.12
0.14
0.16
0.18
0.00
0.50
1.00
1.50
2.00
Main xenolith
Main xenolith (JEOL)
Spinel Patch (JEOL)
Pegmatoidal band (JEOL)
Spinel layer
Spinel layer (JEOL)
RSTX26-53B (fragment)
RSTX26-52 (fragment)
Cr stringer-proximal (JEOL)
Cr stringer-intermediate (JEOL)
Cr stringer-distal (JEOL)
UG1 (JEOL)

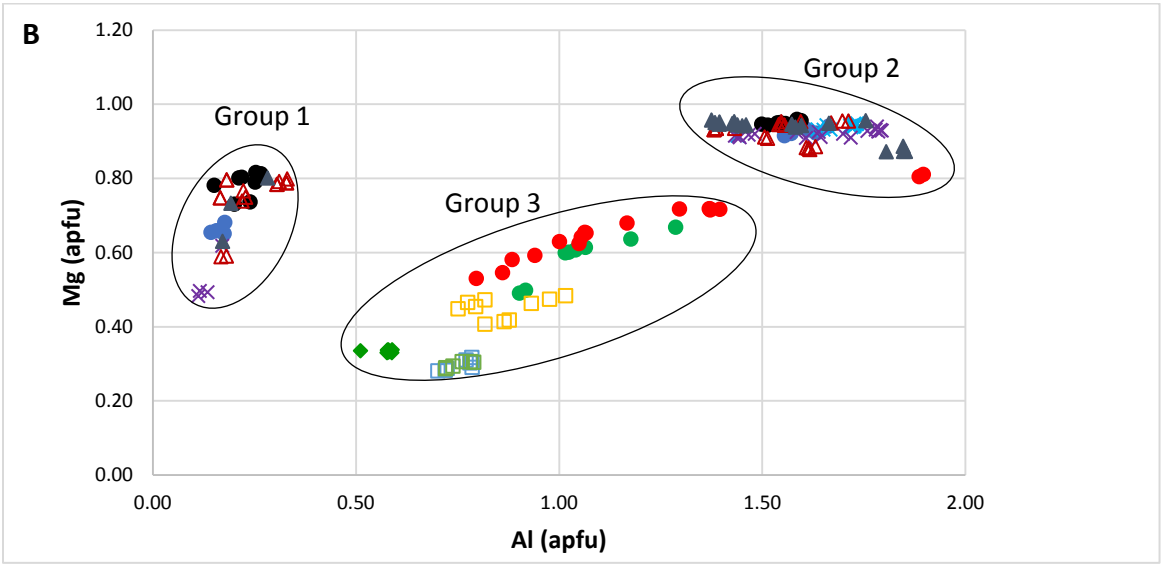
B
Group 1
Group 2
Group 3
Mg (apfu)
Al (apfu)
0.00
0.20
0.40
0.60
0.80
1.00
1.20
0.00
0.50
1.00
1.50
2.00

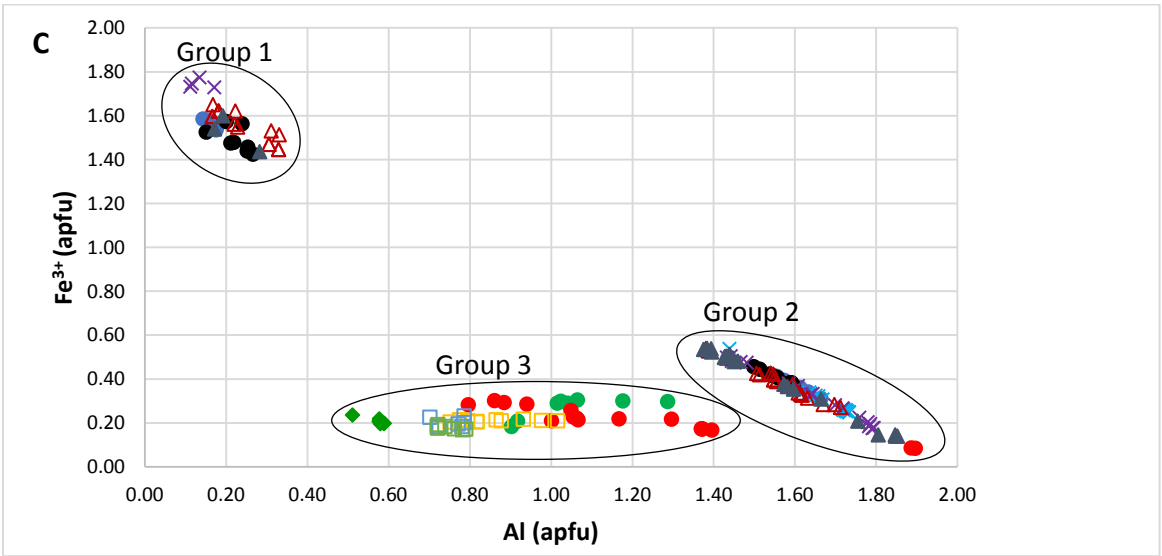
C
Group 1
Group 2
Group 3
Fe3+ (apfu)
Al (apfu)
0.00
0.20
0.40
0.60
0.80
1.00
1.20
1.40
1.60
1.80
2.00
0.00
0.20
0.40
0.60
0.80
1.00
1.20
1.40
1.60
1.80
2.00

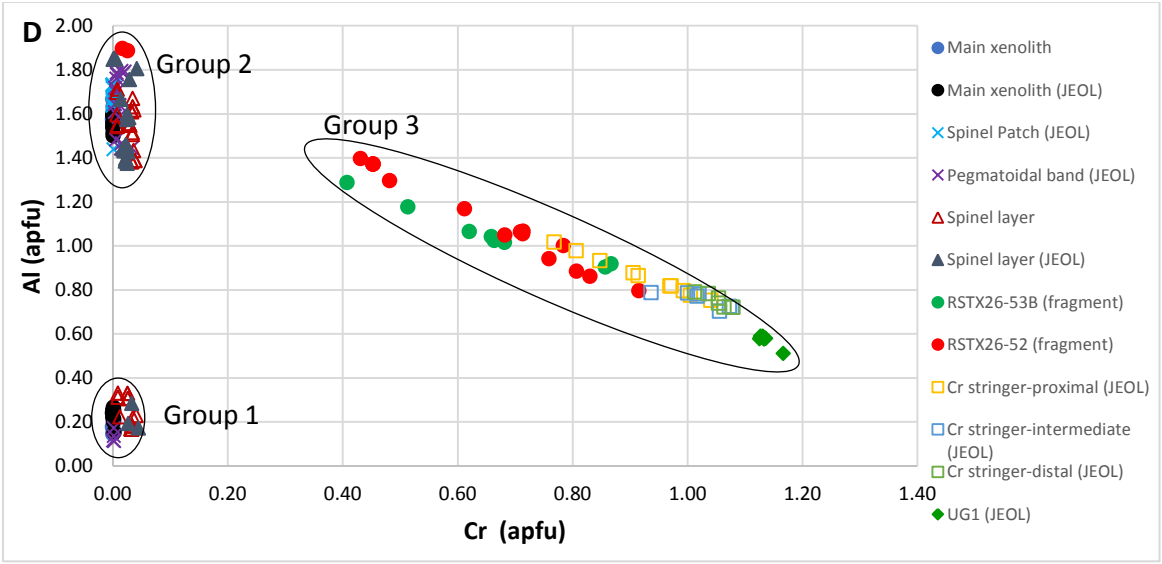
D
Group 2
Group 3
Group 1
Al (apfu)
Cr (apfu)
Main xenolith
Main xenolith (JEOL)
Spinel Patch (JEOL)
Pegmatoidal band (JEOL)
Spinel layer
Spinel layer (JEOL)
RSTX26-53B (fragment)
RSTX26-52 (fragment)
Cr stringer-proximal (JEOL)
Cr stringer-intermediate (JEOL)
Cr stringer-distal (JEOL)
UG1 (JEOL)

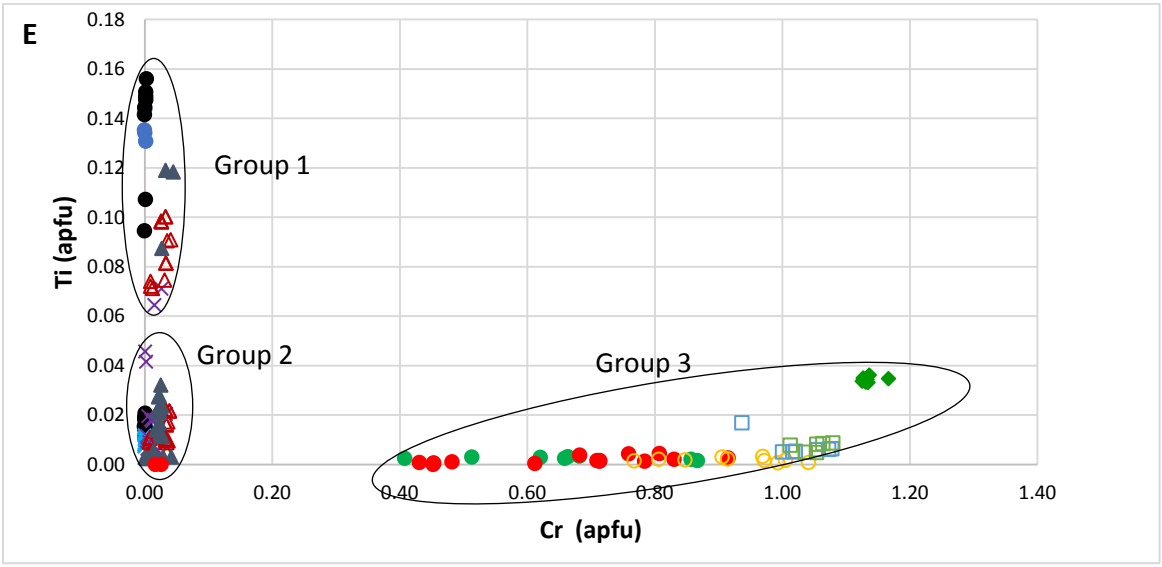
E
Group 1
Group 2
Group 3
Ti (apfu)
Cr (apfu)

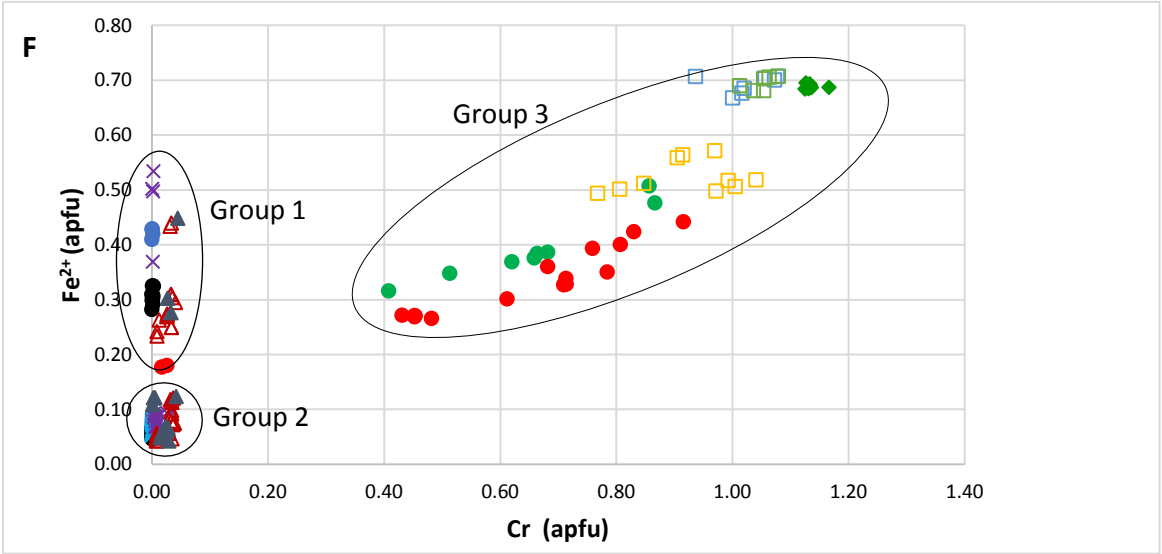
F
Group 3
Group 1
Group 2
Fe2+ (apfu)
Cr (apfu)

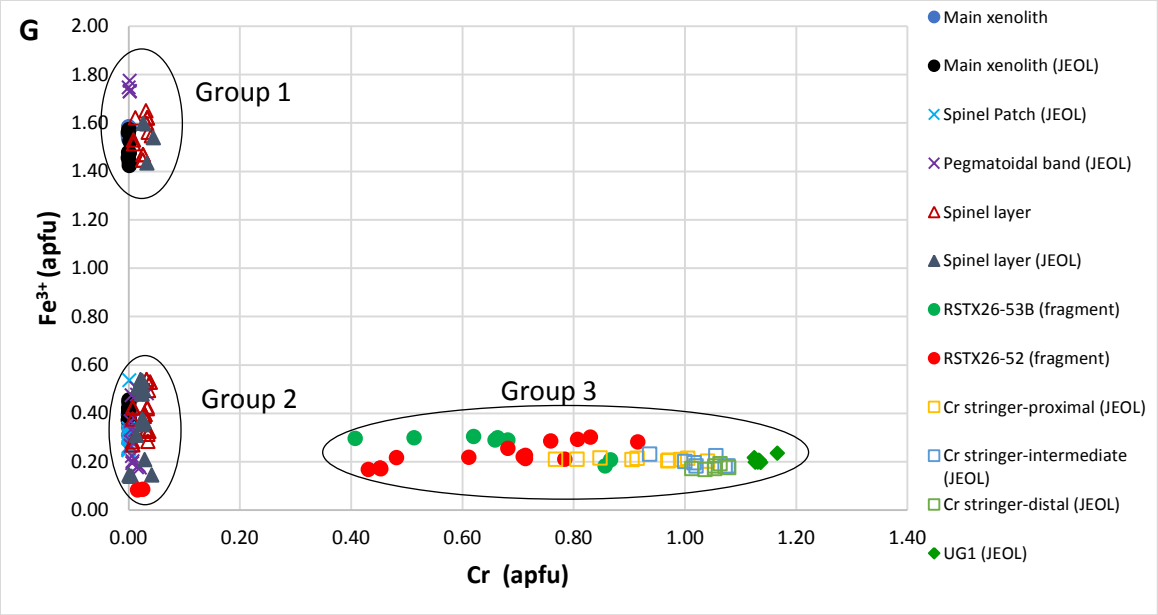
G
Group 1
Group 2
Group 3
Fe3+ (apfu)
Cr (apfu)
2.00
1.80
1.60
1.40
1.20
1.00
0.80
0.60
0.40
0.20
0.00
0.00
0.20
0.40
0.60
0.80
1.00
1.20
1.40
Main xenolith
Main xenolith (JEOL)
Spinel Patch (JEOL)
Pegmatoidal band (JEOL)
Spinel layer
Spinel layer (JEOL)
RSTX26-53B (fragment)
RSTX26-52 (fragment)
Cr stringer-proximal (JEOL)
Cr stringer-intermediate (JEOL)
Cr stringer-distal (JEOL)
UG1 (JEOL)

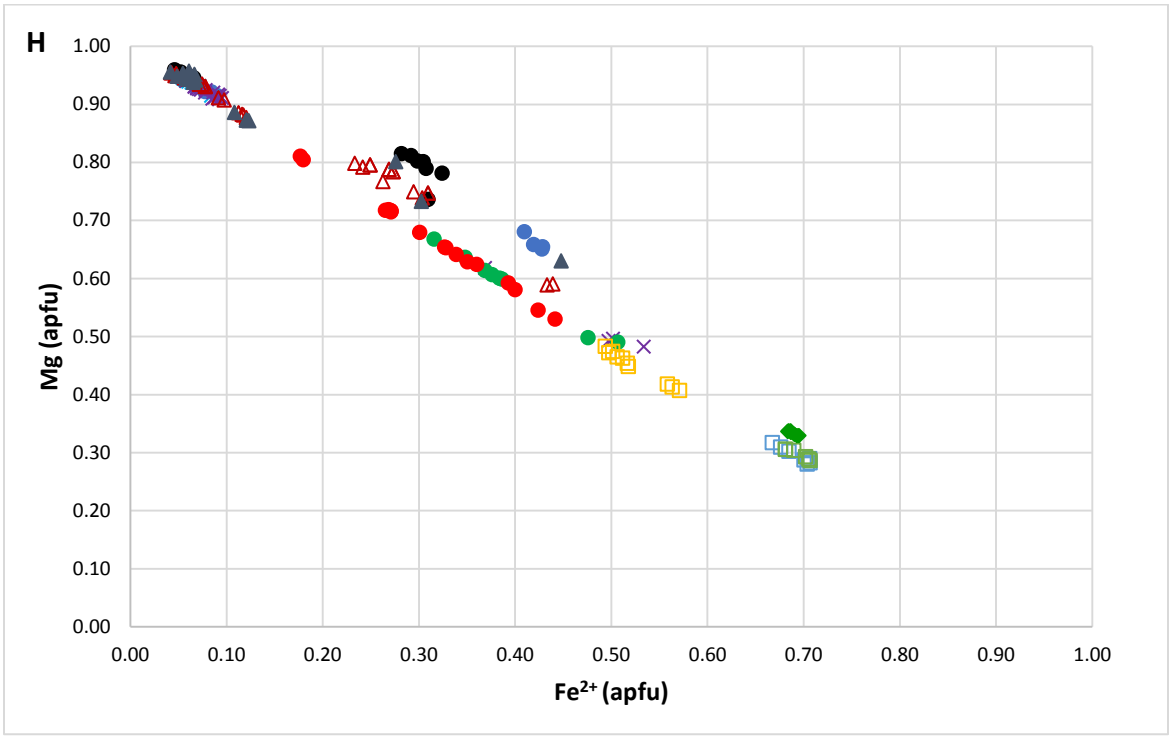
H
Mg (apfu)
Fe2+ (apfu)
1.00
0.90
0.80
0.70
0.60
0.50
0.40
0.30
0.20
0.10
0.00
0.00
0.10
0.20
0.30
0.40
0.50
0.60
0.70
0.80
0.90
1.00

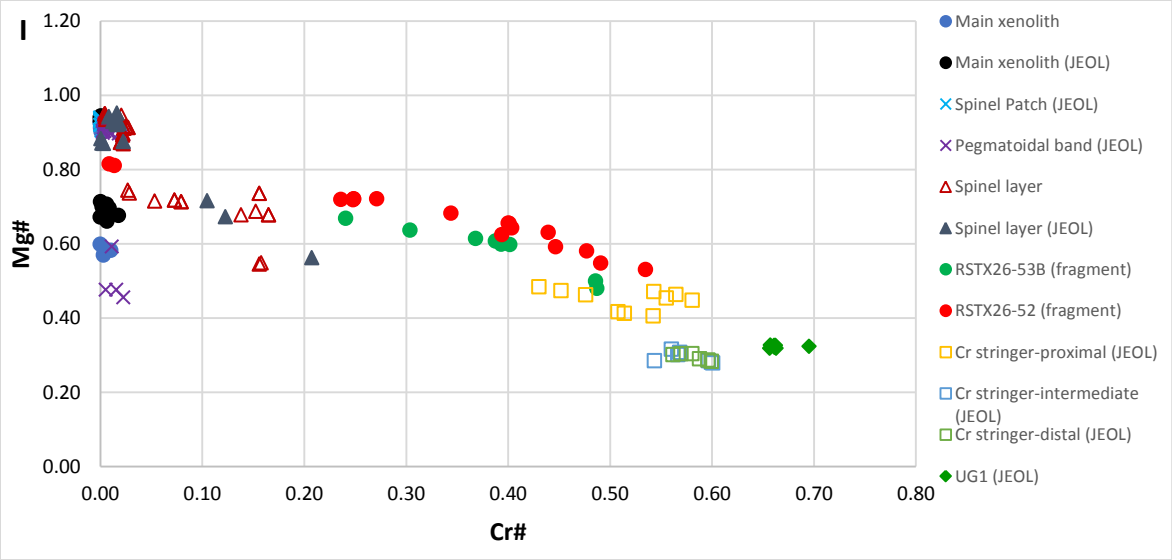

Figure 4.23: A–H are cation-cation plots for spinel throughout the Marikana sample suite and (I) is a Cr# vs Mg# plot showing three distinct clusters representing host spinel and its exsolution lamellae, and zoned, Cr-bearing spinel, respectively.

Table 4. 10: Representative chemical compositions of spinel from the Marikana sample suite

Sample	RSTX26-12 (CAMECA)	RSTX26-12 (CAMECA)	RSTX26-6 (CAMECA)	RSTX26-6 (CAMECA)	RSTX26-53B (CAMECA)	RSTX26-53B (CAMECA)	RSTX26-53B (CAMECA)
comment	host	lamellae	host	lamellae	core	inter	rim
SiO_2	0.04	0.03	0.03	0.02	0.28	0.02	0.01
TiO_2	0.69	5.20	0.64	3.27	0.09	0.14	0.12
Al_2O_3	52.84	4.00	50.37	8.75	26.16	30.67	38.53
Cr_2O_3	0.03	0.03	1.31	1.05	32.34	26.43	18.21
V_2O_3	bdl	bdl	0.01	bdl	0.13	0.19	0.14
Fe_2O_3	19.03	59.61	20.25	58.37	9.76	13.36	13.89
FeO	3.49	14.48	3.34	9.95	17.43	15.00	13.32
MnO	0.45	1.81	0.46	1.43	0.78	0.64	0.61
MgO	24.19	12.74	23.91	15.38	11.54	13.86	15.80
NiO	0.02	0.02	0.01	0.02	0.14	0.13	0.16
ZnO	0.08	0.04	0.06	0.04	0.12	0.03	0.07
Total	100.85	97.94	100.39	98.29	98.77	100.45	100.86
			Number of ions based on 4 Oxygens				
Si	bdl	bdl	bdl	bdl	0.01	bdl	bdl
Ti	0.01	0.14	0.01	0.08	bdl	bdl	bdl
Al	1.60	0.16	1.55	0.32	0.95	1.07	1.29
Cr	bdl	bdl	0.03	0.03	0.79	0.62	0.41
V^{3+}	bdl	bdl	bdl	bdl	bdl	bdl	bdl
Fe^{3+}	0.37	1.56	0.40	1.48	0.23	0.30	0.30
Fe^{2+}	0.08	0.42	0.07	0.28	0.45	0.37	0.32
Mn	0.01	0.05	0.01	0.04	0.02	0.02	0.01
Mg	0.93	0.66	0.93	0.76	0.53	0.61	0.67
Ni	bdl	bdl	bdl	bdl	bdl	bdl	bdl
Zn	bdl	bdl	bdl	bdl	bdl	bdl	bdl
Total	3.00	3.00	3.00	3.00	3.00	3.00	3.00

Table 4.10: *(continued)*

Sample	RSTX26-52 (CAMECA)	RSTX26-52 (CAMECA)	RSTX26-52 (CAMECA)	RSTX26-52 (CAMECA)	RSTX26-1 (JEOL)	RSTX26-3 (JEOL)	RSTX26-3 (JEOL)
comment	interstitial to Mtc	rimming Mtc	Spinel *s.s.*	Ves+Di+ Grt+Mtc	spinel patch	host	lamellae
SiO_2	0.02	0.02	0.04	0.01	0.03	0.03	0.03
TiO_2	0.18	0.03	bdl	0.07	0.46	0.81	5.57
Al_2O_3	26.63	41.91	63.98	29.61	54.52	50.48	5.77
Cr_2O_3	30.99	20.30	1.08	30.31	0.03	0.05	0.05
V_2O_3	0.18	0.09	0.03	0.07	0.02	0.01	0.29
Fe_2O_3	12.06	8.14	4.46	10.49	16.04	20.10	58.50
FeO	15.03	11.59	8.50	13.83	3.04	2.70	10.76
MnO	0.61	0.34	0.31	0.71	0.42	0.45	1.65
MgO	13.15	17.23	21.59	14.19	24.16	24.12	15.80
NiO	0.19	0.21	0.36	0.18	0.03	0.03	0.05
ZnO	0.06	0.08	0.07	0.07			
Total	99.09	99.93	100.42	99.54	98.75	98.78	98.45
			Number of ions based on 4 oxygens				
Si	bdl	bdl	bdl	bdl	bdl	bdl	bdl
Ti	bdl	bdl	bdl	bdl	0.01	0.02	0.14
Al	0.96	1.38	1.89	1.04	1.66	1.57	0.23
Cr	0.75	0.45	0.02	0.72	bdl	bdl	bdl
V^{3+}	bdl	bdl	bdl	bdl	bdl	bdl	0.01
Fe^{3+}	0.28	0.17	0.08	0.24	0.32	0.40	1.48
Fe^{2+}	0.38	0.27	0.18	0.35	0.07	0.06	0.30
Mn	0.02	0.01	0.01	0.02	0.01	0.01	0.05
Mg	0.60	0.72	0.81	0.63	0.93	0.95	0.79
Ni	bdl	bdl	0.01	bdl	bdl	bdl	bdl
Zn	bdl	bdl	bdl	bdl			
Total	3.00	3.00	3.00	3.00	3.00	3.00	3.00

Table 4.10: *(continued)*

Sample	RSTX 26-3 (JEOL)	RSTX 26-3 (JEOL)	RSTX 26-4 (JEOL)	RSTX 26-4 (JEOL)	RSTX 26-5 (JEOL)	RSTX 26-5 (JEOL)	RSTX 26-61 (JEOL)	RSTX 26-62 (JEOL)	RSTX 26-63 (JEOL)	RSTX 26-UG1 (JEOL)
comment	host	lamellae	host	lamellae	host	lamellae	proximal stringer	intermediate stringer	distal stringer	
SiO_2	0.03	0.03	0.03	0.05	0.02	0.04	0.02	0.03	0.04	0.03
TiO_2	0.81	5.57	0.55	2.07	0.68	4.16	0.08	0.30	0.29	1.35
Al_2O_3	50.48	5.77	50.24	3.18	50.34	5.32	23.31	19.66	19.51	14.34
Cr_2O_3	0.05	0.05	0.59	0.06	0.99	1.28	37.03	39.91	40.58	42.43
V_2O_3	0.01	0.29	0.01	0.13	bdl	0.20	0.02	0.17	0.12	0.46
Fe_2O_3	20.10	58.50	19.30	64.82	18.12	58.48	8.85	8.17	7.19	8.16
FeO	2.70	10.76	4.33	15.87	3.29	11.78	19.91	25.46	25.36	24.31
MnO	0.45	1.65	0.50	1.52	0.46	1.55	0.99	0.64	0.51	0.33
MgO	24.12	15.80	22.77	9.80	23.33	14.01	9.59	6.09	6.09	6.61
NiO	0.03	0.05	0.04	0.11	0.01	0.04	0.11	0.10	0.11	0.14
ZnO										
Total	98.78	98.45	98.35	97.60	97.24	96.86	99.90	100.53	99.80	98.15
Number of ions based on 4 oxygens										
Si	bdl	bdl	bdl	bdl	bdl	bdl	bdl	bdl	bdl	bdl
Ti	0.02	0.14	0.01	0.06	0.01	0.11	bdl	0.01	0.01	0.03
Al	1.57	0.23	1.55	0.13	1.58	0.22	0.86	0.75	0.75	0.57
Cr	bdl	bdl	0.01	bdl	0.02	0.04	0.92	1.03	1.05	1.14
V^{3+}	bdl	0.01	bdl	bdl	bdl	0.01	bdl	bdl	bdl	0.01
Fe^{3+}	0.40	1.48	0.41	1.75	0.37	1.52	0.21	0.20	0.18	0.21
Fe^{2+}	0.06	0.30	0.10	0.48	0.07	0.34	0.52	0.69	0.69	0.69
Mn	0.01	0.05	0.01	0.05	0.01	0.05	0.03	0.02	0.01	0.01
Mg	0.95	0.79	0.90	0.52	0.93	0.72	0.45	0.30	0.30	0.33
Ni	bdl	bdl	bdl	bdl	bdl	bdl	bdl	bdl	bdl	bdl
Zn	bdl	bdl	bdl	bdl	bdl	bdl	bdl	bdl	bdl	bdl
Total	3.00	3.00	3.00	2.99	3.00	3.00	3.00	3.00	3.00	3.00

4.3.5.1 Xenolith

The main xenolithic body hosts spinel that exhibits various exsolution patterns (Figure 4.24). The exsolution lamellae are magnetite and are composed of 1.48 - 1.58 Fe^{3+} apfu, 0.09–0.16 Ti apfu, 0.65–0.81 Mg apfu and 0.14–0.27 Al apfu (Appendix 4B). The exsolution lamellae host higher concentrations of Fe^{3+}, Fe^{2+} (≤ 0.43 apfu) and Ti than the host mineral (spinel, *sensu stricto.*). The spinel host is characterised by higher amounts of Mg (0.91–0.96 apfu) and Al (1.51–1.63 apfu). In BSE images, magnetite exsolution lamellae are surrounded by a darker zone which appears to be depleted in Fe (Figure 4.24). Mg# [Mg# = Mg / (Mg + Fe^{2+} + Mn)] ranges from 0.57 to 0.71 in magnetite exsolution lamellae and from 0.90 to 0.95 in the host spinel. No Cr was detected in these spinel grains.

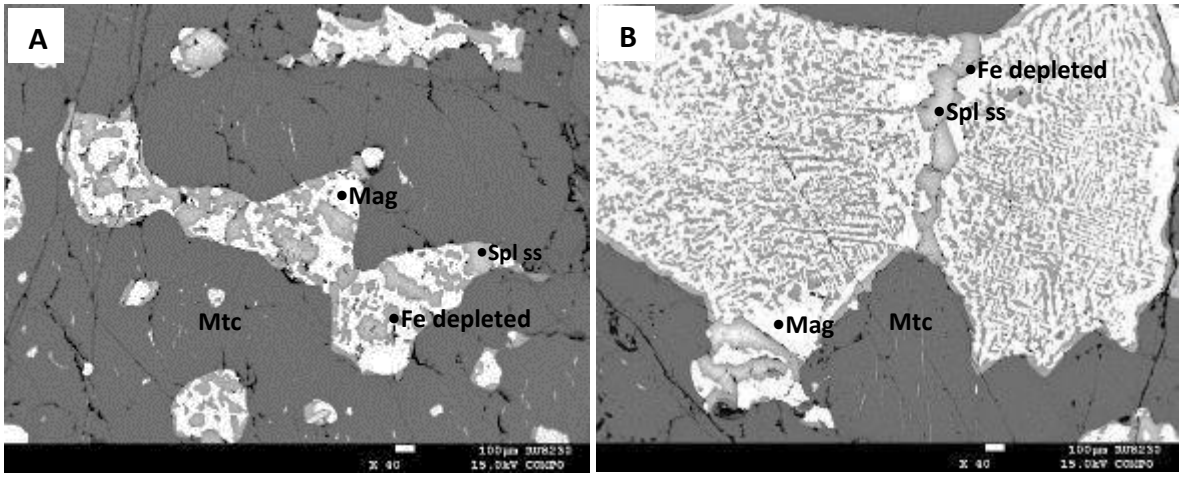

Figure 4.24: BSE images of spinel found in the Marikana main xenolithic body in sample RSTX26-03 (A and B). Bright grey is magnetite surrounding Fe-depleted zones (dark grey) and medium grey is spinel *sensu stricto*. Mtc = monticellite, Mag = magnetite, Spl ss = spinel, *sensu stricto.*

Spinel found in the spinel patch displays no exsolution, and the composition is constant throughout the grains, with 0.94 Mg apfu, 1.73 Al apfu, 0.06 Fe^{2+} apfu and 0.26 Fe^{3+} apfu, and with minor Mn and Ti (both 0.01 apfu); no Cr was detected. It is termed spinel *sensu stricto.,* with Mg# remaining constant at 0.94 apfu. Zoned spinel (Figure 4.25 and 4.26) is found in one sample only: RSTX26-04 (pegmatoidal patch; Figures 3.4, 3.5). In this sample, Fe^{3+} increases from core to rim (from 0.18 to 0.37 apfu) and Al decreases from 1.79 to 1.61 apfu (Figure 4.27).

The rims of the zoned spinel are characterised by magnetite blebs (Figures 3.5, 4.26). Minor amounts of Cr were detected in the cores (≤ 0.2 apfu), decreasing to 0.0 apfu towards the rim (Figure 4.25).

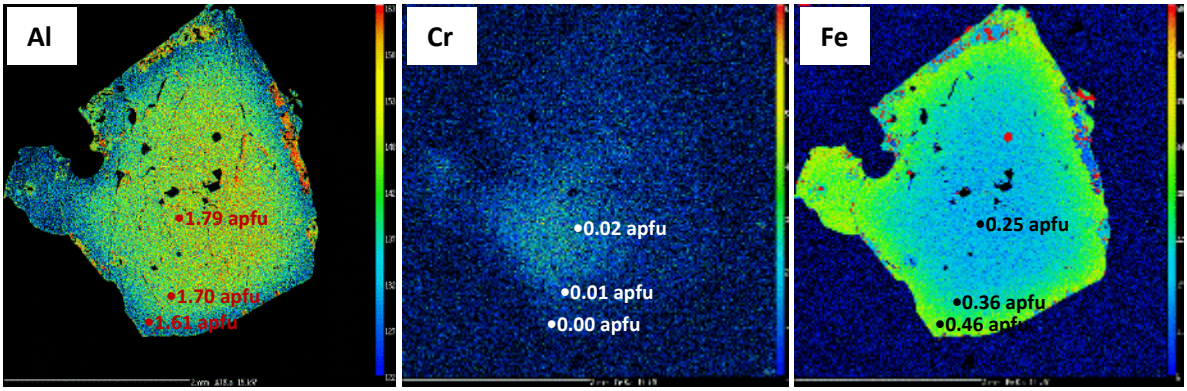

Figure 4.25: Element maps of zoned spinel found in samples containing pegmatoidal monticellite (RSTX26-04) from the Marikana xenolith. Al and Cr decrease towards the rim, while Cr zonation is not symmetrical within the grain. Fe increases towards the rim and is characterised by magnetite blebs, shown in Figure 4.33

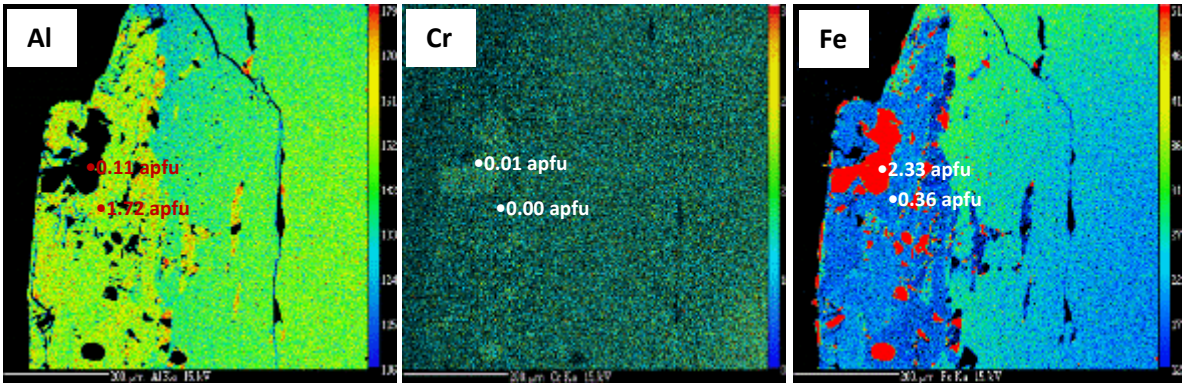

Figure 4.26: Element maps showing the rim of zoned spinel in sample RSTX26-04 from the Marikana xenolith. The left rim of the spinel grain is characterised by magnetite blebs of variable sizes. Al appears to increase towards the rim and Fe appears to decrease in the rim.

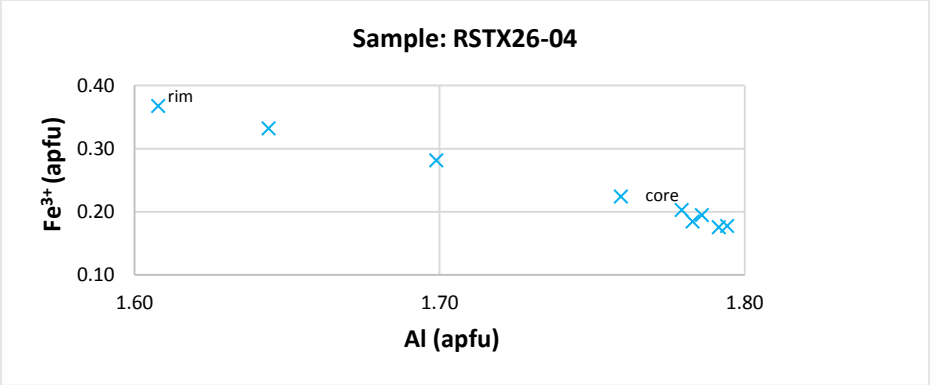

Figure 4.27: Cation-cation correlation diagram for zoned spinel found in samples containing pegmatoidal monticellite (RSTX26-04) from the Marikana xenolith depicting the variation of Fe^{3+} and Al from core to rim.

The spinel layer and layers immediately surrounding it, namely, the forsterite-spinel and forsterite monticellite layers, show similar spinel compositions and textures as the main xenolithic body, that is, exsolution textures (Figure 4.28). Slight variation in chemical composition from the forsterite-spinel layer (A), through the spinel layer (B), and the forsterite-monticellite layer (C) are shown in Figure 4.29. Mg decreases slightly (from 0.95 to 0.87 apfu), Fe^{2+} increases (from 0.04 to 0.12 apfu), Al increases (from 1.39 to 1.85 apfu) and Fe^{3+} decreases (0.54 to 0.14 apfu) from the forsterite-spinel layer through to the forsterite-monticellite layer. The Mg# recorded in host spinel (not the lamellae) in the forsterite-monticellite layer (RSTX26-05C and RSTX26-06C) is slightly higher (0.92–0.93) than the forsterite-spinel layer (RSTX26-05A and RSTX26-06A), where Mg# ranges between 0.87 and 0.91 apfu. Cr content is lower in the forsterite-spinel layer (A) and ranges between 0.01 and 0.03 apfu. The spinel layer itself (B), and the forsterite-monticellite layer (C), exhibit slightly higher Cr values, ranging from 0.02 to 0.05 apfu. Some spinel grains in the forsterite-monticellite layer, in particular sample RSTX26-05, show no exsolution, contain Cr (0.02 to 0.05 apfu) and are green in colour (spinel, *sensu stricto*). Mn remains constant at 0.01 apfu in host spinel, however, the exsolution lamellae contain up to 0.05 Mn apfu. Ti ranges between 0.01 and 0.03 apfu in the host spinel, whereas magnetite exsolution lamellae contain between 0.07 and 0.12 Ti apfu.

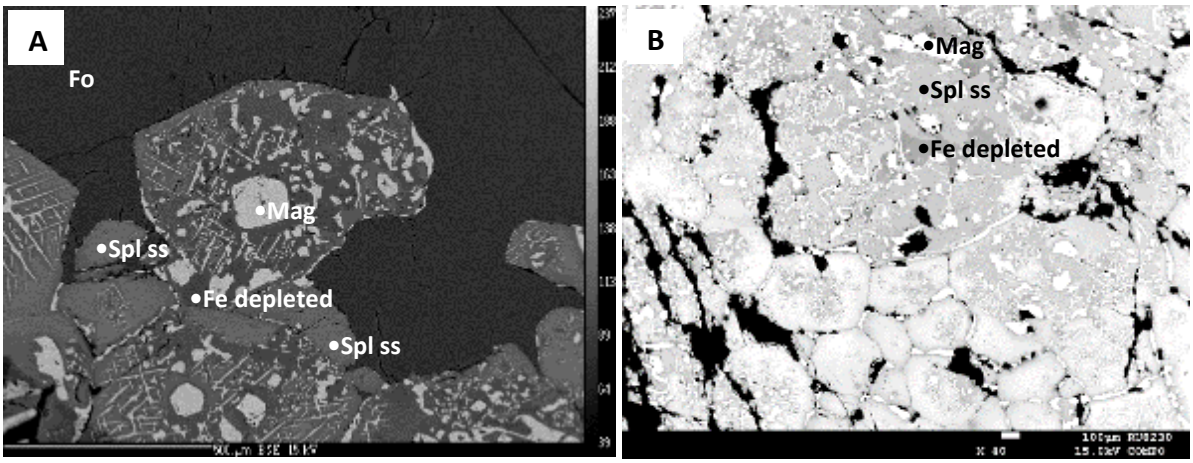

Figure 4.28: BSE image of the spinel layer, sample RSTX26-05 (A) and RSTX26-06 (B). Bright grey is magnetite (Mag), surrounded by Fe-depleted zones (dark grey); medium grey is spinel *sensu sctricto* (Spl ss).

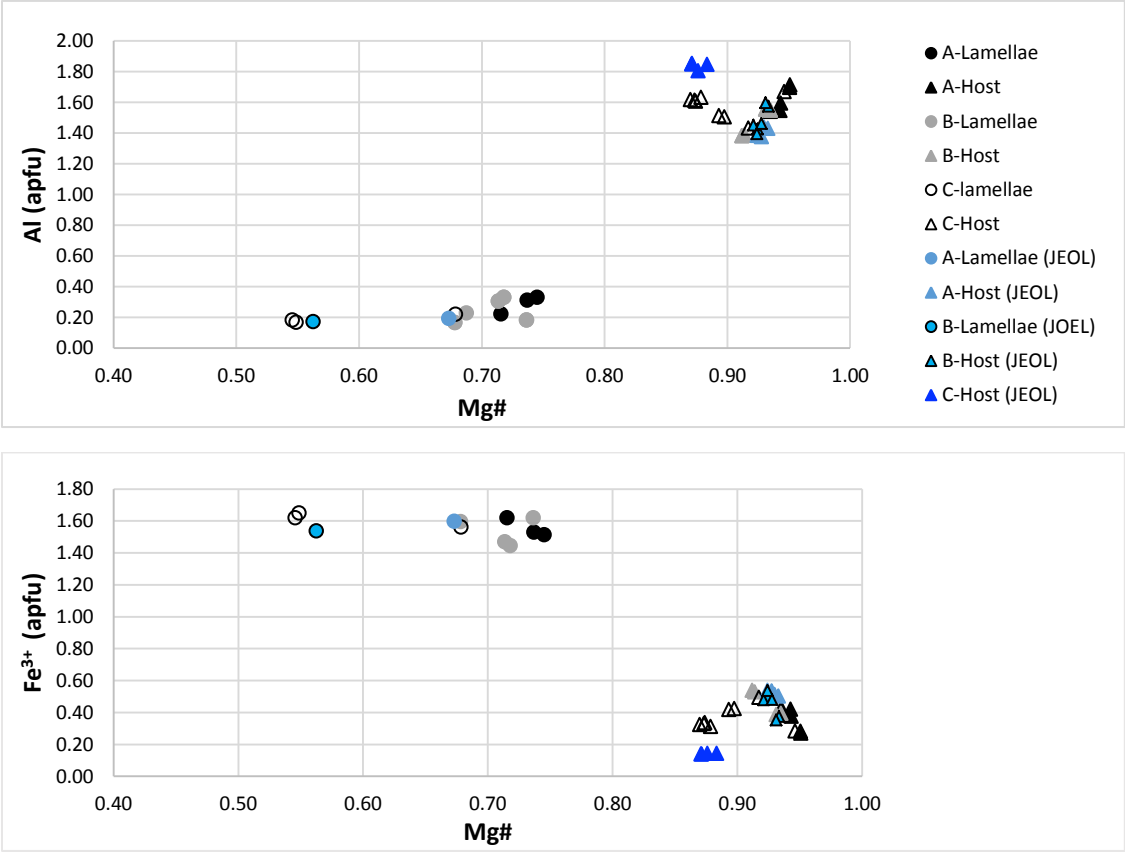

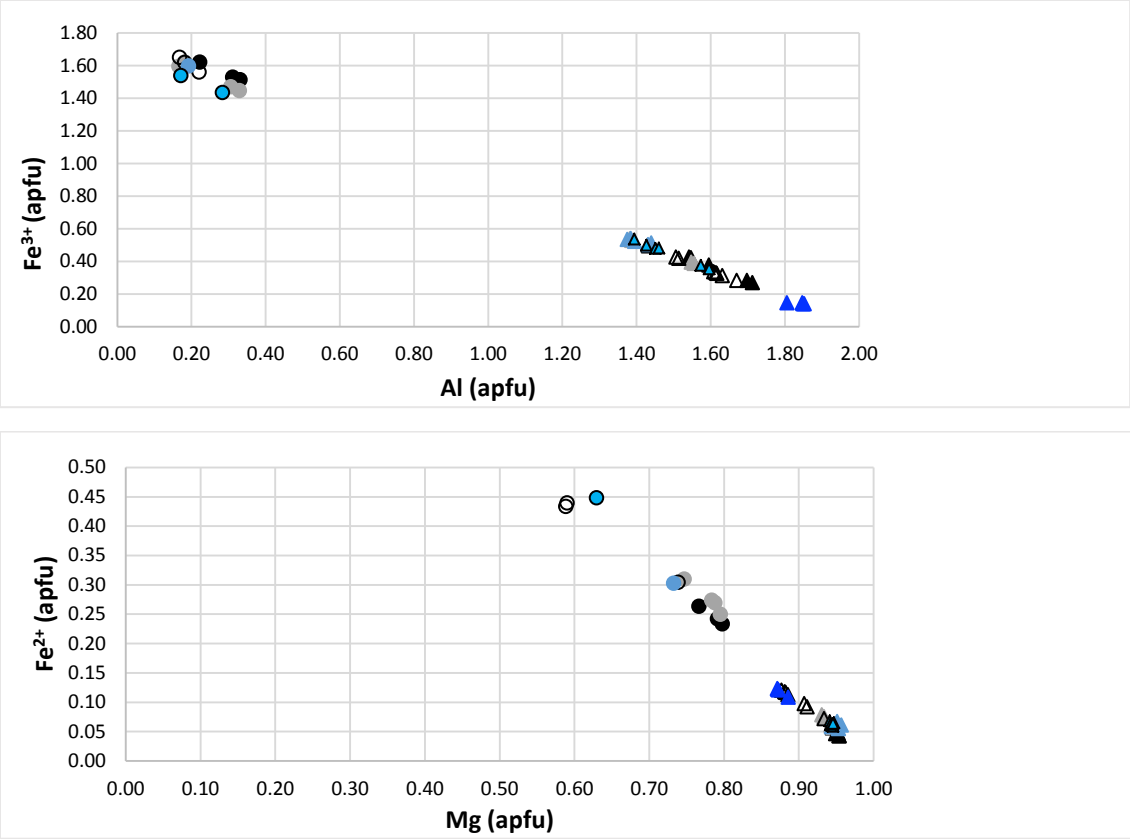

Figure 4.29: Cation-cation correlation diagrams for spinel found in the forsterite-spinel, spinel and monticellite-forsterite layers from the Marikana xenolith (samples RSTX26-05 A, B, C and RSTX26-06 A, B, C).

4.3.5.2 Contact zone – fragment samples

Zoned spinel is found in samples RSTX26-53B and RSTX26-52, which contain calc-silicate fragments. The spinels are Cr-bearing and show similar trends. RSTX26-53B contains Cr-bearing garnet and Al-diopside and contains higher amounts of Cr in spinel cores that decrease toward the rims (Figure 4.8). Mg increases from 0.49 to 0.67 apfu, while Fe^{2+} decreases (from 0.48 apfu to 0.32 apfu) from core to rim (Figure 4.23H). The Cr, Al and Fe^{3+} relationships shown in Figures 4.23 C, D and G are enlarged in Figure 4.30.

In sample RSTX26-53B the Cr content decreases from the core to rim (0.68 to 0.41 apfu), with some grains containing ≤0.87 apfu Cr. The Al content increases from 1.02 to 1.29 apfu from

core to rim, and Fe^{3+} remains relatively constant at ~0.29 apfu. Mg# increases towards the rims from 0.48 to 0.67. Cr# [Cr#= Cr/(Cr + Al)] shows the opposite trend and decreases towards the rim from 0.49 to 0.24 apfu (Figure 4.30).

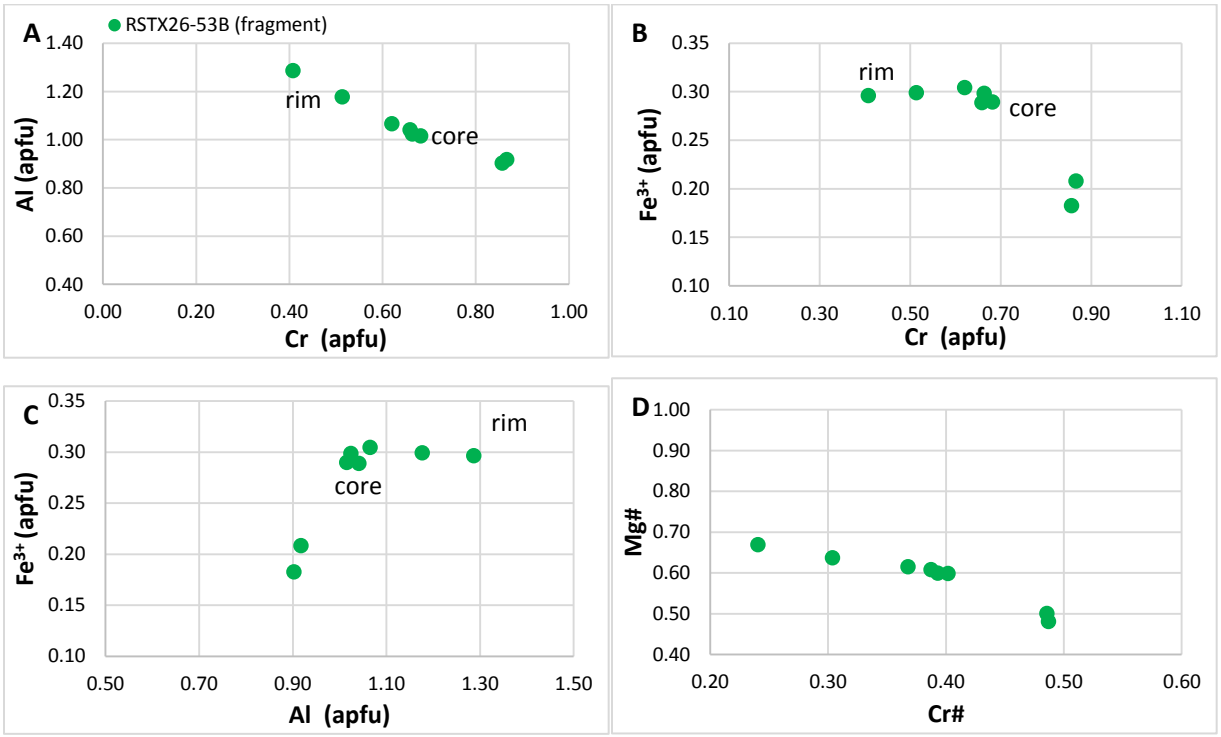

Figure 4.30: Plots depicting the relationship between Cr, Al and Fe^{3+} (A to C) and Mg# vs Cr# (D) for spinel in sample RSTX26-53B from core to rim (from the Marikana contact zone).

Spinel in sample RSTX26-52 occurs in four different mineral assemblages, with some variability in composition, possibly owing to compositional diversity within the sample (Figure 3.10). Sample RSTX26-52 comprises a monticellite fragment with an edge characterised by a band of zoned spinel grains with dark brown cores and light brown rims. This is followed outwards by a highly fractured ~2 mm-thick band of diopside. Adjacent to this band is a layer that comprises monticellite, vesuvianite, diopside and garnet, as described in section 3.3.2 and shown in Figure 3.10. Spinel occurs as: (1) interstitial grains in the monticellite fragment where spinel is zoned and Cr-rich (with 0.81 apfu at the core, decreasing to 0.68 at the rim), and Al increases from 0.89 apfu in the core to 1.05 apfu at the rim (Figure 4.31); (2) forming the discontinuous rim

around the monticellite fragment: these grains are similarly zoned but the Cr# range is not as great as the spinel within the monticellite fragment (Figure 4.31); (3) discrete grains of spinel, *sensu stricto*, occurring in minor amounts in the ~2 mm-thick band of diopside and contains 0.80 apfu Mg, 1.90 apfu Al, 0.18 apfu Fe^{2+}, 0.08 apfu Fe^{3+} and minor Cr and Mn; and (4) zoned spinel occurring with garnet, diopside and vesuvianite and monticellite. This spinel shows Cr-rich cores (0.92 apfu) and Cr-poor rims (0.48 apfu), while Mg increases from 0.53 apfu to 0.72 apfu and Al from 0.80 apfu to 1.30 apfu at the rims, and Fe^{3+} remains relatively steady at ~0.21 apfu. Fe^{2+} exhibits a decrease (from 0.44 apfu to 0.27 apfu) from core to rim, but Mn remains constant at 0.02 apfu. Mg# is highest at the rims of the spinel, while Cr# is the highest at the cores (Figure 4.31).

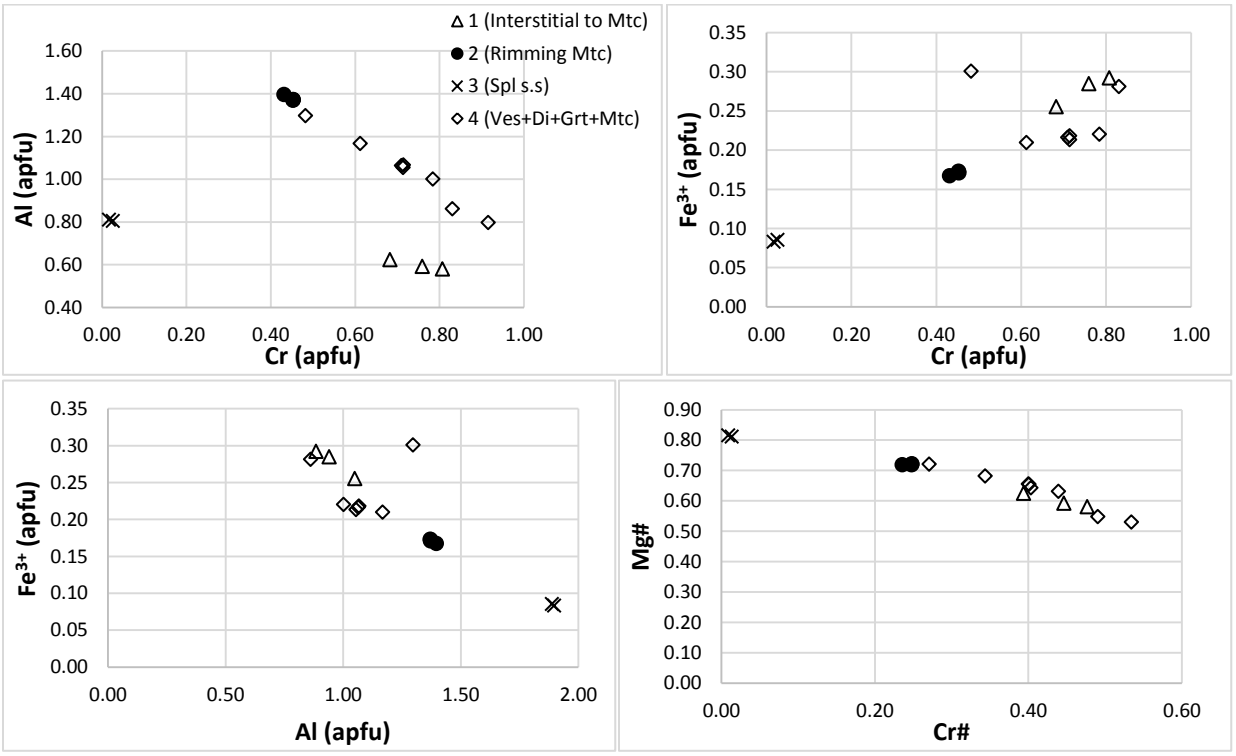

Figure 4.31: Plots depicting the relationship between Cr, Al and Fe^{3+} (A to C) and Mg# vs Cr# (D) for spinel in various mineral associations in sample RSTX26-52 from the Marikana contact zone.

4.3.5.3 Contact zone – chromitite stringers

All spinel analysed from samples collected from the chromitite stringer are chromian. However, compositional variation of Mg, Al, Fe and Cr exists between the proximal chromitite stringer through to the distal chromitite stringer. When considering the overall change in composition of Cr-spinel in a spatial context, from the proximal stringer through to the distal stringer (Figure 4.32), the Cr content is lowest in the proximal stringer and increases towards the distal stringer. Al content behaves inversely and is highest in the proximal stringer. Fe^{3+} remains relatively constant with a slight decrease in the distal sample. Mg content is highest, and Fe^{2+} lowest, in the proximal stringer.

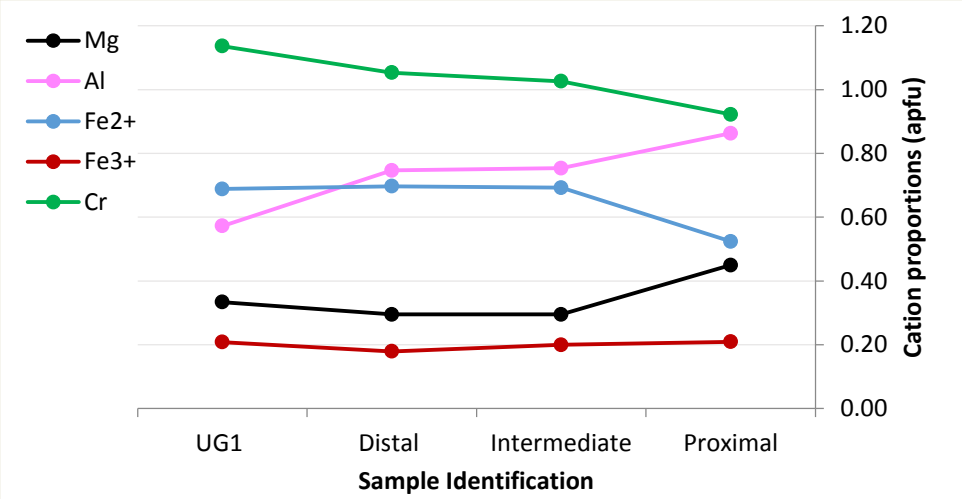

Figure 4.32: Plots showing spinel composition (cations per formula unit) averaged for each sample from the chromitite stringer and UG 1 chromitite layer, showing the overall spatial compositional variation between samples from the Marikana sample suite.

Within the individual stringers compositional heterogeneity is observed on a grain-to-grain basis and/or from core to rim. The stringer proximal to the xenolith, on average, contains the least amount of Cr relative to the intermediate and distal samples. The spinel cores contain 0.99–1.04 apfu Cr and the Cr content decreases towards the rims (0.77 apfu–0.81 apfu). Al increases towards the rim (from 0.75 apfu to 1.02 apfu) and Fe^{3+} remains relatively constant at ~0.21 apfu (Figure 4.33 A to C), Mg increases (0.41 apfu to 0.48 apfu) and Fe^{2+} decreases

(0.57 apfu to 0.49 apfu) (Figure 4.33D). Cr# ranges from 0.58 in the core to 0.43 at the rim (Figure 4.33E). The intermediate stringer exhibits the same core-to-rim trends as the proximal stringer, although cation proportions differ slightly. In the intermediate stringer Cr content decreases from 1.08 to 0.94 apfu and Al increases from 0.70 to 0.79 apfu from core to rim, while Fe^{3+} remains relatively steady at ~0.20 apfu (Figure 4.33 A to C) and Mg and Fe^{2+} remain relatively constant at ~0.30 apfu and 0.69 apfu, respectively. The spinel in the distal stringer does not display significant core-to-rim heterogeneity. Cr ranges from 1.01 apfu to 1.08, Al from 0.72 apfu to 0.79 apfu, Fe^{3+} 0.17 apfu to 0.19 apfu (Figure 4.33 A to C), Mg from 0.29 apfu to 0.31 apfu and Fe^{2+} from 0.68 apfu to 0.71 apfu (Figure 4.33D). Cr# is overall higher in intermediate (ranges from 0.54–0.60) and distal (ranges 0.56–0.60) stringers when compared to the proximal stringer (Figure 4.33E). Spinel in the distal stringer exhibits compositions that approach UG 1 chromitite composition, which has a Cr# of 0.66 (Figure 4.33E). Minor Mn (0.01 apfu–0.03 apfu) and no Ti were detected in all stringers.

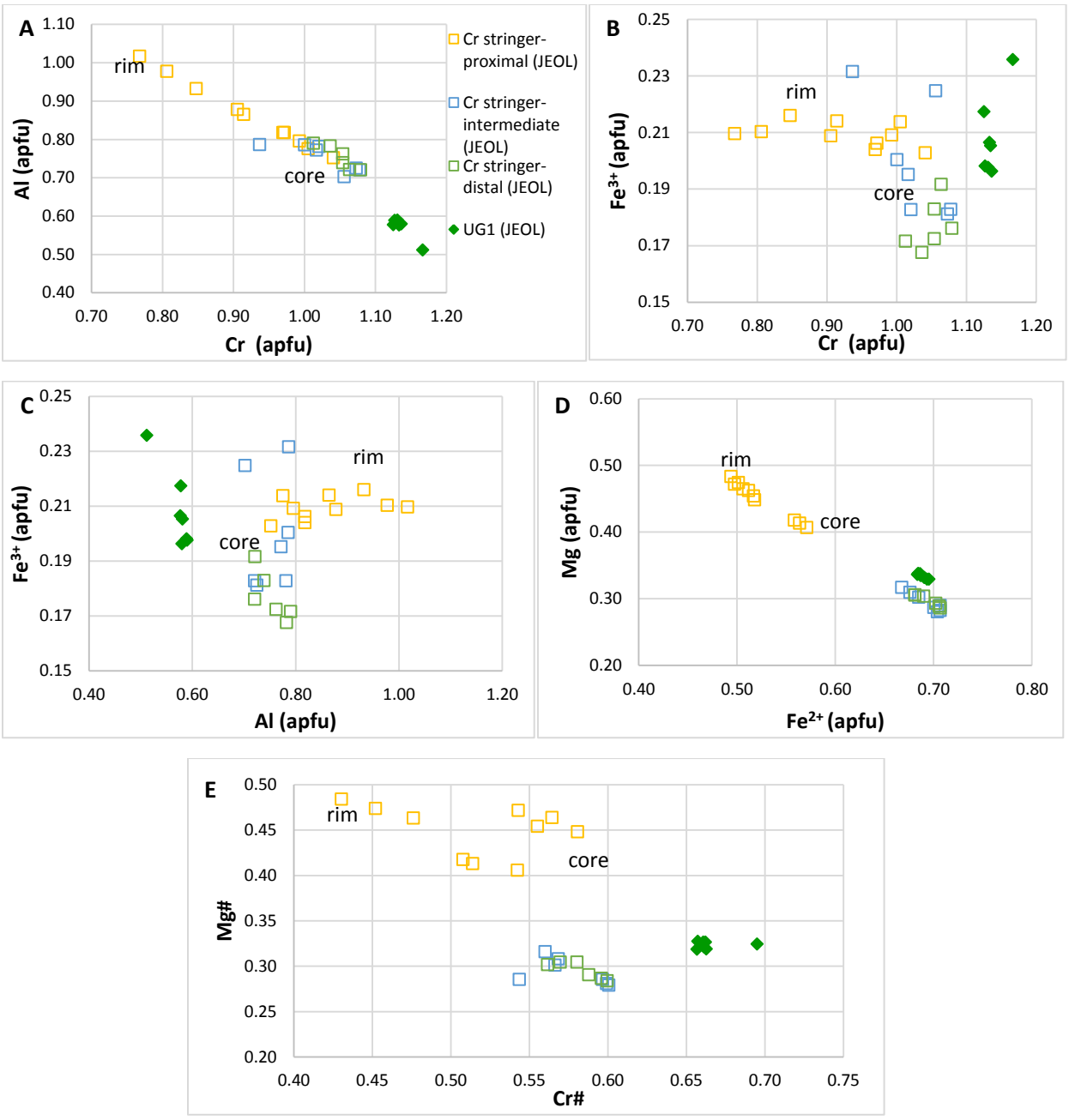

Figure 4.33: Plots depicting relationship between Cr, Al and Fe^{3+} (A to C), Fe^{2+} and Mg (D) and Mg# and Cr# (E) for chromian spinel in the proximal, intermediate and distal chromitite stringer, and chromite in the UG 1 chromitite layer from the Marikana sample suite.

4.3.5.4 Summary

Based on the results, it is evident that three compositional types of spinel are present in the sample suite (Figure 4.23 A-I). Pure phases according to Figure 4.27 do not exist in this system; however, spinel can be broadly classified into three groups. Spinel in Group 1 is magnetite-bearing exsolution lamellae and is found in the xenolithic samples. Group 2 hosts spinel, *sensu stricto,* which is found in the xenolith samples, typically with forsterite and monticellite. Group 3 hosts Cr-bearing spinel and is present in the contact zone, together with the UG 1 chromitite. Cr-spinel cores found in the matrix surrounding calc-silicate fragments and in the Cr-stringers (proximal, intermediate and distal) appear to approach UG 1 chromitite compositions.

4.3.6 Garnet

The general formula of garnet is $X_3Y_2Z_3\varphi_{12}$, where the *X* site is occupied by Ca, Mg, Mn, Fe^{2+}; the *Y* site by Al, Mg, Mn, Ti, Cr, Fe^{3+}; the *Z* site is most frequently occupied by Si, but may also include Fe, Al, Zn, and φ represents O, OH or F (Grew *et al*., 2013). There are seven major endmembers: pyrope, almandine, spessartine, grossular, andradite, uvarovite and hydrogrossular (Deer *et al*., 1989). The chemical compositions of the five garnet endmembers of interest in the samples are: grossular ($Ca_3Al_2Si_3O_{12}$), andradite ($Ca_3(Fe^{3+})_2Si_3O_{12}$), uvarovite ($Ca_3Cr_2Si_3O_{12}$), pyrope ($Mg_3Al_2Si_3O_{12}$) and almandine ($Fe^{2+}{}_3Al_2Si_3O_{12}$). The number of ions is based on twelve oxygens. Garnet is only found in the contact zone, occurs in association with numerous minerals, and shows various textural features (summarised in Table 4.11). Representative analyses of garnet in the sample suite are shown in Table 4.12 and Fe^{2+}/Fe^{3+} estimations were calculated based the method described by Droop (1987). Pure garnet endmembers do not exist in the sample suite. The compositions largely involve three garnet endmembers (grossular, andradite and uvarovite) which occur in abundance throughout the sample suite. Pyrope is abundant in a few samples, whereas almandine is present in minor amounts only. Two ternary diagrams have been used to illustrate the compositional data of garnet: (1) grossular-andradite-uvarovite and (2) pyrope-almandine-uvarovite. Only trace amounts of Mn were recorded, therefore spessartine is not included in the figures.

Table 4. 11: Summary of textures and mineral assemblages associated with garnet from the Marikana sample suite

Sample name	Sample description	Main textural feature	Mineral assemblage
RSTX26-13	Fragment	Zoned grains	Di + Grt + Spl
RSTX26-51	Matrix	Zoned clusters	Di + Grt + Spl
RSTX26-52	Fragment	Zoned grains	Di + Grt + Spl
RSTX26-53 A	Matrix	Zoned grains	Di + Grt + Ves
RSTX26-53 B	Fragment	Zoned grains	Di + Grt + Spl
RSTX26-61	Cr-stringer proximal to xenolith	Zoned grains	Di + Grt + Spl
RSTX26-51	Matrix	Unzoned coronas	Di + Grt + Pl
RSTX26-53 A	Matrix	Unzoned coronas	Di + Grt + Pl
RSTX26-54	Matrix	Unzoned coronas	Di + Grt + Pl
RSTX26-54	Matrix	Unzoned symplectites	Ves + Grt
RSTX26-63	Cr-stringer distal from xenolith	Unzoned grains	Di + Grt + Spl

4.3.6.1 Unzoned grossular garnet

Grossular predominantly occurs as coronas between plagioclase and Al-rich diopside in the matrix of the contact zone. The garnet composition is uniform, with an average composition of Grs_{86}-Adr_{8}-Prp_{3}-Alm_{3} (Figures 4.34 and 4.35). Al content is ~1.72 apfu, Ca ~2.88 apfu, Fe^{3+} ~0.16 apfu, Fe^{2+} ~0.09 apfu, Mg ~0.07 apfu, and Cr ~0.07 apfu. Grossular also occurs in symplectites with vesuvianite and its composition appears to remain constant throughout, with an average composition of Grs_{90}-Adr_{6}-Prp_{1}-Alm_{3}. The average amount of Ca in this grossular symplectite is ~2.89 apfu, Al is ~1.85 apfu, Fe^{3+} ~0.11 apfu, Fe^{2+} ~0.08 apfu, Mg ~0.04 apfu and Cr ~0.01 apfu. Garnet found in the chromitite stringer samples (distal to the xenolith) that occurs together with Cr-spinel, Al-diopside and plagioclase is also homogeneous. This garnet contains significant Cr (~0.59 apfu), with an average composition of Grs_{42}-Adr_{24}-Prp_{7}-Uv_{25} and an Al content of ~0.99 apfu, Ca ~2.72 apfu, Fe^{3+} ~0.56 apfu, Mg ~0.08 apfu and Ti ~0.06 apfu.

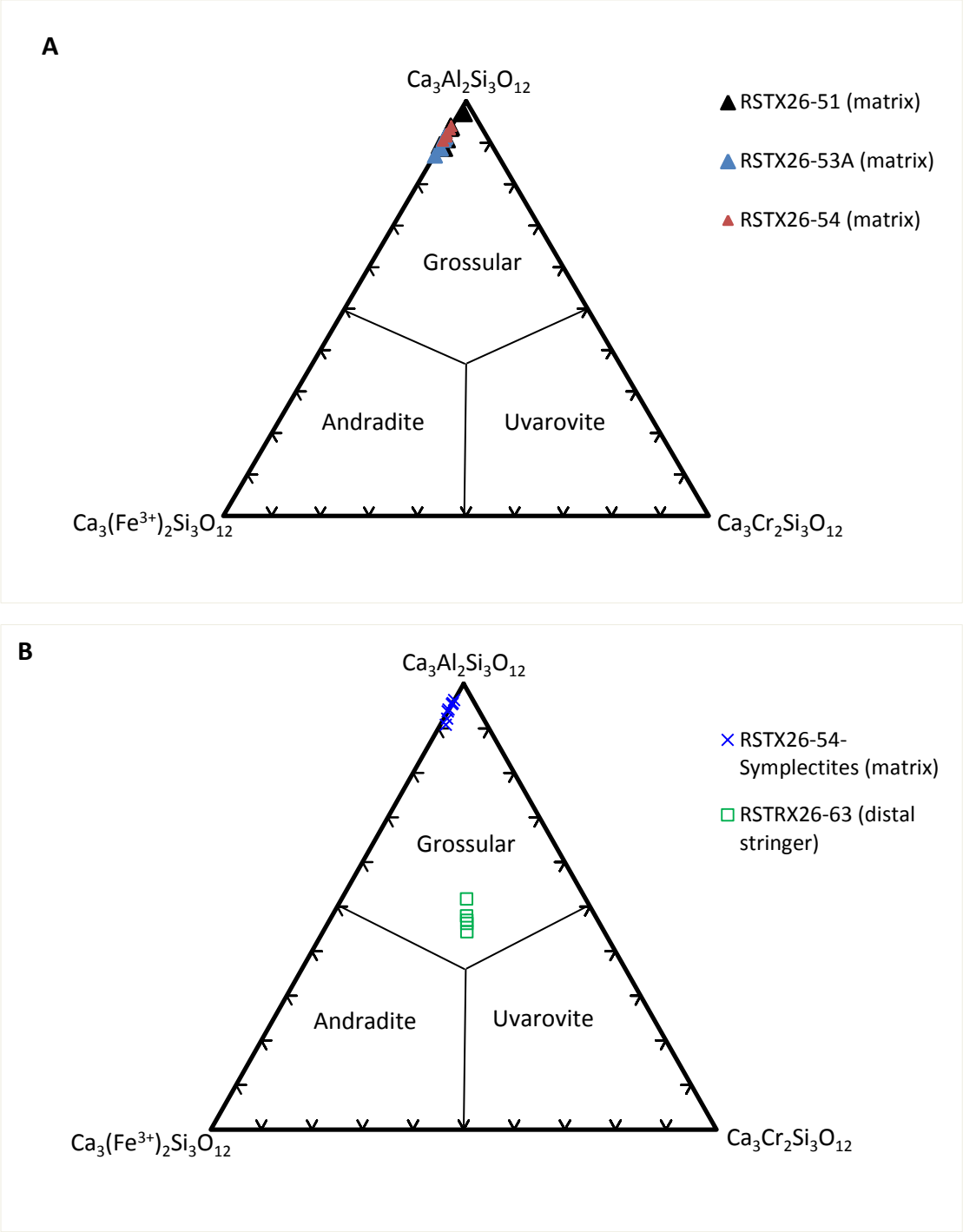

Figure 4.34: Ternary plots for garnet endmembers grossular, andradite and uvarovite representing individual garnet grains, which are unzoned from the Marikana sample suite. (A) depicts grossular coronas between plagioclase and diopside in the contact zone matrix; (B) depicts symplectites in the contact zone matrix and garnet grains found in the distal chromite stringer.

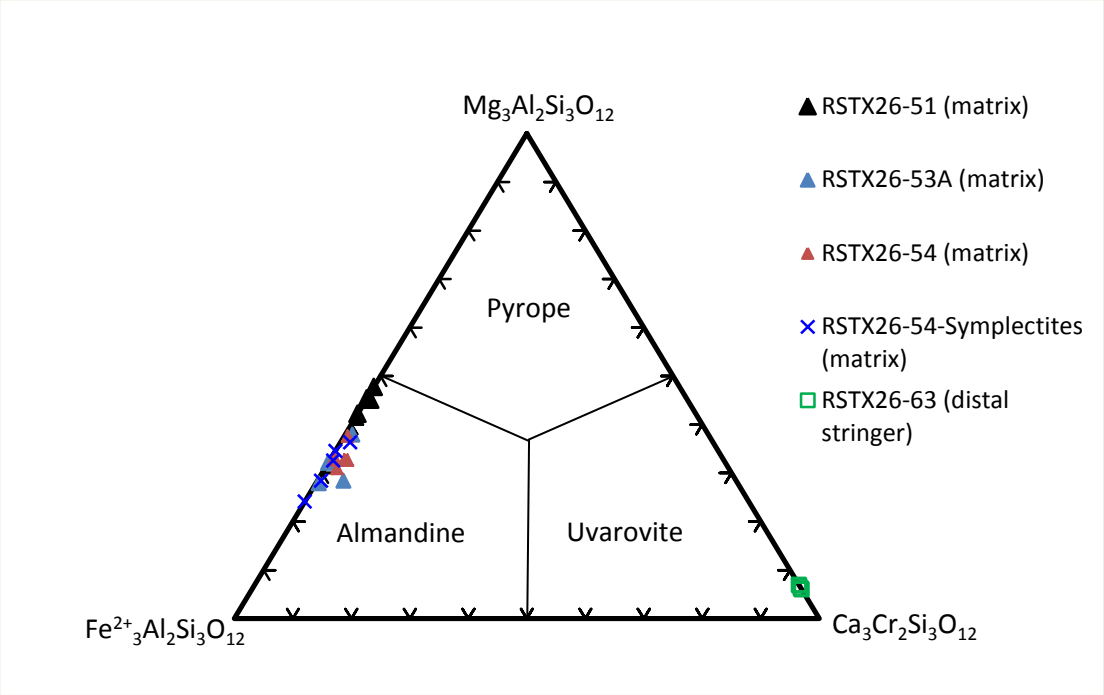

Figure 4.35: Ternary plot for garnet endmembers pyrope, almandine and uvarovite, representing all individual garnet grains which are unzoned from the Marikana sample suite.

4.3.6.2 Zoned garnet

As illustrated in Figures 4.36–4.38, the individual garnet grains in several samples are zoned. These zoned grains are associated with many other minerals (Table 4.11 and figures below). Most commonly zoned garnet occurs with Cr-spinel (which also displays zonation) and Al-diopside in samples that contain calc-silicate rock fragments. This mineral assemblage (Grt + Di + Spl) and the elemental distribution are depicted in Figure 4.8. Based on the mineral chemical data, the Cr content in garnet decreases from core to rim (from 0.64 apfu to bdl apfu) and the rims are enriched in Al (1.91 apfu) relative to the cores (1.01 apfu), while Fe^{3+} and Mg remain relatively constant at ~0.40 apfu and ~0.04 apfu, respectively. Mn was recorded at 0.01 apfu–0.02 apfu.

Garnet associated with vesuvianite and Al-diopside shows two compositional variations (Figures 4.37 and 4.39). Fe^{3+} and Ca increase (from 0.21 apfu to 1.33 apfu, and 1.99 apfu to 2.96 apfu, respectively) towards the rim and can be identified as the light grey material in the BSE image (Figure 4.39), whereas Al, Mg, Cr and Fe^{2+} decrease towards the rim (Al decreases from 0.99 apfu to 0.69 apfu, Cr from 0.15 apfu to bdl apfu, Fe^{2+} from 0.14 apfu to bdl apfu and Mg from 1.41 apfu to bdl apfu). Core compositions are Grs_{44}-Adr_{10}-Prp_{35}-Alm_4-Uv_7 and rims are Adr_{65}-Grs_{35}. Thus, andradite is found at the rim (10 µm–15 µm thick), and grossular-pyrope occurs at the core and intermediate points of the grain. This is the only sample (RSTX26-53A) displaying garnet with a significant Mg content (≤ 1.41 apfu).

Zoned garnet is found in association with Cr-spinel, diopside and plagioclase in samples associated with the proximal chromitite stringer (sample RSTX26-61) (Figure 4.40). The cores are enriched in Cr (0.58 apfu) relative to the rims (0.37 apfu). In some cases, the cores are characterised by single or multiple Cr-spinel inclusions. Al increases towards the rims (from 1.00 apfu to 1.32 apfu), Fe^{3+} decreases from core to rim (from 0.56 apfu to 0.35 apfu) and Mg increases slightly from core to rim (0.06 apfu to 0.08 apfu).

Clusters of garnet (Figures 4.37 and 4.41) are found in samples that contain fragments of calc-silicate rock (RSTX26-51). In thin-section (Figures 3.11 and 3.12), aggregates of xenoblastic garnet grains appear to be poikilitic and display radial subgrains. In some cases, the cores of these clusters are characterised by Cr-spinel (Figure 4.6). The cores of the aggregates are Cr-rich (0.64 apfu), even where Cr-spinel is not present; Cr decreases towards the rims (0.17 apfu). However, the compositional zonation does not appear to be symmetrical throughout the clusters. This feature is exhibited in the element maps (Figure 4.41). The rims are enriched in Al (1.60 apfu which decreases to 1.01 apfu at the cores), whereas Fe^{3+} is slightly higher at the rims (0.24 apfu) than at the cores (0.18); Mg increases from core to rim (0.03 apfu to 0.05 apfu) and Fe^{2+} decreases from core to rim (0.11 apfu to 0.07 apfu).

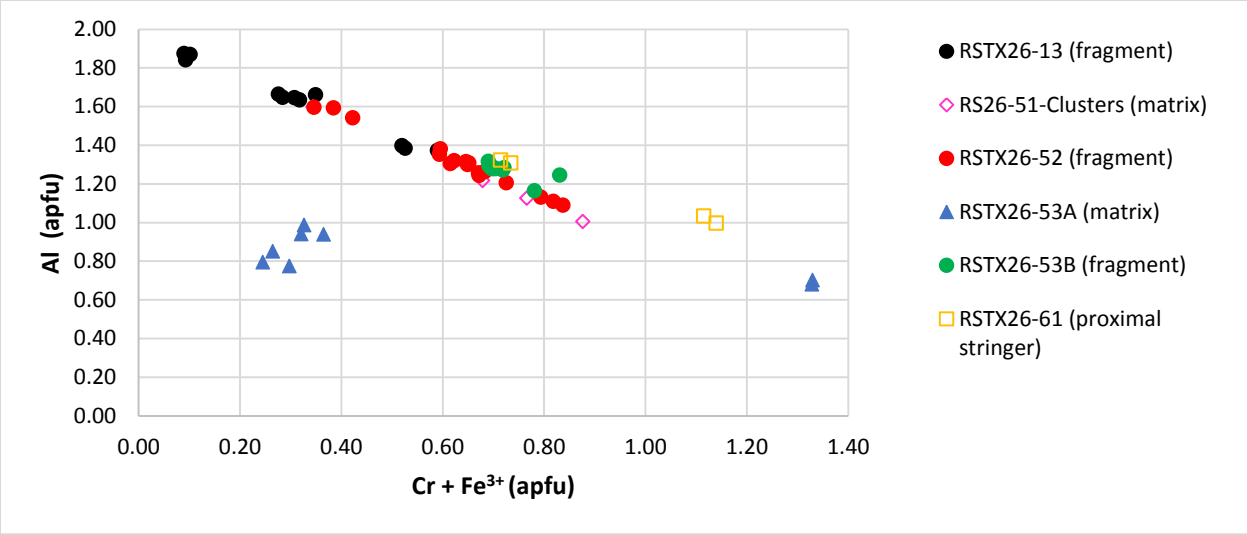

Figure 4.36: Plot showing the relationship between trivalent ions from core to rim in Cr-bearing zoned garnet from the Marikana sample suite.

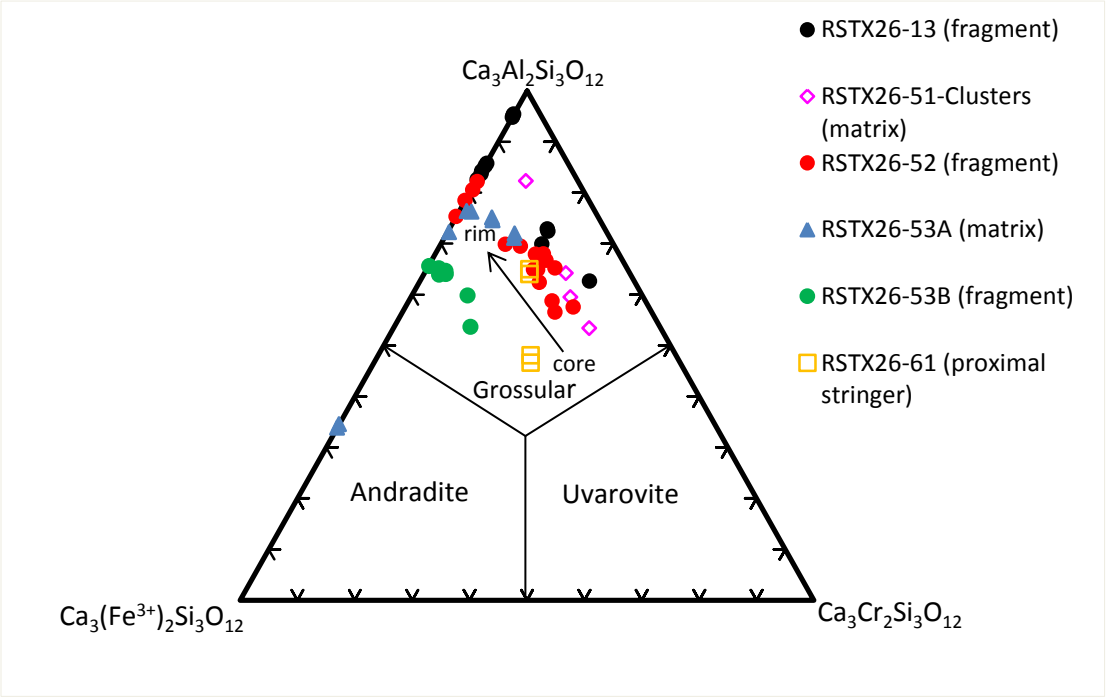

Figure 4.37: Ternary plot for garnet endmembers grossular, andradite and uvarovite, representing all garnet grains which are zoned and were analysed from core to rim from the Marikana sample suite.

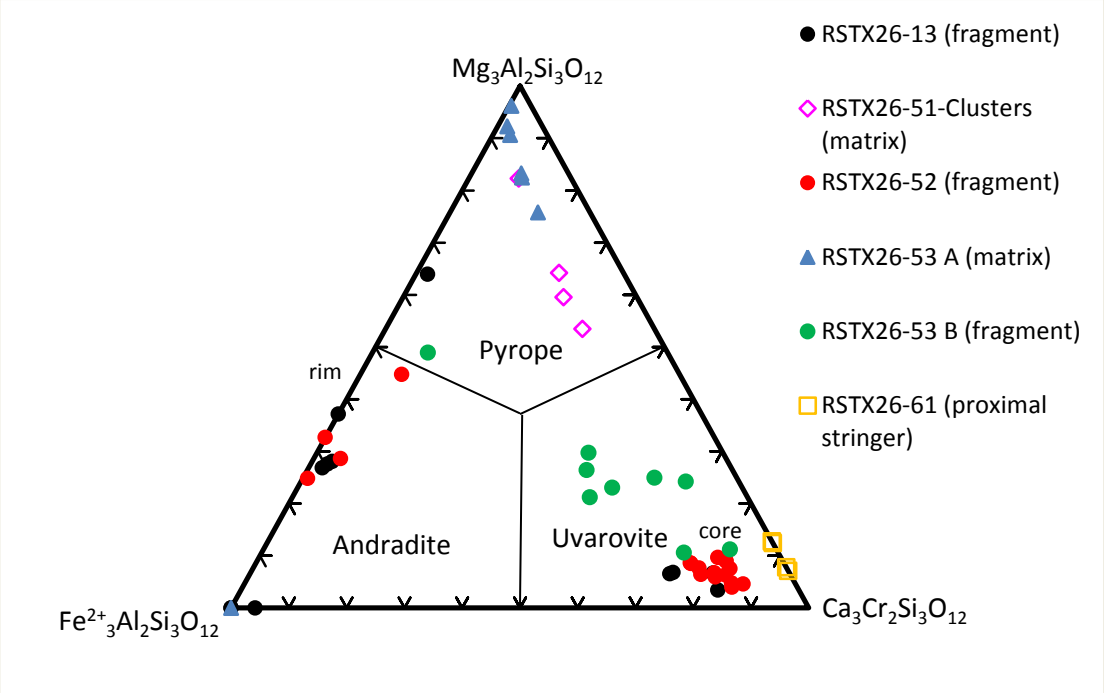

Figure 4.38: Ternary plot for garnet endmembers pyrope, almandine and uvarovite, representing all garnet grains which are zoned and were analysed from core to rim from the Marikana sample suite.

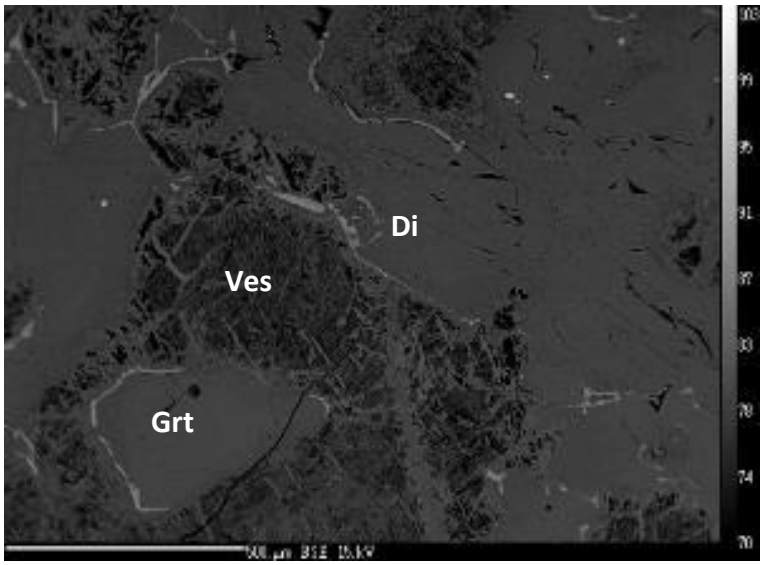

Figure 4.39: BSE image of zoned garnet in sample RSTX26-53A from the Marikana sample suite. The garnet core is grossular- and pyrope-rich, while the narrow rim (light grey) is andradite-rich. Garnet is surrounded by vesuvianite which, in turn, is surrounded by diopside.

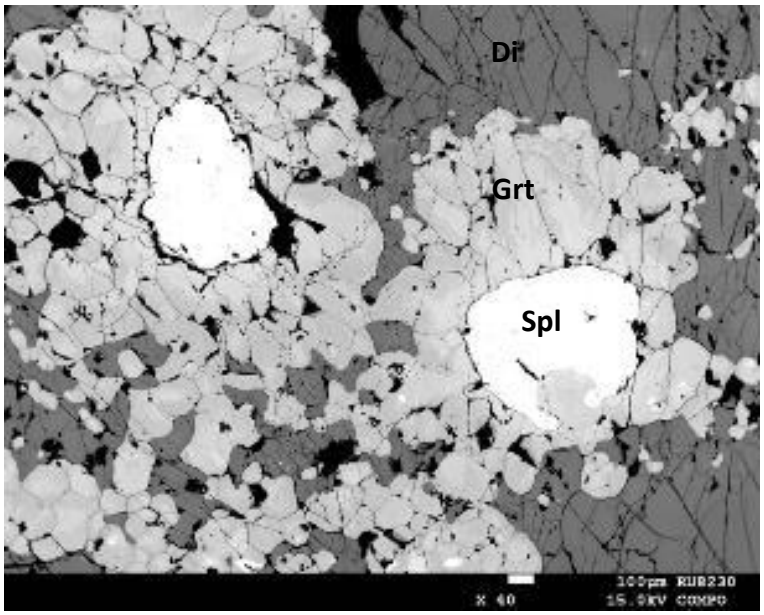

Figure 4.40: BSE image of garnet surrounding Cr-spinel in the proximal chromitite stringer (RSTX26-61) from the Marikana sample suite; garnet displays asymmetrical compositional zonation. The cores of the aggregates are enriched in Cr (uvarovite), while the Ca and Al increase at the rim (grossular).

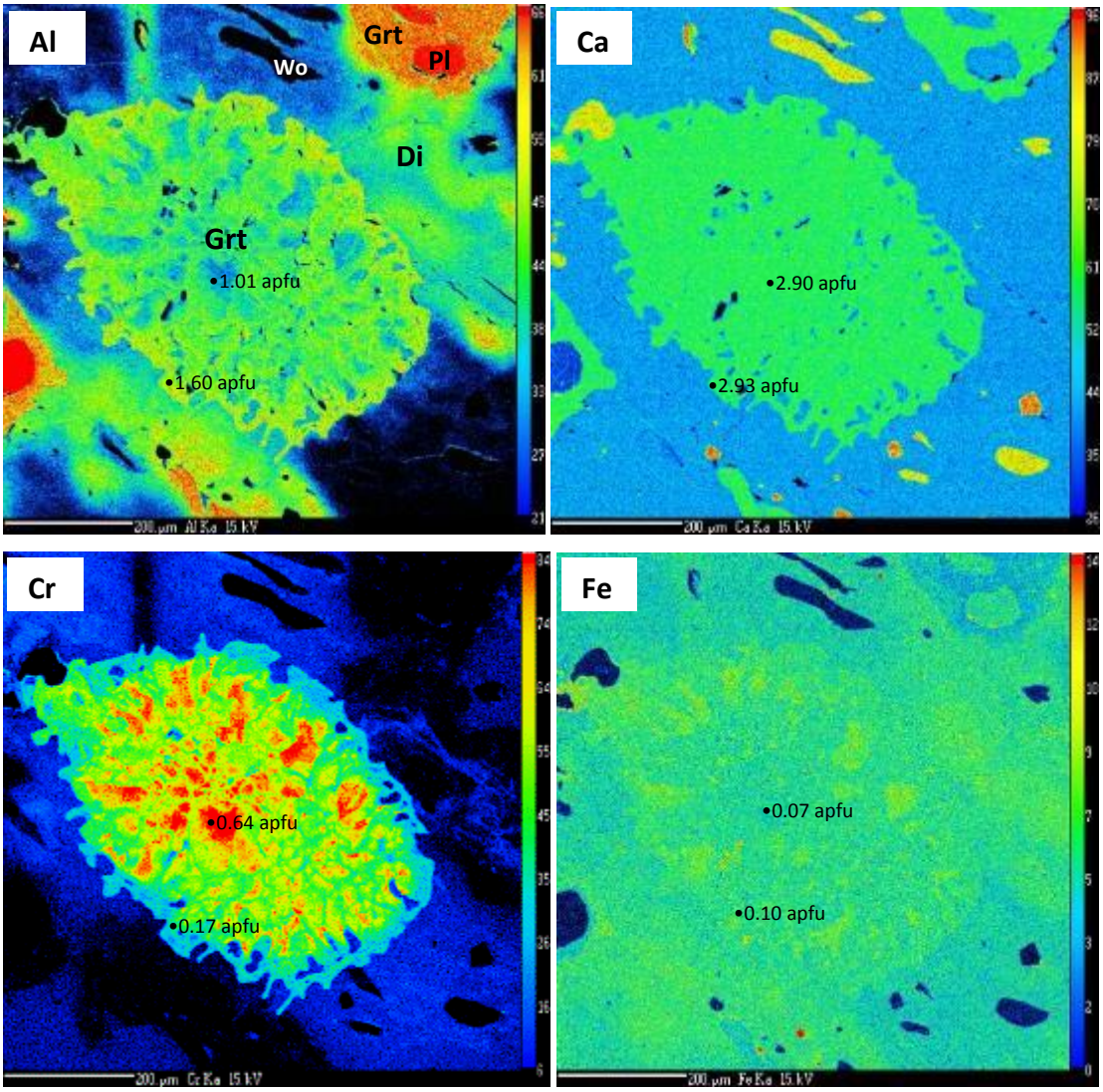

Figure 4.41: Element maps of garnet clusters (RSTX26-51) from the Marikana sample suite exhibiting complex internal zonation, shown petrographically in Figure 3.11. Ca and Fe show little variation; however, Cr is enriched and Al is depleted in the core.

Table 4. 12: Representative chemical compositions of garnet from the Marikana sample suite.

Sample	RSTX 26-53A (CAMECA)	RSTX 26-53A (CAMECA)	RSTX 26-53B (CAMECA)	RSTX 26-53B (CAMECA)	RSTX 26-51 (CAMECA)	RSTX 26-51 (CAMECA)	RSTX 26-52 (CAMECA)	RSTX 26-52 (CAMECA)	RSTX 26-52 (CAMECA)
comment	corona	zoned	core	rim	corona	cluster	core	intermediate	rim
SiO_2	38.91	45.84	37.71	39.17	39.76	38.41	38.64	37.73	37.75
TiO_2	0.12	0.15	1.10	1.02	0.17	0.35	0.45	0.76	0.53
Al_2O_3	16.12	10.07	14.06	12.84	19.64	13.35	17.27	13.90	11.83
Cr_2O_3	0.04	1.03	0.68	1.43	0.13	7.20	0.06	5.65	8.26
FeO	9.15	5.56	10.44	9.36	3.73	4.68	7.05	5.69	5.87
MnO	0.18	0.08	0.15	0.11	0.18	0.02	0.17	0.09	0.04
MgO	0.28	11.66	0.30	2.60	0.43	0.34	0.37	0.42	0.34
CaO	34.84	25.26	35.09	32.90	35.23	34.47	34.81	34.13	34.01
Na_2O	0.01	0.01	0.01	0.01	0.01	0.01	bdl	bdl	bdl
Total	99.64	99.66	99.53	99.44	99.28	98.81	98.82	98.36	98.63
				Number of ions based on 12 oxygens					
Si	3.00	3.40	2.94	3.03	3.04	3.03	2.99	2.98	3.00
Ti	0.01	0.01	0.06	0.06	0.01	0.02	0.03	0.05	0.03
$Al^{(IV)}$	0.01	bdl	bdl	bdl	bdl	bdl	bdl	bdl	bdl
$Al^{(VI)}$	1.45	0.88	1.29	1.18	1.77	1.24	1.58	1.30	1.11
Cr	bdl	0.06	0.04	0.09	0.01	0.45	bdl	0.35	0.52
Fe^{3+}	0.52	0.24	0.65	0.56	0.14	0.21	0.38	0.29	0.30
Fe^{2+}	0.08	0.10	0.03	0.05	0.10	0.09	0.08	0.08	0.09
Mn	0.01	bdl	0.01	0.01	0.01	bdl	0.01	0.01	bdl
Mg	0.03	1.29	0.03	0.29	0.05	0.04	0.04	0.05	0.04
Ca	2.88	2.01	2.93	2.74	2.88	2.91	2.89	2.89	2.90
Na	bdl	bdl	bdl	bdl	bdl	bdl	bdl	bdl	bdl
Total	8.00	8.00	8.00	8.00	8.00	8.00	8.00	8.00	8.00
Prp	1.06	37.85	1.14	8.61	1.60	1.30	1.42	1.64	1.32
Alm	2.70	3.02	0.89	1.68	3.23	3.09	2.50	2.70	3.09
Sps	0.39	0.14	0.32	0.24	0.39	0.04	0.37	0.19	0.09
Grs	70.12	43.65	61.47	56.47	87.19	61.36	75.94	62.31	54.13
Uv	0.10	2.86	2.00	4.24	0.39	22.51	0.17	17.01	25.36
And	25.38	12.13	31.12	26.70	6.78	10.68	18.35	14.17	14.46
Total	99.76	99.65	96.95	97.94	99.58	98.98	98.74	98.01	98.44

Table 4.12: *(continued)*

Sample	RSTX26-54 (CAMECA)	RSTX26-54 (CAMECA)	RSTX26-61 (JEOL)	RSTX26-61 (JEOL)	RSTX26-63 (JEOL)
comment	corona	sym	core	rim	
SiO_2	39.89	39.95	37.87	37.35	36.92
TiO_2	0.12	0.07	0.48	0.85	1.68
Al_2O_3	20.30	20.80	12.51	10.75	11.26
Cr_2O_3	0.04	0.09	8.46	10.24	9.33
Fe2O3			4.71	5.40	5.59
FeO*	3.97	3.00			
MnO	0.20	0.14	0.21	0.18	0.13
MgO	0.42	0.36	0.56	0.66	0.73
CaO	35.42	35.78	33.37	33.01	32.61
Na2O	0.01	bdl	0.03	0.01	0.02
Total	100.35	100.19	98.38	98.48	98.45
	Number of ions based on 12 oxygens				
Si	3.01	3.01	3.01	3.20	2.96
Ti	0.01	bdl	0.03	0.05	0.10
Al(IV)	bdl	bdl	bdl	bdl	bdl
Al(VI)	1.81	1.85	1.18	0.81	1.06
Cr	bdl	0.01	0.53	0.54	0.59
Fe3+	0.16	0.11	0.28	0.27	0.34
Fe2+	0.09	0.08	bdl	bdl	bdl
Mn	0.01	0.01	0.01	0.01	0.01
Mg	0.05	0.04	0.07	0.38	0.09
Ca	2.86	2.89	2.84	2.67	2.80
Na2O	bdl	bdl	bdl	bdl	bdl
Total	8.00	8.00	7.96	7.94	7.95
Prp	1.55	1.34	2.34	11.03	3.00
Alm	3.08	2.54	bdl	bdl	bdl
Sps	0.42	0.29	0.50	0.36	0.31
Grs	86.95	89.90	56.80	44.35	49.14
Uv	0.11	0.27	25.43	27.27	27.31
And	7.58	5.47	13.70	14.53	15.57
Total	99.69	99.81	98.76	97.55	95.32

4.3.7 Vesuvianite

The general formula for vesuvianite is $X_{19}Y_{13}Z_{18}O_{68}W_{10}$, where the *X* site is commonly occupied by Ca, Na; the *Y* site by Al, Mg, Fe, Mn, Ti, Cu, Zn; the *Z* by Si, and the *W* site by OH, F, O (Groat *et al.,* 1992). The number of ions is based on seventy-eight oxygens and representative analyses of vesuvianite are shown in Table 4.13. Vesuvianite found in the contact zone and in samples containing calc-silicate fragments, shows Ca content that varies from 18.74 apfu to 19.96 apfu and Na from 0.01 apfu to 0.28 apfu. Mg varies from 0.92 apfu to 3.60 apfu, Fe from 0.06 apfu to 0.55 apfu, Al from 11.71 apfu to 17.72 apfu and Si from 11.54 apfu to 14.50 apfu. Ti, Cr and Mn occur in negligible amounts (Appendix 4B). F ranges from 0.04 apfu to 0.33 apfu, while Cl occurs in one sample only (RSTX26-54) and shows a wide range (0.01 apfu to 4.67 apfu). The chemical composition is characterised by relatively lower Ca, Mg, Fe, Ti, and higher Al, while Cr occurs in similar amounts when compared to vesuvianite observed in the Eastern Limb (Wallmach *et al*., 1995).

Cation-cation correlation diagrams (Figure 4.42) show the variation in element abundance from core to rim for grains in two samples (RSTX26-52 and RSTX26-53A). By contrast, sample RSTX26-54 contains vermicules of vesuvianite in a symplectitic intergrowth with grossular, and was analysed across the symplectite. The overall trend in Figure 4.42A indicates that the cores of grains appear to be richer in Ca than the rims. There are no distinctive Ca-Na trends in the symplectite. Al increases from core to rim, while Mg and Fe^{2+} decrease from core to rim, and Cr and Mn remain relatively constant (Figure 4.42B – E). The overall trend indicates that all elements (except Al) which occupy the *Y* site decrease from core to rim (Figure 4.42E). There is only one point in sample RSTX26-54 that contains a significant amount of Cl (4.67 apfu) and can be recognised as the outlier in Figure 4.42A as it contains significantly less Ca (18.74 apfu) than other points in the sample.

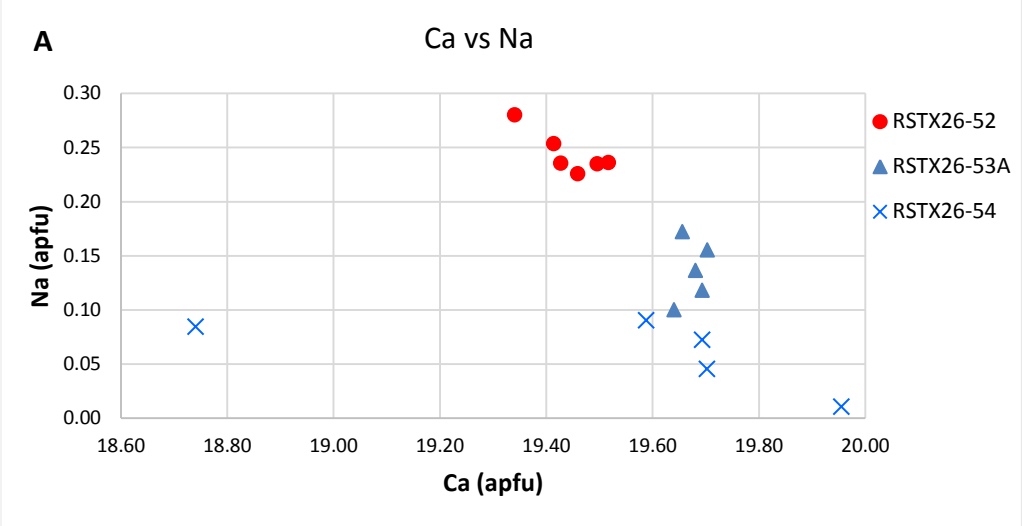
A
Ca vs Na
Na (apfu)
0.30
0.25
0.20
0.15
0.10
0.05
0.00
18.60
18.80
19.00
19.20
19.40
19.60
19.80
20.00
Ca (apfu)
RSTX26-52
RSTX26-53A
RSTX26-54

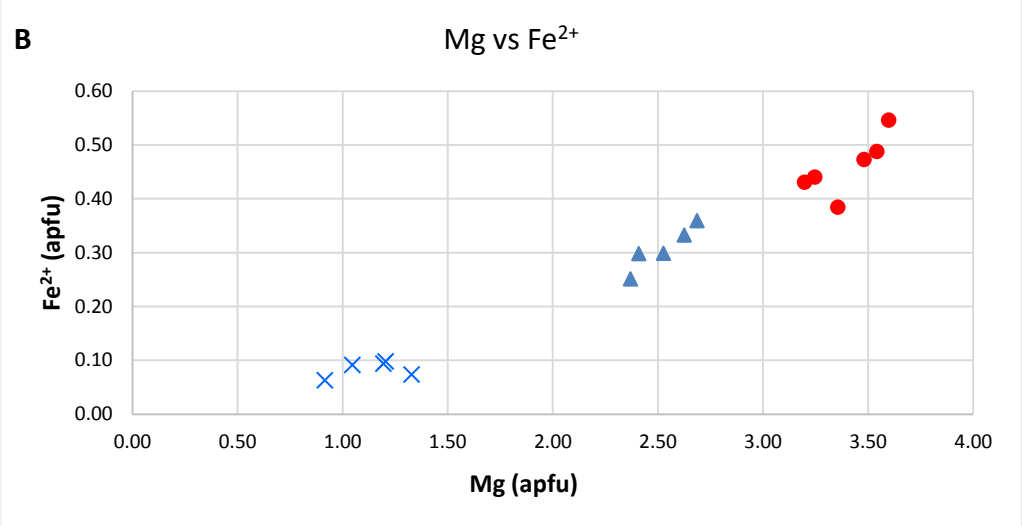
B
Mg vs Fe2+
Fe2+ (apfu)
0.60
0.50
0.40
0.30
0.20
0.10
0.00
0.00
0.50
1.00
1.50
2.00
2.50
3.00
3.50
4.00
Mg (apfu)

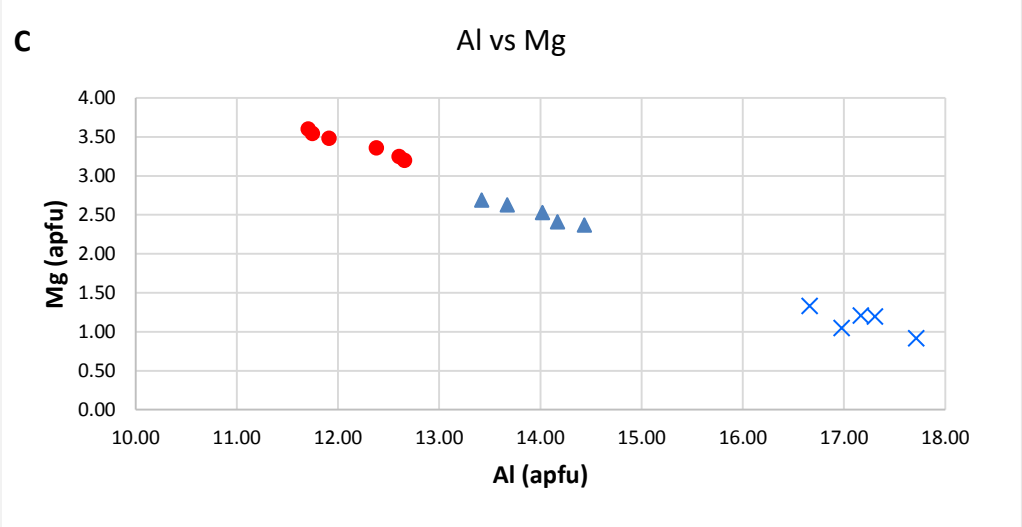
C
Al vs Mg
Mg (apfu)
4.00
3.50
3.00
2.50
2.00
1.50
1.00
0.50
0.00
10.00
11.00
12.00
13.00
14.00
15.00
16.00
17.00
18.00
Al (apfu)

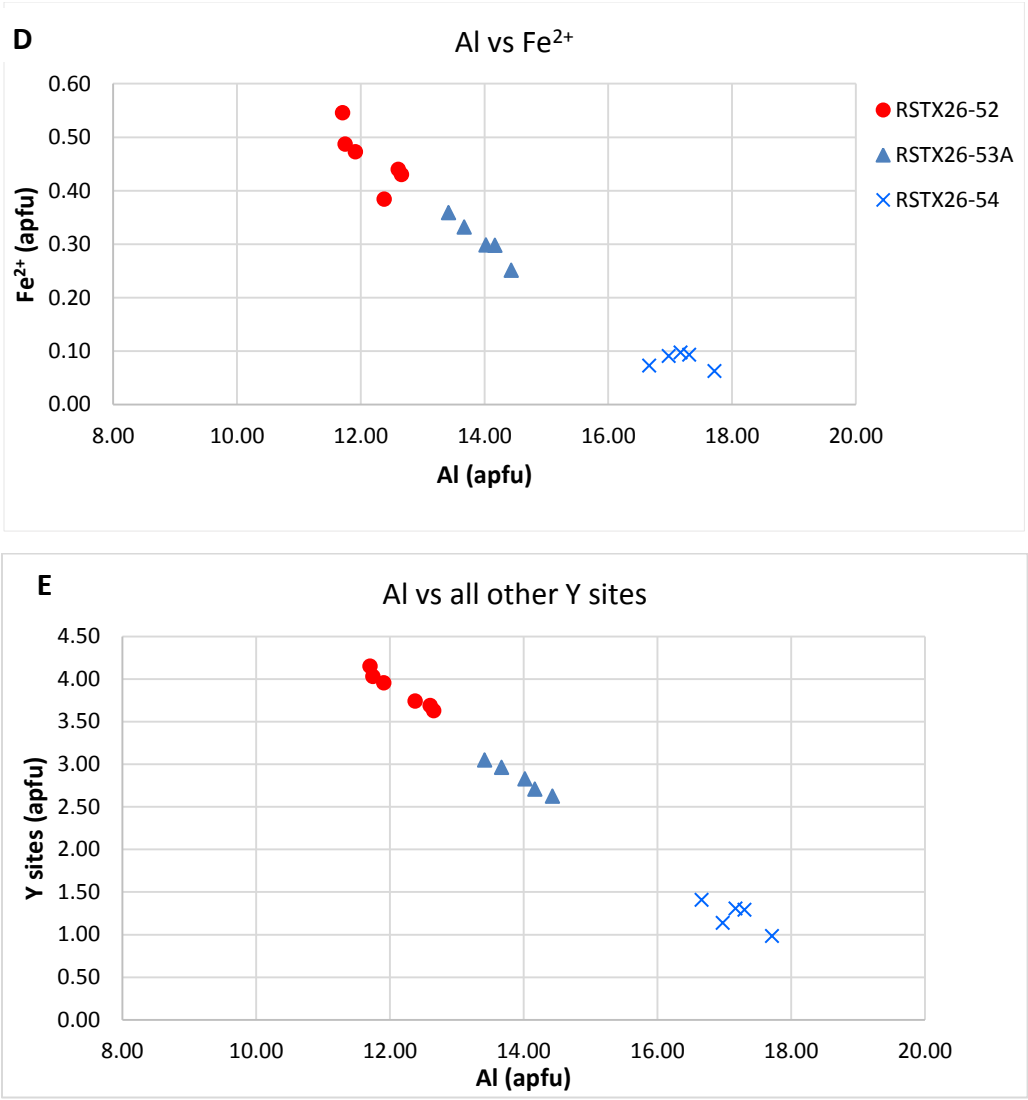

Figure 4.42: Cation-cation correlation diagrams depicting the variation in elemental proportions for vesuvianite in samples RSTX26-52 and RSTX26-53A and in the vesuvianite-garnet symplectites (RSTX26-54) from the Marikana sample suite. (A) depicts the correlation between Ca and Na (in the *X* site). Variations in the *Y* site cations are depicted in B – D.

Table 4. 13: Representative chemical compositions of vesuvianite from the Marikana sample suite.

Sample	RSTX26-52 (CAMECA)	RSTX26-52 (CAMECA)	RSTX26-53A (CAMECA)	RSTX26-53A (CAMECA)	RSTX26-54 (CAMECA)
comment	core	rim	core	rim	symplectite
F	0.05	0.09	0.04	0.15	0.11
Na_2O	0.27	0.27	0.14	0.14	0.06
MgO	4.99	4.80	3.53	3.61	1.54
Al_2O_3	21.90	22.35	25.51	25.13	29.42
SiO_2	30.74	30.35	28.40	28.54	24.15
SO_3	bdl	bdl	bdl	bdl	bdl
Cl	bdl	bdl	bdl	bdl	1.16
CaO	38.94	38.83	39.18	39.03	36.81
TiO_2	bdl	bdl	bdl	0.01	0.01
Cr_2O_3	0.03	0.02	bdl	0.01	0.01
MnO	0.04	0.04	0.02	0.03	0.02
FeO	1.26	1.10	0.76	0.78	0.20
Fe_2O_3	bdl	bdl	bdl	bdl	bdl
H_2O	1.94	1.94	1.94	1.88	1.49
Total	100.17	99.79	99.50	99.28	94.98
			Number of ions based on 78 O, OH		
F	0.08	0.13	0.06	0.22	0.17
Na	0.25	0.24	0.13	0.13	0.06
Mg	3.46	3.35	2.47	2.53	1.14
Al	12.02	12.32	14.10	13.93	17.17
Si	14.32	14.19	13.32	13.42	12.00
Cl	bdl	bdl	bdl	bdl	1.07
Ca	19.43	19.45	19.69	19.67	19.54
Ti	bdl	bdl	bdl	bdl	bdl
Cr	0.01	0.01	bdl	bdl	bdl
Mn	0.02	0.01	0.01	0.01	0.01
Fe^{2+}	0.49	0.43	0.30	0.31	0.08
Fe^{3+}	bdl	bdl	bdl	bdl	bdl
Total	50.08	50.13	50.06	50.22	51.24
OH	9.48	9.34	9.28	9.24	8.81
O^{2-}	62.42	62.47	62.60	62.65	63.11

4.3.8 Summary

Evidence from mineral chemical data indicates that there is definite compositional zonation of mineral assemblages from the xenolith, through the contact zone and into the mottled anorthosite. Monticellite and forsterite are predominantly found in the main xenolithic body and the western contact of the xenolith in the forsterite-spinel and forsterite-monticellite layers. A slight variation in the Mg and Fe content is recorded between the main xenolithic body and the aforementioned layers; Mg decreases while Fe increases from the main xenolithic body to the forsterite-monticellite layer. Apart from this slight variation the overall composition of forsterite and monticellite remains constant.

Pyroxenes are predominantly observed in the contact zone (as clinopyroxene). Clinopyroxene found in the contact zone in samples from the matrix, calc-silicate fragments and chromitite stringer – proximal sample) are characterised by high Al contents (up to ~ 0.86 apfu). The Fe^{3+} in clinopyroxene is also typically higher (up to ~0.22 apfu) than that observed in mottled anorthosite. According to Tracey *et al*. (1978), high Al and Fe^{3+} concentrations are common for clinopyroxenes in contact metamorphic settings. Another distinguishing feature of these clinopyroxenes is their highly calcic composition. Ca, Al and Fe^{3+}-rich clinopyroxene are similar to those observed by Willemse and Bensch (1964) within xenoliths in localities C, D, E, F, G, I and J, and the contact zone in locality A (termed 'fassaite'). Although these clinopyroxenes in this study have been termed diopsides, many samples plot above the typical diopsidic compositions in the pyroxene ternary (Figures 4.4, 4.7 and 4.9), thus indicating an excess Ca content. According to Tracey *et al*. (1978), Owens (2000), Gaeta *et al*. (2009) and Mollo *et al*. (2010), clinopyroxene that is composed of elevated Ca, Al and Fe^{3+}, as identified in this sample suite, is considered enriched in the calcium Tschermak (CaTs) component, which is a common occurrence in clinopyroxene found in contact metamorphic settings. CaTs-rich clinopyroxene samples all lie in Group 1, as demonstrated in Figures 4.10 to 4.14 and may be attributed to their closer proximity to the xenolith or calc-silicate rock fragments compared to samples that lie in Group 2. Wollastonite is found in samples where grossular coronas have formed between plagioclase and CaTs-rich clinopyroxene. The other clinopyroxene-bearing samples found in the

contact zone include the chromitite stringers intermediate and distal to the xenolith. These samples lie in Group 2 with mottled anorthosite. The intermediate sample is termed Al-diopside and shows typically elevated Ca concentrations, but it does not contain high Fe^{3+} values. Therefore, it is not considered as CaTs-enriched. The distal sample shows lower Al and Fe^{3+} values that are similar to mottled anorthosite clinopyroxene, and shows no signs of contamination visually and compositionally. Therefore, clinopyroxene in the distal chromitite stringer and mottled anorthosite can be considered diopsidic in composition. Based on the results presented herein it is evident that the Ca, Al and Fe^{3+} concentrations in pyroxene vary based on their proximity to the xenolith. Willemse and Bensch (1964) noted a similar phenomenon in their study where Ca, Al, Fe^{3+}-rich clinopyroxene (termed 'fassaite' in their study and CaTs clinopyroxene in this study) was found both within the xenoliths themselves and surrounding contact zones. However, in some cases the clinopyroxene becomes diopsidic in composition on the xenolith contacts.

Plagioclase is found in the contact zone matrix and mottled anorthosite. It is always closely associated with CaTs clinopyroxene in the contact zone, where the latter is interstitial to the former, or with grossular coronas that occur between the plagioclase and clinopyroxene grains. Plagioclase composition varies between samples found in the contact zone matrix, which are most calcic (An_{99}); the intermediate chromitite stringer ($An_{94–98}$); to the distal chromitite stringer (zoned grains, with $An_{70–80}$ cores and $An_{60–70}$ rims). The plagioclase from the distal stringer shows compositional similarity compared to the mottled anorthosite.

Spinel occurs in three distinct compositional variations (section 4.3.5). Group 1 comprises magnetite-bearing exsolution lamellae, whereas Group 2 is spinel, *sensu stricto,* that hosts the exsolution lamellae. Both Group 1 and 2 are found in xenolithic samples, namely, the main xenolithic body, forsterite-spinel, spinel and forsterite-monticellite layers. Overall the chemical heterogeneity between and within samples is minor. Group 3 comprises Cr-bearing spinel, which is found in the contact zone and in the UG 1 chromitite. Cr-spinel displays chemical heterogeneity on a core-to-rim basis, where the cores are Cr-rich and rims are Al-rich. The Cr-

spinel in the chromitite stringers, from proximal through to the distal, appear to progressively approach UG 1 chromitite compositions.

Garnet compositions show two major compositional variations; grossular-rich and grossular-andradite-uvarovite-bearing. Unzoned grossular-rich garnet is found as reaction coronas between plagioclase (An_{99}) and Al-diopside and in symplectic intergrowth with vesuvianite in the contact zone. The grossular-andradite-uvarovite-bearing variation is intimately associated with Cr-spinel in most cases, which occurs as inclusions in the garnet. In samples where uvarovite is observed without Cr-spinel at its core (such as clusters demonstrated in Figure 4.41), Cr-spinel-bearing uvarovite is always observed in close proximity. The uvarovitic garnet displays relative Cr enrichment in the core of grains and Al enrichment at its rims.

Overall the chemical data indicates that compositional heterogeneity occurs on a variety of scales, from decimetres between zones, to centimetres within individual zones between samples, and on a grain-to-grain and/or core-to-rim basis within individual samples. The enrichment of Al, Ca, and/or Fe^{3+} in the contact zone appears to be responsible for highly calcic major mineral phases, such as plagioclase, CaTs clinopyroxene and wollastonite.

4.4 Zwartfontein

Five thin-sections were analysed from the Zwartfontein locality by the JEOL instrument at Rhodes University. Table 4.14 provides a summary and brief description of all thin-sections analysed.

Table 4. 14: Summary and brief description of all thin-sections analysed

Borehole	Sample name	Sample description	Mineral assemblage
ZF116	A156-7	Main xenolithic body	Mtc + Fo + Di + Spl
ZF116	A291-1	Contact zone (Parapyroxenite)	Cpx + Pl
ZF116	A312-3	Main xenolithic body	Cal
ZF116 ED1	B882-4	Contact zone	Opx + Cpx + Pl
ZF109 ED1	C435-2	Main xenolithic body	Di + Anh + Cal + Srp

4.4.1 Monticellite and forsterite

Representative analyses of monticellite and forsterite are shown in Table 4.15. Monticellite and forsterite compositions are shown on the Ca-Mg-Fe ternary in Figure 4.43. Both minerals are found in xenolith A156-7 (Figure 3.19) in borehole ZF116. Mg in monticellite ranges from 0.87 to 0.91 apfu, with an average composition of 0.89 apfu. X_{Mg} shows a slight variation from 0.88 to 0.90. Fe ranges from 0.10 to 0.12 apfu, with an average of 0.11 apfu, and Ca is relatively constant at ~0.96 apfu. There is no compositional difference between monticellite grains and monticellite lamellae found in forsterite. Forsterite compositions exhibit little variation, with an average of Fo_{95} and a range from $Fo_{94\text{-}96}$. Mg ranges from 1.86 to 1.88 apfu, Fe ranges from 0.09 to 0.11 apfu and most grains contain an average of 0.01 apfu Ca. Given that monticellite and forsterite are only found in one xenolith and not in the contact zones, it is not possible to make any comparisons similar to the Marikana samples.

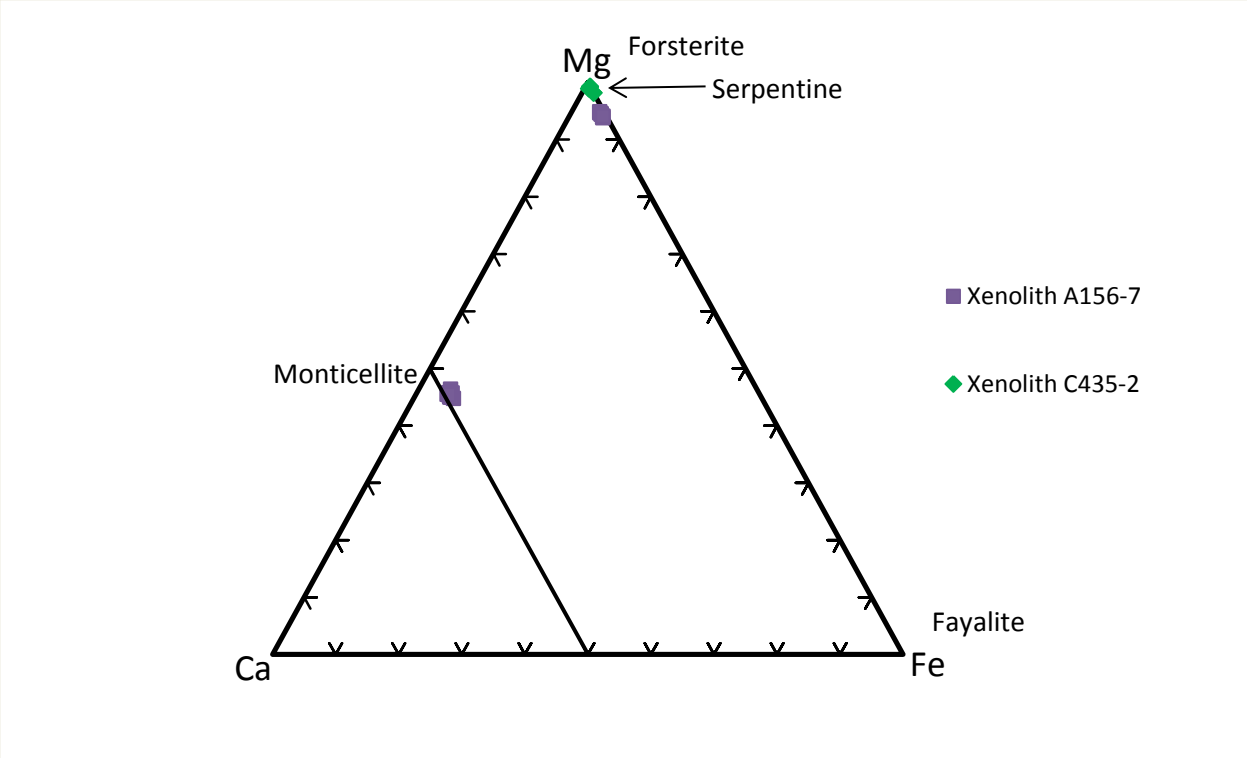

Figure 4.43: Monticellite and forsterite compositions illustrated, based on the proportions of Ca-Mg-Fe for xenolith A156-7 in borehole ZF 116 together with serpentine from xenolith C435-2 in borehole ZF109 ED1 from the Zwartfontein xenoliths.

4.4.2 Serpentine

Serpentine [$Mg_3(Si_2O_5)(OH)_4$] is found in xenolith C435-2. Its composition shows little variability: Si ranges from 1.77 apfu to 1.82 apfu, Al from 0.01 apfu to 0.03 apfu, Fe^{2+} from 0.02 apfu to 0.05 apfu, Mg from 2.61 apfu to 2.65 apfu, and Mn is constant at 0.01 apfu (Figure 4.43). Chemical data compared with Deer *et al*. (1989) indicate that the serpentine may be termed chrysotile. A representative serpentine analysis is shown in Table 4.15.

Table 4. 15: Representative chemical compositions for monticellite, forsterite and serpentine from the Zwartfontein xenoliths

Sample	A156-7 (JEOL)	A156-7 (JEOL)	A156-7 (JEOL)
comment	Mtc	Mtc lamellae	Fo
SiO_2	37.24	37.07	41.11
Al_2O_3	bdl	bdl	0.01
TiO_2	bdl	0.01	0.01
Cr_2O_3	0.03	bdl	0.03
FeO	4.74	5.24	4.89
MnO	1.20	1.31	1.14
MgO	22.17	21.67	51.90
CaO	33.21	32.97	0.54
Na_2O	0.01	bdl	bdl
K_2O	0.02	0.02	0.02
Total	98.63	98.29	99.65
	Number of ions based on 4 Oxygens		
Si	1.01	1.01	0.99
Al	bdl	bdl	bdl
Ti	bdl	bdl	bdl
Cr	bdl	bdl	bdl
Fe^{2+}	0.11	0.12	0.10
Mn	0.03	0.03	0.02
Mg	0.89	0.88	1.87
Ca	0.96	0.96	0.01
Na	bdl	bdl	bdl
K	bdl	bdl	bdl
Total	2.99	2.99	3.01
Mg#	0.89	0.88	0.95

Sample	C435-2 (JEOL)
comment	Srp
SiO_2	41.56
Al_2O_3	0.68
TiO_2	0.01
Cr_2O_3	0.02
FeO	0.83
MnO	0.21
MgO	40.63
CaO	0.11
Na_2O	0.01
K_2O	0.02
H_2O	15.51
Total	99.59
Number of ions based on 4 O, OH	
Si	1.81
Al	0.02
Ti	bdl
Cr	bdl
Fe^{3+}	bdl
Fe^{2+}	0.03
Mn	0.01
Mg	2.63
Ca	0.01
Na	bdl
K	bdl
H	4.50
Total	9.00

4.4.3 Calcite

EMPA confirmed the occurrence of calcite in two xenoliths (sample A312-3 in borehole ZF116, and sample C435-2 in borehole ZF109 ED1). A chemical compositional analysis is provided in Appendix 3. Calcite is composed of 1.99 apfu Ca and negligible amounts of Sr and Mg. Calcite

compositions are almost identical to Western Limb samples, except for the negligible amounts of Ba detected in the Western Limb. No Ba was detected in the Northern Limb calcite.

4.4.4 Anhydrite

The presence of anhydrite ($CaSO_4$) is confirmed in xenolith C435-2 only (Figures 3.20 and 3.21). Anhydrite throughout the sample contains 2.97 apfu – 2.98 apfu S, and 1.00 apfu Ca. It is usually associated with calcite and an extremely fine-crystalline Ca-rich material (however, no accurate chemical data were recorded for this mineral because its microcrystalline grain size compared to the beam diameter).

4.4.5 Pyroxenes

Clinopyroxene is evident in the two xenoliths (A156-7 and C435-2), whereas orthopyroxene is only found in contact zones adjacent to xenoliths (A291-1 and B882-4). Representative analyses for pyroxene are shown in Table 4.16. In xenolith sample A156-7, clinopyroxene is associated with calc-silicate minerals, including monticellite and forsterite. It is diopsidic and ranges from Wo_{49}-En_{50}-Fs_1 to Wo_{54}-En_{39}-Fs_8 (Figure 4.44). It is characterised by a high amount of Al (between 0.30–0.44 Al apfu). Therefore, all clinopyroxene in this sample is termed Al-diopside, according to Morimoto *et al*. (1988), given that it is composed of ≥ 0.1 apfu of Al. Clinopyroxene in xenolith sample C435-2 is partially altered to serpentine and occurs with calcite and anhydrite (and not monticellite and forsterite, such as xenolith A156-7). Compositions range from Wo_{50}-En_{41}-Fs_1 to Wo_{52}-En_{40}-Fs_8 (Figure 4.46). The grains contain similar high amounts of Al (between 0.27–0.32 apfu) and can be termed Al-diopside.

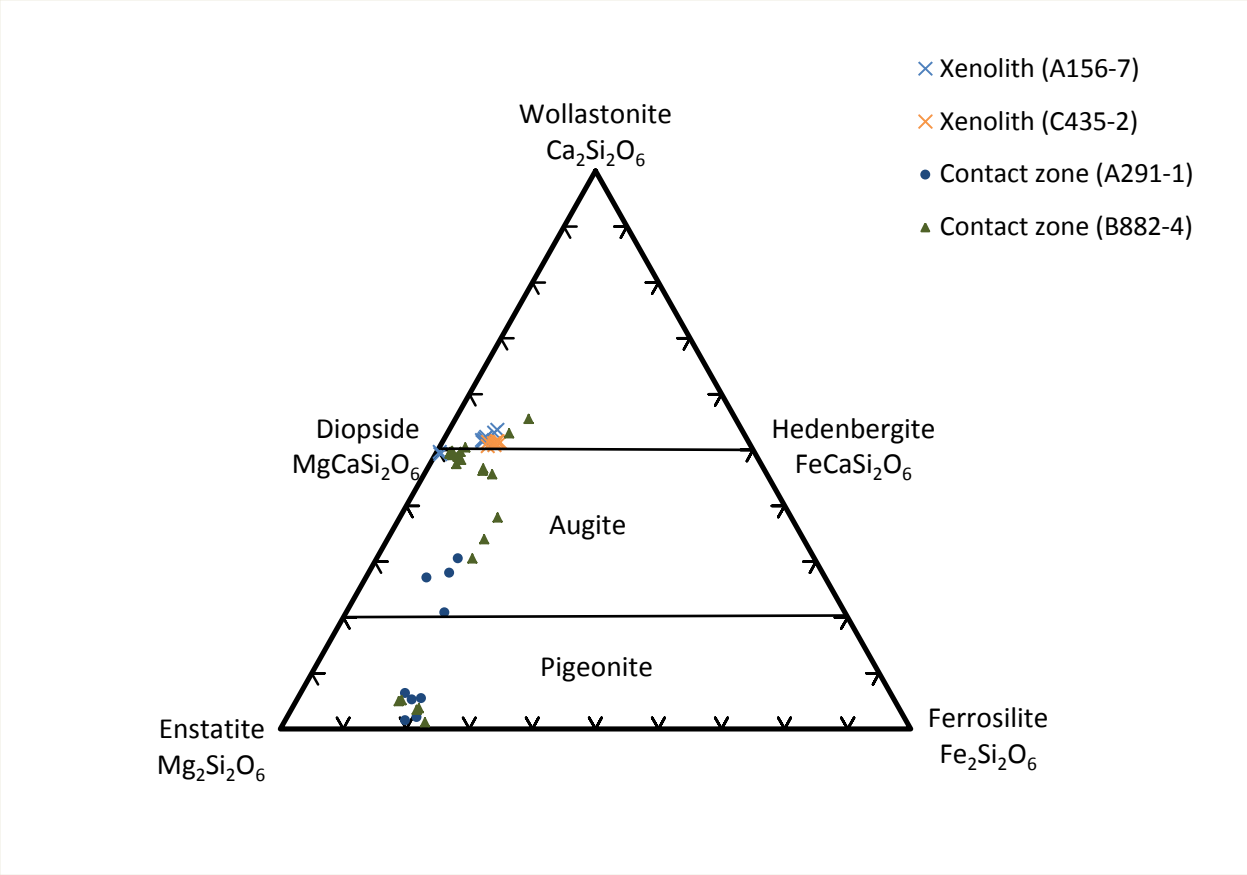

Figure: 4.44: Ternary plot for pyroxene endmembers wollastonite, enstatite and ferrosilite, showing analyses for all pyroxene from the Zwartfontein sample suite.

Both clinopyroxene and orthopyroxene are evident in sample A291-1 from the contact zone. Clinopyroxene contains 0.1–0.4 apfu Al with a compositional range of Wo_{21}-En_{65}-Fs_{14} to Wo_{31}-En_{63}-Fs_{6}. It is significantly less calcic than the Al-diopside in the xenolith and can be considered as Al-rich augite. The composition of orthopyroxene shows a variation from Wo_{2}-En_{81}-Fs_{17} to Wo_{6}-En_{76}-Fs_{19} and is termed enstatite. It contains ~0.06 Al apfu. In sample B882-4, clinopyroxene compositions range from Wo_{46}-En_{45}-Fs_{11} to Wo_{50}-En_{48}-Fs_{2}, with Al ranging from 0.03 apfu to 0.12 apfu. The Al content is higher in diopside and augite associated with orthopyroxene, whereas in the zone where only diopside is present, the Al content is lower. Al-rich augite is present and found only in zones where orthopyroxene occurs. Augite shows a compositional variation of Wo_{31}-En_{54}-Fs_{15} to Wo_{38}-En_{37}-Fs_{16}, with Al ranging from 0.10 apfu to

0.22 apfu. The orthopyroxene exhibits a compositional range between Wo_1-En_{76}-Fs_{22} to Wo_5-En_{79}-Fs_{16}.

Variations in cation proportions with X_{Mg} [X_{Mg} = Mg / (Mg + Fe_T)] for all clinopyroxenes are illustrated in Figures 4.45 A–C. Al-diopside in xenoliths A156-7 and C435-2 shows a slight variation in X_{Mg} from 0.84 to 0.88 and 0.81 to 0.87, respectively. In the contact zone, clinopyroxene has a greater range in X_{Mg}. Sample A291-1 shows variation from 0.80 to 0.87, while sample B882-4 shows a larger range from 0.75 to 0.96. This variation can be attributed to the variable compositional types of clinopyroxene found in this sample; greater X_{Mg} is recorded in the clinopyroxene-rich zone, whereas lower values are observed in clinopyroxene associated with orthopyroxene and plagioclase (Figure 3.23).

The pyroxene Al content in the xenoliths shows smaller ranges than the contact zones. In xenolith A156-7, a range from 0.30 apfu to 0.44 apfu is evident, while xenolith C435-2 exhibits a range from 0.25 apfu to 0.35 apfu. Sample A291-1 from the contact zone shows a greater variation in Al, from 0.09 apfu to 0.36 apfu. The variation in Al content in sample B882-4 is from 0.03 apfu to 0.09 apfu in zones that are clinopyroxene-rich, whereas areas in which orthopyroxene is present show a slightly higher Al content, varying from 0.10 apfu to 0.22 apfu. Fe_T in xenolith A156-7 and xenolith C435-2 shows small ranges from 0.12 apfu to 0.14 apfu, and 0.14 apfu to 0.17 apfu, respectively. From the contact zone, sample A291-1 exhibits a larger variation, from 0.17 apfu to 0.31 apfu. Sample B882-4 shows a similar feature for Fe_T (like X_{Mg} and Al content), where clinopyroxene-rich zones show lower values of 0.04 apfu to 0.09 apfu, and the areas associated with orthopyroxene and plagioclase contain higher Fe_T values, between 0.17 apfu to 0.30 apfu. Ca in clinopyroxene in the xenoliths remains relatively constant at 0.96 apfu to 0.98 apfu, and the contact zone (B882-4) hosts clinopyroxene-rich zones with Ca contents similar to the xenoliths (0.96 apfu to 0.99 apfu). However, clinopyroxene in association with orthopyroxene and plagioclase shows lower Ca contents, between 0.88 apfu to 0.60 apfu.

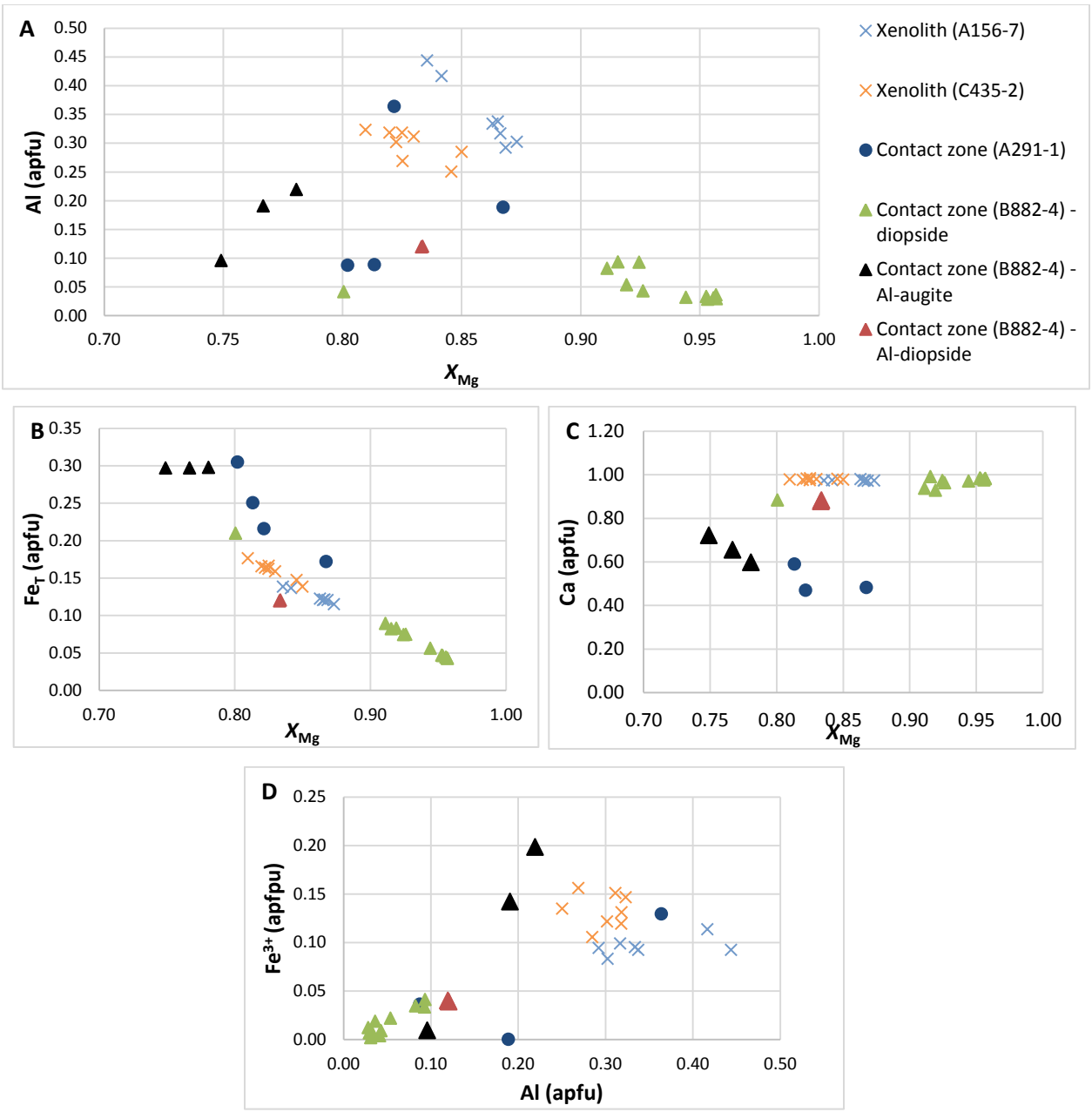

Figure 4.45: Plots depicting cation proportions and X_{Mg} (A–C) and Al vs Fe^{3+} (D), representing all clinopyroxene from the Zwartfontein sample suite.

Table 4. 16: Representative chemical compositions for pyroxene from the Zwartfontein sample suite

Sample	A156-7 (JEOL)	C435-2 (JEOL)	A291-1(JEOL)	A291-1(JEOL)	B882-4 (JEOL)	B882-4 (JEOL)	B882-4 (JEOL)	B882-4 (JEOL)
comment	di	Al-di	Al-aug	opx	opx	di	Al-di	Al-aug
SiO_2	49.01	48.03	51.51	54.61	54.45	53.90	52.10	49.57
TiO_2	0.46	0.17	0.52	0.25	0.08	0.06	0.18	0.11
Al_2O_3	6.50	6.80	4.16	1.39	1.64	1.16	2.77	3.81
Cr_2O_3	0.01	0.04	0.38	0.32	0.41	0.10	0.83	0.27
FeO	3.22	5.17	7.69	12.69	12.58	2.44	5.49	9.48
MnO	0.12	0.05	0.16	0.25	0.29	0.22	0.17	0.30
MgO	14.74	14.00	20.30	28.49	28.28	17.14	15.40	17.43
CaO	24.54	24.68	12.36	1.99	1.99	24.67	22.30	16.38
Na_2O	0.04	0.02	0.77	0.03	0.03	0.05	0.44	0.27
Total	98.64	98.97	97.84	100.03	99.73	99.74	99.67	97.62
				Number of ions based on 6 Oxygens				
Si	1.81	1.78	1.90	1.95	1.95	1.97	1.92	1.86
Ti	0.01	bdl	0.01	0.01	bdl	bdl	bdl	bdl
Al	0.29	0.30	0.18	0.06	0.07	0.05	0.12	0.17
Fe^{3+}	0.07	0.13	0.05	0.03	0.02	0.02	0.04	0.12
Cr^{3+}	bdl	bdl	0.01	0.01	0.01	bdl	0.02	0.01
Fe^{2+}	0.03	0.03	0.19	0.35	0.35	0.06	0.13	0.18
Mn	bdl	bdl	bdl	0.01	0.01	0.01	0.01	0.01
Mg	0.81	0.77	1.11	1.51	1.51	0.93	0.85	0.98
Ca	0.97	0.98	0.49	0.08	0.08	0.96	0.88	0.66
Na	bdl	bdl	0.06	bdl	bdl	bdl	0.03	0.02
Total	4.00	4.00	4.00	4.00	4.00	4.00	4.00	4.00
Wo	53.85	55.04	27.43	3.93	3.93	49.33	47.44	36.24
En	44.71	43.45	62.40	77.97	77.82	47.67	45.57	53.92
Fs	1.44	1.51	10.16	18.10	18.25	3.00	6.99	9.84
Total	100.00	100.00	100.00	100.00	100.00	100.00	100.00	100.00

4.4.6 Feldspar

As in the Western Limb, all feldspars analysed are Ca-rich, therefore only plagioclase feldspars are of interest. Plagioclase is found only in the contact zones, predominantly associated with pyroxene. Representative plagioclase analyses are shown in Table 4.17. Chemical data indicate that plagioclase in sample A291-1 is labradorite (Figure 4.43); however, samples show slight reverse compositional zoning from cores (An_{56-66}) to rims (An_{67}). Al constitutes ~1.53 apfu, Ca ~0.57 apfu and Na ~0.38 apfu, while towards the rims Al comprises ~1.61 apfu, Ca ~0.65 apfu and Na ~0.31 apfu, with the exception of one rim which shows An_{44}). Plagioclase in sample B882-4 is bytownite (An_{70-72}; Al comprises ~1.66 apfu, Ca ~0.70 apfu and Na ~0.27 apfu) and shows a composition range from An_{70}-Ab_{29}-Or_1 to An_{72}-Ab_{26}-Or_2. The relationship between Si, Al and Ca is shown in Figure 4.47.

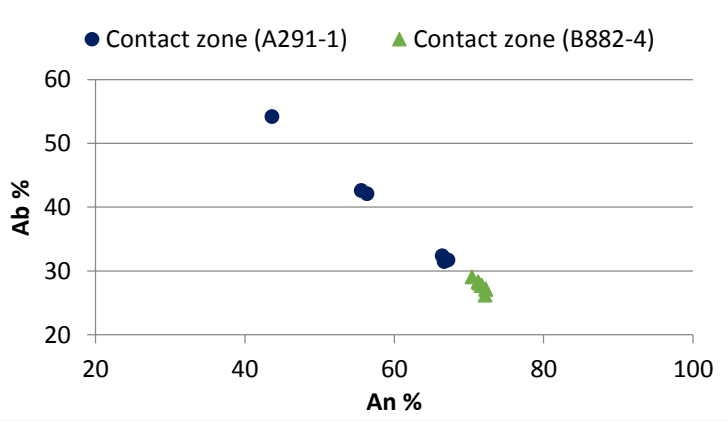

Figure: 4.46: Plot for depicting anorthite and albite proportions for plagioclase from the contact zones in samples A291-1 (borehole ZF 116) and B882-4 (borehole ZF 116 ED1) from the Zwartfontein sample suite.

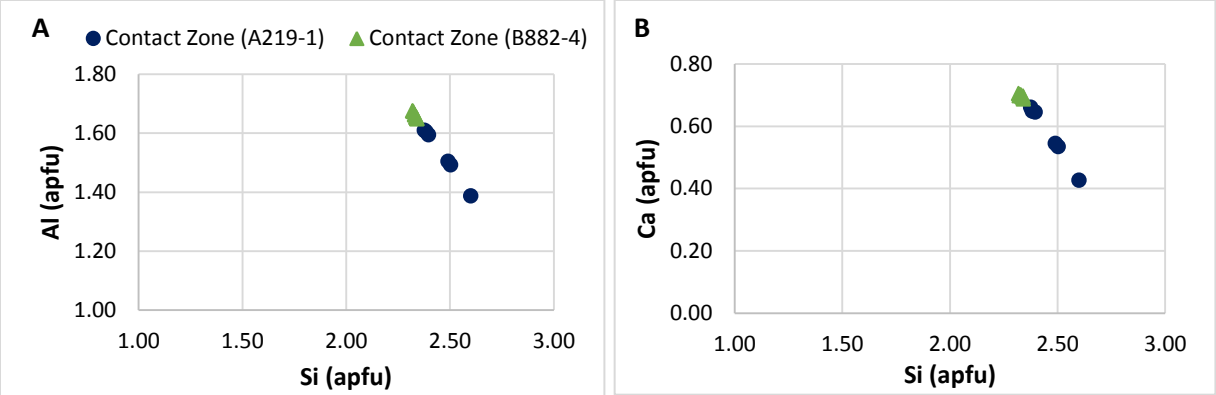

Figure 4.47: Cation-cation correlation diagrams between (A) Si vs Al and (B) Si vs Ca for plagioclase found in samples A291-1 (borehole ZF 116) and B882-4 (borehole ZF 116 ED1) from the Zwartfontein sample suite.

Table 4. 17: Representative chemical compositions of plagioclase from the Zwartfontein sample suite

Sample	B882-4 (JEOL)	A291-1(JEOL)	A291-1(JEOL)
comment		core	rim
SiO_2	51.30	55.18	54.89
Al_2O_3	30.38	29.08	29.09
FeO	0.32	0.17	0.27
CaO	15.61	12.01	12.06
Na_2O	2.75	4.35	4.42
K_2O	0.11	0.26	0.29
Total	100.47	101.06	101.04
Number of ions based on 8 Oxygens			
Si	2.33	2.46	2.45
Al	1.62	1.53	1.53
Fe	0.01	0.01	0.01
Ca	0.76	0.57	0.58
Na	0.24	0.38	0.38
K	0.01	0.01	0.02
Total	4.98	4.96	4.97
Ab	24.65	39.02	39.14
An	74.71	59.46	59.17
Or	0.64	1.52	1.69
Total	100.00	100.00	100.00

4.4.7 Spinel

Spinel is found in only one xenolith (A156-7), and its composition is not as variable as in those found in the Western Limb. Representative analyses of spinel are shown in Table 4.18. Spinel is zoned; however, the range in composition from core to rim is too small to be presented on a ternary diagram, given that all spinel plot in the same compositional space. Three grains were analysed from core to rim (Figure 4.48). Grain 1 shows Mg contents that remain relatively constant, at 0.90 apfu, with a slight decrease towards the rim (0.89 apfu), but Al and Fe^{2+} increase towards the rim from 1.84 apfu to 1.87 apfu, and 0.08 apfu to 0.10 apfu, respectively, and Fe^{3+} decreases from core to rim, from 0.18 apfu to 0.16 apfu. In Grain 2, Mg decreases from core to rim (0.89 apfu to 0.87 apfu), Al and Fe^{2+} increase towards the rim from 1.82 apfu to 1.86 apfu, and 0.10 apfu to 0.12 apfu, respectively, while Fe^{3+} decreases from 0.17 apfu to 0.14 apfu towards the rim. Grain 3 shows the same trends: Mg and Fe^{3+} decrease from core to rim from 0.92 apfu to 0.89 apfu, and 0.15 apfu to 0.14 apfu, respectively. Fe^{2+} and Al increase from core to rim from 1.83 apfu to 1.86 apfu, and 0.07 apfu to 0.09 apfu, respectively.

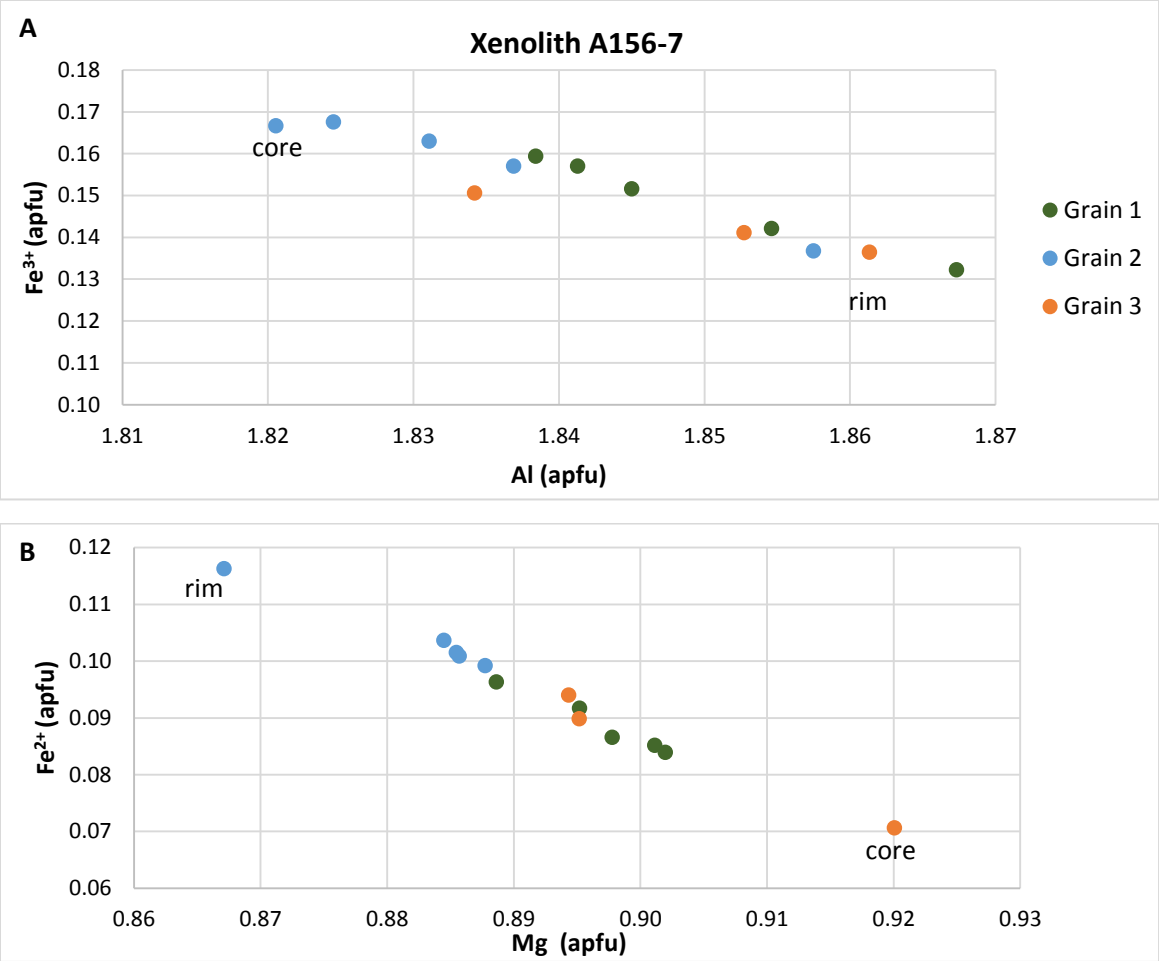

Figure 4.48: Plots showing the variation in cation proportion, Al vs Fe^{3+} (A) and Mg vs Fe^{2+} (B) for spinel grains from core to rim in xenolith A156-7 (borehole ZF 116) from the Zwartfontein xenolith.

Table 4. 18: Representative chemical compositions for spinel in xenolith A156-7 from the Zwartfontein xenolith

Sample A156-7 (JEOL)							
Comment	Grain 1			Grain 2		Grain 3	
	core	inter	rim	core	rim	core	rim
SiO_2	0.03	0.02	bdl	0.03	0.04	0.24	0.04
TiO_2	0.01	0.03	0.01	0.18	0.09	0.06	0.04
Al_2O_3	61.23	61.52	61.80	60.13	60.51	61.74	61.93
Cr_2O_3	0.01	0.05	0.01	0.09	0.03	0.05	0.04
V_2O_3	bdl	bdl	bdl	bdl	bdl	bdl	bdl
Fe_2O_3	8.24	7.65	6.85	8.64	7.83	7.94	7.25
FeO	4.00	4.15	4.49	4.77	4.88	3.35	4.32
MnO	0.70	0.67	0.70	0.77	0.74	0.71	0.69
MgO	23.69	23.62	23.26	23.09	22.87	24.49	23.60
CaO	0.02	bdl	bdl	bdl	0.02	0.04	0.01
NiO	0.01	0.01	bdl	bdl	0.02	bdl	0.01
Total	97.93	97.71	97.13	97.69	97.03	98.62	97.91
Number of ions based on 4 Oxygens							
Si	bdl	bdl	bdl	bdl	bdl	0.01	bdl
Ti	bdl	bdl	bdl	bdl	bdl	bdl	bdl
Al	1.84	1.85	1.87	1.82	1.84	1.83	1.86
Cr	bdl	bdl	bdl	bdl	bdl	bdl	bdl
V^{3+}	bdl	bdl	bdl	bdl	bdl	bdl	bdl
Fe^{3+}	0.16	0.15	0.13	0.17	0.15	0.15	0.14
Fe^{2+}	0.09	0.09	0.10	0.10	0.11	0.07	0.09
Mn	0.02	0.01	0.02	0.02	0.02	0.02	0.01
Mg	0.90	0.90	0.89	0.88	0.88	0.92	0.89
Ca	bdl	bdl	bdl	bdl	bdl	bdl	bdl
Ni	bdl	bdl	bdl	bdl	bdl	bdl	bdl
Total	3.00	3.00	3.00	3.00	3.00	3.00	3.00

4.4.8 Summary

The variation in major mineral chemistry between the Marikana and Zwartfontein sample suites is shown in Table 4.19. Based on the chemical data from the Zwartfontein sample suite it is evident that chemical heterogeneity between samples and within individual samples is less pronounced when compared to the Marikana sample suite. Xenolith A156-7 (Zwartfontein) comprises monticellite with X_{Mg} ~0.89 whereas in the Marikana xenolith X_{Mg} varies from 0.95 to

0.88, with lowest values observed in the pegmatoidal band. Forsterite in Xenolith A156-7 (Zwartfontein) shows X_{Mg}=0.95, whereas in the Marikana xenolith exhibits overall higher X_{Mg} (0.98–0.95), with the lower values observed in the forsterite-monticellite layer. The widespread serpentine in Zwartfontein samples appears to be chrysotile when compared with Deer *et al*. (1989). All orthopyroxene in Zwartfontein is enstatite which is the same for the Marikana sample suite. Clinopyroxene in Zwartfontein exhibits chemical heterogeneity on a sample to sample basis; in the xenoliths (A156-7 and C435-2) clinopyroxene is Al, Fe^{3+} and Ca-rich and considered as CaTs clinopyroxene. In contact zone sample A219 it is augitic with elevated Al concentrations. In contact zone B882-4 Al-rich diopside and augite are present. While the clinopyroxene in the Zwartfontein shows elevated Al concentrations (≤0.44), the CaTs clinopyroxene in the Marikana contact zone shows higher concentrations (0.59–0.77). Plagioclase in the Zwartfontein case is predominately calcic ($An_{60–70}$), with a slight core-to-rim increase in A219, whereas the Marikana sample suite comprises plagioclase with highly variable, and more calcic, compositions (An_{99-60}). Spinel is only found in xenolith A156-7 in Zwartfontein where it exhibits weak core-to-rim chemical heterogeneity and lacks Cr, whereas in the Marikana sample suite spinel is found in all samples and shows highly variable composition both between samples and via internal zoning and exsolution textures. Spinel cores and grains in samples distal to the xenolith are Cr-rich, comparable with UG1 chromite compositions; rims and grains in proximal samples are more aluminous.

Table 4. 19: Summary of major minerals chemistry in the Marikana and Zwartfontein sample suites.

Sample/ Mineral	Marikana						Zwartfontein	
		Contact zone			Igneous rock			
	Xenolith	Forsterite-spinel layer, spinel layer and forsterite-monticellite layer	Calc-silicate rock fragment and surrounding matrix	Chromitite stringer	Mottled Anorthosite	UG1	Xenolith	Contact zone
Monticellite	Mg#=0.93-0.94	Mg#=0.88-0.92					Mg#=0.89	
Forsterite	Mg#=0.97-0.98	Mg#=0.95-0.98					Mg#=0.95	
Pyroxene			Ca=0.99-1.02 Mg=0.47-0.65 Fe^{2+}=bdl-0.07 Fe^{3+}=0.09-0.22 Al=0.60-0.77	**Proximal** Ca=0.98-0.99 Mg=0.48-0.59 Fe^{2+}=0.04-0.07 Fe^{3+}=0.12-0.15 Al=0.62-0.73 **Intermediate** Ca=0.93-0.98 Mg=0.71-0.85 Fe^{2+}=0.11-0.20 Fe^{3+}=bdl-0.04 Al=0.09-0.18 **Distal** Ca=0.87-0.91 Mg=0.84-0.89 Fe^{2+}=0.12-0.16 Fe^{3+}=bdl-0.02 Al=0.08-0.10	Ca=0.82-0.87 Mg=0.78-0.84 Fe^{2+}=0.21-0.33 Fe^{3+}=bdl-0.03 Al=0.03-0.06		Ca=0.97-0.98 Mg=0.70-0.81 Fe^{2+}=0.01-0.05 Fe^{3+}=0.08-0.15 Al=0.25-0.44	Ca=0.47-0.99 Mg=0.84-1.24 Fe^{2+}=0.03-0.27 Fe^{3+}=bdl-0.20 Al=0.04-0.36
Plagioclase			Ca=0.99-1.06 Na=bdl-0.01 K=bdl		Ca=0.92-0.97 Na=0.02-0.05 K=bdl	Ca=0.58-0.79 Na=0.19-0.36 K=0.01-0.02	Ca=0.64-0.79 Na=0.17-0.32 K=0.01	Ca=0.64-0.74 Na=0.25-0.32 K=0.01		Ca=0.43-0.70 Na=0.27-0.53 K=bdl-0.02
Spinel	Mg=0.65-0.96 Fe^{2+}=0.05-0.42 Fe^{3+}=0.23-1.58 Al=0.15-1.79 Cr=0.01-0.03	Mg=0.63-0.95 Fe^{2+}=0.04-0.44 Fe^{3+}=0.14-1.62 Al=0.17-1.85 Cr=bdl-0.04	Mg=0.50-0.72 Fe^{2+}=0.27-0.51 Fe^{3+}=0.17-0.30 Al=0.80-1.40 Cr=0.43-0.87	Mg=0.41-0.48 Fe^{2+}=0.49-0.52 Fe^{3+}=0.20-0.22 Al=0.75-1.02 Cr=0.77-1.04	Mg=0.28-0.34 Fe^{2+}= 0.67-0.71 Fe^{3+}=0.18-0.22 Al=0.70-0.79 Cr=0.94-1.08	Mg=0.29-0.31 Fe^{2+}=0.68-0.71 Fe^{3+}=0.17-0.19 Al=0.72-0.79 C=1.01-1.08		Mg=0.33-0.34 Fe^{2+}=0.68-0.70 Fe^{3+}=0.20-0.24 Al=0.51-0.59 Cr=1.13-1.17	Mg=0.87-0.90 Fe^{2+}=0.07-0.10 Fe^{3+}=0.13-0.17 Al=1.82-1.87 Cr=bdl	

CHAPTER 5: TRACE ELEMENTS IN SPINEL GROUP MINERALS

5.1 Introduction

Trace elements in spinel group minerals were analysed from the Marikana xenolith using laser ablation inductively coupled plasma mass spectrometry (LA-CP-MS) with the aim of determining the variation in trace element concentration in these spinels from the various zones (xenolith and contact zone) for comparison with spinels from the UG 1 chromitite. This was done in order to determine the possible origin of spinels (magmatic or metamorphic or hybrid) and the role the interaction between the xenolith and magma played in the crystallisation of the different spinels. The different spinels analysed are summarised in Table 5.1. The variation in trace element concentrations is much larger than in the major elements as trace-elements are more sensitive to processes than the major elements (White 2013). The following elements were measured: P, Sc, V, Cr, Mn, Co, Ni, Cu, Zn, Ga, Ge, Sr, Y, Zr, Nb, Ru, Sn, Hf, Ta, W and Pb. Of these 21 elements not all were detected in every sample (Table 5.1). Elements analysed, predominantly transition metals, were selected to explore their geochemical behaviour across the sample suite, from xenolith body through contact zone and the UG1 chromitite. Ru, a platinum group element (PGE) was analysed because it is the only PGE that occurs in relatively higher concentrations in chromite compared to other PGEs (Pagé and Barnes, 2016). Lanthanides/REE's were not considered as they have not been detected in chromite in previous studies (Maier and Barnes, 1998). Results of the LA-ICP-MS analysis show that samples can be categorised into two groups comparable with the main xenolithic body or the UG 1 chromitite endmember samples, with one sample found in the contact zone that shows trace element concentrations comparable with both endmembers. No analyses were done for Northern Limb samples, given that a sufficient amount of spinel was not identified throughout the sample suite.

5.2 Previous LA-ICP-MS studies on trace elements in spinels

The crystal structure of spinel is considered stable under low temperatures and pressures (Morton, 1991). However, with increasing temperature and pressure, the structure of spinel can become unstable, especially in mafic/ultramafic rocks and can result in alteration of the structure and chemistry (Buddington and Lindsley, 1964 and Maier and Barnes, 1996). The

spinel structure can easily accommodate trivalent ions with radii between 0.5 Å and 0.7 Å (Hiroshi *et al*., 1980). A study of REEs in minerals found in the Lower, Critical and Main Zones of the RLS (Maier and Barners, 1998) shows that no REEs were detected in chromite. However, according to Hiroshi *et al*. (1980) only REEs with ionic radii between 0.861 Å and 1.045 Å are too large to be favoured in the spinel structure.

Magnetite is considered an important mineral used as a provenance indicator based on its trace element concentration and given that it is commonly found in various depositional environments (Dare *et al.*, 2014 and Duparc *et al*., 2016). Dare *et al*. (2014) studied trace elements in magnetite from various magmatic and hydrothermal ore-forming environments, since magnetite forms under a variety of conditions that include high-temperature crystallisation from sulphide or silicate melts, or low temperature precipitation from hydrothermal fluids. This can result in unique trace elemental signatures as a large number of minor and trace elements can substitute into the magnetite crystal structure (Dare *et al*., 2014). A notable difference between magmatic and hydrothermal magnetite is the behaviour of Ca and Si that are commonly absent in magmatic magnetite, but enriched in some hydrothermal samples. The behaviour of Ni and Cr is considered important as the Ni/Cr ratio is ≤ 1 in magnetite from silicate magmas, and hydrothermal magnetite commonly shows Ni/Cr ratios ≥ 1 (Dare *et al*., 2014). Maier and Barnes (1996) noted that the metamorphism of magnetite in the amphibolite facies resulted in a significant increase in wt% of Ti, V, Cr and Zn in mafic environments.

Chromite is a powerful petrogenetic tool (Irvine, 1965; Rollinson, 2008; Mukherjee 2010), given that processes associated with mantle melting control its chemical composition that is typical of particular tectonic settings (Mukherjee, 2015). Experimental studies (Nielsen *et al*., 1994; Righter *et al*., 2004; Wijbrans *et al*., 2015) indicate that the partitioning of minor and trace elements between chromite and melt is sensitive to oxygen fugacity, temperature and pressure. Sub-solidus fluid-rock interaction affects major, minor and trace element signatures of the primary magmatic chromite (Colás *et al*., 2014; González-Jiménez *et al*., 2015; Mukherjee *et al*., 2015). Fluid-rock interactions can result in; (1) crystallisation of hydrous phases, (2) enrichment of Cr and Fe^{3+} in chromite and (3) change in oxygen fugacity (Evans and Frost 1975; Barnes and Roeder 2001). Therefore, it is difficult to pinpoint which

process is ultimately responsible for altering trace element signatures in magmatic chromite (Colás *et al*., 2014; González-Jiménez *et al*., 2015).

Chromite found in massive unaltered chromitites maintain their original major element compositions, while in metamorphic settings changes in minor and trace element compositions are common (Evans and Frost, 1975; González-Jiménez *et al*., 2013; Colás *et al*., 2014). Often metamorphism causes primary chromite to become chemically zoned with a core enriched in FeO and Cr_2O_3, and depleted in MgO and Al_2O_3, with rims that are enriched in Fe_2O_3 (Evans and Frost, 1975; Barnes, 2000).

Mukherjee *et al*. (2015) investigated the chromite found in mafic/ultramafic rocks in the Nuggihalli greenstone belt and considered both unaltered and altered grains with the aim of comparing trace element concentration of primary magmatic grains versus grains that underwent secondary alteration. Mukherjee *et al*. (2015) noted that variability in trace element concentration at this locality can be caused by; (1) the re-equilibration of chromite with surrounding silicate minerals or interstitial melt (Rollinson, 1995), (2) serpentinisation and metamorphism of the host rock that results in oxidation (Evans and Frost, 1975) and (3) reducing fluids circulating during retrograde metamorphism (González-Jiménez *et al*. 2013). Mukherjee *et al*. (2015) found that unaltered chromite show no variation in trace element concentration. However, altered grains display variation from core to rim, where Zn, Ga, Mn and V decrease towards the rim while Ti and Ni increase in the rim. Altered grains are enriched in Zn, Co, Mn, V and Ga relative to unaltered grains.

Colas *et al*. (2014) studied Ga, Ti, Ni, Zn, Co, Mn, V and Sc in chromite grains of ophiolitic chromitites that underwent stages of metamorphism from high pressure eclogite to amphibolite facies that produced various types of altered chromite. Compared to unmetamorphosed chromite grains the partly altered chromite cores display enrichment in Zn, Co and Mn, and depletion in Ga, Ni and Sc. The altered non-porous crystals are enriched in Ti, Ni, Zn, Co, Mn and Sc and depleted in Ga and suggests that fluids associated with retrogression have altered the original magmatic signature (Proenza *et al*., 2004; Mukherjee *et al*., 2010; Colas *et al*., 2014). The core of zoned chromites are enriched in Zn, Co, and Mn and depleted in Ga, Ni and Sc, this correlates with a decrease in Mg# and Al towards the

rims, and Colas *et al*. (2014) proposed that this trace element signature can be used as a fingerprint to identify amphibolite facies metamorphism in chromites. Colas *et al*. (2014) concluded that metamorphism can seriously alter the primary magmatic signature of minor and trace elements in chromite, even in the cores of grains that show no textural evidence of alteration.

The chromitite grains found in the Eastern Pampean Ranges of Córdoba, Argentina (studied by Colas *et al*. (2016)) contain exsolution lamellae that range in composition from spinel *sensu stricto* to magnetite in composition. Colas *et al*. (2016) constrained the crystal-crystal partition co-efficient between spinel-rich and magnetite-rich phases in chromite; trace elements listed in increasing order of compatibility with the spinel phases are Ti, Sc, Ni, V, Ge, Mn, Cu, Sn, Co, Ga and Zn. There is preferential partitioning of Ti and Sc into the magnetite phase and this agrees with high-temperature chromite/melt experiments (Wijbrans *et al*., 2015; Colas *et al*., 2016).

Table 5. 1: Summary of the different spinels found in the Marikana sample suite and trace elements detected in each sample

Sample name		Sample description	Mineral assemblage	Spinel group	Spinel texture	Elements detected
Xenolith	RSTX26-12	Main xenolith body	Fo + Mtc + Spl	Spinel s.s Magnetite	Exsolution	P, Sc, V, Cr, Mn, Co, Ni, Zn, Ga,Zr,Sn,Nb, Ta,Pb,Hf
	RSTX26-04	Pegmatoidal patch	Mtc + Spl+ Cal	Spinel s.s	Exsolution Zoned	P, Sc, V, Cr, Mn, Co, Ni, Zn, Ga,Zr, Sn,Pb,Hf
Western contact of xenolith	RSTX26-06	Spinel layer	Spl	Spinel s.s Magnetite	Exsolution	P, Sc, V, Cr, Mn, Co, Ni, Zn, Ga,Zr,Sn,Nb, Ta,Hf, Ge, Y
Contact zone	RSTX26-52	Fragment	Di + Grt + Spl + Ves + Mtc	Cr-rich	Zoned	P, Sc, V, Cr, Mn, Co, Ni, Zn, Ga,Zr,Sn,Nb,Ta, Pb, Hf, Ge, Y
	RSTX26-61	Chromitite stringer proximal to xenolith	Di + Grt + Spl	Chromite	Zoned	P, Sc, V, Cr
	RSTX26-63	Chromitite stringer distal to xenolith	Pl + Di + Grt + Spl	Chromite	Homogenous	P, Sc, V, Cr
Igneous rock	RSTX26-UG1	UG 1 chromitite 20 m away from the main xenolithic body	Pl + Spl	Chromite	Homogenous	P, Sc, V, Cr

5.3 Methodology

Trace elements in spinel group minerals were measured using LA-ICP-MS and conducted at the Earthlab at the University of the Witwatersrand, employing an Australian Scientific Instruments (ASI) Resonetics Resolution 193 nm ArF excimer (SE 155) system coupled to a Thermo Scientific Fisher sector-field IC-PMS (Element XR). Measurements were performed in low resolution and electrostatic scanning (E-scan) modes. Data were acquired by single spot analysis (38 μm), using a laser repetition rate of 8 Hz and a fluence of 2.5 Jcm^{-2}. Total signal acquisition time was 60 sec to allow data processing and preparation for the next analysis, comprising 20 seconds of pre-ablation and 10 seconds post-ablation (gas blank) and 30 seconds of ablation measurements. Laser sampling took place in a SE155 dual-

volume ablation cell (Laurin Technic, Canberra, Australia) using a mixed He-Ar atmosphere and a small volume of N_2 to enhance signal stability and sensitivity. The following gas flows were applied: He (300-400 ml/min), Ar (800-1200 ml/min) and N_2 (2-6 ml/min), respectively. Synthetic glass NIST 612 (Jochum *et al*., 2011) served for calibration, USGS natural glasses BC28 and BIR-1 (Gao *et al*., 2002) were analysed as unknowns to evaluate accuracy and precision (shown in Appendix 5). The LA-ICP-MS system was tuned during line scans using NIST 612 glass for maximum sensitivity for ^{6}Li, ^{115}In and ^{238}In, while maintaining oxide levels (ThO^{+}/Th) <0.3%. ^{27}Al was used for internal standardization. Typically, two analyses of the primary calibration standard were obtained at the beginning and end of an experiment, and 10-20 analyses of unknowns were followed by analyses of one primary calibration standard and two to four analyses of the secondary standards for quality control purposes. Prior to each spot analysis surface material was removed using 2 laser pulses. The following masses were measured (40 samples per peak): ^{27}Al, ^{31}P, ^{45}Sc, ^{51}V, ^{52}Cr, ^{53}Cr, ^{55}Mn, ^{54}Fe, ^{57}Fe, ^{59}Co, ^{60}Ni, ^{62}Ni, ^{63}Cu, ^{65}Cu, ^{66}Zn, ^{68}Zn, ^{69}Ga, ^{71}Ga, ^{72}Ge, ^{74}Ge, ^{88}Sr, ^{89}Y, ^{90}Zr, ^{94}Zr, ^{93}Nb, ^{101}Ru, ^{116}Sn, ^{118}Sn, ^{178}Hf, ^{181}Ta, ^{182}W and ^{208}Pb. All isotopes were measured in triple mode, including pulse counting, analog and Faraday cup, depending on signal. Data reduction was performed using the iolite extension to the software Igor Pro (Paton *et al*., 2010, 2011) for 7 thin sections containing spinel from the Marikana sample suite (Appendix 5).

5.4 Results

Binary plots (Figure 5.1 A-G) were employed to represent trace element variation between the main xenolithic body through to the UG 1 chromitite layer. Minute amounts of Cr (Figure 5.1B) are found in spinel in the main xenolithic body and range from 15.17 ppm to 145.80 ppm in magnetite lamellae and from 189.70 ppm to 352.00 ppm in host spinel *sensu stricto.* In the pegmatoidal patch Cr ranges from 4.00 ppm to 61bdl ppm. In the spinel layer a slight increase in Cr is observed and varies from 268.00 ppm to 340bdl ppm in magnetite exsolution lamellae and from 691bdl ppm to 1593bdl ppm in host spinel *sensu stricto.* The remaining samples contain significant concentrations of Cr and are addressed in section 4.3.5.

Magnetite exsolution lamellae in the main xenolithic body show ranges between 5.29 ppm and 34.60 ppm for P, 1.27 ppm and 81.80 for Sc, 8.40 ppm and 194.30 ppm for V, 263.00 ppm and 517bdl for Mn, 4.73 ppm to 43.80 ppm for Co, 12.30 ppm and 130.90 for Ni, 6.00 ppm to 110.90 ppm for Ni and 1.60 ppm to 14.12 ppm for Ga. The host spinel shows higher concentrations for all elements analysed and ranges from 63.20 ppm to 113.00 ppm for P, 10.60 ppm to 159.00 ppm for Sc, 67.30 ppm and 475.00 ppm for V, 274bdl ppm and 1480bdl ppm for Mn, 48.90 ppm and 145.00 ppm for Co, 144.80 ppm and 457.00 ppm for Ni, 517.00 ppm and 762.00 ppm for Zn and 59.90 ppm and 89.00 ppm for Ga.

Trace element concentrations in spinel from the pegmatoidal patch are overall similar to the main xenolithic body with minor ranges in Cr (from 4.00 ppm to 61bdl ppm) and Mn (from 2.00 ppm to 65.00 ppm). In the spinel layer, magnetite exsolution lamellae show ranges from 10.20 ppm to 46.30 ppm for P, from 1.90 ppm to 85.90 ppm for Sc, from 8.75 ppm to 208.80 ppm for V, from 306.00 ppm to 668bdl ppm for Mn, from 4.91 ppm to 63.00 ppm for Co, from 7.39 ppm to 118.00 ppm for Ni, from 61.30 ppm to 150.80 ppm for Zn and, from 6.39 ppm to 17.18 ppm for Ga. The host spinel *sensu stricto* contains overall higher concentration for most elements and ranges from 64.20 ppm to 107.50 ppm for P, from 9.37 ppm to 67.10 ppm for Sc, from 71.60 ppm to 285.00 ppm for V, from 231bdl ppm to 653bdl ppm for Mn, from 40.6 ppm to 66.20 ppm for Co, from 98.20 ppm to 22bdl ppm for Ni, from 458.00 ppm to 770 ppm for Zn, and from 57.10 ppm to 73.70 ppm for Ga.

Sample RSTX26-52 from the contact zone shows an overall decrease in trace element concentrations from core to rim and will be addressed later. RSTX26-61 (chromitite proximal to the main xenolithic body) shows slight ranges for P, from 34.80 ppm to 58.30 ppm, from 0.14 ppm to 0.41 for Sc and, from 514.00 ppm to 1332.00 ppm for V. RSTX26-63 (chromitite distal to the main xenolithic body) shows similar variations from 41.60 ppm to 74.00 ppm for P, from 0.16 ppm to 6.29 ppm for Sc, from 2162.00 to 4326.00 ppm for V. Ranges for the UG 1 chromitite layer are from 39.90 ppm to 63.60 ppm for P, from 8.33 ppm to 10.08 ppm for Sc and, from 3328.00 ppm to 354bdl ppm for V.

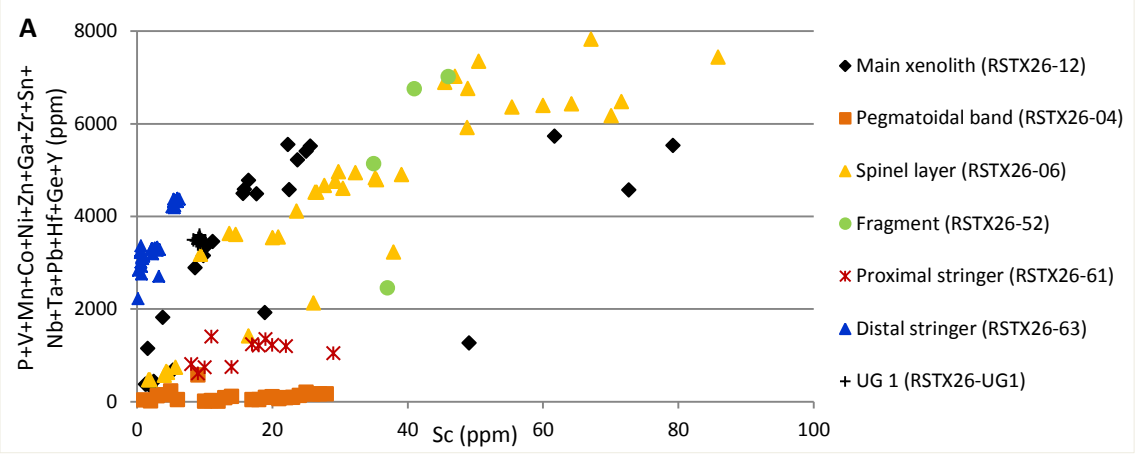
A
P+V+Mn+Co+Ni+Zn+Ga+Zr+Sn+
Nb+Ta+Pb+Hf+Ge+Y (ppm)
8000
6000
4000
2000
0
0
20
40
60
80
100
Sc (ppm)
Main xenolith (RSTX26-12)
Pegmatoidal band (RSTX26-04)
Spinel layer (RSTX26-06)
Fragment (RSTX26-52)
Proximal stringer (RSTX26-61)
Distal stringer (RSTX26-63)
UG 1 (RSTX26-UG1)

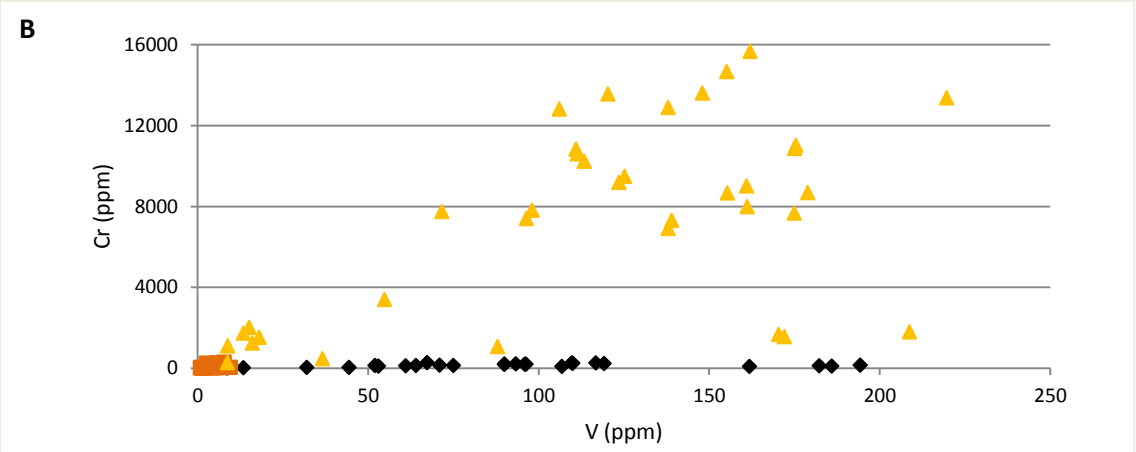
B
16000
12000
8000
4000
0
Cr (ppm)
0
50
100
150
200
250
V (ppm)

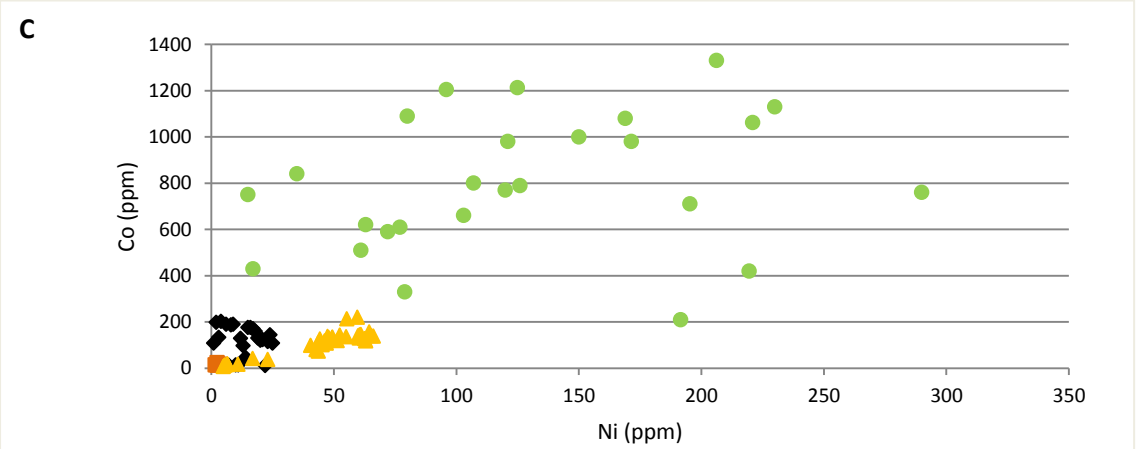
C
1400
1200
1000
800
600
400
200
0
Co (ppm)
0
50
100
150
200
250
300
350
Ni (ppm)

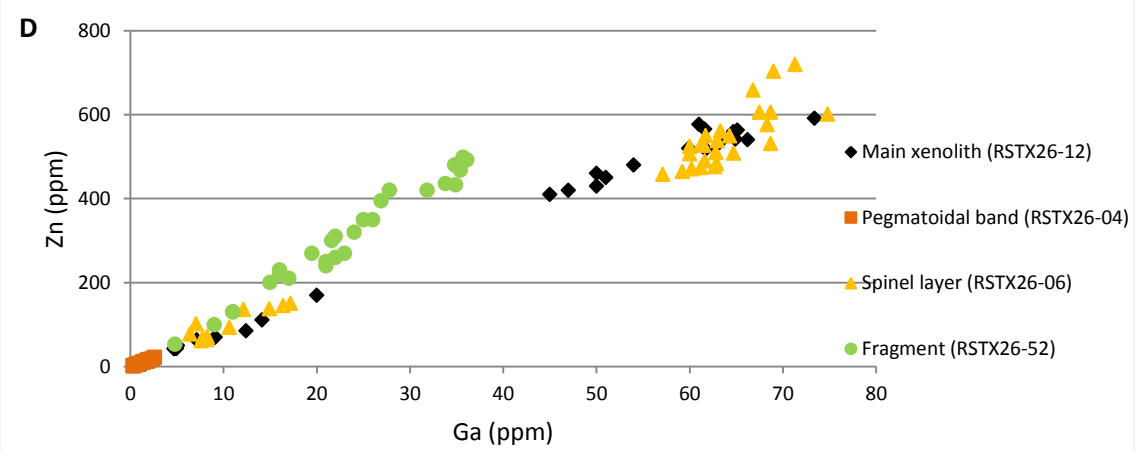
D
800
600
400
200
0
Zn (ppm)
0
10
20
30
40
50
60
70
80
Ga (ppm)
Main xenolith (RSTX26-12)
Pegmatoidal band (RSTX26-04)
Spinel layer (RSTX26-06)
Fragment (RSTX26-52)

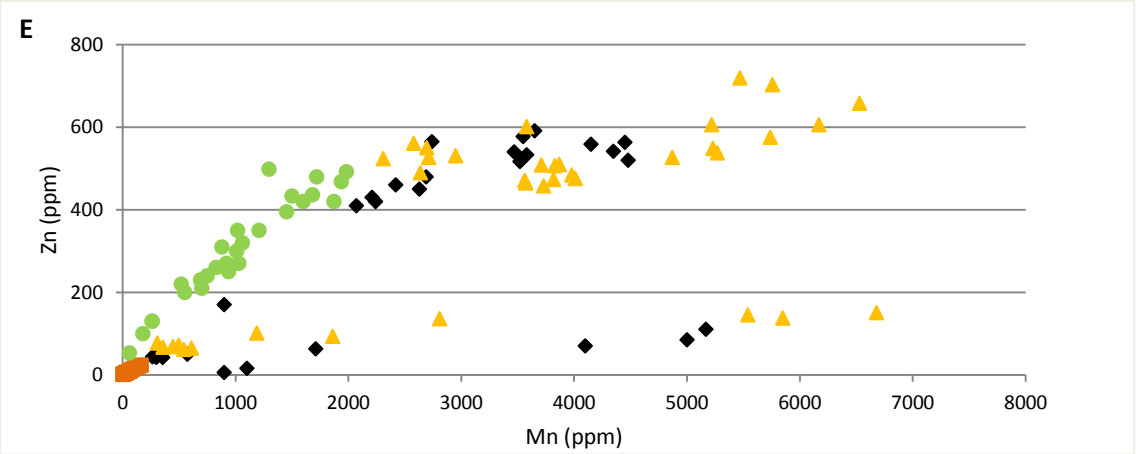
E
800
600
400
200
0
Zn (ppm)
0
1000
2000
3000
4000
5000
6000
7000
8000
Mn (ppm)

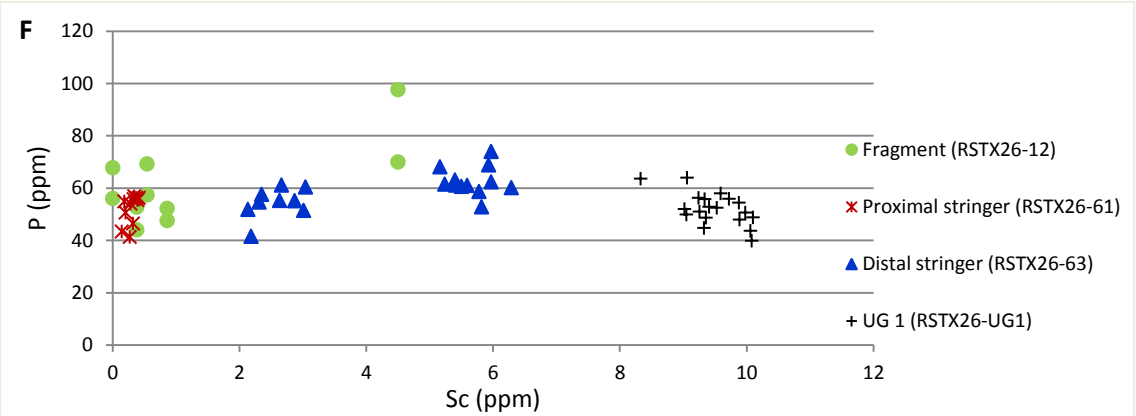
F
120
100
80
60
40
20
0
P (ppm)
0
2
4
6
8
10
12
Sc (ppm)
Fragment (RSTX26-12)
Proximal stringer (RSTX26-61)
Distal stringer (RSTX26-63)
UG 1 (RSTX26-UG1)

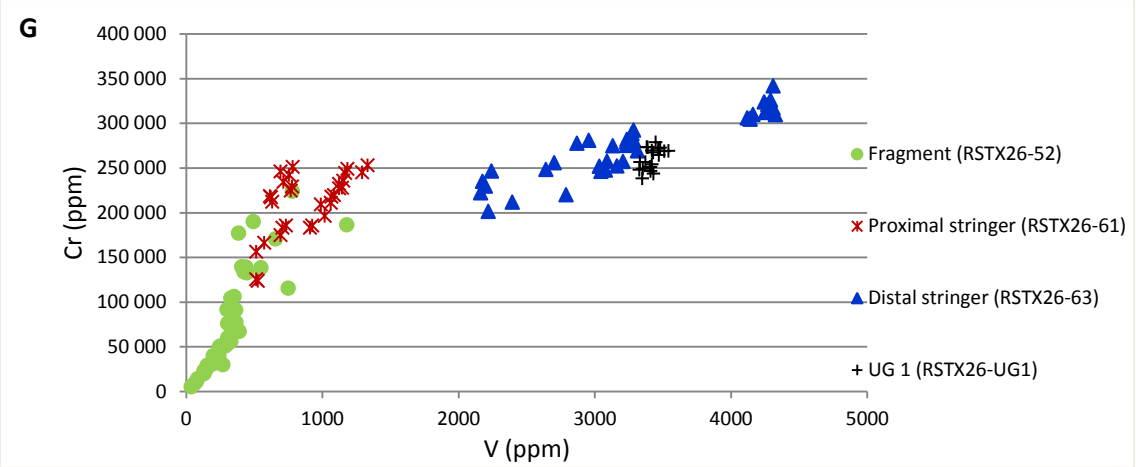

Figure 5.1: Trace element compositional variations in samples from the main xenolithic body through to the UG1 chromitite layer. Variations for Sc versus a sum of the remaining trace elements excluding Cr (A) and Cr, V, Co, Ni, Zn, Ga, Mn, P and Sc (B – G). All figures are shown in terms are of ppm.

In the Figures that follow (Figs 5.2 and 5.3) trace elements were normalized to the two endmember samples (main xenolithic body or UG 1 chromitite) in order to compare the variation in trace element concentration in the contaminated and contact zones with the endmember samples. To illustrate the variation in trace element concentration in the main xenolithic body spinel the average concentration per grain was normalized to the total average concentration of spinel in the main xenolithic body (Figure 5.2). Two compositions of spinel were analysed from the main xenolithic body, namely, host spinel *sensu stricto* and magnetite exsolution lamellae. The exsolution lamellae are depleted in all trace elements analysed compared to spinel *sensu stricto*, with a greater depletion in Sc, Zr and Hf. Spinel *sensu stricto* displays a depletion of Sc, V, Zr, Sn, Hf, ± Mn and ± Co and slight enrichment in P, Cr, Ni, Zn, Ga and Pb. Spinel *sensu stricto* was analysed in the pegmatoidal patch located in the main xenolithic body. This spinel is depleted overall in all elements analysed and shows similar trends compared to the main xenolithic body. Depletion is most prominent in Mn and Zr.

Spinel and magnetite exsolution lamellae were analysed from spinel in the spinel layer (Figure 2.4). The exsolution lamellae are enriched in all elements relative to the main xenolithic body and pegmatoidal patch. It shows depletions of V, Mn, Co, Ni, Zn, Ga and Sn

and enrichment in Cr and ± Zr. Spinel *sensu stricto* shows a slight enrichment in all elements analysed. The Cr concentration for both spinel *sensu stricto* and magnetite exsolution lamellae is anomalous compared to the main xenolithic body. In the contact zone samples containing zoned spinel, with Cr-rich cores and Al-rich rims, were analysed. The spinel shows a greater depletion in Sc compared to all other samples, as well as depletion in Mn, Zn and Ga. However, when compared to other samples it is relatively less depleted in the aforementioned elements. Enrichments occur in Co, Ni, Zn and Cr is anomalously enriched.

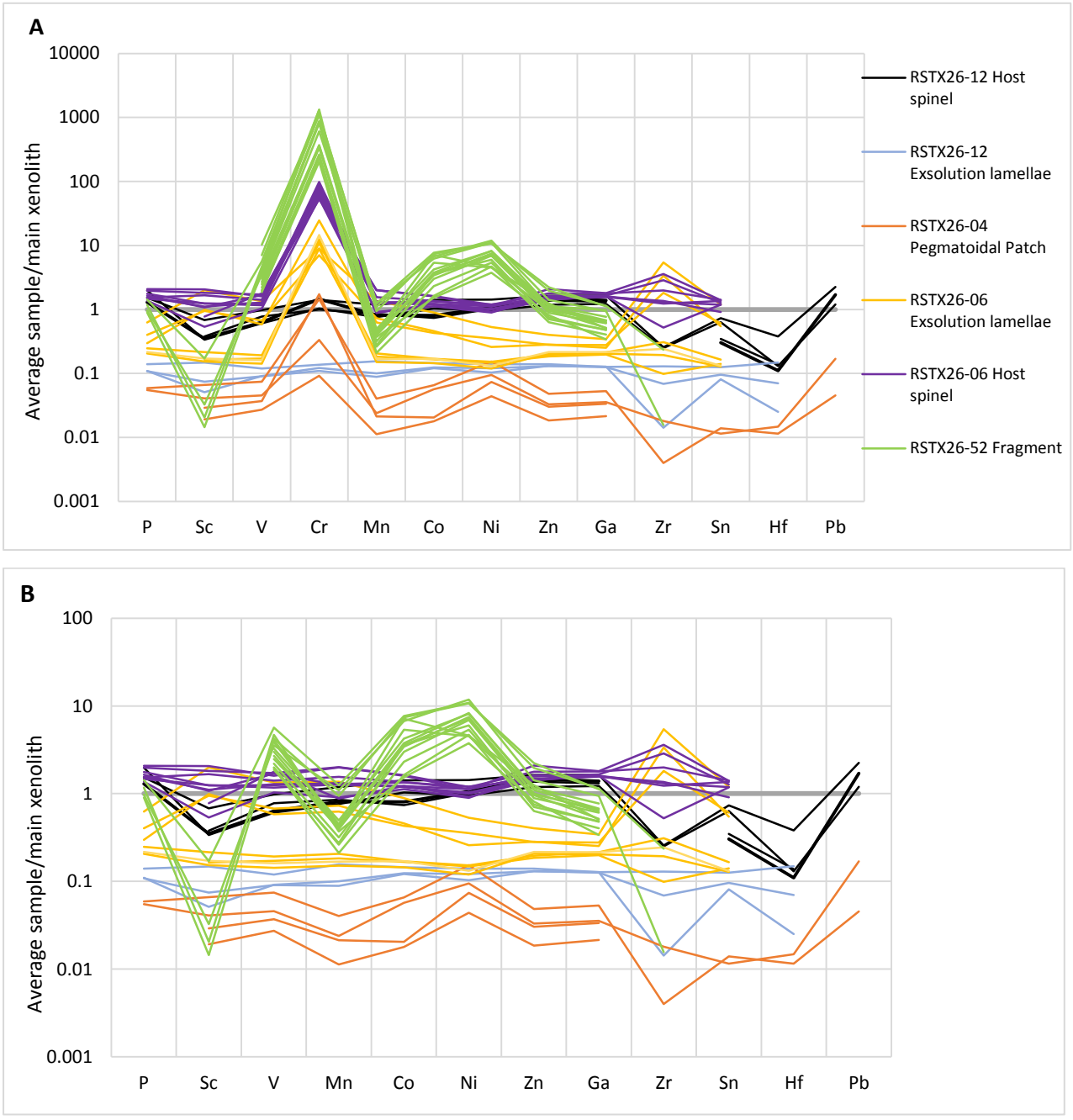

Figure 5.2: Trace element variation diagram for spinel normalized to average main xenolithic body spinel compositions. (A) Showing all relevant trace elements and (B) excluding Cr.

Sample RSTX26-52 from the contact zone containing zoned spinel, with Cr-rich cores and Al-rich rims, together with samples analysed from the proximal and distal chromitite stringers were normalized to the UG 1 chromitite. To illustrate the variation in trace element concentration in the UG 1 chromitite the average concentration per grain was normalized to the total average concentration of the UG 1 chromitite (Figure 5.3). Trace elements

detected in the UG 1 chromitite include, P, Sc, V and Cr and all grains show a similar overall trend, with minor variation in P and Sc. V and Cr concentrations remain consistent through all grains analysed. Sample RSTX26-52 shows depletion in Sc and V when normalized to UG 1 chromitite concentrations. The chromitite stringers, proximal (RSTX26-61) and distal (RSTX26-63) to the xenolith are relatively depleted in Sc and V, while RSTX26-61 shows a greater deal of depletion in Sc. RSTX26-63 shows slight enrichment in Cr compared to UG1 chromite.

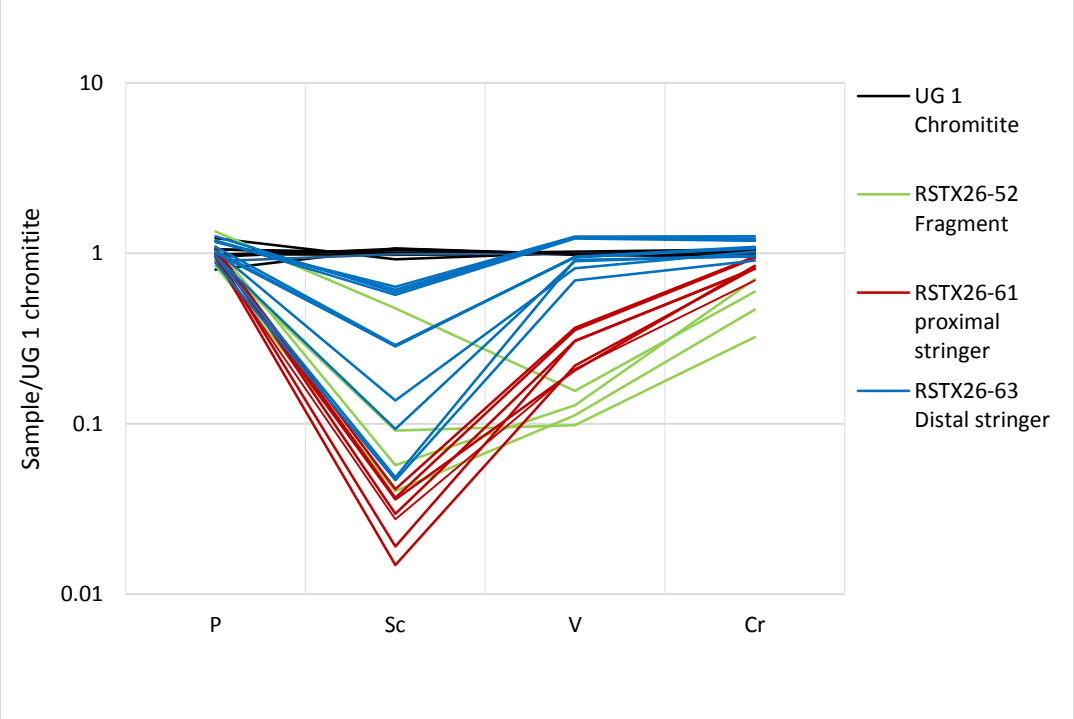

Figure 5.3: Trace element variation diagram for spinel normalized to average UG 1 chromitite compositions.

Spinel analysed in sample RSTX26-52 containing Cr-rich cores and Al-rich rims shows zonation of trace elements. All trace elements detected, namely, V, Mn, Co, Ni, Zn and Ga decrease from core to rim (Figure 5.4). Zoned spinel/chromite is also found in the proximal chromitite stringer, and shows a decrease in P, Sc and V from core to rim. Mn, Co, Ni, Zn and Ga were not detected in this sample.

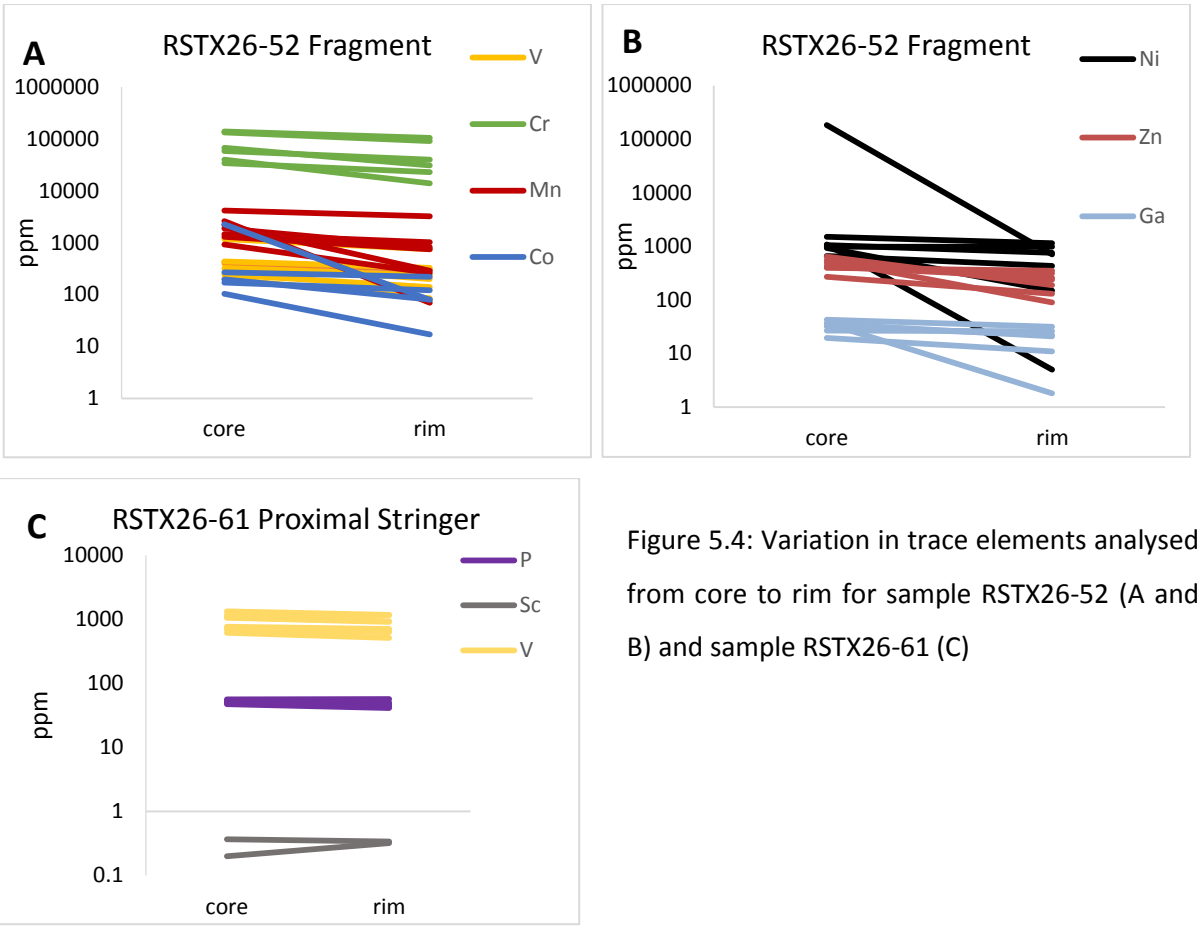

Figure 5.4: Variation in trace elements analysed from core to rim for sample RSTX26-52 (A and B) and sample RSTX26-61 (C)

5.5 Discussion and Summary

The data illustrates that the samples analysed produce trace elemental patterns that can be classified into two groups and affiliated with one endmember, namely the main xenolithic body or the UG 1 chromitite layer. Samples RSTX26-12, RSTX26-04 and RSTX26-06 show patterns that are consistent with the main xenolithic body. RSTX26-61 and RSTX26-63 are consistent with the UG 1 chromitite layer, while RSTX26-52 that located in the contact zone and associated with calc-silicate fragments and Cr-rich spinel shows patterns that are comparable with both the main xenolithic body and UG 1 chromitite layer. As shown in Figure 5.2 Cr is the most significant anomaly that is detected in xenolithic samples. The main xenolithic body has a maximum of 352 ppm Cr detected in spinel *sensu stricto* and lower concentrations in the magnetite exsolution lamellae. Grains analysed from the spinel layer (RSTX26-06) show higher Cr concentrations compared to the main xenolithic body, with a maximum of 15930 ppm detected in spinel *sensu stricto* and 3400 ppm in magnetite exsolution lamellae. Colas *et al*. (2016) studied exsolved phases from chromite during

medium to high grade amphibolite facies metamorphism and the exsolved phases are somewhat texturally similar to those found in this study, namely, magnetite and spinel *sensu stricto.* However, the trace element content differs from exsolved phases in this study as the spinel studied by Colas *et al*. (2016) contains a significant amount of Cr_2O_3 (21 wt% – 33 wt%). Therefore, it can be assumed that exsolved phases in the spinel layer are not predated by Cr-rich minerals according to Colas *et al*. (2016).

There is an increase in Cr concentration in samples closer to the surrounding igneous rock. Trace element concentration of sample RSTX26-52 is highly enriched in Cr, which decreases towards the rim, together with V, Mn, Co, Ni, Zn and Ga (Figure 5.4), while Al, Mg and Fe^{3+} increase towards the rim as noted in section 4.3.5.3. The presence of Mn, Zn, Ga and V may indicate possible alteration of chromite (Colas *et al*. 2014). Given that the aforementioned trace elements are detected in cores of the grain suggests that the cores have been altered as well. The decrease of Ga, V and Cr, given their trivalent ionic nature, behave similarly and are substituted by Fe^{3+} (Mukherjee *et al*., 2015). This phenomenon may be more distinctive in sample RSTX26-52 owing to its close proximity to calc-silicate fragments. Sample RSTX26-52 is enriched in Mn, Co, Ni, Zn and Ga relative to the UG 1 chromitite (these elements were below detection limits) and according to Mukherjee *et al*. (2015) altered chromite grains can be enriched in these trace elements that suggests that secondary alteration processes could have led to the depletion of Cr at the rims.

This zonation in elements depicts the evolution of the system in which decarbonating calc-silicate contaminated the enclosing magma hosting Cr-rich spinel/chromite. Cr-bearing spinel may be the best way to distinguish the two endmembers and may record the evolving contamination. The crystallisation of the chromite grains, like those found in the UG 1 chromitite, is inhibited (in sample RSTX26-52) by the decarbonating xenolith that results in the partitioning of Al, Mg and Fe^{3+} into the spinel, instead of Cr, particularly at the rims of spinel. Similar zonation patterns are exhibited in RSTX26-61, but to a lesser degree. P, Sc, V and Cr were the only elements detected in samples from the chromitite stringer and the UG 1 chromitite. Trace element concentration of the unaltered UG 1 chromitite does not show any major variation and the same can be attributed for the major elements (as indicated by EMP results in section 4.3.5.3). RSTX26-61 and RSTX26-63 show some variation in trace

elements within individual grains and are depleted in Sc and V (few grains RSTX26-63 show a slight enrichment in Sc) relative the UG 1 chromitite. This variation can be the result of decarbonation effects of the xenolith that may have influenced the trace element concentration in samples RSTX26-61 and RSTX26-63, but did not influence the concentration of the UG 1 chromitite located 20 m away from the xenolith. Given that RSTX26-52 shows relatively major variations in trace-element concentration, compared to RSTX26-61 and RSTX26-63, it can be assumed that the effects of the decarbonating xenolith are localised, possibly within zones that are in extremely close proximity to the main xenolithic body or on a smaller scale where calc-silicate fragments locally disturb the original magmatic distribution of trace elements.

CHAPTER 6: OXYGEN ISOTOPES

6.1 Introduction

The study of oxygen isotope ratios provides an opportunity to trace crustal contamination of igneous systems (Sharp, 2007). This geochemical method was employed in order to determine the extent of chemical mass transfer/contamination, on the cm to m scale, of the magmatic sequence adjacent to the xenoliths in Marikana (Western Limb) and Zwartfontein (Northern Limb). The analyses are compared with published data from the rest of the RLS. Mineral separates were selected from the Marikana samples and one borehole (ZF 116) from Zwartfontein. Samples from both localities were chosen in order to determine if the oxygen isotope composition showed any spatial variation on the aforementioned scale. Minerals analysed include, monticellite, forsterite, plagioclase, pyroxene, uvarovitic garnet and spinel. There are no known oxygen isotope data for uvarovitic garnet and spinel from the RLS. Hence, results presented herein for the aforementioned minerals are the first of its kind.

6.2 Theory and concepts

There are three naturally occurring oxygen isotopes, namely ^{16}O, ^{17}O and ^{18}O. The most abundant is ^{16}O, which makes up 99.8%, followed by ^{18}O (0.20%); the least abundant is ^{17}O (0.036%). Given these proportions, the $^{18}O/^{16}O$ ratio is normally used in order to determine oxygen isotopic ratios (Rollinson, 1993; Sharp, 2007). The ratio is expressed by the formula below:

$$\delta^{18}O‰ = [(^{18}O/^{16}O_{(sample)} - {}^{18}O/^{16}O_{(reference)})/ {}^{18}O/^{16}O_{(standard)}] \times 1000$$

For the purpose of this study, all $\delta^{18}O$ values are given relative to Standard Mean Ocean Water (SMOW), which is available and distributed by the International Atomic Energy Agency (IAEA) (Sharp 2007).

The $\delta^{18}O$ values of rocks show significant variation according to the processes and conditions under which they formed. Meteoric water shows the greatest range (-4bdl‰ to +5.70‰), whereas chondritic meteorites, together with Earth's mantle, show little variation,

with an approximate value of +5.70‰. Granites, metamorphic rocks and sediments have elevated $\delta^{18}O$ values; sedimentary rocks have the highest $\delta^{18}O$ values (~+10‰ to +30‰) relative to the mantle. Knowing the accepted $\delta^{18}O$ composition of rocks in different crustal settings can, inter alia, assist in determining contamination of igneous rock by crustal/sedimentary sources (Sharp, 2007).

6.3 Previous oxygen isotope studies in the Rustenburg Layered Suite

Oxygen isotope studies were conducted by Schiffries and Rye (1989) on mineral separates from numerous rock types, including orthopyroxenite, feldspathic pyroxenite, leuconorite, anorthosite, gabbro and diorite in the Eastern Limb. Results showed that plagioclase and pyroxene have similar $\delta^{18}O$ values within the Lower Zone through to the Main Zone of the RLS, with average $\delta^{18}O$ values for plagioclase and pyroxene being +7.1‰ and +6.7‰, respectively. In the Upper Zone, $\delta^{18}O$ values show more variability and are slightly higher for plagioclase (+7.6 ± 0.3‰), whereas pyroxene has similar values to that in other zones. The authors noted that the aforementioned values are higher than those for mantle-derived basalt or gabbro (+6.0‰ and +5.5‰ for plagioclase and pyroxene, respectively). This was attributed to contamination of the RLS magma by a crustal component prior to emplacement into the magma chamber. The most likely contaminant is the Transvaal Supergroup sediments, which exhibit $\delta^{18}O$ values between +9.0‰ and +21.0‰ (Schiffries and Rye, 1989). Reid *et al*. (1993) found plagioclase and pyroxene $\delta^{18}O$ values in samples from the Merensky Reef footwall in the Western Limb similar to those observed by Schiffries and Rye (1989) (approximately +7.10‰ and +6.60‰, respectively). (The range of $\delta^{18}O$ values from previous studies are summarised in Table 6.1).

Harris *et al*. (2005) obtained $\delta^{18}O$ values between +6.1‰ to +8.4‰ for plagioclase and +5.8‰ to +7.6‰ for pyroxene from samples from the Upper and Main Zones, Northern Limb (Bellevue core). They analysed samples from the Marginal and Lower Zones in the Eastern Limb as well, and found that $\delta^{18}O$ values there agree with those of Schiffries and Rye (1989), ranging from +5.7‰ to +6.8‰ for pyroxene and from +5.6‰ to +6.5‰ for olivine. Harris *et al*. (2005) agree that elevated $\delta^{18}O$ values indicate that the RLS magma was contaminated before emplacement, but they proposed a staging chamber hypothesis which

suggests that the contaminant was found in the lower to middle crust and not in the Transvaal Supergroup.

Buick *et al*. (2000) studied $\delta^{18}O$ values of metacarbonates found in the footwall contact aureole beneath the RLS and calc-silicate xenoliths in the Eastern Limb. This investigation found that lower $\delta^{18}O$ values correlate with a higher degree of metamorphism of carbonates in the aureole. Calc-silicate xenoliths containing high-grade minerals show $\delta^{18}O$ values between unmetamorphosed carbonate and the RLS, whereas completely retrogressed xenoliths show lower $\delta^{18}O$ values than partially retrogressed and high-*T* xenoliths. Buick *et al*. (2000) suggested that the $\delta^{18}O$ depletions in samples from the aureole can be attributed to hydrous fluid infiltration derived from the dehydration of non-carbonate rocks such as, metapelites found in the country rocks.

Harris and Chaumba (2001) obtained $\delta^{18}O$ values for plagioclase and pyroxene in the Platreef, Main and Upper Zones, in the Sandsloot area of the Northern Limb. Their results reveal that the Main and Upper Zones show little variation (+7.0‰ to +8.3‰ for plagioclase and +6.1‰ to +7.6‰ for pyroxene). In the Platreef, however, $\delta^{18}O$ values are more variable and higher, showing ranges of +7.40‰ to +10.40‰ for plagioclase, and +6.0‰ to +11.3‰ for pyroxene. Pyroxene found in Platreef pyroxenite displays $\delta^{18}O$ values that are, on average, 2.4‰ higher than Main and Upper Zone pyroxenes. Harris and Chaumba (2001) attributed these elevated values to crustal contamination. The diopsides in parapyroxenite are further 2.5‰ higher than in the pyroxenites.

The unmetamorphosed Malmani dolomite footwall in the Northern Limb has $\delta^{18}O$ values between +19.00‰ and +24.00‰ (Buchanan *et al*., 1981), whereas decarbonated dolomite/calc-silicates exhibit lower values of +12.10‰ to +15.40‰ (Harris and Chaumba, 2001). The dolomitic footwall is the most likely source of elevated values in the Platreef because of its proximity and the presence of multiple xenoliths within the magmatic sequence (Harris and Chaumba, 2001). Its high $\delta^{18}O$ signature has a greater ability to alter the $\delta^{18}O$ per unit assimilated than any other contaminant in the region. Harris and Chaumba (2001) estimated that a total of 18% dolomite assimilation into the Platreef magma, in addition to the prior contamination of the RLS in a staging chamber could account for the

observed patterns. The $\delta^{18}O$ values investigated by Sharman-Harris *et al*. (2005) in the Platreef on the farms Turfspruit and Macalacaskop generally agree with Harris and Chaumba (2001). Sharman-Harris *et al*. (2005) noted that the $\delta^{18}O$ ratios for plagioclase (+5.89‰ to +9.74‰) and pyroxene (+6.54‰ to +8.74‰) are slightly lower when compared to data from Sandsloot, implying that the carbonate footwall on Turfspruit and Macalacaskop might have lower $\delta^{18}O$ ratios. This may be supported by Buick *et al*. (2000) who show oxygen isotope data for calcite from metacarbonate xenoliths and country rocks beneath the RLS that range from ~+13‰ to ~+21‰ where the footwall is the Duitschland Formation, and ~+14‰ to ~+25‰ where the footwall is the Malmani Subgroup.

Pronost *et al*. (2008) considered the isotopic signatures in the Platreef on three farms where the footwall is not dolomite, and found that on the farm Overysel, where the footwall is granitic basement, plagioclase and pyroxene show $\delta^{18}O$ values similar to the main RLS, with ranges from +7.20‰ to +7.50‰ and +6.10‰ to +6.60‰, respectively. On the farms Macalacaskop and Turfspruit, values are slightly elevated, with plagioclase ~+8.00‰ and pyroxene ~+7.30‰, and plagioclase ~+7.60‰ and pyroxene +7.30‰, respectively. These values are lower than the average $\delta^{18}O$ observed in the Sandsloot area of +9.40‰ in plagioclase and +7.70‰ in pyroxene (Harris and Chaumba, 2001). According to Pronost *et al*. (2008) this is an indication that contamination is more significant where the footwall is dolomite.

The $\delta^{18}O$ studies of the RLS indicate that any viable contaminant should have a relatively enriched $\delta^{18}O$ signature. The unaltered dolomite has $\delta^{18}O$ values that range from +19‰ to +25‰ (Buchanan *et al*., 1981; Harris and Chaumba, 2001) and, therefore, 18 % assimilation of dolomitic footwall can raise the $\delta^{18}O$ values to those observed at Sandsloot, as opposed to any other likely contaminants in the region with a lower $\delta^{18}O$ signature, such as quartzite (+10‰ to +13‰), shales (+9‰ to +10‰), and granite (+8‰ to +9‰) (Pronost *et al*., 2008). The percentage of any other contaminant needed to reach $\delta^{18}O$ values observed in Sandsloot is unrealistically high (Harris and Chaumba, 2001; Pronost *et al*., 2008). It should be noted that already decarbonated calc-silicates are less likely contaminants, given their relatively lower $\delta^{18}O$ values (+12.1‰ to +15.4‰), unless exceptionally high levels of assimilation were achieved. However, the decarbonation of carbonate xenoliths within the

Platreef magma might have been the agent which raised the $\delta^{18}O$ value (Harris and Chaumba, 2001; Pronost *et al*., 2008). This may still be possible on other farms where the footwall is not predominantly dolomite and a slightly higher $\delta^{18}O$ value is evident affirming that contamination can be attributed to the $\delta^{18}O$ value of the contaminant, as well as the amount of the contaminant (Pronost *et al*., 2008).

Table 6. 1: Range of O-isotope composition of the RLS and Transvaal Supergroup rocks from published data

Study	Location	$\delta^{18}O_{plag}$ range (‰)	$\delta^{18}O_{pyrox}$ range (‰)	$\delta^{18}O_{carbonate}$ range (‰)
Schiffries and Rye (1989)	Critical Zone, Eastern Limb	6.88-7.48	6.45-6.86	
Reid *et al.,* (1993)	Critical Zone, Western Limb	6.8-7.6	6.2-6.8	
Harris *et al.,* (2005)	Critical Zone, Eastern Limb	6.8-7.1	6.2-6.5	
Harris and Chaumba (2001)	Platreef, Northern Limb (FW: Sandsloot)	9.8-10.4	6.7-8.9	13.0-25.5
	Platreef, Northern Limb (FW: Macalacaskop)	7.3-9.1	6.9-8.7	
Sharman-Harris *et al.,* (2005)	Platreef, Northern Limb (FW: Turfspruit)	7.7-9.7	6.5-7.3	
	Platreef, Northern Limb (FW: Duitschland Formation)	5.9-7.6	6.5-6.7	
	Platreef, Northern Limb (FW: Macalacaskop)	7.2-9.9	6.2-9.2	
Pronost *et al*., (2008)	Platreef, Northern Limb (FW: Turfspruit)	6.8-8.7	6.3-9.7	
	Platreef, Northern Limb (FW: Overysel)	3.6-9.0	6.3-9.3	
Buchanan *et al*., 1981	Malmani Subgroup			19-24
Buick *et al*., 2000	Malmani Subgroup (RLS aureole)			11.0-18.5
Harris and Chaumba (2001)	Malmani Subgroup			21.1-23.2
Pronost *et al*., (2008)	Duitschland Formation			11.8-17.7

6.4 Methodology

Mineral separates including pyroxene, plagioclase, garnet, spinel, monticellite and forsterite were analysed. Samples were selected from the different zones, namely, xenolith, contact zone and host magmatic rock, proximal and distal from the xenoliths, in order to examine the potential oxygen isotopic variation between the xenolith and surrounding lithologies. The analyses were conducted at the Department of Geological Sciences, University of Cape Town, under the supervision of Professor C. Harris. The laser fluorination method was used to obtain the oxygen gas.

Samples were crushed and sieved; the fraction between 250 µm–500 µm was washed and dried. From this fraction mineral separates were hand-picked under a binocular microscope, in some cases after initial magnetic separation, washed with acetone and dried again before laser fluorination. The apparatus used a 20 W New Wave CO_2 laser mounted on a stage. The design of the laser apparatus was first described by Sharpe (1990). A total of 12 samples were loaded into a highly polished pure Ni sample holder at once, and a total weight of 2 mg–4 mg of mineral separates was used for each analysis. Ten samples together with two standards were always loaded in the sample holder. MONGT was used as the standard and originates from a single megacryst of Monastery garnet (Harris *et al*., 2000).

After loading the standards and samples, the Ni holder was placed in an oven at 110 °C for a minimum of 1 hour. Thereafter, the sample holder was transferred to the reaction chamber. The sample chamber was pumped for 1–2 hours, after which 10 kPa of BrF_5 was expanded into the reaction chamber for the first prefluorination for 30 seconds and removed cryogenically using liquid N_2. The sample chamber was left to pump again for >1 hour and a second load of 10 kPa BrF_5 was expanded into the reaction chamber and left overnight before extracting the O_2 gas.

Each sample was reacted using ~10 kPa BrF_5. Once the reaction was complete, any excess BrF_5 and free Br formed by dissociation were frozen into a metal finger using liquid N_2. The remaining gases were passed through a KCl trap, which maintains a temperature of 200 °C in order to remove any F_2 which may have been produced. Thereafter, the gases were

expanded into a stainless-steel double-U trap surrounded by liquid N_2, and pure O_2 gas was collected into a glass storage bottle containing 5 Å molecular sieves.

At the beginning of an O_2 extraction day, a blank was run in order to measure the amount of gas. The blank pressure was < ~1/200 of the sample value of a 1 mg sample. The O isotope ratios of the 12 samples extracted per run were measured off-line using a Finnegan DeltaXP mass spectrometer in dual inlet mode. All data are reported in the familiar δ notation. The O isotopic ratios were measured on O_2 gas and the values were used to determine raw δ values for each sample relative to the SMOW standard. MONGT was calibrated against the UWG-2 garnet standard analysed by Valley *et al*. (1995) using the current laser fluorination system and assuming a $\delta^{18}O$ value of 5.80‰ for UWG-2. Vielzeuf *et al*. (2005) obtained values of 5.3‰ for similar Monastery garnet, which is in relatively good agreement with the values of analysed standards. The MONGT $\delta^{18}O$ values of 5.38‰ were used to normalise raw data according to the SMOW scale (Harris and Vogeli, 2010). It should be noted that the laser fluorination method is more precise than conventional methods (Harris and Vogeli, 2010), therefore results are reported to two decimal places. The obtained $\delta^{18}O$ values for MONGT during the analysis ranged between 5.31‰ and 5.45‰ which agrees well with values recorded by Harris and Vogeli (2010).

6.5 Results

6.5.1 Marikana

Oxygen isotope data were obtained for monticellite, forsterite, plagioclase, pyroxene, uvarovitic garnet and spinel. The analysis of uvarovitic garnet and spinel presented here are novel as no previous data are available or known for these minerals. Marikana samples show variation in $\delta^{18}O$ values between all zones (Table 6.2). The overall trend observed is one of a consistent decrease in $\delta^{18}O$ values, from metasedimentary to more magmatic values, from the centre of the xenolith to the mottled anorthosite, and the range in $\delta^{18}O$ values are greatest in the contact zone (Figure 6.1). The main xenolithic body has $\delta^{18}O$ values between +11.67‰ to +13.47‰ for monticellite, +10.72‰ to +11.27‰ for forsterite and +12.79‰ to +12.98‰ for spinel. Forsterite and spinel found in the spinel layer show a slight decrease in $\delta^{18}O$ values, with ranges from +9.77‰ to +10.57‰ and +11.18‰ to

+11.83‰, respectively. A very consistent decrease between forsterite-spinel pairs from the xenolith to the spinel layer is observed (Figure 6.1). The plagioclase (An_{99}) $\delta^{18}O$ values in the contact zone range from +7.92‰ to +12.67‰, while clinopyroxene ranges from +8.63‰ to +9.93‰ and uvarovitic garnet display values from +9.86‰ to +7.79‰. The $\delta^{18}O$ values of plagioclase and diopside decrease in the host mottled anorthosite: 5 m from the xenolith the plagioclase value is +6.62‰ and 20 m away plagioclase ranges from +6.42‰ to +6.50‰, and diopside shows a value of +5.81‰. The spatial variation in $\delta^{18}O$ values is presented in Figure 6.1.

Table 6. 2: $\delta^{18}O$ values of all samples analysed in this study (‰, SMOW) and the difference between $\delta^{18}O_{plagioclase}$ and $\delta^{18}O_{pyroxene}$ ($\Delta_{plag - pyrox}$) where applicable.

	Sample no.	Zone/Rock type	Mtc	Fo	Spl	Grt	Plag	Cpx	plag - pyrox
Marikana	RSTX26-03	Main calc-silicate xenolith	11.67 13.47	10.72 11.27	12.79 12.98				
	RSTX26-06	Spinel Layer - calc-silicate xenolith		9.77 10.57	11.18 11.83				
	RSTX26-50	Contact zone				8.79 7.96 9.86	12.67 7.92 8.66	9.18 8.63 9.93	+3.49 -0.71 -0.27
	RSTX26-5A	Mottled anorthosite 5 m away from xenolith					6.62		
	RSTX26-20A	Mottled anorthosite 20 m away from xenolith					6.42 6.50	5.81	+0.69
Zwartfontein	A24	Magmatic pyroxenite					6.98 7.11	6.10	+1.01
	A156	Calc-silicate xenolith		11.95 10.02	11.42			9.64	
	A246	Magmatic pyroxenite between xenoliths					7.33 7.77	8.85 6.23	-1.52 +1.54
	A291	Hybridised/ parapyroxenite					8.05	6.33 6.35 6.99* 10.67	-2,62

*Orthopyroxene analysed instead of clinopyroxene

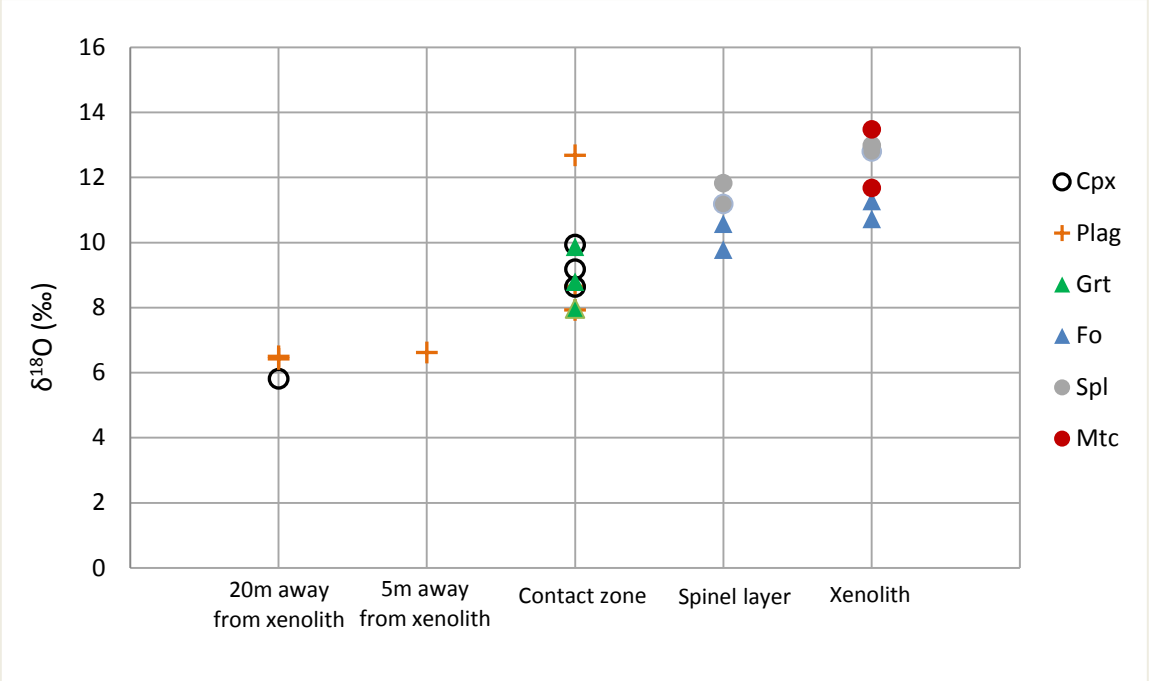

Figure 6.1: Plot showing variation in $\delta^{18}O$ between different zones, from xenolith to mottled anorthosite in the Western Limb.

6.5.2 Zwartfontein

The Zwartfontein samples were selected based on their positions relative to the xenoliths. Minerals analysed include, plagioclase, pyroxene, forsterite and spinel (Figure 6.2). Magmatic pyroxenite (A24) was selected 111 m away from the calc-silicate xenolith and exhibited $\delta^{18}O$ values between +6.98‰ to +7.11‰ for plagioclase and +6.10‰ for clinopyroxene (Table 6.2). The calc-silicate xenolith selected for analysis (A156), which is composed of high-grade metamorphic minerals with no apparent serpentinisation, had $\delta^{18}O$ values of +9.64‰ for diopside, +10.02‰ to +11.95‰ for forsterite, and +11.42‰ for spinel. The next magmatic pyroxenite (A246) between xenoliths was selected and showed values between +7.33‰ and +7.77‰ for plagioclase, and +6.23‰, and +8.85‰ for diopside. The hybridised sample (A291), exhibiting both igneous and metamorphic features (Figure 3.23) showed $\delta^{18}O$ values of +8.05‰ for plagioclase, between +6.33‰ and +10.69‰ for diopside, and +6.99‰ for enstatite.

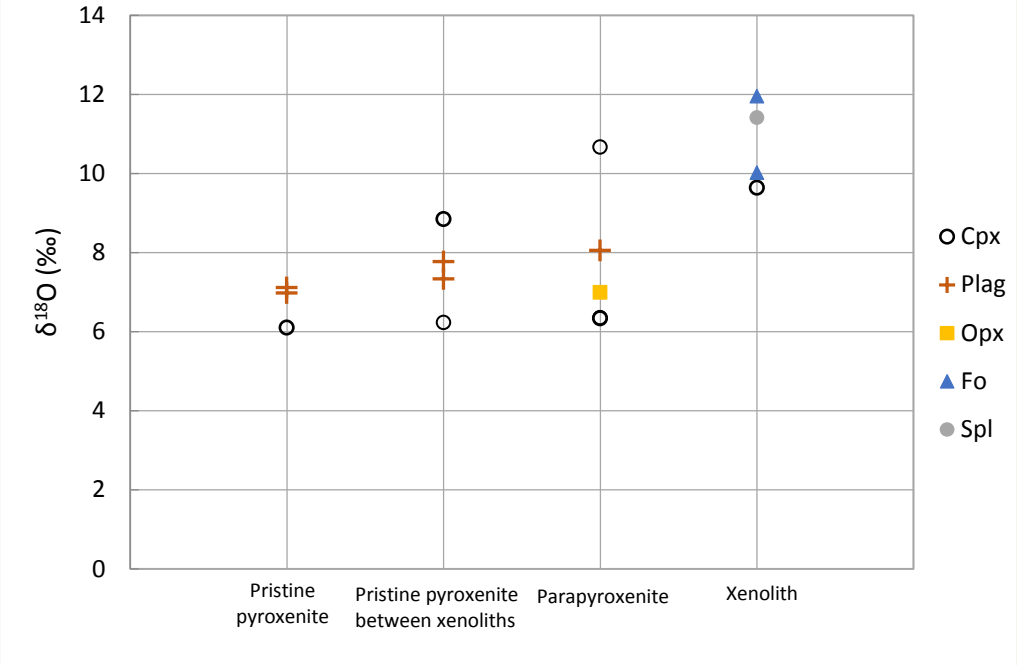

Figure 6.2: Plot showing the variation in $\delta^{18}O$ values between xenoliths and associated lithologies in the Platreef.

6.6 Discussion

6.6.1 Marikana

Mottled anorthosite located 5 m from the main xenolithic body showed a $\delta^{18}O$ value of +6.62‰ for plagioclase. Plagioclase and pyroxene 20 m away showed values from +6.42‰ to +6.50‰, with pyroxene showing a value of +5.81‰. The best way to assess the degree of oxygen isotope equilibrium between minerals that co-exist is the δ – δ plot, where the $\delta^{18}O$ of one mineral is plotted against another (e.g. Gregory and Criss, 1986). One of the most useful of these plots is δ-pyroxene vs δ-plagioclase, which records the $\delta^{18}O$ values of a mineral (plagioclase) that exchanges oxygen relatively rapidly compared to a mineral (pyroxene) that exchanges oxygen less rapidly (Pronost *et al.*, 2008) (Figure 6.3). Closed system cooling and crystallisation would be characterised by data points that fall within isotherms of constant parts per mil difference (Δ) between the co-existing minerals of interest (Gregory and Criss, 1986). Data points that plot away from an isotherm can be considered as being in oxygen isotope magmatic disequilibrium (Pronost *et al.*, 2008). For the purpose of this study, isotherms at 550 °C and 1150 °C have been considered and correlate to $\Delta_{plagioclase\text{-}pyroxene}$ of 1.74‰ and 0.58‰, according to the plagioclase-diopside curve of Chiba (1989). These isotherms were selected because previous workers on the RLS

found that the majority of samples in oxygen isotope magmatic equilibrium plot within this field. The isotherm at 1150 °C represents the crystallisation temperature, and the isotherm at 550 °C represents the closure temperature, hence, oxygen equilibrates between minerals after the crystallisation temperature and ceases at closure temperature (Harris and Chaumba, 2001). Plagioclase and pyroxene 20 m from the xenolith plots within the isotherms (Figure 6.3), indicating that it is in oxygen isotope magmatic equilibrium. These data are consistent with previous studies done in the Critical Zone, Western and Eastern Limbs (Schiffries and Rye, 1989; Reid *et al*., 1993; Harris *et al*., 2005). Hence, no contamination from the decarbonating xenolith is evident 20 m away from the main xenolithic body. No pyroxene data were recorded for mottled anorthosite 5 m away from the xenolith. However, $\delta^{18}O$ values observed for plagioclase (6.62‰) agree with previous investigations done in the Eastern and Western Limbs (Schiffries and Rye, 1989; Reid *et al*., 1993; Harris *et al*., 2005). Hence, no evidence of contamination from the decarbonating xenolith is evident 5 m away from the main xenolithic body.

In the contact zone of the Marikana xenolith, plagioclase (An_{99}) and CaTs-clinopyroxene show $\delta^{18}O$ values between +7.92‰ to +12.67‰, and +8.63‰ to +9.93‰, respectively. These values are not consistent with previously studied samples collected from the Critical Zone, Western and Eastern Limbs (Schiffries and Rye 1989; Reid *et al.,* 1993). According to Harris and Chaumba (2001), higher $\delta^{18}O$ values for plagioclase have been reported in the Platreef region, where the footwall is dolomite (+7.40‰ to +10.40‰). Pyroxene values studied herein are higher than typical RLS values recorded by Schiffries and Rye (1989), Reid *et al.* (1993) and Harris *et al*. (2005). Both plagioclase and pyroxene in the contact zone show a greater affinity with samples that have previously been studied from the Platreef (Harris and Chaumba, 2001). As it seems likely that Platreef $\delta^{18}O$ values have been elevated by the presence of dolomite, the same principle can be applied to plagioclase and pyroxene in the contact zone of the Marikana xenolith. The obvious contaminant is the decarbonating calc-silicate xenolith.

According to Figure 6.3, data from this study collected from the contact zone surrounding the Marikana xenolith show a scattered nature, with two samples plotting below the 1150 °C isotherm and one sample significantly away from both isotherms. Data from

Schiffries and Rye (1989), Reid *et al*. (1993) and Harris *et al*. (2005) plot within the isotherms and are thus considered to be in oxygen isotope magmatic equilibrium. Data that plot in an array away from the isotherms have undergone fluid-rock interaction (Harris and Chaumba, 2001; Pronost *et al*. 2008). Data from Harris and Chaumba (2001) plot between at the 550 °C and 1150 °C isotherms and slightly above the 550 °C isotherm, whereas the data from Sharman-Harris *et al*. (2005) and Pronost *et al*. (2008) plot between at the 550 °C and 1150 °C isotherms and below the 1150 °C isotherm. According to Pronost *et al*., (2008) $\Delta_{plagioclase\text{-}pyroxene} < 0.55‰$ indicates high-temperature fluid-rock interaction and $\Delta_{plagioclase\text{-}pyroxene} > 1.55‰$ indicates low-temperature fluid-rock interaction. Therefore, according to Harris and Chaumba (2001) data that plot above the 550 °C isotherm (Figure 6.3) indicate sub-solidus water-rock interaction. The data that plot within the two isotherms and show elevated $\delta^{18}O$ values for plagioclase and pyroxene, compared to the Western and Eastern Limbs (Schiffries and Rye 1989; Reid *et al.,* 1993; Harris *et al*., 2001), can be attributed to crustal contamination. Data that plot below the 1150 °C isotherm (Sharman-Harris *et al*., 2005; Pronost *et al*., 2008) indicate high-temperature, possibly CO_2-rich fluid interaction originating from decarbonating dolomitic rocks. The $\Delta_{plagioclase\text{-}pyroxene}$ values herein (Table 6.2) indicate that the contact zone may have been subjected to both high-temperature and low-temperature fluid-rock interactions. The trend observed in Figure 6.3 suggests that contamination in the Marikana case took place during the emplacement of the magma or during prograde metamorphism as the majority of the data from the contact zone plot below the 1150 °C isotherm. This implies that the elevated $\delta^{18}O$ values of plagioclase and pyroxene result from a decarbonating xenolith undergoing prograde metamorphism where a CO_2-rich fluid may be responsible for the low $\Delta_{plagioclase\text{-}pyroxene}$ values observed in some of the samples, whereas a late stage H_2O-rich fluid is responsible the high $\Delta_{plagioclase\text{-}pyroxene}$ value (Pronost *et al*., 2008) observed in one sample.

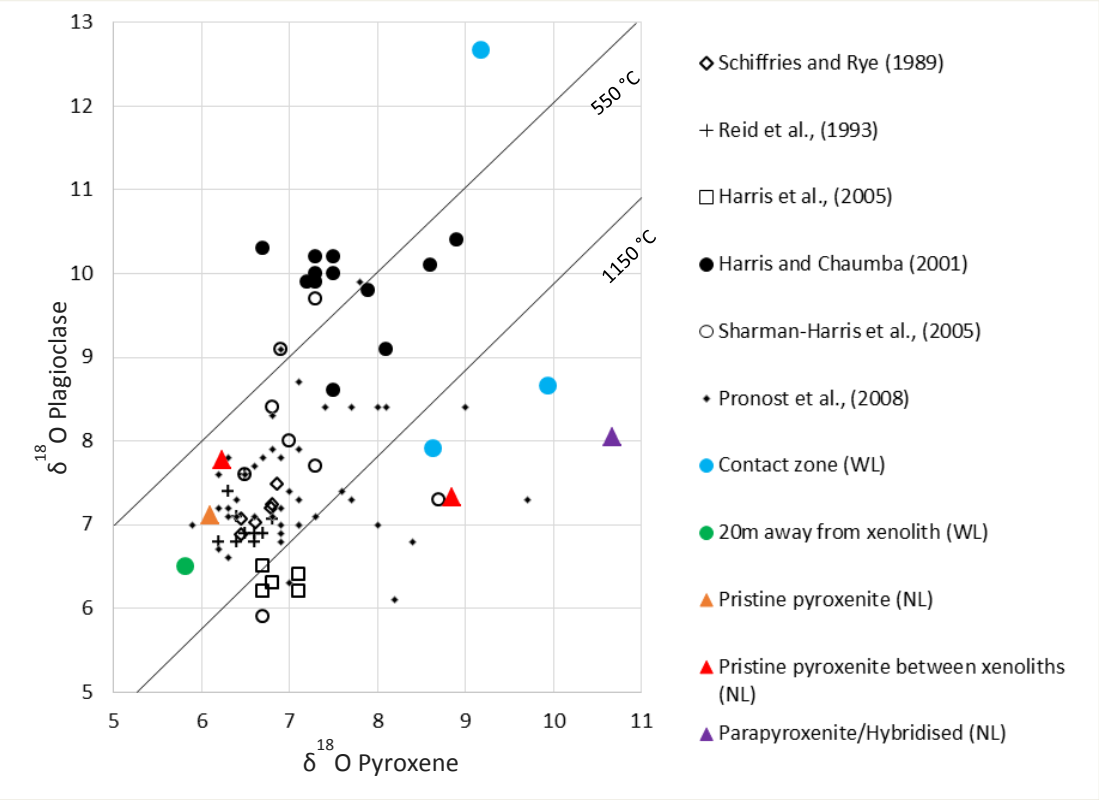

Figure 6.3: Plot of $\delta^{18}O$ values of co-existing pyroxene and plagioclase for data from the Marikana xenolith (WL) shown using circles and the Zwartfontein xenolith (NL) shown using triangles compared with Schiffries and Rye (1989) from the Critical Zone, Eastern Limb; Reid *et al*. (1993) from the Critical Zone, Western Limb; Harris and Chaumba (2001) and Sharman-Harris *et al*. (2005) from the Platreef, Northern Limb; and Harris *et al*. (2005) from the Critical Zone, Eastern Limb. Isotherms for 550 °C and 1150 °C, corresponding to $\Delta_{plagioclase\text{-}pyroxene}$ values of 1.74‰ and 0.58‰ are shown according to Harris and Chaumba (2001).

Samples from the Marikana xenolith have $\delta^{18}O$ values that are consistent with calc-silicate/marble originating from Transvaal Supergroup dolomites after undergoing decarbonation (Buick *et al*., 2000; Pronost *et al*., 2008). Therefore, these samples record much lower $\delta^{18}O$ values than the original carbonate rock. Forsterite and spinel found in the spinel layer have slightly lower $\delta^{18}O$ values when compared to the main xenolith body (Figure 6.1). This feature may be ascribed to a varying degree of decarbonation endured by each zone and implies that the spinel layer has undergone a greater amount of decarbonation owing to its proximity to the magma, than the main xenolithic body, which was not in direct contact with, and at the forefront of, interaction with the magma.

6.6.2 Zwartfontein

Magmatic pyroxenite located farthest from the xenolith has $\delta^{18}O$ values for plagioclase and pyroxene that are consistent with previously published data from the Western and Eastern Limbs (Schiffries and Rye, 1989; Reid *et al*., 1993; Harris *et al.* 2005), as opposed to the Platreef (Harris and Chaumba, 2001; Sharman-Harris *et al*., 2005; Pronost *et al.,* 2008). This could be due to this pyroxenite being found higher in the stratigraphy, and therefore, being less susceptible to the effects of the interaction with the footwall. Pyroxenites located between xenoliths have variable $\delta^{18}O$ values, with one data point consistent with data from the Critical Zone in the Western and Eastern Limbs (Schiffries and Rye, 1989; Reid *et al*., 1993; Harris *et al*., 2005). Both of the aforementioned samples are in oxygen isotope magmatic equilibrium (Figure 6.3). The other sample (from pyroxenite located between xenoliths) is in oxygen isotope magmatic disequilibrium and plots below the 1150 °C isotherm. This sample differs from typical Platreef samples in that the plagioclase has $\delta^{18}O$ values similar to the main RLS (+7.33‰), whereas the co-existing pyroxene has typical Platreef $\delta^{18}O$ values (+8.85‰). The only other sample that shows this feature is the parapyroxenite/hybridised rock, with a plagioclase value of +8.05‰ and pyroxene of 10.67‰; this could be due to alteration effects (Figure 6.3). Harris and Chaumba (2001) noted that, in some cases, the parapyroxenite pyroxene has $\delta^{18}O$ values of ~11.30‰; however, no data for co-existing plagioclase were recorded. Based on the $\Delta_{plagioclase\text{-}pyroxene}$ values for samples that plot below the 1150 °C isotherm it is possible that a high-temperature CO_2-rich fluid is responsible for the oxygen isotope magmatic disequilibrium observed (Pronost *et al*., 2008). These data show an agreement with Sharman-Harris *et al*., (2005) and Pronost *et al*., (2008) (Figure 6.3) and indicate that magmatic interaction with the dolomitic footwall results in elevated $\delta^{18}O$ values observed in plagioclase and pyroxene.

6.7 Summary

The Marikana xenolith and surrounding contact zone preserves a rare case of m-scale heterogeneity. Plagioclase (An_{99}) and clinopyroxene (Tschermak end – member) in the contact zone show $\delta^{18}O$ values that do not agree with previously published data from the Western or Eastern Limbs. It does, however, show values that are in agreement with data published from the Platreef (Harris and Chaumba, 2001; Sharman-Harris *et al*. 2005; Pronost *et al*. 2008). This can be explained by the decarbonating xenoliths that raised the $\delta^{18}O$

values, in the same way that Harris and Chaumba (2001) suggested dolomitic footwall as a source of contamination leading to elevated $\delta^{18}O$ values in the Platreef. Samples collected from the Platreef cores agree with previous studies from the Northern Limb. Platreef igneous rocks surrounding the xenolith show no obvious evidence of input of high $\delta^{18}O$ material derived from the xenoliths. However, it should be noted that the assimilation of the dolomitic footwall in the form of xenoliths is what led to the higher $\delta^{18}O$ values already observed in the Platreef. It is proposed that the contact zone surrounding the Marikana xenolith is a small-scale version of the same events that took place in the "bigger picture" Platreef (Harris and Chaumba, 2001) where contamination by the dolomitic rock and high-temperature CO_2-rich fluids are responsible for elevated $\delta^{18}O$ values and oxygen isotope magmatic disequilibrium.

CHAPTER 7: METAMORPHISM

7.1 Introduction

Bowen's (1940) investigation on the progressive metamorphism of siliceous limestone and dolomite provides a useful framework to describe and interpret the metamorphic history of the Marikana and Zwartfontein xenoliths. Bowen (1940) suggested that changes in carbonates could be observed as series of reactions, with increasing decarbonation occurring at successively hotter temperatures at any given pressure. The typical mineral assemblage observed in the xenoliths is monticellite + forsterite + spinel ± diopside. Prograde metamorphism of the main xenolithic body would have taken place in the presence of a CO_2-rich fluid phase as carbonate minerals broke down. In contrast, retrograde metamorphism is more likely to have been accompanied by hydration of the decarbonated high-grade calc-silicate mineral assemblages.

7.2 Methodology

Petrography, mineral chemistry and the detailed mineralogical framework for interpreting the progressive metamorphism of siliceous limestones and dolostones by Bowen (1940) was employed as the basis to explain the reactions taking place in the xenoliths and surrounding zones. Composition diagrams and pseudosections for the CaO-MgO-SiO_2-CO_2 system were calculated using the thermodynamic calculation software package, Perple_X (version 6.8.6, June 2019) (Connolly 1990, 2009). The thermodynamic data file used was hp633ver.dat, together with appropriate solution models, where necessary, that accommodate for Ca in olivine and therefore, capable of producing monticellite and forsterite. A range of pressures between 0.6–1.6 kbar was considered given the overburden pressure in the Critical Zone at the time of emplacement (Sharpe, 1982). Samples from Zwartfontein were not computed since suitable bulk data were not available, and bulk rock data studied in the Platreef catalogue (Nex *et al.,* 2006) does not correlate well with samples from this study.

7.3 Results

The Marikana main xenolithic body is composed of coarse-crystalline idioblastic to hypidioblastic monticellite, which is the primary Ca-Mg silicate, with lesser amounts of

forsterite and spinel (Figure 3.1) and trace amounts of calcite in some samples (Section 3.2.1). Textures observed in samples from the xenolith show no evidence of disequilibrium or retrograde effects, and it can be assumed that these minerals represent the observed peak metamorphic assemblage. Forsterite is formed at a lower metamorphic grade than monticellite by one of the following reactions (Bowen, 1940):

$$CaMg_3(SiO_3)_4 + 5CaMg(CO_3)_2 \leftrightharpoons 6CaCO_3 + 4Mg_2SiO_4 + 4CO_2 \quad (1)$$

Tremolite dolomite calcite forsterite

$$2CaCO_3 + 3CaMg_3(SiO_3)_4 \leftrightharpoons 5CaMgSi_2O_6 + 2Mg_2SiO_4 + 2CO_2 \quad (2)$$

Calcite tremolite diopside forsterite

The monticellite-forming reaction would most likely be:

$$CaMgSi_2O_6 + Mg_2SiO_4 + 2CaCO_3 \leftrightharpoons 3CaMgSiO_4 + 2CO_2 \quad (3)$$

Diopside forsterite calcite monticellite

Possible spinel-forming reactions according to Wallmach *et al*. (1989) would be:

$$CaCO_3 + 2Mg_2SiO_4 + Ca_2Al_2SiO_7 \leftrightharpoons 3CaMgSiO_4 + MgAl_2O_4 + CO_2 \quad (4)$$

Calcite forsterite gehlenite monticellite spinel

$$2Ca_2Al_2SiO_7 + 2MgO + 2Mg_2SiO_4 \leftrightharpoons 4CaMgSiO_4 + 2MgAl_2O_4 \quad (5)$$

gehlenite periclase forsterite monticellite spinel

The mineralogy of the xenolith can be most simply presented in the CaO-MgO-SiO_2 system with the exception of Al_2O_3 (in spinel), but all relevant phase relationships can be displayed in this system. Figure 7.1 illustrates mineral phases and assemblages based on theoretical data (Connolly 1990, 2009) relevant to the bulk rock composition of the xenolith calculated at various temperatures, fluid composition and P = 1 kbar. According to Figure 7.1A, where $X_{CO_2} = 1$, diopside and forsterite or wollastonite can be present at $T = 600$ °C and remain the only formed minerals until $T = 900$ °C. Higher-grade minerals, such as monticellite and akermanite first appear at $T = 1050$ °C. Merwinite is first formed at $T = 1200$ °C. In Figure 7.1B, where X_{CO_2} is 0.5, forsterite, diopside and wollastonite are the only minerals formed between $T = 600$–750 °C. Akermanite and monticellite form between $T = 900$–1050 °C, reflecting the fact that at lower $X_{CO_2} = 0.5$ the relevant reactions occur at lower temperatures than in the pure fluid end-member system.

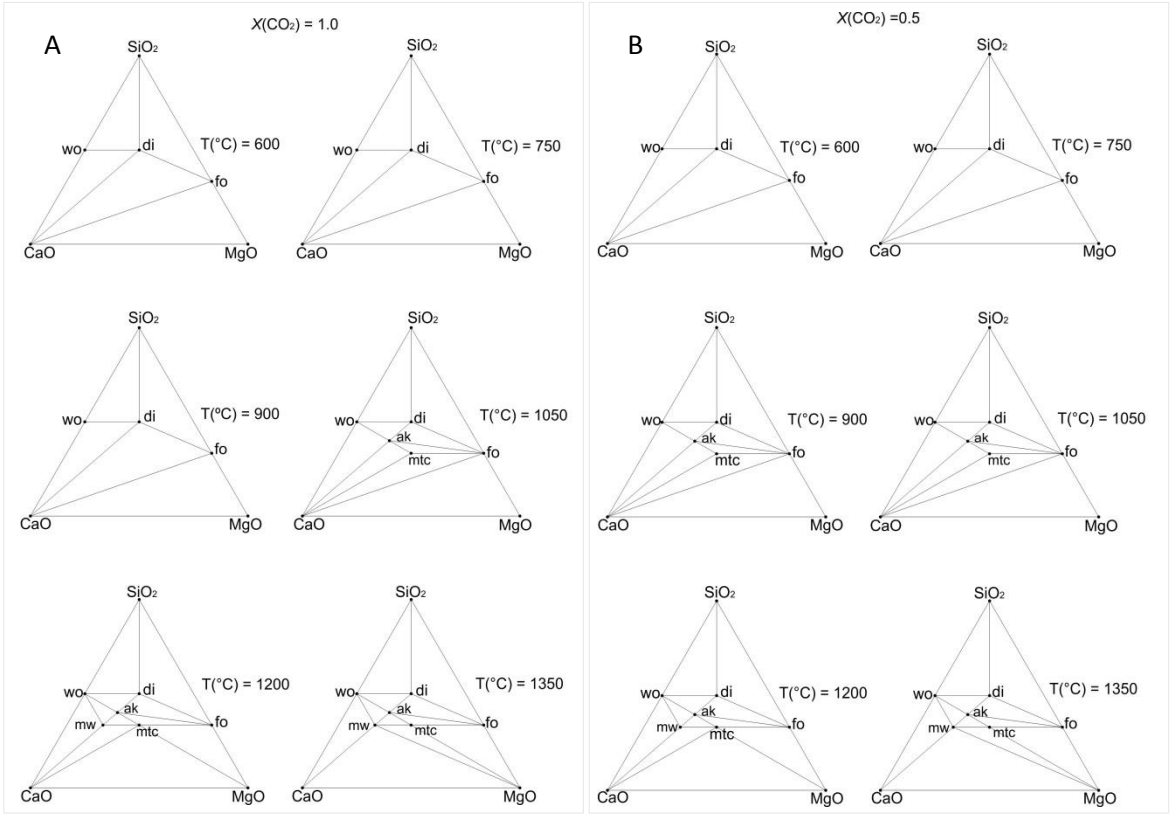

Figure 7.1 A: CaO-MgO-SiO_2 compositional diagram showing possible phases and changes in phase relationships with increasing temperature, constant pressure (1kbar, XCO_2 = 1 (A) and XCO_2 = 0.5. (B): calculated based on theoretical data (Connolly, 1990, 2009). Abbreviations: Wo = wollastonite, Di = diopside, Fo = forsterite, Ak = akermanite, Mtc = monticellite and Mw = merwinite.

Reaction curves relevant to the CaO-MgO-SiO_2-CO_2 minerals and CO_2-bearing fluid were computed considering temperature, pressure, and composition of the fluid phase as variables. The computation (Figure 7.2) is based on theoretical data (Connolly, 1990, 2009) and produces results similar to Sharp *et al*. (1986), Wallmach *et al*. (1989) and Owens (2000). A total of five CO_2-saturated invariant points occur (Table 7.1) and 12 univariant reaction curves link these points (Table 7.2). Although Figure 7.2 represents the reactions taking place in the CaO-MgO-SiO_2-CO_2 system, the mineral assemblage observed in the Marikana xenolith cannot be fully explained using these parameters because Al_2O_3 and FeO_T occur additionally in the xenolith. However, it is necessary to show these outputs as they will become valuable in the discussion.

Table 7. 1: Invariant points in the CaO-MgO-SiO_2-CO_2 system

1. calcite, periclase, monticellite, merwinite, forsterite
2. calcite, monticellite, merwinite, forsterite, akermanite
3. calcite, monticellite, merwinite, forsterite, akermanite
4. calcite, monticellite, forsterite, akermanite, diopside
5. calcite, monticellite, akermanite, wollastonite, diopside

Table 7. 2: Univariant reaction curves in the CaO-MgO-SiO_2-CO_2 system

1. calcite + monticellite = periclase + merwinite
2. calcite + forsterite = periclase + monticellite
3. calcite + forsterite = periclase + merwinite
4. monticellite = merwinite + forsterite
5. calcite + akermanite = merwinite
6. calcite + forsterite + akermanite = monticellite
7. calcite + monticellite + wollastonite = merwinite
8. monticellite + wollastonite = akermanite
9. calcite +forsterite + diopside = monticellite
10. calcite + diopside = akermanite
11. monticellite + diopside = forsterite + akermanite
12. calcite + diopside = monticellite + wollastonite

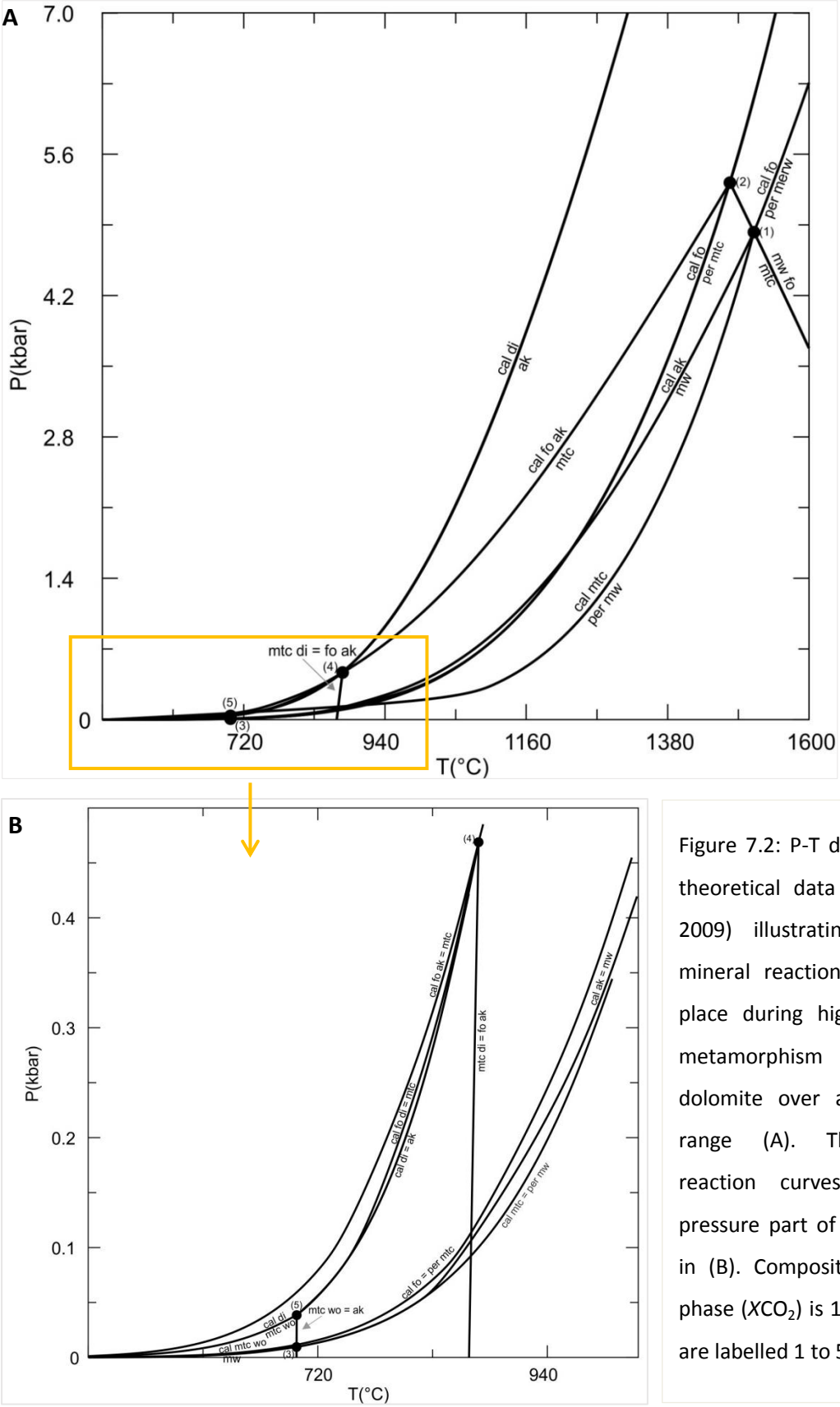

Figure 7.2: P-T diagram based on theoretical data (Connolly 1990, 2009) illustrating the possible mineral reactions that can take place during high-grade contact metamorphism of siliceous dolomite over a wide pressure range (A). The overlapping reaction curves in the low-pressure part of (A) are enlarged in (B). Composition of the fluid phase (XCO_2) is 1. Invariant points are labelled 1 to 5 (see Table 7.1).

A *P-T* pseudosection was computed using the bulk rock composition of the main xenolithic body, including Al_2O_3 and FeO, at variable X_{CO_2} of the fluid phase (Figure 7.3). Possible mineral assemblages for the bulk rock composition at X_{CO_2} of 1.0 and 0.5, respectively, are listed in Table 7.3. This computation results in the generation of the mineral assemblage, Mtc + Fo + Spl, at *T* ~ 900–1050 °C when X_{CO_2} = 1 and *T* ~825–975 °C when X_{CO_2} = 0.5, at *P* = 0.6–1.6 kbar. A decrease in the CO_2 composition of the fluid phase results in the generation of the same mineral phases that are stable at a lower temperature.

Most of the prograde mineral assemblages have similar temperature stability fields at the same pressures when X_{CO_2} = 1 and X_{CO_2} = 0.5, with the exception of forsterite + akermanite + spinel + calcite which is stable over a reduced pressure range when X_{CO_2} = 0.5 (Figure 7.3). The assemblages (1) merwinite + gehlenite + periclase + spinel and (2) larnite + gehlenite + periclase + spinel are stable are a greater pressure range when X_{CO_2} = 0.5 (Table 7.3). A T-X_{CO_2} pseudosection was computed to illustrate the effects that change in the composition of the CO_2-bearing fluid phase has on the mineral assemblages produced at *P* = 1 kbar (Figure 7.4). All possible mineral assemblages generated in Figure 7.3 are reproduced.

Table 7. 3: Temperature and pressure at which mineral assemblages are stable for X_{CO_2} = 1 and 0.5

Mineral assemblage	**X_{CO_2} = 1**		**X_{CO_2} = 0.5**	
	Temperature (°C)	**Pressure (kbar)**	**Temperature (°C)**	**Pressure (kbar)**
Fo + di + hc + cal	600 - 820±5	0.6-1.6	600 - 755±80	0.6 - 1.6
Fo + di + spl + cal	820±5 - 900±80	0.6-1.6	755±80 - 83 ±108	0.6 - 1.6
Fo + ak + spl + cal	900±80 - 920±130	0.6-1.6	880±108 - 975	0.9 - 1.6
Fo + mtc +spl	920±130 - 1050±150	0.6-1.6	830±108 - 980±140	0.6 - 1.6
Mtc + per + spl	1050±150 - 1180±110	0.6-1.6	980±140 -1120±36	0.6 - 1.6
Mw + per + spl	1180±110 - 1280±70	0.6-1.6	1120±36 -1202±148	0.6 - 1.6
Mw + gh + per + spl	1280±70 - 1295±55	0.6 - 0.85	1202±148 - 1238±112	0.6 - 1.4
Lrn + gh + per + spl	1295±55 - 1350	0.6 - 0.7	1238 ±112- 1350	0.6 - 1.3

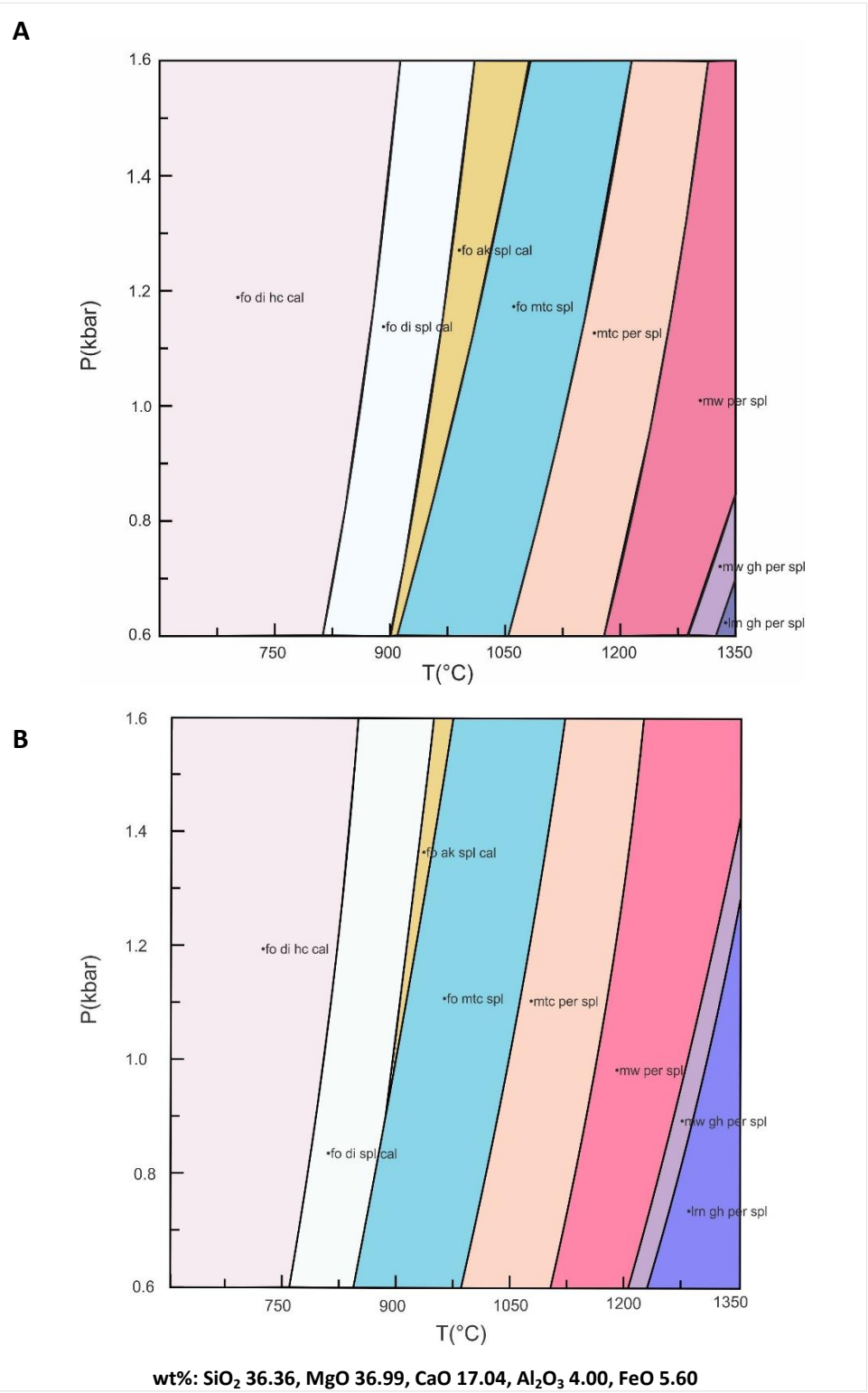

Figure 7.3: Calculated *P-T* pseudosection representing the bulk rock composition of the main xenolithic body considering CaO-MgO-SiO_2 together with Al_2O_3 and FeO for (A) X_{CO_2} = 1. And (B) X_{CO_2} = 0.5. The bulk composition used to calculate this pseudosection is included at the bottom of this diagram.

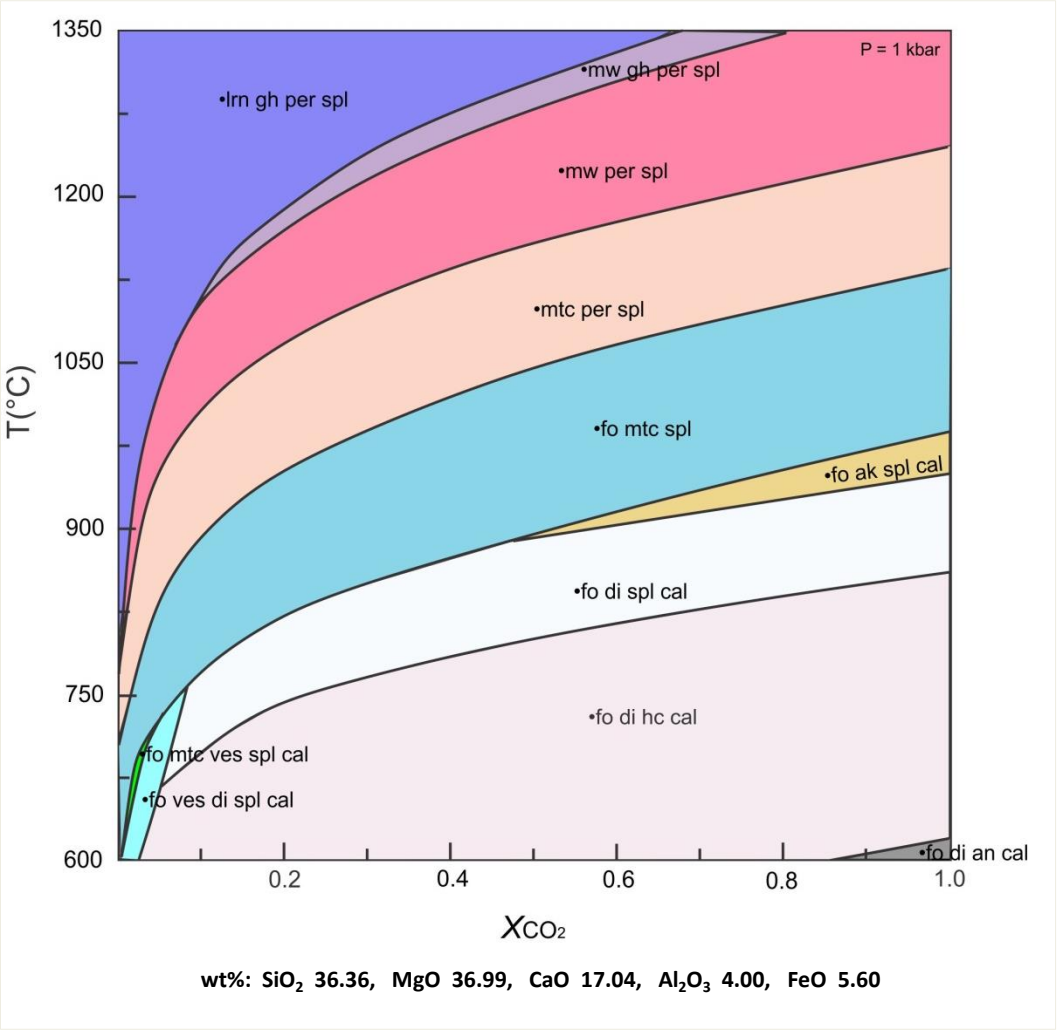

Figure 7.4: Calculated *T*-X_{CO_2} pseudosection representing the bulk rock composition of the main xenolithic body considering CaO-MgO-SiO_2 together with Al_2O_3 and FeO at P = 1 kbar. The bulk composition used to calculate this pseudosection is included at the bottom of this diagram.

7.4 Discussion

Bowen (1940) showed that the progressive metamorphism of siliceous limestones and dolostones produces 10 indicator minerals of metamorphic grade. In order of increasing temperature these minerals are tremolite, forsterite, diopside, periclase, wollastonite, monticellite, akermanite, spurrite, merwinite and larnite. The occurrence of monticellite together with forsterite places the xenolith in the monticellite-forsterite subfacies of the sanidinite facies, as indicated by Fyfe *et al*. (1958), and is indicative of high-temperature, low-pressure contact metamorphism.

7.4.1 Prograde metamorphism

According to the experimental studies of Irvine and Sharpe (1982), the temperature of the Bushveld magma was between 1200–1300 °C and the overburden pressure in the Critical Zone was between 0.6–1.6 kbar at the time of emplacement. Wallmach *et al*. (1989) proposed that the absence of merwinite in the calc-silicate xenoliths found in the Marginal Zone on the Eastern Limb, indicates that temperature and pressure did not exceed 1390 °C and 3.1 kbar, and the absence of periclase indicates that pressure did not exceed 2.4 kbar. According to Irvine and Sharpe (1982) and Wallmach *et al*. (1989), overburden pressure at the time of emplacement in the Marginal Zone was between 1.1 and 2.4 kbar and at P = 0.6–1.6 kbar in the Critical Zone. Based on the studies done by Irvine and Sharpe (1982) and Wallmach *et al*. (1989), pressures between 0.6–1.6 kbar were considered appropriate in this study.

The composition of the fluid phase at peak metamorphic temperatures is considered as $X_{CO_2} = 1$ for and is supported by Wallmach *et al*. (1989) for the following five reasons: (1) It is common that low-temperature fluids are rich in H_2O, while an increasing CO_2 content in fluids correlates to higher-grade metamorphism in a carbonate system (Fyfe *et al*., 1978; Wallmach *et al*., 1989). The decomposition and dehydration of OH-bearing minerals take place at temperatures which are much lower than the temperatures that are attained by this xenolith, according to the observed mineral assemblage. The only OH-bearing mineral found in this sample suite is vesuvianite, which is not found in the main xenolithic body, and which is interpreted as retrograde in origin. (2) According to Wallmach *et al*. (1989), the infiltration of H_2O into a xenolith during prograde metamorphism, in the process of decarbonation, is unlikely. This is because during the process of decarbonation, the reactions taking place allow for partial pressure of the fluid phase to be the same as total pressure, while a much lower partial pressure of the fluid phase exists in the magma surrounding the xenolith. (3) The xenolith is completely surrounded by magma during prograde metamorphism. Given that H_2O is more soluble than CO_2 in magma (Burnham, 1979), if any H_2O is present in the fluid within the xenolith, it would likely diffuse into the magma and result in a CO_2-rich fluid phase in the xenolith. (4) The fast heating and degassing of the xenolith during prograde decarbonation causes loss of volume and

prevents magmatic fluids from infiltrating the xenolith (Wallmach *et al*., 1989). (5) Roedder (1984) has shown that fluid inclusions found in high-grade metamorphic minerals, such as monticellite and akermanite, are CO_2-rich. Based on these factors, it is assumed that $X_{CO_2} = 1$ for prograde metamorphism is a reasonable assumption.

High-grade minerals such as akermanite, periclase, merwinite and larnite are predicted using the bulk rock composition of the xenolith (Figure 7.3). These minerals, with the exception of larnite, have been observed in calc-silicate xenoliths found in the Upper, Critical and Marginal Zones in the Eastern Limb (Willemse and Bensch, 1964; Wallmach *et al*., 1989). Forsterite and monticellite could have been produced by the additional reactions below, as noted in Figure 7.2 and studied experimentally by Walter (1963) and Yoder (1968):

$$3CaMgSiO_4 + CaMgSi_2O_6 \leftrightharpoons 2Ca_2MgSi_2O_7 + Mg_2SiO_4 \quad (6)$$
Monticellite diopside akermanite forsterite

$$Ca_2MgSi_2O_7 + Mg_2SiO_4 + CaCO_3 \leftrightharpoons 3CaMgSiO_4 + CO_2 \quad (7)$$
Akermanite forsterite calcite monticellite

$$CaCO_3 + CaMgSi_2O_6 \leftrightharpoons Ca_2MgSi_2O_7 + CO_2 \quad (8)$$
Calcite diopside akermanite

$$Ca_2MgSi_2O_7 \leftrightharpoons CaMgSiO_4 + CaSiO_3 \quad (9)$$
Akermanite monticellite wollastonite

$$CaCO_3 + SiO_2 \leftrightharpoons CaSiO_3 + CO_2 \quad (10)$$
Calcite quartz wollastonite

Monticellite cannot be produced under low temperature and high X_{CO_2} conditions, therefore it is unlikely that forsterite formed by reaction 6. Monticellite could have been produced by reaction 7 if akermanite was produced in the earlier reaction 8, and assuming that diopside is completely consumed, which is possible as no diopside is evident in the xenolith. Mineral assemblages Cal + Ak + Mtc and Cal + Mtc + Fo are produced by reaction 7. No petrographic evidence exists to support the presence of akermanite. However, reaction 7 could have produced the mineral assemblage containing monticellite and forsterite if akermanite was

consumed. It should be noted that, although minor amounts of calcite are found in the xenolith, it never occurs together with/in mutual contact with both monticellite and forsterite (Figure 3.3). Reaction 9 takes place during retrogression (Wallmach *et al*., 1989), and since no petrographic or textural evidence exists to support the presence of secondary monticellite or retrogressive textures involving monticellite, it is assumed that monticellite did not form as a result of reaction 9 in the main xenolithic body.

Gehlenite, the Al-bearing end-member of akermanite, could have produced spinel in the prograde reaction 4 or the retrograde reaction 5. Given that the formation of gehlenite is favourable according to the bulk rock composition, it is possible that either reaction 4 or 5 is responsible for the development of spinel; however, again, no petrographic evidence was found to assess this. Alternatively, spinel may have formed at lower metamorphic grades from pre-existing Al-bearing minerals such as Mg-Fe chlorite (Wallmach *et al*., 1989).

The observed peak metamorphic assemblage in the Western Limb xenolith is Mtc + Fo + Spl. Metamorphism of lower-grade minerals, calcite, tremolite and dolomite, formed forsterite during reaction 1 or 2 listed above, and monticellite formed by reaction 3. Although the bulk rock composition indicates that formation of higher-grade minerals such as akermanite, periclase, merwinite and larnite is possible (Figure 7.3), there is no evidence to support the presence of these minerals. Based on the observed mineral assemblage in the xenolith, the peak temperature is considered to have been reached at between ~975–1125 °C, at pressures between 0.6–1.6 kbar, with a fluid composition of $X_{CO_2} = 1$ (Figure 7.3A).

Wollastonite occurs as a single large crystal in one sample only (RSTX26-13). The wollastonite-forming reactions include reaction 9 and reaction 10 (Bowen 1940). There is no evidence of wollastonite forming as part of the prograde assemblage in the main xenolithic body, and the bulk rock composition does not favour its formation. However, wollastonite is found in the contact zone and possibly formed by reaction 9 at $T = 700$ °C (Harker and Tuttle, 1956). This does, however, imply that akermanite/melilite-bearing minerals were present on the prograde path in the contact zone. It should be noted that wollastonite is predominantly found as exsolution lamellae in CaTs-clinopyroxene in the contact zone and occurs in the igneous assemblage in a pseudo-ophitic texture as shown Figure 3.12. It does

not form part of any equilibrium assemblage with other minerals and its possible formation will be discussed further in Chapter 8.

Uvarovite is commonly considered to have been formed by metamorphic metasomatic reactions (Proenza *et al*., 1999; Klemme *et al*., 2005) due to the influence of hydrothermal Ca and Si-bearing fluids interacting with chromite (Wan and Yeh, 1984; Proenza *et al*., 1999; Klemme *et al*., 2005). This garnet cannot form without the pre-existing Cr-bearing minerals and is commonly observed replacing chromite grains (Proenza *et al*., 1999). Ca required for the development of uvarovite is likely to originate from the xenolith. Frankel (1959) studied this phenomenon where uvarovite is associated with chromite in the chromitite seams in the Eastern Limb of the Bushveld Complex and will be discussed in Chapter 8.

7.4.2 Retrograde metamorphism

Retrograde minerals in the sample suite include, vesuvianite and garnet, together with textures such as (1) garnet + vesuvianite symplectites, and (2) grossular reaction coronas occurring between plagioclase and clinopyroxene. These are restricted to the contact zone and not observed in the main xenolithic body. From this it is concluded that retrograde hydration by infiltrating fluids affected the contact zone but did not significantly affect the main xenolithic body. Even in the contact zone, this relatively high-temperature retrogression is relatively limited. Low-temperature alterations along small faults displacing the xenolith were not investigated in this study owing to the highly friable, clay-rich, nature of the sample material.

Vesuvianite occurs in symplectites with grossular and as xenoblastic crystals in samples containing garnet, diopside and monticellite. It is generally interpreted to form from one or more of melilite, wollastonite, monticellite and diopside during retrograde hydration of high-grade precursor assemblages (Ito and Arem 1971; Valley *et al*., 1985). According to Shoji (1971), vesuvianite forms between 400–600 °C, with an upper stability limit of 700 °C in the presence of H_2O and $P > 1$ kbar. Figure 7.3 agrees with Shoji (1971) and illustrates that vesuvianite-bearing mineral assemblages are stable to ~750 °C. The presence of vesuvianite allows for the composition of the fluid phase infiltrating the contact zone to be determined.

As shown in Figure 7.4, vesuvianite-bearing assemblages are stable when $X_{CO_2} < 0.1$. This indicates that the fluid phase circulating during retrogression was highly H_2O-rich.

Grossular can also only be stable in the presence of H_2O-rich fluids, where $X_{CO_2} < 0.2$ (Valley *et al*., 1985). It occurs in symplectitic textures with vesuvianite due to replacement reactions (Wallmach *et al*., 1995) of the precursor high-grade minerals. Fe-bearing grossular crystals occur together with vesuvianite (Figure 4.10), and pure grossular occurs as reaction coronas between plagioclase and diopside, and in symplectites (Figures 3.13 and 3.15). Grossular formation is likely to have taken place together with vesuvianite (Wallmach *et al*., 1995) at $T > 500$ °C (Gnos and Armbruster, 2006).

7.5 Summary and conclusion

The peak metamorphic assemblage, Mtc + Fo + Spl, observed in the main xenolithic body indicates temperatures peaked between ~975–1125 °C, at pressures between 0.6–1.6 kbar. No petrographic evidence was found to suggest that higher-grade minerals such as melilite, gehlenite and akermanite could have been present in the xenolith and surrounding zones. On the prograde path, the fluid phase composition was CO_2-rich. No retrograde effects were observed in the main xenolithic body, while in the contact zone, the presence of H_2O-rich fluid facilitated the formation of vesuvianite and grossular at T 700–400 °C.

CHAPTER 8: DISCUSSION AND CONCLUSIONS

8.1 Introduction

The overall aim of this study was to investigate the scales of interaction between calc-silicate xenoliths and the surrounding Bushveld Complex magma in order to establish the role these xenoliths could have played in contamination/metasomatic effects in the host igneous rock assemblage. Previous detailed studies on calc-silicate xenoliths in the Eastern and Northern limbs of the Bushveld Complex have focussed primarily on the metamorphic assemblages within the xenoliths, aimed at establishing peak P-T conditions and their metamorphic history (Willemse and Bensch, 1964; Gain and Mostert, 1982; Wallmach *et al*., 1989 and 1995; Buick *et al*., 2000). Apart from Willemse and Bensch (1964), little to no focus was given to the interaction of these xenoliths with the surrounding magma. However, Gain and Mostert (1982) proposed extensive xenolith-magma interaction in the Platreef and stable isotopic studies by Harris and Chaumba (2001) and Pronost *et al*. (2008) have invoked significant large-scale interaction between the Transvaal Supergroup carbonates and RLS magma in the Northern Limb, although these authors do not specifically discriminate between xenoliths and footwall*, sensu stricto*, as the source of these anomalies.

8.2 Zwartfontein xenoliths

Xenoliths studied from the Platreef at Zwartfontein show two main mineral assemblages - Mtc + Di + Fo + Spl, and Di + Cal + Anh + Srp - and one xenolith comprises mostly calcite, with microcrystalline Mg-rich aggregates that might represent pseudomorphs after forsterite. If, as proposed by Gain and Mostert (1982), larger xenoliths show lesser degrees of alteration and higher – grade metamorphic assemblages compared to smaller xenoliths, this variation in mineralogy may relate to xenolith size and/or the degree of alteration. The xenolith preserving monticellite displays the least amount of alteration. The lower-grade assemblages in the other two xenoliths and the presence of pseudomorphs would then be consistent with them representing either smaller xenoliths or the edges of larger xenoliths and having experienced greater amounts of retrograde hydrothermal alteration.

Gain and Mostert (1982) proposed that extensive alteration zones around xenoliths formed as CO_2, H_2O and possibly S were released from the xenoliths during prograde metamorphism. They maintained that CO_2 was more easily absorbed into the magma compared to H_2O, therefore H_2O may have remained within the confines of the xenolith and caused retrogression and serpentinisation during cooling. Alternatively, H_2O could have resulted in the development of localised pegmatoidal regions in other rock-types in close proximity to the xenoliths (Gain and Mostert, 1982).

In contrast to Gain and Mostert (1982), Appiah-Nimoh (2004), Sharman-Harris *et al*. (2005) and Mavimbela (2013) have suggested that the degree of alteration of Platreef xenoliths is influenced by their distance from the footwall contact. They attributed this to the greater volume of decarbonating and dehydrating footwall and the fact that fluids would be generated progressively later as the contact metamorphic heat front spread downwards into the footwall. Similarly, such fluids would be lower-temperature than, and overprint, those derived from the xenoliths. Extensive serpentinisation of the prograde assemblages has taken place together with development of very fine – crystalline Mg – rich alteration products in xenoliths of this study.

Parapyroxenites are a common feature of the Zwartfontein borehole cores studied herein, consistent with observations from previous studies that have focussed on Platreef interactions with the dolomitic footwall (Harris and Chaumba, 2001, Kinnaird *et al*., 2005; Sharman-Harris *et al*., 2005; Pronost *et al*., 2008; Klemd *et al*., 2020). Clinopyroxene in the Zwartfontein parapyroxenites and calc-silicate xenoliths shows slightly elevated Ca, Fe^{3+} and Al values (section 4.3.3), which are common features of carbonate-magma interactions (Joesten, 1997; Gaeta *et al*., 2009; Whitley *et al*., 2020). These elevated values are absent in Platreef pyroxenite and norite (Harris and Chaumba, 2001; Pronost *et al*., 2008); however, clinopyroxene rich in Ca-Tschermak component, *sensu stricto*, has not been identified in this study or any previous studies. $\delta^{18}O$ values from this study for plagioclase and pyroxene agree with previous studies (Harris and Chaumba, 2001; Sharman-Harris *et al*., 2005; Pronost *et al*., 2008) and are elevated relative to the RLS lithologies at the Marikana locality in the Western Limb (Chapter 6); however, evidence of direct contamination of the magma

by an individual xenolith could not be established in this investigation. Given the evidence of more widespread $\delta^{18}O$ enrichment in the Platreef at Sandsloot (Harris and Chaumba, 2001; Pronost *et al*., 2008) and Tweefontein, Turfspruit and Macalacaskop (Sharman-Harris *et al*., 2005; Pronost *et al*., 2008) it seems likely that it originated from more pervasive fluid movement derived from the footwall to the Platreef. However, it is possible the parapyroxenite could be the product of *in situ* breakdown and assimilation of calc-silicate xenoliths and rafts that may have been completely digested by the magma.

As noted in chapters 2 and 6, the footwall to the xenoliths investigated is primarily Malmani dolomite and granite. Harris and Chaumba (2001) proposed that contamination of the Platreef magma was effected by interaction with this footwall, with up to 18 % assimilation of dolomitic footwall into the magma. The exact mechanism of how dolomite become incorporated is, however, not clear (Harris and Chaumba, 2001; Pronost *et al*., 2008).

8.3 Marikana xenolith

8.3.1 The xenolith and contact zone

Unlike at Zwartfontein and in the Platreef as a whole, carbonate-magma interaction associated with the Marikana xenolith has produced clear spatial variation at a range of scales that can be confirmed in different ways (mineralogy, major and trace mineral chemistry, stable isotopes). Using the definitions of Heinonen *et al*. (2021), the Marikana xenolith appears to display a combination of stoping along its western margin that isolated fragments of the xenolith from the main body and that now lie in a plagioclase-diopside matrix with pseudo – ophitic igneous textures (Figure 8.1), and hybridisation of RLS magma and melt from the metamorphosing xenolith. Both stoping and hybrid layering showing a zonal arrangement are reported from the Eastern Limb xenoliths by Willemse and Bensch (1964). These features and processes, and their implications for a general model of calc-silicate – magma interaction, and specifically for calc-silicate xenoliths in the RLS, are discussed in more detail below.

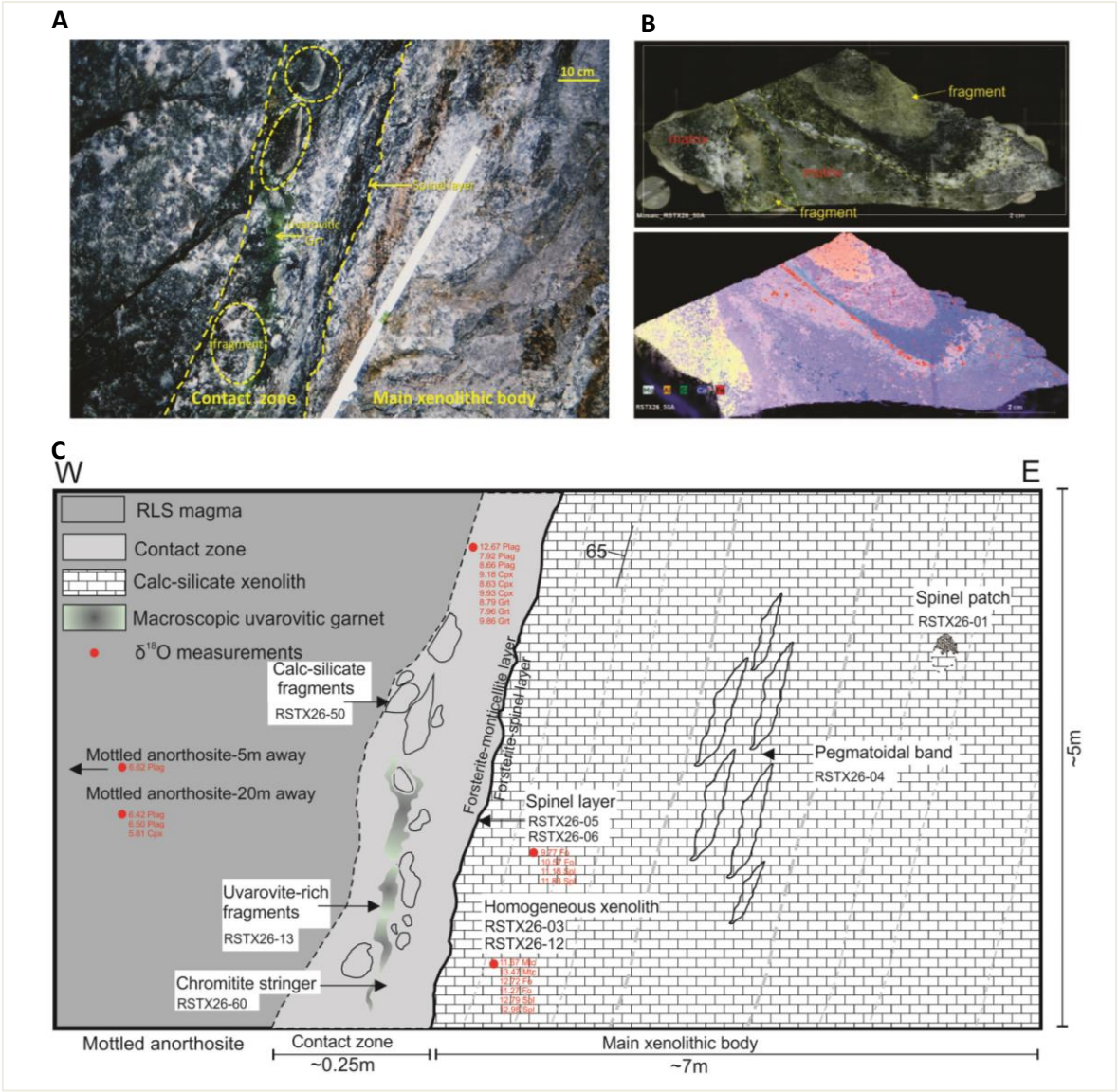

Figure 8.1: The Marikana xenolith and immediate surroundings. (A) Photograph of the sample site showing the xenolith, contact zone and surrounding igneous rock. (B) Enlarged image of calc-silicate rock fragments in the contact zone and corresponding micro-XRF composite of major elements. (C) Schematic diagram of the xenolith and surrounding contact zone showing $\delta^{18}O$ measurements.

The second component of the evolving system is the RLS magma. It is beyond the scope of this study to discuss the contrasting models for the development of magmatic layering, and specifically anorthosite and chromitite layers, in the RLS. However, while the Marikana xenolith currently lies in mottled anorthosite, the presence of the chromitite stringer with strong similarities to the UG 1 chromitite layer needs to be factored into any model. Bulk chemistry of the contact zone samples (section 2.2.3) is broadly consistent with an

anorthosite endmember that has undergone significant Ca, Fe and Mg enrichment at the expense of Al and Si. While Willemse and Bensch (1964) and Mollo *et al*. (2010) maintain that MgO, FeO and Al_2O_3 can migrate into the magmatic component from the xenolith, in general such evidence may not be clearly visible in carbonate-magma systems owing to the facts that many of the localities described in the literature (a) involve limestone, which is largely devoid of these components, and/or (b) involve a mafic to ultramafic magma, in which these components are already present in significant quantities. The presence of anorthositic magma in the Marikana locality is thus unusual and provides an opportunity to investigate the relative extents of diffusion of, for example, Ca vs Mg during xenolith breakdown.

Mottled anorthosite was compared with whole-rock data of anorthosite studied by Maier (1991) located in the Upper Critical Zone (Western Limb). Mottled anorthosite in this study shows little to no variation in composition when compared to Maier (1991; section 5.2). This indicates that the mottled anorthosite surrounding the xenolith is typical RLS anorthosite. In the contact zone, however, Al_2O_3 drops from the average (~30 wt%) for RLS mottled anorthosite to only ~16 wt%. Given that the Al_2O_3 content of the xenolith ranges from only ~3 wt% to ~7 wt%, the contact zone may be considered, at a first approximation, to comprise almost equal contributions of xenolith and magma; however, a more complex pattern emerges with CaO, FeO and MgO (section 2.2.3). In terms of CaO, the contact zone shows values that are almost double that of the anorthosite (and 3-4 times that of norite; Table 2.1). These are at least as high, and commonly exceed, the CaO values of the xenolith itself, indicating significant decarbonation of the xenolith during prograde heating (see also Willemse and Bensch, 1964). The Marikana contact zone confirms Willemse and Bensch's (1964) proposal of greater mobility of Ca versus Mg in the Eastern Limb xenoliths, as MgO in the contact zone (8.6 wt%) is significantly lower than in the xenolith (>26 wt%). Nonetheless, the contact zone is considerably enriched in MgO relative to the anorthosite (~1 wt%; Table 2.1). The contact zone shows a similar FeO content (~6 wt%) to the xenolith, but is significantly higher in FeO relative to the anorthosite (~1 wt%; Table 2.1). This suggests that Fe may have been more mobile than Mg, and perhaps similar to Ca. Should a future opportunity arise, more closely spaced sampling might be able to further investigate length scales of diffusion of these components; however, it must be noted that the contact

zone is texturally highly heterogeneous, may have involved mechanical stoping that implies a non-static system, and contains evidence in the form of the chromitite stringer that suggests significant bulk movement between the xenolith and its host prior to magma crystallisation (see section 8.6).

O isotopes (chapter 6) confirm that xenolith contamination effects of the magma are restricted to the contact zone. $\delta^{18}O$ values of 6.62‰ for plagioclase in mottled anorthosite 5 m away from the xenolith are indistinguishable from those located 20 m away (6.42‰ – 6.50‰) from the xenolith and are consistent with the magmatic values obtained by previous studies in the Critical Zone in the Western and Eastern Limbs (Schiffries and Rye, 1989; Reid *et al*., 1993; Harris *et al*., 2005).

Decarbonation of the calc-silicate xenolith involves reactions that took place during prograde metamorphism where dolomite was the main reactant (chapter 7). $\delta^{18}O$ values in the xenolith for monticellite and forsterite are comparatively lower than unaltered dolomites from the Malmani Subgroup (Buchanan *et al*., 1981) and Duitschland Formation (Buick *et al*., 2000) but are consistent with the lowering expected from metamorphism (Buick *et al*., 2000). The presence of a forsterite-spinel layer (Figure 2.4) at the edge of the xenolith resembles a pattern recorded by Willemse and Bensch (1964) in a calc-silicate xenolith located in the Upper Zone of the Eastern Limb, which they attributed to loss of CaO or $CaCO_3$ from the xenolith, leaving an MgO-enriched core. According to Willemse and Bensch (1964) and Wenzel *et al*. (2002), during devolatilization of the xenolith calcium carbonate is more soluble than magnesium silicate; therefore, calcium carbonate would migrate away from the xenolith leaving behind a Mg-rich, forsterite-rich layer (Wenzel *et al*., 2002). However, in the Marikana xenolith the forsterite-spinel layer forms part of a package that includes a forsterite-monticellite layer further outboard of the xenolith core. Owing to limited exposure, it could also not be established if the forsterite-spinel layer is continuous around the xenolith. Finally, the orientation of the layer is consistent with the presumed relict sedimentary bedding in the xenolith. From this, we conclude that the spinel layer is an artefact of sedimentary bedding in the protolith rather than the product of differential diffusion effects during prograde decarbonation.

The enrichment of Ca in the contact zone seen in the bulk rock compositional data is confirmed in the extremely calcic compositions of plagioclase (An_{99}; section 4.3.4), Ca-Tschermak-rich clinopyroxene (section 4.3.3) and wollastonite inclusions found in the clinopyroxene that we interpret as exsolution lamellae (Figures 3.12 and 4.6). Reaction coronas involving plagioclase and clinopyroxene that occur in association with calc-silicate fragments are also another sign that the contact zone is compositionally anomalous (Figures 3.13 and 4.6). The clinopyroxene in the contact zone is a solid solution between diopside and Ca-Tschermak's components, which is a common characteristic of contact metamorphic settings that involve carbonate – magma interaction (Tilley and Harwood, 1931; Joesten, 1977; Gaeta *et al*., 2009; Whitley *et al*., 2020) and is attributed to $CaCO_3$ assimilation into the magma (Gaeta *et al*., 2009; Mollo *et al*., 2010). Furthermore, the presence of Fe^{3+} in the clinopyroxene implies that this contamination of the magma by the xenolith was accompanied by an increase in oxygen fugacity during crystallisation, as also noted by Tracey *et al*. (1978), Owens (2000) and Wenzel *et al*. (2002). According to Wenzel *et al*. (2002), more oxidising conditions in the magma would favour crystallisation of olivine with higher *Mg#* and spinel with lower *Cr#*. Olivine is not found in the magmatic matrix of the contact zone; however, chromite does show systematic shifts in major and trace elements that are consistent with increased oxidation (sections 4.3.5.3 and 5.4).

Wollastonite is only present as inclusions in the Ca-Tschermak-rich clinopyroxene in the pseudo-ophitic igneous matrix assemblage in the contact zone (Figure 3.12). As such, it cannot be interpreted as a retrograde phase signifying hydrous fluid conditions, as is most commonly inferred in metamorphic studies of calc-silicate systems (e.g., Harker and Tuttle, (1956); Hochella *et al*. (1982); Mathavan and Fernado, (2001)). Based on its occurrence as oriented inclusions, it is interpreted as exsolution lamellae produced during cooling of the clinopyroxene when large-radius Ca ions were expelled from the shrinking crystal lattice. This may imply that the temperature of crystallisation would have exceeded the normal range for wollastonite stability.

At some point in their post-crystallisation history, cumulus plagioclase and intercumulus clinopyroxene became unstable in the contact zone, leading to development of grossular coronas (Figure 3.12A). Wallmach *et al*. (1995) interpreted grossular as a product of hydrous

fluid influx during retrogression (Grammatikopoulos and Clark, 2006) at ~600/700 °C. Given the presence of grossular-vesuvianite symplectites in the vicinity of the calc-silicate fragments in the contact zone, the grossular corona texture between the Ca-Tschermak-rich clinopyroxene and plagioclase is interpreted as having formed in response to post-magmatic fluid infiltration that catalysed partial reaction between the two phases.

In contrast to the grossular, uvarovite is interpreted as having formed by a different process. The pure uvarovite endmember does not exist in nature: instead it is normally associated with significant amounts of grossular and andradite solid-solution (Proenza *et al*., 1999). This phenomenon is observed in uvarovite within this sample suite. According to Frankel (1959), who studied the occurrence of uvarovite in the Lower Group chromitite seams in the Eastern Limb, it is only possible for uvarovite to form if chromium is already present in the system in the form of chromite, with the addition of CaO into the system also being required. He concluded that pockets of uvarovite developed where calc-silicate xenoliths were completely digested. Uvarovite found in the sample suite is intimately associated with Cr – spinel (Figures 3.12B and 4.40). Where uvarovite occurs without the presence of Cr – spinel, complete replacement of the latter is inferred (Figure 3.12A and 4.41). According to Frankel (1959), Wan and Yeh, (1984), Proenza *et al*. (1999) and Klemme *et al*. (2005), although uvarovitic garnet forms in the presence of chromite by metasomatic reactions, it is unclear whether they regard this as "igneous crystallisation" or "metamorphic recrystallisation" (Wan and Yeh, 1984; Viswanathiah *et al*. 1979; Graham *et al*., 1996; Arai *et al*., 1999). However, all agree that uvarovite cannot develop without the presence of pre-existing Cr-bearing minerals, particularly Cr-rich spinel. This indicates that chromite would have already crystallised before the addition of CaO into the contact zone. The formation of uvarovite requires the addition of Ca and Si (Frankel, 1959; Wan and Yeh, 1984) to the Cr and Al that derive from the Cr – spinel.

EMP and trace element analysis of zoned Cr-bearing spinels in the contact zone show that Cr, V, Mn, Co, Ni, Zn and Ga decrease towards the rims, whereas Al, Mg and Fe^{3+} increase (section 5.4). In comparison, trace elements analysed from UG 1 chromitite do not exhibit core to rim zoning. This difference is attributed to increasing levels of hybridisation of the anorthositic magma closest to the decarbonating xenolith. Taken together with the EMPA

and X-ray mapping data for the uvarovite garnet (section 4.3.6.2), which show that the garnet also displays core to rim zoning towards lower Cr and higher Al, Mg and Fe^{3+} (section 4.3.6.2), all of these features are consistent with a magma in which chromite spinel had started to crystallise but that then became overwhelmed by xenolith components. Based on this, we suggest that uvarovite in this case is igneous-metasomatic as it crystallised directly from the contaminated magma, seeded by already-nucleated chromite grains and that it is thus contemporaneous with, or even predates, the plagioclase-clinopyroxene texture. The zoned margins of the Cr-spinel cores to the uvarovite clusters may also indicate the first signs of this contamination and hybridisation of the magma.

The chromitite stringer proximal to the xenolith, on average, contains the least amount of Cr relative to the intermediate and distal samples. The intermediate stringer exhibits the same core-to-rim trends as the proximal samples, although cation proportions differ slightly. In the proximal and intermediate stringer Cr content decreases and Al increases from core to rim, and Fe^{3+} remains relatively constant (Figure 4.33 A to C). The distal stringer does not display core-to-rim heterogeneity. This indicates that effects of the decarbonating xenolith are more pronounced in the proximal and intermediate stringers and is reiterated by the amount of uvarovitic garnet associated with each stringer. Based on Figures 2.12, 3.14 and 3.15 it is evident that uvarovitic garnet is more dominant in the proximal stringer compared to the distal stringer. In addition, both garnet and spinel are similarly zoned; garnet cores are uvarovite-rich ($Ca_3Cr_2Si_3O_{12}$) and rims are grossular-rich ($Ca_3Al_2Si_3O_{12}$); Cr-spinel inclusions show Cr-rich cores and Al-rich rims. This may indicate that the magma-cumulate matrix surrounding the stringers became more Al-rich as the contact zone evolved via increasing contamination from the xenolith.

8.3.2 Origin of the chromitite stringer and spinel layer

Spinel data obtained from the Marikana locality, together with UG 1 chromitite data, are compared with the global dataset of Barnes and Roeder (2001) in Figure 8.2. The ternary plots show the 50^{th} and 90^{th} percentile contours for 681 chromite analyses from layered intrusions and 341 spinel analyses from high-grade metasedimentary rocks (Barnes and Roeder, 2001). These geological settings show distinct differences that allow investigation of

the Marikana spinel data. Based on section 4.3.5, three spinel compositional types occur within the Marikana sample suite, namely: (1) Cr-rich spinel and chromite found in the contact zone and UG 1 chromitite; (2) spinel, *sensu stricto,* located in the main xenolithic body and the spinel layer at its margin; and (3) magnetite exsolution lamellae hosted in spinel, *sensu stricto.* Based on textural analysis, these can be separated into magmatic (1) and metasedimentary (2 + 3), however, as discussed below, some evidence exists for transitional compositions that are interpreted as tracking magma hybridisation in the contact zone.

Figure 8.2A shows that chromite grains from the UG 1 chromitite layer plot mainly within the 90th percentile contour of all chromite analysed from layered intrusions. Chromite from the chromitite stringer distal and intermediate to the xenolith plot between the 90th and 50th percentile contours, with some analyses plotting outside the contours. In contrast, analyses from the proximal chromitite stringer plot outside the 50th percentile contour. Zoned Cr – rich spinel that is found in samples containing calc-silicate fragments plots close to the 50th percentile contour, although the cores are comparable with the UG 1 chromite composition, whereas the Al-rich rims show a greater affinity with high grade metasedimentary spinel (Figure 8.2B). The spinels from the core of the xenolith and its marginal spinel layer lack significant Cr and do not plot within the percentile contours calculated for chromite in layered intrusions. Spinel, *sensu stricto,* plots within the 50th percentile contour for spinel in high grade metasedimentary rocks (Figure 8.2B), whereas the Fe-rich (magnetite) exsolution lamellae do not plot within the contours. From this we conclude that Cr – rich spinel in the contact zone and chromite originate from the same source, namely, the RLS magma, whereas the Mg, Al, Fe – rich spinel that contains varying amounts of magnetite exsolution is metasedimentary in origin and related to the xenolith. However, as seen in Figure 8.2, zoned spinels in the contact zone evolve from a magmatic type towards a more metasedimentary type.

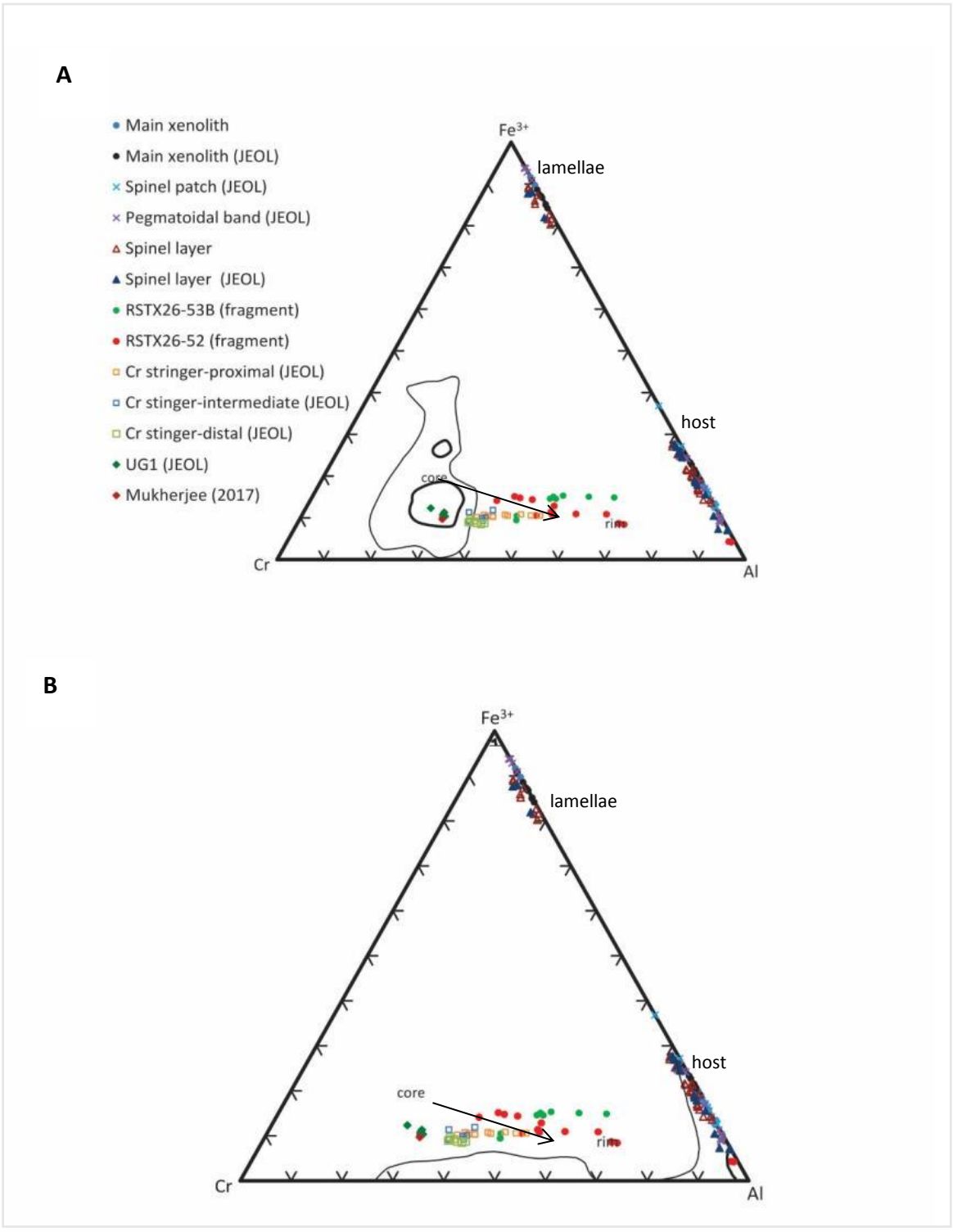

Figure 8.2: Data density plot of the global spinel dataset of chromite in layered intrusions (A), and high-grade metasedimentary rocks (B) compiled by Barnes and Roeder (2001), compared with spinel from the current study and chromite from the UG 1 chromitite. The data density plots represent the 50th (thin line) and 90th (thick line) percentile contours calculated from the full Barnes and Roeder (2001) dataset.

Potential mechanisms that control the crystallisation of chromite in magmas need to be considered owing to the presence of the UG 1 chromitite 20 m away from the xenolith and the chromitite stringer in the contact zone. There are several suggested ways for chromite to crystallise within RLS magmas (Kinnaird *et al*., 2002): (1) injection of chromite-phyric magma into the chamber. This requires the precipitation of chromite at a greater depth and its entrainment in a rising magma prior to emplacement; (2) increased pressure in the magma chamber would stabilise spinel and orthopyroxene at the expense of the olivine and plagioclase at crustal pressures (1-10 kbar); therefore, alternating chromite and/or orthopyroxenite layers and dunite or anorthosite layers could reflect varying pressure conditions in the magma chamber. However, the magnitude of change required to shift magma composition from a cotectic to a field of chromite-only is not certain; (3) crystal settling in a large magma chamber induced by gravity; (4) mixing between resident and new magma; (5) contamination by a siliceous component; and (6) contamination by a siliceous component of the new magma and subsequent mixing with resident magma. The proposed model of chromitite formation in the Bushveld Complex by Kinnaird *et al*. (2002) suggests that extreme variation in strontium isotope compositions observed in chromitites, compared to the under- and overlying lithologies, cannot be attributed to the contamination of new mantle-derived magma mixing with resident magma alone. The proposed model (Kinnaird *et al*., 2002) involves aspects of crustal contamination of the new magma by a SiO_2-bearing roof-rock melt (later crystallised to granophyre) and subsequent mixing of the new magma with resident magma. This model accounts for the extreme changes in strontium isotope ratios in chromitites. Applying this model to the Marikana samples, at first glance, the chromite may then be considered to have crystallised as a result of interaction between the xenolith and the RLS magma to produce the chromitite stringer found in the contact zone. This would have taken place in the early stages of prograde metamorphism of the xenolith. However, given that the xenolith is not highly siliceous as noted in section 2.2.3, the mechanisms proposed by Kinnaird *et al*., (2002) may not be sufficient to explain the origin of the chromitite stringer in this case. Therefore, the different spinel minerals in this study must be considered in order to investigate other possibilities that may have resulted in the presence of Cr in the contact zone. Primarily, the question is whether the Cr-rich spinel/chromite formed *in situ* or whether it was derived from a pre-existing layer.

The spinel layer at the westernmost edge of the xenolith is composed of spinel, *sensu stricto,* with magnetite exsolution lamellae and shows polygonal granoblastic textures. Willemse and Bensch (1964) suggested that spinel associated with calc-silicate xenoliths in the Eastern Limb was sedimentary in origin, as dolomitic rocks interlayered with pelitic bands from the Pretoria Group are spinel-bearing (Willemse and Bensch, 1964). A few calc-silicate xenoliths studied by Willemse and Bensch (1964) that were originally banded sedimentary rocks, contain zones in which the spinel concentration is so high it led to macroscopically identifiable dark bands.

Irrespective of the mechanism by which essentially monomineralic chromitite layers formed in the RLS, or the bulk intrusion mechanism of the RLS magma(s) that led to the isolation and incorporation of country rock xenoliths, it is necessary to consider the significance of the chromitite stringer in the contact zone adjacent to the Marikana xenolith for evolution of the magma-xenolith system.

The Critical Zone (CZ) in the Western Limb contains a number of chromitite layers (Figure 1.4), from LG 1 to 7 in the LCZ, MG1 and 2 in the middle CZ, MG 3 and 4 near the base of the UCZ, to the UG 1 and 2 chromitite layers in the upper parts of the UCZ. The host rock for most of the CZ is predominately pyroxenite, with some norite and anorthosite in the UCZ. The Marikana xenolith is located ~20 m vertically below the UG 1 chromitite that is being mined, and no significant chromitite unit occurs along-strike. Only the UG 1 and UG 2 chromitites are hosted in anorthosite. Given the bulk rock compositional evidence that suggests that the contact zone hosting the chromitite stringer is anorthositic in origin, and the similarity of the chromite compositions to the UG 1 chromites analysed by Mukherjee (2017), the UG 1 chromitite appears to be the most likely source of the chromitite stringer. This is further supported by the fact that chromitite stringers are generally absent between the MG 4 and UG 1 chromitite layers (Eales and Cawthorn, 1996; Lee 1996; Kinnaird *et al*., 2002; Kinnaird, 2005; Cawthorn, 2015). While Scoon and Costin (2018) noted stringers with thicknesses of up to a few millimetres in the UCZ in the Eastern Limb, it is not comparable with the stringer studied herein that has a total thickness of ~7 cm. It is, therefore, assumed that the stringer in this case is a unique occurrence of disrupted UG 1 chromitite.

If a UG 1 derivation for the chromitite stringer adjacent to the xenolith is proposed, then a mechanism to explain its out-of-sequence position is needed. The best explanation would be that the xenolith sank downwards through the still-forming chromitite, entraining, and possibly internally disrupting, part of the layer. This would require that the underlying anorthosite itself could not have been crystalline at the time, which raises interesting constraints on the formation of layering in the RLS. While a typical carbonate has a density of ~2.7-2.8 g/cm^3 (Schön, 2011), anorthosite a density of ~2.8 g/cm^3, pyroxenite 3.2 g/cm^3 and norite a density of ~2.9 g/cm^3 (Jones, 2015), two important qualifying observations of the Marikana scenario are that (a) as the xenolith undergoes metamorphism, its density would approach ~3.2 g/cm^3 (the densities of both forsterite and monticellite), and (b) the magmatic component was not solid, so its density at the time would have been lower than the solid-rock values listed above, possibly as low as ~2.6-2.7 g/cm^3 (L.D. Ashwal, pers. comm. 2021). Apart from the viscosity of the magmatic layers into which it was sinking, which would have varied as a function of the level of crystallisation, the distance that the xenolith would have been able to sink would be related to its volume, shape and the nature of the contact with the magma. Willemse and Bensch (1964) commented that xenoliths in the Eastern Limb are commonly elongate parallel to their bedding and that the bedding is discordant in terms of both strike and dip relative to the RLS layering. The steep westerly dip of inferred bedding in the Marikana xenolith (section 2.2.1) contrasts with the shallow northerly dip of the magmatic layering. It suggests that, while the xenolith may have originally comprised a subhorizontally-oriented slab, it rotated and speared downwards into the underlying crystal mush prior to the latter attaining sufficient viscosity to block further sinking. Owing to limited exposure, the present shape of the xenolith is unknown, but it could have undergone further *in situ* rounding by thermal corrosion which would have been enhanced at the slab ends.

While no signs of flow alignment or strain of plagioclase have been found in the mottled anorthosite flanking the xenolith, a model invoking a UG 1 origin for the chromitite stringer requires a significant level of crystallisation of the underlying anorthosite prior to UG 1 formation (and, thus, prior to sinking of the xenolith). Depending on its timing relative to the main decarbonation reactions, descent of the xenolith through the magmatic crystalline mush may have led to a mechanically evolving contact zone. For instance, magmatic units

contaminated by the initial decarbonation may now lie significantly above, and separated from, the xenolith, and the contamination zone may have undergone thinning caused by viscous drag during sinking. Although outcrop is limited, the slight downward convergence of the calc-silicate fragments towards the main xenolith edge suggested in Figure 8.1 would be consistent with sinking-induced attenuation. Similarly, the preferred vertical elongation of the uvarovitic garnet lenses and stringers is compatible with flow-induced stretching in the magmatic envelope around the sinking xenolith. Such extension may have increased the surface area exposed to the contamination front, and thus aided more complete replacement of chromite grains in these aggregates by uvarovite.

8.3.3 Constraints on fluid sources

Although evidence from the Marikana xenolith points to a protolith comprising both carbonate and silicate layers and components, the carbonate component dominates. Mafic-ultramafic magmas also carry limited hydrous fluid, and several studies have suggested that initial crystallisation of magma against a xenolith may restrict exchange between the xenolith and magma (Wallmach *et al*., 1995; Owens, 2000; Gaeta *et al*., 2009; Mollo *et al*., 2010). Consequently, it is reasonable to expect that the prograde-to-peak evolution of the xenolith would have been dominated by a CO_2-rich fluid phase, with any hydrous component likely being minor and preferentially partitioned into anatectic melts derived from pelitic layers that escaped the system. Once metamorphic decarbonation depleted the CO_2 source, however, fluid composition would inevitably have evolved to more hydrous compositions. While evidence for this hydrous fluid overprint is widespread, several alternative models for the fluid source have been proposed in previous studies, including:

1. trapped hydrous fluid in the xenolith (autometasomatism);
2. magmatic fluid (wet Main Zone magma or linked to slightly younger Lebowa Granite Suite intrusion);
3. dehydrating footwall during contact metamorphism; and
4. fluids linked to greenschist facies dynamothermal metamorphism associated with the penecontemporaneous Limpopo Orogeny to the north of the Bushveld Complex (e.g., Hales, 2020).

Stable isotope studies indicate that the RLS experienced widespread hydrothermal fluid infiltration that Schiffries and Rye (1990) suggested originated from dehydration of Transvaal Supergroup footwall rocks during contact metamorphism. Based on H and C isotopic data they estimated that the maximum temperature at which fluid-rock interaction took place was 710 °C, with late-stage veins in anorthosite in the Critical Zone corresponding to temperatures of ~300 °C (Schiffries and Rye, 1990).

Previous workers examining calc-silicate xenoliths in the Eastern Limb observed relatively pristine peak metamorphic assemblages in xenoliths in the Marginal and Critical Zones (Wallmach *et al*., 1986) but strong retrogression in other xenoliths in the Upper Zone (Wallmach *et al*., 1995 and Buick *et al*., 2000). Wallmach *et al.* (1986) proposed that conditions in the Marginal and Critical Zones remained dry whereas the presence of hydrous minerals such as vesuvianite, wollastonite and grossular in the Upper Zone xenoliths suggests relatively high-T retrograde fluid infiltration (Wallmach *et al*., 1995). If, as suggested by Schiffries and Rye (1990) and Buick *et al*. (2000), retrograde fluids were derived from dehydration of the Transvaal Supergroup footwall, it is unclear why stratigrahically-lower xenoliths in the Marginal and Critical Zones were bypassed and only those in the Upper Zone were affected. However, there is abundant evidence, particularly in the Eastern Limb, that the RLS was significantly disrupted by footwall diapirs and faults that developed penecontemporaneously with crystallisation of the RLS (Gerya *et al*., 2003). This could have resulted in localised focussing of this fluid, leaving other parts of the RLS relatively unaffected. Schweitzer and Hatton (1995) suggested that the RLS itself is a source of hydrothermal fluids. Sharpe (1985) suggested that the magma forming the Main Zone was injected around a similar time as the Critical Zone and that the elevated parts of this magma crystallised to the Upper Zone, which released fluids that led to pervasive hydration of the Upper Zone xenoliths. Fluids linked to the intrusion and emplacement of the Lebowa Suite granites above the RLS could also be a source of hydrothermal fluids operating in the higher stratigraphic levels of the RLS magma chamber (Wallmach *et al*., 1995).

Upon re-analysis of the xenoliths found in the Marginal and Upper Zones, Buick *et al*. (2000) recorded the presence of low-*T* hydrous minerals, including three F-bearing minerals - foshagite, cuspidine and hillebrandite that indicate F-bearing fluids circulating between

~250 °C and 400 °C. Therefore, using the analogy of Wallmach *et al.* (1995), both the Marginal and Upper Zones experienced 'wet' conditions. The occurrence of vesuvianite and grossular in the Western Limb xenolith studied herein indicates the presence of hydrous fluid infiltration. This may imply that these hydrous fluids infiltrated the Critical Zone as well. It is likely that the fluid was derived from dehydration reactions that took place in the footwall, which is supported by Buick *et al*. (2000) and Benson *et al*. (2020).

In the Platreef, the paucity of high-grade assemblages in the calc-silicate xenoliths (Gain and Mostert 1982; Yudovskaya and Kinnaird, 2010; this study) and extensive serpentinisation is interpreted as indicating voluminous retrograde fluid infiltration; consistent with the stable isotope results of Harris and Chaumba (2001). As this has been studied by Gain and Mostert (1982); Harris and Chaumba (2001); Pronost *et al*., (2008), no further discussion is presented here. Further work is possible to document the very fine-grained low-T aggregates in both the Marikana and Zwartfontein xenoliths, to evaluate whether similar assemblages to those identified by Buick *et al*. (2000) occur.

8.4 Comparison with other studies in the RLS

In the Eastern Limb of the RLS Willemse and Bensch (1964) studied calc-silicate xenoliths in the Marginal and Upper Zones, Wallmach *et al*. (1989) studied examples from the Marginal and Critical Zones, while Wallmach *et al*. (1995) studied xenoliths in the Upper Zone. Buick *et al*. (2000) re-analysed xenoliths in the Marginal and Upper Zones. Collectively, these authors report similar findings with the major focus being on metamorphic mineral assemblages found within the xenolith in order to determine $P - T - X_{CO_2}$ conditions. Willemse and Bensch (1964) is the exception in that their study included information about the magmatic rocks immediately surrounding the xenoliths wherever these were exposed. Key findings from all the above studies include the estimates of peak metamorphic temperature in excess of 1200 °C and slightly variable peak pressure based on the overburden load, although the latter is primarily based on RLS and hanging wall thickness estimates. The key high – grade minerals are periclase, monticellite, akermanite and merwinite. Of these minerals, only monticellite is observed in this study. The observed peak assemblage in the Marikana xenolith, Mtc + Fo + Spl, is stable between ~975 and 1125 °C

(Figure 7.3), slightly lower than the maximum temperatures in the Eastern Limb xenoliths. Based on stratigraphic considerations, overburden load pressure at the time of metamorphism is estimated at 0.6 – 1.6 kbar, similar to Wallmach *et al*.'s (1989) estimate for the only other xenolith studied in the Critical Zone.

In the Northern Limb, Gain and Mostert (1982) document alteration zones (composed of low-grade minerals and serpentinisation) surrounding xenoliths in the Platreef, and Kinnaird *et al*. (2005) found xenoliths that are partly assimilated and cause local contamination of the magma in the Platreef and Main Zone. Xenoliths in the Upper Zone crop out over a vertical interval of up to 160 m (Wallmach *et al*., 1995), indicating a substantial volume, yet all are retrogressed. It is possible, but seems unlikely, that the lack of high-grade cores in the Upper Zone xenoliths could be a function of selective exposure, or that the opposite may be true for the Marginal and Critical Zones xenoliths, where it is possible that only relatively unaltered xenoliths are exposed. It is important to note that alteration in these xenoliths refers to retrogression to relatively coarse-grained vesuvianite-grossular assemblages (and serpentinisation in the Northern Limb), thus, none of the Upper Zone or Northern Limb examples provide an opportunity to study contact zones where high-temperature carbonate-magma interactions could have taken place.

In their interpretation of the Platreef, Gain and Mostert (1982) depicted three possible of scenarios to explain different widths of contamination around xenoliths (Figure 1.7). Example 1 shows a uniformly shaped xenolith surrounded by a uniform contact zone. In example 2, an irregularly shaped xenolith is surrounded by a contact zone that may be wider in areas where protrusions occur in the original shape of the xenolith. Example 3 depicts an originally large xenolith that has undergone physical breakup through fracturing and fragmentation into smaller pieces, greatly increasing the surface area in contact with the magma and thus producing a relatively larger contact zone. While Gain and Mostert's (1982) model is aimed at explaining the xenolith-parapyroxenite relationships in the Northern Limb, it is possible that the different levels of preservation of high-grade assemblages / overprinting by retrograde assemblages in the Eastern Limb may reflect similar gross-scale variation in contact relationships and the degree of *in situ* disruption of the xenoliths by the

RLS magma. However, there appears to be little evidence that Willemse and Bensch (1964) observed wide zones of hybridisation in the magmatic rocks around the Eastern Limb xenoliths and, for the most part, the equivalent hybridisation domains appear to be on a similar scale, or smaller, than those associated with the Marikana xenolith.

Given the location of the Marikana xenolith in the sidewall underground at Lonmin, Marikana where its true dimensions are impossible to determine, it is difficult to determine with certainty which of the scenarios in Figure 1.7 represent its true nature. However, the Marikana xenolith presents a rare and unique occurrence where prograde and retrograde metamorphism, as well as carbonate-magma interactions, are preserved in a relatively small but well-exposed outcrop. It is proposed that the contact zone be considered as a magmatic skarn equivalent to those observed by Tilley and Harwood (1931), Joesten (1977), Owens (2000), Gaeta *et al*. (2009) and Whitley *et al*. (2020) at the interface between magma and a carbonate-rich rock. Carbonate assimilation, possibly in the form of $CaCO_3$ in solution or as melt (Wenzel *et al*., 2002; Gaeta *et al*., 2009; Mollo *et al*., 2010), into the surrounding magma resulted in: (1) the depletion of Ca and Ca-bearing minerals at the western layer of the xenolith and spinel layer (Figure 2.4; see also Wenzel *et al*., 2002); although the possibility of protolith layering cannot be ruled out; (2) Ca-rich minerals, such as plagioclase (An_{99}), Ca-Tschermak-rich clinopyroxene with wollastonite inclusions, and uvarovitic garnet, as well as the subsequent development of grossular garnet, in the contact zone adjacent to the xenolith; and (3) elevated $\delta^{18}O$ values in plagioclase and clinopyroxene in the contact zone compared to the adjacent mottled anorthosite. The exact mechanism by which the incorporation of carbonate into the magma took place is uncertain for the Marikana and Zwartfontein cases. This uncertainty is expressed by numerous previous workers (Wenzel *et al*., 2002; Gaeta *et al*., 2009; Pronost *et al*., 2008). While the assimilation of calcite melt into the magma has been proposed, no evidence for this is observed in the Marikana and Zwartfontein xenoliths as well as by any previous workers mentioned above (section 8.2), with the exception of Whitley *et al*. (2020). The stability of liquidus phases was not impacted by carbonate assimilation in this study as is noted by Harris and Chaumba (2001) and Pronost *et al*. (2008). The presence of Ca-Tschermak-rich clinopyroxene associated with the Marikana xenolith is the first recorded occurrence in the RLS. However, this does not imply

changes in the stability of liquidus phases as clinopyroxene is an inter-cumulus phase at this stratigraphic level in the CZ.

8.5 Model

The following model (Figure 8.3) is proposed in an attempt to explain the spatial and temporal relationship between the Marikana xenolith and CZ magma. This model envisages that the CZ magma entrapped the carbonate xenolith at a point in the crystallisation history after the UG 1 chromitite layer has already begun to crystallise, in accordance with the mechanism described by Kinnaird *et al*. (2002; section 8.3.2). It should be noted that at this time the magma may or may not have been partially crystalline.

As soon as the xenolith became entrapped in the magma it underwent prograde metamorphism (as suggested in section 7.3) (Figure 8.3A) during which significant decarbonation resulted in a rapid increase of the xenolith's density. The xenolith then began to sink through the magma. As prograde metamorphism continued the following processes occurred: (1) the migration of Ca in the form of $CaCO_3$. Based on the physical and chemical evidence presented herein, it can be assumed that the migration of $CaCO_3$ predominantly takes place where the magma is in direct contact with the xenolith (Figure 8.3B). In this case the forsterite-spinel layer (Figure 2.4) may be considered the first line of evidence of this migration; similar to the phenomenon recorded by Willemse and Bensch (1964) and Wenzel *et al*., (2002). Both the aforementioned authors agree that during devolatilisation of the xenolith, calcium carbonate is more soluble than magnesium silicate; therefore, calcium carbonate would migrate away from the xenolith leaving behind an Mg – rich assemblage. (2) In the contact zone the cm-scale fragments comprising calc-silicate mineral assemblageFs (in a plagioclase + clinopyroxene matrix, as shown in Figure 8.1) that are irregular to round in nature indicate that the xenolith was being mechanically disrupted (Joesten, 1977; Heinonen *et al*., 2021). (3) The enrichment of Ca in the contact zone drove the crystallisation of extremely calcic plagioclase (An_{99}, in section 4.3.4) and Ca-Tschermak-rich clinopyroxene (4.3.3). (4) The transfer of mass from the xenolith to the contact zone is also recorded in the elevated $\delta^{18}O$ measurements for plagioclase and clinopyroxene (compared to mottled anorthosite). In this case the magma surrounding the xenolith was subjected to the localised infiltration of CO_2-rich fluid, at high temperatures, originating

from decarbonating xenolith. This agrees with the suggestion that a CO_2-rich fluid was present during prograde metamorphism as explained in section 7.4.1 and implies that mass transfer shown by $\delta^{18}O$ measurements took place during prograde metamorphism. Therefore, the interaction between the decarbonating xenolith and magma resulted in the development of the contact zone.

It is speculated that on the xenolith's descent it passed through the partially-crystalline UG 1 chromitite layer (Figure 8.3B), before coming to a halt ~20 m below the UG 1. The disruption/splitting of the chromitite stringer maybe reflect the inherent morphology of the UG 1, as previous authors have noted that it comprises multiple thin layers or stringers that even splay off the main layer in some cases (Nex, 2004; Mukherjee *et al*., 2017; Pebane and Latypov, 2017). Alternatively, the UG 1 chromitite layer could have split into multiple thinner layers during expulsion of fluids and/or melts from the decarbonating xenolith. The sinking xenolith would have finally come to rest when the viscosity of the anorthosite mush increased enough to inhibit further sinking.

After the xenolith stopped sinking it is assumed that the effects of prograde metamorphism and the outward migration of CaO (in the form of $CaCO_3$) were still occurring. In addition to the aforementioned effects that the migration of CaO had on the xenolith and contact zone, the composition of Cr-spinel in the chromitite stringer was also affected. Within the individual stringers, compositional heterogeneity is observed on a grain-to-grain basis and/or from core to rim. The strong compositional variation shown in the three stringers indicates that the scale of contamination is limited (cm-scale).

Once the RLS magma cooled it was subjected to fluid infiltration (Figure 8.3C; section 8.4.3), which resulted in retrograde hydration of the contact zone forming vesuvianite and grossular. Their distribution in the highly heterogeneous contact zone is restricted to the comparatively Al-rich zones adjacent to calc-silicate fragments. The ingress of the H_2O-rich fluid also favoured the development of grossular-vesuvianite symplectites and likely catalysed the grossular reaction coronas between plagioclase and diopside (Figure 3.12).

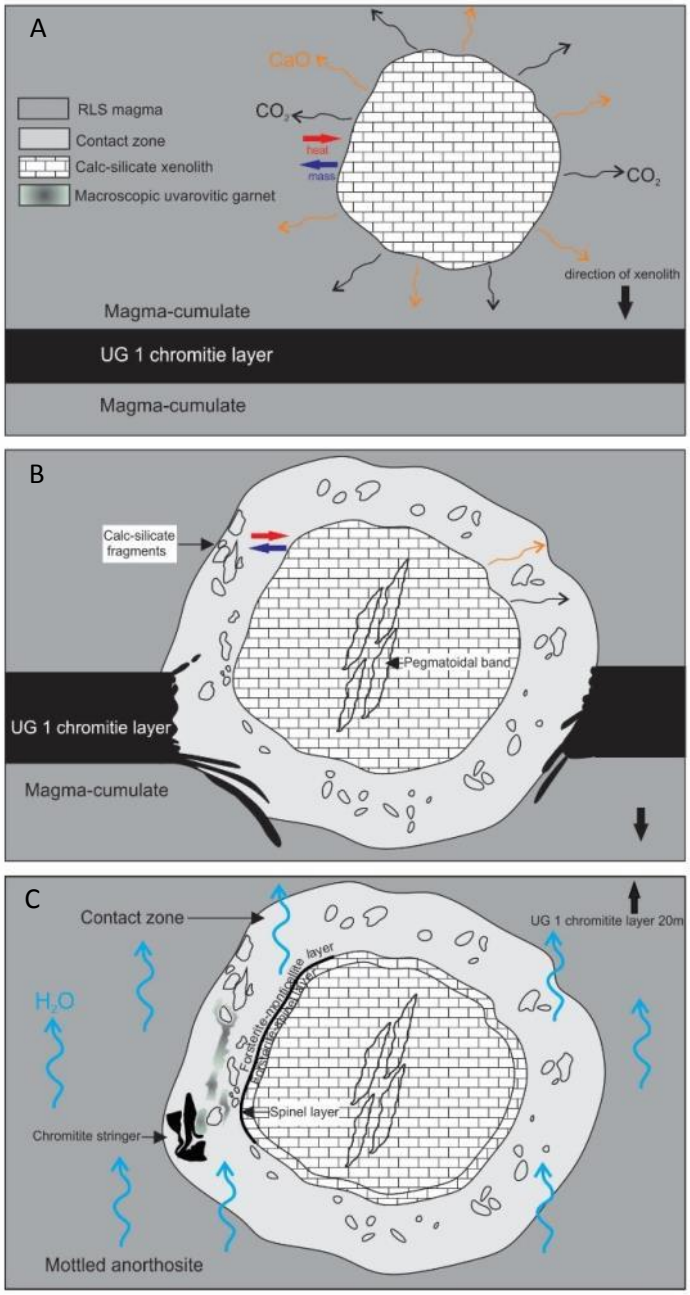

Figure 8.3: Proposed model illustrating the spatial and temporal relationships between the Marikana xenolith and CZ magma. (A) As soon as the xenolith is entrapped in the magma it undergoes prograde metamorphism resulting in the decarbonation, dehydration and subsequent development of the contact zone as mass, CO_2 and CaO migrate away from the xenolith. An increase in density causes the xenolith to sink, breaking through and entraining portions of the partially crystalline UG 1 chromitite layer. (B). The xenolith continues to sink until the viscosity of the anorthosite mush increases enough to inhibit the sinking. (C) Hydrous fluids infiltrating the RLS derived from dehydration of the Transvaal Supergroup footwall cause retrogression in the contact zone. The spherical shape of the xenolith is assumed for the purpose of simplicity.

8.6 Conclusions

This study investigated the interaction between calc-silicate xenoliths and magma in the mafic-ultramafic RLS in the Western and Northern Limbs of the Bushveld Complex. Bulk rock geochemical, petrographic, mineral chemical, micro-XRF and stable isotope analysis of the two suites of samples indicate that:

- Calc-silicate xenoliths vary in size from a few centimetres to tens of kilometres and originate from carbonate horizons or formations from the Transvaal Supergroup.
- The peak metamorphic assemblage in the Marikana xenolith - monticellite + forsterite + spinel - indicates peak T between ~975–1125 °C at P between 0.6–1.6 kbar with a fluid composition of X_{CO_2} = 1. Retrograde minerals, vesuvianite and grossular, are found in the contact zone between the xenolith and the silicate host rock. Textures such as (1) garnet + vesuvianite symplectites, and (2) grossular reaction coronas occurring between plagioclase and diopside indicate hydrous fluid (X_{CO_2} < 0.1) infiltration at T between 400–700 °C.
- The Marikana xenolith displays a combination of stoping by, and hybridisation of, the RLS magma along its western margin. Isolated fragments of the xenolith from the main body now lie in a plagioclase-clinopyroxene matrix with pseudo-ophitic igneous texture that is the product of hybridisation of RLS magma by carbonate fluids and/or melt from the xenolith. Bulk and mineral-scale compositional variation show a zonal arrangement in the hybridised contact zone, with decreasing xenolith influence over a distance of ~25 cm.
- Bulk CaO values in the contact zone are double that of host anorthosite and as high as the xenolith itself. This is an indication of significant decarbonation of the xenolith during prograde metamorphism. Ca was more mobile than Mg, leading to CaO enrichment in the contact zone and MgO enrichment in the xenolith. The bulk FeO contents in the xenolith and contact zone are similar, but are higher compared to anorthosite, suggesting that Fe may have been more mobile than Mg.
- The Ca enrichment in the contact zone seen in the bulk rock compositional data is confirmed by calcic compositions of plagioclase (An_{99}), Ca-Tschermak clinopyroxene and wollastonite inclusions in clinopyroxene that are interpreted as an exsolution

feature. Plagioclase-clinopyroxene reaction coronas defined by grossular garnet also indicate that the contact zone is compositionally anomalous. The elevated Fe^{3+} in the clinopyroxene in the contact zone indicates that the contamination of the magma by the xenolith also involved an increase in oxygen fugacity during crystallization.

- Elevated O isotopes confirm that xenolith contamination effects of the magma are restricted to the contact zone. $\delta^{18}O$ values of 6.62‰ for plagioclase in mottled anorthosite 5 m away from the xenolith are indistinguishable from those located 20 m away (6.42‰ – 6.50‰) from the xenolith. Elevated $\delta^{18}O$ values are recorded for plagioclase and clinopyroxene in the contact zone (7.62‰–12.67‰ and 8.63‰–9.8‰, respectively).
- Three spinel compositional types occur within the Marikana sample suite: (1) Cr-rich spinel; (2) spinel, *sensu stricto*; and (3) magnetite exsolution lamellae hosted in spinel, *sensu stricto*.
- The spinel layer at the western edge of the xenolith is composed of spinel, *sensu stricto,* with magnetite exsolution lamellae. The spinel composition in this layer is consistent with a sedimentary source, and the layer orientation is consistent with relict sedimentary bedding in the xenolith. The layer is thus an artefact of the protolith rather than a magmatic feature.
- The apparent entrainment of calc-silicate fragments and uvarovitic garnet stringers, and out-of-sequence chromitite stringer in the contact zone suggest that decarbonation increased the density of the xenolith and caused it to sink through semi-crystallised magma and the partially crystalline UG 1 chromitite layer. Sinking of the xenolith stopped once the magma attained sufficient viscosity.
- Mineral chemical analysis of spinels in the contact zone indicate that initial magmatic-derived chromite cores were subsequently overgrown by spinel with an increasing metasedimentary-derived component, and that increasing Ca levels from the decarbonating xenolith eventually led to poikilitic uvarovitic garnet crystallising directly from the contaminated magma as overgrowths on the chromite grains.
- Our model for the evolution of the Marikana xenolith includes stoping, hybridisation and entrainment of the UG 1 chromitite layer during sinking in which case the underlying anorthosite itself could not have been crystalline at the time.

- Calc-silicate xenoliths at Zwartfontein locally preserve a peak monticellite + forsterite + diopside + spinel assemblage, but retrograde re-equilibration dominated by serpentine is ubiquitous. Marginal contamination effects by individual xenoliths on the magma are less apparent, possibly owing to the high degree of contamination that has already taken place close to the dolomitic footwall. The extreme calcic plagioclase and clinopyroxene compositions seen at Marikana are not observed. Stable isotopes show elevated $\delta^{18}O$ values, ranging from 7.33‰–8.05‰ and 6.23‰–10.67‰ for plagioclase and pyroxene, respectively, that agree with previous studies from the Northern Limb.
- It is concluded that the Marikana xenolith and contact zone preserves a localised example of rare and unique interactions between a calc-silicate xenolith and surrounding magma.

REFERENCES

Alexandre, P., Andreoli, M. A., Jamison, A. and Gibson, R. L. (2006). $^{40}Ar/^{39}Ar$ age constraints on low-grade metamorphism and cleavage development in the Transvaal Supergroup (central Kaapvaal craton, South Africa): implications for the tectonic setting of the Bushveld Igneous Complex. *South African Journal of Geology*, **109**, 393–410.

Appiah-Nimoh, F. (2004). A Geological Study of the Platreef at Potgietersrus Platinum Mine with Emphasis on the Magmatic Processes, Contamination and Metasomatism. MSc. Thesis (unpubl). University of Johannesburg, Johannesburg, 66 pp.

Arai, S., Prichard, H.M., Matsumoto, I. and Fisher, P.C. (1999) Platinum-group minerals in podiform chromitite from the Kamuikotan zone, Hokkaido, northern Japan. *Resource Geology*, **49**, 39–47.

Armitage, P., McDonald, I., Edwards, S. and Manby, G. (2002). Platinum-group element mineralization in the Platreef and calc-silicate footwall at Sandsloot, Potgietersrus District, South Africa. *Applied Earth Science*, **111(1),** 36–45.

Armstrong, R., Compston, W., Retief, E., Williams, I.T. and Welke, H. (1991). Zircon ion microprobe studies bearing on the age and evolution of the Witwatersrand triad. *Precambrian Research*, **53(3-4)**, 243–266.

Ashwal, L., Webb, S., Knoper, M. and Mare, L. (2005). Physical and mineralogical properties of Bushveld rocks: magnetic susceptibility, density and mineral chemistry profiles in the 2950 m Bellevue drill core, Northern Lobe, *South African Journal of Geology*, **108**, 199–232.

Barbieri, M., Penta, A. and Turi, B. (1975). Oxygen and strontium isotope ratios in some ejecta from the Alban Hills volcanic area, Roman Comagmatic Region. *Contributions to Mineralogy and Petrology*, **51**, 127–133.

Barnes, C., Prestvik, T., Sundvoll, B. and Surratt, D. (2005). Pervasive assimilation of carbonate and silicate rocks in the Hortavaer igneous complex, north-central Norway. *Lithos*, **80**, 179–199.

Barnes, S. J. (2000). Chromite in komatiites, II. Modification during greenschist to mid-amphibolite facies metamorphism, *Journal of Petrology*, **41**, 387–409.

Barnes, S. J. and Roeder, P. L. (2001). The range of spinel compositions in terrestrial mafic and ultramafic rocks. *Journal of petrology*, **42(12),** 2279–2302.

Barnes, S. J. and Maier, W. D. (2002). Platinum-group element distributions in the Rustenburg layered suite of the Bushveld Complex, South Africa. *In* The Geology, Geochemistry, Mineralogy and Mineral Beneficiation of Platinum-Group Elements. Edited by L.J. Cabri, Canadian Institute of Mining, Metallurgy and Petroleum, Special Volume 54, p.431–458.

Bates, R.L. and Jackson, J.A. (1987). *Glossary of Geology* (third edition). American Geological Institute, Alexander, Virginia.

Benson, E., Connolly, J.A.D. and Boudreau, A.E. (2020). Crustal fluid contamination in the Bushveld Complex, South Africa: An analogue for subduction zone fluid migration, *International Geological Review*, **62**, 1845–1861.

Borisova, A. Y., Martel, C., Gouy, S., Pratomo, I., Sumarti, S., Toutain, J.-P., Bindeman, I. N., de Parseval, P. and Métaxian, J.P. (2013). Highly explosive 2010 Merapi eruption: evidence for shallow-level crustal assimilation and hybrid fluid. *Journal of Volcanology and Geothermal Research*, **261**, 193–208.

Bowen, N. L. (1940). Progressive metamorphism of siliceous limestone and dolomite. *The Journal of Geology*, **48(3)**, 225–274.

Buchanan, D., Nolan, J., Suddaby, P., Rouse, J., Viljoen, M. and Davenport, J. (1981). The genesis of sulfide mineralization in a portion of the Potgietersrus Limb of the Bushveld Complex. *Economic Geology*, **76(3)**, 568–579.

Buddington, A.F. and Lindsley, D.H. (1964). Iron-titanium oxide minerals and synthetic Equivalents. *Journal of Petrology*, **5**, 310–357.

Buick, I. S., Gibson, R.L., Cartwright, I., Maas,R., Wallmach, T. and Uken,R. (2000). Fluid flow in metacarbonates associated with emplacement of the Bushveld Complex, South Africa. *Journal of Geochemical Exploration*. **69–70**, 391–395.

Buick, I. S., Gibson, R., Wallmach, T. and Metz, J. (2000). The occurrence of cuspidine, foshagite and hillebrandite in calc-silicate xenoliths from the Bushveld Complex, South Africa. *South African Journal of Geology*, **103(3-4)**, 249–254.

Buick, I. S., Maas, R. and Gibson, R. (2001). Precise U–Pb titanite age constraints on the emplacement of the Bushveld Complex, South Africa. *Journal of the Geological Society*, **158(1)**, 3–6.

Buick, I. S., Uken, R., Gibson, R.L. and Wallmach, T. (1998). High- δ13C Paleoproterozoic carbonates from the Transvaal Supergroup, South Africa. *Geology*, **26(10)**, 875 – 878

Burnham, C. W. (1979). Magmas and hydrothermal fluids. In: Barnes, H.L. (Ed.) Geochemistry of Hydrothermal Ore Deposits John Wiley and Sons, New York, 136–168.

Cameron, E. N. (1978). The lower zone of the eastern Bushveld Complex in the Olifants River trough. *Journal of Petrology*, **19(3)**, 437–462.

Campbell, G. (2011). Exploration geophysics of the Bushveld Complex in South Africa. *The Leading Edge*, **30(6)**, 622–638.

Carr, B.B., Clarke, A.B. and de' Michieli Vitturi, M. (2018). Earthquake induced variations in extrusion rate: A numerical modelling approach to the 2006 eruption of Merapi Volcano (Indonesia). *Earth and Planetary Science Letters*, **482**, 377–387.

Catuneanu, O. and Eriksson, P. G. (1999). The sequence stratigraphic concept and the Precambrian rock record: an example from the 2.7–2.1 Ga Transvaal Supergroup, Kaapvaal craton. *Precambrian Research*, **97(3-4)**, 215–251.

Cawthorn, R. (1999). The platinum and palladium resources of the Bushveld Complex. *South African Journal of Science*, **95**, 481–489.

Cawthorn, R. and Lee, C. (1998). Field excursion guide to the Bushveld Complex. Paper presented at the 8th international platinum symposium. Geological Society of South Africa and South African Institute of Mining and Metallurgy.

Cawthorn, R. and Webb, S. (2001). Connectivity between the western and eastern limbs of the Bushveld Complex. *Tectonophysics*, **330(3-4)**, 195–209.

Cawthorn, R. G. and Ashwal, L. D. (2009). Origin of anorthosite and magnetitite layers in the Bushveld Complex, constrained by major element compositions of plagioclase. *Journal of Petrology*, **50(9)**, 1607–1637.

Cawthorn, R. G., Lee, C. A., Schouwstra, R. P. and Mellowship, P. (2002). Relationship between PGE and PGM in the Bushveld Complex. *The Canadian Mineralogist*, **40(2)**, 311–328.

Cawthorn, R. G. and Walraven, F. (1998). Emplacement and crystallization time for the Bushveld Complex. *Journal of Petrology*, **39(9)**, 1669–1687.

Chadwick, J. P., Troll, V. R., Ginibre, C., Morgan, D., Gertisser, R., Waight, T. E. and Davidson, J. P. (2007). Carbonate assimilation at Merapi Volcano, Java, Indonesia: insights from crystal isotope stratigraphy. *Journal of Petrology*, **48**, 1793–1812.

Chiarabba, C., Amato, A. and Delaney, P. T. (1997). Crustal structure, evolution, and volcanic unrest of the Alban Hills, Central Italy. *Bullettin of Volcanology,* **59**, 161–170.

Chiba, H., Chacko, T., Clayton, R. N. and Goldsmith, J. R. (1989). Oxygen isotope fractionations involving diopside, forsterite, magnetite, and calcite: Application to geothermometry. *Geochimica et Cosmochimica Acta*, **53(11)**, 2985–2995.

Colás, V., González-Jiménez, J. M., Griffin, W. L., Fanlo, I., Gervilla, F., O'Reilly, S.Y, Pearson, N. J, Kerestedjian, T. and Proenza, J.A. (2014). Fingerprints of metamorphism in chromite: new insights from minor and trace elements, *Chemical Geology***, 389**,137–152.

Colás, V., Padrón-Navarta, J. A., González-Jiménez, J.M., Griffin, W.L., Fanlo, I., O'Reilly, S.Y., Gervilla, F., Proenza, J,A., Pearson, N.J. and Escayola, M.P. (2016). Compositional effects on the solubility of minor and trace elements in oxide spinel minerals: Insights from crystal-crystal partition coefficients in chromite exsolution, *American Mineralogist*, **101**, 1360–1372.

Connolly, J.A.D. (1990). Multivariant phase diagrams: an algorithm based on generalized thermodynamics. *American Journal of Science*, **290**, 666–718.

Connolly, J. A. D. (2009). The geodynamic equation of state: What and how. *Geochemistry, Geophysics, Geosystems*, **10**, 1–19.

Dare, S.A.S., Barnes S.J., Beaudoin, G., Méric, J., Boutroy, E. and Potvin- Doucet, C. (2014). Trace elements in magnetite as petrogenetic indicators, *Miner Deposita*, **49**, 785–796.

Deer, W.A., Howie, R.A. and Zussman, J. (1989). *An Introduction to the Rock Forming Mineral* (second edition), Longman Scientific and and Technical, England, 696pp.

Droop, G. T. R. (1987). A general equation for estimation of Fe3+ concentrations in ferromagnesian silicates and oxides from microprobe analysis, using stoichiometry criteria. *Mineralogical Magazine*, **51**, 431–435.

Duparc, Q., Dare, S.A.S., Cousineau, P.A. and Goutier, J. (2016). Magnetite chemistry as a provenance indicator in Archean metamorphosed sedimentary rocks, *Journal of Sedimentary Research*, **86**, 542–563.

Eales, H.V. and Cawthorn, R.G., 1996. The Bushveld Complex. In: Cawthorn, R.G. (Ed.), *Layered Intrusions*. Elsevier, Amsterdam, pp. 181–229.

Eales, H.V., De Klerk, W.J., Butcher, A.R. and Kruger, F.J. (1990). The cyclic unit beneath the UG1 chromitite (UG1FW unit) at RPM Union Section Platinum Mine- Rosetta Stone of the Bushveld Complex Upper Critical Zone?. *Mineralogical Magazine*, **54**, 23-43.

Eales, H., De Klerk, W. and Butcher, A. (1990). The cyclic unit beneath the UG1 chromitite (UGIFW unit) at RPM Union Section Platinum Mine—Rosetta Stone of the Bushveld Upper Critical Zone? *Mineralogical Magazine*. **54(374)**, 23–43.

Eriksson, P., Altermann, W., Catuneanu, O., Van der Merwe, R. and Bumby, A. (2001). Major influences on the evolution of the 2.67–2.1 Ga Transvaal basin, Kaapvaal craton. *Sedimentary Geology*, **141**, 205–231.

Eriksson, P. and Clendenin, C. (1990). A review of the Transvaal Sequence, South Africa. *Journal of African Earth Sciences (and the Middle East)*, **10(1-2)**, 101–116.

Eriksson, P., Hattingh, P. and Altermann, W. (1995). An overview of the geology of the Transvaal Sequence and Bushveld Complex, South Africa. *Mineralium Deposita*, **30(2)**, 98–111.

Evans, B. W. and Frost, B. R. (1975) Chrome-spinel in progressive metamorphism— a preliminary analysis. *Geochimica et Cosmochimica Acta*, **39**, 959–972.

Frankel, J. (1959). Uvarovite garnet and South African jade (hydrogrossular) from the Bushveld complex, Transvaal. *American Mineralogist: Journal of Earth and Planetary Materials*, **44(5-6)**, 565–591.

Freda, C., Gaeta, M., Misiti, V., Mollo, S., Dolfi, D. and Scarlato, P. (2008). Magma-carbonate interaction: an experimental study on ultrapotassic rocks from Alban Hills (Central Italy). *Lithos*, **101**, 397–415.

Fyfe, W., Price, N. and Thompson, A. (1978). Fluids in the earth's crust. Amsterdam. Elsevier. 383pp.

Fyfe, W.S., Turner, F.J. and Verhoogen, J. (1958). Metamorphic reactions and metamorphic facies. Geological Society of America Memoir, 73, 259 pp.

Gaeta, M., Di Rocco, T. and Freda, C. (2009). Carbonate assimilation in open magmatic systems: the role of melt-bearing skarns and cumulate-forming processes. *Journal of Petrology*, **50**, 361–385.

Gain, S. B. and Mostert, A. (1982). The geological setting of the platinoid and base metal sulfide mineralization in the Platreef of the Bushveld Complex in Drenthe, north of Potgietersrus. *Economic Geology*, **77(6)**, 1395–1404.

Gao, S., Liu, X., Yuan, H., Hattendorf, B., Günther, D., Chen, L. and Hu, S. (2002). Determination of forty two major and trace elements in USGS and NIST SRM glasses by laser ablation inductively coupled plasma mass spectro-metry. *Geostandards Newsletter*, **26(2)**, 181–196.

Gary, M., McAfee, R. and Wolf, C. L. (1972). *Glossary of Geology*. American Geological Institute. Washington DC, United States, 805pp.

Gerya, T.V., Uken, R., Reinhardt, J., Watkeys M.K., Maresch, W.V. and Clarke, B.M. (2003). Cold fingers in a hot magma: Numerical modeling of country-rock diapirs in the Bushveld Complex, South Africa, *Geology*, **39**, 753-756.

González-Jiménez, J.M., Augé, T., Gervilla, F., Bailly, L., Proenza, J.A. and Griffin, W.L. (2011). Mineralogy and geochemistry of platinum-rich chromitites from the mantle-crust transition zone at Ouen Island, New Caledonia ophiolite, *Canadian Mineralogist*, **49**, 1549–1569.

González-Jiménez, J.M., Locmelis, M., Belousova, E., Griffin, W.L., Gervilla, F., Kerestedjian, T.N., Pearson, N.J. and Sergeeva, I. (2013). Genesis and tectonic implications of podiform chromitites in the metamorphosed Ultramafic Massif of Dobromirtsi (Bulgaria), *Gondwana Research*, **27**,555–574.

Good, N. and De Wit, M. J. (1997). The Thabazimbi-Murchison lineament of the Kaapvaal craton, South Africa: 2700 Ma of episodic deformation. *Journal of the Geological Society*, **154(1)**, 93–97.

Gnos, E. and Armbuster. (2006), Relationship among metamorphic grade, vesuvianite "rod polytypism," and vesuvianite composition. *American Mineralogist*, **91**, 862 – 870.

Graham, I.T., Franklin, B.J. and Marshall, B. (1996). Chemistry and mineralogy of podiform chromitite deposits, southern NSW, Australia: A guide to their origin and evolution. *Mineralogy and Petrology*, **57**, 129–150.

Grammatikopoulos, T.A. and Clark, A.H. (2006). A comparative study of wollastonite skarn genesis in the Central Metasedimentary Belt, southeastern Ontario, Canada. *Ore Geology Reviews*, **29**, 146–161.

Gregory, R.T. and Criss, R.E. (1986). Isotopic exchange in open and closed systems. *Rev Mineral,* **16**, 91–127.

Grew, E. S., Locock, A. J., Mills, S. J., Galuskina, I. O., Galuskin, E. V. and Hålenius, U. (2013). Nomenclature of the garnet supergroup. *American Mineralogist***, 98(4)**, 785–811.

Groat, L. A., Hawthorne, F. C. and Ercit, T. S. (1992). The chemistry of vesuvianite. *Canadian Mineralogist*, **30(1)**, 19–48.

Hales, M.P. (2020). Structural and kinematic analysis of a pseudotachylite-bearing fault system within the upper Critical Zone of the Bushveld Complex, South Africa. Master's thesis (unpubl). University of the Witwatersrand, Johannesburg, 112pp.

Hannah, J. L., Bekker, A., Stein, H. J., Markey, R. J. and Holland, H. D. (2004). Primitive Os and 2316 Ma age for marine shale: implications for Paleoproterozoic glacial events and the rise of atmospheric oxygen. *Earth and Planetary Science Letters*, **225(1-2)**, 43–52.

Harker, R. and Tuttle, O. (1956). The lower limit of stability of akermanite ($Ca_2MgSi_2O_7$). *American Journal of Science*, **254(8)**, 468–478.

Harris, C. and Chaumba, J. B. (2001). Crustal contamination and fluid–rock interaction during the formation of the Platreef, northern limb of the Bushveld Complex, South Africa. *Journal of Petrology*, **42(7)**, 1321–1347.

Harris, C., Pronost, J. J., Ashwal, L. D. and Cawthorn, R. G. (2004). Oxygen and hydrogen isotope stratigraphy of the Rustenburg Layered Suite, Bushveld Complex: constraints on crustal contamination. *Journal of Petrology*, **46(3)**, 579–601.

Harris, C., Smith, H. S. and le Roex, A. P. (2000). Oxygen isotope composition of phenocrysts from Tristan da Cunha and Gough Island lavas: variation with fractional crystallization and evidence for assimilation. *Contributions to Mineralogy and Petrology*, **138(2)**, 164–175.

Harris, C. and Vogeli, J. (2010). Oxygen isotope composition of garnet in the Peninsula Granite, Cape Granite Suite, South Africa: constraints on melting and emplacement mechanisms. *South African Journal of Geology*, **113(4)**, 401–412.

Hartzer, F. (1995). Transvaal Supergroup inliers: geology, tectonic development and relationship with the Bushveld Complex, South Africa. *Journal of African Earth Sciences*, **21(4)**, 521–547.

Heinonen, J.S., Kieran, A.I., Heinonen, A., Fred, R., Virtanen, V.J., Bohrsom, A. and Spera, F.J. (2021). From Binary Mixing to Magma Chamber Simulator – Geochemical Modeling of Assimilation in Magmatic Systems. In: Masotta, M., Beier, C. and Mollo, S. (Eds), Crustal Magmatic System Evolution: Anatomy, Architecture and Physico-Chemical Processes. Wiley.

Henry, D. (1999). Cuspidine-bearing skarn from Chesney Vale, Victoria. *Australian Journal of Earth Sciences*, **46(2)**, 251–260.

Hiroshi, N., Schreiber, H. D. and Morris, R. V. (1980). Experimental mineral/liquid partition coefficients of the rare earth elements (REE), Sc and Sr for perovskite, spinel and melilite, *Earth and Planetary Science Letters*, **46**, 431–437.

Hochella, M., Liou, J., Keskinen, M. and Kim, H. (1982). Synthesis and stability relations of magnesium idocrase. *Economic Geology*, **77(4)**, 798–808.

Holwell, D. A. and McDonald, I. (2006). Petrology, geochemistry and the mechanisms determining the distribution of platinum-group element and base metal sulphide mineralisation in the Platreef at Overysel, northern Bushveld Complex, South Africa. *Mineralium Deposita*, **41(6)**, 575–598.

Hulbert, L. J. and Von Gruenewaldt, G. (1982). Nickel, copper, and platinum mineralization in the lower zone of the Bushveld Complex, south of Potgietersrus. *Economic Geology*, **77(6)**, 1296–1306.

Iacono Marziano, G., Gaillard, F. and Pichavant, M. (2008). Limestone assimilation by basaltic magmas: an experimental re-assessment and application to Italian volcanoes. *Contributions to Mineralogy and Petrology*, **155**, 719–738.

Irvine, T.N. (1965). Chromian spinel as a petrogenetic indicator. Part I, *Canadian Journal of Earth Sciences,* **2**, 648–671.

Irvine, T. and Sharpe, M. (1982). Source-rock compositions and depths of origin of Bushveld and Stillwater magmas. *Carnegie Institute of Washington Yearbook*, **81**, 294-303.

Ito, J., and Arem, J. E. (1970). Idocrase: Synthesis, phase relations and crystal chemistry1. *American Mineralogist: Journal of Earth and Planetary Materials*, **55(5-6)**, 880–912.

Jochum, K. P., Weis, U., Stoll, B., Kuzmin, D., Yang, Q., Raczek, I. and Günther, D. (2011). Determination of reference values for NIST SRM 610–617 glasses following ISO guidelines. *Geostandards and Geoanalytical Research*, **35(4)**, 397–429.

Joesten, R.H. (1977). Mineralogical and chemical evolution of contaminated igneous rocks at a gabbro-limestone contact, Christmas Mountains, Big Bend region, Texas. *Geological Society of America Bulletin*, **88**, 1515-1529.

Johnson, T.E., Brown, M. and White, R.W. (2010). Petrogenetic modelling of strongly residual metapelitic xenoliths within the southern Platreef, Bushveld Complex, South Africa. *Journal of Metamorpic Geology*, **28**, 269-291.

Johson, T.E., White, R.W. and Brown, M. (2011). A year in the life of an aluminous metapelite xenolith—The role of heating rates, reaction overstep, H2O retention and melt loss. *Lithos*, **124**, 132-143.

Jones, M.Q.W. (2015). Thermophysical properties of rocks from the Bushveld Complex. *The Journal of the Southern African Institute of Mining and Metallurgy*, **115**, 153–160.

Kinnaird, J. A. (2005). *The Bushveld large igneous province*, University of the Witwatersrand, Johannesburg. 39pp.

Kinnaird, J.A., Kruger, F., Nex, P. and Cawthorn, R. (2002). Chromitite formation—a key to understanding processes of platinum enrichment. *Applied Earth Science*, **111(1)**, 23–35.

Kinnaird, J. A. (2005). Geochemical evidence for multiphase emplacement in the southern Platreef. *Applied Earth Science*, **114(4)**, 225–242.

Kinnaird, J. A., Hutchinson, D., Schurmann, L., Nex, P. and de Lange, R. (2005). Petrology and mineralisation of the southern Platreef: northern limb of the Bushveld Complex, South Africa. *Mineralium Deposita*, **40(5)**, 576–597.

Klemd, R., Beinlich, A., Kern, M., Junge, M., Martin, M.R. and Schouwstra, R. (2020). Magmatic PGE Sulphide Mineralization in Clinopyroxenite from the Platreef, Bushveld Complex, South Africa, *Minerals*, **10**, 1–28.

Kennedy, W. Q. (1959). The formation of a diffusion-reaction skarn by pure thermal metamorphism. *Mineralogical Magazine*, **32**, 26–31.

Klemme, S., Van Miltenburg, J. C., Javorsky, P.J. and Wastin, F. (2005). Thermodynamic properties of uvarovite garnet ($Ca_3Cr_2Si_3O_{12}$), *American Mineralogist*, **90**, 663–666.

Koovarjee, B. (2015). Petrographic and geochemical analysis of a calc-silicate xenolith and adjacent hybridized zone in the Critical Zone of the Western Complex, Rowland Shaft, Lonmin Platinum, Marikana. Honours thesis (unpubl). University of the Witwatersrand, Johannesburg, 74pp.

Le Bas, M.J. (1965). The contamination of a gabbro by Carboniferous limestone at Carlingford, Co. Louth. *Mineralogical Magazine*, **34**, 292–302.

Lee, C. (1996). A review of mineralization in the Bushveld Complex and some other layered intrusions *Developments in Petrology*, **15**, 103–145.

Maier, W. D. (1991). Geochemical and petrological trends in the UG2-Merensky Unit interval of the Upper Critical Zone in the Western Bushveld Complex. PhD Thesis (unpubl). Rhodes University, Grahamstown, 253 pp.

Maier, W. D., Arndt, N. T. and Curl, E. A. (2000). Progressive crustal contamination of the Bushveld Complex: evidence from Nd isotopic analyses of the cumulate rocks. *Contributions to Mineralogy and Petrology*, **140(3)**, 316–327.

Maier, W.D., and Barnes S.J. (1996). Unusually high concentrations of magnetite at Cara´ıba and other Cu-sulfide deposits in the Cura¸ca´ valley, Bahia, Brazil, *The Canadian Mineralogist*, **34**, 717–731.

Maier, W.D. and Barnes, S.J. (1998). Concentrations of rare earth elements in silicate rocks of the Lower, Critical and Main Zones of the Bushveld Complex. *Chemical Geology*, **150**, 85–103.

Manyeruke, T. D., Maier, W. D. and Barnes, S.-J. (2005). Major and trace element geochemistry of the Platreef on the farm Townlands, northern Bushveld Complex. *South African Journal of Geology*, **108(3)**, 381–396.

Mathavan, V. and Fernado, G.W.A.R. 2001. Reactions and textures in grossular-wollastonite–scapolite calc–silicate granulites from Maligawila, Sri Lanka: evidence for high temperature isobaric cooling in the meta-sediments of the Highland Complex. *Lithos*, **59**, 217–232.

Mavimbela, P.K. (2013). Metamorphism in the Contact Aureole of the Eastern Limb of the Bushveld Complex, South Africa. MSc. Thesis (unpubl). University of Pretoria, Pretoria, 119 pp.

McDonald, I., Holwell, D. A. and Armitage, P. E. (2005). Geochemistry and mineralogy of the Platreef and "Critical Zone" of the northern lobe of the Bushveld Complex, South Africa: implications for Bushveld stratigraphy and the development of PGE mineralisation. *Mineralium Deposita*, **40(5)**, 526–549.

Mitchell, A. and Scoon, R. (2012). The Platreef of the Bushveld Complex, South Africa: a new hypothesis of multiple, non-sequential magma replenishment based on observations at the Akanani project, north-west of Mokopane. *South African Journal of Geology*, **115(4)**, 535-550.

Mollo, S., Gaeta, M., Freda, C., Di Rocco, T., Misiti, V. and Scarlato, P. (2010). Carbonate assimilation in magmas: a reappraisal based on experimental petrology. *Lithos* **114**, 503–514.

Morimoto, N., Fabries, J., Ferguson, A.K., Ginzburg, I.V., Ross, M., Seifert, F.A.m Zussman, J., Aoki, K. and Gottardi, G. (1988). Nomenclature of Pyroxenes. *Mineralogy and Petrology*, **39**, 55-79.

Morse, S.A. (1981) Kiglapait geochemistry IV: the major elements. *Geochimica et Cosmochimica Acta*, **45**, 461–479.

Morton, A.C. (1991). Geochemical studies of detrital heavy minerals and their applicationto provenance research. In Morton, A.C., Todds, S.P., and Haughton, P.D.W (Ed.), Developments in Sedimentary Provenance Studies: Geological Society of London, Special Publication, **57**, 31–45.

Mukherjee, R., Latypov, R. and Balakrishna. (2017). An intrusive origin of some UG-1 chromitite layers in the Bushveld Igneous Complex, South Africa: Insights from field relationships. *Ore Geology Reviews*, **90**, 94–109.

Mukherjee, R., Mondal, S.K., Gonzalez-Jimenez, J.M., Griffin, W.L., Pearson, N.J. and O'Reilly, S.Y. (2015). Trace-element fingerprints of chromite, magnetite and sulphides from the 3.1 Ga ultramafic–mafic rocks of the Nuggihalli greenstone belt, Western Dharwar craton (India). *Contrib Mineral Petrol,* **169**, 1–23.

Mukherjee, R., Mondal, S.K., Rosing, M.T. and Frei, R. (2010). Compositional variations in the Mesoarchean chromites of the Nuggihalli schist belt, Western Dharwar craton (India): potential parental melts and implications for tectonic setting, *Contrib Mineral Petrol,* **160**, 865–885.

Neuendorf, K.K.E., Mehl, J.P. and Jackson, J. A. (2005). *Glossary of Geology*, 5th Edition. American Geological Institute, Alexandria, Virginia, United States, 779pp.

Nex, P. A. M. (2004). Formation of bifurcating chromitite layers of the UG1 in the Bushveld Igneous Complex, an analogy with sand volcanoes. *Journal of the Geological Society, London* **161**, 903–909.

Nex, P.A.M. (2005). The structural setting of mineralisation on Tweefontein Hill, northern limb of the Bushveld Complex, South Africa. *Applied Earth Science*, **114(4)**, 243–251.

Nex, P.A.M. and Kinnaird, J.A. (2004). The Platreef: it is not as easy as A, B, C, Geoscience Africa 2004, Abstract Volume, University of the Witwatersrand, Johannesburg, South Africa, 494–495.

Nex, P.A.M., Kinnaird, J.A., Jones, B. and Colloty, A. (2006). *Platreef Rock Type Definitions and Descriptions.* Anglo Platinum training manual, 281pp.

Nielsen, R.L., Forsythe, L.M., Gallahan, W.E. and Fisk, M.R. (1994). Major-and trace-element magnetite-melt equilibria, *Chemical Geology*, **117**, 167–191.

Norrish, K. and Hutton, J. (1969). An accurate X-ray spectrographic method for the analysis of a wide range of geological samples. *Geochimica et Cosmochimica Acta*, **33(4)**, 431–453.

Nyama, N., Nex, P. and Yao, Y. (2005). Preliminary petrological studies of the Platreef on Tweefontein Hill, Bushveld Igneous Complex, South Africa. Paper presented at the Extended Abstracts. 10th International Platinum Symposium. University of Oulu, Finland.

Owens, B. E. (2000). High-temperature contact metamorphism of calc-silicate xenoliths in the Kiglapait Intrusion, Labrador. *American Mineralogist*, **85(11-12)**, 1595–1605.

Pagė, P. and Barnes, S.J. (2016). The influence of chromite on osmium, iridium, ruthenium and rhodium distribution during early magmatic processes. *Chemical Geology*, **420**, 51–68

Paton, C., Hellstrom, J., Paul, B., Woodhead, J. and Hergt, J. (2011). Iolite: Freeware for the visualisation and processing of mass spectrometric data. *Journal of Analytical Atomic Spectrometry*, **26(12)**, 2508–2518.

Paton, C., Woodhead, J. D., Hellstrom, J. C., Hergt, J. M., Greig, A. and Maas, R. (2010). Improved laser ablation U-Pb zircon geochronology through robust downhole fractionation correction. *Geochemistry, Geophysics, Geosystems*, **11(3)**, 1–36.

Pebane, M. and Latypov, R. (2017). The significance of magmatic erosion for bifurcation of UG1 chromitite layers in the Bushveld Complex. *Ore Geology Reviews*, **90**, 65–93.

Penniston-Dorland, S. C., Mathez, E. A., Wing, B. A., Farquhar, J. and Kinnaird, J. A. (2012). Multiple sulfur isotope evidence for surface-derived sulfur in the Bushveld Complex. *Earth and Planetary Science Letters*. **337**, 236–242.

Proenza, J., Ortega-Gutiérrez, F., Camprubí, A., Tritlla, J., Elías-Herrera, M. and Reyes-Salas, M., (2004). Paleozoic serpentinite-enclosed chromitites from Tehuitzingo (Acatlán Complex, southern Mexico): a petrological and mineralogical study, *Journal of South American Earth Sciences*, **16 (8)**, 649–666.

Proenza, J., Solė, J. and Melgarejo, J.C. (1999). Uvarovite in podiform chromitite: The Moa – Baracoa ophiolitic massif, Cuba. *The Canadian Mineralogist*, **37**, 679–690.

Pronost, J., Harris, C. and Pin, C. (2008). Relationship between footwall composition, crustal contamination, and fluid–rock interaction in the Platreef, Bushveld Complex, South Africa. *Mineralium Deposita*, **43(8)**, 825–848.

Reid, D., Cawthorn, R., Kruger, F. and Tredoux, M. (1993). Isotope and trace-element patterns below the Merensky Reef, Bushveld Complex, South Africa: evidence for fluids? *Chemical Geology*, **106(1-2)**, 171–186.

Righter, K., Campbell, A., Humayun, M. and Hervig, R. (2004). Partitioning of Ru, Rh, Pd, Re, Ir, and Au between Cr-bearing spinel, olivine, pyroxene and silicate melts, *Geochimica et Cosmochimica Acta*, **68**, 867–880.

Roedder, E. (1984). Reviews in mineralogy; Fluid inclusions, *Mineralogical Society of America*, **12**, 361–380.

Rollinson, H. R. (1993). *Using geochemical data: evaluation, presentation, interpretation*. Pearson Education Limited, England, 352pp.

Rollinson, H. (1995). The relationship between chromite chemistry and the tectonic setting of Archean ultramafic rocks. In Blenkinsop, T.G. and Tromps, P. (Ed.) Sub-Saharan Econ Geol Amsterdam, Balkema, 7–23.

Rollinson, H. (2008). The geochemistry of mantle chromitites from the northern part of the Oman ophiolite: inferred parental melt compositions, *Contrib Mineral Petrol*, **156**, 273-288

Schiffries, C. M. and Rye, D. M. (1989). Stable isotopic systematics of the Bushveld Complex; I, Constraints of magmatic processes in layered intrusions. *American Journal of Science*, **289(7)**, 841–873.

Schiffries, C. M. and Rye, D. M. 1990. Stable isotopic systematics of the Bushveld Complex: II. Constraints on hydrothermal processes in layered intrusions. *American Journal Science*, **290**,209–245.

Schön, J. H. (2011). Density. In: Schön, J. H. (Eds), Handbook of Petroleum Exploration and Production. Elsevier, Amsterdam, 97–105.

Schweitzer, J. and Hatton, C. (1995). Chemical Alteration within the Volcanic Roof Rocks of the Bushveld Complex, *Economic Geology*, **90**, 2218–2231.

Schweitzer, J., Hatton, C. and De Waal, S. (1997). Link between the granitic and volcanic rocks of the Bushveld Complex, South Africa. *Journal of African Earth Sciences*, **24(1-2)**, 95–104.

Scoon, R. N. and Costin, G. (2018). Chemistry, Morphology and Origin of Magmatic-Reaction Chromite Stringers Associated with Anorthosite in the Upper Critical Zone at Winnaarshoek, Eastern Limb of the Bushveld Complex. *Journal of Petrology*, **59(8)**, 1551–1578.

Sharman-Harris, E., Kinnaird, J., Harris, C. and Horstmann, U. (2005). A new look at sulphide mineralisation of the northern limb, Bushveld Complex: a stable isotope study. *Applied Earth Science*, **114(4)**, 252–263.

Sharpe, M. R. 1985. Strontium isotope evidence for preserved density stratification in the main zone of the Bushveld Complex, South Africa. *Nature*, **316**, 119–126.

Sharp, Z., Essene, E. J., Anovitz, L. M., Metz, G. W., Westrum Jr, E. F., Hemingway, B. and Valley, J. (1986). The heat capacity of a natural monticellite and phase equilibria in the system CaO-MgO-SiO_2-CO_2. *Geochimica et Cosmochimica Acta*, **50(7)**, 1475–1484.

Sharp, Z., (2007), *Principles of stable isotope geochemistry*, Pearson Prentice Hall, New Jersey, 344pp.

Shoji, T. 1975. Role of temperature and CO2 pressure in the formation of skarn and its bearing on mineralization. *Economic Geology,* **70**,739–749.

Smith, D. S., Basson, I. J. and Reid, D. L. (2004). Normal reef subfacies of the Merensky Reef at Northam platinum mine, Zwartklip facies, western Bushveld Complex, South Africa. *The Canadian Mineralogist*, **42(2)**, 243–260.

Tilley, C.E. and Harwood, H.F. (1931). The dolerite-chalk contact of Scawt Hill, Co. Antrim. The production of basic alkali-rocks by assimilation of limestone by basaltic magma. *Mineralogical Magazine*, **22**, 439–468.

Tracy, R., Jaffe, H. and Robinson, P. (1978). Monticellite marble at Cascade Mountain, Adirondack Mountains, New York. *American Mineralogist*, **63(9-10)**, 991–999.

Valley, J., Peacor, D., Bowman, J., Essene, E. J. and Allard, M. (1985). Crystal chemistry of a Mg-vesuvianite and implications of phase equilibria in the system CaO-MgO-Al_2O_3-SiO_2-H_2O-CO_2. *Journal of Metamorphic Geology*, **3(2)**, 137–153.

Valley, J. W., Kitchen, N., Kohn, M. J., Niendorf, C. R. and Spicuzza, M. J. (1995). UWG-2, a garnet standard for oxygen isotope ratios: strategies for high precision and accuracy with laser heating. *Geochimica et Cosmochimica Acta*, **59(24)**, 5223–5231.

Van der Merwe, M. (1976). The layered sequence of the Potgietersrus limb of the Bushveld Complex. *Economic Geology*, **71(7)**, 1337–1351.

Vielzeuf, D. and Montel, J. M. (1994). Partial melting of metagreywackes. Part I. Fluid-absent experiments and phase relationships. *Contributions to Mineralogy and Petrology*, **117(4)**, 375–393.

Viswanathiah, M.N., Shankara, M.A. and Janardhan, A.S. (1979). Note on the origin of chrome grossular garnet (Uvarovite) in calc-silicate from Bandihalli, Tumkur-District, Karnataka. *Journal of the Geological Society of India*, **20**, 507–511

Wagner, P.A. (1929). *The Platinum Deposits and Mines of South Africa.* Oliver and Boyd, Edinburgh, U.K, 326pp.

Wallmach, T., Hatton, C.J. and Droop, G. T. (1989). Extreme facies of contact metamorphism developed in calc-silicate xenoliths in the eastern Bushveld Complex. Canadian Mineralogist, **27**, 509–523.

Wallmach, T., Hatton, C., De Waal, S. and Gibson, R. (1995). Retrogressive hydration of calc-silicate xenoliths in the eastern Bushveld Complex: evidence for late magmatic fluid movement. *Journal of African Earth Sciences*, **21(4)**, 633–646.

Walraven, F. (1995). Zircon Pb-evaporation age determinations of the oak tree formation, Chuniespoort group, Transvaal sequence: implications for Transvaal-Griqualand west basin correlations. *South African Journal of Geology*, **98(1)**, 58–67.

Walraven, F., Armstrong, R. and Kruger, F. (1990). A chronostratigraphic framework for the north-central Kaapvaal craton, the Bushveld Complex and the Vredefort structure. *Tectonophysics*, **171(1-4)**, 23–48.

Walter, L. (1963). Experimental studies on Bowen's decarbonation series; [Part] 1, PT univariant equilibria of the'monticellite'and'akermanite'reactions. *American Journal of Science,* **261(5)**, 488–500.

Wan, H.M. and Yeh C.L. (1982). Uvarovite and grossular from Fengtien nephrite deposits, eastern Taiwan, *Mineralogical Magazine*, **48**, 31–37.

Wenzel, T., Baumgartner, L. P., Brugmann, G.E., Konnikov, E. G. and Kislov, E. V. (2002). Partial Melting and Assimilation of Dolomitic Xenoliths by Mafic Magma: the Ioko-Dovyren Intrusion (North Baikal Region, Russia). *Journal of Petrology*, **4**, 2049–2074

White, J. (1994). The Potgietersrus Prospect, geology and exploration history. Paper presented at the Proceedings XVth CMMI Congress Johannesburg, SAIMM, **3**, 173 –181.

White, W.M. (2013). *Geochemistry* (first edition), Wiley-Blackwell, UK, 668pp.

Whitley, S., Halama, R., Gertisser, R., Preece, K., Deegan, F. M. and Troll, V. R. (2020). Magmatic and metasomatic effects of magma-carbonate interaction recorded in calc-silicate xenoliths from Merapi volcano (Indonesia), *Journal of Petrology*, **61**, 1–38.

Whitney D.L. and Evans B. W. (2010). Abbreviations for names of rock-forming minerals, *American Mineralogist,* **95**, 185–187.

Wilson, A.H. (2015). The Earliest Stages of Emplacement of the Eastern Bushveld Complex: Development of the Lower Zone, Marginal Zone and Basal Ultramafic Sequence, *Journal of Petrology*, **56**, 347–388.

Wilson, A.H., Zeh, A. and Gerdes, A. (2017). In Situ Sr isotopes in Plagioclase and Trace Element Systematics in the Lowest Part of the Eastern Bushveld Complex: Dynamic Processes in an Evolving Magma Chamber. *Journal of Petrology*, **58**, 327–360.

Wijbrans, C., Klemme, S., Berndt, J. and Vollmer, C. (2015). Experimental determination of trace element partition coefficients between spinel and silicate melt: the influence of chemical composition and oxygen fugacity. *Contributions to Mineralogy and Petrology*, **169**, 1–33.

Willemse, J. and Bensch, J. (1964). Inclusions of the original carbonate rocks in Gabbro and Norite of the Eastern part of the Bushveld Complex. *South African Journal of Geology*, **67(1)**, 1-87.

Winter, J.D. (2010). *Principles of Igneous and Metamorphic Petrology* (second edition), Pearson Prentice Hall, USA, 720pp.

Yoder Jr, H. (1968). Akermanite and related melilite-bearing assemblages. *Carnegie Institute Washington Yearbook*, **66**, 471–477.

Yudovskaya, M. A. and Kinnaird, J. A. (2010). Chromite in the Platreef (Bushveld Complex, South Africa): occurrence and evolution of its chemical composition. *Mineralium Deposita*, **45(4)**, 369–391.

Zeh, A., Ovtcharova, M., Wilson, A. H. and Schaltegger, U. (2015). The Bushveld Complex was emplaced and cooled in less than one million years–results of zirconology, and geotectonic implications. *Earth and Planetary Science Letters*, **418**, 103–114.

APPENDICES

Appendix 1A: Sample preparation and methodology for X-ray fluorescence

Samples were analysed for major and minor elements using X-ray fluorescence (XRF) at the Earth laboratory, School of Geosciences, University of the Witwatersrand. Samples were crushed and milled into a fine powder, thereafter the powder was ignited at 1100 °C for 40 minutes. Major elements were determined using the Norrish Fusion technique using in-house correction procedures and using a Panalytical X-ray fluorescence spectrometer, samples were analysed at 50kV and 50mA. Major elements were fused using Johnson Matthey Spectrolflux 105 at 1000°C and raw data corrected using in-house software. Standard calibrations were made up using synthetic oxide mixtures and international standard rocks as well as in-house controls. Sample weight used was 0.35 gm and flux weight 2.0 gm. Calibration standards were primary International Reference Materials USGS series (USA) and NIM series (South Africa). Precision is taken as 1% for elements in abundance of greater than 5% by weight, and 5% for elements in abundance less than 5%. The instrument used was the Panalytical Axios x-ray spectrometer. Standard calibrations use BCR2, NIM-P, NIM-D, W-2, NIM-S, GSP-2, NIM-N, NIM-G, PCC1, BHVO2, AGV2, G2 DTS1.

Trace elements were determined on pressed pellets using a Moviol solution binder. Standardization was carried out using International Reference Materials USGS series (USA) and NIM series (South Africa). Precision was determined on the basis of counting time and is taken as 5% for elements in abundance greater than 100 ppm, and 10% for elements in abundance between 10 and 100 ppm. The instrument used was the Philips PW2404 x-ray spectrometer.

Appendix 1B: Whole rock and trace element geochemistry of samples from the Marikana sample suite and Eales *et al*. (1990)

Sample ID	RSTX26-12	RSTX26-06A	RSTX26-06C	RSTX26-50	RSTX26-A5	RSTX26-A20	Average of 6 norites near top UG1 unit (Eales *et al*., 1990)	Average of 4 norites at the base of noritic suite (Eales *et al*., 1990)
(wt %)								
SiO_2	36.13	34.23	33.92	40.96	48.93	49.1	52.68	52.05
Al_2O_3	3.98	2.65	6.78	15.88	30.87	29.6	11.75	14.81
Fe_2O_3	0.62	1.02	0.65	0.71	0.09	0.17	0.78	0.72
FeO	5.01	8.23	5.26	5.72	0.73	1.35	7.77	7.21
Fe_{total}	5.63	9.25	5.91	6.43	0.82	1.52	8.55	7.93
MnO	0.53	0.57	0.56	0.14	0.01	0.02	0.17	0.16
MgO	36.77	52.73	25.63	8.62	0.46	1.26	19.14	15.27
CaO	16.93	1.02	27.11	26.34	15.2	14.6	6.31	8.17
Na_2O	0.03	0.06	bdl	0.04	2.43	2.4	1.14	1.46
K_2O	0.03	0.03	0.03	0.03	0.18	0.18	0.13	0.05
TiO_2	0.20	0.28	0.19	0.53	0.05	0.07	0.11	0.08
P_2O_5	0.01	0.01	0.01	0.01	0.01	0.01	0.02	0.01
Cr_2O_3	<0.01	0.04	0.27	1.23	0.01	0.01		
NiO	0.01	0.01	0.01	0.02	bdl	bdl		
TOTAL	**100.25**	**100.88**	**100.42**	**100.23**	**98.97**	**98.77**	**100.34**	**100.28**
LOI	0.32	1.02	0.79	0.54	0.6	0.3		
(ppm)								
Sc	28.52	24.43	27.51	39.53	13.30	13.70	22	23
V	7.85	18.51	16.15	421.79	10.60	20.20	118	101
Cr	27.74	244.9	1726.78	6852.35	12.60	77.10	2005	1665
Co	22.81	34.29	24.22	21.84	3.20	13.10	75	64
Ni	54.26	92.34	109.24	176.19	7.80	22.80	404	339
Cu	16.7	21.37	63.27	17.54	10.30	15.10	12	12
Zn	47.22	57.27	71.46	11.67	7.50	12.70	62	56
Ga	4.58	3.15	8.26	14.41	20.10	19.70		
Rb	bdl	bdl	bdl	bdl	bdl	0.40	1.2	1.9
Sr	2.62	4.15	21.29	37.53	438.90	431.80	178	223
Y	7.84	2.11	9.84	18.98	1.00	1.40	3.00	2.9
Zr	7.3	27.27	14.63	110.28	17.90	18.00	5.6	3.2
Nb	bdl	0.02	1.97	0.44	bdl	1.00		
Mo	bdl	bdl	bdl	bdl	bdl	1.00		
Ba	15.86	9.92	8.67	2.76	80.90	85.80		
Pb	2.37	2.07	6.9	0.21	bdl	1.20		
Th	bdl	bdl	bdl	bdl	bdl	bdl		
U	bdl	bdl	bdl	bdl	bdl	bdl		

Appendix 1C: Methodology for micro-X-ray fluorescence

Hand samples RSTX26-05, RSTS26-50 and RSTX26-60 were cut into slabs approximately 1 cm –2 cm thick at the School of Geosciences, University of the Witwatersrand, in preparation for micro-XRF analysis. The analyses were conducted at the Mineralogy Department, Mintek, Johannesburg. All cut slabs were scanned imaged prior to element mapping using the Bruker M4 Tornado micro-XRF instrument. All element maps were produced using the parameters outlined in the table below.

Sample ID	**RSTX26-50A**	**RSTX26-05A**	**RSTX26-60**
	Mapping Parameters		
Width	110 mm (2200 pixel)	112 mm (2240 pixel)	140 mm (2800 pixel)
Height	48 mm (960 pixel)	37 mm (740 pixel)	40 mm (800 pixel)
Pixel Size	50 µm	50 µm	50 µm
Total Pixel Count	2112000 pixel	1657600 pixel	2240000 pixel
	Acquisition parameters		
Pixel time	10 ms/pixel	10 ms/pixel	10 ms/pixel
	Tube parameter		
High voltage	50 kV	50 kV	50 kV
Anode current	599 µA	599 µA	599 µA
Filter	Empty	Empty	Empty
Optic	Lens	Lens	Lens
Spot Size	20 µm	20 µm	20 µm
Chamber at	Air 2 mbar	Air 2 mbar	Air 2 mbar
Anode current	Rh	Rh	Rh

Appendix 1D: Whole rock and trace element geochemistry of samples from the Platreef (Nex *et al.*, 2006)

	N2	**N3**	**N24**	**N31**	**N35**	**N17**	**N7**	**N30**	**N18**	**N19**
	Calc silicate	Calc silicate	Calc silicate	Calc silicate	Calc silicate	Feldspathic pyroxenite	Para pyroxenite	Para pyroxenite	Pyroxenite	Pyroxenite
(wt%)										
SiO_2	36.23	47.39	44.24	46.83	49.82	48.01	49.20	48.79	51.44	48.54
TiO_2	0.05	0.05	0.16	0.16	0.25	0.16	0.22	0.28	0.33	0.17
Al_2O_3	3.97	1.95	6.35	12.49	13.49	13.32	5.21	3.27	6.30	13.88
Fe_2O_3	17.89	1.22	6.41	9.89	11.23	9.47	5.16	17.46	13.07	13.26
MnO	0.70	0.28	0.29	12.28	0.21	0.15	0.86	0.39	0.25	0.19
MgO	4.41	21.01	23.69	1.90	9.67	15.46	13.12	8.24	21.11	12.30
CaO	31.88	23.44	8.05	12.21	10.83	8.19	23.98	21.16	5.14	8.45
Na_2O	bdl	bdl	bdl	0.05	2.52	1.50	bdl	0.16	0.87	1.83
K_2O	bdl	bdl	bdl	bdl	bdl	0.05	bdl	0.44	bdl	bdl
P_2O_5	bdl	bdl	bdl	0.14	0.01	0.13	0.01	0.01	0.03	0.01
TOTAL	**98.97**	**98.73**	**99.19**	**99.84**	**98.57**	**97.46**	**99.03**	**100.54**	**98.86**	**99.53**
%LOI	3.84	3.39	1bdl	3.89	0.54	1.02	1.27	0.34	0.32	0.90
(ppm)										
Rb	9	7	8	8	9	20	8	19	15	13
Sr	32	27	17	14	208	214	23	46	76	206
Y	9	5	15	36	13	6	8	8	11	6
Zr	24	23	27	79	24	21	39	60	53	32
Nb	<3	<3	<3	4	<3	<3	<3	<3	3	<3
Co	14	6	14	26	56	56	25	26	153	95
Ni	99	<6	40	11	195	379	44	277	5761	1420
Cu	21	<6	<6	16	101	39	12	147	1862	1610
Zn	25	45	26	47	73	60	28	37	85	82
TiO2	0.05	0.05	0.14	0.15	0.26	0.15	0.19	0.29	0.39	0.18
V	<12	<12	<12	47	191	158	190	87	194	77
Cr	43	26	46	103	179	1158	24	61	2021	652
Ba	<20	<20	<20	<20	67	116	<20	104	80	61
Pb	108	<9	<9	27	<9	<9	9	22	19	22
Ga	<10	<10	<10	20	16	10	<10	<10	<10	16
La	16	17	19	54	20	17	19	16	18	15
Ce	21	18	12	55	<12	18	24	18	23	22
Sc	76	45	18	28	42	26	64	42	26	25
Th	<12	<12	<12	<12	<12	<12	<12	<12	<12	<12
As	15	<12	<12	<12	<12	<12	<12	27	<12	<12
U	11	<9	<9	18	<9	<9	<9	15	<9	<9

Appendix 2: Sample description for borehole core from Zwartfontein

BOREHOLE ZF 116					
Sample no.	Depth (m)		Sample description	Thin-sections	Sulphides (based on Hand samples only)
	From	To			
ZF116/24	1208.06	1209.05	Dark grey. Fine-medium grained (2-5 mm). Pred. pyroxene w/ minor biotite and sulphides. Cross-cut by horizontal veins composed of serpentine and talc. PYROXENITE	A24-1.	5% pyrite chalcopyrite (1-2 mm) disseminations
ZF116/44	1224.08	1225.19	Dark grey-black. Medium to coarse-grained (5-9 mm). pred. olivine (serpentinized) and pyroxene w/ accessory biotite. Bottom 40 cm shows a higher degree of serpentinisation. HARZBURGITE	A44-8A A44-8B	Magnetite associated with serpentinisation
ZF116/85	1259.11	1260.04	Grey-green. Coarse-grained (5-11 mm). Inhomogeneous. Pred. pyroxene w/ minor amounts of plagioclase and sulphides. PARAPYROXENITE		5% pyrite and pyrrhotite minor chalcopyrite. medium to coarse grained interstitial/ network/ inter-cumulus. disseminated
ZF116/117	1287.18	1288.20	Light grey-green. Medium to coarse-grained (3-12 mm). Inhomogeneous pred. pyroxene w/ minor plagioclase and biotite. Cross-cut by serpentine veins. Vuggs filled with biotite and calcite. PARAPYROXENITE	A117-3	
ZF116/127	1295.28	1296.28	Mottled grey-green. Medium to coarse-grained (3-10 mm). Inhomogeneous. Pyroxene w/ minor biotite and plagioclase. Vuggs filled with biotite and calcite. PARAPYROXENITE		
ZF116/141	1307.49	1307.87	Grey-red. Medium-grained. (3-5 mm) highly oxidised. Inhomogeneous. Pred. pyroxene w/ biotite. Vuggs filled with biotite and calcite. PARAPYROXENITE		
ZF116/155-156.1	1319.17	1319.71	Grey-red. Medium-grained. (3-5 mm) highly oxidised. Inhomogeneous. Pred. pyroxene w/ biotite and minor spinel. Vuggs filled with biotite and calcite. PARAPYROXENITE		

ZF116/156.2	1319.71	1319.91	Grey-pale green. Medium to coarse-grained (3-11 mm). Inhomogeneous. Pred. clinopyroxene. Forsterite and Ca-bearing silicates w/ black fine to coarse-grained (1-8 mm) spinel and minor. CALC-SILICATE	A156-7	
ZF116/156.3-156.8	1319.91	1321.00	Grey-red. Medium-grained. (3-5 mm) highly oxidised. Inhomogeneous. Pred. pyroxene w/ biotite and minor spinel. Vuggs filled with biotite and calcite. PARAPYROXENITE		
ZF116/160-162	1323.45	1326.06	Pale cream to grey-green. Medium to coarse-grained (3-12 mm). Inhomogeneous. Pred. clinopyroxene forsterite and Ca-bearing silicates w/ black fine to coarse-grained spinel and minor serpentinisation. Bottom 40 cm is horizontally cross-cut by serpentine veins. CALC-SILICATE	A160-3	
ZF116/170	1331.13	1331.99	Grey. Medium-grained (3-5 mm). Inhomogeneous. Pred. pyroxene w/ minor biotite sulphides. Top 45 cm is cross-cut by horizontal veins and highly serpentinized. Vuggs filled with biotite and calcite PARAPYROXENITE		<1% pyrite. pyrrhotite. chalcopyrite disseminations (1-3mm)
ZF116/208	1363.13	1364.09	Grey-green. Medium-grained (3-5 mm). Pred. pyroxene w/ interstitial plagioclase and minor biotite and sulphides. Few cross-cutting serpentine veins. PYROXENITE		<1% pyrite. pyrrhotite. chalcopyrite disseminations (1-5mm)
ZF116/227-228	1379.06	1381.30	Grey-green. Medium to coarse-grained (3-15 mm). Inhomogeneous. Pred. pyroxene w/ plagioclase and minor biotite and sulphides. Cross-cut by serpentine and talc veins. PARAPYROXENITE	A228-5	<1% pyrite. pyrrhotite and chalcopyrite disseminations and net-textured (1-3 mm)
ZF116/229	1381.30	1381.90	Grey-green. Coarse-grained (5-13 mm). Pred. pyroxene w/ interstitial plagioclase and minor biotite and sulphides. PYROXENITE		<1% pyrite and pyrrhotite disseminations (1-2 mm)
ZF116/244	1395.24	1396.04	Grey-green. Medium grained (3-5 mm). Pred. pyroxene and interstitial plagioclase w/ minor sulphides. Few cross-cutting serpentine veins. FELDSPATHIC PYROXENITE		<1% pyrite. and chalcopyrite disseminations (1-3 mm)
ZF116/246	1397.04	1398.10	Grey-green. Medium grained (3-5 mm). Pred. pyroxene and interstitial plagioclase w/ minor sulphides. Few cross-cutting serpentine and talc veins. FELDSPATHIC PYROXENITE	A246-9	<1% pyrite. and chalcopyrite disseminations (1-5 mm)
ZF116/288	1434.64	1435.61	Green-grey. Coarse grained (5-15 mm). Pred. pyroxene and interstitial plagioclase w/ minor sulphides and biotite. Pegmatoidal texture. Few cross-cutting serpentine veins. FELSPATHIC PYROXENITE		

ZF116/289-291	1435.61	1439.21	Pale green to grey. Medium to coarse-grained (3-17 mm). Inhomogeneous. Pred. clinopyroxene and serpentine w/ forsterite and minor calcite and spinel. Bottom 25 cm is pred. cumulus pyroxene w/ interstitial plagioclase. Displaying an igneous-like texture. PARAPYROXENITE	A289-1 A290-1 A291-1	<1% pyrite and pyrrhotite disseminations (1-2 mm)
ZF116/293-295	1439.21	1442.00	Pale green to dark grey. Medium to coarse-grained (3 -6 mm). Inhomogeneous. Pred. clinopyroxene and serpentine w/ forsterite and Ca-bearing silicates and minor calcite. It is characterized by up to 25 cm of course to pegmatitic (5 mm to 2 cm) igneous-like texted zones. pred. pyroxene w/ interstitial plagioclase and minor biotite and sulphides. PARAPYROXENITE	A295-2A A295-2B	<1% pyrite and pyrrhotite disseminations (>1 mm)
ZF116/298	1443.09	1444.07	Grey-green. Fine to medium grained (1-5 mm). Inhomogeneous. Pred. pyroxene and serpentine w/ Ca-bearing silicates and minor biotite. Cross-cut by serpentine veins. PARAPYROXENITE		
ZF116/307.5	1451.06	1451.84	Dark grey. Medium-grained (3-5 mm). Pred. pyroxene w/ minor interstitial plagioclase and accessory biotite. PYROXENITE	A307-1	
ZF116/307.6-309.3	1451.84	1453.24	Pale cream. Grey-green. Medium to coarse-grained (3-12 mm). Inhomogeneous. Pred. clinopyroxene forsterite and Ca-bearing silicates w/ black. Fine-grained spinel (~1 mm). Few cross-cutting serpentine veins. CALC-SILICATE	A308-1 A309-1	
ZF116/309.4-312	1453.24	1455.68	Grey-black. Yellow and pale green. Fine-grained (<1-2 mm). Remnant sedimentary layering evident. Pred. Ca-bearing silicates and calcite. Cross-cutting serpentine veins. CALC-SILICATE/METASEDIMENT	A312-3	
ZF116/313.1-313.7	1455.68	1456.53	Grey-green. Fine to coarse-grained (1-9 mm). Inhomogeneous. Pred. pyroxene w/ serpentine. Few cross-cutting serpentine veins. PARAPYROXENITE		
ZF116/313.8-314	1456.53	1458.16	Grey-green. Medium to coarse-grained (3-9 mm). Pred. pyroxene w/ interstitial plagioclase. Top 35 cm is characterized by white. Plagioclase rich zone. The modal abundance of plagioclase ranges from >10-25% in the bottom 1.33 m. PYROXENITE		
ZF116/327	1469.06	147bdl	Grey. Medium-grained (3-5 mm).pred. pyroxene w/ interstitial plagioclase (>10%) and minor biotite. GABBRONORITE	A327-1	

ZF116/347	1487.30	1488.27	Dark grey. Fine-medium grained (2-5 mm). Pred. pyroxene w/ minor interstitial plagioclase. The bottom 23 cm is plagioclase rich (>40%) w/ minor sulphides. PYROXENITE		>2% pyrrhotite and chalcopyrite. net-textured
ZF116/358	1495.65	1497.25	Grey. Fine to medium-grained (1-5 mm).pred. pyroxene w/ interstitial plagioclase (>10%) and minor biotite. FELDSPATHIC PYROXENITE		
ZF116/382-387	1515.26	1521.08	Grey-green. Fine to coarse-grained (1-11 mm). Inhomogeneous. Pred. pyroxene w/ serpentine. Forsterite. Ca-bearing silicates and minor biotite. Cross-cutting serpentine veins. Top 50 cm displays an igneous-like texture w/ pyroxene and interstitial plagioclase. PARAPYROXENITE	A382-5 A385-7	

BOREHOLE ZF116 ED1					
Sample no.	**Depth (m)**		**Sample description**	**Thin-sections**	**Sulphides (based on Hand samples only)**
	From	**To**			
ZF116ED1/702	1364.26	1365.00	Dark grey. Medium-grained (3-5 mm). Pred. pyroxene w/ minor interstitial plagioclase and accessory biotite and sulphides. PYROXENITE	B702-1	
ZF116ED1/720	1379.00	138bdl	Grey-green. Coarse-grained to pegmatitic (5 mm-3 cm). Inhomogeneous. Pred. pyroxene w/ some interstitial plagioclase. Ca-bearing silicates. Serpentine and minor sulphides. PARAPYROXENITE	B720-3	>1% pyrite and pyrrhotite. 1-3mm disseminations
ZF116ED1/804	1450.03	1451.73	Grey. Medium to coarse-grained (3-9 mm). Pred. pyroxene w/ interstitial plagioclase (>10%). minor biotite and sulphides. FELDSPHATIC PYROXENITE		>1% pyrite and pyrrhotite 1-5mm disseminated interstitial
ZF116ED1/805.1-805.8	1451.73	1452.73	Pale cream. Grey-green. Medium to coarse-grained (3-12 mm). Inhomogeneous. Pred. clinopyroxene. Forsterite and Ca-bearing silicates w/ black. Fine-grained spinel (~1 mm). CALC-SILICATE	B805-6	

ZF116ED1/805.9-808.2	1452.73	1455.18	Grey-black. Yellow and pale green. Fine-grained (<1-2 mm). Remnant sedimentary layering evident. Pred. Ca-bearing silicates and calcite. Cross-cutting serpentine veins. CALC-SILICATE/METASEDIMENT	B806-4	
ZF116ED1/808.3-808.7	1455.18	1456.00	Grey-green. Medium to coarse-grained (3-15 mm). Pred. pyroxene w/ interstitial plagioclase (>10%). minor biotite and sulphides. Characterized by inhomogeneous zones green-cream fine-grained material. FELDSPATHIC PYROXENITE		
ZF116ED1/810	1456.07	1457.43	Pale cream. Green-grey. Fine to coarse grained (1-7 mm). Inhomogeneous. Pred. Ca-bearing silicates and pyroxene. Some cross-cutting veins. CALC-SILICATE		
ZF116ED1/811	1457.43	1458.08	Dark grey. Medium-grained (3-5 mm). Pred. pyroxene w/ minor interstitial plagioclase and accessory sulphides. PYROXENITE	B811-1	>1% pyrite and pyrrhotite (1mm) disseminations
ZF116ED1/843	1484.11	1485.11	Grey-green. Medium-grained (3-5 mm). Pred. pyroxene w/ interstitial plagioclase (>10%) and minor biotite. Characterized by a ~25 cm thick zone rich in Ca-bearing silicates and/or calcite. PYROXENITE		
ZF116ED1/846	1487.16	1488.20	Grey-green. Fine to medium-grained (1-5 mm). Pred. pyroxene w/ interstitial plagioclase (10-30%). FELDSPATHIC PYROXENITE		
ZF116ED1/882-884	1517.12	1520.18	Pale cream-white. Green and grey-black. Fine to coarse grained (1 mm- 2 cm) inhomogeneous. Pred. clinopyroxene. Forsterite. Ca-bearing silicates and minor plagioclase. Few cross-cutting veins. CALC-SILICATE/ HYBRID	B882-4A B882-4B B882-5A B882-5B B884-2 B884-3	

BOREHOLE ZF24 D1					
Sample no.	**Depth (m)**		**Sample description**	**Thin-sections**	**Sulphides (based on Hand samples only)**
	From	**To**			
ZF24D1/280-281	1228.88	1231.81	Grey-green w/ purple hue. Fine to coarse-grained (1-7 mm). Pred. pyroxene. Ca-bearing silicates. Anhydrite. Some serpentinisation and minor sulphides. CALC-SILICATE/ HYBRID	D280-1 D281-1	>1% pyrite disseminations

BOREHOLE ZF109 ED1					
Sample no.	**Depth (m)**		**Sample description**	**Thin-sections**	**Sulphides (based on Hand samples only)**
	From	**To**			
ZF109ED1/324-325	1071.48	1073.30	Dark grey. Fine to medium grained (1-5 mm). Pred. pyroxene w/ minor interstitial plagioclase (<10%). some biotite/ phlogopite and sulphides. Characterized by 20 cm thick zone. Coarse-grained to pegmatitic of similar composition, but more abundant in plagioclase (>10%). PYROXENITE	C325-4	>2% pyrite. chalcopyrite and pyrrhotite. (1-10mm) disseminations
ZF109ED1/326-327	1073.30	1074.73	Dark grey-black. Fine to coarse-grained (<1-6 mm). Inhomogeneous. Pred. pyroxene. Forsterite. Ca-bearing silicates. Minor plagioclase and biotite/phlogopite and sulphides. Some irregular cross-cutting serpentine veins. Remnant sedimentary layering/structures evident. CALC-SILICATE/ HYBRID	C326-2 C327-3 C327-5A C327-5B	<1% pyrite and chalcopyrite (1-5mm) disseminations
ZF109ED1/328-329	1074.73	1076.51	Dark grey. Medium to coarse-grained (3-8 mm). Pred. pyroxene w/ minor interstitial plagioclase (<10%) and sulphides. Few cross-cutting veins. PYROXENITE	C329-1	<1% pyrite and chalcopyrite (1-5mm) disseminations
ZF109ED1/331.1-331.3	1076.51	1077.09	Dark grey. Medium to coarse-grained (3-8 mm). Pred. pyroxene w/ minor interstitial plagioclase (<10%) and sulphides. Few cross-cutting veins. PYROXENITE		<1% pyrite and chalcopyrite (1-2mm) disseminations
ZF109ED1/331.4-334	1077.09	1080.33	Dark grey to green. Fine to coarse-grained (1-9 mm). Inhomogeneous. Pred. pyroxene, serpentine. Ca-bearing silicates w/ plagioclase and minor sulphides. Numerous cross-cutting serpentine veins. PRARPYROXENITE/ HYBRID	C332-2	<5% pyrrhotite. chalcopyrite (1-5mm) disseminations

ZF109ED1/336	1080.33	1081.67	Top 37 cm; grey-green. Medium-grained (3-5 mm) pred. pyroxene and serpentine. It grades into light grey fine to coarse grained (1-6 mm). Pred. pyroxene w/ interstitial plagioclase (>15%) and some sulphides. FELDSPATHIC PYROXENITE		>5% chalcopyrite. pyrrhotite disseminations (1-10 mm)
ZF109ED1/429-431	1156.18	1158.37	Grey-green. Fine to coarse grained (1-10 mm). Inhomogeneous. Pred. pyroxene, serpentine, Ca-bearing silicates, forsterite, minor plagioclase and sulphides. Bottom 20 cm displays a pegmatitic texture (5mm - 2.5cm). w/ pyroxene and interstitial plagioclase PARAPYROXENITE	C431-5 C431-7A C431-7B	>5% chalcopyrite. pyrrhotite disseminations (1-10 mm
ZF109ED1/433-435	1158.37	1160.64	Green-grey. Coarse-grained (5-15 mm). Pred. clinopyroxene, forsterite, Ca-silicates w/ minor calcite and serpentine. CALC-SILICATE	C434-0 C435-2	
ZF109ED1/436-438	1160.64	1163.69	Dark grey. Fine to medium grained (1-5 mm). Pred. pyroxene with minor interstitial plagioclase (<10%) and sulphides. Characterized by a 46 cm thick zone; pred. forsterite with vuggs filled with calcite and pyrite. The plagioclase modal abundance increases (~15%) towards this zone. PYROXENITE	C436-1 C437-5 C438-6	>5% chalcopyrite. pyrrhotite disseminations (1-10 mm

Appendix 3A: Thin – section descriptions for Marikana samples

Thin-section no.	Zone	Sample description	Transmitted light
RSTX26-01	Xenolith	Spinel patch	Coarse-crystalline monticellite with medium to fine-crystalline zoned spinel. All monticellite and spinel are idioblastic to hypidioblastic. Minor amounts of interstitial calcite occur. Sub-parallel fracturing exhibited in monticellite. Alteration veins cross-cut all minerals and are filled with micro-crystalline rust coloured mineral.
RSTX26-03	Xenolith	Unaltered xenolith	Coarse-crystalline monticellite and forsterite with sub-ordinate amounts of spinel inclusions. Sub-parallel fracturing is exhibited in monticellite. All minerals are idioblastic to hypidioblastic. Alteration veins cross-cut all minerals and are filled with micro-crystalline rust coloured mineral.
RSTX26-04	Xenolith	Pegmatoidal band	Coarse - crystalline to pegmatoidal monticellite occurs with medium to fine-crystalline zoned spinel inclusions. Monticellite exhibits sub - parallel fracturing. Medium spinel crystals exhibit zonation and contain minor amounts of calcite at their cores.
RSTX26-05	Xenolith	Forsterite-spinel layer, spinel layer and forsterite-monticellite layer	Sample is divided into three layers. (A) Coarse - crystalline idioblastic to hypidioblastic forsterite with medium - crystalline zoned spinel. (B) Medium - crystalline spinel rich layer exhibiting polygonal granoblastic texture with minor amounts of forsterite. (C) Medium - crystalline hypidioblastic forsterite with fine - crystalline. Idioblastic spinel and minor hypidioblastic monticellite. The sample is cross - cut by veins.
RSTX26-06 x2	Xenolith	Forsterite-spinel layer, spinel layer and forsterite-monticellite layer	Sample is divided into three layers. (A) Coarse - crystalline idioblastic to hypidioblastic forsterite with medium - crystalline zoned spinel. (B) Medium - crystalline spinel rich layer exhibiting polygonal granoblastic texture with minor amounts of forsterite. (C) Medium - crystalline hypidioblastic forsterite with fine - crystalline. Idioblastic spinel and minor hypidioblastic monticellite. The sample is cross - cut by veins.
RSTX26-12	Xenolith	Unaltered xenolith	Coarse-crystalline monticellite and forsterite with sub-ordinate amounts of spinel inclusions. Sub-parallel fracturing exhibited in monticellite. All minerals are idioblastic to hypidioblastic. Alteration veins cross-cut all minerals and are filled with micro-crystalline rust coloured mineral.
RSTX26-13 x 2	Contact	Calc - silicate fragment	Medium - crystalline garnet surrounded by highly fractured medium - crystalline diopside. Minor spinel occurs at garnet cores. The sample is characterized by a single 2cm long wollastonite fragment.

RSTX26-51	Contact	Matrix	Medium - crystalline euhedral to subhedral plagioclase with interstitial diopside. The sample is characterized by randomly positioned garnet aggregates/clusters. In some cases garnet appears to host spinel inclusions.
RSTX26-52	Contact	Calc - silicate fragment	A single 1.5 cm long monticellite fragment occurs. Mineral zonation appears to take place adjacent to the fragment. The edge of the fragment comprises fine-crystalline. Idioblastic. Zoned spinel. This is followed by a highly fractured band of medium-crystalline diopside. Next to the diopside band medium – crystalline, hypidioblastic monticellite, diopside, garnet and vesuvianite occur with minor amounts of zoned spinel.
RSTX26-53A	Contact	Matrix	Medium - crystalline euhedral to subhedral plagioclase with interstitial diopside. The sample is characterized by medium - crystalline xenoblastic garnet and vesuvianite together with fine symplectites.
RSTX26-53B	Contact	Calc - silicate fragment	Medium - crystalline garnet surrounded by highly fractured medium - crystalline diopside. Garnet crystals are characterized by fine - crystalline. idioblastic spinel at the core
RSTX26-54	Contact	Matrix	Highly altered medium - crystalline subhedral - anhedral plagioclase with interstitial diopside and minor amounts of calcite. The sample is characterized by very fine symplectites
RSTX26-61	Contact	Chromitite stringer proximal to xenolith	Medium - crystalline garnet surrounded by highly fractured medium - crystalline diopside. Garnet crystals are characterized by fine - crystalline. idioblastic spinel at the core
RSTX26-62	Contact	Chromitite stringer intermediate to xenolith	Highly altered, medium - grained. Subhedral - anhedral plagioclase with sericite and interstitial cpx and opx. Spinel occurs as euhedral inclusions in plagioclase. cpx and opx and in some case is surrounded by a thin layer of garnet.
RSTX26-63	Contact	Chromitite stringer distal to xenolith	Altered medium - grained. Subhedral - anhedral plagioclase with sericite and interstitial cpx and opx. Spinel occurs as inclusions in plagioclase. cpx and opx and in some case is surrounded by a thin layer of garnet. The sample is characterized by fine plagioclase - cpx symplectites.
RSTX26-A5	Host rock	Mottled anorthosite 5 m west of xenolith	Medium - grained. Euhedral - subhedral plagioclase with medium - grained of fine - grained cpx and opx.
RSTX26-A20	Host rock	Mottled anorthosite 20 m west of xenolith	Medium - grained. Euhedral - subhedral plagioclase with medium - grained of fine - grained cpx and opx.
RSTX26-UG1	UG1 chromitite layer	UG1 chromitite layer 20 m west of xenolith	Medium to fine - grained. Euhedral chromite with interstitial plagioclase and minor amounts of cpx and opx.

Appendix 3B: Thin – section descriptions for Zwartfontein samples

BOREHOLE ZF 116				
Sample no.	**Rock type**	**Thin-section no.**	**Transmitted Light**	**Reflected Light**
ZF116/24	Pyroxenite	A24-1.	Medium-grained cumulus cpx and opx with minor interstitial plagioclase which show signs of alteration in the form of sericite. Minor biotite occurs. The sample is cross-cut by a talc (?) vein.	Minor fine-grained disseminated magnetite associated with the talc (?) vein
ZF116/44	Serpentinite/ Harzburgite	A44-8A	Highly serpentinised. Medium-grained opx and olivine with oxides and minor biotite	All sulphides are associated with serpentinisation. Fine-grained magnetite occurs as disseminations and veinlets which often cross-cut disseminated pyrite. In some cases pyrite is rimmed by chalcopyrite
ZF116/44	Serpentinite/ Harzburgite	A44-8B	Highly serpentinised. Medium-grained opx and olivine with oxides and minor biotite	All sulphides are associated with serpentinisation. Fine-grained magnetite occurs as disseminations and veinlets which often cross-cut disseminated pyrite. In some cases pyrite is rimmed by chalcopyrite
ZF116/117	Parapyroxenite	A117-3	Medium-grained. altered cumulus cpx and forsterite with very minor interstitial plagioclase and vuggs occur	N/A
ZF116/156.2	Calc-silicate	A156-7	Medium-grained monticellite. Forsterite and cpx. Some grains are altered to fine-grained Ca-silicates and minor interstitial calcite. Medium to fine-grained spinel occurs	Fine to medium-grained disseminated magnetite. which often hosts fine-grained pyrite inclusions
ZF116/160-162	Calc-silicate	A160-3	Medium to fine-grained monticellite, forsterite and cpx. Numerous grains are altered to fine-grained Ca-silicates. Interstitial and individual grains of calcite occur	N/A
ZF116/227-228	Serpentinite	A228-5	Entirely serpentinised grains with minor amounts of very fine-grained Ca-silicates that occur as discontinuous veins	Very minor disseminated magnetite

ZF116/246	Pyroxenite	A246-9	Medium-grained cumulus opx and cpx with interstitial plagioclase with some sericitisation. Associated with minor amounts of biotite and cross-cut by serpentine veins	Very minor disseminations of pyrite rimmed by chalcopyrite
ZF116/289-291	Calc-silicate/ hybrid	A289-1	Medium-grained highly serpentinised grains + forsterite and cpx with minor interstitial calcite. Some grain have been altered to very fine-grained Ca-silicates and appear to be associated with veins	Very minor disseminated magnetite
ZF116/289-291	Calc-silicate/ hybrid	A290-6	Medium-grained serpentinised grains + forsterite and minor monticellite some grains are altered to very fine-grained Ca-silicates while others appear to be cross-cut by this very fine-grained material. interstitial and individual grains of calcite	N/A
ZF116/289-292	Parapyroxenite	A291-1	Medium to coarse-grained serpentinised grains + highly altered cumulus opx and cpx with minor interstitial plagioclase and few biotite laths	Fine to coarse-grained disseminated pyrrhotite often rimmed and/ or cross-cut by either pyrite or pentlandite which is associated with minor chalcopyrite. Minor disseminations of magnetite are associated with serpentinised zones
ZF116/293-295	Calc-silicate	A295-2A	Medium-grained serpentinised grains, forsterite, cpx and minor monticellite. Some grains are altered to very fine-grained Ca-silicates, while others are cross-cut by this alteration. calcite occurs interstitially and as veins	Very minor disseminations of fine-grained pyrrhotite associated with pyrite and chalcopyrite and cross-cut by magnetite
ZF116/293-295	Serpentinite/ Calc-silicate	A295-2B	Highly serpentinised grains occur with medium-grained forsterite (associated with very fine-grained Ca-silicates) and minor calcite	Very minor disseminated magnetite associated with serpentine
ZF116/307.5	Feldspathic Pyroxenite	A307-1	Pegmatoidal cumulus cpx and opx with interstitial plagioclase with minor biotite, calcite and oxides. Grains have been sericitised	Minor fine-grained disseminated pyrite and chalcopyrite
ZF116/307.6-309.3	Calc-silicate	A308-1	Fine to medium-grained forsterite. Cpx, other Ca-silicates and calcite. Ca-silicates are altered to finer material and associated with serpentine	N/A
ZF116/307.6-309.3	Serpentine	A309-1	Complete serpentinisation and/ or alteration of all minerals. Minor amounts of Ca-silicates and calcite occur	Very minor fine-grained disseminated pyrite

ZF116/309.4-312	Calc-silicate/ Metasediment	A312-3	Layered fine to medium-grained calcite, serpentine and very fine-grained Ca-silicates. The degree of serpentinisation is variable between layers	N/A
ZF116/327	Gabbronorite	A327-1	Medium to coarse-grained cumulus opx. cpx and plagioclase with minor biotite. Some zones of sericitisation occur.	Minor fine-grained disseminated pyrite in some cases rimmed by pyrite
ZF116/382-385	Calc-silicate/ Hybrid	A382-5	Medium-grained forsterite. cpx with some biotite. very minor plagioclase (highly sericitised) and interstitial calcite. Very fine-grained Ca-silicates occur. Some areas cross-cut by serpentine veins.	Very minor fine-grained disseminated chalcopyrite
ZF116/385-387	Calc-silicate	A385-7	Fine to medium-grained cpx and forsterite. Some alteration to very fine-grained Ca-silicates and minor calcite. Some zones are highly serpentinised.	N/A

BOREHOLE ZF116 ED1				
Sample no.	**Rock type**	**Thin-section no.**	**Transmitted Light**	**Reflected Light**
ZF116ED1/702	Feldsphatic Pyroxenite	B702-1	Medium-grained cumulus opx and cpx with interstitial plagioclase. Minor sulphides and biotite	Minor fine-grained disseminated pyrrhotite associated with pyrite and magnetite and rimmed by chalcopyrite
ZF116ED1/720	Serpentinite	B720-3	Complete serpentinisation and/or alteration of minerals. Very minor amounts of cpx appear to be present and very fine-grained Ca-silicates are associated with serpentine	Veinlets of magnetite associated with serpentine
ZF116ED1/805.1-805.8	Serpentinite Calc-silicate	B805-6	Highly serpentinised material with fine to medium grained calcite and minor cpx. Very fine-grained Ca-silicates occur.	N/A
ZF116ED1/805.9-808.2	Calc-silicate/ Metasediment	B806-4	Layered fine to medium-grained calcite, serpentine and very fine-grained Ca-silicates. The degree of serpentinisation is variable between layers	N/A
ZF116ED1/811	Pyroxenite	B811-1	Medium to coarse-grained cpx and opx with interstitial plagioclase which shows some sericitisation. Biotite (and phlogopite) occurs	Fine-grained disseminated magnetite and minor pyrite rimmed by chalcopyrite

ZF116ED1/882-884	Calc-silicate/ Hybrid	B882-4A	Medium to coarse-grained plagioclase. Opx. and cpx. Minor Ca-silicates (monticellite?), calcite and oxides. Some zones are highly altered	Fine-grained disseminated magnetite and pyrrhotite associated with
ZF116ED1/882-884	Calc-silicate	B882-4B	Fine to coarse-grained cpx, forsterite and other minor Ca-silicates (monticellite?). Minor serpentine	Few pyrite veinlets associated with minor magnetite
ZF116ED1/882-884	Calc-silicate/ Hybrid	B882-5A	Pred. cpx with variable grain size; fine to coarse-grained with opx and plagioclase. Some mineral are altered very fine-grained Ca-silicates	Minor fine-grained disseminated pyrite
ZF116ED1/882-884	Calc-silicate/ Hybrid	B882-5B	Fine to medium-grained monticellite and forsterite cross-cut by numerous serpentine veins. A large portion is completely altered to fine-grained material giving the area brown-turbid appearance. Some grains are completely serpentinised	Fine-grained magnetite in serpentine veins
ZF116ED1/882-884	Calc-silicate/ Hybrid	B884-2	Pred. medium-grained forsterite with minor monticellite and calcite. Some zones are serpentinised. another zone is cross-cut numerous serpentine veins	N/A
ZF116ED1/882-884	Calc-silicate/ Serpentinite	B884-3	Most grains are serpentinised some minor forsterite. cpx and calcite. Few grains are altered to very fine-grained Ca-silicates	Very fine-grained disseminated pyrite

BOREHOLE ZF24 D1				
Sample no.	**Rock type**	**Thin-section no.**	**Transmitted Light**	**Reflected Light**
ZF24D1/280-281	Calc-silicate/ Hybrid	D280-1	Fine to coarse-grained forsterite and cpx with minor calcite. Some grains have been altered to very fine-grained Ca-silicates	Medium to coarse-grained interstitial to disseminated pyrite associated with minor chalcopyrite
ZF24D1/280-281	Calc-silicate/ Hybrid	D281-1	Dominated by coarse-grained anhydrite. associated with fine to medium-grained cpx	N/A

BOREHOLE ZF109 ED1				
Sample no.	**Rock type**	**Thin-section no.**	**Transmitted Light**	**Reflected Light**
ZF109ED1/324-325	Pyroxenite	C325-4	Medium to coarse-grained opx and cpx (some enclose olivine) with interstitial plagioclase and minor biotite. Some zones are highly sercitised	Some interstitial fine-grained pyrrhotite associated with pyrite. chalcopyrite and minor magnetite
ZF109ED1/326-327	Calc-silicate/ Hybrid	C326-2	Fine to medium-grained forsterite. cpx and minor opx and oxides. Some zones are serpentinised	Fine-grained disseminations of pyrrhotite associated with pyrite and chalcopyrite in some cases. The sulphide disseminations are pred. concentrated serpentine veinlets
ZF109ED1/326-327	Calc-silicate/ Hybrid	C327-3	Fine to medium-grained forsterite. cpx and minor opx and oxides. Some zones are sericitised and few grains are serpentinised.	Minor disseminations of fine-grained pyrrhotite
ZF109ED1/326-327	Calc-silicate/ Hybrid	C327-5A	Fine to medium-grained forsterite and highly serpentinised material.	Fine-grained disseminations of pyrrhotite associated with pyrite, chalcopyrite and magnetite. The sulphide disseminations are pred. concentrated serpentine veinlets
ZF109ED1/326-327	Calc-silicate/ Hybrid	C327-5B	Medium-grained forsterite and cpx and minor phlogopite and oxides. Some zones are highly serpentinised and some grains are cross-cut by serpentine veins	Fine to coarse-grained disseminated pyrrhotite associated with chalcopyrite and in some cases minor magnetite
ZF109ED1/328-329	Pyroxenite	C329-1	Medium grained cumulus cpx and opx with interstitial plagioclase. The minerals are sericitised to difference degrees and also show a turbid-brown alteration	Fine-grained disseminations of magnetite. Fine to medium-grained pyrrhotite associated with minor pyrite and rimmed by chalcopyrite occur interstitially
ZF109ED1/331.4-334	Hybrid/ Serpentinite	C332-2	Highly serpentinised material with medium-grained forsterite and calcite. Some grains show turbid-brown alteration	Fine-grained disseminations of pyrrhotite associated with pyrite, chalcopyrite and magnetite.
ZF109ED1/429-431	Hybrid	C431-5	Medium-grained forsterite. cpx and calcite. Some zones are highly serpentinised and grains are cross-cut by numerous serpentine veins	Medium-grained interstitial pyrrhotite associated with either pyrite or pentlandite and rimmed by chalcopyrite. minor magnetite is associated in few cases
ZF109ED1/429-431	Parapyroxenite	C431-7A	Medium to coarse-grained cumulus cpx and plagioclase with minor forsterite, biotite and phlogopite and Ca-silicates (monticellite). Grains show different degrees of alteration	Some fine-grained disseminated pyrrhotite associated with pyrite and cross-cut by chalcopyrite in some cases. Fractures are filled with pyrite

ZF109ED1/429-431	Calc-silicate	C431-7B	Fine to medium-grained forsterite. cpx and monticellite. Few grains are completely serpentinised and other are cross-cut by serpentine veins	Some fine-grained disseminated pyrite associated with chalcopyrite. and magnetite
ZF109ED1/433-435	Calc-silicate	C434-0	Pred. medium-grained cpx with some calcite and anhydrite. Numerous areas are highly serpentinised and very fine-grained Ca-silicates (monticellite?/ wollastonite?) often occur in association with serpentine grains. Some cpx grains are cross-cut by serpentine veins. Minor phlogopite occurs	N/A
ZF109ED1/433-435	Calc-silicate	C435-2	Pred. medium-grained cpx with some calcite and anhydrite. Numerous areas are highly serpentinised and very fine-grained Ca-silicates (monticellite?/ wollastonite?) often occur in association with serpentine grains	Very minor fine-grained magnetite
ZF109ED1/436-438	Pyroxenite	C436-1	Medium-grained cumulus opx and opx with minor interstitial plagioclase and biotite. Some grains are sericitised	Some fine-grained disseminated pyrrhotite. associated with pyrite or pentlandite and chalcopyrite. Minor fine-grained magnetite disseminations occur
ZF109ED1/436-438	Calc-silicate	C437-5	Pred. fine-grained forsterite and cpx with calcite filled vuggs	Very minor fine-grained disseminated pyrite and chalcopyrite
ZF109ED1/436-438	Pyroxenite	C438-6	Medium-grained cumulus opx and opx with minor interstitial plagioclase and biotite. Some grains are sericitised	Fine to medium-grained disseminated of pyrrhotite. chalcopyrite and pentlandite intimately associated with each other

Appendix 4A: Electron microprobe analysis methodology

Eight samples were quantitatively analysed using a CAMECA SX – 5FE EMPA equipped with 5 wavelength dispersive spectrometers located at the MMU (Microscopy and Microanalysis Unit) of the University of the Witwatersrand. Analytical conditions were 15 kV acceleration voltage and 20 nA beam current. Natural and synthetic standards were used for calibration. A focused electron beam was used during quantitative analysis; the only exceptions were for feldspars and vesuvianite where a 5 µm beam diameter was used. Counting times were 20 seconds on the peak and 10 seconds in total on the background for all elements. Commercial "SPI" standards were used. Analyses of spinel were standardized for Si on a diopside standard. Al on almandine, V on vanadium metal, Mg on diopside, Mn on rhodonite, Ni on nickel metal, Ti on rutile, Zn on willemite and Cr on Cr-oxide. Analyses of garnet were standardized for Al/Si/Ca/Fe on almandine, Mg on pyrope, Ti on rutile, Mn on rhodonite and Cr on Cr-oxide. Plagioclase and wollastonite were standardized for Si/Al/Ca on plagioclase, Fe on almandine, Na on albite and K on orthoclase. Pyroxenes and monticellite analyses were standardized for Si/Ca/Mg on diopside, Al/Fe on almandine, Na on jadeite, K on orthoclase, Mn on rhodonite, Ti on rutile and Cr on Cr-oxide. Analyses of olivine were standardized for Mg on olivine, Si on diopside, Al on plagioclase, Fe on almandine, Mn on rhodonite and Ni on nickel metal. The data were collected with CAMECA software. An automated X-PHI matrix algorithm was applied to correct for differential matrix effects. Oxygen was calculated by stoichiometry. A total of 302 analyses were done.

Owing to prolonged downtime of the CAMECA instrument, quantitative mineral chemical analyses were obtained for 14 samples by using four wavelength dispersive spectrometers on a JEOL JXA-8230 electron probe micro-analyser at Rhodes University. The beam was generated by a tungsten cathode; 15 kV acceleration voltage, 20 nA current and beam sizes of 1 µm, 10 µm or 20 µm were applied to the minerals depending on their sensitivity to beam effects. Counts for Ca, Mg, Fe, K, Si, Na, F, Al, Mn, Ti, Cr, V and Ni were measured on K-alpha peaks. Counting times were 10 seconds on the peak and 10 seconds in total on the background for all elements. Commercial "SPI" standards were used. Analyses of chromite and spinel were standardized for Si on an olivine standard, Al on chromite or plagioclase, V on vanadium metal, Mg/Fe on pyrope or hematite, Mn on manganese metal, Ni on nickel metal, Ca on plagioclase, Ti on rutile and Cr on chromite. Analyses of pyroxene, garnet, monticellite, olivine and serpentine were standardised for Al on kaersutite, Si/Mg/Fe on pyrope, Ti on rutile, Na on jadeite, Mn on rhodonite, Ca on plagioclase, K on orthoclase and Cr on chromite. Plagioclase was standardized for Si/Al/Ca on plagioclase, Ti/Mg/Fe on kaersutite, Na on jadeite, Mn on rhodonite, F on MgF_2 and K on orthoclase. Carbonates and anhydrite analyses were standardized for Si on olivine, Mg/Fe on pyrope, Mn on rhodonite, Ba/S on barite, Ca on plagioclase/anhydrite and Sr on celestite. Unknown acquisitions were peaked on the samples before each point analysis. The data were collected with JEOL software. An automated ZAF matrix algorithm was applied to correct for differential matrix effects. Oxygen was calculated by stoichiometry. A total of 459 points were analysed.

Appendix 4B: Electron microprobe data expressed as oxides (wt %) and recalculated atoms per unit formula for Marikana samples

MONTICELLITE															
Sample	**RSTX26-12 (CAMECA)**				**RSTX26-6 (CAMECA)**				**RSTX26-1 (JEOL)**						
Analysis #	**1**	**2**	**3**	**4**	**1**	**2**	**3**	**4**	**31**	**32**	**33**	**34**	**35**	**36**	**37**
SiO_2	37.66	37.66	37.79	37.50	37.34	37.34	37.45	37.35	37.98	37.99	37.80	37.95	37.67	37.94	38.42
Al_2O_3	bdl	bdl	0.01	bdl	bdl	0.01	0.01	bdl	bdl	bdl	0.01	bdl	bdl	bdl	0.01
TiO_2	0.03	0.03	0.03	0.02	0.03	0.01	0.02	0.03	0.04	0.07	bdl	0.03	0.03	0.06	bdl
Cr_2O_3	0.02	0.03	bdl	0.01	0.05	bdl	0.01	0.01	0.06	0.06	bdl	bdl	0.08	0.03	0.04
FeO	2.80	2.74	2.81	2.76	4.05	3.91	3.16	3.37	2.61	2.55	2.64	2.53	2.70	2.50	2.65
MnO	0.60	0.58	0.53	0.55	0.55	0.61	0.58	0.55	0.56	0.47		0.49	0.56	0.46	0.49
MgO	23.96	24.10	24.20	24.04	23.34	23.03	23.66	23.93	24.32	24.31	24.14	24.16	24.92	24.21	24.58
CaO	34.13	34.08	33.84	34.05	33.67	33.63	33.67	33.50	33.74	33.96	33.85	33.93	33.73	33.86	33.77
Na_2O	0.01	0.01	0.01	0.01	0.01	0.01	0.02	0.01	bdl	bdl	0.01	bdl	bdl	bdl	bdl
K_2O	0.01	bdl	bdl	bdl	bdl	bdl	bdl	bdl	0.03	0.02	0.02	0.02	0.03	0.01	0.01
Total	**99.22**	**99.23**	**99.22**	**98.94**	**99.04**	**98.55**	**98.58**	**98.75**	**99.33**	**99.42**	**98.45**	**99.11**	**99.72**	**99.07**	**99.97**
Number of ions based on 4 Oxygens															
Si	1.00	1.00	1.00	1.00	1.00	1.00	1.00	1.00	1.00	1.00	1.01	1.01	0.99	1.01	1.01
Al	bdl	bdl	bdl	bdl	bdl	bdl	bdl	bdl	bdl	bdl	bdl	bdl	bdl	bdl	bdl
Ti	bdl	bdl	bdl	bdl	bdl	bdl	bdl	bdl	bdl	bdl	bdl	bdl	bdl	bdl	bdl
Cr	bdl	bdl	bdl	bdl	bdl	bdl	bdl	bdl	bdl	bdl	bdl	bdl	bdl	bdl	bdl
Fe^{2+}	0.06	0.06	0.06	0.06	0.09	0.09	0.07	0.08	0.06	0.06	0.06	0.06	0.06	0.06	0.06
Mn	0.01	0.01	0.01	0.01	0.01	0.01	0.01	0.01	0.01	0.01	bdl	0.01	0.01	0.01	0.01
Mg	0.95	0.95	0.96	0.95	0.93	0.92	0.94	0.95	0.96	0.96	0.96	0.96	0.98	0.96	0.96
Ca	0.97	0.97	0.96	0.97	0.97	0.97	0.97	0.96	0.96	0.96	0.97	0.96	0.95	0.96	0.95
Na	bdl	bdl	bdl	bdl	bdl	bdl	bdl	bdl	bdl	bdl	bdl	bdl	bdl	bdl	bdl
K	bdl	bdl	bdl	bdl	bdl	bdl	bdl	bdl	bdl	bdl	bdl	bdl	bdl	bdl	bdl
Total	**3.00**	**3.00**	**3.00**	**3.00**	**3.00**	**3.00**	**3.00**	**3.00**	**2.99**	**2.99**	**2.99**	**2.99**	**3.00**	**2.99**	**2.99**
Mg#	**0.94**	**0.94**	**0.94**	**0.94**	**0.91**	**0.91**	**0.93**	**0.93**	**0.94**	**0.94**	**0.94**	**0.94**	**0.94**	**0.95**	**0.94**

MONTICELLITE

Sample	RSTX26-1 (JEOL)								RSTX26-3 (JEOL)						
Analysis #	38	39	40	41	42	43	44	45	46	47	48	49	64	65	66
SiO_2	37.78	37.63	37.69	37.74	37.83	37.76	37.90	37.77	38.14	38.10	38.09	38.19	37.37	38.29	37.67
Al_2O_3	bdl	bdl	bdl	bdl	0.01	bdl	0.01	0.01	bdl	bdl	bdl	0.01	0.02	bdl	0.04
TiO_2	0.05	bdl	0.06	bdl	0.04	bdl	0.08	0.04	0.03	0.06	bdl	bdl	0.04	0.08	0.02
Cr_2O_3	bdl	bdl	bdl	bdl	bdl	0.03	bdl	bdl	bdl	0.05	bdl	bdl	0.05	0.01	bdl
FeO	2.43	2.41	2.74	2.33	3.02	2.62	2.35	2.58	2.23	2.03	2.11	2.08	2.21	2.32	2.01
MnO	0.55	0.63	0.47	0.51	0.61	0.50	0.46	0.49	0.61	0.53	0.55	0.51	0.54	0.65	0.52
MgO	24.03	24.23	24.51	23.98	23.89	24.15	24.42	24.34	24.65	24.51	24.76	25.02	24.33	24.60	24.81
CaO	33.95	34.01	33.88	33.95	33.40	33.66	33.76	33.69	33.60	34.08	34.02	34.07	33.80	33.58	33.99
Na_2O	bdl	bdl	bdl	bdl	bdl	bdl	bdl	bdl	0.01	bdl	bdl	0.01	bdl	0.03	bdl
K_2O	0.01	0.02	bdl	0.01	0.03	0.03	0.01	0.02	0.01	0.02	0.03	0.02	0.02	0.04	0.02
Total	**98.80**	**98.93**	**99.33**	**98.52**	**98.83**	**98.75**	**98.99**	**98.93**	**99.28**	**99.37**	**99.55**	**99.90**	**98.37**	**99.58**	**99.08**
	Number of ions based on 4 Oxygens														
Si	1.01	1.00	1.00	1.01	1.01	1.01	1.00	1.00	1.01	1.01	1.00	1.00	1.00	1.01	1.00
Al	bdl	bdl	bdl	bdl	bdl	bdl	bdl	bdl	bdl	bdl	bdl	bdl	bdl	bdl	bdl
Ti	bdl	bdl	bdl	bdl	bdl	bdl	bdl	bdl	bdl	bdl	bdl	bdl	bdl	bdl	bdl
Cr	bdl	bdl	bdl	bdl	bdl	bdl	bdl	bdl	bdl	bdl	bdl	bdl	bdl	bdl	bdl
Fe^{2+}	0.05	0.05	0.06	0.05	0.07	0.06	0.05	0.06	0.05	0.04	0.05	0.05	0.05	0.05	0.04
Mn	0.01	0.01	0.01	0.01	0.01	0.01	0.01	0.01	0.01	0.01	0.01	0.01	0.01	0.01	0.01
Mg	0.95	0.96	0.97	0.95	0.95	0.96	0.97	0.96	0.97	0.96	0.97	0.98	0.97	0.97	0.98
Ca	0.97	0.97	0.96	0.97	0.95	0.96	0.96	0.96	0.95	0.96	0.96	0.96	0.97	0.95	0.96
Na	bdl	bdl	bdl	bdl	bdl	bdl	bdl	bdl	bdl	bdl	bdl	bdl	bdl	bdl	bdl
K	bdl	bdl	bdl	bdl	bdl	bdl	bdl	bdl	bdl	bdl	bdl	bdl	bdl	bdl	bdl
Total	**2.99**	**3.00**	**3.00**	**2.99**	**2.99**	**2.99**	**2.99**	**3.00**	**2.99**	**2.99**	**3.00**	**3.00**	**3.00**	**2.99**	**3.00**
Mg#	**0.95**	**0.95**	**0.94**	**0.95**	**0.93**	**0.94**	**0.95**	**0.94**	**0.95**	**0.96**	**0.95**	**0.96**	**0.95**	**0.95**	**0.96**

MONTICELLITE

Sample	RSTX26-4 (JEOL)										RSTX26-5 (JEOL)			
Analysis #	67	68	69	70	71	72	73	74	75	76	90	91	92	93
SiO_2	37.71	37.84	37.22	37.59	37.57	37.82	37.64	37.88	38.06	37.67	37.43	36.82	36.93	37.14
Al_2O_3	bdl	bdl	bdl	0.02	bdl	bdl	0.01	0.01	bdl	bdl	bdl	0.01	bdl	bdl
TiO_2	0.02	0.01	0.06	bdl	0.04	0.02	0.02	bdl	0.07	0.01	0.06	0.04	bdl	0.05
Cr_2O_3	bdl	bdl	0.04	bdl	0.06	0.04	0.10	0.06	0.03	0.01	0.02	bdl	0.04	0.04
FeO	3.00	3.10	3.50	3.89	3.82	3.46	2.60	2.70	2.85	3.23	5.41	5.41	5.59	5.39
MnO	0.56	0.60	0.62	0.59	0.55	0.59	0.50	0.55	0.55	0.56	0.59	0.62	0.63	0.71
MgO	23.88	24.18	23.85	23.36	23.19	23.41	24.12	24.19	23.91	23.77	22.01	21.95	22.02	22.14
CaO	33.59	33.95	33.33	33.61	33.86	33.72	33.82	33.71	33.62	33.39	32.89	32.68	32.99	32.77
Na_2O	0.02	bdl	0.01	bdl	bdl	bdl	0.02	0.01	0.02	bdl	0.02	0.01	0.01	0.02
K_2O	0.02	0.01	0.01	0.03	0.01	0.01	0.04	0.03	0.02	0.01	0.02	0.03	0.02	0.01
Total	**98.80**	**99.70**	**98.65**	**99.09**	**99.11**	**99.06**	**98.86**	**99.14**	**99.12**	**98.65**	**98.44**	**97.56**	**98.24**	**98.26**
Number of ions based on 4 Oxygens														
Si	1.01	1.00	1.00	1.00	1.00	1.01	1.00	1.00	1.01	1.01	1.01	1.01	1.00	1.01
Al	bdl	bdl	bdl	bdl	bdl	bdl	bdl	bdl	bdl	bdl	bdl	bdl	bdl	bdl
Ti	bdl	bdl	bdl	bdl	bdl	bdl	bdl	bdl	bdl	bdl	bdl	bdl	bdl	bdl
Cr	bdl	bdl	bdl	bdl	bdl	bdl	bdl	bdl	bdl	bdl	bdl	bdl	bdl	bdl
Fe^{2+}	0.07	0.07	0.08	0.09	0.09	0.08	0.06	0.06	0.06	0.07	0.12	0.12	0.13	0.12
Mn	0.01	0.01	0.01	0.01	0.01	0.01	0.01	0.01	0.01	0.01	0.01	0.01	0.01	0.02
Mg	0.95	0.95	0.95	0.93	0.92	0.93	0.96	0.96	0.95	0.95	0.89	0.89	0.89	0.89
Ca	0.96	0.96	0.96	0.96	0.97	0.96	0.96	0.96	0.96	0.96	0.95	0.96	0.96	0.95
Na	bdl	bdl	bdl	bdl	bdl	bdl	bdl	bdl	bdl	bdl	bdl	bdl	bdl	bdl
K	bdl	bdl	bdl	bdl	bdl	bdl	bdl	bdl	bdl	bdl	bdl	bdl	bdl	bdl
Total	**3.00**	**3.00**	**3.00**	**3.00**	**3.00**	**2.99**	**3.00**	**2.99**	**2.99**	**2.99**	**2.99**	**2.99**	**3.00**	**2.99**
Mg#	**0.93**	**0.93**	**0.92**	**0.91**	**0.92**	**0.92**	**0.94**	**0.94**	**0.94**	**0.93**	**0.88**	**0.88**	**0.88**	**0.88**

FORSTERITE

Sample	RSTX26-12 (CAMECA)				RSTX26-6 CAMECA)									
Analysis #	1	2	3	4	4	6	7	8	9	10	11	12	13	14
SiO_2	42.22	42.20	42.14	42.07	42.00	41.78	41.92	41.84	42.19	42.23	41.88	42.08	42.05	41.54
Al_2O_3	0.02	0.02	0.02	0.02	0.01	0.03	0.02	0.02	bdl	bdl	bdl	0.04	0.01	0.01
TiO_2	0.02	0.02	0.01	0.02	0.02	bdl	0.01	0.01	0.01	0.03	0.02	0.01	0.01	0.01
Cr_2O_3	0.01	0.02	bdl	bdl	0.03	bdl	bdl	bdl	bdl	0.03	bdl	0.04	0.03	bdl
FeO	3.17	3.11	2.84	3.14	3.67	3.77	4.06	4.13	2.37	2.28	2.27	2.37	2.08	2.08
MnO	0.59	0.53	0.54	0.53	0.58	0.53	0.53	0.53	0.47	0.46	0.47	0.52	0.50	0.48
MgO	54.77	54.85	54.81	54.46	53.96	54.27	53.83	53.79	55.32	55.01	55.29	55.22	55.56	55.57
CaO	0.52	0.50	0.68	0.70	0.75	0.74	0.45	0.53	0.50	0.45	0.67	0.74	0.67	0.61
Na_2O	0.01	bdl	bdl	bdl	bdl	bdl	bdl	bdl	0.01	bdl	bdl	bdl	bdl	0.01
K_2O	bdl	bdl	bdl	bdl	bdl	bdl	bdl	0.01	bdl	bdl	bdl	bdl	bdl	bdl
Total	**101.33**	**101.25**	**101.04**	**100.94**	**101.02**	**101.12**	**100.82**	**100.86**	**100.87**	**100.49**	**100.60**	**101.02**	**100.91**	**100.31**
					Number of ions based on 4 Oxygens									
Si	0.99	0.99	0.99	0.99	0.99	0.99	1.00	0.99	0.99	1.00	0.99	0.99	0.99	0.98
Al	bdl	bdl	bdl	bdl	bdl	bdl	bdl	bdl	bdl	bdl	bdl	bdl	bdl	bdl
Ti	bdl	bdl	bdl	bdl	bdl	bdl	bdl	bdl	bdl	bdl	bdl	bdl	bdl	bdl
Cr	bdl	bdl	bdl	bdl	bdl	bdl	bdl	bdl	bdl	bdl	bdl	bdl	bdl	bdl
Fe^{2+}	0.06	0.06	0.06	0.06	0.07	0.07	0.08	0.08	0.05	0.05	0.04	0.05	0.04	0.04
Mn	0.01	0.01	0.01	0.01	0.01	0.01	0.01	0.01	0.01	0.01	0.01	0.01	0.01	0.01
Mg	1.92	1.93	1.93	1.92	1.91	1.92	1.91	1.90	1.94	1.94	1.95	1.94	1.95	1.96
Ca	0.01	0.01	0.02	0.02	0.02	0.02	0.01	0.01	0.01	0.01	0.02	0.02	0.02	0.02
Na	bdl	bdl	bdl	bdl	bdl	bdl	bdl	bdl	bdl	bdl	bdl	bdl	bdl	bdl
K	bdl	bdl	bdl	bdl	bdl	bdl	bdl	bdl	bdl	bdl	bdl	bdl	bdl	bdl
Total	**3.01**	**3.01**	**3.01**	**3.00**	**3.00**	**3.01**	**3.00**	**3.01**	**3.01**	**3.00**	**3.01**	**3.01**	**3.01**	**3.02**
Mg#	**0.97**	**0.97**	**0.97**	**0.97**	**0.96**	**0.96**	**0.96**	**0.96**	**0.98**	**0.98**	**0.98**	**0.98**	**0.98**	**0.98**

FORSTERITE

Sample	RSTX26-3 (JEOL)													
Analysis #	50	51	52	53	54	55	56	57	58	59	60	61	62	63
SiO_2	42.42	42.09	42.21	41.80	41.90	41.87	41.85	42.07	42.26	41.57	41.93	41.90	42.91	41.96
Al_2O_3	bdl	0.01	0.02	0.63	bdl	0.02	0.02	0.01	0.02	0.03	0.05	bdl	0.02	0.02
TiO_2	0.01	bdl	0.07	0.02	0.03	0.05	0.04	0.04	0.04	0.06	0.01	bdl	0.11	bdl
Cr_2O_3	0.04	0.01	0.04	bdl	bdl	0.02	bdl	0.04	bdl	0.08	0.02	0.04	bdl	0.03
FeO	2.15	1.91	1.90	2.08	2.20	2.13	2.35	2.06	2.08	2.22	2.11	2.14	2.07	2.41
MnO	0.54	0.48	0.42	0.50	0.53	0.54	0.51	0.54	0.47	0.54	0.56	0.50	0.52	0.56
MgO	55.46	55.87	55.95	55.20	55.02	54.77	54.91	54.99	55.76	54.76	54.99	55.28	56.79	54.97
CaO	0.42	0.45	0.59	0.43	0.57	0.73	0.57	0.57	0.47	0.78	0.66	0.47	0.54	0.65
Na_2O	bdl	0.02	0.01	bdl	bdl	bdl	bdl	bdl	bdl	bdl	bdl	bdl	0.01	bdl
K_2O	0.02	0.03	0.02	0.03	0.02	0.01	0.02	0.02	0.01	0.01	0.02	0.01	0.01	0.01
Total	**101.06**	**100.86**	**101.23**	**100.70**	**100.26**	**100.14**	**100.26**	**100.34**	**101.10**	**100.05**	**100.35**	**100.35**	**102.98**	**100.62**
	Number of ions based on 4 Oxygens													
Si	1.00	0.99	0.99	0.99	0.99	0.99	0.99	1.00	0.99	0.99	0.99	0.99	0.99	0.99
Al	bdl	bdl	bdl	0.02	bdl	bdl	bdl	bdl	bdl	bdl	bdl	bdl	bdl	bdl
Ti	bdl	bdl	bdl	bdl	bdl	bdl	bdl	bdl	bdl	bdl	bdl	bdl	bdl	bdl
Cr	bdl	bdl	bdl	bdl	bdl	bdl	bdl	bdl	bdl	bdl	bdl	bdl	bdl	bdl
Fe^{2+}	0.04	0.04	0.04	0.04	0.04	0.04	0.05	0.04	0.04	0.04	0.04	0.04	0.04	0.05
Mn	0.01	0.01	0.01	0.01	0.01	0.01	0.01	0.01	0.01	0.01	0.01	0.01	0.01	0.01
Mg	1.94	1.96	1.96	1.94	1.94	1.94	1.94	1.94	1.95	1.94	1.94	1.95	1.95	1.94
Ca	0.01	0.01	0.01	0.01	0.01	0.02	0.01	0.01	0.01	0.02	0.02	0.01	0.01	0.02
Na	bdl	bdl	bdl	bdl	bdl	bdl	bdl	bdl	bdl	bdl	bdl	bdl	bdl	bdl
K	bdl	bdl	bdl	bdl	bdl	bdl	bdl	bdl	bdl	bdl	bdl	bdl	bdl	bdl
Total	**3.00**	**3.01**	**3.01**	**3.01**	**3.01**	**3.01**	**3.01**	**3.00**	**3.01**	**3.01**	**3.01**	**3.01**	**3.01**	**3.01**
Mg#	**0.98**	**0.98**	**0.98**	**0.98**	**0.98**	**0.98**	**0.98**	**0.98**	**0.98**	**0.98**	**0.98**	**0.98**	**0.98**	**0.98**

FORSTERITE										
Sample	**RSTX26-5 (JEOL)**									
Analysis #	80	81	82	83	84	85	86	87	88	89
SiO_2	42.09	41.83	41.98	41.67	41.99	41.61	41.34	41.49	41.56	41.68
Al_2O_3	0.01	0.01	0.01	0.01	0.01	0.02	0.01	0.01	0.01	bdl
TiO_2	0.01	0.05	bdl	bdl	0.06	0.02	0.02	0.02	bdl	0.01
Cr_2O_3	0.04	bdl	bdl	0.05	0.02	bdl	0.01	0.04	bdl	0.01
FeO	1.74	2.06	2.44	2.62	2.27	1.91	4.02	4.57	5.06	5.59
MnO	0.54	0.51	0.56	0.46	0.47	0.44	0.47	0.50	0.52	0.54
MgO	55.17	54.79	54.44	54.14	54.54	54.74	53.29	52.77	53.03	52.77
CaO	0.54	0.65	0.35	0.61	0.78	0.66	0.38	0.53	0.60	0.72
Na_2O	bdl	bdl	bdl	0.02	bdl	bdl	bdl	0.03	bdl	0.01
K_2O	0.02	0.02	0.03	0.01	0.03	0.03	0.03	0.03	0.01	bdl
Total	**100.15**	**99.92**	**99.80**	**99.60**	**100.17**	**99.43**	**99.56**	**99.98**	**100.77**	**101.31**
	Number of ions based on 4 Oxygens									
Si	1.00	0.99	1.00	1.00	1.00	0.99	0.99	1.00	0.99	0.99
Al	bdl	bdl	bdl	bdl	bdl	bdl	bdl	bdl	bdl	bdl
Ti	bdl	bdl	bdl	bdl	bdl	bdl	bdl	bdl	bdl	bdl
Cr	bdl	bdl	bdl	bdl	bdl	bdl	bdl	bdl	bdl	bdl
Fe^{2+}	0.03	0.04	0.05	0.05	0.05	0.04	0.08	0.09	0.10	0.11
Mn	0.01	0.01	0.01	0.01	0.01	0.01	0.01	0.01	0.01	0.01
Mg	1.95	1.94	1.93	1.93	1.93	1.95	1.91	1.89	1.89	1.87
Ca	0.01	0.02	0.01	0.02	0.02	0.02	0.01	0.01	0.02	0.02
Na	bdl	bdl	bdl	bdl	bdl	bdl	bdl	bdl	bdl	bdl
K	bdl	bdl	bdl	bdl	bdl	bdl	bdl	bdl	bdl	bdl
Total	**3.00**	**3.00**	**3.00**	**3.00**	**3.00**	**3.01**	**3.01**	**3.00**	**3.01**	**3.01**
Mg#	**0.98**	**0.98**	**0.98**	**0.97**	**0.98**	**0.98**	**0.96**	**0.95**	**0.95**	**0.94**

CALCITE					
Sample	**RSTX26-1 (JEOL)**		**RSTX24-4 (JEOL)**		
Analysis #	**1**	**2**	**1**	**2**	**3**
CaO	53.87	53.80	54.64	54.39	53.40
MgO	0.08	0.09	0.01	0.03	0.02
FeO	0.02	bdl	0.11	0.18	0.04
SrO	0.24	0.21	0.25	0.22	0.24
BaO	0.01	0.03	0.08	0.06	bdl
MnO	bdl	bdl	bdl	0.06	0.03
CO_2	42.48	42.42	43.09	42.97	42.08
Total	**96.70**	**96.55**	**98.17**	**97.91**	**95.82**
	Number of ions based on 6 Oxygens				
Ca	1.99	1.99	1.99	1.99	1.99
Mg	bdl	0.01	bdl	bdl	bdl
Mn	bdl	bdl	bdl	bdl	bdl
Fe	bdl	bdl	bdl	bdl	bdl
Sr	bdl	bdl	bdl	bdl	bdl
Ba	bdl	bdl	bdl	bdl	bdl
C	**2.00**	**2.00**	**2.00**	**2.00**	**2.00**
O	**6.00**	**6.00**	**6.00**	**6.00**	**6.00**

VESUVIANITE

Sample	RSTX26-52 (CAMECA)						RSTX26-53A (CAMECA)					RSTX26-54 (CAMECA)				
Analysis #	1	2	3	4	5	6	1	2	3	4	5	1	2	3	4	5
Comment	c	r	c	r	c	r	r	i	i	c	r	sym	sym	sym	sym	sym
F	0.05	0.06	0.03	0.08	0.08	0.13	0.12	0.07	0.03	0.05	0.18	0.11	0.06	0.16	0.03	0.19
Na_2O	0.25	0.26	0.26	0.28	0.31	0.26	0.11	0.19	0.15	0.13	0.17	0.05	0.01	0.08	0.1	0.08
MgO	4.68	4.59	5.1	5	5.18	4.81	3.39	3.77	3.61	3.45	3.82	1.31	1.63	1.73	1.72	1.29
Al_2O_3	22.98	22.98	21.4	21.64	21.32	22.44	26.12	24.83	25.34	25.67	24.13	32.06	25.87	31.18	31.52	26.48
SiO_2	30.06	30.03	31.05	30.94	31.12	30.09	28.13	28.94	28.39	28.4	28.94	24.62	21.88	25.16	25.16	23.92
SO_3	bdl	bdl	bdl	bdl	bdl	bdl	bdl	bdl	bdl	bdl	bdl	bdl	bdl	bdl	bdl	bdl
Cl	bdl	bdl	bdl	bdl	bdl	bdl	bdl	bdl	bdl	bdl	bdl	0.01	0.72	0	0	5.06
CaO	39.02	38.79	39.06	38.79	38.74	38.91	39.09	39.26	39.12	39.24	38.97	39.22	34.08	39.34	39.24	32.15
TiO_2	bdl	bdl	bdl	bdl	0.01	bdl	0.01	0.01	bdl	bdl	bdl	0.01	0.01	0.01	bdl	bdl
Cr_2O_3	0.04	bdl	0.03	bdl	0.01	0.05	bdl	bdl	bdl	bdl	0.02	0.03	bdl	bdl	bdl	0.02
MnO	0.04	0.03	0.04	0.03	0.05	0.05	0.02	0.03	0.01	0.02	0.03	bdl	0.02	0.01	0.01	0.08
FeO	1.13	1.10	1.25	1.21	1.4	0.98	0.64	0.85	0.76	0.76	0.91	0.16	0.16	0.25	0.24	0.2
Fe_2O_3	bdl	bdl	bdl	bdl	bdl	bdl	bdl	bdl	bdl	bdl	bdl	bdl	bdl	bdl	bdl	bdl
H_2O	1.94	1.93	1.95	1.92	1.92	1.98	1.9	1.92	1.94	1.93	1.85	1.9	1.45	1.88	1.95	0.28
Total	**100.19**	**99.77**	**100.17**	**99.89**	**100.14**	**99.7**	**99.53**	**99.87**	**99.35**	**99.65**	**99.02**	**99.48**	**85.89**	**99.8**	**99.97**	**89.75**
							Number of ions based on 78 O. OH									
F	0.07	0.09	0.04	0.12	0.12	0.19	0.18	0.10	0.04	0.07	0.27	0.16	0.10	0.24	0.04	0.33
Na	0.23	0.24	0.23	0.25	0.28	0.24	0.10	0.17	0.14	0.12	0.16	0.05	0.01	0.07	0.09	0.08
Mg	3.25	3.20	3.54	3.48	3.60	3.36	2.37	2.63	2.53	2.41	2.69	0.92	1.33	1.20	1.19	1.05
Al	12.61	12.66	11.75	11.91	11.71	12.38	14.44	13.67	14.02	14.17	13.42	17.72	16.66	17.17	17.31	16.98
Si	13.99	14.04	14.46	14.45	14.50	14.09	13.19	13.52	13.33	13.30	13.66	11.54	11.96	11.76	11.72	13.01
Cl	bdl	bdl	bdl	bdl	bdl	bdl	bdl	bdl	bdl	bdl	bdl	0.01	0.67	bdl	bdl	4.67
Ca	19.46	19.43	19.50	19.41	19.34	19.52	19.64	19.66	19.68	19.69	19.70	19.70	19.96	19.69	19.59	18.74
Ti	bdl	bdl	bdl	bdl	bdl	bdl	bdl	bdl	bdl	bdl	bdl	bdl	bdl	bdl	bdl	bdl
Cr	0.01	bdl	0.01	bdl	bdl	0.02	bdl	bdl	bdl	bdl	0.01	0.01	bdl	bdl	bdl	0.01
Mn	0.02	0.01	0.02	0.01	0.02	0.02	0.01	0.01	bdl	0.01	0.01	bdl	0.01	bdl	bdl	0.04
Fe^{2+}	0.44	0.43	0.49	0.47	0.55	0.38	0.25	0.33	0.30	0.30	0.36	0.06	0.07	0.10	0.09	0.09
Fe^{3+}	bdl	bdl	bdl	bdl	bdl	bdl	bdl	bdl	bdl	bdl	bdl	bdl	bdl	bdl	bdl	bdl
Total	**50.07**	**50.09**	**50.04**	**50.12**	**50.12**	**50.19**	**50.18**	**50.10**	**50.04**	**50.07**	**50.27**	**50.17**	**50.77**	**50.24**	**50.04**	**54.99**
OH	**9.53**	**9.40**	**9.44**	**9.33**	**9.47**	**9.29**	**9.15**	**9.36**	**9.33**	**9.24**	**9.32**	**9.11**	**9.37**	**9.29**	**9.23**	**7.06**
O^{2-}	**62.38**	**62.50**	**62.45**	**62.57**	**62.44**	**62.34**	**62.73**	**62.56**	**62.55**	**62.66**	**62.58**	**62.78**	**62.57**	**62.61**	**62.66**	**64.93**

*c = core. i = intermediate. r = rim. sym = symplectite

GARNET

Sample	RSTX26-53A (CAMECA)													
Analysis #	**1**	**2**	**3**	**4**	**5**	**6**	**7**	**8**	**9**	**10**	**11**	**12**	**13**	**14**
Comment	**cn**	**cn**	**cn**	**cn**	**cn**	**i**	**i**	**i**	**i**	**i**	**i**	**r**	**r**	**r**
SiO_2	39.55	39.43	39.59	39.73	39.66	44.76	45.38	44.53	46.36	47.14	46.87	44.23	37.21	37.18
TiO_2	0.23	0.21	0.19	0.09	0.10	0.15	0.20	0.20	0.14	0.13	0.08	bdl	0.02	bdl
Al_2O_3	19.11	19.12	19.72	19.86	19.97	10.67	10.78	11.18	9.74	9.14	8.91	1.40	7.29	7.78
Cr_2O_3	0.15	0.07	0.01	bdl	0.02	2.62	1.46	1.41	0.42	0.23	0.06	bdl	bdl	bdl
FeO*	5.41	5.43	4.44	4.23	4.18	5.61	5.81	5.76	5.38	5.21	5.56	12.63	20.39	19.97
MnO	0.22	0.24	0.23	0.23	0.22	0.04	0.06	0.06	0.09	0.10	0.11	0.22	0.06	0.07
MgO	0.36	0.34	0.41	0.41	0.46	10.65	11.07	10.88	12.04	12.50	12.84	12.31	bdl	bdl
CaO	34.72	35.12	34.82	35.19	35.25	25.18	25.43	25.00	25.32	25.38	25.23	29.83	34.22	34.55
Na_2O	0.01	0.01	0.01	bdl	bdl	0.02	0.01	0.01	0.01	0.02	bdl	0.01	bdl	0.01
Total	**99.76**	**99.97**	**99.42**	**99.74**	**99.86**	**99.70**	**100.20**	**99.03**	**99.50**	**99.85**	**99.66**	**100.63**	**99.19**	**99.56**
						Number of ions based on 12 Oxygens								
Si	3.02	3.00	3.02	3.02	3.01	3.34	3.36	3.33	3.44	3.48	3.46	3.31	2.99	2.97
Ti	0.01	0.01	0.01	0.01	0.01	0.01	0.01	0.01	0.01	0.01	bdl	bdl	bdl	bdl
Al(IV)	bdl	bdl	bdl	bdl	bdl	bdl	bdl	bdl	bdl	bdl	bdl	bdl	0.01	0.03
Al(VI)	1.72	1.72	1.77	1.78	1.79	0.94	0.94	0.99	0.85	0.79	0.78	0.12	0.68	0.70
Cr	0.01	bdl	bdl	bdl	bdl	0.15	0.09	0.08	0.02	0.01	bdl	bdl	bdl	bdl
Fe^{3+}	0.21	0.25	0.16	0.17	0.18	0.21	0.24	0.24	0.24	0.23	0.29	1.26	1.33	1.33
Fe^{2+}	0.13	0.09	0.12	0.10	0.08	0.14	0.12	0.12	0.09	0.09	0.05	-0.47	0.04	bdl
Mn	0.01	0.02	0.01	0.01	0.01	bdl	bdl	bdl	0.01	0.01	0.01	0.01	bdl	bdl
Mg	0.04	0.04	0.05	0.05	0.05	1.19	1.22	1.21	1.33	1.37	1.41	1.37	bdl	bdl
Ca	2.84	2.86	2.85	2.87	2.87	2.01	2.02	2.01	2.01	2.00	1.99	2.39	2.95	2.96
Na	bdl	bdl	bdl	bdl	bdl	bdl	bdl	bdl	bdl	bdl	bdl	bdl	bdl	bdl
Total	**8.00**	**8.00**	**8.00**	**8.00**	**8.00**	**8.00**	**8.00**	**8.00**	**8.00**	**8.00**	**8.00**	**8.00**	**8.00**	**8.00**
Prp	1	1	2	2	2	35	36	36	39	40	41	42	0	0
Alm	4	3	4	3	3	4	4	4	3	3	1	-14	1	0
Sps	0	1	0	0	0	0	0	0	0	0	0	0	0	0
Grs	83	82	86	86	86	43	44	45	44	44	41	6	33	34
Uv	0	0	0	0	0	7	4	4	1	1	0	0	0	0
And	10	12	8	8	9	10	11	11	12	13	16	66	65	65
Total	100	99	99	100	100	100	99	99	100	100	100	100	100	100

*c = core. r = rim. cn = corona

GARNET

Sample	RSTX26-53B (CAMECA)								RSTX26-51 (CAMECA)										
Analysis #	1	2	3	4	5	6	8	9	1	2	3	4	5	6	7	8	9	10	11
Comment	c	i	i	i	i	i	r	i	r	r	r	r	r	r	r	c	c	c	r
SiO_2	37.34	37.30	37.65	37.99	37.51	37.37	38.01	37.67	39.75	39.70	39.61	39.80	39.53	40.29	39.65	37.94	38.03	38.40	39.26
TiO_2	1.37	1.24	1.26	0.97	1.25	1.38	0.79	1.08	0.19	0.14	0.15	0.16	0.22	0.19	0.17	0.39	0.41	0.35	0.23
Al_2O_3	12.52	13.90	13.96	13.91	14.02	13.82	14.40	13.87	20.07	20.71	20.65	20.64	19.73	16.58	19.09	10.66	11.98	13.09	17.65
Cr_2O_3	3.05	1.25	1.13	0.90	0.67	0.90	0.06	0.87	0.24	bdl	bdl	0.01	bdl	0.26	0.37	10.16	8.35	7.51	2.78
FeO*	9.92	10.05	10.05	10.87	10.38	10.41	10.92	10.42	3.71	2.95	2.94	3.01	4.29	4.63	4.58	4.94	5.25	4.69	3.83
MnO	0.07	0.13	0.14	0.13	0.15	0.16	0.16	0.13	0.17	0.15	0.20	0.15	0.21	0.21	0.19	bdl	bdl	bdl	0.08
MgO	0.35	0.34	0.35	0.28	0.32	0.37	0.23	0.28	0.45	0.48	0.48	0.50	0.40	0.31	0.38	0.28	0.35	0.31	0.41
CaO	34.47	34.88	35.10	35.15	34.98	34.72	35.21	35.05	35.59	35.64	35.45	35.56	35.57	33.50	35.27	34.17	33.96	34.49	35.26
Na_2O	0.01	0.01	0.01	bdl	bdl	bdl	0.02	bdl	0.01	bdl	bdl	0.01	bdl	0.07	bdl	bdl	0.01	bdl	0.01
Total	**99.10**	**99.10**	**99.65**	**100.20**	**99.28**	**99.13**	**99.80**	**99.37**	**100.18**	**99.77**	**99.48**	**99.84**	**99.95**	**96.04**	**99.70**	**98.54**	**98.34**	**98.84**	**99.51**
Number of ions based on 12 Oxygens																			
Si	2.95	2.93	2.94	2.95	2.93	2.93	2.95	2.95	3.01	3.00	3.01	3.01	3.00	3.20	3.02	3.04	3.03	3.03	3.02
Ti	0.08	0.07	0.07	0.06	0.07	0.08	0.05	0.06	0.01	0.01	0.01	0.01	0.01	0.01	0.01	0.02	0.02	0.02	0.01
Al(IV)	bdl	bdl	bdl	bdl	bdl	bdl	bdl	bdl	bdl	bdl	bdl	bdl	bdl	bdl	bdl	bdl	bdl	bdl	bdl
Al(VI)	1.16	1.28	1.28	1.27	1.29	1.28	1.32	1.28	1.79	1.85	1.85	1.84	1.76	1.55	1.72	1.01	1.13	1.22	1.60
Cr	0.19	0.08	0.07	0.06	0.04	0.06	bdl	0.05	0.01	bdl	bdl	bdl	bdl	0.02	0.02	0.64	0.53	0.47	0.17
Fe^{3+}	0.59	0.64	0.63	0.66	0.65	0.64	0.69	0.65	0.17	0.13	0.12	0.12	0.21	0.03	0.20	0.23	0.24	0.21	0.18
Fe^{2+}	0.06	0.02	0.02	0.04	0.03	0.04	0.02	0.03	0.07	0.06	0.07	0.07	0.06	0.28	0.10	0.10	0.11	0.10	0.07
Mn	bdl	0.01	0.01	0.01	0.01	0.01	0.01	0.01	0.01	0.01	0.01	0.01	0.01	0.01	0.01	bdl	bdl	bdl	0.01
Mg	0.04	0.04	0.04	0.03	0.04	0.04	0.03	0.03	0.05	0.05	0.05	0.06	0.05	0.04	0.04	0.03	0.04	0.04	0.05
Ca	2.91	2.93	2.93	2.92	2.93	2.92	2.93	2.94	2.88	2.89	2.88	2.88	2.89	2.85	2.88	2.93	2.90	2.92	2.90
Na	bdl	bdl	bdl	bdl	bdl	bdl	bdl	bdl	bdl	bdl	bdl	bdl	bdl	0.01	bdl	bdl	bdl	bdl	bdl
Total	**8.00**	**8.00**	**8.00**	**8.00**	**8.00**	**8.00**	**8.00**	**8.00**	**8.00**	**8.00**	**8.00**	**8.00**	**8.00**	**8.00**	**8.00**	**8.00**	**8.00**	**8.00**	**8.00**
Prp	**1**	**1**	**1**	**1**	**1**	**1**	**1**	**1**	**2**	**2**	**2**	**2**	**2**	**1**	**1**	**1**	**1**	**1**	**2**
Alm	**2**	**1**	**1**	**1**	**1**	**1**	**1**	**1**	**2**	**2**	**2**	**2**	**2**	**9**	**3**	**3**	**4**	**3**	**2**
Sps	**0**	**0**	**0**	**0**	**0**	**0**	**0**	**0**	**0**	**0**	**0**	**0**	**0**	**0**	**0**	**0**	**0**	**0**	**0**
Grs	**58**	**60**	**61**	**60**	**61**	**60**	**63**	**61**	**87**	**89**	**89**	**89**	**85**	**86**	**84**	**51**	**56**	**61**	**78**
Uv	**9**	**4**	**3**	**3**	**2**	**3**	**0**	**3**	**1**	**0**	**0**	**0**	**0**	**1**	**1**	**32**	**26**	**23**	**8**
And	**29**	**30**	**30**	**32**	**31**	**30**	**33**	**31**	**8**	**6**	**6**	**6**	**10**	**2**	**10**	**12**	**12**	**10**	**9**
Total	**100**	**97**	**96**	**97**	**97**	**96**	**98**	**97**	**100**	**100**	**100**	**100**	**99**	**99**	**100**	**99**	**99**	**99**	**99**

*c=core. i = intermediate. r = rim

GARNET

Sample	RSTX26-52 (CAMECA)																
Analysis #	1	2	3	4	5	6	7	8	9	10	11	12	13	14	15	16	17
Comment	i	i	i	i	i	r	r	r	i	c	c	i	i	c	c	c	c
SiO_2	37.80	37.57	37.77	37.43	37.87	38.59	38.74	38.60	37.96	37.51	37.34	37.46	37.84	37.82	38.02	37.91	37.92
TiO_2	0.72	0.93	0.79	0.91	0.56	0.40	0.47	0.48	0.66	0.62	1.06	1.15	0.63	0.50	0.48	0.48	0.51
Al_2O_3	14.16	14.14	13.98	14.00	13.55	16.86	17.47	17.48	14.58	11.78	13.40	13.95	14.91	11.63	12.94	12.09	13.29
Cr_2O_3	5.78	5.44	6.25	5.79	6.06	bdl	0.08	0.09	4.42	8.95	6.84	5.78	3.60	8.17	6.48	7.67	5.71
FeO*	5.32	5.28	4.95	5.31	5.75	7.61	6.84	6.69	6.15	5.09	5.12	5.36	6.70	6.40	6.33	6.11	6.30
MnO	0.11	0.10	0.06	0.08	0.07	0.16	0.18	0.17	0.11	0.02	0.09	0.10	0.16	0.05	0.05	0.05	0.02
MgO	0.50	0.51	0.44	0.49	0.36	0.30	0.38	0.43	0.39	0.37	0.44	0.44	0.31	0.30	0.37	0.34	0.37
CaO	34.25	34.14	34.30	34.09	34.24	34.90	34.59	34.94	34.25	33.90	33.74	33.87	34.39	34.01	34.12	34.12	33.99
Na_2O	bdl	bdl	0.01	bdl	0.01	bdl	bdl	0.01	bdl	bdl	bdl	bdl	bdl	bdl	bdl	bdl	bdl
Total	**98.64**	**98.11**	**98.55**	**98.10**	**98.47**	**98.82**	**98.75**	**98.89**	**98.52**	**98.24**	**98.03**	**98.11**	**98.54**	**98.88**	**98.79**	**98.77**	**98.11**
							Number of ions based on 12 Oxygens										
Si	2.98	2.97	2.98	2.97	3.00	2.99	3.00	2.98	2.99	3.00	2.97	2.97	2.97	3.01	3.01	3.01	3.01
Ti	0.04	0.06	0.05	0.05	0.03	0.02	0.03	0.03	0.04	0.04	0.06	0.07	0.04	0.03	0.03	0.03	0.03
Al(IV)	bdl	bdl	bdl	bdl	bdl	bdl	bdl	bdl	bdl	bdl	bdl	bdl	bdl	bdl	bdl	bdl	bdl
Al(VI)	1.31	1.32	1.30	1.31	1.26	1.54	1.60	1.59	1.35	1.11	1.26	1.30	1.38	1.09	1.21	1.13	1.24
Cr	0.36	0.34	0.39	0.36	0.38	bdl	bdl	0.01	0.28	0.57	0.43	0.36	0.22	0.51	0.40	0.48	0.36
Fe^{3+}	0.29	0.28	0.26	0.29	0.30	0.42	0.34	0.38	0.32	0.25	0.24	0.25	0.37	0.32	0.32	0.31	0.31
Fe^{2+}	0.06	0.07	0.07	0.06	0.08	0.07	0.10	0.05	0.09	0.09	0.10	0.10	0.07	0.10	0.10	0.09	0.11
Mn	0.01	0.01	bdl	0.01	bdl	0.01	0.01	0.01	0.01	bdl	0.01	0.01	0.01	bdl	bdl	bdl	bdl
Mg	0.06	0.06	0.05	0.06	0.04	0.03	0.04	0.05	0.05	0.04	0.05	0.05	0.04	0.04	0.04	0.04	0.04
Ca	2.89	2.89	2.90	2.89	2.90	2.90	2.87	2.89	2.89	2.90	2.88	2.88	2.90	2.90	2.89	2.90	2.89
Na	bdl	bdl	bdl	bdl	bdl	bdl	bdl	bdl	bdl	bdl	bdl	bdl	bdl	bdl	bdl	bdl	bdl
Total	**8.00**	**8.00**	**8.00**	**8.00**	**8.00**	**8.00**	**8.00**	**8.00**	**8.00**	**8.00**	**8.00**	**8.00**	**8.00**	**8.00**	**8.00**	**8.00**	**8.00**
Prp	**2**	**2**	**2**	**2**	**1**	**1**	**1**	**2**	**2**	**1**	**2**	**2**	**1**	**1**	**1**	**1**	**1**
Alm	**2**	**2**	**2**	**2**	**3**	**2**	**3**	**2**	**3**	**3**	**3**	**3**	**2**	**3**	**3**	**3**	**3**
Sps	**0**	**0**	**0**	**0**	**0**	**0**	**0**	**0**	**0**	**0**	**0**	**0**	**0**	**0**	**0**	**0**	**0**
Grs	**64**	**63**	**62**	**62**	**61**	**75**	**77**	**76**	**65**	**54**	**60**	**62**	**66**	**53**	**59**	**55**	**61**
Uv	**18**	**16**	**19**	**17**	**18**	**0**	**0**	**0**	**13**	**28**	**20**	**17**	**11**	**25**	**20**	**24**	**18**
And	**14**	**13**	**12**	**14**	**15**	**20**	**16**	**18**	**15**	**12**	**11**	**12**	**18**	**16**	**16**	**15**	**15**
Total	**100**	**97**	**98**	**97**	**98**	**99**	**99**	**99**	**98**	**98**	**97**	**97**	**98**	**99**	**99**	**99**	**99**

*c=core, i = intermediate, r = rim

GARNET

Sample	RSTX26-54 (CAMECA)												
Analysis #	1	2	3	4	5	6	7	8	9	10	11	12	13
Comment	cn	cn	cn	cn	cn	cn	sym	sym	sym	sym	sym	sym	sym
SiO_2	40.12	39.78	39.99	39.94	39.65	39.88	39.97	39.73	40.22	40.27	39.54	39.84	40.08
TiO_2	0.04	0.17	0.15	0.17	0.11	0.09	0.04	0.14	bdl	0.05	0.13	0.07	0.05
Al_2O_3	20.68	20.11	19.88	19.96	20.51	20.66	21.53	20.54	21.07	21.20	19.96	20.53	20.75
Cr_2O_3	0.01	0.03	0.09	0.04	0.01	0.05	0.02	0.24	bdl	0.01	0.37	bdl	0.01
FeO*	3.44	4.27	4.26	4.39	3.93	3.52	2.41	3.69	2.63	2.64	3.48	3.12	3.02
MnO	0.18	0.18	0.17	0.23	0.23	0.19	0.10	0.16	0.06	0.16	0.15	0.19	0.15
MgO	0.44	0.34	0.43	0.41	0.46	0.41	0.34	0.44	0.14	0.41	0.47	0.35	0.36
CaO	35.50	35.56	35.36	35.52	35.16	35.39	35.98	35.32	36.69	35.76	35.48	35.68	35.58
Na2O	bdl	0.01	bdl	bdl	0.01	0.01	bdl	bdl	bdl	bdl	bdl	bdl	bdl
Total	**100.41**	**100.45**	**100.33**	**100.66**	**100.07**	**100.20**	**100.39**	**100.26**	**100.81**	**100.50**	**99.58**	**99.78**	**10bdl**
					Number of ions based on 12 Oxygens								
Si	3.02	3.00	3.02	3.01	3.00	3.01	3.00	3.00	3.01	3.02	3.01	3.02	3.03
Ti	bdl	0.01	0.01	0.01	0.01	0.01	bdl	0.01	bdl	bdl	0.01	bdl	bdl
Al(IV)	bdl	bdl	bdl	bdl	bdl	bdl	bdl	bdl	bdl	bdl	bdl	bdl	bdl
Al(VI)	1.84	1.79	1.77	1.77	1.83	1.84	1.91	1.83	1.86	1.88	1.79	1.83	1.85
Cr	bdl	bdl	0.01	bdl	bdl	bdl	bdl	0.01	bdl	bdl	0.02	bdl	bdl
Fe^{3+}	0.12	0.19	0.16	0.19	0.16	0.13	0.09	0.14	0.12	0.07	0.16	0.12	0.09
Fe^{2+}	0.10	0.08	0.11	0.09	0.09	0.09	0.06	0.09	0.05	0.09	0.06	0.07	0.10
Mn	0.01	0.01	0.01	0.01	0.01	0.01	0.01	0.01	bdl	0.01	0.01	0.01	0.01
Mg	0.05	0.04	0.05	0.05	0.05	0.05	0.04	0.05	0.02	0.05	0.05	0.04	0.04
Ca	2.86	2.88	2.86	2.87	2.85	2.86	2.89	2.86	2.94	2.88	2.89	2.90	2.88
Na	bdl	bdl	bdl	bdl	bdl	bdl	bdl	bdl	bdl	bdl	bdl	bdl	bdl
Total	**8.00**	**8.00**	**8.00**	**8.00**	**8.00**	**8.00**	**8.00**	**8.00**	**8.00**	**8.00**	**8.00**	**8.00**	**8.00**
Prp	**2**	**1**	**2**	**2**	**2**	**2**	**1**	**2**	**1**	**2**	**2**	**1**	**1**
Alm	**3**	**3**	**4**	**3**	**3**	**3**	**2**	**3**	**2**	**3**	**2**	**2**	**3**
Sps	**0**	**0**	**0**	**0**	**0**	**0**	**0**	**0**	**0**	**0**	**0**	**0**	**0**
Grs	**89**	**86**	**86**	**85**	**87**	**88**	**92**	**87**	**92**	**91**	**87**	**90**	**90**
Uv	**0**	**0**	**0**	**0**	**0**	**0**	**0**	**1**	**0**	**0**	**1**	**0**	**0**
And	**6**	**9**	**8**	**9**	**8**	**6**	**4**	**7**	**6**	**3**	**8**	**6**	**4**
Total	**100**	**100**	**100**	**100**	**100**	**100**	**100**	**100**	**100**	**100**	**100**	**100**	**100**

*cn = corona, sym = symplectite

GARNET

Sample	RSTX26-61 (JEOL)											RSTX26-63 (JEOL)				
Analysis #	1	2	3	4	5	6	7	8	9	10	11	1	2	3	4	5
Comment	c	r	c	r	c	i	c	c	c	c	r					
SiO_2	37.79	37.79	38.01	37.60	38.28	37.75	37.86	37.32	37.11	37.11	37.36	37.09	36.49	36.86	36.69	37.47
TiO_2	0.47	0.47	0.37	0.48	0.44	0.63	0.56	0.61	0.97	1.11	1.04	1.66	2.08	1.72	1.68	1.26
Al_2O_3	11.71	11.71	14.10	12.19	14.34	11.04	12.15	10.82	10.41	10.17	10.22	10.96	10.98	11.09	11.24	12.02
Cr_2O_3	9.60	9.60	6.04	9.38	5.91	10.25	9.13	10.26	10.53	10.73	10.55	10.11	9.33	9.12	9.58	8.51
Fe_2O_3	3.83	4.61	5.13	4.42	5.20	5.08	4.90	5.37	5.68	5.43	5.64	5.83	5.53	5.77	5.31	5.50
MnO	0.17	0.17	0.21	0.30	0.21	0.19	0.24	0.23	0.17	0.14	0.15	0.14	0.11	0.14	0.16	0.11
MgO	0.49	0.49	0.65	0.53	0.61	0.61	0.59	0.63	0.65	0.73	0.70	0.65	0.75	0.80	0.69	0.75
CaO	33.50	33.50	33.34	33.11	33.48	33.27	33.41	33.13	32.95	32.79	32.76	32.51	32.52	32.52	32.69	32.82
Na2O	0.04	0.04	0.01	0.03	0.02	0.03	0.02	0.02	0.01	0.02	0.01	0.02	0.03	0.03	0.03	0.02
Total	**98.65**	**98.38**	**97.88**	**98.03**	**98.46**	**98.85**	**98.86**	**98.38**	**98.49**	**98.21**	**98.45**	**98.45**	**98.45**	**98.45**	**98.45**	**98.45**
Number of ions based on 12 Oxygens																
Si	3.03	3.01	3.01	3.01	3.01	3.00	2.99	2.98	2.99	3.00	4.05	2.96	2.94	2.96	2.95	2.98
Ti	0.03	0.02	0.03	0.03	0.04	0.03	0.04	0.06	0.07	0.06	0.01	0.10	0.13	0.10	0.10	0.08
Al(IV)	bdl	bdl	bdl	bdl	bdl	bdl	bdl	bdl	bdl	bdl	bdl	bdl	bdl	bdl	bdl	bdl
Al(VI)	1.11	1.32	1.15	1.33	1.04	1.14	1.02	0.99	0.96	0.97	0.12	1.03	1.04	1.05	1.07	1.13
Cr	0.61	0.38	0.59	0.37	0.65	0.57	0.65	0.67	0.68	0.67	0.03	0.64	0.59	0.58	0.61	0.54
Fe^{3+}	0.23	0.31	0.27	0.31	0.30	0.29	0.32	0.34	0.33	0.34	0.03	0.35	0.34	0.35	0.32	0.33
Fe^{2+}	bdl	bdl	bdl	bdl	bdl	bdl	bdl	bdl	bdl	bdl	bdl	bdl	bdl	bdl	bdl	bdl
Mn	0.01	0.01	0.02	0.01	0.01	0.02	0.02	0.01	0.01	0.01	0.01	0.01	0.01	0.01	0.01	0.01
Mg	0.06	0.08	0.06	0.07	0.07	0.07	0.07	0.08	0.09	0.08	1.59	0.08	0.09	0.10	0.08	0.09
Ca	2.88	2.83	2.84	2.82	2.84	2.84	2.85	2.84	2.83	2.82	2.01	2.78	2.81	2.80	2.81	2.80
Na	0.01	bdl	bdl	bdl	bdl	bdl	bdl	bdl	bdl	bdl	bdl	bdl	bdl	bdl	bdl	bdl
Total	**7.97**	**7.96**	**7.97**	**7.96**	**7.96**	**7.97**	**7.97**	**7.96**	**7.96**	**7.95**	**7.86**	**7.94**	**7.95**	**7.95**	**7.96**	**7.95**
Prp	**2**	**3**	**2**	**2**	**2**	**2**	**3**	**3**	**3**	**3**	**44**	**3**	**3**	**3**	**3**	**3**
Alm	**0**	**0**	**0**	**0**	**0**	**0**	**0**	**0**	**0**	**0**	**0**	**0**	**0**	**0**	**0**	**0**
Sps	**0**	**0**	**1**	**0**	**0**	**1**	**1**	**0**	**0**	**0**	**0**	**0**	**0**	**0**	**0**	**0**
Grs	**55**	**64**	**55**	**64**	**50**	**54**	**49**	**46**	**46**	**46**	**35**	**47**	**48**	**49**	**49**	**53**
Uv	**30**	**18**	**28**	**18**	**31**	**27**	**31**	**32**	**32**	**32**	**10**	**29**	**27**	**27**	**28**	**25**
And	**11**	**15**	**13**	**15**	**15**	**14**	**15**	**16**	**16**	**16**	**9**	**16**	**15**	**16**	**15**	**15**
Total	**99**	**100**	**99**	**99**	**98**	**98**	**98**	**97**	**97**	**97**	**98**	**95**	**94**	**95**	**95**	**96**

* c=core. i = intermediate. r = rim

FELDSPAR

Sample	RSTX26-53A (CAMECA)										RSTX26-51 (CAMECA)														
Analysis #	**1**	**2**	**3**	**4**	**5**	**6**	**7**	**8**	**9**	**10**	**1**	**2**	**3**	**4**	**5**	**6**	**7**	**8**	**9**	**10**	**11**	**12**	**13**	**14**	**15**
SiO_2	43.24	42.91	43.33	43.24	43.02	43.14	43.02	42.91	42.34	42.96	42.7	42.72	42.55	42.65	42.77	42.46	42.77	42.91	43.12	43.08	42.99	43.06	42.81	42.94	42.96
Al_2O_3	36.35	36.24	36.37	36.31	36.56	36.26	36.35	36.31	35.98	36.33	36.28	36.16	35.97	36.12	35.77	35.86	36.28	36.41	36.5	36.51	36.46	36.37	36.3	36.22	36.22
FeO	0.18	0.07	0.09	0.14	0.11	0.17	0.15	0.12	0.15	0.22	0.13	0.11	0.12	0.11	0.15	0.14	0.16	0.08	0.08	0.08	0.07	0.19	0.16	0.20	0.17
CaO	20.02	19.76	20.25	19.88	20.17	19.84	19.99	19.76	19.59	20.02	19.89	19.94	19.8	19.89	19.63	19.52	19.8	19.74	19.87	19.88	20.11	20.04	19.92	19.84	19.83
Na_2O	0.03	0.02	0.01	0.05	0.02	0.03	0.06	0.02	0.03	0.04	0.04	0.01	0.03	0.05	0.06	0.09	0.06	0.01	0.03	bdl	0.02	0.03	0.03	0.02	0.03
K_2O	0.01	0.01	bdl	0.01	0.01	0.01	0.02	0.02	0.01	bdl	0.02	0.03	0.02	0.03	0.06	0.06	0.05	bdl	0.02	0.01	0.02	0.02	0.02	0.02	0.01
BaO	0.05	0.01	0.04	0.02	0.04	bdl	0.02	0.02	0.03	0.04	bdl	0.01	0.02	0.03	0.03	0.06	0.02	0.03	0.02	0.03	0.01	0.03	0.04	0.04	0.02
Total	**99.88**	**99.02**	**100.1**	**99.7**	**99.93**	**99.45**	**99.6**	**99.16**	**98.13**	**99.61**	**99.06**	**98.98**	**98.51**	**98.88**	**98.47**	**98.19**	**99.14**	**99.18**	**99.64**	**99.6**	**99.68**	**99.74**	**99.28**	**99.3**	**99.24**
	Number of ions based on 8 Oxygens																								
Si	2.01	2.01	2.01	2.01	2.00	2.01	2.00	2.00	2.00	2.00	2.00	2.00	2.00	2.00	2.01	2.00	2.00	2.00	2.00	2.00	2.00	2.00	2.00	2.00	2.01
Al	1.99	2.00	1.99	1.99	2.00	1.99	1.99	2.00	2.00	1.99	2.00	2.00	1.99	2.00	1.98	1.99	2.00	2.00	2.00	2.00	2.00	1.99	2.00	1.99	1.99
Fe	0.01	bdl	bdl	0.01	bdl	0.01	0.01	bdl	0.01	0.01	0.01	bdl	bdl	bdl	0.01	0.01	0.01	bdl	bdl	bdl	bdl	0.01	0.01	0.01	0.01
Ca	1.00	0.99	1.00	0.99	1.00	0.99	1.00	0.99	0.99	1.00	1.00	1.00	1.00	1.00	0.99	0.99	0.99	0.99	0.99	0.99	1.00	1.00	1.00	0.99	0.99
Na	bdl	bdl	bdl	bdl	bdl	bdl	0.01	bdl	bdl	bdl	bdl	bdl	bdl	bdl	0.01	0.01	0.01	bdl	bdl	bdl	bdl	bdl	bdl	bdl	bdl
K	bdl	bdl	bdl	bdl	bdl	bdl	bdl	bdl	bdl	bdl	bdl	bdl	bdl	bdl	bdl	bdl	bdl	bdl	bdl	bdl	bdl	bdl	bdl	bdl	bdl
Ba	bdl	bdl	bdl	bdl	bdl	bdl	bdl	bdl	bdl	bdl	bdl	bdl	bdl	bdl	bdl	bdl	bdl	bdl	bdl	bdl	bdl	bdl	bdl	bdl	bdl
Total	**5.00**	**5.00**	**5.00**	**5.00**	**5.01**	**5.00**	**5.00**	**5.00**	**5.00**	**5.01**	**5.00**	**5.00**	**5.00**	**5.01**	**5.00**	**5.00**	**5.01**	**5.00**	**5.00**	**5.00**	**5.00**	**5.00**	**5.00**	**5.00**	**5.00**
Ab	**0**	**0**	**0**	**0**	**0**	**0**	**1**	**0**	**0**	**0**	**0**	**0**	**0**	**0**	**1**	**1**	**1**	**0**	**0**	**0**	**0**	**0**	**0**	**0**	**0**
An	**100**	**100**	**100**	**99**	**100**	**100**	**99**	**100**	**100**	**100**	**100**	**100**	**100**	**99**	**99**	**99**	**99**	**100**	**100**	**100**	**100**	**100**	**100**	**100**	**100**
Or	**0**	**0**	**0**	**0**	**0**	**0**	**0**	**0**	**0**	**0**	**0**	**0**	**0**	**0**	**0**	**0**	**0**	**0**	**0**	**0**	**0**	**0**	**0**	**0**	**0**
Total	**100**	**100**	**100**	**100**	**100**	**100**	**100**	**100**	**100**	**100**	**100**	**100**	**100**	**100**	**100**	**100**	**100**	**100**	**100**	**100**	**100**	**100**	**100**	**100**	**100**

FELDSPAR

Sample	RSTX26-54 (CAMECA)												RSTX26-62 (JEOL)									
Analysis #	**1**	**2**	**3**	**4**	**5**	**6**	**7**	**8**	**9**	**10**	**11**	**12**	**53**	**54**	**55**	**56**	**57**	**58**	**59**	**60**	**61**	**62**
SiO_2	43.29	43.19	43.25	42.98	42.98	43.13	42.94	42.94	42.99	42.77	41.81	42.74	45.14	44.94	45.34	45.04	45.54	45.74	45.47	45.75	45.80	44.68
Al_2O_3	36.53	36.5	36.6	36.43	36.33	36.63	36.64	36.5	36.39	36.13	35.52	35.97	35.56	35.28	35.42	35.65	35.12	34.82	35.69	35.28	35.22	35.68
FeO	0.09	0.05	0.05	0.06	0.08	0.14	0.1	0.02	0.03	0.02	0.03	0.06	0.23	0.24	0.13	0.21	0.20	0.27	0.11	0.12	0.12	0.16
CaO	20.03	20.01	19.87	19.9	20	19.91	20.15	19.94	20.06	20.03	20.95	19.94	19.39	19.22	19.55	19.43	19.10	18.65	19.17	18.79	19.08	19.67
Na_2O	0.02	0.01	0.02	0.05	0.02	0.01	0.02	0.01	0.01	0.02	bdl	0.01	0.29	0.37	0.19	0.22	0.56	0.69	0.36	0.60	0.59	0.19
K_2O	bdl	bdl	bdl	0.02	bdl	bdl	bdl	bdl	0.01	0.01	bdl	bdl	0.03	0.03	0.03	0.02	0.04	0.03	0.04	0.04	0.02	0.04
BaO	0.03	0.04	0.03	0.04	0.01	0.04	0.02	0.04	0.02	0.02	0.03	0.04										
Total	**99.99**	**99.8**	**99.82**	**99.5**	**99.42**	**99.86**	**99.9**	**99.45**	**99.51**	**99**	**98.34**	**98.76**	**100.63**	**100.08**	**100.66**	**100.58**	**100.56**	**100.21**	**100.82**	**100.60**	**100.82**	**100.41**
	Number of ions based on 8 Oxygens																					
Si	2.01	2.00	2.01	2.00	2.00	2.00	1.99	2.00	2.00	2.00	1.98	2.01	2.07	2.07	2.08	2.07	2.09	2.10	2.08	2.09	2.09	2.06
Al	1.99	2.00	2.00	2.00	1.99	2.00	2.00	2.00	2.00	1.99	1.98	1.99	1.92	1.92	1.91	1.93	1.90	1.89	1.92	1.90	1.90	1.94
Fe	bdl	bdl	bdl	bdl	bdl	0.01	bdl	bdl	bdl	bdl	bdl	bdl	0.01	0.01	0.01	0.01	0.01	0.01	bdl	bdl	bdl	0.01
Ca	0.99	0.99	0.99	0.99	1.00	0.99	1.00	0.99	1.00	1.00	1.06	1.00	0.95	0.96	0.96	0.94	0.92	0.94	0.92	0.93	0.97	0.69
Na	bdl	bdl	bdl	bdl	bdl	bdl	bdl	bdl	bdl	bdl	bdl	bdl	0.03	0.02	0.02	0.05	0.06	0.03	0.05	0.05	0.02	0.27
K	bdl	bdl	bdl	bdl	bdl	bdl	bdl	bdl	bdl	bdl	bdl	bdl	bdl	bdl	bdl	bdl	bdl	bdl	bdl	bdl	bdl	0.02
Ba	bdl	bdl	bdl	bdl	bdl	bdl	bdl	bdl	bdl	bdl	bdl	bdl										
Total	**5.00**	**5.00**	**5.00**	**5.00**	**5.00**	**5.00**	**5.01**	**5.00**	**5.00**	**5.00**	**5.03**	**5.00**	**4.99**	**4.98**	**4.97**	**4.99**	**4.98**	**4.97**	**4.98**	**4.99**	**4.98**	**4.97**
Ab	**0**	**0**	**0**	**0**	**0**	**0**	**0**	**0**	**0**	**0**	**0**	**0**	**3**	**3**	**2**	**2**	**5**	**6**	**3**	**5**	**5**	**2**
An	**100**	**100**	**100**	**99**	**100**	**100**	**100**	**100**	**100**	**100**	**100**	**100**	**97**	**96**	**98**	**98**	**95**	**94**	**97**	**94**	**95**	**98**
Or	**0**	**0**	**0**	**0**	**0**	**0**	**0**	**0**	**0**	**0**	**0**	**0**	**0**	**0**	**0**	**0**	**0**	**0**	**0**	**0**	**0**	**0**
Total	**100**	**100**	**100**	**100**	**100**	**100**	**100**	**100**	**100**	**100**	**100**	**100**	**100**	**100**	**100**	**100**	**100**	**100**	**100**	**100**	**100**	**100**

FELDSPAR

Sample	RSTX26-63 (JEOL)																				
Analysis #	**63**	**64**	**65**	**66**	**67**	**68**	**69**	**70**	**71**	**72**	**73**	**74**	**75**	**76**	**77**	**78**	**79**	**80**	**81**	**82**	**83**
SiO_2	51.88	50.35	52.42	54.08	49.39	51.26	54.21	50.07	49.38	51.22	53.55	50.62	50.99	53.13	50.15	54.29	44.75	44.95	44.63	44.23	44.49
Al_2O_3	30.70	31.83	30.32	29.41	32.48	31.41	29.13	31.54	32.78	31.34	29.92	31.58	31.62	30.16	31.93	29.70	35.88	35.95	35.83	35.89	35.79
FeO	0.23	0.23	0.31	0.15	0.19	0.13	0.13	0.20	0.14	0.15	0.15	0.11	0.13	0.10	0.08	0.15	0.07	0.04	0.04	0.12	0.04
CaO	14.18	15.44	13.88	12.40	16.18	14.92	12.03	15.27	16.24	14.71	13.08	14.91	14.64	13.22	15.66	12.46	19.70	19.84	19.95	19.76	19.80
Na_2O	3.07	2.41	3.15	3.85	2.19	2.82	4.08	2.49	2.06	2.90	3.90	2.75	2.88	3.69	2.48	4.13	0.14	0.12	0.10	0.18	0.20
K_2O	0.32	0.22	0.29	0.61	0.16	0.21	0.34	0.13	0.14	0.21	0.28	0.15	0.13	0.23	0.14	0.33	0.04	0.02	0.02	0.02	0.03
Total	**100.37**	**100.49**	**100.37**	**100.49**	**100.58**	**100.75**	**99.91**	**99.71**	**100.75**	**100.53**	**100.87**	**100.12**	**100.40**	**100.53**	**100.43**	**101.05**	**100.57**	**100.92**	**100.57**	**100.20**	**100.34**
									Number of ions based on 8 Oxygens												
Si	2.35	2.28	2.37	2.43	2.24	2.32	2.45	2.29	2.24	2.32	2.40	2.30	2.31	2.39	2.28	2.43	2.05	2.06	2.05	2.04	2.05
Al	1.64	1.70	1.62	1.56	1.74	1.67	1.55	1.70	1.75	1.67	1.58	1.69	1.69	1.60	1.71	1.57	1.94	1.94	1.94	1.95	1.94
Fe	0.01	0.01	0.01	0.01	0.01	bdl	0.01	0.01	0.01	0.01	0.01	bdl	bdl	bdl	bdl	0.01	bdl	bdl	bdl	bdl	bdl
Ca	0.75	0.67	0.60	0.79	0.72	0.58	0.75	0.79	0.71	0.63	0.73	0.71	0.64	0.76	0.60	0.97	0.97	0.98	0.98	0.98	0.98
Na	0.21	0.28	0.34	0.19	0.25	0.36	0.22	0.18	0.25	0.34	0.24	0.25	0.32	0.22	0.36	0.01	0.01	0.01	0.02	0.02	0.02
K	0.01	0.02	0.03	0.01	0.01	0.02	0.01	0.01	0.01	0.02	0.01	0.01	0.01	0.01	0.02	bdl	bdl	bdl	bdl	bdl	bdl
Total	**4.97**	**4.96**	**4.96**	**4.99**	**4.97**	**4.95**	**4.98**	**4.98**	**4.98**	**4.98**	**4.97**	**4.97**	**4.98**	**4.99**	**4.96**	**4.98**	**4.98**	**4.99**	**4.99**	**4.99**	**4.99**
Ab	**28**	**22**	**29**	**35**	**19**	**25**	**37**	**23**	**19**	**26**	**34**	**25**	**26**	**33**	**22**	**37**	**1**	**1**	**1**	**2**	**2**
An	**70**	**77**	**70**	**62**	**80**	**74**	**61**	**77**	**81**	**73**	**64**	**74**	**73**	**66**	**77**	**61**	**98**	**99**	**99**	**98**	**98**
Or	**2**	**1**	**2**	**4**	**1**	**1**	**2**	**1**	**1**	**1**	**2**	**1**	**1**	**1**	**1**	**2**	**0**	**0**	**0**	**0**	**0**
Total	**100**	**100**	**100**	**100**	**100**	**100**	**100**	**100**	**100**	**100**	**100**	**100**	**100**	**100**	**100**	**100**	**100**	**100**	**100**	**100**	**100**

FELDSPAR

Sample	RSTX26-A5 (JEOL)																		
Analysis #	**5**	**6**	**7**	**8**	**9**	**10**	**11**	**12**	**13**	**14**	**15**	**16**	**17**	**18**	**19**	**20**	**21**	**22**	**23**
SiO_2	50.74	50.79	51.51	51.27	52.30	51.54	50.41	50.41	50.75	50.47	50.94	50.54	50.96	51.25	48.69	50.38	50.49	50.65	50.56
Al_2O_3	31.51	31.51	31.32	30.83	31.61	31.11	31.51	31.63	31.77	31.78	31.90	31.60	31.06	31.51	32.64	31.77	31.58	31.77	31.99
FeO	0.19	0.27	0.22	0.19	0.18	0.20	0.20	0.23	0.21	0.23	0.24	0.22	0.20	0.18	0.21	0.25	0.27	0.24	0.25
CaO	14.83	14.98	14.70	14.34	14.71	14.51	15.03	15.24	15.29	15.21	15.19	14.99	14.41	14.86	16.15	14.99	15.10	15.00	15.34
Na_2O	2.68	2.66	2.86	2.84	3.01	2.94	2.72	2.51	2.54	2.57	2.55	2.68	2.95	2.71	1.95	2.73	2.56	2.59	2.50
K_2O	0.19	0.19	0.23	0.23	0.20	0.18	0.18	0.20	0.19	0.19	0.16	0.20	0.20	0.18	0.12	0.16	0.18	0.18	0.19
Total	**100.13**	**100.39**	**100.83**	**99.71**	**102.00**	**100.48**	**100.06**	**100.20**	**100.74**	**100.44**	**100.97**	**100.23**	**99.78**	**100.69**	**99.77**	**100.27**	**100.18**	**100.42**	**100.83**
								Number of ions based on 8 Oxygens											
Si	2.31	2.30	2.32	2.34	2.33	2.33	2.30	2.29	2.29	2.29	2.30	2.30	2.32	2.31	2.23	2.29	2.30	2.30	2.28
Al	1.69	1.68	1.67	1.66	1.66	1.66	1.69	1.70	1.69	1.70	1.70	1.69	1.67	1.68	1.76	1.70	1.69	1.70	1.70
Fe	0.01	0.01	0.01	0.01	0.01	0.01	0.01	0.01	0.01	0.01	0.01	0.01	0.01	0.01	0.01	0.01	0.01	0.01	0.01
Ca	0.72	0.73	0.71	0.70	0.70	0.70	0.73	0.74	0.74	0.74	0.73	0.73	0.70	0.72	0.79	0.73	0.74	0.73	0.74
Na	0.24	0.23	0.25	0.25	0.26	0.26	0.24	0.22	0.22	0.23	0.22	0.24	0.26	0.24	0.17	0.24	0.23	0.23	0.22
K	0.01	0.01	0.01	0.01	0.01	0.01	0.01	0.01	0.01	0.01	0.01	0.01	0.01	0.01	0.01	0.01	0.01	0.01	0.01
Total	**4.97**	**4.97**	**4.97**	**4.96**	**4.97**	**4.97**	**4.98**	**4.97**	**4.97**	**4.98**	**4.97**	**4.97**	**4.98**	**4.97**	**4.97**	**4.98**	**4.97**	**4.97**	**4.97**
Ab	**24**	**24**	**26**	**26**	**27**	**27**	**24**	**23**	**23**	**23**	**23**	**24**	**27**	**25**	**18**	**25**	**23**	**24**	**23**
An	**74**	**75**	**73**	**73**	**72**	**72**	**75**	**76**	**76**	**76**	**76**	**75**	**72**	**74**	**81**	**75**	**76**	**75**	**76**
Or	**1**	**1**	**1**	**1**	**1**	**1**	**1**	**1**	**1**	**1**	**1**	**1**	**1**	**1**	**1**	**1**	**1**	**1**	**1**
Total	**100**	**100**	**100**	**100**	**100**	**100**	**100**	**100**	**100**	**100**	**100**	**100**	**100**	**100**	**100**	**100**	**100**	**100**	**100**

FELDSPAR

Sample	RSTX26-A5 (JEOL)									RSTX26-A20 (JEOL)									
Analysis #	**24**	**25**	**26**	**27**	**28**	**29**	**30**	**31**	**32**	**33**	**34**	**35**	**36**	**37**	**38**	**39**	**40**	**41**	**42**	**43**
SiO_2	50.24	50.57	50.63	50.18	50.80	50.87	51.13	50.45	50.73	51.33	51.28	51.40	51.30	50.15	51.63	50.80	51.66	50.94	50.72	51.60
Al_2O_3	31.81	31.92	31.38	29.47	31.48	31.89	31.72	31.87	31.72	31.65	31.41	31.52	31.53	31.86	31.46	31.71	31.58	31.61	31.63	31.07
FeO	0.28	0.28	0.32	0.19	0.26	0.26	0.32	0.24	0.23	0.39	0.37	0.35	0.43	0.36	0.34	0.34	0.33	0.37	0.35	0.33
CaO	15.24	15.01	14.87	13.53	14.80	15.04	15.03	15.12	15.02	14.93	15.05	15.00	15.22	15.23	14.88	15.21	14.79	15.02	15.02	14.69
Na_2O	2.51	2.57	2.52	2.96	2.61	2.73	2.56	2.58	2.60	2.66	2.70	2.57	2.64	2.39	2.64	2.52	2.73	2.55	2.58	2.73
K_2O	0.17	0.15	0.17	0.15	0.20	0.12	0.18	0.19	0.18	0.21	0.22	0.19	0.21	0.20	0.22	0.20	0.22	0.20	0.23	0.25
Total	100.26	100.50	99.89	**96.47**	**100.14**	**100.90**	**100.95**	**100.44**	**100.48**	**101.17**	**101.03**	**101.03**	**101.33**	**100.19**	**101.17**	**100.78**	**101.31**	**100.70**	**100.52**	**100.66**
	Number of ions based on 8 Oxygens																			
Si	2.29	2.29	2.31	2.36	2.31	2.30	2.31	2.29	2.30	2.31	2.31	2.32	2.31	2.28	2.32	2.30	2.32	2.30	2.30	2.33
Al	1.71	1.71	1.69	1.63	1.69	1.70	1.69	1.70	1.69	1.68	1.67	1.67	1.67	1.71	1.67	1.69	1.67	1.68	1.69	1.65
Fe	0.01	0.01	0.01	0.01	0.01	0.01	0.01	0.01	0.01	0.01	0.01	0.01	0.02	0.01	0.01	0.01	0.01	0.01	0.01	0.01
Ca	0.74	0.73	0.73	0.68	0.72	0.73	0.73	0.73	0.73	0.72	0.73	0.72	0.73	0.74	0.72	0.74	0.71	0.73	0.73	0.71
Na	0.22	0.23	0.22	0.27	0.23	0.24	0.22	0.23	0.23	0.23	0.24	0.22	0.23	0.21	0.23	0.22	0.24	0.22	0.23	0.24
K	0.01	0.01	0.01	0.01	0.01	0.01	0.01	0.01	0.01	0.01	0.01	0.01	0.01	0.01	0.01	0.01	0.01	0.01	0.01	0.01
Total	4.98	4.97	4.96	**4.96**	**4.97**	**4.98**	**4.96**	**4.97**	**4.97**	**4.97**	**4.97**	**4.96**	**4.97**	**4.97**	**4.96**	**4.97**	**4.97**	**4.97**	**4.97**	**4.96**
Ab	23	23	23	**28**	**24**	**25**	**23**	**23**	**24**	**24**	**24**	**23**	**24**	**22**	**24**	**23**	**25**	**23**	**23**	**25**
An	76	76	76	**71**	**75**	**75**	**76**	**76**	**75**	**75**	**75**	**75**	**75**	**77**	**75**	**76**	**74**	**76**	**75**	**74**
Or	1	1	1	**1**	**1**	**1**	**1**	**1**	**1**	**1**	**1**	**1**	**1**	**1**	**1**	**1**	**1**	**1**	**1**	**2**
Total	**100**	**100**	**100**	**100**	**100**	**100**	**100**	**100**	**100**	**100**	**100**	**100**	**100**	**100**	**100**	**100**	**100**	**100**	**100**	**100**

FELDSPAR

Sample	RSTX26-A20 (JEOL)			RSTX26-UG1 (JEOL)				
Analysis #	**44**	**45**	**46**	**47**	**48**	**49**	**50**	**51**
SiO_2	50.36	52.68	51.97	51.93	56.92	52.76	50.09	51.50
Al_2O_3	31.76	29.99	31.05	31.00	1.34	30.37	31.44	31.36
FeO	0.40	0.17	0.13	0.12	9.61	0.19	0.15	0.15
CaO	15.20	13.18	14.01	14.04	0.44	13.21	14.98	14.56
Na_2O	2.48	3.62	3.23	3.23	bdl	3.69	2.57	2.86
K_2O	0.22	0.14	0.10	0.12	0.02	0.20	0.15	0.17
Total	**100.43**	**99.77**	**100.48**	**100.43**	**68.32**	**100.41**	**99.38**	**100.59**
	Number of ions based on 8 Oxygens							
Si	2.29	2.39	2.35	2.35	2.65	2.38	2.29	2.33
Al	1.70	1.60	1.65	1.65	0.07	1.62	1.70	1.67
Fe	0.02	0.01	bdl	bdl	0.37	0.01	0.01	0.01
Ca	0.74	0.64	0.68	0.68	0.02	0.64	0.74	0.70
Na	0.22	0.32	0.28	0.28	bdl	0.32	0.23	0.25
K	0.01	0.01	0.01	0.01	bdl	0.01	0.01	0.01
Total	**4.97**	**4.97**	**4.97**	**4.97**	**3.12**	**4.98**	**4.97**	**4.97**
Ab	**23**	**33**	**29**	**29**	**0**	**33**	**23**	**26**
An	**76**	**66**	**70**	**70**	**96**	**66**	**76**	**73**
Or	**1**	**1**	**1**	**1**	**4**	**1**	**1**	**1**
Total	**100**	**100**	**100**	**100**	**100**	**100**	**100**	**100**

PYROXENE																		
Sample	**RSTX26-53A (CAMECA)**									**RSTX26-53B**								
Analysis #	**1**	**2**	**3**	**4**	**5**	**6**	**7**	**8**	**9**	**1**	**2**	**3**	**4**	**5**	**6**	**7**	**8**	**9**
Comment	**cn**	**cn**	**cn**	**cn**	**cn**	**cn**	**Wo**	**cn**	**cn**									**r**
SiO_2	43.69	43.77	43.54	43.2	43.18	44.1	51.03	41.18	40.35	41.21	35.21	35.18	35.16	38.13	34.75	34.86	35.01	40.53
TiO_2	0.29	0.27	0.31	0.3	0.33	0.35	0.03	0.19	0.42	1.3	0	0.01	bdl	bdl	bdl	bdl	bdl	1.53
Al_2O_3	14.52	14.06	15.03	15.35	15.07	13.87	0.06	18.68	18.4	14.41	15.24	15.07	14.98	10.71	15.48	15.84	15.79	14.99
Cr_2O_3	bdl	bdl	0.01	0.04	0.17	0.16	bdl	0.18	0.59	0.45	0.01	bdl	0.02	0.01	bdl	0.01	0.02	0.95
FeO	5.31	5.33	5.42	5.15	5.29	5.41	0.28	4.77	4.74	7.1	0.99	1.07	1.21	1.42	1.29	1.18	0.91	7.14
MnO	0.09	0.09	0.09	0.08	0.08	0.08	0.11	0.05	0.05	0.06	0.05	0.05	0.04	0.04	0.06	0.02	0.04	0.05
MgO	10.23	10.49	9.96	9.94	10.06	10.56	0	9.19	9.22	10.06	7.63	7.76	7.74	8.96	7.33	7.4	7.56	9.8
CaO	24.99	24.91	25.14	25.1	25.19	25.27	47.28	25.39	25.35	24.83	40.18	40.27	40.2	40.02	39.86	40.01	39.86	24.96
Na_2O	0.02	bdl	0.03	0.02	bdl	0.02	0.01	0.01	bdl	bdl	0.36	0.37	0.36	0.45	0.37	0.31	0.36	0.01
Total	**99.12**	**98.92**	**99.5**	**99.16**	**99.37**	**99.8**	**98.79**	**99.63**	**99.12**	**99.42**	**99.31**	**99.41**	**99.35**	**99.29**	**98.77**	**99.32**	**99.19**	**99.95**
							Number of ions based on 6 Oxygens											
Si	1.62	1.63	1.61	1.60	1.60	1.63	2.00	1.52	1.50	1.54	1.29	1.29	1.29	1.40	1.28	1.28	1.28	1.51
Ti	0.01	0.01	0.01	0.01	0.01	0.01	bdl	0.01	0.01	0.04	bdl	bdl	bdl	bdl	bdl	bdl	bdl	0.04
Al	0.64	0.62	0.66	0.67	0.66	0.60	bdl	0.81	0.81	0.63	0.66	0.65	0.65	0.46	0.67	0.68	0.68	0.66
Fe^{3+}	0.10	0.11	0.10	0.10	0.11	0.12	bdl	0.13	0.15	0.20	0.03	0.03	0.04	0.04	0.04	0.04	0.03	0.21
Cr^{3+}	bdl	bdl	bdl	bdl	bdl	bdl	bdl	0.01	0.02	0.01	bdl	bdl	bdl	bdl	bdl	bdl	bdl	0.03
Fe^{2+}	0.06	0.06	0.07	0.06	0.05	0.05	0.01	0.01	bdl	0.02	bdl	bdl	bdl	bdl	bdl	bdl	bdl	0.01
Mn	bdl	bdl	bdl	bdl	bdl	bdl	bdl	bdl	bdl	bdl	bdl	bdl	bdl	bdl	bdl	bdl	bdl	bdl
Mg	0.57	0.58	0.55	0.55	0.56	0.58	bdl	0.51	0.51	0.56	0.42	0.42	0.42	0.49	0.40	0.40	0.41	0.54
Ca	1.00	0.99	1.00	1.00	1.00	1.00	1.98	1.00	1.01	0.99	1.58	1.58	1.58	1.57	1.57	1.57	1.57	1.00
Na	bdl	bdl	bdl	bdl	bdl	bdl	bdl	bdl	bdl	bdl	0.03	0.03	0.03	0.03	0.03	0.02	0.03	bdl
Total	**4.00**	**4.00**	**4.00**	**4.00**	**4.00**	**4.00**	**4.00**	**4.00**	**4.00**	**4.00**	**4.00**	**4.00**	**4.00**	**4.00**	**4.00**	**4.00**	**4.00**	**4.00**
Wo	**61**	**61**	**62**	**62**	**62**	**61**	**100**	**66**	**66**	**63**	**79**	**79**	**79**	**76**	**80**	**80**	**79**	**64**
En	**35**	**36**	**34**	**34**	**35**	**36**	**0**	**33**	**34**	**36**	**21**	**21**	**21**	**24**	**20**	**20**	**21**	**35**
Fs	**4**	**4**	**4**	**4**	**3**	**3**	**0**	**1**	**0**	**1**	**0**	**0**	**0**	**0**	**0**	**0**	**0**	**1**
Total	**100**	**100**	**100**	**100**	**100**	**100**	**100**	**100**	**100**	**100**	**100**	**100**	**100**	**100**	**100**	**100**	**100**	**100**

*cn = corona, Wo = wollastonite

PYROXENE

Sample	RSTX26-53B							RSTX26-51 (CAMECA)									
Analysis #	10	11	12	13	14	15	16	1	2	3	4	5	6	7	8	9	10
Comment	c	c	r	c	i	r	r	cn	cn	cn	cn	cn	cn	cn	cn	cn	cn
SiO_2	38.89	39.47	39.58	37.52	37.54	41.47	40.87	43.38	45.74	45.69	49.86	49.19	44.47	40.11	45.79	42.71	43.33
TiO_2	1.67	1.68	1.69	4.1	4.1	1.84	2.05	0.39	0.32	0.31	0.27	0.32	0.22	0.27	0.2	0.44	0.47
Al_2O_3	15.34	15.65	15.42	16.35	16.64	13.9	14.65	15.51	11.32	11.49	4.45	5.81	13.49	19.33	10.94	16.1	15.3
Cr_2O_3	1.46	1.62	1.59	0.44	0.56	0.26	0.35	0.46	0.73	0.9	0.92	1.16	0.04	0	0	0.14	0.06
FeO	6.81	6.85	6.93	6.2	6.18	6.89	6.56	4.09	3.94	3.55	3.61	3.68	4.19	4.51	3.72	4.49	4.46
MnO	0.04	0.05	0.02	0.07	0.08	0.09	0.07	0.01	0.03	0.06	0.11	0.1	0.02	0.05	0.1	0.05	0.05
MgO	9.12	9.2	9.26	8.91	8.97	10.24	9.93	10.46	12.05	12.25	14.73	13.83	11.26	8.65	12.57	10.05	10.44
CaO	24.93	24.7	24.82	24.39	24.42	24.68	24.8	25.47	25.23	25.18	25.3	25.07	25.29	24.8	25.31	25.02	25.22
Na_2O	0.02	0.01	bdl	0.02	0.02	0.02	0.01	bdl	bdl	0.01	0.02	0.01	0.01	0.01	0.02	0.01	0.02
Total	**98.26**	**99.22**	**99.31**	**97.98**	**98.49**	**99.37**	**99.28**	**99.77**	**99.36**	**99.43**	**99.25**	**99.16**	**98.98**	**97.72**	**98.63**	**99**	**99.33**
								Number of ions based on 6 Oxygens									
Si	1.48	1.48	1.49	1.43	1.42	1.55	1.53	1.60	1.69	1.69	1.84	1.82	1.65	1.51	1.70	1.59	1.60
Ti	0.05	0.05	0.05	0.12	0.12	0.05	0.06	0.01	0.01	0.01	0.01	0.01	0.01	0.01	0.01	0.01	0.01
Al	0.69	0.69	0.68	0.73	0.74	0.61	0.65	0.67	0.49	0.50	0.19	0.25	0.59	0.86	0.48	0.70	0.67
Fe^{3+}	0.22	0.20	0.20	0.16	0.16	0.18	0.17	0.10	0.09	0.09	0.08	0.05	0.10	0.11	0.12	0.10	0.10
Cr^{3+}	0.04	0.05	0.05	0.01	0.02	0.01	0.01	0.01	0.02	0.03	0.03	0.03	bdl	bdl	bdl	bdl	bdl
Fe^{2+}	bdl	0.02	0.02	0.04	0.04	0.04	0.04	0.03	0.04	0.02	0.03	0.07	0.03	0.03	bdl	0.04	0.04
Mn	bdl	bdl	bdl	bdl	bdl	bdl	bdl	bdl	bdl	bdl	bdl	bdl	bdl	bdl	bdl	bdl	bdl
Mg	0.52	0.52	0.52	0.51	0.51	0.57	0.55	0.57	0.66	0.67	0.81	0.76	0.62	0.48	0.69	0.56	0.58
Ca	1.01	0.99	1.00	1.00	0.99	0.99	0.99	1.00	1.00	1.00	1.00	1.00	1.00	1.00	1.01	1.00	1.00
Na	bdl	bdl	bdl	bdl	bdl	bdl	bdl	bdl	bdl	bdl	bdl	bdl	bdl	bdl	bdl	bdl	bdl
Total	**4.00**	**4.00**	**4.00**	**4.00**	**4.00**	**4.00**	**4.00**	**4.00**	**4.00**	**4.00**	**4.00**	**4.00**	**4.00**	**4.00**	**4.00**	**4.00**	**4.00**
Wo	**66**	**65**	**65**	**65**	**65**	**62**	**63**	**62**	**59**	**59**	**54**	**54**	**61**	**66**	**59**	**62**	**62**
En	**34**	**34**	**34**	**33**	**33**	**36**	**35**	**36**	**39**	**40**	**44**	**42**	**38**	**32**	**41**	**35**	**36**
Fs	**0**	**1**	**1**	**3**	**2**	**2**	**2**	**2**	**2**	**1**	**2**	**4**	**2**	**2**	**0**	**3**	**2**
Total	**100**	**100**	**100**	**100**	**100**	**100**	**100**	**100**	**100**	**100**	**100**	**100**	**100**	**100**	**100**	**100**	**100**

*cn = corona, r = rim, i = intermediate, c = core

PYROXENE

Sample	RSTX26-52 (CAMECA)							
Analysis #	**3**	**4**	**5**	**6**	**7**	**8**	**9**	**10**
Comment	**i**	**i**	**i**	**i**	**r**	**r**	**r**	**r**
SiO_2	45.83	45.55	44.32	44.99	43.36	43.26	40.85	40.71
TiO_2	0.25	0.25	0.35	0.24	0.24	0.24	0.66	0.86
Al_2O_3	9.68	9.82	11.57	11.31	13.88	13.5	14.88	15.51
Cr_2O_3	0.44	0.49	0.64	0.63	0.05	0	1.66	1.38
FeO	4.8	4.7	5.15	5.02	5.61	5.62	6.38	6.59
MnO	0.03	0.03	0.05	0.03	0.04	0.05	0.05	0.08
MgO	12.67	12.66	11.6	11.76	10.81	10.86	9.11	8.79
CaO	24.63	24.77	24.67	24.73	24.92	24.81	24.35	24.6
Na_2O	bdl	bdl	bdl	0.01	0.01	0.01	bdl	bdl
Total	**98.3**	**98.27**	**98.35**	**98.71**	**98.91**	**98.34**	**97.94**	**98.52**
	Number of ions based on 6 Oxygens							
Si	1.71	1.70	1.66	1.68	1.61	1.62	1.55	1.54
Ti	0.01	0.01	0.01	0.01	0.01	0.01	0.02	0.02
Al	0.43	0.43	0.51	0.50	0.61	0.60	0.67	0.69
Fe^{3+}	0.12	0.14	0.13	0.12	0.15	0.15	0.14	0.14
Cr^{3+}	0.01	0.01	0.02	0.02	bdl	bdl	0.05	0.04
Fe^{2+}	0.03	0.01	0.03	0.04	0.02	0.02	0.06	0.07
Mn	bdl	bdl	bdl	bdl	bdl	bdl	bdl	bdl
Mg	0.71	0.71	0.65	0.65	0.60	0.61	0.52	0.50
Ca	0.99	0.99	0.99	0.99	0.99	0.99	0.99	1.00
Na	bdl	bdl	bdl	bdl	bdl	bdl	bdl	bdl
Total	**4.00**	**4.00**	**4.00**	**4.00**	**4.00**	**4.00**	**4.00**	**4.00**
Wo	**57**	**58**	**59**	**59**	**61**	**61**	**63**	**64**
En	**41**	**41**	**39**	**39**	**37**	**37**	**33**	**32**
Fs	**2**	**1**	**2**	**2**	**1**	**1**	**4**	**4**
Total	**100**	**100**	**100**	**100**	**100**	**100**	**100**	**100**

*i = intermediate, r = rim

PYROXENE

Sample	RSTX26-13 (CAMECA)							RSTX26-61(JEOL)										
Analysis#	1	2	3	4	5	6	7	8	95	96	97	98	99	100	101	102	103	104
Comment					Wo	Wo	Wo	Wo										
SiO_2	39.94	39.88	40.59	41.45	51.59	51.08	51.7	51.93	40.01	40.44	40.83	42.68	41.65	41.36	41.83	41.96	41.56	40.93
TiO_2	0.43	0.42	0.47	0.49	0.01	0.02	bdl	0.01	0.49	0.50	0.54	0.65	0.54	0.51	0.59	0.52	0.46	0.63
Al_2O_3	16.6	16.99	15.62	15.36	0.09	0.10	0.10	0.11	16.93	16.53	16.45	14.13	16.49	16.38	15.47	14.89	16.02	15.90
Cr_2O_3	1.93	1.87	1.49	0.69	bdl	0.05	bdl	0.01	1.13	1.79	0.36	0.28	0.44	0.45	0.40	0.43	0.45	1.64
FeO	6.18	6.59	6.51	6.62	0.24	0.16	0.29	0.23	6.20	6.29	6.15	5.39	6.25	6.17	6.45	6.48	5.89	5.71
MnO	0.03	0.08	0.09	0.13	0.12	0.17	0.14	0.14	0.12	0.13	0.09	0.07	0.10	0.11	0.10	0.13	0.07	0.07
MgO	8.51	7.95	8.96	9.33	0.04	bdl	0.02	bdl	8.54	8.61	9.04	10.58	9.19	9.22	9.38	9.73	9.70	9.17
CaO	25.41	24.71	24.84	24.92	47.22	47.26	47.23	47.38	24.35	24.42	24.46	24.62	24.62	24.46	24.59	24.56	24.47	24.32
Na_2O	bdl	0.04	0.03	0.01	0.01	0.02	bdl	0.01	bdl	0.01	0.02	bdl	0.05	0.02	bdl	bdl	0.01	bdl
Total	**99.03**	**98.49**	**98.6**	**98.99**	**99.31**	**98.84**	**99.48**	**99.81**	**97.767**	**98.702**	**97.912**	**98.396**	**99.263**	**98.651**	**98.808**	**98.688**	**98.625**	**98.37**
								Number of ions based on 6 Oxygens										
Si	1.50	1.51	1.53	1.55	2.01	2.00	2.01	2.01	1.52	1.52	1.54	1.60	1.55	1.55	1.57	1.57	1.56	1.54
Ti	0.01	0.01	0.01	0.01	bdl	bdl	bdl	bdl	0.01	0.01	0.02	0.02	0.02	0.01	0.02	0.01	0.01	0.02
Al	0.74	0.76	0.69	0.68	bdl	bdl	bdl	0.01	0.76	0.73	0.73	0.62	0.72	0.72	0.68	0.66	0.71	0.71
Fe^{3+}	0.18	0.15	0.18	0.17	bdl	bdl	bdl	bdl	0.14	0.14	0.14	0.13	0.13	0.13	0.13	0.15	0.14	0.12
Cr^{3+}	0.06	0.06	0.04	0.02	bdl	bdl	bdl	bdl	0.03	0.05	0.01	0.01	0.01	0.01	0.01	0.01	0.01	0.05
Fe^{2+}	0.01	0.06	0.03	0.04	0.01	0.01	0.01	0.01	0.06	0.06	0.05	0.04	0.06	0.06	0.07	0.05	0.04	0.06
Mn	bdl	bdl	bdl	bdl	bdl	0.01	bdl	bdl	bdl	bdl	bdl	bdl	bdl	bdl	bdl	bdl	bdl	bdl
Mg	0.48	0.45	0.50	0.52	bdl	bdl	bdl	bdl	0.48	0.48	0.51	0.59	0.51	0.52	0.52	0.54	0.54	0.52
Ca	1.02	1.00	1.00	1.00	1.97	1.98	1.97	1.97	0.99	0.99	0.99	0.99	0.98	0.98	0.99	0.99	0.98	0.98
Na	bdl	bdl	bdl	bdl	bdl	bdl	bdl	bdl	bdl	bdl	bdl	bdl	bdl	bdl	bdl	bdl	bdl	bdl
Total	**4.00**	**4.00**	**4.00**	**4.00**	**4.00**	**4.00**	**4.00**	**4.00**	**4.00**	**4.00**	**4.00**	**4.00**	**4.00**	**4.00**	**4.00**	**4.00**	**4.00**	**4.00**
Wo	**68**	**66**	**65**	**64**	**99**	**100**	**99**	**100**	**65**	**64**	**64**	**61**	**63**	**63**	**62**	**62**	**63**	**63**
En	**32**	**30**	**33**	**33**	**0**	**0**	**0**	**0**	**32**	**32**	**33**	**37**	**33**	**33**	**33**	**34**	**35**	**33**
Fs	**1**	**4**	**2**	**3**	**0**	**0**	**0**	**0**	**4**	**4**	**3**	**2**	**4**	**4**	**4**	**3**	**3**	**4**
Total	**100**	**100**	**100**	**100**	**100**	**100**	**100**	**100**	**100**	**100**	**100**	**100**	**100**	**100**	**100**	**100**	**100**	**100**

*Wo = Wollastonite

PYROXENE																		
Sample	**RSTX26-62 (JEOL)**										**RSTX26-63(JEOL)**							
Analysis#	**105**	**106**	**107**	**108**	**109**	**110**	**111**	**112**	**113**	**114**	**115**	**116**	**117**	**118**	**119**	**120**	**121**	**122**
SiO_2	52.37	51.36	52.46	50.99	52.05	50.89	51.99	51.11	52.45	52.61	52.54	52.81	52.73	53.13	52.82	52.93	52.86	53.00
TiO_2	0.21	0.19	0.16	0.21	0.22	0.39	0.38	0.40	0.23	0.27	0.24	0.31	0.25	0.31	0.24	0.30	0.27	0.29
Al_2O_3	2.03	2.09	2.16	2.97	2.11	3.80	2.95	4.03	2.14	2.15	2.01	2.08	2.00	2.06	2.19	1.98	2.01	2.02
Cr_2O_3	0.82	0.71	0.70	0.16	0.81	0.90	0.74	0.93	0.80	0.74	0.80	0.87	0.89	0.86	0.87	0.95	0.76	0.75
FeO	4.89	7.48	5.19	7.63	6.44	4.60	4.54	4.42	4.05	4.28	4.34	4.75	4.73	4.53	4.86	5.11	4.77	4.68
MnO	0.09	0.18	0.13	0.17	0.18	0.16	0.14	0.15	0.14	0.14	0.07	0.16	0.13	0.15	0.16	0.13	0.11	0.14
MgO	14.73	13.03	14.26	12.73	13.72	14.27	14.67	14.30	15.31	15.37	15.25	15.76	15.28	15.37	15.74	16.01	15.91	15.93
CaO	24.60	24.09	24.30	24.40	23.97	24.15	24.20	24.20	24.25	23.41	23.88	22.07	22.94	23.02	21.58	21.13	22.08	22.33
Na_2O	0.08	0.22	0.09	0.11	0.10	0.11	0.12	0.17	0.17	0.21	0.29	0.44	0.38	0.37	0.46	0.47	0.37	0.40
Total	**99.745**	**99.109**	**99.358**	**99.257**	**99.494**	**99.165**	**99.606**	**99.53**	**99.363**	**98.965**	**99.138**	**98.801**	**98.957**	**99.411**	**98.458**	**98.542**	**98.763**	**99.145**
							Number of ions based on 6 Oxygens											
Si	1.94	1.93	1.95	1.91	1.94	1.89	1.92	1.89	1.94	1.95	1.94	1.95	1.95	1.96	1.96	1.96	1.95	1.95
Ti	0.01	0.01	bdl	0.01	0.01	0.01	0.01	0.01	0.01	0.01	0.01	0.01	0.01	0.01	0.01	0.01	0.01	0.01
Al	0.09	0.09	0.09	0.13	0.09	0.17	0.13	0.18	0.09	0.09	0.09	0.09	0.09	0.09	0.10	0.09	0.09	0.09
Fe^{3+}	0.01	0.04	bdl	0.03	bdl	0.01	bdl	0.01	0.01	bdl	0.02	bdl	bdl	bdl	bdl	bdl	bdl	bdl
Cr^{3+}	0.02	0.02	0.02	bdl	0.02	0.03	0.02	0.03	0.02	0.02	0.02	0.03	0.03	0.02	0.03	0.03	0.02	0.02
Fe^{2+}	0.14	0.20	0.16	0.20	0.20	0.13	0.14	0.13	0.11	0.13	0.12	0.15	0.15	0.14	0.15	0.16	0.15	0.14
Mn	bdl	0.01	bdl	0.01	0.01	0.01	bdl	bdl	bdl	bdl	bdl	0.01	bdl	bdl	bdl	bdl	bdl	bdl
Mg	0.81	0.73	0.79	0.71	0.76	0.79	0.81	0.79	0.84	0.85	0.84	0.87	0.84	0.84	0.87	0.88	0.88	0.87
Ca	0.97	0.97	0.97	0.98	0.96	0.96	0.96	0.96	0.96	0.93	0.95	0.87	0.91	0.91	0.86	0.84	0.87	0.88
Na	0.01	0.02	0.01	0.01	0.01	0.01	0.01	0.01	0.01	0.01	0.02	0.03	0.03	0.03	0.03	0.03	0.03	0.03
Total	**4.00**	**4.00**	**4.00**	**4.00**	**4.00**	**4.00**	**4.00**	**4.00**	**4.00**	**4.00**	**4.00**	**4.00**	**4.00**	**4.00**	**4.00**	**4.00**	**4.00**	**4.00**
Wo	**51**	**51**	**50**	**52**	**50**	**51**	**50**	**51**	**50**	**49**	**50**	**46**	**48**	**48**	**46**	**45**	**46**	**46**
En	**42**	**38**	**41**	**38**	**40**	**42**	**42**	**42**	**44**	**44**	**44**	**46**	**44**	**45**	**46**	**47**	**46**	**46**
Fs	**7**	**10**	**8**	**11**	**10**	**7**	**7**	**7**	**6**	**7**	**6**	**8**	**8**	**7**	**8**	**8**	**8**	**8**
Total	**100**	**100**	**100**	**100**	**100**	**100**	**100**	**100**	**100**	**100**	**100**	**100**	**100**	**100**	**100**	**100**	**100**	**100**

PYROXENE

Sample	RSTX26-63(JEOL)						RSTX26-A20 (JEOL)							
Analysis #	**123**	**124**	**125**	**126**	**127**	**128**	**23**	**24**	**25**	**26**	**27**	**28**	**29**	**30**
SiO_2	53.24	53.18	43.69	52.853	51.544	39.273	52.01	51.78	52.80	52.20	51.98	52.30	51.96	52.1
TiO_2	0.21	0.25	0.03	0.187	0.386	0.066	0.61	0.58	0.44	0.48	0.53	0.30	0.28	0.28
Al_2O_3	1.74	1.94	35.71	1.995	2.866	30.592	1.28	1.26	1.42	1.24	1.32	0.64	0.65	0.74
Cr_2O_3	0.57	0.77	0.06	0.026	0.035	0	0.32	0.25	0.36	0.37	0.29	0.11	0.04	0.12
FeO	4.62	4.43	0.07	5.653	4.974	0.219	10.23	10.10	10.11	10.42	9.58	23.89	22.48	21.44
MnO	0.11	0.20	0.02	0.114	0.066	0	0.21	0.26	0.24	0.23	0.23	0.38	0.46	0.36
MgO	16.18	15.96	0.01	14.728	14.854	0.552	13.89	13.81	13.81	14.00	13.88	21.40	20.78	20.28
CaO	22.59	22.56	19.29	24.251	24.219	20.034	20.33	20.49	20.31	20.22	21.09	0.95	2.69	4.21
Na_2O	0.36	0.35	0.15	0.109	0.094	0.163	0.20	0.24	0.19	0.20	0.18	0.01	0.01	0.03
Total	**99.25**	**99.28**	**98.88**	**99.81**	**98.94**	**90.74**	**98.87**	**98.516**	**99.493**	**99.164**	**98.892**	**99.964**	**99.347**	**99.531**
						Number of ions based on 6 Oxygens								
Si	1.96	1.96	1.64	1.95	1.91	1.60	1.97	1.96	1.98	1.97	1.96	1.96	1.96	1.96
Ti	0.01	0.01	bdl	0.01	0.01	bdl	0.02	0.02	0.01	0.01	0.01	0.01	0.01	0.01
Al	0.08	0.08	1.57	0.09	0.13	1.47	0.06	0.06	0.06	0.06	0.06	0.03	0.03	0.03
Fe^{3+}	0.01	bdl	bdl	0.01	0.03	bdl	bdl	bdl	bdl	bdl	bdl	0.03	0.03	0.03
Cr^{3+}	0.02	0.02	bdl	bdl	bdl	bdl	0.01	0.01	0.01	0.01	0.01	bdl	bdl	bdl
Fe^{2+}	0.13	0.14	bdl	0.17	0.12	0.01	0.32	0.32	0.32	0.33	0.30	0.72	0.67	0.64
Mn	bdl	0.01	bdl	bdl	bdl	bdl	0.01	0.01	0.01	0.01	0.01	0.01	0.01	0.01
Mg	0.89	0.88	bdl	0.81	0.82	0.03	0.78	0.78	0.77	0.79	0.78	1.20	1.17	1.14
Ca	0.89	0.89	0.77	0.96	0.96	0.87	0.82	0.83	0.82	0.82	0.85	0.04	0.11	0.17
Na	0.03	0.02	0.01	0.01	0.01	0.01	0.01	0.02	0.01	0.01	0.01	bdl	bdl	bdl
Total	**4.00**	**4.00**	**4.00**	**4.00**	**4.00**	**4.00**	**4.00**	**4.00**	**4.00**	**4.00**	**4.00**	**4.00**	**4.00**	**4.00**
Wo	**47**	**47**	**100**	**50**	**50**	**96**	**43**	**43**	**43**	**42**	**44**	**2**	**6**	**9**
En	**46**	**46**	**0**	**42**	**43**	**4**	**41**	**40**	**41**	**41**	**40**	**61**	**60**	**58**
Fs	**7**	**7**	**0**	**9**	**6**	**1**	**17**	**17**	**17**	**17**	**16**	**37**	**35**	**33**
Total	**100**	**100**	**100**	**100**	**100**	**100**	**100**	**100**	**100**	**100**	**100**	**100**	**100**	**100**

SPINEL

Sample	RSTX26-12 (CAMECA)										RSTX26-6 (CAMECA)						
Analysis #	**1**	**2**	**3**	**4**	**5**	**6**	**7**	**8**	**9**	**10**	**1**	**2**	**3**	**4**	**5**	**6**	**7**
SiO_2	0.03	0.02	0.03	0.04	0.03	0.05	0.03	0.01	0.05	0.05	0.02	0.02	0.04	0.02	0.02	0.03	0.04
TiO_2	0.63	4.99	0.62	5.09	0.78	5.20	0.81	5.51	0.72	0.56	0.27	2.80	0.54	0.22	2.98	0.56	0.47
Al_2O_3	54.09	3.83	53.21	3.48	51.77	4.36	51.02	4.31	51.06	55.89	57.37	5.59	50.54	57.73	8.00	50.40	52.64
Cr_2O_3	0.03	0.06	0.04	0.02	bdl	bdl	0.06	0.02	0.06	0.01	0.38	0.47	0.40	0.41	0.35	0.40	0.36
V_2O_3	bdl	bdl	bdl	bdl	bdl	bdl	bdl	bdl	0.02	bdl	0.01	bdl	bdl	bdl	bdl	bdl	bdl
Fe_2O_3	17.68	60.18	18.68	60.05	20.26	59.43	2bdl	58.77	21.20	16.35	15.01	63.65	21.57	14.24	61.47	21.87	19.48
FeO	3.63	14.39	3.28	14.62	3.05	14.15	3.86	14.74	4.17	2.92	2.01	9.29	2.20	2.02	8.75	2.58	2.22
MnO	0.48	1.78	0.45	1.74	0.45	1.55	0.48	2.17	0.42	0.40	0.35	1.46	0.45	0.31	1.45	0.43	0.43
MgO	24.15	12.67	24.27	12.52	24.39	13.19	23.64	12.58	23.75	24.96	25.50	15.20	24.60	25.43	16.06	24.44	24.85
NiO	0.02	0.04	0.04	0.02	0.05	bdl	bdl	0.03	bdl	0.01	0.01	0.03	bdl	0.02	bdl	bdl	bdl
ZnO	0.13	0.02	0.09	0.02	0.06	0.06	0.04	0.04	0.06	0.07	0.1	0	0.09	0.06	0.04	0.06	0.03
Total	**100.87**	**97.98**	**100.71**	**97.59**	**100.84**	**97.99**	**99.94**	**98.19**	**101.51**	**101.22**	**101.02**	**98.50**	**100.43**	**100.47**	**99.12**	**100.77**	**100.52**
							Number of ions based on 4 Oxygens										
Si	bdl	bdl	bdl	bdl	bdl	bdl	bdl	bdl	bdl	bdl	bdl	bdl	bdl	bdl	bdl	bdl	bdl
Ti	0.01	0.13	0.01	0.13	0.02	0.14	0.02	0.14	0.01	0.01	0.01	0.07	0.01	bdl	0.07	0.01	0.01
Al	1.63	0.16	1.61	0.14	1.57	0.18	1.57	0.18	1.56	1.67	1.70	0.22	1.55	1.71	0.31	1.54	1.60
Cr	bdl	bdl	bdl	bdl	bdl	bdl	bdl	bdl	bdl	bdl	0.01	0.01	0.01	0.01	0.01	0.01	0.01
V^{3+}	bdl	bdl	bdl	bdl	bdl	bdl	bdl	bdl	bdl	bdl	bdl	bdl	bdl	bdl	bdl	bdl	bdl
Fe^{3+}	0.34	1.58	0.36	1.58	0.39	1.55	0.39	1.53	0.41	0.31	0.28	1.62	0.42	0.27	1.53	0.43	0.38
Fe^{2+}	0.08	0.42	0.07	0.43	0.07	0.41	0.08	0.43	0.09	0.06	0.04	0.26	0.05	0.04	0.24	0.06	0.05
Mn	0.01	0.05	0.01	0.05	0.01	0.05	0.01	0.06	0.01	0.01	0.01	0.04	0.01	0.01	0.04	0.01	0.01
Mg	0.92	0.66	0.93	0.65	0.94	0.68	0.92	0.65	0.91	0.94	0.95	0.77	0.95	0.95	0.79	0.95	0.95
Ni	bdl	bdl	bdl	bdl	bdl	bdl	bdl	bdl	bdl	bdl	bdl	bdl	bdl	bdl	bdl	bdl	bdl
Zn	bdl	bdl	bdl	bdl	bdl	bdl	bdl	bdl	bdl	bdl	bdl	bdl	bdl	bdl	bdl	bdl	bdl
Total	**3.00**	**3.00**	**3.00**	**3.00**	**3.00**	**3.00**	**3.00**	**3.00**	**3.00**	**3.00**	**3.00**	**3.00**	**3.00**	**3.00**	**3.00**	**3.00**	**3.00**

SPINEL

Sample	RSTX26-6 (CAMECA)																
Analysis #	**8**	**9**	**10**	**11**	**12**	**13**	**14**	**15**	**16**	**17**	**18**	**19**	**20**	**21**	**22**	**23**	**24**
SiO_2	0.03	0.03	0.03	0.08	0.03	0.01	0.05	0.02	0.02	0.02	0.01	0.04	0.03	0.02	0.01	0.02	0.03
TiO_2	2.91	1.10	1.07	0.62	0.63	3.13	3.84	3.96	3.91	3.58	0.27	0.86	3.56	3.09	2.84	0.81	0.83
Al_2O_3	8.52	43.65	43.63	51.11	49.89	4.47	4.07	8.47	7.78	5.74	56.00	45.69	5.53	4.39	4.08	48.85	48.64
Cr_2O_3	0.35	1.55	1.82	1.37	1.44	1.23	1.20	0.99	1.00	1.54	1.75	1.73	1.32	1.21	1.14	1.64	1.64
V_2O_3	bdl	bdl	bdl	0.04	0.01	bdl	bdl	bdl	bdl					bdl	bdl	bdl	bdl
Fe_2O_3	61.00	26.67	26.04	19.96	19.94	62.26	61.12	58.16	58.46	60.86	14.92	24.70	61.34	61.36	62.74	21.18	21.53
FeO	8.46	3.48	3.32	2.81	2.56	8.62	10.66	9.73	9.78	10.43	2.19	3.23	10.74	14.97	14.82	4.44	4.18
MnO	1.42	0.52	0.57	0.42	0.42	1.20	1.53	1.45	1.46	1.60	0.35	0.55	1.61	1.76	1.71	0.49	0.55
MgO	16.24	23.25	23.23	24.51	24.11	15.43	14.44	16.00	15.74	14.88	25.17	23.56	14.66	11.29	11.30	23.16	23.27
NiO	0.01	0.01	0.03	0.02	0.04	bdl	bdl	0.01	0.03	0.04	bdl	bdl	0.05	bdl	0.04	bdl	0.06
ZnO	0.08	0.11	0	0.05	0.04	0.07	0.02	0.06	0	0.04	0.13	0	0.06	0.01	0.05	0.03	0.05
Total	**99.02**	**100.37**	**99.74**	**100.99**	**99.11**	**96.43**	**96.93**	**98.84**	**98.17**	**98.72**	**100.79**	**100.36**	**98.90**	**98.10**	**98.73**	**100.62**	**100.78**
							Number of ions based on 4 Oxygens										
Si	bdl	bdl	bdl	bdl	bdl	bdl	bdl	bdl	bdl	bdl	bdl	bdl	bdl	bdl	bdl	bdl	bdl
Ti	0.07	0.02	0.02	0.01	0.01	0.08	0.10	0.10	0.10	0.09	0.01	0.02	0.09	0.08	0.07	0.02	0.02
Al	0.33	1.38	1.39	1.56	1.55	0.18	0.17	0.33	0.31	0.23	1.67	1.43	0.22	0.18	0.17	1.51	1.51
Cr	0.01	0.03	0.04	0.03	0.03	0.03	0.03	0.03	0.03	0.04	0.04	0.04	0.04	0.03	0.03	0.03	0.03
V^{3+}	bdl	bdl	bdl	bdl	bdl	bdl	bdl	bdl	bdl	bdl	bdl	bdl	bdl	bdl	bdl	bdl	bdl
Fe^{3+}	1.51	0.54	0.53	0.39	0.40	1.62	1.60	1.45	1.47	1.55	0.28	0.49	1.56	1.62	1.65	0.42	0.43
Fe^{2+}	0.23	0.08	0.07	0.06	0.06	0.25	0.31	0.27	0.27	0.29	0.05	0.07	0.30	0.44	0.43	0.10	0.09
Mn	0.04	0.01	0.01	0.01	0.01	0.04	0.04	0.04	0.04	0.05	0.01	0.01	0.05	0.05	0.05	0.01	0.01
Mg	0.80	0.93	0.93	0.94	0.95	0.80	0.75	0.79	0.78	0.75	0.95	0.93	0.74	0.59	0.59	0.91	0.91
Ni	bdl	bdl	bdl	bdl	bdl	bdl	bdl	bdl	bdl	bdl	bdl	bdl	bdl	bdl	bdl	bdl	bdl
Zn	bdl	bdl	bdl	bdl	bdl	bdl	bdl	bdl	bdl	bdl	bdl	bdl	bdl	bdl	bdl	bdl	bdl
Total	**3.00**	**3.00**	**3.00**	**3.00**	**3.00**	**3.00**	**3.00**	**3.00**	**3.00**	**3.00**	**3.00**	**3.00**	**3.00**	**3.00**	**3.00**	**3.00**	**3.00**

SPINEL

Sample	RSTX26-6 (CAMECA)													RSTX26-13 (CAMECA)	
Analysis #	**25**	**26**	**27**	**28**	**29**	**30**	**31**	**32**	**33**	**34**	**35**	**36**	**37**	**1**	**2**
SiO_2	0.05	0.02	0.01	0.03	0.03	0.03	0.08	0.03	0.01	0.05	0.02	0.02	0.03	0.80	0.02
TiO_2	0.51	0.49	0.54	0.46	1.10	1.07	0.62	0.63	3.13	3.84	3.96	3.91	0.07	0.09	0.11
Al_2O_3	52.31	52.80	52.77	53.76	43.65	43.63	51.11	49.89	4.47	4.07	8.47	7.78	24.69	24.32	29.48
Cr_2O_3	1.60	1.80	1.57	1.71	1.55	1.82	1.37	1.44	1.23	1.20	0.99	1.00	34.78	34.42	27.82
V_2O_3	bdl	bdl	0.05	0.05	bdl	bdl	0.04	0.01	bdl	bdl	bdl	bdl	0.08	0.11	0.20
Fe_2O_3	17.11	16.65	16.92	16.16	26.67	26.04	19.96	19.94	62.26	61.12	58.16	58.46	8.77	7.70	12.81
FeO	5.33	5.54	5.41	5.23	3.48	3.32	2.81	2.56	8.62	10.66	9.73	9.78	18.05	19.24	15.00
MnO	0.49	0.48	0.47	0.45	0.52	0.57	0.42	0.42	1.20	1.53	1.45	1.46	0.83	0.89	0.62
MgO	22.70	22.65	22.78	23.07	23.25	23.23	24.51	24.11	15.43	14.44	16.00	15.74	10.59	10.44	13.58
NiO	0.02	bdl	bdl	0.01	0.01	0.03	0.02	0.04	bdl	bdl	0.01	0.03	0.11	0.15	0.15
ZnO	0.06	0.1	0.09	0.09	0.11	0	0.05	0.04	0.07	0.02	0.06	0	0.17	0.12	0.06
Total	**100.18**	**100.54**	**100.61**	**101.02**	**100.37**	**99.74**	**100.99**	**99.11**	**96.43**	**96.93**	**98.84**	**98.17**	**98.17**	**98.28**	**99.85**
						Number of ions based on 4 Oxygens									
Si	bdl	bdl	bdl	bdl	bdl	bdl	bdl	bdl	bdl	bdl	bdl	bdl	bdl	0.03	bdl
Ti	0.01	0.01	0.01	0.01	0.02	0.02	0.01	0.01	0.08	0.10	0.10	0.10	bdl	bdl	bdl
Al	1.61	1.62	1.61	1.63	1.38	1.39	1.56	1.55	0.18	0.17	0.33	0.31	0.92	0.90	1.04
Cr	0.03	0.04	0.03	0.03	0.03	0.04	0.03	0.03	0.03	0.03	0.03	0.03	0.87	0.86	0.66
V^{3+}	bdl	bdl	bdl	bdl	bdl	bdl	bdl	bdl	bdl	bdl	bdl	bdl	bdl	bdl	bdl
Fe^{3+}	0.34	0.33	0.33	0.31	0.54	0.53	0.39	0.40	1.62	1.60	1.45	1.47	0.21	0.18	0.29
Fe^{2+}	0.12	0.12	0.12	0.11	0.08	0.07	0.06	0.06	0.25	0.31	0.27	0.27	0.48	0.51	0.38
Mn	0.01	0.01	0.01	0.01	0.01	0.01	0.01	0.01	0.04	0.04	0.04	0.04	0.02	0.02	0.02
Mg	0.88	0.88	0.88	0.89	0.93	0.93	0.94	0.95	0.80	0.75	0.79	0.78	0.50	0.49	0.61
Ni	bdl	bdl	bdl	bdl	bdl	bdl	bdl	bdl	bdl	bdl	bdl	bdl	bdl	bdl	bdl
Zn	bdl	bdl	bdl	bdl	bdl	bdl	bdl	bdl	bdl	bdl	bdl	bdl	bdl	bdl	bdl
Total	**3.00**	**3.00**	**3.00**	**3.00**	**3.00**	**3.00**	**3.00**	**3.00**	**3.00**	**3.00**	**3.00**	**3.00**	**3.00**	**3.00**	**3.00**

SPINEL

Sample	RSTX26-3B (JEOL)						RSTX26-52 (CAMECA)										
Analysis #	**1**	**2**	**3**	**4**	**5**	**6**	**1**	**2**	**3**	**4**	**5**	**6**	**7**	**8**	**9**	**10**	**11**
SiO_2	0.02	0.03	bdl	0.01	0.01	0.01	0.02	0.01	0.02	0.01	bdl	bdl	0.01	0.05	0.02	0.01	bdl
TiO_2	0.15	0.14	0.13	0.14	0.12	0.11	0.09	0.05	0.07	0.06	0.02	0.07	0.06	bdl	bdl	bdl	0.03
Al_2O_3	28.88	28.96	30.45	34.39	38.53	21.22	23.01	39.11	30.70	28.46	34.12	30.63	30.14	64.10	63.85	41.90	41.57
Cr_2O_3	28.92	27.99	26.44	22.37	18.21	36.36	33.07	21.68	30.53	33.25	26.67	30.58	30.41	0.85	1.31	20.60	20.49
V_2O_3	0.21	0.22	0.16	0.16	0.14	0.02	0.07	0.09	0.07	0.05	0.05	0.12	0.07	0.03	0.03	0.09	0.09
Fe_2O_3	12.90	13.22	13.62	13.69	13.89	11.74	12.58	10.22	9.96	9.34	9.99	9.60	10.14	4.41	4.52	8.26	8.11
FeO	15.49	15.30	14.86	14.34	13.32	16.58	15.96	11.28	13.30	14.04	12.40	13.28	13.64	8.43	8.58	11.66	11.55
MnO	0.64	0.69	0.64	0.59	0.61	0.99	0.93	0.49	0.64	0.67	0.61	0.63	0.66	0.29	0.33	0.37	0.32
MgO	13.46	13.42	13.87	14.70	15.80	11.16	11.52	17.10	14.92	14.13	15.69	14.82	14.49	21.66	21.52	17.25	17.17
NiO	0.12	0.10	0.13	0.15	0.16	0.17	0.24	0.24	0.17	0.16	0.17	0.14	0.16	0.33	0.39	0.19	0.18
ZnO	0	0.01	0.05	0.05	0.07	0.02	0.1	0.09	0.06	0.09	0.07	0.09	0.06	0.06	0.08	0.1	0.09
Total	**100.79**	**100.07**	**100.35**	**100.58**	**100.86**	**98.38**	**97.59**	**100.36**	**100.44**	**100.26**	**99.79**	**99.96**	**99.85**	**100.20**	**100.63**	**100.43**	**99.60**
							Number of ions based on 4 Oxygens										
Si	bdl	bdl	bdl	bdl	bdl	bdl	bdl	bdl	bdl	bdl	bdl	bdl	bdl	bdl	bdl	bdl	bdl
Ti	bdl	bdl	bdl	bdl	bdl	bdl	bdl	bdl	bdl	bdl	bdl	bdl	bdl	bdl	bdl	bdl	bdl
Al	1.02	1.02	1.07	1.18	1.29	0.80	0.86	1.30	1.06	1.00	1.17	1.07	1.05	1.90	1.89	1.37	1.37
Cr	0.68	0.66	0.62	0.51	0.41	0.92	0.83	0.48	0.71	0.78	0.61	0.71	0.71	0.02	0.03	0.45	0.45
V^{3+}	0.01	0.01	bdl	bdl	bdl	bdl	bdl	bdl	bdl	bdl	bdl	bdl	bdl	bdl	bdl	bdl	bdl
Fe^{3+}	0.29	0.30	0.30	0.30	0.30	0.28	0.30	0.22	0.22	0.21	0.22	0.21	0.23	0.08	0.09	0.17	0.17
Fe^{2+}	0.39	0.38	0.37	0.35	0.32	0.44	0.42	0.27	0.33	0.35	0.30	0.33	0.34	0.18	0.18	0.27	0.27
Mn	0.02	0.02	0.02	0.01	0.01	0.03	0.03	0.01	0.02	0.02	0.02	0.02	0.02	0.01	0.01	0.01	0.01
Mg	0.60	0.60	0.61	0.64	0.67	0.53	0.55	0.72	0.65	0.63	0.68	0.65	0.64	0.81	0.80	0.71	0.72
Ni	bdl	bdl	bdl	bdl	bdl	bdl	bdl	0.01	0.01	bdl	bdl	bdl	bdl	bdl	0.01	0.01	bdl	bdl
Zn	bdl	bdl	bdl	bdl	bdl	bdl	bdl	bdl	bdl	bdl	bdl	bdl	bdl	bdl	bdl	bdl	bdl
Total	**3.00**	**3.00**	**3.00**	**3.00**	**3.00**	**3.00**	**3.00**	**3.00**	**3.00**	**3.00**	**3.00**	**3.00**	**3.00**	**3.00**	**3.00**	**3.00**	**3.00**

SPINEL

Sample	RSTX26-52 (CAMECA)						RSTX26-1 (JEOL)										
Analysis #	**12**	**13**	**15**	**16**	**17**	**18**	**15**	**16**	**17**	**18**	**19**	**20**	**21**	**22**	**23**	**24**	**25**
SiO_2	0.02	0.03	0.03	0.02	0.02	bdl	0.05	0.06	0.01	bdl	0.03	0.06	0.03	0.04	bdl	0.01	0.05
TiO_2	0.03	0.04	0.19	0.19	0.17	0.51	0.51	0.54	0.58	0.55	0.60	0.44	0.42	0.46	0.40	0.41	0.42
Al_2O_3	41.61	42.55	24.18	26.11	29.59	53.71	55.26	53.55	37.07	46.84	52.83	56.97	56.43	57.10	57.12	56.77	57.18
Cr_2O_3	20.51	19.59	32.88	31.41	28.68	0.02	0.06	0.02	0.02	0.07	bdl	0.07	0.01	bdl	0.05	0.03	bdl
V_2O_3	0.09	0.08	0.17	0.20	0.16	bdl	0.03	bdl	0.06	0.05	0.01	bdl	0.05	bdl	0.01	bdl	bdl
Fe_2O_3	8.22	7.98	12.51	12.39	11.28	16.31	15.94	16.45	33.88	27.35	17.10	13.36	13.43	13.13	13.28	13.32	13.09
FeO	11.50	11.65	15.40	15.37	14.31	2.53	3.30	3.18	6.29	3.85	3.26	2.73	2.94	2.44	2.69	2.80	2.57
MnO	0.34	0.34	0.69	0.57	0.56	0.46	0.40	0.45	0.74	0.55	0.40	0.40	0.33	0.41	0.38	0.37	0.41
MgO	17.25	17.25	12.54	12.99	13.91	24.17	24.39	23.88	19.88	23.54	23.79	24.67	24.32	24.78	24.60	24.44	24.70
NiO	0.25	0.23	0.21	0.16	0.19	0.02	bdl	0.05	bdl	bdl	bdl	0.03	0.05	0.07	0.05	0.06	0.05
ZnO	0.04	0.07	0.06	0.06	0.07												
Total	**99.86**	**99.81**	**98.86**	**99.47**	**98.94**	**97.74**	**99.94**	**98.18**	**98.54**	**102.80**	**98.03**	**98.72**	**98.00**	**98.42**	**98.58**	**98.22**	**98.46**
							Number of ions based on 4 Oxygens										
Si	bdl	bdl	bdl	bdl	bdl	bdl	bdl	bdl	bdl	bdl	bdl	bdl	bdl	bdl	bdl	bdl	bdl
Ti	bdl	bdl	bdl	bdl	bdl	0.01	0.01	0.01	0.01	0.01	0.01	0.01	0.01	0.01	0.01	0.01	0.01
Al	1.37	1.40	0.89	0.94	1.05	1.66	1.67	1.65	1.25	1.44	1.64	1.72	1.72	1.73	1.73	1.72	1.73
Cr	0.45	0.43	0.81	0.76	0.68	bdl	bdl	bdl	bdl	bdl	bdl	bdl	bdl	bdl	bdl	bdl	bdl
V^{3+}	bdl	bdl	bdl	bdl	bdl	bdl	bdl	bdl	bdl	bdl	bdl	bdl	bdl	bdl	bdl	bdl	bdl
Fe^{3+}	0.17	0.17	0.29	0.29	0.26	0.32	0.31	0.32	0.73	0.54	0.34	0.26	0.26	0.25	0.26	0.26	0.25
Fe^{2+}	0.27	0.27	0.40	0.39	0.36	0.06	0.07	0.07	0.15	0.08	0.07	0.06	0.06	0.05	0.06	0.06	0.06
Mn	0.01	0.01	0.02	0.01	0.01	0.01	0.01	0.01	0.02	0.01	0.01	0.01	0.01	0.01	0.01	0.01	0.01
Mg	0.72	0.72	0.58	0.59	0.62	0.94	0.93	0.93	0.84	0.91	0.93	0.94	0.94	0.95	0.94	0.94	0.94
Ni	0.01	0.01	0.01	bdl	bdl	bdl	bdl	bdl	bdl	bdl	bdl	bdl	bdl	bdl	bdl	bdl	bdl
Zn	bdl	bdl	bdl	bdl	bdl	bdl	bdl	bdl	bdl	bdl	bdl	bdl	bdl	bdl	bdl	bdl	bdl
Total	**3.00**	**3.00**	**3.00**	**3.00**	**3.00**	**3.00**	**3.00**	**3.00**	**3.00**	**3.00**	**3.00**	**3.00**	**3.00**	**3.00**	**3.00**	**3.00**	**3.00**

SPINEL

Sample	RSTX26-1 (JEOL)						RSTX26-3 (JEOL)										
Analysis #	**26**	**27**	**28**	**29**	**30**	**31**	**32**	**33**	**34**	**35**	**37**	**38**	**39**	**40**	**41**	**42**	**43**
SiO_2	0.02	0.04	0.04	0.03	0.03	0.10	0.04	0.06	0.04	0.02	0.01	0.02	bdl	0.06	0.01	0.01	0.02
TiO_2	0.43	0.43	0.41	0.38	0.40	4.17	3.67	0.94	0.56	5.67	0.91	0.96	6.08	5.76	6.00	0.71	0.80
Al_2O_3	56.79	56.82	57.37	57.70	57.27	4.99	5.94	47.98	51.49	6.50	49.92	49.20	3.77	5.58	5.40	51.83	52.07
Cr_2O_3	0.02	0.02	bdl	bdl	0.06	0.05	bdl	0.05	0.07	bdl	0.02	0.05	0.10	0.01	0.07	0.03	bdl
V_2O_3	0.03	0.01	0.04	0.05	bdl	0.16	0.21	0.01	bdl	0.22	bdl	bdl	0.34	0.33	0.31	0.06	0.02
Fe_2O_3	13.22	13.69	12.82	13.02	13.25	61.15	60.55	22.01	19.37	58.29	20.34	20.73	59.33	58.85	58.70	19.25	18.96
FeO	2.63	2.75	2.45	2.53	2.73	11.38	10.80	2.86	2.38	10.16	2.71	2.52	11.36	10.71	10.90	2.35	2.41
MnO	0.42	0.41	0.35	0.36	0.39	1.71	1.71	0.55	0.43	1.58	0.44	0.49	1.69	1.61	1.59	0.38	0.37
MgO	24.53	24.64	24.81	24.91	24.67	14.45	14.41	23.62	24.29	16.48	24.02	23.94	15.35	16.13	16.09	24.56	24.65
NiO	0.04	0.04	0.03	0.02	0.05	bdl	0.04	0.03	bdl	0.04	0.03	0.11	0.09	0.02	0.03	0.03	bdl
Total	98.12	98.84	98.33	99.00	98.85	98.16	97.35	98.10	98.63	98.95	98.41	98.02	98.10	99.07	99.10	99.21	99.30
							Number of ions based on 4 Oxygens										
Si	bdl	bdl	bdl	bdl	bdl	bdl	bdl	bdl	bdl	bdl	bdl	bdl	bdl	bdl	bdl	bdl	bdl
Ti	0.01	0.01	0.01	0.01	0.01	0.11	0.09	0.02	0.01	0.14	0.02	0.02	0.16	0.14	0.15	0.01	0.02
Al	1.72	1.72	1.73	1.73	1.73	0.20	0.24	1.51	1.59	0.25	1.56	1.54	0.15	0.22	0.21	1.59	1.60
Cr	bdl	bdl	bdl	bdl	bdl	bdl	bdl	bdl	bdl	bdl	bdl	bdl	bdl	bdl	bdl	bdl	bdl
V^{3+}	bdl	bdl	bdl	bdl	bdl	bdl	0.01	bdl	bdl	0.01	bdl	bdl	0.01	0.01	0.01	bdl	bdl
Fe^{3+}	0.26	0.26	0.25	0.25	0.26	1.57	1.56	0.44	0.38	1.46	0.41	0.42	1.52	1.48	1.48	0.38	0.37
Fe^{2+}	0.06	0.06	0.05	0.05	0.06	0.33	0.31	0.06	0.05	0.28	0.06	0.06	0.32	0.30	0.30	0.05	0.05
Mn	0.01	0.01	0.01	0.01	0.01	0.05	0.05	0.01	0.01	0.04	0.01	0.01	0.05	0.05	0.05	0.01	0.01
Mg	0.94	0.94	0.95	0.95	0.94	0.74	0.74	0.94	0.95	0.81	0.95	0.95	0.78	0.80	0.80	0.95	0.96
Ni	bdl	bdl	bdl	bdl	bdl	bdl	bdl	bdl	bdl	bdl	bdl	bdl	bdl	bdl	bdl	bdl	bdl
Total	**3.00**	**3.00**	**3.00**	**3.00**	**3.00**	**3.00**	**3.00**	**3.00**	**3.00**	**3.00**	**3.00**	**3.00**	**3.00**	**3.00**	**3.00**	**3.00**	**3.00**

SPINEL

Sample	RSTX26-3 (JEOL)						RSTX26-4 (JEOL)										
Analysis #	**44**	**45**	**46**	**47**	**48**	**49**	**50**	**51**	**52**	**53**	**54**	**55**	**56**	**57**	**58**	**59**	**60**
SiO_2	0.06	0.06	0.01	0.03	0.04	0.03	0.01	0.03	0.02	0.03	0.02	0.01	0.04	0.05	0.03	0.04	0.02
TiO_2	1.04	5.91	5.88	0.96	0.75	0.46	0.27	0.34	0.29	0.30	0.30	0.26	0.30	0.46	1.00	0.25	0.42
Al_2O_3	47.87	6.82	6.36	49.39	51.56	53.47	58.43	60.05	59.53	60.16	59.51	59.07	55.60	52.01	2.65	56.49	52.51
Cr_2O_3	0.05	0.06	0.07	0.02	0.04	0.21	0.31	0.91	1.04	0.77	0.35	0.37	0.27	0.19	0.21	0.20	0.57
V_2O_3	bdl	0.30	0.32	bdl	bdl	bdl	bdl	bdl	bdl	bdl	bdl	bdl	0.02	bdl	0.03	bdl	bdl
Fe_2O_3	22.74	57.01	56.73	21.25	19.43	16.90	11.64	9.74	9.13	9.32	10.14	10.53	14.40	18.61	66.08	13.70	16.59
FeO	2.97	10.51	10.92	2.71	2.11	4.02	3.24	2.75	3.13	3.27	3.35	3.13	3.58	4.21	15.88	3.96	3.32
MnO	0.48	1.59	1.77	0.50	0.44	0.43	0.40	0.42	0.33	0.35	0.35	0.35	0.42	0.42	1.50	0.45	0.44
MgO	23.87	16.40	15.72	24.11	24.66	23.45	24.35	25.03	24.44	24.62	24.40	24.44	23.81	23.24	9.04	23.65	23.43
NiO	0.01	0.06	0.07	bdl	0.03	0.06	bdl	0.02	0.08	0.05	0.06	bdl	bdl	0.02	0.04	0.01	0.04
Total	**99.09**	**98.73**	**97.85**	**98.97**	**99.06**	**99.03**	**98.64**	**99.28**	**97.98**	**98.87**	**98.47**	**98.16**	**98.46**	**99.21**	**96.47**	**98.74**	**97.34**
							Number of ions based on 4 Oxygens										
Si	bdl	bdl	bdl	bdl	bdl	bdl	bdl	bdl	bdl	bdl	bdl	bdl	bdl	bdl	bdl	bdl	bdl
Ti	0.02	0.15	0.15	0.02	0.01	0.01	0.01	0.01	0.01	0.01	0.01	0.01	0.01	0.01	0.03	bdl	0.01
Al	1.50	0.27	0.25	1.54	1.59	1.64	1.76	1.78	1.79	1.79	1.79	1.78	1.70	1.61	0.11	1.72	1.64
Cr	bdl	bdl	bdl	bdl	bdl	bdl	0.01	0.02	0.02	0.02	0.01	0.01	0.01	bdl	0.01	bdl	0.01
V^{3+}	bdl	0.01	0.01	bdl	bdl	bdl	bdl	bdl	bdl	bdl	bdl	bdl	bdl	bdl	bdl	bdl	bdl
Fe^{3+}	0.45	1.42	1.44	0.42	0.38	0.33	0.22	0.18	0.18	0.18	0.19	0.20	0.28	0.37	1.82	0.27	0.33
Fe^{2+}	0.07	0.29	0.31	0.06	0.05	0.09	0.07	0.06	0.07	0.07	0.07	0.07	0.08	0.09	0.49	0.09	0.07
Mn	0.01	0.04	0.05	0.01	0.01	0.01	0.01	0.01	0.01	0.01	0.01	0.01	0.01	0.01	0.05	0.01	0.01
Mg	0.95	0.81	0.79	0.95	0.96	0.91	0.93	0.94	0.93	0.93	0.93	0.93	0.92	0.91	0.49	0.91	0.92
Ni	bdl	bdl	bdl	bdl	bdl	bdl	bdl	bdl	bdl	bdl	bdl	bdl	bdl	bdl	bdl	bdl	bdl
Total	**3.00**	**3.00**	**3.00**	**3.00**	**3.00**	**3.00**	**3.00**	**3.00**	**3.00**	**3.00**	**3.00**	**3.00**	**3.00**	**3.00**	**3.00**	**3.00**	**3.00**

SPINEL

Sample	RSTX26-4 (JEOL)											RSTX26-5 (JEOL					
Analysis #	**61**	**62**	**63**	**64**	**65**	**66**	**67**	**68**	**111**	**112**	**113**	**69**	**70**	**71**	**72**	**73**	**74**
SiO_2	0.05	0.04	0.05	0.02	0.04	0.07	0.08	0.06	0.05	0.02	0.04	0.01	bdl	0.02	0.03	0.04	0.02
TiO_2	0.58	0.87	0.89	0.96	1.00	0.90	2.61	2.40	1.54	1.73	1.36	1.57	1.33	1.04	0.67	3.35	0.28
Al_2O_3	50.36	46.56	45.05	45.04	44.57	46.47	2.63	2.75	3.20	4.14	43.41	42.65	43.01	43.88	43.81	4.70	53.85
Cr_2O_3	0.49	0.27	1.55	0.66	1.23	0.74	0.09	0.02	0.08	0.07	1.07	1.17	1.01	0.90	0.81	0.98	0.68
V_2O_3	bdl	bdl	0.04	bdl	bdl	0.03	0.18	0.12	0.07	0.16	0.07	bdl	bdl	0.05	bdl	0.15	bdl
Fe_2O_3	18.88	23.35	23.55	24.62	24.21	23.67	63.54	64.84	65.63	65.26	25.46	25.96	26.24	24.19	24.44	61.14	15.64
FeO	3.51	3.83	4.19	4.04	4.07	4.07	17.62	16.77	16.55	12.52	2.93	2.67	2.77	2.37	2.50	10.41	2.22
MnO	0.41	0.46	0.53	0.58	0.53	0.53	1.33	1.42	1.45	1.86	0.46	0.58	0.63	0.58	0.55	1.81	0.40
MgO	23.23	22.86	22.46	22.57	22.49	22.97	8.94	9.30	9.20	11.77	23.41	23.47	23.33	23.11	22.71	14.15	24.25
NiO	0.03	0.06	0.06	0.06	0.08	0.01	0.06	0.16	0.10	0.11	bdl	0.04	bdl	0.03	bdl	0.02	bdl
Total	**97.52**	**98.31**	**98.35**	**98.54**	**98.21**	**99.46**	**97.08**	**97.84**	**97.86**	**97.63**	**98.20**	**98.12**	**98.31**	**96.17**	**95.50**	**96.76**	**97.34**
							Number of ions based on 4 Oxygens										
Si	bdl	bdl	bdl	bdl	bdl	bdl	bdl	bdl	bdl	bdl	bdl	bdl	bdl	bdl	bdl	bdl	bdl
Ti	0.01	0.02	0.02	0.02	0.02	0.02	0.07	0.06	0.04	0.05	0.03	0.03	0.03	0.02	0.01	0.09	0.01
Al	1.58	1.48	1.44	1.44	1.43	1.47	0.11	0.12	0.14	0.17	1.40	1.38	1.38	1.43	1.44	0.19	1.66
Cr	0.01	0.01	0.03	0.01	0.03	0.02	bdl	bdl	bdl	bdl	0.02	0.03	0.02	0.02	0.02	0.03	0.01
V^{3+}	bdl	bdl	bdl	bdl	bdl	bdl	0.01	bdl	bdl	bdl	bdl	bdl	bdl	bdl	bdl	bdl	bdl
Fe^{3+}	0.38	0.47	0.48	0.50	0.50	0.48	1.73	1.75	1.77	1.73	0.52	0.53	0.54	0.50	0.51	1.60	0.31
Fe^{2+}	0.08	0.09	0.10	0.09	0.09	0.09	0.53	0.50	0.50	0.37	0.07	0.06	0.06	0.05	0.06	0.30	0.05
Mn	0.01	0.01	0.01	0.01	0.01	0.01	0.04	0.04	0.04	0.06	0.01	0.01	0.01	0.01	0.01	0.05	0.01
Mg	0.92	0.92	0.91	0.91	0.91	0.92	0.48	0.50	0.49	0.62	0.95	0.96	0.95	0.95	0.94	0.73	0.95
Ni	bdl	bdl	bdl	bdl	bdl	bdl	bdl	bdl	bdl	bdl	bdl	bdl	bdl	bdl	bdl	bdl	bdl
Total	**3.00**	**3.00**	**3.00**	**3.00**	**3.00**	**3.00**	**2.98**	**2.98**	**2.99**	**3.00**	**3.00**	**3.00**	**3.00**	**3.00**	**3.00**	**3.00**	**3.00**

SPINEL

Sample	RSTX26-5 (JEOL														
Analysis #	**75**	**76**	**77**	**78**	**79**	**80**	**81**	**82**	**83**	**84**	**85**	**86**	**88**	**89**	**90**
SiO_2	0.01	0.05	0.03	0.02	0.02	0.05	0.01	0.04	0.01	0.03	0.01	bdl	0.03	0.02	0.05
TiO_2	1.15	1.02	0.82	0.65	0.60	4.69	1.10	4.45	0.17	0.56	0.15	0.12	0.16	0.13	1.32
Al_2O_3	44.16	45.21	45.50	50.74	51.06	7.13	42.83	4.12	57.77	50.32	60.81	59.71	60.39	60.06	14.88
Cr_2O_3	1.24	1.14	1.08	1.18	1.22	1.24	1.03	1.61	1.43	1.33	0.05	0.13	2.08	0.26	42.56
V_2O_3	0.01	bdl	bdl	bdl	bdl	0.28	bdl	0.17	bdl	bdl	bdl	0.02	bdl	bdl	0.42
Fe_2O_3	24.15	23.39	23.45	18.96	17.69	56.55	25.82	57.76	10.74	18.22	7.47	7.04	7.60	7.11	7.81
FeO	2.81	2.99	2.66	2.66	2.78	9.78	2.75	15.14	1.94	2.94	5.03	5.50	5.81	5.52	24.34
MnO	0.54	0.54	0.56	0.40	0.35	1.46	0.60	1.38	0.25	0.35	0.38	0.35	0.41	0.43	0.32
MgO	23.18	23.19	23.26	24.12	23.84	15.94	22.97	11.94	24.86	23.59	23.06	22.24	23.05	22.42	6.74
NiO	bdl	bdl	bdl	bdl	bdl	0.07	bdl	0.02	0.04	0.04	0.02	0.02	bdl	bdl	0.15
Total	**97.25**	**97.54**	**97.37**	**98.72**	**97.55**	**97.19**	**97.09**	**96.62**	**97.21**	**97.37**	**97.00**	**95.12**	**99.51**	**95.96**	**98.58**
						Number of ions based on 4 Oxygens									
Si	bdl	bdl	bdl	bdl	bdl	bdl	bdl	bdl	bdl	bdl	bdl	bdl	bdl	bdl	bdl
Ti	0.02	0.02	0.02	0.01	0.01	0.12	0.02	0.12	bdl	0.01	bdl	bdl	bdl	bdl	0.03
Al	1.43	1.45	1.46	1.57	1.60	0.28	1.39	0.17	1.76	1.58	1.85	1.85	1.81	1.85	0.59
Cr	0.03	0.02	0.02	0.02	0.03	0.03	0.02	0.04	0.03	0.03	bdl	bdl	0.04	0.01	1.13
V^{3+}	bdl	bdl	bdl	bdl	bdl	0.01	bdl	bdl	bdl	bdl	bdl	bdl	bdl	bdl	0.01
Fe^{3+}	0.50	0.48	0.48	0.38	0.35	1.43	0.54	1.54	0.21	0.37	0.14	0.14	0.15	0.14	0.20
Fe^{2+}	0.06	0.07	0.06	0.06	0.06	0.28	0.06	0.45	0.04	0.07	0.11	0.12	0.12	0.12	0.68
Mn	0.01	0.01	0.01	0.01	0.01	0.04	0.01	0.04	0.01	0.01	0.01	0.01	0.01	0.01	0.01
Mg	0.95	0.94	0.94	0.95	0.94	0.80	0.95	0.63	0.96	0.94	0.89	0.87	0.87	0.87	0.34
Ni	bdl	bdl	bdl	bdl	bdl	bdl	bdl	bdl	bdl	bdl	bdl	bdl	bdl	bdl	bdl
Total	**3.00**	**3.00**	**3.00**	**3.00**	**3.00**	**3.00**	**3.00**	**3.00**	**3.00**	**3.00**	**3.00**	**3.00**	**3.00**	**3.00**	**3.00**

SPINEL

Sample	RSTX26-61 (JEOL)										RSTX26-62 (JEOL)						
Analysis #	**14**	**15**	**16**	**17**	**18**		**20**	**21**	**22**	**23**	**24**	**25**	**26**	**28**	**29**	**30**	**31**
SiO_2	0.03	0.01	0.01	0.02	0.01	0.05	bdl	bdl	0.01	0.05	0.04	0.01	0.03	0.04	bdl	0.02	0.03
TiO_2	0.07	0.03	0.07	0.09	0.08	0.07	0.13	0.09	0.14	0.25	0.26	0.22	0.70	0.21	0.21	0.24	0.20
Al_2O_3	20.73	21.10	21.75	27.05	25.53	28.30	23.45	23.40	21.73	18.93	18.66	20.42	20.76	20.28	20.55	18.05	20.45
Cr_2O_3	40.07	39.28	38.54	33.28	34.60	31.88	36.06	36.88	38.40	41.77	41.61	39.78	36.86	39.83	39.02	40.47	40.37
V_2O_3	bdl	bdl	bdl	0.02	bdl	bdl	0.07	0.08	0.03	0.21	0.12	0.15	0.34	0.14	0.12	0.12	0.04
Fe_2O_3	8.95	8.69	8.59	9.12	9.26	9.14	8.74	9.07	8.49	7.41	7.41	7.48	9.57	8.03	8.21	9.05	6.86
FeO	19.07	19.32	18.65	19.56	19.75	19.38	21.02	21.48	21.37	25.77	25.80	25.23	26.28	25.03	24.62	25.49	25.08
MnO	1.13	1.05	1.12	0.95	0.92	0.82	0.90	0.89	0.90	0.64	0.56	0.57	0.68	0.69	0.64	0.74	0.61
MgO	9.82	9.52	9.92	10.37	10.01	10.64	8.82	8.83	8.54	5.92	5.78	6.25	6.04	6.43	6.55	5.70	6.31
NiO	0.07	0.09	0.10	0.12	0.16	0.17	0.11	0.08	0.07	0.11	0.12	0.10	0.11	0.07	0.12	0.08	0.10
Total	**99.93**	**99.10**	**98.75**	**100.57**	**100.31**	**100.43**	**99.29**	**100.80**	**99.67**	**101.05**	**100.36**	**100.21**	**101.38**	**100.74**	**100.04**	**99.96**	**100.06**
							Number of ions based on 4 Oxygens										
Si	bdl	bdl	bdl	bdl	bdl	bdl	bdl	bdl	bdl	bdl	bdl	bdl	bdl	bdl	bdl	bdl	bdl
Ti	bdl	bdl	bdl	bdl	bdl	bdl	bdl	bdl	bdl	0.01	0.01	0.01	0.02	0.01	0.01	0.01	bdl
Al	0.78	0.80	0.82	0.98	0.93	1.02	0.88	0.86	0.82	0.73	0.72	0.78	0.79	0.77	0.79	0.70	0.78
Cr	1.01	0.99	0.97	0.81	0.85	0.77	0.91	0.91	0.97	1.07	1.08	1.02	0.94	1.02	1.00	1.06	1.04
V^{3+}	bdl	bdl	bdl	bdl	bdl	bdl	bdl	bdl	bdl	0.01	bdl	bdl	0.01	bdl	bdl	bdl	bdl
Fe^{3+}	0.21	0.21	0.21	0.21	0.22	0.21	0.21	0.21	0.20	0.18	0.18	0.18	0.23	0.20	0.20	0.22	0.17
Fe^{2+}	0.51	0.52	0.50	0.50	0.51	0.49	0.56	0.56	0.57	0.70	0.71	0.68	0.71	0.68	0.67	0.70	0.68
Mn	0.03	0.03	0.03	0.02	0.02	0.02	0.02	0.02	0.02	0.02	0.02	0.02	0.02	0.02	0.02	0.02	0.02
Mg	0.46	0.45	0.47	0.47	0.46	0.48	0.42	0.41	0.41	0.29	0.28	0.30	0.29	0.31	0.32	0.28	0.31
Ni	bdl	bdl	bdl	bdl	bdl	bdl	bdl	bdl	bdl	bdl	bdl	bdl	bdl	bdl	bdl	bdl	bdl
Total	**3.00**	**3.00**	**3.00**	**3.00**	**3.00**	**3.00**	**3.00**	**3.00**	**3.00**	**3.00**	**3.00**	**3.00**	**3.00**	**3.00**	**3.00**	**3.00**	**3.00**

SPINEL

Sample	RSTX26-63 (JEOL)					RSTX26-UG1 (JEOL)						
Analysis #	**32**	**33**	**34**	**35**	**36**	**6**	**7**	**8**	**9**	**10**	**11**	**12**
SiO_2	0.03	0.02	0.07	0.02	0.08	0.01	0.02	0.04	0.05	0.02	0.02	0.04
TiO_2	0.20	0.34	0.33	0.35	0.32	1.33	1.32	1.44	1.39	1.30	1.36	0.03
Al_2O_3	19.87	18.72	19.05	18.47	20.52	14.51	14.67	14.68	14.90	12.24	14.53	20.03
Cr_2O_3	40.98	41.16	40.53	41.23	39.20	42.15	42.71	42.89	42.51	41.61	42.60	41.35
V_2O_3	bdl	0.19	0.11	0.19	0.19	0.44	0.43	0.46	0.45	0.53	0.50	bdl
Fe_2O_3	7.04	7.79	7.38	7.07	6.97	8.55	8.12	7.78	7.85	8.83	8.15	8.46
FeO	25.03	25.80	25.51	25.53	25.24	24.20	24.57	24.49	24.79	23.15	24.63	19.44
MnO	0.58	0.47	0.47	0.51	0.44	0.34	0.36	0.31	0.31	0.31	0.34	1.24
MgO	6.30	5.92	5.97	5.79	6.23	6.68	6.62	6.75	6.59	6.32	6.56	9.44
NiO	0.12	0.07	0.09	0.09	0.17	0.16	0.07	0.19	0.13	0.18	0.11	0.11
Total	**100.14**	**100.48**	**99.51**	**99.24**	**99.35**	**98.35**	**98.86**	**99.02**	**98.97**	**94.49**	**98.80**	**100.14**
					Number of ions based on 4 Oxygens							
Si	bdl	bdl	bdl	bdl	bdl	bdl	bdl	bdl	bdl	bdl	bdl	bdl
Ti	bdl	0.01	0.01	0.01	0.01	0.03	0.03	0.04	0.03	0.03	0.03	bdl
Al	0.76	0.72	0.74	0.72	0.79	0.58	0.58	0.58	0.59	0.51	0.58	0.75
Cr	1.05	1.06	1.05	1.08	1.01	1.13	1.13	1.14	1.13	1.17	1.13	1.04
V^{3+}	bdl	0.01	bdl	bdl	bdl	0.01	0.01	0.01	0.01	0.01	0.01	bdl
Fe^{3+}	0.17	0.19	0.18	0.18	0.17	0.22	0.21	0.20	0.20	0.24	0.21	0.20
Fe^{2+}	0.68	0.71	0.70	0.71	0.69	0.68	0.69	0.69	0.70	0.69	0.69	0.52
Mn	0.02	0.01	0.01	0.01	0.01	0.01	0.01	0.01	0.01	0.01	0.01	0.03
Mg	0.31	0.29	0.29	0.29	0.30	0.34	0.33	0.34	0.33	0.33	0.33	0.45
Ni	bdl	bdl	bdl	bdl	bdl	bdl	bdl	0.01	bdl	0.01	bdl	bdl
Total	**3.00**	**3.00**	**3.00**	**3.00**	**3.00**	**3.00**	**3.00**	**3.00**	**3.00**	**3.00**	**3.00**	**3.00**

Appendix 4C: Electron microprobe data expressed as oxides (wt %) and recalculated atoms per unit formula for Zwartfontein samples

MONTICELLITE																	
Sample	**A156-7 (JEOL)**																
Analysis #	**133**	**134**	**135**	**136**	**137**	**138**	**139**	**150**	**151**	**152**	**153**	**158**	**159**	**160**	**161**	**164**	**165**
Comment	**Lam**	**G**	**G**	**G**	**G**	**G**	**G**	**Fine gr**	**Fine gr**	**Fine gr**	**Fine gr**	**Lam**	**G**	**G**	**G**	**Fine gr**	**Fine gr**
SiO_2	36.98	37.27	37.23	36.98	37.06	37.03	37.25	37.85	38.06	39.31	39.41	37.16	37.77	37.27	37.30	37.49	37.46
Al_2O_3	bdl	bdl	bdl	bdl	bdl	bdl	0.01	0.05	0.01	18.81	20.45	bdl	bdl	0.01	0.02	bdl	0.01
TiO_2	bdl	0.01	bdl	bdl	bdl	0.03	bdl	0.01	bdl	bdl	bdl	0.03	bdl	bdl	bdl	bdl	bdl
Cr_2O_3	bdl	0.06	bdl	0.08	bdl	bdl	0.01	0.01	bdl	bdl	bdl	0.01	0.08	0.08	bdl	0.01	bdl
FeO	5.42	4.67	4.84	4.90	4.81	4.93	5.05	1.05	0.20	3.96	2.38	5.06	4.43	4.65	4.39	4.31	4.51
MnO	1.32	1.16	1.24	1.21	1.21	1.13	1.16	0.36	0.75	0.08	0.05	1.29	1.18	1.21	1.26	1.15	1.19
MgO	21.44	22.10	22.00	22.28	21.85	21.92	21.83	24.67	25.05	0.18	0.57	21.89	22.82	22.44	22.26	22.20	22.19
CaO	32.63	32.94	33.16	33.00	33.30	33.52	33.22	34.68	34.81	35.62	35.65	33.31	33.27	33.24	33.26	33.65	33.62
Na_2O	bdl	0.01	0.01	bdl	bdl	0.01	bdl	0.02	bdl	bdl	0.02	bdl	bdl	0.03	bdl	bdl	0.01
K_2O	0.02	0.03	bdl	0.03	0.02	0.03	0.03	bdl	0.03	0.04	0.01	0.02	bdl	0.02	0.02	0.02	0.01
Total	**97.81**	**98.26**	**98.48**	**98.48**	**98.25**	**98.59**	**98.56**	**98.70**	**98.91**	**98.00**	**98.53**	**98.77**	**99.57**	**98.93**	**98.52**	**98.84**	**99.00**
								Number of ions based on 4 Oxygens									
Si	1.01	1.01	1.01	1.00	1.01	1.00	1.01	1.00	1.00	1.02	1.01	1.00	1.01	1.00	1.01	1.01	1.01
Al	bdl	bdl	bdl	bdl	bdl	bdl	bdl	bdl	bdl	0.58	0.62	bdl	bdl	bdl	bdl	bdl	bdl
Ti	bdl	bdl	bdl	bdl	bdl	bdl	bdl	bdl	bdl	bdl	bdl	bdl	bdl	bdl	bdl	bdl	bdl
Cr	bdl	bdl	bdl	bdl	bdl	bdl	bdl	bdl	bdl	bdl	bdl	bdl	bdl	bdl	bdl	bdl	bdl
Fe^{2+}	0.12	0.11	0.11	0.11	0.11	0.11	0.11	0.02	bdl	0.09	0.05	0.11	0.10	0.10	0.10	0.10	0.10
Mn	0.03	0.03	0.03	0.03	0.03	0.03	0.03	0.01	0.02	bdl	bdl	0.03	0.03	0.03	0.03	0.03	0.03
Mg	0.87	0.89	0.89	0.90	0.88	0.88	0.88	0.97	0.99	0.01	0.02	0.88	0.91	0.90	0.90	0.89	0.89
Ca	0.95	0.96	0.96	0.96	0.97	0.97	0.96	0.98	0.98	0.99	0.98	0.96	0.95	0.96	0.96	0.97	0.97
Na	bdl	bdl	bdl	bdl	bdl	bdl	bdl	bdl	bdl	bdl	bdl	bdl	bdl	bdl	bdl	bdl	bdl
K	bdl	bdl	bdl	bdl	bdl	bdl	bdl	bdl	bdl	bdl	bdl	bdl	bdl	bdl	bdl	bdl	bdl
Total	**2.99**	**2.99**	**2.99**	**3.00**	**2.99**	**3.00**	**2.99**	**3.00**	**3.00**	**2.69**	**2.68**	**3.00**	**2.99**	**3.00**	**2.99**	**2.99**	**2.99**
Mg#	**0.88**	**0.89**	**0.89**	**0.89**	**0.89**	**0.89**	**0.89**	**0.98**	**1.00**	**0.08**	**0.30**	**0.89**	**0.90**	**0.90**	**0.90**	**0.90**	**0.90**

FORSTERITE				
Sample	**A156-7 (JEOL)**			
Analysis #	**129**	**130**	**131**	**132**
SiO_2	41.18	41.14	41.06	41.07
Al_2O_3	bdl	0.02	0.03	0.01
TiO_2	0.01	bdl	bdl	0.01
Cr_2O_3	0.06	0.06	bdl	0.02
FeO	5.29	4.48	4.37	5.41
MnO	1.24	1.06	1.05	1.21
MgO	51.54	52.20	52.08	51.79
CaO	0.53	0.58	0.50	0.54
Na_2O	bdl	bdl	bdl	bdl
K_2O	0.03	0.02	0.03	0.03
Total	**99.88**	**99.55**	**99.12**	**100.07**
	Number of ions based on 4 Oxygens			
Si	1.00	0.99	1.00	0.99
Al	bdl	bdl	bdl	bdl
Ti	bdl	bdl	bdl	bdl
Cr	bdl	bdl	bdl	bdl
Fe^{2+}	0.11	0.09	0.09	0.11
Mn	0.03	0.02	0.02	0.02
Mg	1.86	1.88	1.88	1.87
Ca	0.01	0.02	0.01	0.01
Na	bdl	bdl	bdl	bdl
K	bdl	bdl	bdl	bdl
Total	**3.00**	**3.01**	**3.00**	**3.01**
Mg#	**0.95**	**0.95**	**0.96**	**0.94**

CALCITE

Sample	C435-2 (JEOL)			A312-2 (JEOL)				
Analysis #	**1**	**2**	**3**	**1**	**2**	**3**	**4**	**5**
CaO	53.62	53.39	54.02	53.28	54.04	54.62	54.25	54.31
MgO	0.10	0.12	0.11	0.01	0.01	0.05	0.02	0.03
FeO	bdl	0.03	bdl	0.02	bdl	0.01	0.03	0.04
SrO	0.20	0.23	0.22	0.18	0.10	0.23	0.22	0.18
BaO	bdl	0.01	0.01	0.01	0.01	0.02	0.02	0.03
MnO	bdl	0.01	bdl	bdl	0.01	0.01	0.04	bdl
CO_2	**42.27**	**42.16**	**42.61**	**41.92**	**42.47**	**43.03**	**42.74**	**42.76**
Total	**96.19**	**95.95**	**96.97**	**95.42**	**96.63**	**97.97**	**97.32**	**97.34**
			Number of ions based on 6 Oxygens					
Ca	1.99	1.99	1.99	2.00	2.00	1.99	1.99	1.99
Mg	0.01	0.01	0.01	bdl	bdl	bdl	bdl	bdl
Mn	bdl	bdl	bdl	bdl	bdl	bdl	bdl	bdl
Fe	bdl	bdl	bdl	bdl	bdl	bdl	bdl	bdl
Sr	bdl	bdl	bdl	bdl	bdl	bdl	bdl	bdl
Ba	bdl	bdl	bdl	bdl	bdl	bdl	bdl	bdl
C	**2.00**	**2.00**	**2.00**	**2.00**	**2.00**	**2.00**	**2.00**	**2.00**
O	**6.00**	**6.00**	**6.00**	**6.00**	**6.00**	**6.00**	**6.00**	**6.00**

ANHYDRITE

Sample	C435-2 (JEOL)			
Analysis #	**1**	**2**	**3**	**4**
SO_3	57.42	57.50	57.98	57.90
BaO	0.02	bdl	bdl	0.02
CaO	41.81	42.10	41.83	42.06
SrO	0.19	0.26	0.16	0.19
Total	**99.43**	**99.87**	**99.97**	**100.17**
	Number of ions based on 4 Oxygens			
S	2.97	**2.97**	2.98	2.97
Ba	bdl	bdl	bdl	
Ca	1.03	1.03	1.02	1.03
Sr	bdl	bdl	bdl	bdl
Total	**4.00**	**4.00**	**4.00**	**4.00**

SERPENTINE

Sample	C435-2 (JEOL)					
Analysis #	**1**	**2**	**3**	**4**	**5**	**6**
SiO_2	41.80	41.05	42.26	40.10	42.08	42.07
TiO_2	bdl	bdl	0.02	bdl	bdl	0.02
Al_2O_3	0.47	0.46	0.71	1.25	0.45	0.76
Cr_2O_3	bdl	0.03	bdl	0.05	0.03	0.02
FeO	0.61	1.42	0.68	1.35	0.45	0.50
MnO	0.20	0.15	0.30	0.32	0.15	0.15
MgO	40.92	40.21	40.51	40.09	41.30	40.74
CaO	0.10	0.09	0.28	0.10	0.07	0.04
Na_2O	bdl	bdl	0.01	bdl	bdl	0.02
K_2O	0.02	0.03	0.04	0.01	0.01	0.03
H_2O	**15.56**	**15.38**	**15.61**	**15.30**	**15.65**	**15.56**
Total	**99.66**	**98.81**	**100.42**	**98.56**	**100.19**	**99.92**
	Number of ions based on 4 O. OH					
Si	1.81	1.80	1.82	1.77	1.81	1.82
Ti	bdl	bdl	bdl	bdl	bdl	bdl
Al	0.01	0.01	0.02	0.03	0.01	0.02
Cr	bdl	bdl	bdl	bdl	bdl	bdl
Fe^{+3}	bdl	bdl	bdl	bdl	bdl	bdl
Fe^{+2}	0.02	0.05	0.02	0.05	0.02	0.02
Mn	0.01	0.01	0.01	0.01	0.01	0.01
Mg	2.64	2.63	2.61	2.63	2.65	2.63
Ca	bdl	bdl	0.01	bdl	bdl	bdl
Na	bdl	bdl	bdl	bdl	bdl	bdl
K	bdl	bdl	bdl	bdl	bdl	bdl
H	**4.50**	**4.50**	**4.50**	**4.50**	**4.50**	**4.50**
Total	**9.00**	**9.00**	**9.00**	**9.00**	**9.00**	**9.00**

FELDSPAR

Sample	B882-4 (JEOL)										A291-1(JEOL)					
Analysis #	**85**	**86**	**87**	**88**	**89**	**90**	**91**	**92**	**93**	**94**	**95**	**96**	**97**	**98**	**99**	**100**
SiO_2	52.31	52.19	47.33	45.42	51.84	51.80	51.91	51.51	51.38	51.42	58.64	55.79	53.54	52.83	56.21	53.21
Al_2O_3	31.66	31.20	23.15	22.49	31.12	31.14	31.04	31.21	31.41	31.51	26.52	28.59	30.22	30.35	28.44	30.41
FeO	0.30	0.31	0.74	1.30	0.23	0.28	0.27	0.25	0.32	0.17	0.18	0.15	0.20	0.20	0.17	0.44
CaO	14.68	14.49	24.94	23.04	14.36	14.42	14.23	14.41	14.40	14.57	8.98	11.39	13.45	13.70	11.20	13.51
Na_2O	3.04	3.10	0.06	0.02	3.15	3.14	3.24	3.08	2.89	3.03	6.17	4.70	3.62	3.58	4.75	3.52
K_2O	0.12	0.12	0.03	0.03	0.08	0.09	0.09	0.09	0.28	0.09	0.37	0.27	0.20	0.31	0.30	0.19
Total	102.11	101.40	96.25	92.31	100.79	100.87	100.79	100.55	100.67	100.81	100.86	100.88	101.23	100.98	101.07	101.28
							Number of ions based on 8 Oxygens									
Si	2.33	2.34	2.32	2.27	2.34	2.34	2.34	2.33	2.32	2.32	2.60	2.49	2.40	2.38	2.50	2.38
Al	1.66	1.65	1.34	1.32	1.65	1.65	1.65	1.66	1.67	1.68	1.39	1.50	1.59	1.61	1.49	1.61
Fe	0.01	0.01	0.03	0.05	0.01	0.01	0.01	0.01	0.01	0.01	0.01	0.01	0.01	0.01	0.01	0.02
Ca	0.70	0.70	1.31	1.23	0.69	0.70	0.69	0.70	0.70	0.70	0.43	0.54	0.64	0.66	0.53	0.65
Na	0.26	0.27	0.01	bdl	0.28	0.27	0.28	0.27	0.25	0.27	0.53	0.41	0.31	0.31	0.41	0.31
K	0.01	0.01	bdl	bdl	bdl	0.01	0.01	0.01	0.02	0.01	0.02	0.02	0.01	0.02	0.02	0.01
Total	**4.97**	**4.97**	**5.01**	**4.88**	**4.97**	**4.98**	**4.98**	**4.98**	**4.97**	**4.98**	**4.97**	**4.97**	**4.97**	**4.98**	**4.96**	**4.97**
Ab	**27**	**28**	**0**	**0**	**28**	**28**	**29**	**28**	**26**	**27**	**54**	**42**	**32**	**31**	**43**	**32**
An	**72**	**72**	**99**	**100**	**71**	**71**	**70**	**72**	**72**	**72**	**44**	**56**	**66**	**67**	**56**	**67**
Or	**1**	**1**	**0**	**0**	**0**	**1**	**1**	**1**	**2**	**1**	**2**	**2**	**1**	**2**	**2**	**1**
Total	**100**	**100**	**100**	**100**	**100**	**100**	**100**	**100**	**100**	**100**	**100**	**100**	**100**	**100**	**100**	**100**

PYROXENE

Sample	A156-7 (JEOL)									B882-4 (JEOL)							
Analysis #	**140**	**141**	**142**	**143**	**144**	**145**	**146**	**162**	**163**	**166**	**167**	**168**	**169**	**170**	**171**	**172**	**173**
SiO_2	47.93	44.65	54.76	45.43	55.16	47.66	48.53	48.68	48.25	54.35	49.38	54.45	55.08	52.01	52.19	47.33	53.77
TiO_2	0.43	1.88	0.02	1.34	0.02	0.14	0.23	0.05	0.05	0.12	bdl	0.08	0.07	0.17	0.18	0.04	0.08
Al_2O_3	7.24	10.01	1.35	9.45	1.54	7.66	6.68	6.92	7.66	1.45	4.34	1.70	1.57	2.78	2.76	4.93	1.98
Cr_2O_3	bdl	bdl	0.06	bdl	0.03	bdl	bdl	bdl	0.04	0.37	0.25	0.49	0.29	0.85	0.81	0.39	0.44
FeO	3.91	4.41	0.33	4.37	0.51	3.86	3.90	3.71	3.96	12.88	9.54	10.97	10.80	5.45	5.53	9.42	14.53
MnO	0.14	0.15	0.07	0.18	0.03	0.16	0.10	0.16	0.14	0.25	0.40	0.25	0.22	0.16	0.19	0.20	0.35
MgO	14.22	12.56	18.06	13.02	18.15	13.90	14.43	14.32	14.00	27.76	17.60	28.83	29.21	15.30	15.49	18.81	27.80
CaO	24.49	24.17	24.99	24.33	24.90	24.26	24.44	24.49	24.75	2.49	16.43	2.65	2.56	22.33	22.27	14.75	0.59
Na_2O	0.02	0.02	0.06	0.05	0.03	0.04	0.05	0.04	0.01	0.06	0.27	0.03	0.02	0.46	0.43	0.18	bdl
Total	**98.38**	**97.85**	**99.70**	**98.16**	**100.37**	**97.69**	**98.36**	**98.37**	**98.85**	**99.73**	**98.20**	**99.46**	**99.82**	**99.50**	**99.84**	**96.05**	**99.54**
							Number of ions based on 6 Oxygens										
Si	1.78	1.68	1.98	1.70	1.98	1.78	1.80	1.81	1.78	1.95	1.84	1.94	1.95	1.92	1.92	1.79	1.94
Ti	0.01	0.05	bdl	0.04	bdl	bdl	0.01	bdl	bdl	bdl	bdl	bdl	bdl	bdl	0.01	bdl	bdl
Al	0.32	0.44	0.06	0.42	0.07	0.34	0.29	0.30	0.33	0.06	0.19	0.07	0.07	0.12	0.12	0.22	0.08
Fe^{3+}	0.10	0.09	bdl	0.11	bdl	0.09	0.09	0.08	0.10	0.03	0.14	0.03	0.02	0.04	0.04	0.20	0.03
Cr^{3+}	bdl	bdl	bdl	bdl	bdl	bdl	bdl	bdl	bdl	0.01	0.01	0.01	0.01	0.02	0.02	0.01	0.01
Fe^{2+}	0.02	0.05	0.01	0.02	0.02	0.03	0.03	0.03	0.03	0.36	0.16	0.30	0.30	0.13	0.13	0.10	0.41
Mn	bdl	bdl	bdl	0.01	bdl	0.01	bdl	0.01	bdl	0.01	0.01	0.01	0.01	bdl	0.01	0.01	0.01
Mg	0.79	0.70	0.97	0.73	0.97	0.77	0.80	0.79	0.77	1.48	0.98	1.53	1.54	0.84	0.85	1.06	1.49
Ca	0.98	0.97	0.97	0.97	0.96	0.97	0.97	0.97	0.98	0.10	0.66	0.10	0.10	0.88	0.88	0.60	0.02
Na	bdl	bdl	bdl	bdl	bdl	bdl	bdl	bdl	bdl	bdl	0.02	bdl	bdl	0.03	0.03	0.01	bdl
Total	**4.00**	**4.00**	**4.00**	**4.00**	**4.00**	**4.00**	**4.00**	**4.00**	**4.00**	**4.00**	**4.00**	**4.00**	**4.00**	**4.00**	**4.00**	**4.00**	**4.00**
Wo	**55**	**56**	**50**	**57**	**49**	**55**	**54**	**54**	**55**	**5**	**37**	**5**	**5**	**48**	**47**	**34**	**1**
En	**44**	**41**	**50**	**42**	**50**	**44**	**44**	**44**	**43**	**77**	**55**	**79**	**79**	**45**	**46**	**60**	**77**
Fs	**1**	**3**	**1**	**1**	**1**	**2**	**1**	**2**	**2**	**18**	**9**	**15**	**16**	**7**	**7**	**6**	**21**
Total	**100**	**100**	**100**	**100**	**100**	**100**	**100**	**100**	**100**	**100**	**100**	**100**	**100**	**100**	**100**	**100**	**100**

PYROXENE

Sample	B882-4 (JEOL)																
Analysis #	**174**	**175**	**176**	**177**	**178**	**179**	**180**	**182**	**183**	**185**	**186**	**187**	**188**	**189**	**190**	**193**	**194**
SiO_2	54.62	54.42	51.98	53.52	54.20	53.05	53.65	42.82	46.36	53.80	54.66	53.22	54.39	52.93	54.35	54.62	54.46
TiO_2	0.06	0.09	0.29	0.06	0.05	0.08	0.10	0.03	0.04	0.02	0.01	0.10	0.01	0.05	0.02	0.11	0.14
Al_2O_3	1.44	1.68	2.18	0.95	1.01	1.92	1.25	13.66	9.97	0.84	0.69	2.17	0.66	2.17	0.78	0.73	0.74
Cr_2O_3	0.35	0.49	0.17	0.28	0.07	0.48	0.27	bdl	0.01	0.06	bdl	0.01	bdl	0.01	0.01	bdl	0.05
FeO	13.10	13.17	9.48	6.78	2.46	2.93	2.73	6.62	5.91	1.41	1.42	2.46	1.54	2.70	1.54	1.47	1.86
MnO	0.32	0.33	0.31	0.19	0.13	0.34	0.33	0.10	0.17	0.26	0.25	0.20	0.21	0.22	0.17	0.13	0.18
MgO	28.22	27.86	15.87	15.27	17.30	16.86	17.39	10.43	12.50	17.50	17.66	16.87	17.57	16.42	17.42	17.76	17.62
CaO	1.77	1.88	17.96	22.29	24.73	23.98	23.74	24.56	24.75	25.03	25.31	25.02	25.21	25.37	25.25	25.14	24.99
Na_2O	0.03	0.01	0.35	0.30	0.01	0.13	0.11	bdl	0.01	bdl	bdl	0.01	0.02	bdl	0.02	bdl	bdl
Total	99.90	99.94	98.59	99.64	99.94	99.76	99.56	98.21	99.72	98.91	99.99	100.07	99.61	99.87	99.56	99.96	100.03
							Number of ions based on 6 Oxygens										
Si	1.95	1.95	1.95	1.98	1.97	1.94	1.96	1.61	1.71	1.97	1.98	1.93	1.98	1.93	1.98	1.98	1.98
Ti	bdl	bdl	0.01	bdl	bdl	bdl	bdl	bdl	bdl	bdl	bdl	bdl	bdl	bdl	bdl	bdl	bdl
Al	0.06	0.07	0.10	0.04	0.04	0.08	0.05	0.60	0.43	0.04	0.03	0.09	0.03	0.09	0.03	0.03	0.03
Fe^{3+}	0.02	0.02	0.01	bdl	0.01	0.03	0.02	0.17	0.14	0.02	0.01	0.03	0.01	0.04	0.01	bdl	0.01
Cr^{3+}	0.01	0.01	0.01	0.01	bdl	0.01	0.01	bdl	bdl	bdl	bdl	bdl	bdl	bdl	bdl	bdl	bdl
Fe^{2+}	0.37	0.38	0.29	0.21	0.07	0.06	0.06	0.03	0.04	0.02	0.04	0.04	0.03	0.04	0.04	0.04	0.05
Mn	0.01	0.01	0.01	0.01	bdl	0.01	0.01	bdl	0.01	0.01	0.01	0.01	0.01	0.01	0.01	bdl	0.01
Mg	1.50	1.49	0.89	0.84	0.94	0.92	0.95	0.58	0.69	0.96	0.95	0.91	0.95	0.89	0.95	0.96	0.95
Ca	0.07	0.07	0.72	0.88	0.96	0.94	0.93	0.99	0.98	0.98	0.98	0.97	0.98	0.99	0.99	0.98	0.97
Na	bdl	bdl	0.03	0.02	bdl	0.01	0.01	bdl	bdl	bdl	bdl	bdl	bdl	bdl	bdl	bdl	bdl
Total	**4.00**	**4.00**	**4.00**	**4.00**	**4.00**	**4.00**	**4.00**	**4.00**	**4.00**	**4.00**	**4.00**	**4.00**	**4.00**	**4.00**	**4.00**	**4.00**	**4.00**
Wo	**3**	**4**	**38**	**46**	**49**	**49**	**48**	**62**	**57**	**50**	**50**	**50**	**50**	**51**	**50**	**49**	**49**
En	**77**	**77**	**47**	**44**	**48**	**48**	**49**	**36**	**40**	**49**	**48**	**47**	**48**	**46**	**48**	**49**	**48**
Fs	**19**	**20**	**15**	**11**	**3**	**3**	**3**	**2**	**2**	**1**	**2**	**2**	**2**	**2**	**2**	**2**	**3**
Total	**100**	**100**	**100**	**100**	**100**	**100**	**100**	**100**	**100**	**100**	**100**	**100**	**100**	**100**	**100**	**100**	**100**

PYROXENE

Sample	C435-2 (JEOL)								A291-1(JEOL)									
Analysis #	**195**	**196**	**197**	**198**	**211**	**212**	**213**	**214**	**215**	**216**	**217**	**218**	**219**	**220**	**221**	**222**	**223**	**224**
SiO_2	48.14	48.62	47.34	48.96	47.60	47.56	48.04	48.01	54.47	53.28	54.67	47.53	52.31	52.92	55.06	54.89	54.32	54.29
TiO_2	0.08	0.13	0.24	0.20	0.21	0.22	0.15	0.16	0.74	0.55	0.31	0.88	0.24	0.41	0.07	0.03	0.07	0.27
Al_2O_3	6.15	6.52	7.10	5.78	7.42	6.84	7.33	7.30	1.29	2.06	1.13	8.22	4.31	2.07	1.46	1.42	1.51	1.54
Cr_2O_3	0.04	0.01	0.02	0.08	0.03	0.02	0.05	0.07	0.22	0.31	0.19	0.43	0.25	0.55	0.39	0.39	0.40	0.37
FeO	5.37	4.48	5.12	4.80	5.71	5.23	5.27	5.36	13.95	10.10	13.55	6.88	5.53	8.23	10.98	12.77	12.09	12.83
MnO	0.07	0.04	0.01	0.07	0.03	0.07	0.05	0.05	0.28	0.20	0.27	0.13	0.08	0.22	0.22	0.24	0.23	0.29
MgO	14.21	14.23	14.00	14.75	13.64	13.60	13.92	13.67	28.34	22.98	28.54	17.78	20.32	20.13	28.48	29.77	28.35	27.46
CaO	24.76	24.62	24.59	24.91	24.72	24.49	24.69	24.64	1.25	10.49	1.10	11.70	12.11	15.13	3.30	0.79	2.72	2.80
Na_2O	0.04	0.05	0.02	0.01	0.03	0.01	0.01	0.01	0.01	0.15	0.01	1.74	0.94	0.24	0.08	bdl	0.06	0.02
Total	98.86	98.68	98.44	99.56	99.38	98.03	99.51	99.27	100.54	100.10	99.76	95.29	96.09	99.90	100.02	100.29	99.72	99.86
									Number of ions based on 6 Oxygens									
Si	1.79	1.80	1.76	1.80	1.76	1.78	1.77	1.78	1.94	1.92	1.96	1.79	1.95	1.93	1.96	1.94	1.94	1.95
Ti	bdl	bdl	0.01	0.01	0.01	0.01	bdl	bdl	0.02	0.01	0.01	0.02	0.01	0.01	bdl	bdl	bdl	0.01
Al	0.27	0.28	0.31	0.25	0.32	0.30	0.32	0.32	0.05	0.09	0.05	0.36	0.19	0.09	0.06	0.06	0.06	0.06
Fe^{3+}	0.16	0.11	0.15	0.13	0.15	0.12	0.13	0.12	0.02	0.04	0.01	0.13	bdl	0.04	0.02	0.04	0.05	0.02
Cr^{3+}	bdl	bdl	bdl	bdl	bdl	bdl	bdl	bdl	0.01	0.01	0.01	0.01	0.01	0.02	0.01	0.01	0.01	0.01
Fe^{2+}	0.01	0.03	0.01	0.01	0.03	0.04	0.03	0.05	0.40	0.27	0.39	0.09	0.17	0.22	0.31	0.34	0.31	0.37
Mn	bdl	bdl	bdl	bdl	bdl	bdl	bdl	bdl	0.01	0.01	0.01	bdl	bdl	0.01	0.01	0.01	0.01	0.01
Mg	0.79	0.79	0.78	0.81	0.75	0.76	0.77	0.75	1.51	1.24	1.52	1.00	1.13	1.09	1.51	1.57	1.51	1.47
Ca	0.98	0.98	0.98	0.98	0.98	0.98	0.98	0.98	0.05	0.41	0.04	0.47	0.48	0.59	0.13	0.03	0.10	0.11
Na	bdl	bdl	bdl	bdl	bdl	bdl	bdl	bdl	bdl	0.01	bdl	0.13	0.07	0.02	0.01	bdl	bdl	bdl
Total	**4.00**	**4.00**	**4.00**	**4.00**	**4.00**	**4.00**	**4.00**	**4.00**	**4.00**	**4.00**	**4.00**	**4.00**	**4.00**	**4.00**	**4.00**	**4.00**	**4.00**	**4.00**
Wo	**55**	**54**	**56**	**54**	**56**	**55**	**55**	**55**	**2**	**21**	**2**	**30**	**27**	**31**	**6**	**2**	**5**	**6**
En	**44**	**44**	**44**	**45**	**43**	**43**	**43**	**42**	**77**	**65**	**78**	**64**	**63**	**58**	**78**	**81**	**78**	**76**
Fs	**1**	**2**	**0**	**1**	**2**	**2**	**2**	**3**	**20**	**14**	**20**	**6**	**10**	**11**	**16**	**17**	**16**	**19**
Total	**100**	**100**	**100**	**100**	**100**	**100**	**100**	**100**	**100**	**100**	**100**	**100**	**100**	**100**	**100**	**100**	**100**	**100**

SPINEL													
Sample	**A156-7 (JEOL)**												
Analysis #	**92**	**93**	**94**	**95**	**96**	**97**	**98**	**99**	**100**	**101**	**102**	**103**	**104**
SiO_2	0.04	0.03	bdl	0.02	0.03	0.03	0.03	0.05	0.04	0.04	0.05	0.24	0.03
TiO_2	0.01	bdl	0.01	0.03	0.03	0.13	0.12	0.07	0.22	0.07	0.08	0.06	0.01
Al_2O_3	61.25	61.21	61.80	61.37	61.67	60.24	60.36	60.42	60.02	60.76	61.87	61.74	61.99
Cr_2O_3	bdl	0.02	0.01	0.06	0.04	0.07	bdl	0.03	0.11	0.05	0.04	0.05	0.03
V_2O_3	bdl	bdl	bdl	bdl	bdl	bdl	bdl	bdl	0.01	bdl	bdl	bdl	bdl
Fe_2O_3	8.32	8.17	6.85	7.89	7.40	8.67	8.41	8.09	8.60	7.00	7.38	7.94	7.12
FeO	3.94	4.05	4.49	4.30	3.99	4.72	4.61	4.68	4.81	5.36	4.42	3.35	4.22
MnO	0.66	0.74	0.70	0.66	0.68	0.75	0.71	0.74	0.79	0.77	0.66	0.71	0.72
MgO	23.77	23.60	23.26	23.55	23.70	23.12	23.14	23.04	23.06	22.43	23.62	24.49	23.58
CaO	0.02	0.02	bdl	bdl	bdl	bdl	bdl	bdl	bdl	0.05	0.01	0.04	bdl
NiO	0.03	bdl	bdl	bdl	0.01	bdl	0.03	bdl	bdl	0.04	bdl	bdl	0.01
Total	**98.02**	**97.84**	**97.13**	**97.88**	**97.55**	**97.73**	**97.40**	**97.12**	**97.65**	**96.56**	**98.13**	**98.62**	**97.69**
						Number of ions based on 4 Oxygens							
Si	bdl	bdl	bdl	bdl	bdl	bdl	bdl	bdl	bdl	bdl	bdl	0.01	bdl
Ti	bdl	bdl	bdl	bdl	bdl	bdl	bdl	bdl	bdl	bdl	bdl	bdl	bdl
Al	1.84	1.84	1.87	1.85	1.85	1.82	1.83	1.84	1.82	1.86	1.85	1.83	1.86
Cr	bdl	bdl	bdl	bdl	bdl	bdl	bdl	bdl	bdl	bdl	bdl	bdl	bdl
V^{3+}	bdl	bdl	bdl	bdl	bdl	bdl	bdl	bdl	bdl	bdl	bdl	bdl	bdl
Fe^{3+}	0.16	0.16	0.13	0.15	0.14	0.17	0.16	0.16	0.17	0.14	0.14	0.15	0.14
Fe^{2+}	0.08	0.09	0.10	0.09	0.09	0.10	0.10	0.10	0.10	0.12	0.09	0.07	0.09
Mn	0.01	0.02	0.02	0.01	0.01	0.02	0.02	0.02	0.02	0.02	0.01	0.02	0.02
Mg	0.90	0.90	0.89	0.90	0.90	0.89	0.89	0.89	0.88	0.87	0.89	0.92	0.90
Ca	bdl	bdl	bdl	bdl	bdl	bdl	bdl	bdl	bdl	bdl	bdl	bdl	bdl
Ni	bdl	bdl	bdl	bdl	bdl	bdl	bdl	bdl	bdl	bdl	bdl	bdl	bdl
Total	**3.00**	**3.00**	**3.00**	**3.00**	**3.00**	**3.00**	**3.00**	**3.00**	**3.00**	**3.00**	**3.00**	**3.00**	**3.00**

Appendix 5: LA-ICP-MS analyses for spinel from the Marikana sample suite and spinel standards

Sample-analysis#	P	Sc	V	Cr	Mn	Co	Ni	Cu	Zn	Ga	Ge	Y	Zr	Nb	Sn	Hf	Ta	W	Pb
BC28_1	60.8	19.3	8840.00	1224.00	820.00	80.00	220.00	bdl	300.00	23.00	bdl	bdl	5.7	0.73	0.25	0.12	0.038	bdl	bdl
BC28_2	42.8	19.9	8510.00	1130.00	820.00	123.00	280.00	bdl	310.00	26.00	bdl	bdl	6.5	0.66	0.58	0.30	0.051	bdl	bdl
BC28_3	44.9	20.4	9030.00	1158.00	810.00	96.00	290.00	bdl	310.00	29.00	bdl	bdl	5.4	0.61	0.70	0.32	0.034	bdl	bdl
BC28_4	64.7	24.4	10080.00	1326.00	1250.00	122.00	400.00	3.6	510.00	41.00	bdl	bdl	10.3	0.96	1.51	0.24	0.101	bdl	0.59
BC28_5	61.00	23.7	10870.00	1393.00	1330.00	193.00	410.00	bdl	330.00	40.00	bdl	bdl	5.1	1.11	1.33	0.30	0.101	bdl	bdl
BIR1_1	98.6	42.92	332.70	353.80	1127.00	56.20	188.70	127.20	85.20	15.25	1.22	14.04	13.05	0.507	0.96	0.577	0.034	blod	3.60
BIR1_2	75.2	42.81	330.30	334.50	1064.00	54.90	185.60	124.10	82.50	14.35	1.75	13.60	13.02	0.491	0.86	0.509	0.0300	blod	3.66
BIR1_3	73.2	42.94	336.30	341.00	1042.00	55.80	188.04	126.10	86.80	14.57	1.71	13.68	13.23	0.491	1.00	0.600	0.029	blod	3.81
BIR1_4	81.4	43.12	327.30	331.00	1011.00	53.47	181.20	123.20	85.00	14.95	1.45	14.01	13.01	0.480	0.82	0.521	0.0252	0.037	3.62
BIR1_5	90.8	43.05	330.50	352.80	1038.00	53.98	182.50	130.20	85.90	15.35	1.57	14.02	13.09	0.488	0.94	0.494	0.035	blod	3.74
G_NIST612_1	49.7	40.80	38.74	36.0	36.4	35.0	38.3	37.0	36.2	36.0	35.1	38.0	37.8	40.0	38.2	35.19	39.94	40.00	38.7
G_NIST612_2	50.5	41.18	39.0	35.9	39.1	35.6	40.0	37.0	38.2	36.0	35.0	38.0	38.8	40.2	38.3	35.5	40.6	40.1	38.1
G_NIST612_3	53.5	41.35	39.45	36.5	37.9	35.0	38.7	37.3	37.3	36.1	35.1	38.1	38.4	39.9	37.7	34.46	39.62	39.7	38.7
G_NIST612_4	52.7	41.4	39.1	35.3	39.2	34.0	38.1	36.7	39.6	35.5	34.4	37.9	37.0	40.0	37.2	34.6	40.3	40.1	38.4
G_NIST612_5	48.4	40.41	38.62	36.2	37.5	34.9	38.5	37.0	39.8	36.0	35.3	37.99	37.5	39.97	37.9	35.2	39.9	40.0	38.7
G_NIST612_6	61.0	41.07	39.5	36.4	38.4	35.0	40.3	37.2	37.6	36.4	36.4	38.1	39.2	40.4	38.5	35.2	40.02	40.1	38.7
G_NIST612_7	47.5	41.29	39.29	35.6	38.8	34.9	38.1	36.9	37.3	36.2	34.1	37.8	37.9	39.7	38.0	34.0	39.9	40.0	38.3
G_NIST612_8	59.6	40.90	39.2	36.5	38.1	34.6	38.2	37.1	39.0	37.3	35.6	38.0	38.9	40.0	39.1	35.2	40.0	40.4	39.7
G_NIST612_9	47.6	41.0	39.2	35.6	37.8	35.1	40.1	36.5	38.1	34.0	31.9	38.1	38.1	40.2	35.9	34.9	39.8	39.0	37.4
G_NIST612_10	54.4	40.79	38.71	37.1	37.1	34.6	37.4	37.4	39.3	37.1	34.6	37.5	36.1	39.8	37.9	34.9	39.9	40.3	39.7
G_NIST612_11	44.3	41.33	38.75	35.6	36.8	36.5	39.5	36.5	37.4	36.3	35.3	38.09	38.5	40.0	39.0	35.2	40.1	40.6	38.3
G_NIST612_12	52.6	40.96	39.98	36.3	38.7	35.4	40.5	37.4	38.0	36.4	35.9	38.05	38.5	40.08	39.3	36.0	40.9	40.2	38.9
G_NIST612_13	54.0	40.3	38.49	36.0	37.6	33.6	38.1	36.6	37.2	35.2	34.9	37.9	37.0	39.8	37.4	34.5	39.4	39.8	38.2

Main xenolith body (RSTX26-12)

Sample-analysis#	P	Sc	V	Cr	Mn	Co	Ni	Cu	Zn	Ga	Ge	Y	Zr	Nb	Sn	Hf	Ta	W	Pb
RSTX26-12 - 1	96.60	16.50	96.30	190.30	3650.00	61.90	199.10	bdl	591.00	73.40	bdl	bdl	4.80	bdl	3.03	0.25	bdl	bdl	0.09
RSTX26-12 - 2	bdl	1.60	22.00	bdl	900.00	bdl	34.00	bdl	170.00	20.00	bdl	bdl	bdl	bdl	bdl	bdl	bdl	bdl	bdl
RSTX26-12 - 3	bdl	3.80	32.00	30.00	1400.00	bdl	68.00	bdl	290.00	32.00	bdl	bdl	bdl	bdl	bdl	bdl	bdl	bdl	bdl
RSTX26-12 - 4	20.50	49.10	106.80	77.20	1100.00	bdl	19.00	bdl	16.00	2.20	bdl	bdl	3.00	bdl	1.10	0.53	bdl	bdl	0.00
RSTX26-12 - 5	bdl	11.20	64.00	127.00	2690.00	31.00	134.00	bdl	480.00	54.00	bdl	bdl	bdl	bdl	1.72	0.14	bdl	bdl	0.01
RSTX26-12 - 6	87.60	22.31	110.00	244.00	4450.00	65.50	202.10	bdl	563.00	65.10	bdl	bdl	3.03	bdl	3.57	0.49	bdl	bdl	bdl
RSTX26-12 - 7	7.37	5.32	13.46	20.40	572.00	6.31	18.60	bdl	50.10	5.06	bdl	bdl	3.48	bdl	0.51	0.28	bdl	bdl	bdl
RSTX26-12 - 8	76.80	25.60	119.20	225.00	4480.00	64.10	190.00	bdl	520.00	59.90	bdl	bdl	4.08	bdl	3.63	0.83	bdl	bdl	bdl
RSTX26-12 - 9	6.26	2.49	9.05	17.49	354.00	5.02	14.67	bdl	42.50	4.70	bdl	bdl	1.46	bdl	0.25	0.12	bdl	bdl	bdl
RSTX26-12 - 10	75.00	25.00	116.80	256.00	4350.00	58.30	187.00	bdl	542.00	64.90	bdl	bdl	4.90	bdl	4.40	0.87	bdl	bdl	bdl
RSTX26-12 - 11	78.40	23.74	109.70	254.10	4150.00	59.50	190.00	bdl	559.00	64.70	bdl	bdl	7.50	bdl	3.37	1.02	bdl	bdl	0.10
RSTX26-12 - 12	5.44	1.42	8.40	17.33	300.00	4.77	14.26	bdl	43.20	4.83	bdl	bdl	0.17	bdl	0.23	0.04	bdl	bdl	bdl
RSTX26-12 - 13	5.32	1.28	8.76	16.51	296.00	4.95	14.60	bdl	43.00	4.96	bdl	bdl	0.38	bdl	0.26	0.03	bdl	bdl	bdl
RSTX26-12 - 14	34.60	79.20	182.30	118.30	5000.00	33.00	129.00	bdl	85.00	12.40	bdl	bdl	42.00	bdl	8.70	4.80	bdl	bdl	bdl
RSTX26-12 - 15	33.70	72.70	161.80	86.60	4100.00	24.00	97.00	bdl	70.00	9.10	bdl	bdl	65.00	0.06	6.70	5.60	0.02	bdl	bdl
RSTX26-12 - 16	11.84	18.90	44.40	39.40	1710.00	15.54	46.90	bdl	63.60	7.13	bdl	bdl	18.60	0.01	2.44	1.87	0.01	bdl	bdl
RSTX26-12 - 17	87.50	15.70	93.30	202.90	3470.00	52.80	175.80	bdl	540.00	66.20	bdl	bdl	4.08	bdl	2.47	0.31	bdl	bdl	0.30
RSTX26-12 - 18	73.90	15.87	95.90	198.10	3580.00	57.10	175.80	bdl	533.00	63.20	bdl	bdl	2.33	bdl	2.55	0.39	bdl	bdl	bdl
RSTX26-12 - 19	67.00	17.68	90.00	190.20	3520.00	55.90	171.10	bdl	517.00	61.70	bdl	bdl	2.52	bdl	1.92	0.39	bdl	bdl	bdl
RSTX26-12 - 20	71.40	22.50	89.90	189.70	3550.00	56.30	160.20	bdl	577.00	61.00	bdl	bdl	10.70	bdl	1.90	0.95	bdl	bdl	0.05
RSTX26-12 - 21	28.00	61.70	186.00	106.30	5170.00	43.80	130.90	bdl	110.90	14.12	bdl	bdl	37.70	0.08	8.61	4.08	0.01	bdl	0.05
RSTX26-12 - 22	bdl	9.80	75.00	135.00	2420.00	29.00	121.00	bdl	460.00	50.00	bdl	bdl	bdl	bdl	1.05	0.18	bdl	bdl	bdl
RSTX26-12 - 23	bdl	10.20	71.00	142.00	2630.00	29.00	124.00	bdl	450.00	51.00	bdl	bdl	bdl	bdl	1.05	0.19	bdl	bdl	bdl
RSTX26-12 - 24	5.29	1.97	8.50	15.17	263.00	4.73	12.30	bdl	43.60	4.81	bdl	bdl	1.32	bdl	0.29	0.09	0.00	bdl	bdl
RSTX26-12 - 25	113.00	159.00	475.00	352.00	14800.00	145.00	457.00	bdl	762.00	89.00	bdl	bdl	182.00	bdl	19.80	10.70	0.05	bdl	0.05
RSTX26-12 - 26	bdl	7.40	61.00	120.00	2210.00	28.00	115.00	bdl	430.00	50.00	bdl	bdl	bdl	bdl	0.88	bdl	bdl	bdl	0.05
RSTX26-12 - 27	27.40	81.80	194.30	145.80	900.00	bdl	15.00	bdl	6.00	1.60	bdl	bdl	3.00	bdl	1.40	0.53	bdl	bdl	0.02
RSTX26-12 - 28	63.20	10.60	67.30	273.20	2740.00	48.90	144.80	bdl	565.00	61.60	bdl	bdl	bdl	bdl	1.00	0.15	bdl	bdl	0.13
RSTX26-12 - 29	bdl	7.80	52.00	128.00	2070.00	14.00	109.00	bdl	410.00	45.00	bdl	bdl	bdl	bdl	0.83	bdl	bdl	bdl	bdl
RSTX26-12 - 30																			

Pegmatoidal band (RSTX26-04)

Sample-analysis#	P	Sc	V	Cr	Mn	Co	Ni	Cu	Zn	Ga	Ge	Y	Zr	Nb	Sn	Hf	Ta	W	Pb
RSTX26-04 - 1	bdl	0.25	2.10	43.00	26.00	bdl	4.60	bdl	5.20	0.73	bdl	bdl	bdl	bdl	bdl	bdl	bdl	bdl	bdl
RSTX26-04 - 2	bdl	0.06	1.00	31.00	7.00	bdl	1.90	bdl	2.30	0.31	bdl	bdl	bdl	bdl	bdl	bdl	bdl	bdl	bdl
RSTX26-04 - 3	bdl	1.23	5.10	129.00	93.00	1.20	14.80	bdl	12.90	1.86	bdl	bdl	bdl	bdl	0.02	0.01	bdl	bdl	bdl
RSTX26-04 - 4	bdl	1.59	6.00	27.00	106.00	1.60	17.00	bdl	16.40	1.89	bdl	bdl	0.21	bdl	0.02	0.02	bdl	bdl	0.01
RSTX26-04 - 5	2.69	3.10	9.60	37.70	165.00	3.88	23.50	bdl	22.06	2.59	bdl	bdl	0.48	bdl	0.06	0.03	bdl	bdl	0.02
RSTX26-04 - 6	bdl	0.25	1.90	9.00	29.00	bdl	6.10	bdl	6.70	0.80	bdl	bdl	bdl	bdl	bdl	bdl	bdl	bdl	bdl
RSTX26-04 - 7	bdl	bdl	bdl	bdl	bdl	bdl	bdl	bdl	bdl	bdl	bdl	bdl	bdl	bdl	bdl	bdl	bdl	bdl	bdl
RSTX26-04 - 8 2	bdl	bdl	bdl	bdl	bdl	bdl	bdl	bdl	bdl	bdl	bdl	bdl	bdl	bdl	bdl	bdl	bdl	bdl	bdl
RSTX26-04 - 9	bdl	bdl	1.30	7.00	4.00	bdl	1.00	bdl	2.00	0.35	bdl	bdl	bdl	bdl	bdl	bdl	bdl	bdl	bdl
RSTX26-04 - 10	bdl	0.09	1.60	11.00	14.00	bdl	2.50	bdl	3.70	0.53	bdl	bdl	bdl	bdl	bdl	bdl	bdl	bdl	bdl
RSTX26-04 - 11	bdl	0.06	0.80	4.00	6.00	bdl	1.40	bdl	2.10	0.32	bdl	bdl	bdl	bdl	bdl	bdl	bdl	bdl	bdl
RSTX26-04 - 12	bdl	0.88	4.10	21.00	60.00	bdl	8.70	bdl	10.10	1.27	bdl	bdl	bdl	bdl	bdl	0.01	bdl	bdl	bdl
RSTX26-04 - 13	bdl	0.99	5.00	21.00	83.00	0.70	12.60	bdl	12.80	1.66	bdl	bdl	bdl	bdl	bdl	0.01	bdl	bdl	bdl
RSTX26-04 - 15	bdl	bdl	bdl	bdl	bdl	bdl	bdl	bdl	bdl	bdl	bdl	bdl	bdl	bdl	bdl	bdl	bdl	bdl	bdl
RSTX26-04 - 16	bdl	bdl	0.54	bdl	2.00	bdl	0.50	bdl	2.20	0.32	bdl	bdl	bdl	bdl	bdl	bdl	bdl	bdl	bdl
RSTX26-04 - 17	bdl	0.31	1.70	25.00	30.00	bdl	4.40	bdl	5.10	0.71	bdl	bdl	bdl	bdl	bdl	bdl	bdl	bdl	bdl
RSTX26-04 - 18	bdl	0.35	1.80	16.00	28.00	bdl	4.30	bdl	5.40	0.78	bdl	bdl	bdl	bdl	bdl	bdl	bdl	bdl	bdl
RSTX26-04 - 19	bdl	0.86	4.00	24.00	67.00	bdl	9.90	bdl	10.10	1.42	bdl	bdl	bdl	bdl	bdl	0.01	bdl	bdl	bdl
RSTX26-04 - 20	bdl	0.85	3.70	610.00	79.00	0.80	9.70	bdl	11.90	1.46	bdl	bdl	bdl	bdl	bdl	0.01	bdl	bdl	bdl
RSTX26-04 - 21	bdl	0.56	2.60	250.00	46.00	bdl	6.30	bdl	7.20	0.91	bdl	bdl	bdl	bdl	bdl	bdl	bdl	bdl	bdl
RSTX26-04 - 22	bdl	0.86	3.80	39.00	63.00	bdl	9.60	bdl	10.50	1.38	bdl	bdl	bdl	bdl	bdl	0.01	bdl	bdl	bdl
RSTX26-04 - 23	bdl	0.80	3.80	61.00	66.00	bdl	9.70	bdl	10.70	1.40	bdl	bdl	bdl	bdl	bdl	bdl	bdl	bdl	bdl
RSTX26-04 - 24	bdl	1.49	5.50	255.00	99.00	1.60	15.10	bdl	13.40	1.73	bdl	bdl	0.03	bdl	0.03	0.02	bdl	bdl	bdl
RSTX26-04 - 25	2.88	2.03	7.82	294.60	142.50	3.86	21.17	bdl	18.72	2.39	bdl	bdl	0.13	bdl	0.05	0.03	bdl	bdl	0.00
RSTX26-04 - 26	bdl	1.55	6.70	144.00	113.00	2.40	17.60	bdl	15.90	1.96	bdl	bdl	bdl	bdl	0.04	0.01	bdl	bdl	0.00
RSTX26-04 - 27	bdl	1.94	7.50	161.00	123.00	2.40	18.00	bdl	15.80	2.01	bdl	bdl	0.07	bdl	0.05	0.01	bdl	bdl	bdl
RSTX26-04 - 28	bdl	1.69	7.40	157.00	122.00	2.60	19.50	bdl	16.30	2.09	bdl	bdl	bdl	bdl	0.04	0.01	bdl	bdl	0.00

Spinel layer (RSTX26-06)

Sample-analysis#	P	Sc	V	Cr	Mn	Co	Ni	Cu	Zn	Ga	Ge	Y	Zr	Nb	Sn	Hf	Ta	W	Pb
RSTX26_06 - 1	10.78	1.72	8.87	1104.00	357.00	5.30	11.41	bdl	67.30	7.86	bdl	bdl	0.55	bdl	0.11	bdl	bdl	bdl	bdl
RSTX26_06 - 2	10.20	1.90	8.75	268.90	306.40	4.91	7.39	bdl	77.20	6.39	0.15	0.16	47.00	0.02	0.12	bdl	bdl	bdl	bdl
RSTX26_06 - 3	38.00	71.60	172.10	1550.00	5850.00	43.70	74.00	bdl	137.60	14.90	bdl	0.07	146.00	0.29	4.70	bdl	0.10	bdl	bdl
RSTX26_06 - 4	14.86	16.50	36.60	464.00	1190.00	10.90	17.40	bdl	101.60	7.05	bdl	0.11	42.00	0.08	0.97	bdl	0.02	bdl	bdl
RSTX26_06 - 5	46.30	85.90	208.80	1790.00	6680.00	63.00	118.00	bdl	150.80	17.18	bdl	0.07	146.00	0.31	5.61	bdl	0.13	bdl	bdl
RSTX26_06 - 6	37.40	70.10	170.40	1670.00	5540.00	42.80	81.10	bdl	145.50	16.40	bdl	bdl	135.30	0.26	5.54	bdl	0.11	bdl	bdl
RSTX26_06 - 7	23.50	37.90	88.00	1066.00	2810.00	23.00	37.40	bdl	136.50	12.13	bdl	0.07	93.00	0.17	2.36	bdl	0.07	bdl	bdl
RSTX26_06 - 8	107.50	48.90	139.00	7300.00	5470.00	62.60	127.70	bdl	719.00	71.30	bdl	0.15	61.90	bdl	3.47	bdl	0.05	bdl	bdl
RSTX26_06 - 9	99.00	67.10	175.00	7660.00	6530.00	65.40	140.10	bdl	658.00	66.80	1.20	0.16	83.50	0.08	5.50	bdl	0.05	bdl	bdl
RSTX26_06 - 10	99.30	47.00	138.00	6910.00	5760.00	60.40	130.00	bdl	703.00	69.00	bdl	bdl	61.00	0.06	3.65	bdl	0.04	bdl	bdl
RSTX26_06 - 11	92.10	50.50	161.20	7980.00	6170.00	60.50	144.90	bdl	606.00	68.70	bdl	bdl	40.10	bdl	4.34	bdl	0.02	bdl	bdl
RSTX26_06 - 12	100.90	45.50	161.00	9020.00	5740.00	66.20	139.20	bdl	576.00	68.30	bdl	0.19	36.00	bdl	4.16	bdl	bdl	bdl	bdl
RSTX26_06 - 13	491.00	114.00	100.00	10550.00	18000.00	132.70	357.00	bdl	822.00	73.70	5.60	6.06	18.70	bdl	2.28	bdl	bdl	bdl	bdl
RSTX26_06 - 14	69.30	26.34	175.40	11020.00	3571.00	47.00	108.70	bdl	465.00	59.20	bdl	bdl	23.20	0.05	4.19	bdl	bdl	bdl	bdl
RSTX26_06 - 15	79.50	26.58	175.10	10860.00	3562.00	45.20	101.30	bdl	471.00	60.20	bdl	bdl	23.30	0.06	4.10	bdl	bdl	bdl	bdl
RSTX26_06 - 16	93.00	32.30	125.20	9490.00	3980.00	51.40	120.00	bdl	484.00	62.90	bdl	bdl	24.10	bdl	3.97	bdl	bdl	bdl	bdl
RSTX26_06 - 17	87.90	29.80	123.50	9190.00	4010.00	49.50	134.90	bdl	476.00	62.70	bdl	bdl	12.90	bdl	3.86	bdl	bdl	bdl	bdl
RSTX26_06 - 18	84.30	35.40	111.30	10600.00	3830.00	43.70	110.70	bdl	507.00	60.00	1.16	0.19	37.20	bdl	3.32	bdl	bdl	bdl	bdl
RSTX26_06 - 19	12.10	5.68	18.05	1526.00	610.00	6.62	18.20	bdl	64.90	8.23	bdl	bdl	5.94	0.01	0.50	bdl	bdl	bdl	bdl
RSTX26_06 - 20	74.00	35.20	113.40	10240.00	3870.00	47.20	119.40	bdl	510.00	62.80	bdl	bdl	35.60	0.06	2.77	bdl	bdl	bdl	bdl
RSTX26_06 - 21	70.10	30.43	106.10	12820.00	3730.00	46.30	118.90	bdl	458.00	57.10	bdl	bdl	16.60	bdl	2.73	bdl	bdl	bdl	bdl
RSTX26_06 - 22	bdl	4.34	16.10	1237.00	542.00	6.52	17.58	bdl	61.30	7.61	bdl	bdl	1.89	bdl	0.43	bdl	bdl	bdl	bdl
RSTX26_06 - 23	78.70	55.40	148.00	13600.00	5230.00	59.90	141.00	bdl	549.00	64.30	bdl	0.23	82.00	bdl	4.24	bdl	0.05	bdl	bdl
RSTX26_06 - 24	70.10	48.80	138.00	12890.00	4870.00	55.00	136.40	bdl	527.00	61.50	bdl	0.22	59.20	bdl	4.03	bdl	0.03	bdl	bdl
RSTX26_06 - 25	76.60	27.70	111.00	10840.00	3710.00	44.40	126.80	bdl	508.00	64.70	bdl	bdl	23.80	bdl	3.26	bdl	bdl	bdl	bdl
RSTX26_06 - 26	64.20	14.60	96.40	7400.00	2713.00	43.90	104.30	bdl	527.00	61.20	1.15	bdl	bdl	bdl	1.59	bdl	bdl	bdl	bdl
RSTX26_06 - 27	69.80	13.63	98.10	7810.00	2694.00	44.00	109.00	bdl	550.00	61.70	bdl	bdl	bdl	bdl	1.62	bdl	bdl	bdl	bdl
RSTX26_06 - 28	71.70	9.37	71.60	7740.00	2310.00	40.60	98.20	bdl	524.00	60.00	bdl	bdl	4.10	bdl	1.24	bdl	0.03	bdl	bdl
RSTX26_06 - 29	141.00	281.00	640.00	18900.00	17800.00	162.00	315.00	bdl	770.00	89.20	bdl	bdl	115.00	bdl	18.80	bdl	bdl	bdl	bdl

Sample-analysis#	P	Sc	V	Cr	Mn	Co	Ni	Cu	Zn	Ga	Ge	Y	Zr	Nb	Sn	Hf	Ta	W	Pb
RSTX26_06 - 31	71.10	23.57	219.70	13370.00	2950.00	55.30	214.00	bdl	531.00	68.70	bdl	bdl	bdl	bdl	1.99	bdl	bdl	bdl	bdl
RSTX26_06 - 32	bdl	20.04	155.40	8670.00	2578.00	48.10	130.40	bdl	561.00	63.30	bdl	0.30	bdl	bdl	1.51	bdl	bdl	bdl	bdl
RSTX26_06 - 33	bdl	20.88	178.90	8680.00	2638.00	47.50	137.70	bdl	490.00	61.60	bdl	bdl	bdl	bdl	2.38	bdl	bdl	bdl	bdl
RSTX26_06 - 34	14.60	26.10	54.80	3400.00	1860.00	16.86	42.40	bdl	93.50	10.61	0.25	0.05	34.90	0.03	1.83	bdl	0.01	bdl	bdl
RSTX26_06 - 35	76.20	60.00	155.20	14670.00	5270.00	61.10	146.40	bdl	538.00	63.00	bdl	0.22	76.50	0.07	5.17	bdl	bdl	bdl	bdl
RSTX26_06 - 36	78.80	64.20	162.00	15670.00	5220.00	64.50	157.20	bdl	606.00	67.50	bdl	bdl	66.20	0.10	4.84	bdl	bdl	bdl	bdl
RSTX26_06 - 37	10.09	4.05	13.40	1730.00	447.00	5.66	14.29	bdl	68.70	7.79	bdl	bdl	3.70	0.01	0.39	bdl	bdl	bdl	bdl
RSTX26_06 - 38	76.00	29.30	120.30	13550.00	3819.00	52.40	143.50	bdl	473.80	61.20	bdl	bdl	10.00	bdl	3.57	bdl	bdl	bdl	bdl
RSTX26_06 - 39	10.59	4.53	15.10	2010.00	498.00	6.66	15.70	bdl	71.70	8.26	bdl	0.03	4.66	0.01	0.40	bdl	bdl	bdl	bdl
Fragment (RSTX26-52)																			
RSTX26-52 - 1	34.70	bdl	317.60	58900.00	1452.00	171.40	981.00	bdl	395.00	26.90	bdl	bdl	bdl	0.08	bdl	bdl	bdl	bdl	bdl
RSTX26-52 - 2	bdl	bdl	290.00	51000.00	1210.00	150.00	1000.00	bdl	350.00	25.00	bdl	bdl	bdl	0.06	bdl	bdl	bdl	bdl	bdl
RSTX26-52 - 3	bdl	bdl	240.00	40000.00	1020.00	121.00	980.00	bdl	350.00	26.00	bdl	bdl	bdl	bdl	bdl	bdl	bdl	bdl	bdl
RSTX26-52 - 4	bdl	bdl	243.00	50000.00	1010.00	120.00	770.00	bdl	300.00	21.60	bdl	bdl	bdl	0.04	bdl	bdl	bdl	bdl	bdl
RSTX26-52 - 5	bdl	bdl	131.00	23000.00	550.00	61.00	510.00	bdl	200.00	15.00	bdl	bdl	bdl	0.03	bdl	bdl	bdl	bdl	0.02
RSTX26-52 - 6	bdl	bdl	270.00	30000.00	690.00	72.00	590.00	bdl	230.00	16.00	bdl	bdl	bdl	0.02	bdl	bdl	bdl	bdl	bdl
RSTX26-52 - 7	bdl	bdl	200.00	40000.00	920.00	103.00	660.00	bdl	270.00	19.50	bdl	bdl	bdl	bdl	bdl	bdl	bdl	bdl	bdl
RSTX26-52 - 8	bdl	bdl	85.00	14000.00	260.00	17.00	430.00	bdl	130.00	11.00	bdl	bdl	bdl	bdl	bdl	bdl	bdl	bdl	bdl
RSTX26-52 - 9	bdl	bdl	202.00	35000.00	880.00	107.00	800.00	bdl	310.00	22.00	bdl	bdl	bdl	0.04	bdl	bdl	bdl	bdl	bdl
RSTX26-52 - 10	bdl	bdl	304.00	60000.00	1600.00	169.00	1080.00	bdl	420.00	27.80	bdl	bdl	bdl	0.07	bdl	bdl	bdl	bdl	bdl
RSTX26-52 - 11	bdl	bdl	255.00	51000.00	1030.00	126.00	790.00	bdl	270.00	23.00	bdl	bdl	bdl	0.06	bdl	bdl	bdl	bdl	0.13
RSTX26-52 - 12	bdl	bdl	132.00	20000.00	520.00	63.00	620.00	bdl	220.00	16.00	bdl	bdl	bdl	0.03	bdl	bdl	bdl	bdl	bdl
RSTX26-52 - 13	bdl	bdl	bdl	bdl	bdl	bdl	bdl	bdl	bdl	bdl	bdl	bdl	bdl	bdl	bdl	bdl	bdl	bdl	bdl
RSTX26-52 - 14	bdl	bdl	bdl	bdl	bdl	bdl	bdl	bdl	bdl	bdl	bdl	bdl	bdl	bdl	bdl	bdl	bdl	bdl	bdl
RSTX26-52 - 15	35.20	bdl	334.50	65000.00	1682.00	206.20	1330.00	bdl	436.00	33.80	bdl	bdl	bdl	0.07	bdl	bdl	bdl	bdl	bdl
RSTX26-52 - 16	bdl	bdl	155.00	29000.00	700.00	77.00	610.00	bdl	210.00	17.00	bdl	bdl	bdl	bdl	bdl	bdl	bdl	bdl	0.00
RSTX26-52 - 17	bdl	bdl	37.00	5200.00	60.00	bdl	210.00	bdl	53.00	4.80	bdl	bdl	bdl	bdl	bdl	bdl	bdl	bdl	bdl
RSTX26-52 - 18	38.50	bdl	302.80	53300.00	1500.00	191.60	1213.00	bdl	433.00	34.90	bdl	bdl	bdl	0.05	bdl	bdl	bdl	bdl	bdl
RSTX26-52 - 19	bdl	bdl	240.00	40000.00	1060.00	125.00	840.00	bdl	320.00	24.00	bdl	bdl	bdl	0.06	bdl	bdl	bdl	bdl	bdl

Sample-analysis#	P	Sc	V	Cr	Mn	Co	Ni	Cu	Zn	Ga	Ge	Y	Zr	Nb	Sn	Hf	Ta	W	Pb
RSTX26-52 - 20	bdl	bdl	76.00	10900.00	260.00	35.00	420.00	bdl	130.00	11.00	bdl	bdl	bdl	bdl	bdl	bdl	bdl	bdl	bdl
RSTX26-52 - 21	48.40	bdl	353.50	73800.00	1938.00	219.60	1130.00	bdl	468.00	35.40	bdl	bdl	bdl	0.08	bdl	bdl	bdl	bdl	bdl
RSTX26-52 - 22	41.10	bdl	367.00	77100.00	1983.00	230.00	1204.00	bdl	492.00	36.10	bdl	bdl	bdl	0.09	bdl	bdl	bdl	bdl	bdl
RSTX26-52 - 23	bdl	bdl	157.00	27000.00	940.00	96.00	750.00	bdl	250.00	21.00	bdl	bdl	bdl	bdl	bdl	bdl	bdl	bdl	bdl
RSTX26-52 - 24	bdl	bdl	55.00	7800.00	180.00	15.00	330.00	bdl	100.00	9.00	bdl	bdl	bdl	bdl	bdl	bdl	bdl	bdl	0.05
RSTX26-52 - 25	59.60	bdl	244.00	34120.00	1298.00	2280.00	185000.00	bdl	498.00	35.69	1.51	bdl	bdl	bdl	0.60	bdl	0.01	bdl	4100.00
RSTX26-52 - 26	bdl	bdl	140.00	23000.00	750.00	79.00	710.00	bdl	240.00	21.00	bdl	bdl	bdl	bdl	bdl	bdl	bdl	bdl	bdl
RSTX26-52 - 27	29.80	bdl	390.00	67300.00	1872.00	195.40	1062.00	bdl	420.00	31.86	bdl	bdl	bdl	0.06	bdl	bdl	bdl	bdl	bdl
RSTX26-52 - 28	bdl	bdl	328.00	56000.00	1720.00	221.00	1090.00	bdl	480.00	34.80	bdl	bdl	bdl	0.06	bdl	bdl	bdl	bdl	0.24
RSTX26-52 - 29	bdl	bdl	200.00	31000.00	830.00	80.00	760.00	bdl	260.00	22.00	bdl	bdl	bdl	0.03	bdl	bdl	bdl	bdl	bdl
RSTX26-52 - 30	44.10	bdl	351.40	106100.00	bdl	bdl	bdl	bdl	bdl	bdl	bdl	bdl	bdl	bdl	bdl	bdl	bdl	bdl	bdl
RSTX26-52 - 31	67.80	0.00	446.00	132600.00	2800.00	290.00	1280.00	bdl	740.00	43.00	bdl	bdl	bdl	0.10	bdl	bdl	bdl	bdl	bdl
RSTX26-52 - 32	41.00	bdl	299.50	91600.00	290.00	bdl	150.00	bdl	90.00	4.60	bdl	bdl	bdl	bdl	bdl	bdl	bdl	bdl	bdl
RSTX26-52 - 33	62.30	bdl	425.50	133800.00	2200.00	210.00	930.00	bdl	550.00	35.00	bdl	bdl	bdl	0.07	bdl	bdl	bdl	bdl	bdl
RSTX26-52 - 34	35.30	bdl	327.70	104300.00	70.00	bdl	5.00	bdl	190.00	1.80	bdl	0.54	bdl	0.19	bdl	bdl	bdl	bdl	bdl
RSTX26-52 - 35	52.70	0.38	438.00	139100.00	2600.00	280.00	1090.00	bdl	640.00	37.00	bdl	bdl	bdl	0.09	bdl	bdl	bdl	bdl	0.10
RSTX26-52 - 36	45.40	bdl	385.70	177100.00	bdl	bdl	bdl	bdl	bdl	bdl	bdl	bdl	bdl	bdl	bdl	bdl	bdl	bdl	bdl
RSTX26-52 - 37	69.20	0.54	492.00	190100.00	1100.00	60.00	450.00	bdl	270.00	13.00	bdl	bdl	bdl	bdl	bdl	bdl	bdl	bdl	bdl
RSTX26-52 - 38	51.00	bdl	550.00	138500.00	bdl	bdl	bdl	bdl	bdl	bdl	bdl	bdl	bdl	bdl	bdl	bdl	bdl	bdl	bdl
RSTX26-52 - 39	76.80	bdl	781.00	224100.00	bdl	bdl	bdl	bdl	bdl	bdl	bdl	bdl	bdl	bdl	bdl	bdl	bdl	bdl	bdl
RSTX26-52 - 40	42.40	bdl	407.70	139400.00	bdl	bdl	bdl	bdl	bdl	bdl	bdl	bdl	bdl	bdl	bdl	bdl	bdl	bdl	bdl
RSTX26-52 - 41	97.60	4.50	655.00	170800.00	3700.00	300.00	1300.00	bdl	650.00	44.00	bdl	1.67	4.50	0.47	bdl	bdl	bdl	bdl	0.22
RSTX26-52 - 42	57.80	bdl	750.00	115600.00	3220.00	220.00	1148.00	bdl	316.00	31.80	bdl	bdl	bdl	0.10	bdl	bdl	bdl	bdl	bdl
RSTX26-52 - 43	77.50	bdl	1180.00	186500.00	4200.00	269.00	1510.00	bdl	430.00	43.00	bdl	bdl	bdl	0.16	bdl	bdl	bdl	bdl	bdl
RSTX26-52 - 44	43.50	bdl	304.00	76200.00	2769.00	210.00	1047.00	bdl	380.00	26.40	bdl	bdl	bdl	0.11	bdl	bdl	bdl	bdl	bdl
RSTX26-52 - 45	47.10	bdl	335.00	83700.00	3197.00	256.00	1319.00	bdl	460.00	33.60	bdl	bdl	bdl	0.08	bdl	bdl	bdl	bdl	bdl
RSTX26-52 - 46	52.20	0.86	365.00	91100.00	3780.00	321.00	1879.00	bdl	571.00	48.30	0.61	0.03	0.30	0.14	0.09	bdl	0.02	bdl	0.22

Proximal chromitite stringer (RSTX26-61)

Sample-analysis#	P	Sc	V	Cr	Mn	Co	Ni	Cu	Zn	Ga	Ge	Y	Zr	Nb	Sn	Hf	Ta	W	Pb
RSTX26-61 - 1	52.00	bdl	692.00	246400.00	bdl	bdl	bdl	bdl	bdl	bdl	bdl	bdl	bdl	bdl	bdl	bdl	bdl	bdl	bdl
RSTX26-61 - 2	46.90	bdl	714.00	234300.00	bdl	bdl	bdl	bdl	bdl	bdl	bdl	bdl	bdl	bdl	bdl	bdl	bdl	bdl	bdl
RSTX26-61 - 3	50.30	bdl	632.00	212300.00	bdl	bdl	bdl	bdl	bdl	bdl	bdl	bdl	bdl	bdl	bdl	bdl	bdl	bdl	bdl
RSTX26-61 - 4	47.40	bdl	616.00	218500.00	bdl	bdl	bdl	bdl	bdl	bdl	bdl	bdl	bdl	bdl	bdl	bdl	bdl	bdl	bdl
RSTX26-61 - 5	51.00	bdl	622.00	217400.00	bdl	bdl	bdl	bdl	bdl	bdl	bdl	bdl	bdl	bdl	bdl	bdl	bdl	bdl	bdl
RSTX26-61 - 6	41.40	bdl	514.00	156500.00	bdl	bdl	bdl	bdl	bdl	bdl	bdl	bdl	bdl	bdl	bdl	bdl	bdl	bdl	bdl
RSTX26-61 - 7	58.00	bdl	782.00	251200.00	bdl	bdl	bdl	bdl	bdl	bdl	bdl	bdl	bdl	bdl	bdl	bdl	bdl	bdl	bdl
RSTX26-61 - 8	56.20	0.41	756.90	242300.00	bdl	bdl	bdl	bdl	bdl	bdl	bdl	bdl	bdl	bdl	bdl	bdl	bdl	bdl	bdl
RSTX26-61 - 9	41.30	0.27	572.00	166400.00	bdl	bdl	bdl	bdl	bdl	bdl	bdl	bdl	bdl	bdl	bdl	bdl	bdl	bdl	bdl
RSTX26-61 - 10	46.50	0.32	694.00	175000.00	bdl	bdl	bdl	bdl	bdl	bdl	bdl	bdl	bdl	bdl	bdl	bdl	bdl	bdl	bdl
RSTX26-61 - 11	50.60	0.20	732.00	185700.00	bdl	bdl	bdl	bdl	bdl	bdl	bdl	bdl	bdl	bdl	bdl	bdl	bdl	bdl	bdl
RSTX26-61 - 12	37.60	bdl	526.00	123600.00	bdl	bdl	bdl	bdl	bdl	bdl	bdl	bdl	bdl	bdl	bdl	bdl	bdl	bdl	bdl
RSTX26-61 - 13	34.80	bdl	515.00	125500.00	bdl	bdl	bdl	bdl	bdl	bdl	bdl	bdl	bdl	bdl	bdl	bdl	bdl	bdl	bdl
RSTX26-61 - 14	43.40	0.14	706.00	183200.00	bdl	bdl	bdl	bdl	bdl	bdl	bdl	bdl	bdl	bdl	bdl	bdl	bdl	bdl	bdl
RSTX26-61 - 15	49.70	bdl	769.00	224700.00	bdl	bdl	bdl	bdl	bdl	bdl	bdl	bdl	bdl	bdl	bdl	bdl	bdl	bdl	bdl
RSTX26-61 - 16	56.10	bdl	777.00	229400.00	bdl	bdl	bdl	bdl	bdl	bdl	bdl	bdl	bdl	bdl	bdl	bdl	bdl	bdl	bdl
RSTX26-61 - 17	56.20	0.37	1184.00	249200.00	bdl	bdl	bdl	bdl	bdl	bdl	bdl	bdl	bdl	bdl	bdl	bdl	bdl	bdl	bdl
RSTX26-61 - 18	56.90	0.34	1153.00	236000.00	bdl	bdl	bdl	bdl	bdl	bdl	bdl	bdl	bdl	bdl	bdl	bdl	bdl	bdl	bdl
RSTX26-61 - 19	55.80	0.33	1292.00	245300.00	bdl	bdl	bdl	bdl	bdl	bdl	bdl	bdl	bdl	bdl	bdl	bdl	bdl	bdl	bdl
RSTX26-61 - 20	55.40	0.39	1167.00	244300.00	bdl	bdl	bdl	bdl	bdl	bdl	bdl	bdl	bdl	bdl	bdl	bdl	bdl	bdl	bdl
RSTX26-61 - 21	54.90	bdl	1332.00	253100.00	bdl	bdl	bdl	bdl	bdl	bdl	bdl	bdl	bdl	bdl	bdl	bdl	bdl	bdl	bdl
RSTX26-61 - 22	54.90	0.18	1143.00	228000.00	bdl	bdl	bdl	bdl	bdl	bdl	bdl	bdl	bdl	bdl	bdl	bdl	bdl	bdl	bdl
RSTX26-61 - 23	47.40	bdl	926.00	185800.00	bdl	bdl	bdl	bdl	bdl	bdl	bdl	bdl	bdl	bdl	bdl	bdl	bdl	bdl	bdl
RSTX26-61 - 24	53.40	bdl	1066.00	217800.00	bdl	bdl	bdl	bdl	bdl	bdl	bdl	bdl	bdl	bdl	bdl	bdl	bdl	bdl	bdl
RSTX26-61 - 25	44.10	bdl	908.00	183300.00	bdl	bdl	bdl	bdl	bdl	bdl	bdl	bdl	bdl	bdl	bdl	bdl	bdl	bdl	bdl
RSTX26-61 - 26	52.00	bdl	1061.00	211000.00	bdl	bdl	bdl	bdl	bdl	bdl	bdl	bdl	bdl	bdl	bdl	bdl	bdl	bdl	bdl
RSTX26-61 - 27	56.10	bdl	1086.00	219600.00	bdl	bdl	bdl	bdl	bdl	bdl	bdl	bdl	bdl	bdl	bdl	bdl	bdl	bdl	bdl
RSTX26-61 - 28	58.30	bdl	1124.00	227400.00	bdl	bdl	bdl	bdl	bdl	bdl	bdl	bdl	bdl	bdl	bdl	bdl	bdl	bdl	bdl
RSTX26-61 - 29	54.00	0.28	990.00	209400.00	bdl	bdl	bdl	bdl	bdl	bdl	bdl	bdl	bdl	bdl	bdl	bdl	bdl	bdl	bdl

Sample-analysis#	P	Sc	V	Cr	Mn	Co	Ni	Cu	Zn	Ga	Ge	Y	Zr	Nb	Sn	Hf	Ta	W	Pb
RSTX26-61 - 30	56.90	bdl	1124.00	232300.00	bdl	bdl	bdl	bdl	bdl	bdl	bdl	bdl	bdl	bdl	bdl	bdl	bdl	bdl	bdl
RSTX26-61 - 31	bdl	bdl	1017.00	196500.00	bdl	bdl	bdl	bdl	bdl	bdl	bdl	bdl	bdl	bdl	bdl	bdl	bdl	bdl	bdl
Distal chromitite stringer (RSTX26-63)																			
RSTX26-63 - 1	74.00	5.97	4244.00	323900.00	bdl	bdl	bdl	bdl	bdl	bdl	bdl	bdl	bdl	bdl	bdl	bdl	bdl	bdl	bdl
RSTX26-63 - 2	58.70	5.78	4290.00	326100.00	bdl	bdl	bdl	bdl	bdl	bdl	bdl	bdl	bdl	bdl	bdl	bdl	bdl	bdl	bdl
RSTX26-63 - 3	61.10	5.41	4310.00	317000.00	bdl	bdl	bdl	bdl	bdl	bdl	bdl	bdl	bdl	bdl	bdl	bdl	bdl	bdl	bdl
RSTX26-63 - 4	68.10	5.16	4138.00	305400.00	bdl	bdl	bdl	bdl	bdl	bdl	bdl	bdl	bdl	bdl	bdl	bdl	bdl	bdl	bdl
RSTX26-63 - 5	63.10	5.40	4250.00	312000.00	bdl	bdl	bdl	bdl	bdl	bdl	bdl	bdl	bdl	bdl	bdl	bdl	bdl	bdl	bdl
RSTX26-63 - 6	60.70	5.50	4120.00	306000.00	bdl	bdl	bdl	bdl	bdl	bdl	bdl	bdl	bdl	bdl	bdl	bdl	bdl	bdl	bdl
RSTX26-63 - 7	61.50	5.24	4140.00	304500.00	bdl	bdl	bdl	bdl	bdl	bdl	bdl	bdl	bdl	bdl	bdl	bdl	bdl	bdl	bdl
RSTX26-63 - 8	62.40	5.97	4326.00	309500.00	bdl	bdl	bdl	bdl	bdl	bdl	bdl	bdl	bdl	bdl	bdl	bdl	bdl	bdl	bdl
RSTX26-63 - 9	61.00	5.59	4161.00	310000.00	bdl	bdl	bdl	bdl	bdl	bdl	bdl	bdl	bdl	bdl	bdl	bdl	bdl	bdl	bdl
RSTX26-63 - 10	52.80	5.82	4271.00	317200.00	bdl	bdl	bdl	bdl	bdl	bdl	bdl	bdl	bdl	bdl	bdl	bdl	bdl	bdl	bdl
RSTX26-63 - 11	68.90	5.93	4270.00	321000.00	bdl	bdl	bdl	bdl	bdl	bdl	bdl	bdl	bdl	bdl	bdl	bdl	bdl	bdl	bdl
RSTX26-63 - 12	60.20	6.29	4310.00	342000.00	bdl	bdl	bdl	bdl	bdl	bdl	bdl	bdl	bdl	bdl	bdl	bdl	bdl	bdl	bdl
RSTX26-63 - 13	46.80	0.59	3314.00	269000.00	bdl	bdl	bdl	bdl	bdl	bdl	bdl	bdl	bdl	bdl	bdl	bdl	bdl	bdl	bdl
RSTX26-63 - 14	52.10	0.54	3207.00	257400.00	bdl	bdl	bdl	bdl	bdl	bdl	bdl	bdl	bdl	bdl	bdl	bdl	bdl	bdl	bdl
RSTX26-63 - 15	52.80	0.50	3162.00	252300.00	bdl	bdl	bdl	bdl	bdl	bdl	bdl	bdl	bdl	bdl	bdl	bdl	bdl	bdl	bdl
RSTX26-63 - 16	49.00	0.20	2790.00	220100.00	bdl	bdl	bdl	bdl	bdl	bdl	bdl	bdl	bdl	bdl	bdl	bdl	bdl	bdl	bdl
RSTX26-63 - 17	45.50	bdl	2395.00	211700.00	bdl	bdl	bdl	bdl	bdl	bdl	bdl	bdl	bdl	bdl	bdl	bdl	bdl	bdl	bdl
RSTX26-63 - 18	44.70	bdl	2217.00	201600.00	bdl	bdl	bdl	bdl	bdl	bdl	bdl	bdl	bdl	bdl	bdl	bdl	bdl	bdl	bdl
RSTX26-63 - 19	52.10	0.67	2702.00	255900.00	bdl	bdl	bdl	bdl	bdl	bdl	bdl	bdl	bdl	bdl	bdl	bdl	bdl	bdl	bdl
RSTX26-63 - 20	64.80	3.22	2641.00	248500.00	bdl	bdl	bdl	bdl	bdl	bdl	bdl	bdl	bdl	bdl	bdl	bdl	bdl	bdl	bdl
RSTX26-63 - 21	52.10	0.61	2956.00	281000.00	bdl	bdl	bdl	bdl	bdl	bdl	bdl	bdl	bdl	bdl	bdl	bdl	bdl	bdl	bdl
RSTX26-63 - 22	47.90	0.68	2869.00	277800.00	bdl	bdl	bdl	bdl	bdl	bdl	bdl	bdl	bdl	bdl	bdl	bdl	bdl	bdl	bdl
RSTX26-63 - 23	48.80	0.74	3078.00	247600.00	bdl	bdl	bdl	bdl	bdl	bdl	bdl	bdl	bdl	bdl	bdl	bdl	bdl	bdl	bdl
RSTX26-63 - 24	53.10	0.89	3033.00	251800.00	bdl	bdl	bdl	bdl	bdl	bdl	bdl	bdl	bdl	bdl	bdl	bdl	bdl	bdl	bdl
RSTX26-63 - 25	47.70	1.01	3089.00	257800.00	bdl	bdl	bdl	bdl	bdl	bdl	bdl	bdl	bdl	bdl	bdl	bdl	bdl	bdl	bdl
RSTX26-63 - 26	47.20	0.72	3046.00	246100.00	bdl	bdl	bdl	bdl	bdl	bdl	bdl	bdl	bdl	bdl	bdl	bdl	bdl	bdl	bdl
RSTX26-63 - 27	45.50	0.16	2175.00	235100.00	bdl	bdl	bdl	bdl	bdl	bdl	bdl	bdl	bdl	bdl	bdl	bdl	bdl	bdl	bdl

Sample-analysis#	P	Sc	V	Cr	Mn	Co	Ni	Cu	Zn	Ga	Ge	Y	Zr	Nb	Sn	Hf	Ta	W	Pb
RSTX26-63 - 28	43.60	bdl	2242.00	246600.00	bdl	bdl	bdl	bdl	bdl	bdl	bdl	bdl	bdl	bdl	bdl	bdl	bdl	bdl	bdl
RSTX26-63 - 29	49.20	bdl	2162.00	222200.00	bdl	bdl	bdl	bdl	bdl	bdl	bdl	bdl	bdl	bdl	bdl	bdl	bdl	bdl	bdl
RSTX26-63 - 30	43.40	bdl	2198.00	229800.00	bdl	bdl	bdl	bdl	bdl	bdl	bdl	bdl	bdl	bdl	bdl	bdl	bdl	bdl	bdl
RSTX26-63 - 31	60.40	3.04	3236.00	275600.00	bdl	bdl	bdl	bdl	bdl	bdl	bdl	bdl	bdl	bdl	bdl	bdl	bdl	bdl	bdl
RSTX26-63 - 32	55.10	2.87	3234.00	279200.00	bdl	bdl	bdl	bdl	bdl	bdl	bdl	bdl	bdl	bdl	bdl	bdl	bdl	bdl	bdl
RSTX26-63 - 33	41.60	2.18	3263.00	280000.00	bdl	bdl	bdl	bdl	bdl	bdl	bdl	bdl	bdl	bdl	bdl	bdl	bdl	bdl	bdl
RSTX26-63 - 34	51.50	3.01	3283.00	282000.00	bdl	bdl	bdl	bdl	bdl	bdl	bdl	bdl	bdl	bdl	bdl	bdl	bdl	bdl	bdl
RSTX26-63 - 35	bdl	2.92	3270.00	288100.00	bdl	bdl	bdl	bdl	bdl	bdl	bdl	bdl	bdl	bdl	bdl	bdl	bdl	bdl	bdl
RSTX26-63 - 36	61.10	2.66	3250.00	276500.00	bdl	bdl	bdl	bdl	bdl	bdl	bdl	bdl	bdl	bdl	bdl	bdl	bdl	bdl	bdl
RSTX26-63 - 37	57.60	2.35	3133.00	275000.00	bdl	bdl	bdl	bdl	bdl	bdl	bdl	bdl	bdl	bdl	bdl	bdl	bdl	bdl	bdl
RSTX26-63 - 38	51.80	2.13	3235.00	282100.00	bdl	bdl	bdl	bdl	bdl	bdl	bdl	bdl	bdl	bdl	bdl	bdl	bdl	bdl	bdl
RSTX26-63 - 39	54.70	2.31	3240.00	275100.00	bdl	bdl	bdl	bdl	bdl	bdl	bdl	bdl	bdl	bdl	bdl	bdl	bdl	bdl	bdl
RSTX26-63 - 40	55.30	2.63	3260.00	283000.00	bdl	bdl	bdl	bdl	bdl	bdl	bdl	bdl	bdl	bdl	bdl	bdl	bdl	bdl	bdl
RSTX26-63 - 41	bdl	3.03	3273.00	288900.00	bdl	bdl	bdl	bdl	bdl	bdl	bdl	bdl	bdl	bdl	bdl	bdl	bdl	bdl	bdl
RSTX26-63 - 42	bdl	3.32	3284.00	292500.00	bdl	bdl	bdl	bdl	bdl	bdl	bdl	bdl	bdl	bdl	bdl	bdl	bdl	bdl	bdl
							UG1 chromitite layer (RSTX-26UG1)												
RSTX26-UG1 - 1	55.70	9.34	3480.00	272700.00	bdl	bdl	bdl	bdl	bdl	bdl	bdl	bdl	bdl	bdl	bdl	bdl	bdl	bdl	bdl
RSTX26-UG1 - 2	56.30	9.24	3540.00	269200.00	bdl	bdl	bdl	bdl	bdl	bdl	bdl	bdl	bdl	bdl	bdl	bdl	bdl	bdl	bdl
RSTX26-UG1 - 3	52.40	9.53	3448.00	278700.00	bdl	bdl	bdl	bdl	bdl	bdl	bdl	bdl	bdl	bdl	bdl	bdl	bdl	bdl	bdl
RSTX26-UG1 - 4	52.80	9.41	3382.00	273400.00	bdl	bdl	bdl	bdl	bdl	bdl	bdl	bdl	bdl	bdl	bdl	bdl	bdl	bdl	bdl
RSTX26-UG1 - 5	49.90	9.05	3388.00	273100.00	bdl	bdl	bdl	bdl	bdl	bdl	bdl	bdl	bdl	bdl	bdl	bdl	bdl	bdl	bdl
RSTX26-UG1 - 6	bdl	8.76	3470.00	264400.00	bdl	bdl	bdl	bdl	bdl	bdl	bdl	bdl	bdl	bdl	bdl	bdl	bdl	bdl	bdl
RSTX26-UG1 - 7	64.00	9.06	3465.00	271600.00	bdl	bdl	bdl	bdl	bdl	bdl	bdl	bdl	bdl	bdl	bdl	bdl	bdl	bdl	bdl
RSTX26-UG1 - 8	63.60	8.33	3428.00	267500.00	bdl	bdl	bdl	bdl	bdl	bdl	bdl	bdl	bdl	bdl	bdl	bdl	bdl	bdl	bdl
RSTX26-UG1 - 9	58.00	9.59	3419.00	269600.00	bdl	bdl	bdl	bdl	bdl	bdl	bdl	bdl	bdl	bdl	bdl	bdl	bdl	bdl	bdl
RSTX26-UG1 - 10	55.90	9.72	3372.00	256700.00	bdl	bdl	bdl	bdl	bdl	bdl	bdl	bdl	bdl	bdl	bdl	bdl	bdl	bdl	bdl
RSTX26-UG1 - 11	51.00	9.26	3510.00	268700.00	bdl	bdl	bdl	bdl	bdl	bdl	bdl	bdl	bdl	bdl	bdl	bdl	bdl	bdl	bdl
RSTX26-UG1 - 12	43.60	10.06	3332.00	256600.00	bdl	bdl	bdl	bdl	bdl	bdl	bdl	bdl	bdl	bdl	bdl	bdl	bdl	bdl	bdl
RSTX26-UG1 - 13	39.90	10.08	3420.00	254100.00	bdl	bdl	bdl	bdl	bdl	bdl	bdl	bdl	bdl	bdl	bdl	bdl	bdl	bdl	bdl

Sample-analysis#	P	Sc	V	Cr	Mn	Co	Ni	Cu	Zn	Ga	Ge	Y	Zr	Nb	Sn	Hf	Ta	W	Pb
RSTX26-UG1 - 14	50.60	9.98	3328.00	247900.00	bdl	bdl	bdl	bdl	bdl	bdl	bdl	bdl	bdl	bdl	bdl	bdl	bdl	bdl	bdl
RSTX26-UG1 - 15	48.80	10.10	3352.00	249100.00	bdl	bdl	bdl	bdl	bdl	bdl	bdl	bdl	bdl	bdl	bdl	bdl	bdl	bdl	bdl
RSTX26-UG1 - 16	44.70	9.33	3405.00	251300.00	bdl	bdl	bdl	bdl	bdl	bdl	bdl	bdl	bdl	bdl	bdl	bdl	bdl	bdl	bdl
RSTX26-UG1 - 17	48.70	9.36	3430.00	243600.00	bdl	bdl	bdl	bdl	bdl	bdl	bdl	bdl	bdl	bdl	bdl	bdl	bdl	bdl	bdl
RSTX26-UG1 - 18	47.90	9.89	3410.00	250900.00	bdl	bdl	bdl	bdl	bdl	bdl	bdl	bdl	bdl	bdl	bdl	bdl	bdl	bdl	bdl
RSTX26-UG1 - 19	54.40	9.88	3410.00	246600.00	bdl	bdl	bdl	bdl	bdl	bdl	bdl	bdl	bdl	bdl	bdl	bdl	bdl	bdl	bdl
RSTX26-UG1 - 20	52.00	9.02	3348.00	238200.00	bdl	bdl	bdl	bdl	bdl	bdl	bdl	bdl	bdl	bdl	bdl	bdl	bdl	bdl	bdl